

A selective laser melting and solution heat treatment refined Al–12Si alloy with a controllable ultrafine eutectic microstructure and 25% tensile ductility

X.P. Li^a, X.J. Wang^{a,b,1}, M. Saunders^c, A. Suvorova^c, L.C. Zhang^d, Y.J. Liu^d, M.H. Fang^b, Z.H. Huang^b, T.B. Sercombe^{a,*}

^a The University of Western Australia, School of Mechanical and Chemical Engineering, Perth, WA 6009, Australia

^b China University of Geosciences (Beijing), School of Materials Science and Technology, Beijing 100083, China

^c The University of Western Australia, Centre for Microscopy, Characterisation and Analysis, Perth, WA 6009, Australia

^d Edith Cowan University, School of Mechanical Engineering, Perth, WA 6027, Australia

ARTICLE INFO

Article history:

Received 15 January 2015

Revised 13 May 2015

Accepted 14 May 2015

Keywords:

Al–Si alloys

Selective laser melting

Solution heat treatment

Eutectic microstructure

Mechanical properties

ABSTRACT

This study shows that a eutectic Al–12Si alloy with controllable ultrafine microstructure and excellent mechanical properties can be achieved by using selective laser melting and subsequent solution heat treatment. This provides a novel and promising approach to the refinement of eutectic Al–Si alloys. Unlike Al–12Si alloys fabricated and refined by traditional methods, the as-fabricated Al–12Si in this study contains nano-sized spherical Si particles surrounding a supersaturated Al matrix. During solution heat treatment, precipitation and coalescence of the Si particles occur, which decreases the Si concentration in the matrix and sub-micron to micron-sized spherical particles embedded in an Al matrix form. The as-fabricated Al–12Si exhibits significantly better tensile properties than the traditionally produced counterparts; while the solution treated Al–12Si has an extremely high ductility of approximately 25%. Importantly, the mechanical properties of the Al–12Si can be tailored through controlling the precipitation and coalescence of the Si particles by varying the solution heat treatment time. A detailed transmission electron microscopy study was conducted to investigate this Al–12Si alloy with ultrafine eutectic microstructure. The excellent tensile properties have been attributed to the refined eutectic microstructure containing spherical Si particles. The formation of this unique microstructure is due to the super heating and an extremely high cooling rate during selective laser melting and the subsequent solution heat treatment, which enables Si to grow along its most stable plane {111}Si.

Crown Copyright © 2015 Published by Elsevier Ltd. on behalf of Acta Materialia Inc. All rights reserved.

1. Introduction

The Al–Si casting alloys are extensively used in automotive and aerospace industries due to their light weight, good mechanical properties and low recycling costs [1–3]. The mechanical properties of Al–Si alloys are largely dictated by the morphology of the eutectic silicon [4,5], with the coarse, acicular silicon acting as crack initiation sites in conventionally cast material, resulting in low ductility. As a consequence, refinement of the eutectic microstructure of Al–Si alloys, first reported in 1920 [6], has been extensively investigated [4,7–13] since and is a critical step in improving their mechanical properties (specifically strength and ductility) to meet the ever-growing application demands in

automotive and aerospace industries. This is becoming more imperative as the worldwide energy and environment problems worsen.

The refinement of the Si phase can be achieved by controlling the nucleation and growth of the eutectic grains. Usually, two different methods of refinement are used: elemental additions [14–17] and rapid solidification [18–21]. Although the use of chemical elements can result in reduced fluidity and higher cost, its major disadvantage is the rapid loss of the refining elements from evaporation or oxidation [22]. In addition, the selection of appropriate elements depends on many factors, such as the composition of the alloy, type and quantity of the modifying elements and interactions between the modifying elements. Thus, this modification approach is complex and sometimes hard to control. For example, it has been reported that the combined addition of Sr and Na does not further enhance the modification effect on the eutectic microstructure of a hypoeutectic Al–Si alloy due to the loss of

* Corresponding author.

E-mail address: tim.sercombe@uwa.edu.au (T.B. Sercombe).

¹ Shandong Academy of Sciences, Jinan, Shandong Province, China.

modifying elements as a result of vaporisation or oxidation promoted by Na [22]. In contrast, a combined addition of Sr and B into near-eutectic Al–Si alloys can significantly decrease the size of the eutectic grains at a cooling rate of 10 K/s [12]. The addition of B varies the nucleation mechanism of the eutectic, while Sr increases the undercooling of the melt. However, the addition of modifying elements can be detrimental to the density of the alloys by inducing a higher porosity. This has been attributed to the changes in hydrogen content, oxide permeability and surface tension [9].

An alternate approach to refine the microstructure is to increase the cooling rate [23,24]. Rapid solidification can significantly improve the mechanical properties of cast Al–Si components [25]. However, microstructural uniformity is only possible if the entire casting solidifies at a high cooling rate. For the vast majority of castings, this is not possible and therefore this method of Si refinement is limited to small, thin parts, such as ribbons, filaments and flakes [19–21]. For example, melting spinning has been successfully used to modify the eutectic microstructure of some Al–Si alloys [26,27]. Although submicron or nano-sized Si particles (50–200 nm) formed, the size and geometry of samples are severely constrained, with only ribbons (thickness < 200 µm) or small rods able to be produced. This greatly limits the possible applications of melt spinning. To circumvent the abovementioned drawbacks and realise the thermal modification of eutectic microstructure in a large scale part, selective laser melting (SLM), an emerging additive manufacturing technique, is adopted. SLM fabricates components layer by layer, which enables the fabrication of complex-geometry components [28]. Due to the laser heating only a very small volume of material and the short laser interaction time, the process has very high heating and cooling rates (10^3 – 10^8 K/s) [29] which has been shown to result in the formation of metastable phases [30,31]. Following this, the high heating and cooling rate would induce large super heating and undercooling and this will tend to enhance the nucleation rate and suppress the grain growth in the Al–Si alloy. This unique characteristic makes SLM a promising candidate for producing a refined microstructure and therefore enhanced properties. In recent work [32], the annealing of Al–12Si samples produced by SLM was performed at temperatures <450 °C for 6 h. This work concluded that the microstructure becomes coarser with increasing annealing temperature, which led to an increase in ductility (elongation ~15%) and decrease in strength (~95 MPa). Rietveld analysis was performed on X-ray diffraction (XRD) data, which showed that the as-processed Al matrix was supersaturated in Si, which was rejected during heat treatment.

In this study, we perform a systematic investigation into the influence of selective laser melting and subsequent conventional solution heat treatment on the eutectic microstructure and on the resultant mechanical properties of Al–12Si alloy. A detailed transmission electron microscopy (TEM) investigation of the eutectic microstructure of the Al–12Si alloy which exhibits excellent mechanical properties (elongation ~25% with a tensile strength ~190 MPa) after solution heat treatment has also been conducted. The relationship between the SLM processing, eutectic microstructure and mechanical properties is discussed. A possible underlying mechanism for the formation of this novel eutectic microstructure is also proposed. This study provides new insights into the modification of Al–Si alloys through SLM and solution heat treatment to achieve the desired mechanical properties without the need for the addition of other elements.

2. Experimental procedures

2.1. Fabrication and solution treatment of Al–12Si specimens

Al–12Si specimens ($4 \times 4 \times 4$ mm³) and tensile bars (shown in Fig. 1) were produced on a Realizer SLM-100 machine (Realizer

GmbH, Germany) which is equipped with a fibre laser, which has a laser wavelength of 1.06 µm and maximum power of 200 W at the part bed. Al–12Si (in wt.%) powder ($d_{50} \sim 38$ µm, TLS Technik, Germany) was used. An inert, high purity argon gas atmosphere was used during processing to minimise oxidation. The laser scan speed and laser power were 500 mm/s and 200 W, respectively, which has been shown to produce the best properties [33]. The powder layer thickness was fixed at 50 µm and the scan spacing at 150 µm, while the substrate was heated to 200 °C. Solution heat treatment of specimens was performed in air at 500 °C for up to 4 h, followed by water quenching.

2.2. Microstructure and mechanical properties characterisation

The eutectic microstructure of the Al–12Si specimens after both fabrication and solution heat treatment was characterised using a FEI Verios 460 scanning electron microscope (SEM, acceleration voltage 5 kV, working distance 6 mm). The size and morphology of the Si particles were investigated by imaging analysis software Image Pro Plus. At least ten different regions on each sample were taken for image analysis.

The growth of Si particles, orientation relationship (OR) between Si and Al and the chemical analyses of the Al–12Si specimens were investigated using either a JEOL 2100 transmission electron microscope (TEM) or FEI Titan G2 80–200 TEM with ChemiSTEM technology at 200 kV. TEM samples were mechanically polished and finally thinned by a Precision Ion Polishing System (Gatan PIPS™) where low-angle and low-current polishing conditions were used in conjunction with a liquid nitrogen cold stage.

The residual stresses within the Al–12Si alloy before and after the solution heat treatment were characterised by the Raman peak shift of the Si [34]. Raman spectra were acquired at room temperature with a confocal Raman backscattering technique (WITec alpha 300RA+) using a 532 nm excitation wavelength. The laser light was coupled into the microscope using a single-mode fibre and brought on to the sample using a dichroic mirror and a 100× microscope objective (NA 0.9). The spatial resolution is about 100 nm with a spectral resolution of 0.02 cm⁻¹.

Tensile tests were carried out on machined specimens (gauge length $\sim 4 \times 6 \times 15$ mm³), using an Instron 5982 machine at a constant strain rate of 1 mm/min. Strain was measured with a 10 mm gauge length extensometer. Samples were aligned perpendicular to the build direction as shown in Fig. 1.

2.3. Estimation of temperature distribution during SLM

Since the laser–material interaction time is usually on the order of 100 µs and the interaction volume is less than 50 µm, it is not practical to measure the temperature distribution within the Al–12Si melt pool during SLM. Therefore, a finite element modelling

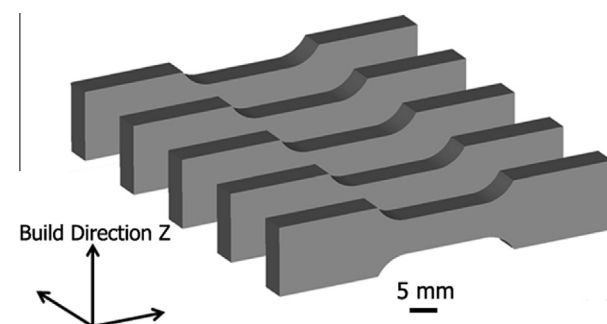


Fig. 1. A schematic illustration showing the orientation of the tensile bars and the axis system used.

(FEM) method using a multi-physics-based computational model based on the heat transfer theory in the heat transient mode of COMSOL™ was used to estimate the temperature distribution. For Al–12Si alloys, the laser absorption is very low ~5% at the 1.06 μm wavelength used [35]. However, many factors such as the size and morphology of the powder particles, the surface and roughness of the samples will influence the actual absorption co-efficient of a material. In general, the laser absorption for a powder sample is 3–5 times higher than a thin film sample with the same composition [36,37]. Therefore, in this work, the absorption co-efficient was set to 20%. For simplification, the simulation was carried out on an Al-based thin film with the same composition as the powder and there was no gap between the last and current layer. The thickness of this thin film was set to 100 μm. The laser power and scan speed were set to be 200 W and 500 mm/s in the simulation, respectively, the same value as we used for the SLM processing.

3. Results and discussion

3.1. Eutectic microstructure after SLM and upon solution heat treatment

The microstructure of the Al–12Si alloy in the as-processed condition and after different solution heat treatment times is shown in Fig. 2. Unlike the eutectic microstructure of cast Al–12Si alloys where large rod- or needle-like Si particles form in the Al matrix, a novel eutectic microstructure with very fine spherical Si particles has formed, as shown in Fig. 2a. Two distinct regions can be observed: one significantly coarser than the other. This indicates that these two regions have different thermal histories. It has been reported [38] that the microstructure of Selective Laser Melted aluminium is affected by the heat generated by both the overlapping scan lines and creation of subsequent layers. Both these processes cause localised partial heat treatment and coarsening of the microstructure, as shown in Fig. 2a. Upon solution heat treatment, it can be seen (Fig. 2b–e) that the eutectic Si particles have grown and are up to ~2 μm in diameter. After solution heat treatment the abovementioned differences in the scale of the microstructure appear much less distinct; both larger and smaller Si particles distribute relatively homogeneously in the Al matrix.

To investigate the changes in size and morphology of the eutectic Si particles upon solution heat treatment, detailed image analysis was conducted on SEM images obtained after different solution treated times. Results are shown in Fig. 3 and Table 1. It can be seen from Fig. 3 and Table 1 that when the Al–12Si was solution treated less than 30 min most of the Si particles are less than 1 μm and particles below 0.16 μm account for 50% of the total Si particles. After longer solution heat treatment times (from 30 min up to 2 h), some of the Si particles have coarsened to a diameter of ~2 μm, increasing the d_{90} in Table 1. However, it appears that times longer than 2 h have no significant effect on the size of the Si particles. Although there are larger Si particles that form after 2 h solution heat treatment, Si particles less than 0.2 μm can still be observed in the Al matrix and account for 50% of the total Si particles observed. Hence it appears that some of the smaller Si particles that have formed in the microstructure remain almost unchanged through subsequent solution treatment, while others coarsen as would be expected. This leads us to presume that the growth of the eutectic Si particles, apart from the impact of different thermal histories during SLM, may also be influenced by the chemical inhomogeneity within the as-processed alloy. This is detailed further is Section 3.2 below.

During the early stages of solution treatment, the number of Si particles decreases while the total area of Si increases as shown in

Fig. 3. The decrease in the number of particles is likely a result of both particle coalescence as well as Ostwald ripening, where the large particles grow at the expense of the small ones. An increase in the area fraction of Si particles indicates that in the as-processed condition, the Al matrix is supersaturated and during heat treatment the excess Si precipitates out. It is apparent that most of the Si particles after solution treatment remain spherical, with only a small fraction becoming elongated particles.

3.2. Si content in the Al matrix

It is well known that rapidly cooling an alloy can result in significant extended (non-equilibrium) solid solubility. The eutectic structure as shown in Fig. 2 consists of cellular Al grains which are surrounded by Si particles with a spherical morphology and less than 100 nm in diameter. This structure is similar to those reported in Al–Si alloy specimens fabricated by melt spinning [26,27], where the reported Si content in the Al matrix reaches about 6% after the rapid solidification. The content of Si in the Al matrix before and after solution heat treatment was measured using TEM energy-dispersive X-ray spectroscopy (EDX) mapping. Fig. 4 shows the mapping results in scanning transmission electron microscopy (STEM) mode of the distribution of Al and Si in the as-fabricated and solution treated Al–12Si alloys. A quantitative analysis of the results shows that in the as-fabricated condition, the Si content was ~7 wt.% in the Al, which far exceeds the maximum solubility of 1.6 wt.% and is even slightly greater than what has been reported in melt spinning [26,27]. However, upon solution treatment the Si content in the Al drops rapidly to ~2 wt.% after just 15 min and then to the equilibrium concentration of 1.6 wt.% after 30 min, as shown in Fig. 4f. Longer solution treatment times have no influence on the Si content in Al, which remains ~1.6 wt.%. Hence it appears that after very short solution treatment times (<15 min), the supersaturated Si precipitates from the Al to form tiny eutectic Si particles, as can be seen from Figs. 2b and 4b. Upon further solution heat treatment, the Si content in the Al matrix drops to the equilibrium concentration and therefore no more precipitation of Si occurs and the area fraction of Si remains constant (Fig. 3). However, continued growth of the Si particles occurs at longer times most likely through a combination of Ostwald ripening and coalescence of adjacent small Si particles, which can be seen from the initial joining neck between two neighbouring Si particles in Fig. 4c and the elongated shape of the large Si particles in Fig. 4d and e.

3.3. Mechanisms for the formation and growth of eutectic Si particles

It is known that the solidification microstructure of Al–Si alloys can be influenced by super heating with a finer and/or more uniform microstructure along with increased strength and ductility in samples that have undergone significant superheat prior to solidification [39–43]. The underlying reason has been attributed to the existence of two characteristic temperatures, the dissolution temperature T_d and the branching temperature T_b . Below T_d , the liquid contains aluminium and silicon-rich particles which have been inherited from the solid material. Once the T_d has been exceeded, these particles begin to melt and above the branching temperature, T_b , molten alloy can be considered homogenous. Between T_d and T_b , Al-rich and Si-rich regions 10–200 nm in size co-exist within the molten pool [39]. This inhomogeneous microstructure will remain in the solidified alloys if the cooling rate is high enough ($>10^3$ K/s). According to previous studies, T_d and T_b of Al–12Si alloys should be around 1080 ± 30 and $1290 \pm 30^\circ\text{C}$, respectively [39,44]. This temperature is much higher than the liquidus temperature of Al–12Si alloys (577°C). Given that measuring the temperature in the melt pool in such a short

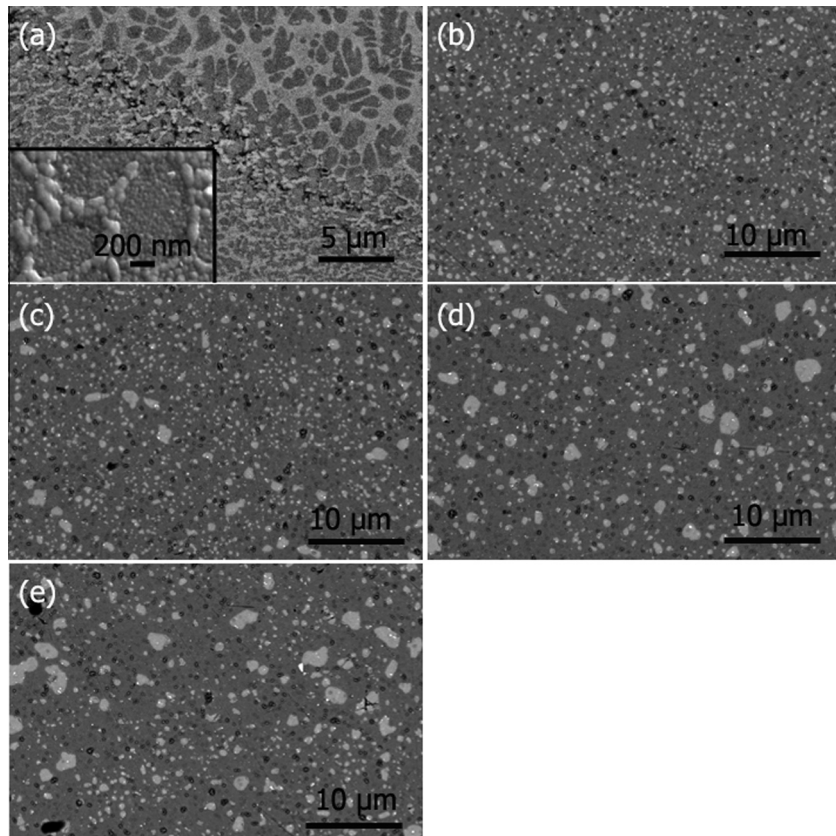


Fig. 2. Back-scattered SEM images of the eutectic microstructure of the Al-12Si alloy in the (a) as-fabricated condition in which the two distinct regions in the as-fabricated Al-12Si alloy: coarse Si and fine Si regions can be observed and after solution treatment at 500 °C for (b) 15 min; (c) 30 min; (d) 2 h; and (e) 4 h. The light grey areas are Si particles. The inset in (a) is high resolution secondary electron image showing that the Si forms small ~50 nm particles. Note the scale bar in (a) is different from the scale bars in (b) to (e).

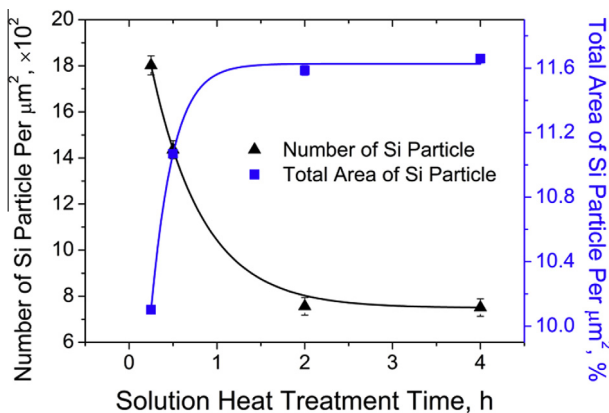


Fig. 3. The Si particle number and total Si particle area as a function of solution treatment time based on the SEM images shown in Fig. 2.

Table 1

Summary of the eutectic Si particle size (μm) in the Al-12Si alloy with different solution heat treatment times. d_x ($x = 10, 50$ or 90) means $x\%$ of the Si particles has a diameter less than d_x . \bar{d} means the average diameter.

Solution heat treatment time	d_{10} (μm)	d_{50} (μm)	d_{90} (μm)	\bar{d} (μm)
15 min	0.11	0.16	0.47	0.23
30 min	0.11	0.17	0.68	0.27
2 h	0.11	0.20	0.77	0.36
4 h	0.11	0.20	0.78	0.36

time is currently not possible, the temperature distribution upon heating within the melt pool in this study was estimated based on the transient heat transfer model using COMSOL™ [45] (the details of the approach have been given previously [46]) and the results are shown in Fig. 5. The maximum temperature is at the centre of the molten pool and reaches about 1439 °C, which lies above T_b of Al-12Si alloy. However, it can be seen that the temperature of a large portion of the melt pool lies in between T_d and T_b of Al-12Si alloy (see the shaded area in Fig. 5a). Hence, a large portion of the Al-12Si alloy melt pool probably undergoes a super heating in the temperature range between T_b and T_d . This will lead to an inhomogeneous microstructure of the molten pool of Al-12Si. In addition, the short interaction time between laser and material and the formation of liquid oscillations or capillary waves will also tend to make the microstructure within the molten pool inhomogeneous [47]. Hence, an inhomogeneous microstructure consisting of nano-sized Al-rich and Si-rich regions is expected, benefiting the heterogeneous nucleation and enhancement of the nucleation rate. The cooling rate is also estimated (based on the simulation) to be above 10^3 K/s for most parts of the melt pool, as shown in Fig. 5b. This super-high cooling rate will help retain the abovementioned inhomogeneous microstructure. Therefore, Si particles around 10–100 nm in size and a supersaturated Al matrix are expected to form in the as-fabricated Al-12Si alloy, and has been observed as shown in Fig. 4a. The growth of these nano-sized Si particles within the microstructure of the as-fabricated Al-12Si alloy upon heat treatment is further discussed below.

Fig. 6a shows energy filtered TEM (EFTEM) images of the eutectic Si particles embedded in the Al matrix after heat treatment for 15 min at 500 °C. The spherical Si particles have a diameter of less

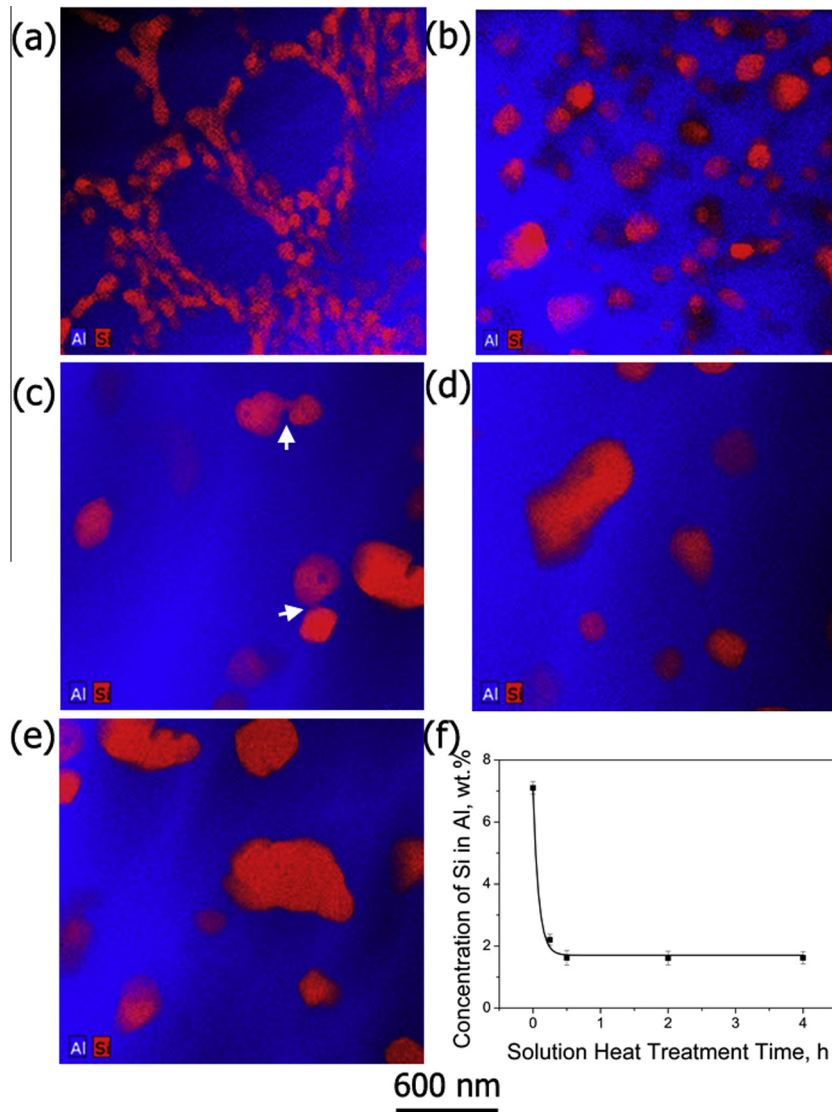


Fig. 4. STEM-EDX maps of the Al and Si distribution in the Al-12Si alloy in the (a) as-fabricated condition and after solution treatment at 500 °C for (b) 15 min; (c) 30 min; (d) 2 h; and (e) 4 h; (f) Concentration of Si in Al at different solution heat treatment times. White arrows in (c) shows the position of the joining neck between adjacent Si particles.

than 100 nm and are located at the Al grain boundaries. The electron energy loss spectroscopy (EELS) spectra of the Al grain and Si particle are shown in Fig. 6b, where the onset and shape of the ionisation edges for the Al grain and Si particles illustrates the valence and bonding state for Al atoms and Si atoms in these two regions. No Si particles are observed inside the Al grains, which indicates that during solution heat treatment, precipitation of the excess Si in the Al matrix occurs at the Al grain boundaries. This is consistent with the results shown in Fig. 4b and further implies that the growth or coalescence of the Si particles also occurs along the Al grain boundaries.

The morphology of the eutectic Si phase, which is directly related to its nucleation and growth processes, is critical in modifying the mechanical properties of Al-12Si alloy. Apart from the interfacial energy $\gamma_{\text{Al/Si}}$ between Al and Si phases, other kinetics or thermodynamic factors such as the wettability (normally expressed by the contact angle θ_c) and the local concentration of Al and Si atoms also play a key role in determining the eutectic microstructure upon solidification [9,48,49]. During conventional casting or for a cooling rate below 10 K/s, the growth direction of

eutectic Si is usually $\langle 110 \rangle$ or $\langle 100 \rangle$ [50] and forms a rod- or needle-like coarse microstructure (usually tens to hundreds of microns in size). This rod-like and needle-like morphology with its coarse microstructure is well known to severely reduce the ductility of Al-12Si alloys. In contrast, the spherical, nano-sized eutectic Si in our materials results in enhanced mechanical properties, especially ductility [9]. To investigate the underlying mechanism for the formation of the rounded eutectic Si, the orientation relationship (OR) between Al grains and Si phases has been determined. The interface between the Al and Si particle is shown in the bright field (BF) TEM image in Fig. 7a. The interface was tilted to edge-on position and overlapped diffraction patterns were taken at the boundaries of Al and Si, as shown Fig. 7b. Both Al and Si have a cubic structure and the OR determined from Fig. 7b can be expressed as $(111)_{\text{Si}}|| (200)_{\text{Al}}$. A high resolution TEM (HRTEM) image is taken along the same zone axis, shown in Fig. 7c, where the parallel lattice fringes of the $(111)_{\text{Si}}$ and $(200)_{\text{Al}}$ planes can be clearly seen at the interface between Al and Si phases. It shows that an epitaxial relationship exists between the eutectic Si and Al. This is different from previously reported observations at low

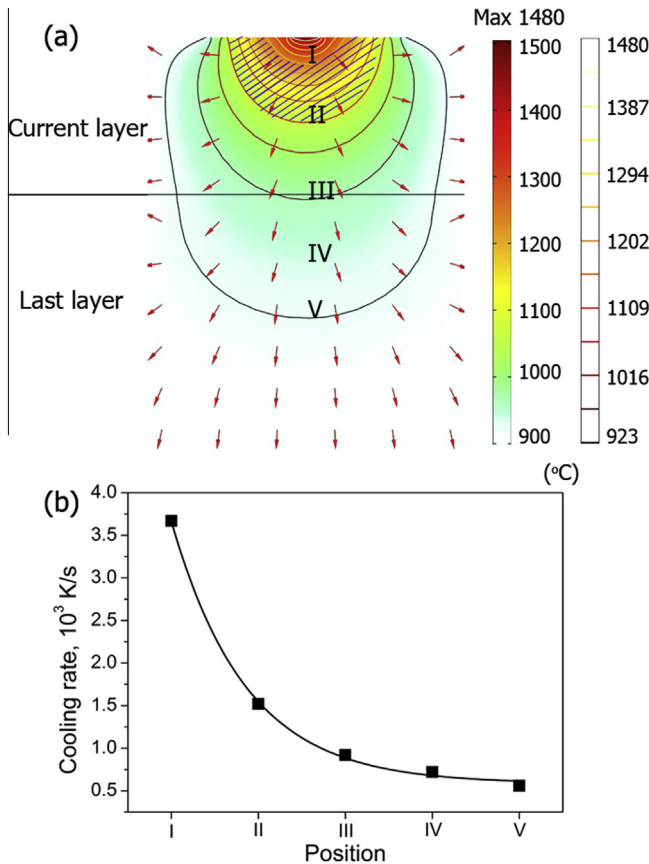


Fig. 5. (a) Temperature distribution of the Al-12Si molten pool upon heating during SLM based on COMSOL™ modelling. (b) Estimated cooling rates at the positions marked I–V in (a). Red arrows schematically show the direction of heat transfer. Shaded area shows the region of the melt pool undergoing a temperature between T_b and T_d . (For interpretation of the references to colour in this figure legend, the reader is referred to the web version of this article.)

temperature or at low cooling rate, where the Si particle grows within the dendrite microstructure of Al grains, especially at the arms and tips of the dendrite [9].

In this study, the Si and Al form Si-rich and Al-rich regions in the melt with a size below 100 nm. Upon rapid cooling, these regions are mostly retained and the growth during cooling is greatly restrained. When heat treated at a high temperature, the Si phase undergoes a thermally activated growth process. This enables the Si phase to grow along the most stable plane with the lowest free energy: the most dense-packed plane {111}_{Si}. This is why the Si phase grows into a spherical morphology.

3.4. Residual stress

The high heating and cooling rate experienced during SLM causes high temperature gradients and thermal fluctuations to occur [51]. This results in severe thermal and residual stresses to form within the fabricated components [51], which has been characterised by the Raman peak shift of Si within the Al-12Si alloy [34]. Fig. 8 shows the position of the Raman peak of Si in the as-processed Al-12Si alloy and solution treated Al-12Si with different times. The corresponding Raman intensity mapping results are also shown as inset in Fig. 8. The lower wave number of the Si line ($\sim 517.6 \text{ cm}^{-1}$ compared with 520.7 cm^{-1} stress-free Si [52]) in the as-fabricated Al-12Si alloy indicates that the Si in the as-fabricated Al-12Si alloy contains significant residual tensile stresses. The Raman shift becomes smaller upon solution treatment, implying that the stress is relaxed through solution treatment. These residual stresses together with the nano-sized Si particles and ultrafine Al matrix in the as-fabricated Al-12Si alloy would introduce a large number of dislocations and boundaries into the components. These dislocations and boundaries could act as paths for fast diffusion which is critical to precipitation and growth of the Si particles. Compared to conventionally fabricated Al-Si alloys, this substantial diffusivity can lead to enhanced recovery which also benefits the tensile ductility or stable plasticity.

3.5. Mechanical properties

The variation of the mechanical properties of the fabricated Al-12Si alloy after different solution heat treatment times is shown in Fig. 9. It has been previously reported that the as-fabricated properties exceed that of castings [33]. After solution heat treatment of

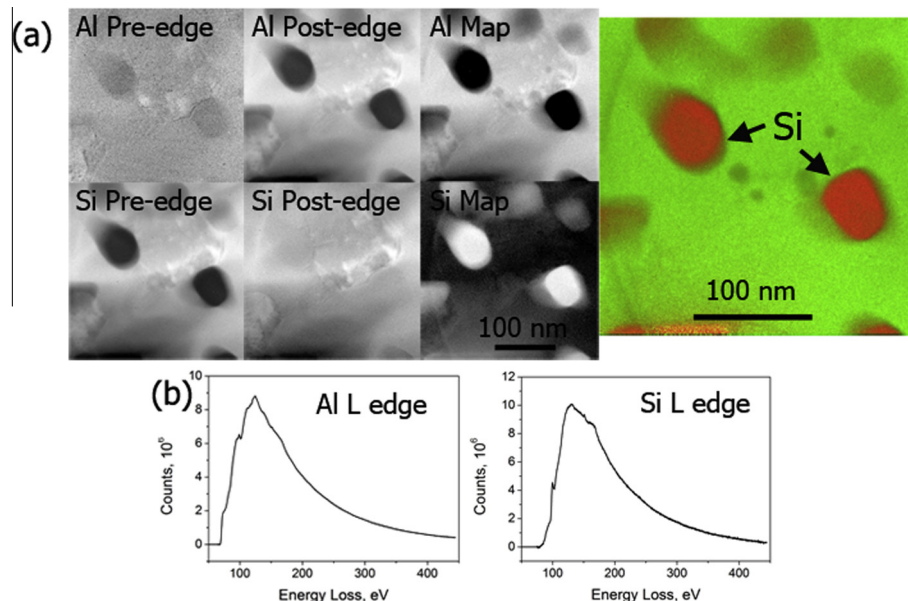


Fig. 6. (a) EFTEM images of the eutectic Si particles embedded in the Al matrix after solution heat treatment for 1 h at 500 °C. (b) EELS spectra of the Al grain and Si particle.

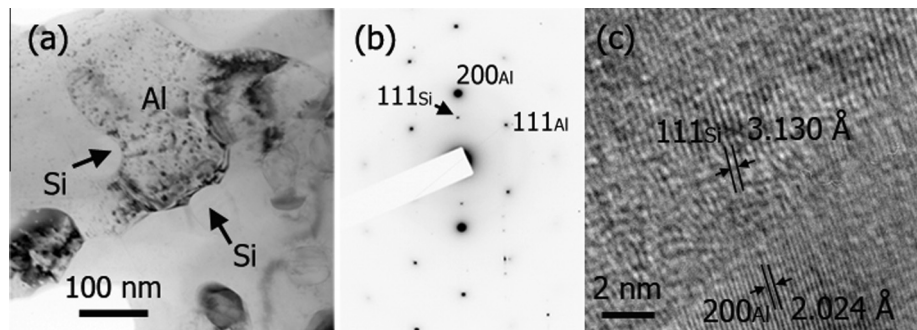


Fig. 7. (a) A bright field TEM image showing the interface between Al grain and Si particles. (b) A selected area diffraction pattern taken at the interface when tilted to edge-on position. (c) A HRTEM image showing the epitaxial relationship of Si.

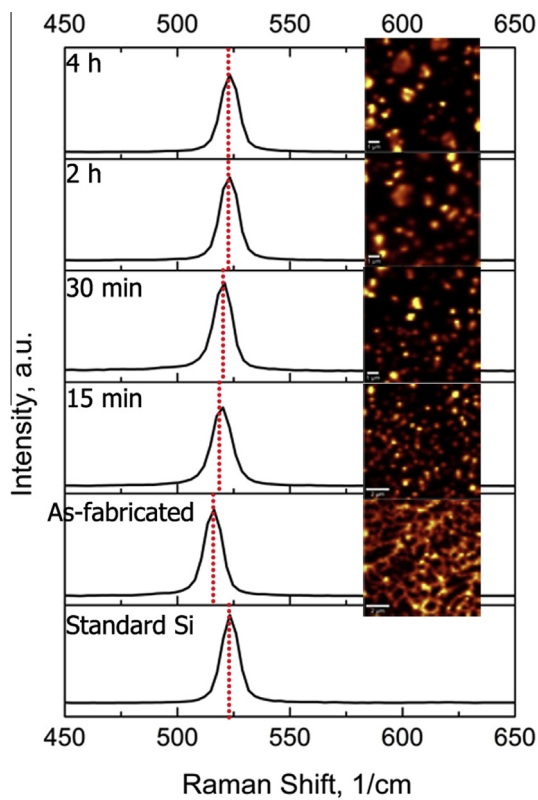


Fig. 8. Raman spectra from the Si particles in the Al-12Si alloys solution treated with different times. Inset shows the Raman intensity mapping of the corresponding Al-12Si alloys measure in the region of 500–550 cm⁻¹. The Raman spectrum for a standard Si is also shown. There is a gradual increase in the Raman shift during heat treatment.

just 15 min, a large increase in ductility and decrease in strength can be observed. When further increasing the solution treatment time to 30 min, the elongation increases to about 25% and the yield and tensile strength decreases to approximately 110 and 190 MPa, respectively. However, no further change in the mechanical properties occurs after longer times. It seems that the mechanical properties of the Al-12Si reach a plateau after 30 min solution heat treatment.

Fig. 10 shows the fracture surface of the Al-12Si alloys before and after solution heat treatment. A typical brittle failure with regular cleavage planes can be seen in the as-fabricated Al-12Si alloy, which is consistent with the low ductility shown in Fig. 9. When the material has been heat treated for just 15 min, equiaxed dimples with an average size around 2 μm were observed across the

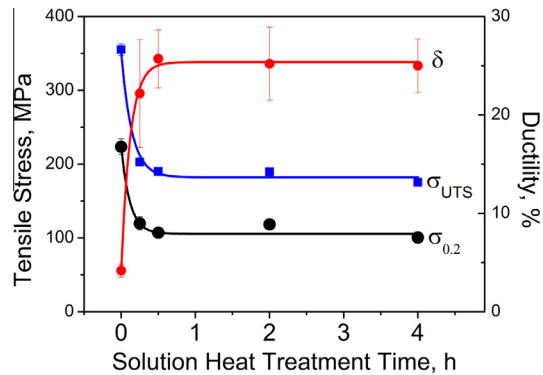


Fig. 9. The variation of mechanical properties of the Al-12Si alloy upon solution heat treatment at different times. δ , $\sigma_{0.2}$ and σ_{UTS} represent the ductility, yield strength and ultimate tensile strength, respectively.

whole fracture surface, as shown in Fig. 10b, which is indicative of a highly ductile fracture. As the solution treatment time is increased further, the size of the equiaxed dimples increases (Fig. 10c–e) and are approximately 5 μm after 4 h. A careful observation shows that the edges of the dimples pass through both Al grains and eutectic Si particles, signifying that the eutectic Si particles no longer act as the main sites triggering fracture.

It is well recognised that the size and morphology of the eutectic Si particles have an important impact on the mechanical properties of the Al-Si alloys [9]. In the conventional casting of Al-Si alloys, due to the faster growth rate of the Si phase compared to the Al phase during solidification, plate-like, rod-like and needle-like eutectic Si phases tend to form in the Al matrix [4,9]. In tensile loading, this kind of morphology of Si phases causes localised shearing to occur at a very early stage of the plastic deformation. This localised shearing can easily initiate cracks and promote crack propagation, triggering a fast fracture with a nominal plastic strain of only a few per cent. In the present study the nano-sized spherical Si particles that form in the as-fabricated Al-12Si alloy can ease the localised shearing and hence suppress the crack initiation and propagation. Therefore, there is enhanced tensile ductility in the as-fabricated Al-12Si components compared with cast material. The high strength of the as-processed material is likely a result of the non-equilibrium solubility of Si in the Al matrix as well as the refinement of the eutectic Si particles and ultrafine Al matrix. However, the relative contribution of these three factors to the enhancement of tensile strength is still unknown.

The influence of solution heat treatment on the strength and ductility of Al-Si alloys is dictated by many factors such as number, morphology and size of the Si phases, initial hardening rate and

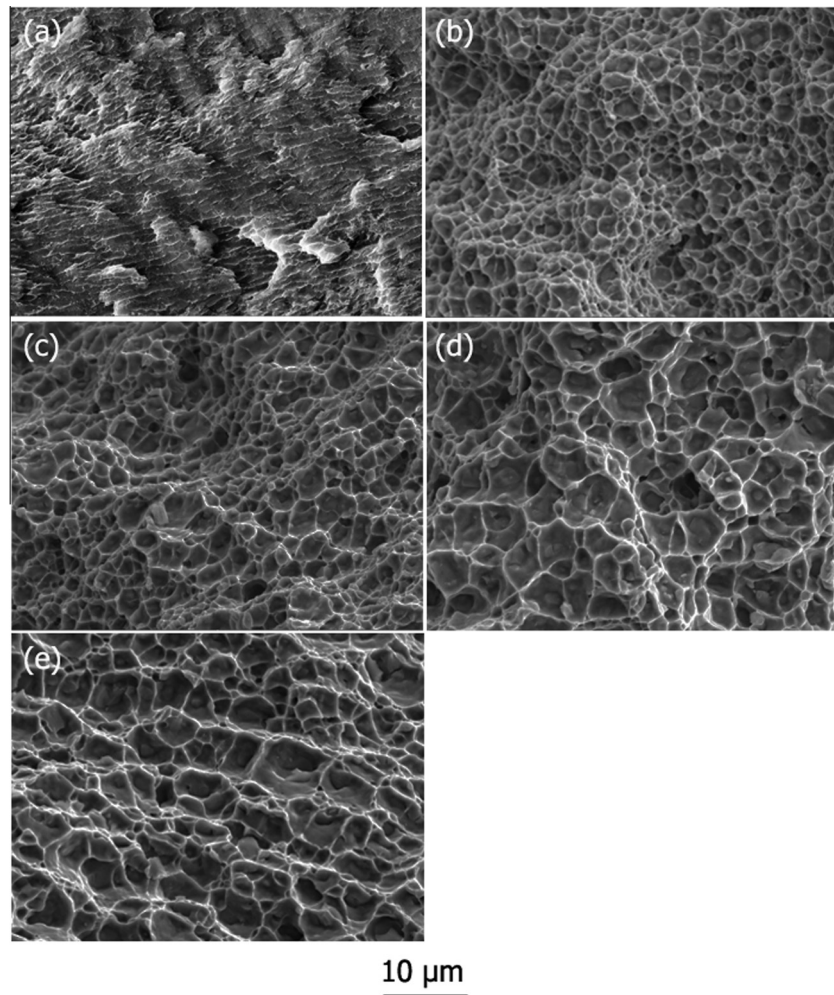


Fig. 10. SEM images (secondary electron images) of the fracture surface of the Al-12Si alloys with different solution heat treatment times (a) as-fabricated; (b) 15 min; (c) 30 min; (d) 2 h; and (e) 4 h, respectively.

recovery rate [53]. The last two factors are closely related to the solute content in the solid solution, which in this study is the Si content in the Al matrix. Upon solution treatment, the Si trapped in the Al matrix rapidly precipitates out onto the existing Si particles which sit at the Al grain boundaries, as shown in Fig. 7, thus reducing the solid solution strengthening. This also results in an increase in the volume fraction of Si (Fig. 3). The Si particles also coarsen during the early phases of the heat treatment through both coalescence of small Si particles as well as Ostwald ripening, which result in both an increase in size (Table 1) and decrease in the number of particles (Fig. 3). However, these processes appear to stop after ~ 2 h and the system reaches equilibrium. All of these together act to reduce tensile strength of the Al-12Si components. The Si content (and hence solid solution strengthening it creates) in the Al matrix drops rapidly during solution heat treatment and remains constant for times longer than 30 min. Hence, the strength of the Al-12Si also drops abruptly and is constant for times greater than 30 min. As to the tensile ductility of the solution treated Al-12Si alloys in this study, two aspects need to be considered. Firstly, the decrease in the number of Si particles and increase in size favour the reduction of localised stress or strain. Secondly, solution treatment reduces the residual stresses which have built up during the SLM process (Fig. 8). These two aspects benefit the enhancement of the tensile ductility of the solution treated Al-12Si components [1].

4. Conclusion

In this work, we have shown that, similar to melting spinning, selective laser melting (SLM) features rapid cooling rates during processing. This enables the formation of an ultrafine eutectic microstructure in an Al-12Si alloy. Unlike the eutectic microstructure observed in Al-12Si alloys fabricated by conventional methods or refined by addition of minor elements, the eutectic microstructure is characterised by spherical nano-sized Si particles embedded in the Al matrix. This ultrafine eutectic microstructure gives rise to significantly better tensile properties compared to traditionally fabricated Al-12Si parts.

Upon solution treatment, the size of the eutectic Si particles, which are critical to the mechanical properties of Al-12Si parts increases with increasing the solution treatment time. The bimodal distribution of the Si particle size is retained. However, the coarse and fine Si particles distribute homogeneously in the Al matrix. Based on the detailed TEM study, it was found that spherical Si particles with a diameter below 100 nm formed at the Al grain boundaries as a result of the extremely high cooling rate during SLM. Together with the inhomogeneous chemical distribution, this enables the Si to grow along its most stable plane $\{111\}_{\text{Si}}$ during solution treatment. This micro-sized eutectic microstructure was believed to be the underlying reason for the very high tensile ductility $\sim 25\%$ of the Al-12Si alloy.

This study shows that Al–12Si alloy with exceptional tensile properties and ultrafine eutectic microstructure can be obtained by selective laser melting and subsequent solution treatment. The eutectic microstructure of Al–12Si alloys, especially the size of the Si particles, can be tailored effectively by varying the solution treatment time. This provides important insights into refinement of Al–Si alloys without the addition of other elements.

Acknowledgements

This work was supported by the Australian Research Council (ARC) Discovery Project DP130103592 and ECM Research Development Grant, The University of Western Australia (UWA). The authors also acknowledge the facilities, and the scientific and technical assistance of the Australian Microscopy & Microanalysis Research Facility at the Centre for Microscopy, Characterisation & Analysis, The University of Western Australia, a facility funded by the University, State and Commonwealth Governments.

References

- [1] I. Gutierrez-Urrutia, M.A. Munoz-Morris, D.G. Morris, *Acta Mater.* 55 (2007) 1319–1330.
- [2] M.A. Moustafa, F.H. Samuel, H.W. Doty, *J. Mater. Sci.* 38 (2003) 4523–4534.
- [3] B. Li, H. Wang, J. Jie, Z. Wei, *Mater. Des.* 32 (2011) 1617–1622.
- [4] S.D. McDonald, K. Nogita, A.K. Dahle, *Acta Mater.* 52 (2004) 4273–4280.
- [5] Y.-C. Tsai, C.-Y. Chou, S.-L. Lee, C.-K. Lin, J.-C. Lin, S.W. Lim, *J. Alloys Compd.* 487 (2009) 157–162.
- [6] Pacz A. Alloy. US Patent 1387900. 1921.
- [7] P. Mohanty, J.E. Gruzleski, *Acta Mater.* 44 (1996) 3749–3760.
- [8] D. Qiu, J.A. Taylor, M.X. Zhang, P.M. Kelly, *Acta Mater.* 55 (2007) 1447–1456.
- [9] S. Hegde, K.N. Prabhu, *J. Mater. Sci.* 43 (2008) 3009–3027.
- [10] J. Asensio-Lozano, B. Suarez-Pena, *Scripta Mater.* 54 (2006) 943–947.
- [11] X. Jian, T.T. Meek, Q. Han, *Scripta Mater.* 54 (2006) 893–896.
- [12] H. Liao, M. Zhang, Q. Wu, H. Wang, G. Sun, *Scripta Mater.* 57 (2007) 1121–1124.
- [13] B. Suarez-Pena, J. Asensio-Lozano, *Scripta Mater.* 54 (2006) 1543–1548.
- [14] H.Y. Geng, Y.X. Li, C. Xiang, W. Xue, *Scripta Mater.* 53 (2005) 69–73.
- [15] S. Farahany, A. Ourdjini, T.A. Abu Bakar, M.H. Idris, *Metall. Mater. Trans. A* 45 (2014) 1085–1088.
- [16] F. Wang, Z. Liu, D. Qiu, J.A. Taylor, M.A. Easton, M.-X. Zhang, *Acta Mater.* 61 (2013) 360–370.
- [17] K. Narayan Prabhu, B.N. Ravishankar, *Mater. Sci. Eng., A* 360 (2003) 293–298.
- [18] L. Pedersen, L. Arnborg, *Metall. Mater. Trans. A* 32 (2001) 525–532.
- [19] Y. Birol, *J. Alloys Compd.* 439 (2007) 81–86.
- [20] A.M. Bastawros, M.Z. Said, *J. Mater. Sci.* 28 (1993) 1143–1146.
- [21] Y. Birol, *J. Mater. Sci.* 31 (1996) 2139–2143.
- [22] L. Lu, K. Nogita, A.K. Dahle, *Mater. Sci. Eng., A* 399 (2005) 244–253.
- [23] R. Trivedi, F. Jin, I.E. Anderson, *Acta Mater.* 51 (2003) 289–300.
- [24] M. Gremaud, D.R. Allen, M. Rappaz, J.H. Perepezko, *Acta Mater.* 44 (1996) 2669–2681.
- [25] E. Karakose, M. Keskin, *J. Alloys Compd.* 479 (2009) 230–236.
- [26] Z. Chen, Y. Lei, H. Zhang, *J. Alloys Compd.* 509 (2011) 7473–7477.
- [27] J.H. Li, M.Z. Zarif, G. Dehm, P. Schumacher, *Philos. Mag.* 92 (2012) 3789–3805.
- [28] D.D. Gu, W. Meiners, K. Wissenbach, R. Poprawe, *Int. Mater. Rev.* 57 (2012) 133–164.
- [29] T. Vilaro, V. Kottman-Rexerodt, M. Thomas, C. Colin, P. Bertrand, L. Thivillon, et al., *Adv. Mater. Res.* 586 (2010) 89.
- [30] X.P. Li, C.W. Kang, H. Huang, L.C. Zhang, T.B. Sercombe, *Mater. Sci. Eng., A* 606 (2014) 370–379.
- [31] X.P. Li, C.W. Kang, H. Huang, T.B. Sercombe, *Mater. Des.* 63 (2014) 407–411.
- [32] K.G. Prashanth, S. Scudino, H.J. Klaus, K.B. Surreddi, L. Löber, Z. Wang, A.K. Chaubey, U. Kühn, J. Eckert, *Mater. Sci. Eng., A* 590 (2014) 153–160.
- [33] X.J. Wang, L.C. Zhang, M.H. Fang, T.B. Sercombe, *Mater. Sci. Eng., A* 597 (2014) 370–375.
- [34] Z. Xiao, Y. Yang, X. Luo, B. Huang, *Appl. Phys. Lett.* (2014) 081611.
- [35] R.C. Weast, S.M. Selby, *CRC Handbook of Chemistry and Physics*, CTC Press, 1981.
- [36] L.K. Ang, Y.Y. Lau, R.M. Gilgenbach, H.L. Spindler, *Appl. Phys. Lett.* 70 (1997) 696–698.
- [37] S.C. Stacy, X. Zhang, M. Pantoya, B. Weeks, *Int. J. Heat Mass Transfer* 73 (2014) 595–599.
- [38] L. Thijss, K. Kempen, J.P. Kruth, J.V. Humbeeck, *Acta Mater.* 61 (2013) 1809–1819.
- [39] M. Calvo-Dahlborg, P.S. Popel, M.J. Kramer, M. Besser, J.R. Morris, U. Dahlborg, *J. Alloys Compd.* 550 (2013) 9–22.
- [40] W.D. Griffiths, D.G. McCartney, *Mater. Sci. Eng., A* 216 (1996) 47–60.
- [41] S. Nafisi, D. Emadi, M.T. Shehata, R. Ghomashchi, *Mater. Sci. Eng., A* 432 (2006) 71–83.
- [42] M. Gupta, E.J. Lavernia, *J. Mater. Process. Technol.* 54 (1995) 261–270.
- [43] J. Wang, S. He, B. Sun, Q. Guo, M. Nishio, *J. Mater. Process. Technol.* 141 (2003) 29–34.
- [44] I.G. Brodova, P.S. Popel, G.I. Eskin, in: J.N. Fridlyander, D.G. Eskin (Eds.), *Liquid Metal Processing: Application to Aluminium Alloy Production, Advances in Metallic Alloys*, Taylor & Francis, London, 2002.
- [45] S. Katakam, J.Y. Hwang, H. Vora, S.P. Harimkar, R. Banerjee, N.B. Dahotre, *Scripta Mater.* 66 (2012) 538–541.
- [46] X.P. Li, M. Roberts, Y.J. Liu, C.W. Kang, H. Huang, T.B. Sercombe, *Mater. Des.* 65 (2015) 1–6.
- [47] W.D. Liu, L.M. Ye, K.X. Liu, *J. Appl. Phys.* 109 (2011) 043109–09–5.
- [48] M. Asta, C. Beckermann, A. Karma, W. Kurz, R. Napolitano, M. Plapp, G. Purdy, M. Rappaz, R. Trivedi, *Acta Mater.* 57 (2009) 941–971.
- [49] D. Qiu, M.-X. Zhang, *J. Alloys Compd.* 586 (2014) 39–44.
- [50] J. Zhang, H. Yu, S.B. Kang, J.H. Cho, G. Min, V.Y. Stetsenko, *J. Alloys Compd.* 541 (2012) 157–162.
- [51] K. Dai, L. Shaw, *Acta Mater.* 49 (2001) 4171–4181.
- [52] G. Viera, S. Huet, L. Boufendi, *J. Appl. Phys.* 90 (2001) 4175–4183.
- [53] Y. Chen, M. Weyland, C.R. Hutchinson, *Acta Mater.* 61 (2013) 5877–5894.



Selective laser melting of AlSi10Mg alloy: Process optimisation and mechanical properties development

Noriko Read^a, Wei Wang^a, Khamis Essa^b, Moataz M. Attallah^{a,*}

^a School of Metallurgy and Materials, University of Birmingham, Edgbaston, Birmingham B15 2TT, UK

^b School of Mechanical Engineering, University of Birmingham, Edgbaston, Birmingham B15 2TT, UK



ARTICLE INFO

Article history:

Received 22 July 2014

Accepted 15 September 2014

Available online 7 October 2014

Keywords:

Selective laser melting
Aluminium alloys
Mechanical properties

ABSTRACT

The influence of selective laser melting (SLM) process parameters (laser power, scan speed, scan spacing, and island size using a Concept Laser M2 system) on the porosity development in AlSi10Mg alloy builds has been investigated, using statistical design of experimental approach, correlated with the energy density model. A two-factor interaction model showed that the laser power, scan speed, and the interaction between the scan speed and scan spacing have the major influence on the porosity development in the builds. By driving the statistical method to minimise the porosity fraction, optimum process parameters were obtained. The optimum build parameters were validated, and subsequently used to build rod-shaped samples to assess the room temperature and high temperature (creep) mechanical properties. The samples produced using SLM showed better strength and elongation properties, compared to die cast Al-alloys of similar composition. Creep results showed better rupture life than cast alloy, with a good agreement with the Larson–Miller literature data for this alloy composition.

© 2014 Elsevier Ltd. All rights reserved.

1. Introduction

Additive layer manufacturing (ALM) has been used for more than 30 years and is now widely used for various materials [1–4]. Although there are many types of production machines, they are all similar, in the sense that they produce three-dimensional shapes by combining a number of two-dimensional slices. In recent years, ALM has been developed for “rapid manufacturing” of metallic components using, electron beam melting (EBM), direct laser fabrication (DLF), and selective laser melting (SLM) [5,6]. Aerospace manufacturers are focusing on the SLM powder-bed technology for Ti-alloy and Ni-superalloy components [7,8] where the potential cost reduction, fewer steps in the production process and design-freedom are among the factors driving this technology. There has been an increasing number of reports on ALM of Al-alloys recently, because of the demand from the industrial field for lightweight structures with complex geometries [6,9].

AlSi10Mg alloy is a traditional cast alloy that is often used for die-casting. Because of its high strength and good mechanical properties, this alloy has been widely used in the automotive and aerospace industry. Because of its near eutectic composition of Al and Si, it has good weldability. Mg plays an important role in age

hardening as β' and Mg_2Si (β -phase) [10]. Recently, various reports have been published of the microstructure using a processing parameter study of SLM-fabricated AlSi10Mg [11,12].

There are many factors that affect the final quality of the SLM samples, including the feedstock material characteristics (powder size, morphology and size distribution). The laser heat input is another source important parameter, as it controls the degree of consolidation of the powder particles, or could potentially aggravate defect formation by creating turbulences in the melt pool that can form a keyhole-like defect in the extreme conditions. One of the approaches to represent the laser heat input is using the energy density function Ψ [6], which is given as

$$\Psi = \frac{P}{v \cdot h \cdot t} \quad (1)$$

where P and v are respectively the laser power and scan speed, h is scan spacing, and t is layer thickness. Some studies [3] used the energy density concept to correlate the porosity development with the heat input, but the trend was generally inconsistent, although it identified an optimum energy density level where the build density was the maximum.

Alternatively, the use of design of experiments (DOE) techniques such as the Response Surface Method, and statistical analysis using the analysis of variance (ANOVA), have been shown to be useful approaches to study the effect of many parameters in material processing applications. Response Surface design of experiment and

* Corresponding author. Tel.: +44 121 414 7842.

E-mail address: M.M.Attallah@Bham.ac.uk (M.M. Attallah).

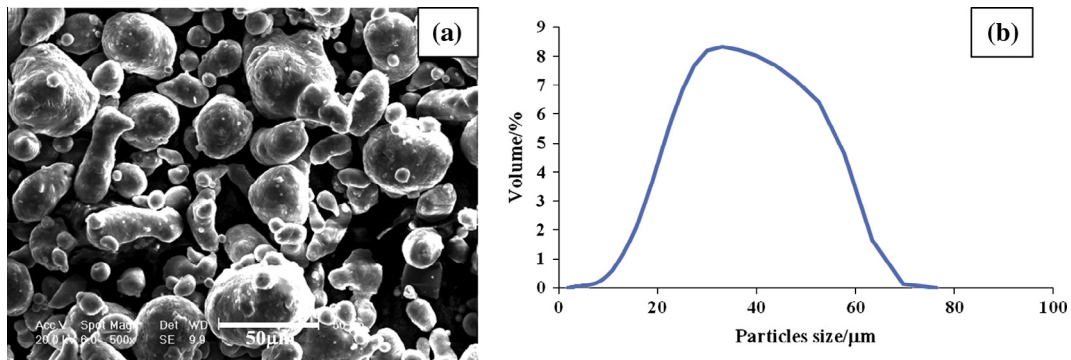


Fig. 1. (a) SEM micrograph, showing the morphology of the AlSi10Mg powder, and (b) the powder size distribution.

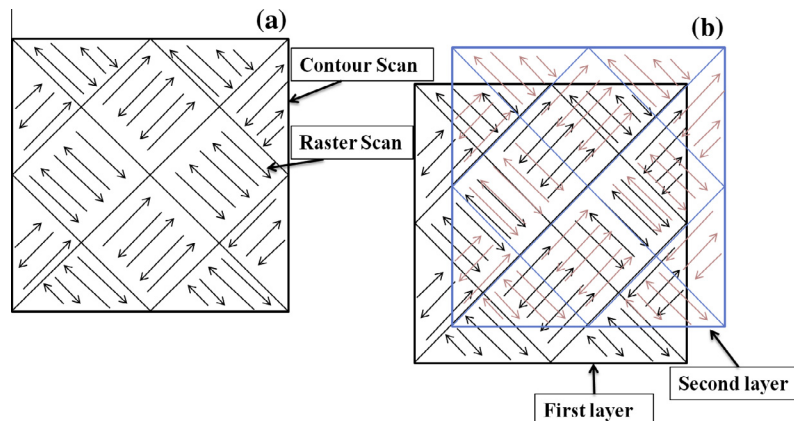


Fig. 2. Schematic illustration of the island scan strategy, showing (a) each layer is divided into square (islands) and the inside of island is raster scanned, then (b) the successive layers are displaced 1 mm in the X and Y-directions.

ANOVA technique have been used for the significance of selective laser sintering (SLS) process variables on surface roughness [13]. Similarly, Carter [14] used response surface method and ANOVA techniques to optimise SLM for CMSX-486 Ni-superalloy, by studying the impact of the process parameters (laser power, scan speed, scan spacing and island size) on crack density and porosity fraction.

This paper focuses on the influence of SLM parameters for fabricating AlSi10Mg. Statistical experimental design was adopted to optimise the process parameters to minimise the defects (pores or cracks). Mechanical tests were performed on samples manufactured using optimised parameters that gave minimum porosity and voids. In this paper, the term “pore” includes spherical pores and irregular voids that are observed in the laser processed samples. The influence of the build orientation (vertically and horizontally built samples) on the tensile properties was investigated. In addition, high temperature mechanical (creep) properties were also measured for horizontally built samples.

2. Experimental details

2.1. Material

The AlSi10Mg powder, the composition of which is shown in Table 1, was supplied by LPW Technology Ltd. The size range was 20–63 μm, as measured using Coulter LS230 laser diffraction particle size analyser.

Fig. 1(a) shows a Scanning Electron Microscope (SEM) micrograph of the powder. It is obvious that the powder particles are not spherical. The particles show a very irregular morphology, with

many small irregular satellite particles attached to the big particles. These irregular shape with small satellite particles were observed elsewhere [15,16]. The particle size distribution affects the powder flowability for in powder bed systems, as well as their melting behaviour [6]. Fig. 1(b) shows the size distribution of the powder, which had an average particle size of ~35 μm. The slightly unsymmetrical distribution is potentially caused by the irregular powder morphology, and the potential agglomeration of the powder particles during the measurement. Despite the irregular morphology, the powder had a reasonable flowability and Hausner's ratio for SLM.

2.2. Statistical design of experiment (DoE) using response surface

The response surface methodology is a statistical technique to generate an experimental design to find an approximate model between the input and output parameters, and to optimise the process responses (e.g. towards a maximum and a minimum). It is a collection of statistical and mathematical methods that are useful for modelling and analysing engineering problems. In this technique, the main objective is to optimise the response surface, which is influenced by various process parameters. The response

Table 1
Chemical composition of the investigated AlSi10Mg alloy (Wt.%).

Si	Fe	Mn	Mg	Ni	Zn	Pb	Sn	Ti	Al
9.92	0.137	0.004	0.291	0.04	0.01	0.004	0.003	0.006	Bal

Table 2

The range of matrix building parameters.

Parameter	Units	Levels				
		-2	-1	0	1	2
Laser power	W	100	125	150	175	200
Scan speed	mm/s	700	1025	1350	1675	2000
Hatch spacing (a_1)		0.2	0.35	0.5	0.65	0.8
Island size	mm	2.0	3.5	5.0	6.5	8.0

Table 3

Response surface model coefficients for cracking density and porosity fraction.

Coefficient	The corresponding value
b_0	-12.76
b_1	$+2.07 \times 10^{-1}$
b_2	$+1.02 \times 10^{-2}$
b_3	-20.44
b_4	+5.50
b_5	-1.39×10^{-4}
b_6	-2.32×10^{-1}
b_7	-2.4×10^{-2}
b_8	$+5.01 \times 10^{-2}$
b_9	-8.37×10^{-4}
b_{10}	-1.45

surface Y can be expressed by a second order polynomial (regression) equation as shown in Eq. (2).

$$Y = b_0 + \sum b_i x_i + \sum b_{ii} x_i^2 + \sum b_{ij} x_i x_j. \quad (2)$$

The experimental design procedure using the response surface methodology can be summarised as follows:

- Identification of the key process parameters.
- Selection of the upper and lower limit of the process parameters.
- Selection of the output response.
- Developing the experimental design matrix.
- Conducting the experiments as per the design matrix.
- Recording the output response.
- Developing a mathematical model to relate the process parameters with the output response.
- Optimising that model using genetic algorithm.

2.3. SLM

All specimens were fabricated using a Concept Laser M2 Cusing® SLM (laser powder-bed) system. The M2 system has a Yb-Fibre laser, with laser power up to 200 W, 150 μm laser track width, with laser scan speed up to 7000 mm/s. All specimens were built using a Z-increment (vertical) of 30 μm . All processing was

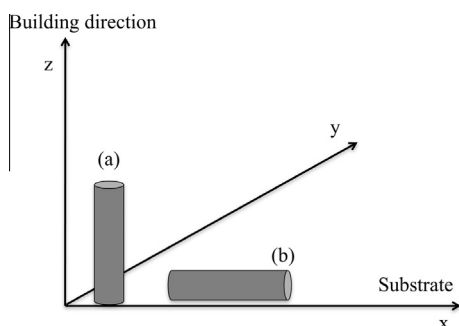


Fig. 3. Schematic drawing of horizontal and vertical samples for the mechanical tests.

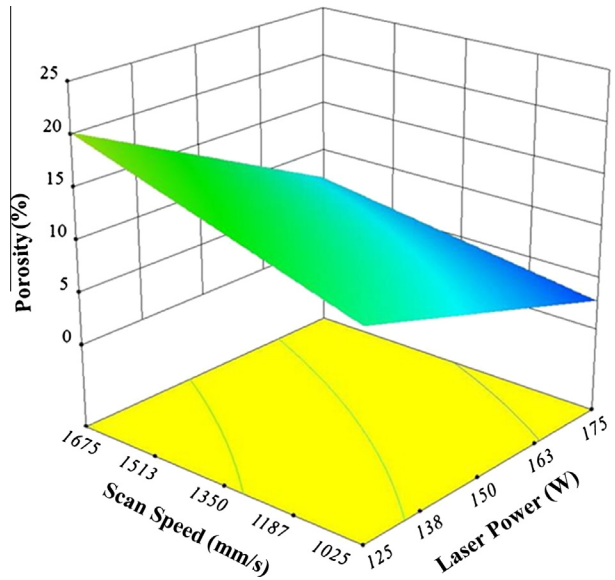


Fig. 4. Response surface plot showing the effect of the laser power and scan speed on the porosity, at 0.5 hatch-spacing a_1 and 5 mm island size.

carried out in an Argon atmosphere with an oxygen-content <0.1%. An “island scanning strategy” was adopted to fabricate specimens [17], in which the filled layer is divided into several square (islands) with each island being built randomly and continuously. Inside each island, the laser is raster-scanned individually. After selective melting the islands, laser scans are carried out around the perimeter of the layer to improve the surface finish. For each subsequent layer, these islands are translated by 1 mm in the X and Y-directions, as illustrated in Fig. 2. The aim of the island deposition strategy is to balance the residual stresses in the build [18].

2.4. Sample build and preparation

To perform the DoE and parametric optimisation, 27 parametric combinations were used to fabricate samples using a fractional factorial DoE. All samples were 10 mm × 10 mm × 10 mm cubes. Since Concept Laser M2 uses a dimensionless number hatch spacing a_1 instead of scan spacing, a_1 parameter was used for this study. a_1 is defined as,

$$a_1(\text{Hatch spacing}) = \text{Scan spacing } h/\text{laser track width} \\ (\text{constant}, 150 \mu\text{m})$$

Table 2 shows the range and levels of the investigated key process variables.

2.5. Porosity and microstructural analysis

To characterise the area fraction and density of cracks and/or pores in the material, all samples were cut in the transverse direction (X-Y plane) 3 mm from the top of the build, mounted in conducting Bakelite, and polished to a 0.05 μm finish. Samples were analysed using a Zeiss Axioskop microscope, with an Axioskop 2® image analyser and AxioVision® software. For each sample, 25 images were collected from the centre. Image threshold was applied to determine the porosity content (porosity %), using ImageJ Software [19]. Table 3 summarises the findings of porosity % and the parametric combinations. No solidification cracks were observed, which was expected as AlSi10Mg alloy has a generally low crack sensitivity [16], although oxide film crack-like features were observed. The microstructure of the samples was examined

Table 4

Matrix building parameters and % porosity.

Run	Laser power (W)	Scan speed (mm/s)	Hatch spacing a_1 ($h/150 \mu\text{m}$)	Island size (mm)	Porosity (%)
1	125	1675	0.35	6.5	16.1
2	125	1675	0.65	3.5	24.7
3	125	1025	0.65	6.5	9.4
4	150	1350	0.8	5	10.8
5	125	1675	0.65	6.5	29.9
6	150	700	0.5	5	10.4
7	150	1350	0.5	5	9.9
8	125	1675	0.35	3.5	15.4
9	175	1025	0.65	6.5	1.7
10	175	1675	0.65	6.5	5.5
11	125	1025	0.35	3.5	11.8
12	150	1350	0.2	5	10.5
13	125	1025	0.35	6.5	14.1
14	150	1350	0.5	2	7.5
15	100	1350	0.5	5	20.5
16	150	1350	0.5	5	10.1
17	175	1025	0.35	6.5	3.5
18	125	1025	0.65	3.5	9.3
19	175	1675	0.35	6.5	6.4
20	175	1675	0.65	3.5	13.1
21	200	1350	0.5	5	0.8
22	150	2000	0.5	5	18.0
23	175	1675	0.35	3.5	6.8
24	150	1350	0.5	5	5.5
25	150	1350	0.5	8	7.3
26	175	1025	0.65	3.5	0.8
27	175	1025	0.35	3.5	2.4

in a JEOL 6060 scanning electron microscope (SEM), equipped with a back-scattered electron (BSE) detector, and operated at 20 kV.

2.6. Mechanical testing

Rod-shape samples were fabricated using the optimised parameters that produced the lowest porosity. Samples were built vertically and horizontally, as shown in Fig. 3. In the 'vertical' samples, the long boundary of the sample is parallel to the building direction, whereas the long boundary of the sample is perpendicular

to the building direction in the 'horizontal' samples. Tensile tests were performed in accordance with BS EN 2002-1:2005 [20]. All mechanical test results are the average of 3 samples. In addition, creep tests were performed at the following conditions 180 °C/200 MPa, 150 °C/200 MPa, and 180 °C/150 MPa for the horizontal samples, in accordance with BS EN 2002-5:2007 [21]. For each creep test, samples were kept at the test temperature for a minimum of 30 min prior to the test. For the 150 °C/200 MPa and 180 °C/150 MPa conditions, tests were stopped at 20 h. Fracture surface observation was performed using SEM after the creep test.

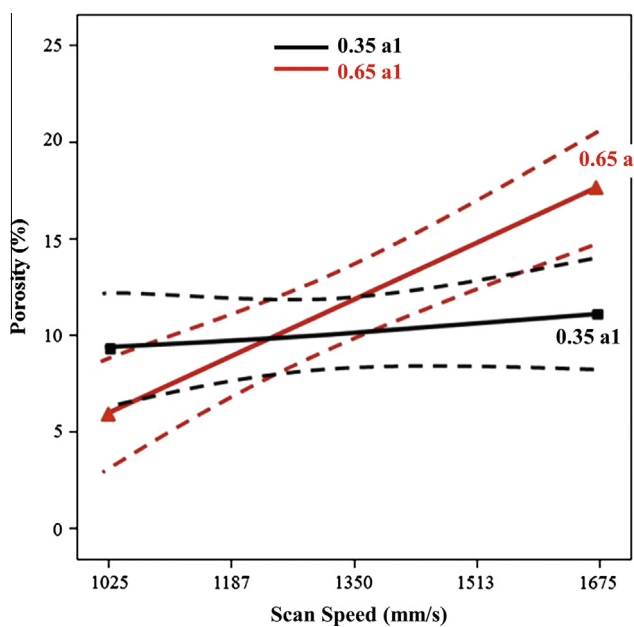


Fig. 5. The impact of the interaction effect of scan speed and hatch spacing on the porosity, at 150 W laser power and 5 mm island size. The solid lines represent model prediction while the dash lines represent the variation of the actual data around the model prediction.

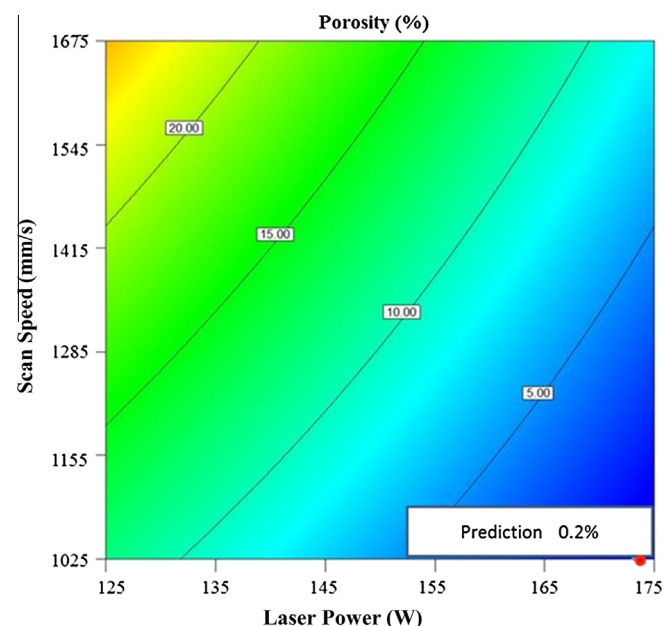
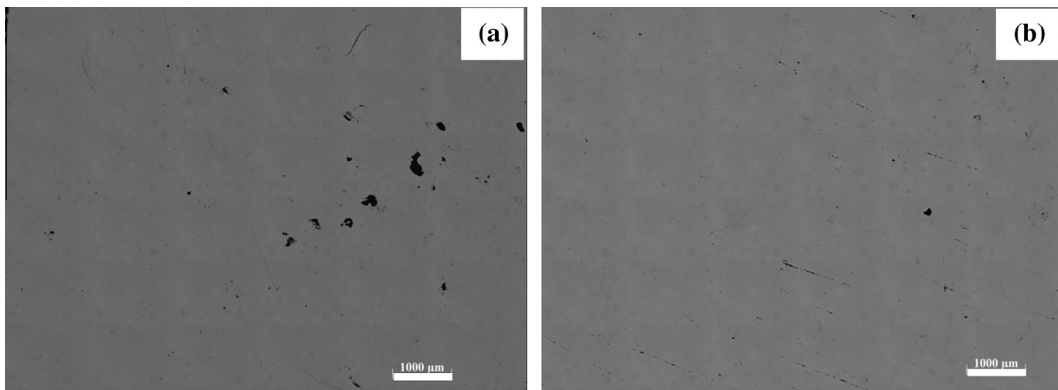
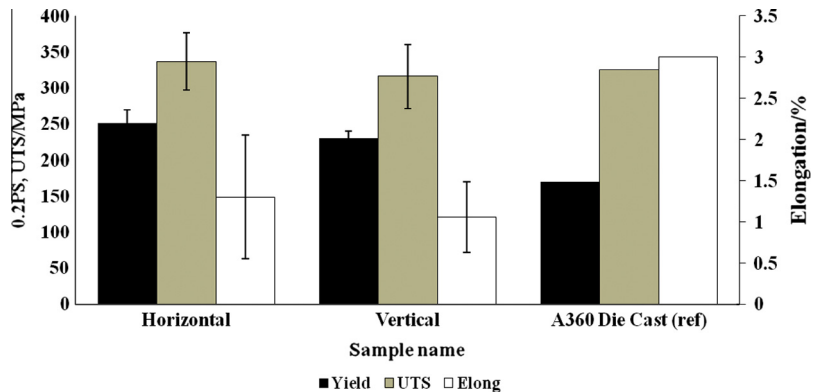


Fig. 6. Predicted optimum laser power and scan speed for minimum porosity.

Table 5

Predicted building parameter and actual porosity %.

Samples	Power (W)	Scan speed (mm/s)	Hatch spacing a_1 ($h/150 \mu\text{m}$)	Island size (mm)	Porosity (%)	
					Predicted	Measured
A	175	1035	0.65	5.9	0.2	0.37
B	173	1025	0.65	6.5	0.2	0.38
C	175	1030	0.64	6	0.2	0.46
D	174	1026	0.65	6.2	0	0.61
E	175	1025	0.65	5.6	0	0.29

**Fig. 7.** Optical micrograph images of (a) sample D and (b) sample E shown in Table 5.**Fig. 8.** Tensile properties of SLM fabricated AlSi10Mg alloy, compared to die cast A360 alloy [24].

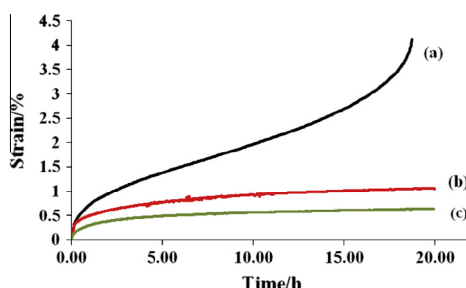
3. Results and discussion

3.1. ANOVA results

The response surface for porosity is a function of laser power (P), scan speed (v), hatch spacing (a_1), and island size (Z) and can be expressed as follows:

$$\begin{aligned} \text{Response} = & b_0 + b_1(P) + b_2(v) + b_3(h) + b_4(Z) + b_5(Pv) \\ & + b_6(Pa_1) + b_7(PZ) + b_8(a_1 v) + b_9(vZ) \\ & + b_{10}(Za_1) \end{aligned} \quad (3)$$

where b_0 is the average response, and b_1, b_2, \dots, b_{10} are the model coefficients that depend on the main and interaction effects of the process parameters. The value of the coefficients for the porosity is shown in Table 4. The R^2 -value, a measure of model fit, showed that each of the models described the relationship between the

**Fig. 9.** Creep curves of SLM fabricated AlSi10Mg alloy (horizontal samples) at the following conditions: (a) 180 °C/200 MPa, (b) 150 °C/200 MPa, and (c) 180 °C/150 MPa.

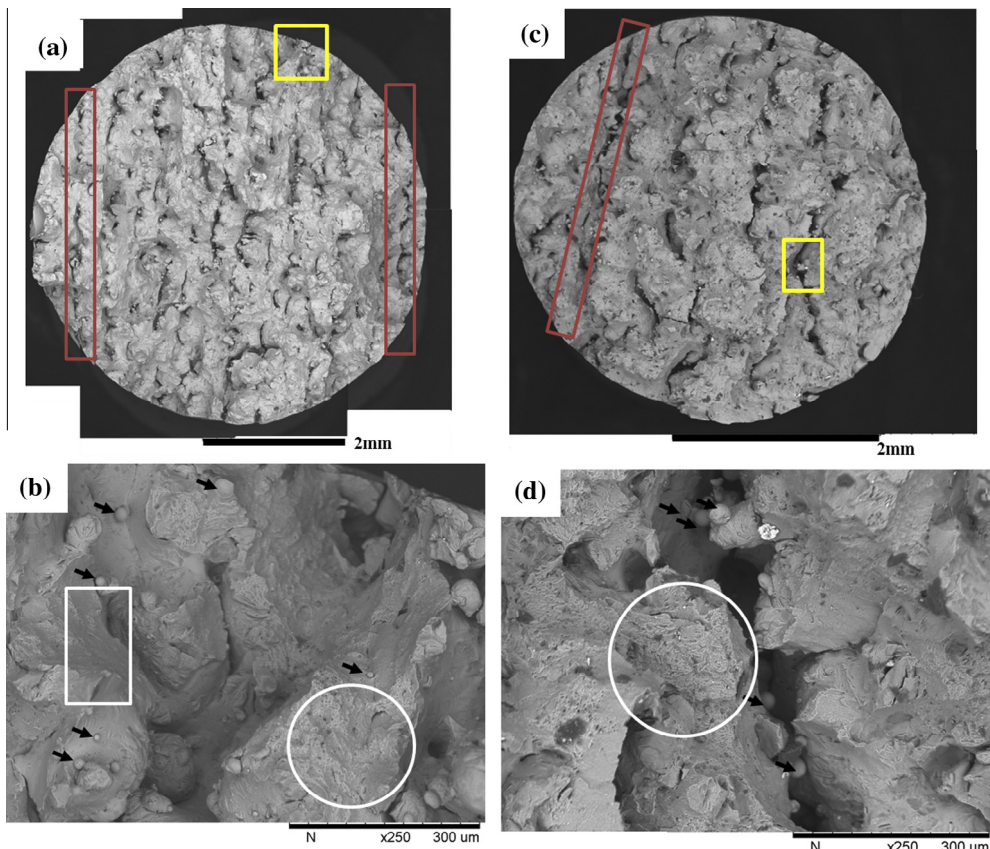


Fig. 10. Backscattered SEM fractographs of SLM fabricated AlSi10Mg horizontal samples, showing (a) RT tensile test sample, (b) enlarged image, shown in yellow square in (a), (c) creep test sample, tested at 180 °C/200 MPa and (d) enlarged image, shown in yellow square in (c). Dimples-containing areas are circled, and the smooth areas are labelled using white rectangles. Unmelted particles are arrowed. (For interpretation of the references to colour in this figure legend, the reader is referred to the web version of this article.)

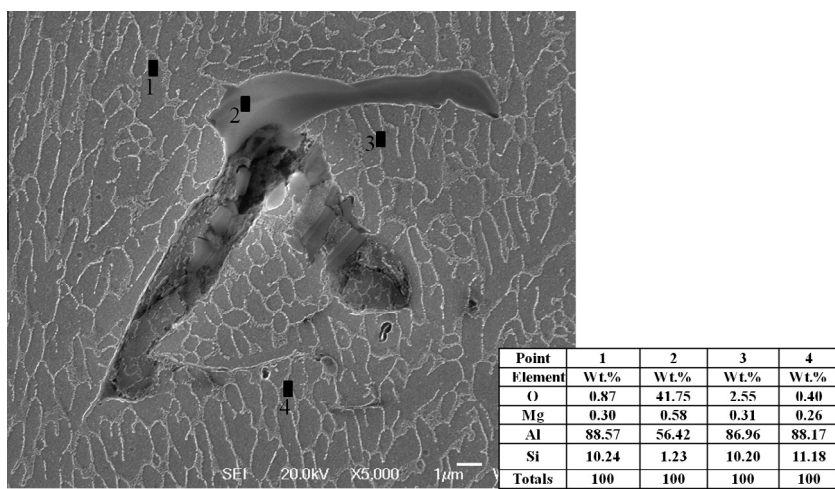


Fig. 11. Secondary electron SEM images of irregular shape porosity showing an oxide film defect. The areas numbered have been analysed using EDX, as shown in the table.

process parameters and porosity was 0.87. The ANOVA indicates that, within the investigated range of parameters, the porosity is mainly affected by laser power, scan speed and the interaction between the scan speed and hatch spacing. The island size was found unlikely to have any influence on porosity.

Fig. 4 shows the response surface model prediction of porosity with respect to laser power and scan speed. It shows that decreasing the laser power and increasing the scan speed both result in an

increased porosity. The influence of the laser power on porosity formation appears to be more significant at high scan speeds, and likewise the influence of the scan speed is more significant at lower laser power. A reduction in the laser power and an increase in the scan speed both have the effect of reducing the energy input into the material, as such these will result in the reduction of the melt pool which will lead to the formation of porosity due to the incomplete consolidation, and may ultimately

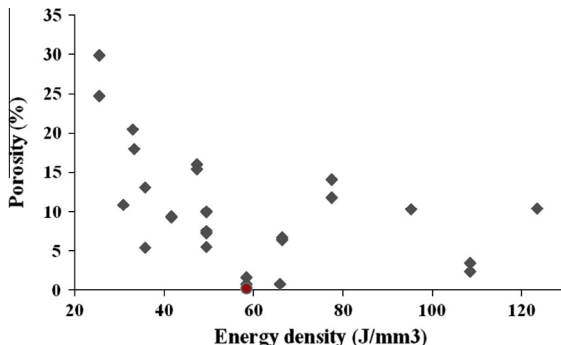


Fig. 12. Porosity variation versus the energy density. The diamond points show the result of the data from Table 3, and the circle shows the predicted parameter E , shown in Table 5.

lead to the breakdown of the SLM process. The relationship between energy input and porosity was also considered in Ti-alloys [22].

Fig. 5 shows the interaction effect between the scan speed and hatch spacing on the porosity. A low hatch spacing a_1 of 0.35 appears to eliminate the effect of the scan speed on the porosity; whereas a high hatch spacing a_1 of 0.65 significantly increases the effect of scan speed on porosity fraction. Likewise, an increase in the hatch spacing will ultimately result in porosity formation due to the lack of sufficient overlap between the laser scan tracks, leading to incomplete consolidation. Since the laser power, scan speed, and hatch spacing can individually control the heat input, it is conceivable that porosity formation can be mitigated using one of these parameters (within the investigated process window) to increase the heat input (e.g. use slow scan speed to fully consolidate the melt pool). It is important to state that these deductions are only valid within the investigated process window, since other mechanisms for porosity formation (e.g. melt pool turbulence or evaporation) could be triggered outside the investigated range. By considering the results presented in Figs. 4 and 5, it can be seen that in order to eliminate or minimise the porosity within the material, a high laser power, at low scan speed with a small hatch spacing should be used.

3.2. Process optimisation

During the optimisation, the objective function was set to minimise the porosity. The genetic algorithm was used to predict the process parameters based on the objective function. The equations modelling the response of porosity with respect to the four key process parameters (shown in Eq. (3) and the related coefficients listed in Table 4) were solved simultaneously. Fig. 6 shows the contour plot for the optimisation function to obtain minimum porosity for a range of laser powers and scan speeds. Kempen et al. [11] suggested optimum process parameter of 200 W, 1400 mm/s, with scan spacing 105 µm. Additionally, Brandl et al. [23] used 250 W, 500 mm/s, 150 µm scan spacing, with 50 µm layer thickness to achieve defect-free SLM of the AlSi10Mg alloy.

3.3. Validation build

To confirm the relationship between the predicted optimum parameter sets and porosity, 5 samples were built using the optimised parameters. Table 5 shows the set of predicted parameters and the measured porosity. Fig. 7 shows micrographs for samples D and E. In sample D, irregular shaped voids (some of them are 200–300 µm in size), rather than spherical, but the overall level of these irregular voids was very low. The irregular pores are most

likely caused by improper powder spreading, especially as they were infrequent.

3.4. Mechanical tests

Fig. 8 shows the tensile test results of horizontal and vertical samples together with data from die cast samples [24]. All samples were built using the parameters set E, shown in Table 5. There is no major influence for the build orientation on the tensile properties, although the horizontal samples show ~10% high strength. Fig. 9 shows the time-strain curves of horizontal samples, for test conditions: (a) 180 °C/200 MPa, (b) 150 °C/200 MPa, and (c) 180 °C/150 MPa. All the strain-time relations show normal creep behaviour, such as primary, secondary and tertiary creep. For test condition (a), the sample ruptured at 18.7 h. Using creep rupture data [24] for Larson miller plot for the same alloy, the predicted rupture time was 14.8 h.

Fig. 10 shows the fractography of the samples tested to failure, for room temperature tensile tests (a,b) and creep tests (c,d). From these images, fracture surface are very rough and irregular. Deep cracks are generally obvious throughout the samples, interestingly all aligned in the same direction. At high magnifications, the fracture surface appears to contain a mix of small dimples and smooth areas. Moreover, fine unmelted powder particles are observed on both surfaces, Fig. 10(b) and (d), which could be due to the presence of thick oxide layers on the particles, which did not enable a full consolidation to occur locally where they existed. These un-bonded regions give rise to large cracks in the failed samples. The fracture surfaces are very similar in both the tension and creep samples, although a larger number of deep cracks was observed in the samples tested in tension. Furthermore, the crack surfaces appear smoother in the tension samples, than those of the creep samples. Similar fracture surfaces have been observed in the SLM of AA6061 [16]. The influence of these un-bonded regions on the tensile properties is small, because their effect on the reduction of the load-bearing cross section is small, but these defects may influence fatigue properties, especially if they are formed near to the surface.

Fig. 11 shows micrographs of the irregular voids. From the EDX data obtained from the areas arrowed in (b), it appears that area 2 is very high in oxygen, suggesting that this irregular void is associated with the presence of an oxide layer which prevented bonding. The analysis for oxygen, particularly on a rough surface, will not be quantitatively accurate, but the large difference between area 2 and other areas is considered as highly significant.

3.5. Rationalising the porosity formation using the energy density

Fig. 12 shows a plot of porosity versus the energy density for the data previously provided in Table 2. The red dot indicates the predicted optimum parameter, E , previously provided in Table 5. The graph shows that at low energy density (<50 J/mm³) corresponds to a high porosity due to the lack of consolidation. The porosity content then decreases with increasing the energy density. This result supports the energy threshold for the full consolidation shown by Fig. 5. However, when the energy density exceeds approximately 60 J/mm³, the porosity content starts to scatter beyond that level until 120 J/mm³. In this region other defects, such as keyhole formation (due to vapourisation), have been observed within the material. Olakanmi also indicated that there is a certain threshold energy density that gives maximum material density, which is 60–75 J/mm³ for Al, Al-Si and Al-Mg alloys [15]. Further in depth studies would be required to understand the factors governing this threshold level in various materials.

4. Conclusions

This study has shown the following:

- A statistical method has been used to evaluate the influence of process parameters on the porosity of SLMed AlSi10Mg, which shows the trends of porosity in the SLM fabricated samples.
- There is a critical energy density point that gives the minimum pore fraction for this alloy, approximately 60 J/m^3 .
- The build direction does not strongly influence the tensile or creep strength of SLMed AlSi10Mg. Both building directions show higher strength than die cast A360, although the elongation is inferior to that of A360.
- Fracture surfaces show the presence of significant amounts of un-melted powder, which give rise to local cracking. Further work is required to see if it is possible to eliminate these regions.

Acknowledgements

The authors would like to acknowledge the financial support from MicroTurbo/Safran Group. The support of the Materials and Components for Missiles (MCM) Innovation and Technology Partnership (ITP), and the Defence Science and Technology Laboratory (Dstl) is highly appreciated.

References

- [1] Casavola C, Campanelli SL, Pappalettere C. Preliminary investigation on distribution of residual stress generated by the selective laser melting process. *J Strain Anal Eng Des* 2009;44:93–104.
- [2] Osakada K, Shiomi M. Flexible manufacturing of metallic products by selective laser melting of powder. *Int J Mach Tools Manuf* 2006;46:1188–93.
- [3] Olakanmi EO, Cochrane RF, Dalgarno KW. Densification mechanism and microstructural evolution in selective laser sintering of Al-12Si powders. *J Mater Process Technol* 2011;211:113–21.
- [4] Yan C, Shi Y, Yang J, Liu J. Preparation and selective laser sintering of nylon-12 coated metal powders and post processing. *J Mater Process Technol* 2009;209:5785–92.
- [5] Vutova K, Vassileva V, Koleva E, Georgieva E, Mladenov G, Mollov D, et al. Investigation of electron beam melting and refining of titanium and tantalum scrap. *J Mater Process Technol* 2010;210:1089–94.
- [6] Liu A, Chua CK, Leong KF. Properties of test coupons fabricated by selective laser melting. *Key Eng Mater* 2010;447–448:780–4.
- [7] Gu D, Wang Z, Shen Y, Li Q, Li Y. In-situ TiC particle reinforced Ti-Al matrix composites: powder preparation by mechanical alloying and selective laser melting behavior. *Appl Surf Sci* 2009;255:9230–40.
- [8] Amato KN, Gaytan SM, Murr LE, Martinez E, Shindo PW, Hernandez J, et al. Microstructures and mechanical behavior of Inconel 718 fabricated by selective laser melting. *Acta Mater* 2012;60:2229–39.
- [9] Dadbakhsh S, Hao L. Effect of Al alloys on selective laser melting behaviour and microstructure of in situ formed particle reinforced composites. *J Alloy Compd* 2012;541:328–34.
- [10] Gupta AK, Lloyd DJ, Court SA. Precipitation hardening in Al–Mg–Si alloys with and without excess Si. *Mater Sci Eng* 2001;A316:11–7.
- [11] Thijs L, Kempen K, Kruth J-P, Humbeeck JV. Fine-structured aluminium products with controllable texture by selective laser melting of pre-alloyed AlSi10Mg powder. *Acta Mater* 2013;61:1809–19.
- [12] Kempen K, Thijs L, Humbeeck JV, Kruth J-P. Mechanical properties of AlSi10Mg produced by selective laser melting. *Phys Procedia* 2012;39:439–46.
- [13] Bacchewar PB, Singhal SK, Pandey PM. Statistical modelling and optimization of surface roughness in the selective laser sintering process. *Proc Inst Mech Eng Part B: J Eng Manuf* 2007;221:35–52.
- [14] Carter LN. Selective laser melting of Ni-superalloys for high temperature applications. Birmingham: University of Birmingham; 2013.
- [15] Olakanmi EO. Selective laser sintering/melting (SLS/SLM) of pure Al, Al-Mg, and Al-Si powders: Effect of processing conditions and powder properties. *J Mater Process Technol* 2013;213:1387–405.
- [16] Louvis E, Fox P, Sutcliffe CJ. Selective laser melting of aluminium components. *J Mater Process Technol* 2011;211:275–84.
- [17] Thijs L, Verhaeghe F, Craeghs T, Humbeeck JV, Kruth J-P. A study of the microstructural evolution during selective laser melting of Ti-6Al-4V. *Acta Mater* 2010;58:3303–12.
- [18] Hofmann Group. Hofmann Innovation Group Website – Concept Laser. <<http://www.hofmann-innovation.com/en/technologies/direct-cusing-manufacturing.html>>. 2012 [accessed 30.05.14].
- [19] Rasband W. ImageJ. U.S. National Institutes of Health, Bethesda, Maryland, USA. <<http://imagej.nih.gov/ij>>; 1997–2014.
- [20] British Standards Institution. Aerospace series. Metallic materials. Test methods. Tensile testing at room temperature (BS EN 2002-1:2005); 2006.
- [21] British Standards Institution. Aerospace series. Metallic materials. Test methods. Tensile testing at elevated temperature (BS EN 2002-2:2005); 2006.
- [22] Gong H, Raff K, Starr T, Stucker B. The effects of processing parameters on defect regularity in Ti-6Al-4V parts fabricated by selective laser melting and electron beam melting. in: The 24th international SFF symposium: An additive manufacturing conference. The University Of Texas at Austin; 2013.
- [23] Brandl E, Heckenberger U, Holzinger V, Buchbinder D. Additive manufactured AlSi10Mg samples using Selective Laser Melting (SLM): microstructure, high cycle fatigue, and fracture behavior. *Mater Des* 2012;34:159–69.
- [24] Kaufman JG, In: Kaufman JG, editor. Properties of aluminum alloys tensile creep and fatigue data at high and low temperatures. Materials Park (Ohio); ASM International (Washington (D.C)); 1999. p. 264.

See discussions, stats, and author profiles for this publication at: <https://www.researchgate.net/publication/257922422>

From Powders to Dense Metal Parts: Characterization of a Commercial AlSiMg Alloy Processed through Direct Metal Laser Sintering

Article in Materials · March 2013

DOI: 10.3390/ma6030856

CITATIONS

210

READS

867

6 authors, including:



Diego Manfredi
Politecnico di Torino
145 PUBLICATIONS 3,067 CITATIONS

[SEE PROFILE](#)



Flaviana Calignano
Politecnico di Torino
143 PUBLICATIONS 2,970 CITATIONS

[SEE PROFILE](#)



Manickavasagam Krishnan
Singapore
11 PUBLICATIONS 472 CITATIONS

[SEE PROFILE](#)



Elisa Paola Ambrosio
Politecnico di Torino
67 PUBLICATIONS 1,804 CITATIONS

[SEE PROFILE](#)

Some of the authors of this publication are also working on these related projects:



Corrosion and Additive Manufacturing [View project](#)



Lattice structures [View project](#)

Article

From Powders to Dense Metal Parts: Characterization of a Commercial AlSiMg Alloy Processed through Direct Metal Laser Sintering

Diego Manfredi ^{1,*}, Flaviana Calignano ¹, Manickavasagam Krishnan ^{1,2}, Riccardo Canali ^{1,3}, Elisa Paola Ambrosio ¹ and Eleonora Atzeni ²

¹ Center for Space Human Robotics @Polito, Istituto Italiano di Tecnologia, Corso Trento 21, Torino 10129, Italy; E-Mails: flaviana.calignano@iit.it (F.C.); manickavasagam.krishnan@iit.it (M.K.); riccardo.canali@iit.it (R.C.); elisa.ambrosio@iit.it (E.P.A.)

² Department of Management and Production Engineering, Politecnico di Torino, Corso Duca degli Abruzzi 24, Torino 10129, Italy; E-Mail: eleonora.atzeni@polito.it

³ Department of Applied Science and Technology, Politecnico di Torino, Corso Duca degli Abruzzi 24, Torino 10129, Italy

* Author to whom correspondence should be addressed; E-Mail: diego.manfredi@iit.it; Tel.: +39-011-090-3406; Fax: +39-011-090-3401.

Received: 24 December 2012; in revised form: 25 February 2013 / Accepted: 1 March 2013 /

Published: 6 March 2013

Abstract: In this paper, a characterization of an AlSiMg alloy processed by direct metal laser sintering (DMLS) is presented, from the analysis of the starting powders, in terms of size, morphology and chemical composition, through to the evaluation of mechanical and microstructural properties of specimens built along different orientations parallel and perpendicular to the powder deposition plane. With respect to a similar aluminum alloy as-fabricated, a higher yield strength of about 40% due to the very fine microstructure, closely related to the mechanisms involved in this additive process is observed.

Keywords: additive manufacturing (AM); direct metal laser sintering (DMLS); aluminum alloys; light microscopy; electron microscopy; mechanical characterization

1. Introduction

Additive manufacturing (AM) of metal end-useable parts is well recognized as an interesting alternative to other conventional or unconventional processes for medium batch production, thanks to its capability to produce complex shapes and integrated parts of a high strength-to-weight ratio [1]. Furthermore, AM techniques have the potential to achieve zero wastage through the use of recycling within the processes. This also results in a reduction in emissions, because fewer raw materials need to be produced. Usually, in molding processes, e.g., die casting, lots of energy and resources are consumed to produce tools like dies and moulds. By contrast AM techniques provide almost unchallenged freedom for design without the need for part-specific tooling [2]. Moreover, in comparison to conventional manufacturing technologies AM techniques do not directly use toxic chemicals, such as lubricant or coolant [3]. Additive technologies directly translate virtual three-dimensional models into physical parts in a quick and easy process. Basically the data is sliced into a series of thin sections, then combined into the AM machine, which subsequently adds them together in a layered sequence [4]. As reported in literature, available AM techniques for the production of metal parts use an energy beam source to create the sections by locally and selectively melting a powder bed [5]. Different approaches can be distinguished:

- Indirect processing, using metal powders mixed with polymer binders;
- Liquid-phase sintering, using a mixture of two metal powders or a metal alloy;
- Full melting, the most recently developed method, using a single metal powder that is fully melted, as the name implies.

The result of the first two approaches is a two-phase material, with a low-melting temperature constituent: they have mainly been used in the past with applications in rapid tooling. By contrast, it could be stated that full melting of metal powders is now suitable for the production of end-useable metal parts [6–13]. However, the performances of the part, in terms of mechanical properties, residual porosity, dimensional accuracy and surface roughness, is closely related to the complex mechanisms involved in heat adsorption and transmission of powders and in melting and consolidation of powders [14–17].

Various European companies produce machines based on laser systems for direct melting or sintering of metal powders beds [18]. In this study, a direct metal laser sintering (DMLS) machine from EOS GmbH able to process reactive materials, such as cobalt–chromium, titanium and even aluminum alloys, thanks to its laser power and to the inert atmosphere in the building chamber, has been used. Aluminum powder, in particular, broadens the range of possible applications of DMLS to lightweight structural components. To be confident about designing parts for structural applications with this technological process and the material selected, using, for example, FEA (Finite Element Analysis), it is fundamental to have a mechanical characterization of the parts that can be fabricated in different orientations with respect to the powder deposition plane. Very recently, Brandl *et al.* investigated the microstructure of samples manufactured by a Selective Laser Melting (SLM) using an AlSi10Mg powder alloy with a Trumpf TrumaForm LF130 machine: these samples were fabricated for high cycle fatigue and machined afterwards [19]. Buchbinder *et al.* [20] explored the use of newly designed SLM machine equipped with a high power laser up to 1 KW, focusing on the increase of building rate performances, thus, on the laser parameters settings. Olakanmi *et al.* [21,22] investigated

the effects of particle size distribution, particle packing arrangement and chemical constitution on the laser sintering of hypoeutectic Al–Si powders and the effect of the processing parameters on the densification mechanism and microstructural evolution in laser sintered Al-12Si powders. Another research group explored the feasibility of introducing high strength aluminum alloys for industrial applications, concentrating mainly on the production of custom powder systems with different particle sizes and different distributions of elementary components [23]. In addition, common materials science literature has some references to the use of aluminum and its alloys for metal matrix composites by additive manufacturing, even though this route is still at an initial stage [24–26]. On the basis of the previous considerations, the present work deals with an experimental characterization of an AlSiMg alloy starting from the commercial powders distribution and chemical analyses through to the estimation of the mechanical properties of parts produced with a DMLS machine in four different building orientations and, subsequently, post-treated only by means of shot-peening. Hence the effect of the DMLS process on the microstructure of the final components before and after tensile tests was evaluated by light and electron microscopy.

2. Materials and Methods

The AlSiMg powders supplied by EOS GmbH were characterized by a Field Emission Scanning Electron Microscope (FESEM, Zeiss SupraTM 40) in order to evaluate their shape and dimensions and then by means of laser granulometry (Fritsch model Analysette 22 Compact) to estimate their size distribution (with volume assumption). The powder chemical composition was assessed through an Inductively Coupled Plasma (ICP) test, in compliance with ISO/IEC 17025; this type of analysis reveals the percentage in weight of the main alloying elements.

The aluminum alloy specimens for the physical and mechanical characterization were prepared by DMLS with an EOSINT M270 Xtended version. In this machine, a powerful Yb (Ytterbium) fiber laser system in an Ar atmosphere is used to melt powders with a continuous power up to 200 W. The detail of the DMLS process, together with the choice of the process parameters to obtain a part with the highest density and the best surface finishing, were described in an earlier study [27], and the values are given in Table 1. As explained in this previous study, the machine employs different parameters for the core of a part, for its lower and upper surfaces parallel to the building plane and for the lateral outer surface, called the contour, as illustrated in Figure 1a. The core and the skin correspond to 2-dimensional surfaces scanned by the laser source, while the contour corresponds to a 1-dimensional closed-type line. First of all, the contour of the layer structure is exposed; then, all of the inner area delimited by the contour is scanned through hatching: the laser beam moves line after line several times (Figure 1b), and the distance between the lines is called the hatching distance. Finally a second exposure of the exterior part contour is carried out to make sure that the part edges correspond exactly to the CAD data, and that part can thus be built with the correct dimensions.

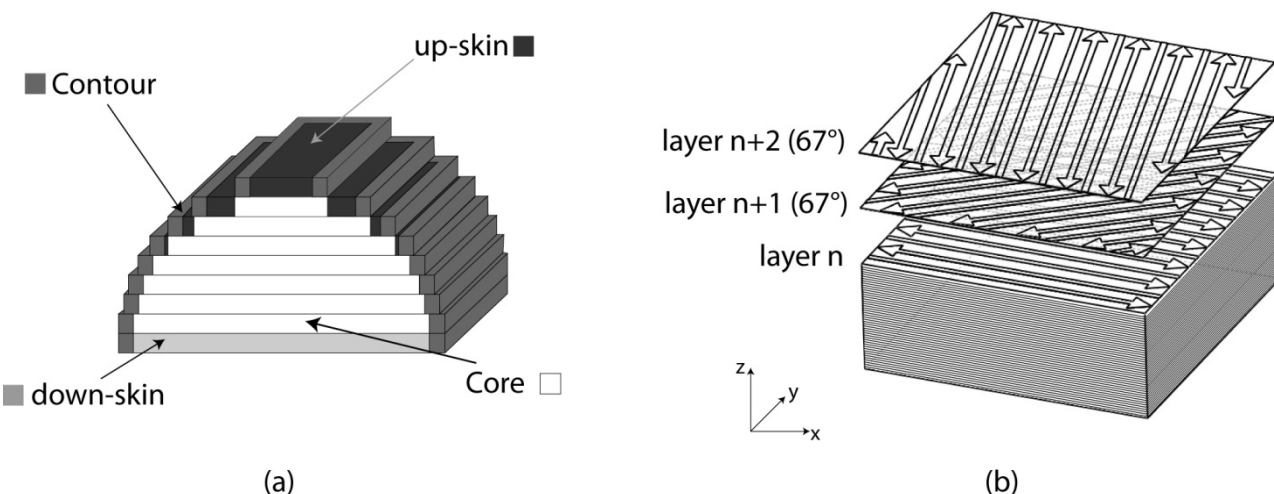
Layer thickness and scanning strategy are also fundamental parameters. The thinner the powder layer, the greater the degree of interlayer bonding and, so, the higher the final density that can be obtained. However, if a too small value is chosen, the speed of manufacturing (and, therefore, the cost) become too slow.

As regards the scanning strategy associated to the core and to the skin, a certain degree of rotation between the layers leads to a better overlapping of these. This should make the properties of the parts obtained more isotropic in comparison with more conventional scanning strategies made of layers with unidirectional vectors or at least with a cross-ply pattern. As shown in Figure 1b, in this study, the direction of scanning is rotated of 67° between consecutive layers. The skin is made up of three layers.

Table 1. Direct metal laser sintering (DMLS) process parameters employed.

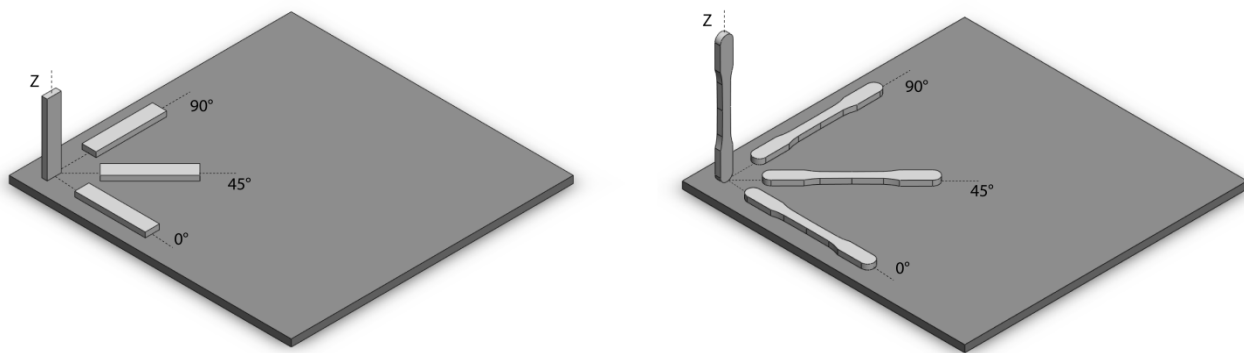
Parameters	Skin	Core	Contour
Scan speed (v) [mm/s]	900	800	900
Laser power (P) [W]	120	195	80
Hatching distance (h_d) [mm]	0.1	0.17	—
Layer thickness [μm]	30	30	—
Laser spot size [mm]	0.01	0.01	0.01

Figure 1. The scanning strategy employed in this work: (a) the parameters considered with different power and scanning speed; (b) the non-contour area of each layer is rotated of 67° in comparison to the previous one.



All samples for physical and mechanical evaluations were fabricated along different orientations using the above mentioned optimized parameters and scanning strategy. The orientations considered (see Figure 2) are along the z axis, called the “build direction”, and along three directions on the building platform (xy -plane): parallel to the direction of the powder deposition (0°), along the normal axis to it (90°) and at 45° between them. Samples of rectangular shape and $50 \times 10 \times 5$ mm size were produced to analyze the density, hardness and Young’s Modulus (Figure 2a). Considering tensile tests, five specimens for each orientation were built according to the standard ASTM E8M and along the above described orientations (Figure 2b). To verify the reliability and reproducibility of the process, the fabrication of these samples was repeated twice.

Figure 2. The four different orientations considered for producing DMLS aluminum alloy specimens.



Due to the high thermal gradients, this process fabricates parts with high residual thermal stresses. In order to avoid the bending of the parts, before removing them from the building platform, it was necessary to perform an annealing for 2 h at 300 °C. The samples were then shot-peened (Ecoblast/F machine, by Silco S.r.l.—Italy) to improve the surface quality and integrity. As a result of previous analysis [27], in this study, glass beads of 200 μm diameter with an air pressure value of 8 bar for several seconds were used. These beads produce a clean, bright, satin-finished surface, with an R_a average value of 3 μm without dimensional change or contamination of the parts.

The density of the specimens was measured by the water displacement method (Archimedes), and the measurements were expressed using the mean value. The standard deviation is less than 0.05 g/cm³. Then, samples were polished down to 1 μm diamond paste to allow Vickers microhardness measurements performed by a Leitz instrument (load 50 g for 30 s): fifteen measurements were done to calculate a mean hardness value for each orientation. Elastic modulus was evaluated by an impulse excitation technique involving the analysis of the transient natural vibration, by means of a GrindoSonic MK5 instrument, according to the standard ASTM C1259. For microstructure analyses, the DMLS samples were cross-sectioned perpendicular and parallel to the building platform, then polished down to colloidal silica suspension (size 0.05 μm) and etched with Weck's reagent (KMnO₄ and NaOH in distilled water) for 15 s; after that, they were observed by an optical microscope (Reichert Young MF3) and by FESEM. All the microstructural images refer to the core of the parts.

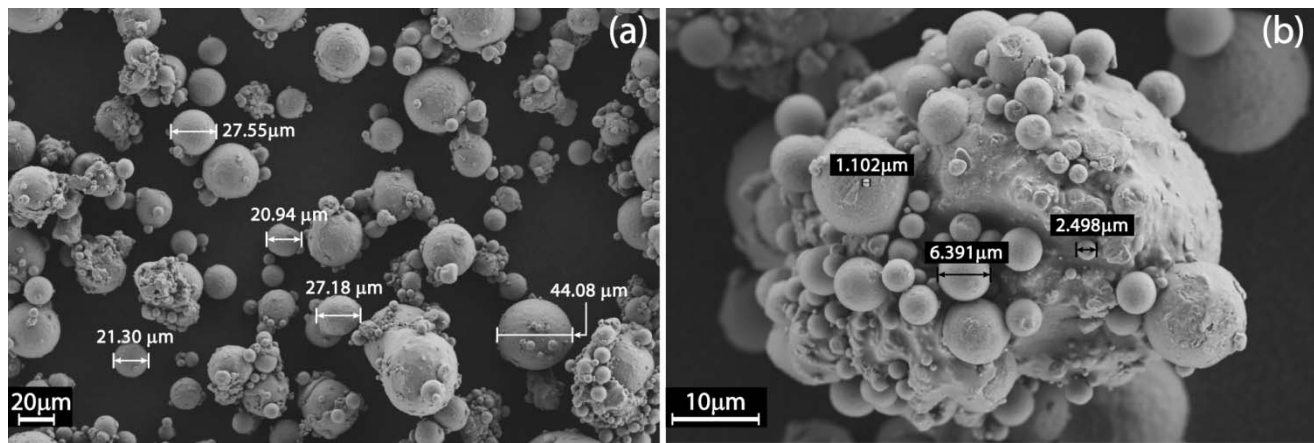
Finally, tensile tests were performed on an EASYDUR 3MZ—5000 testing machine, with a free-running crosshead speed of 2 mm/min: strain was measured by a piezo-electric extensometer. After rupture, the fracture surfaces were observed by Field emission scanning electron microscopy (FESEM).

3. Results

3.1. Powder Characterization

As illustrated by Figure 3a, the as-received gas atomized aluminum alloy powder particles are spherical and quite regular in shape, ranging in dimensions from 1 to 44 μm , with an average around 21–27 μm .

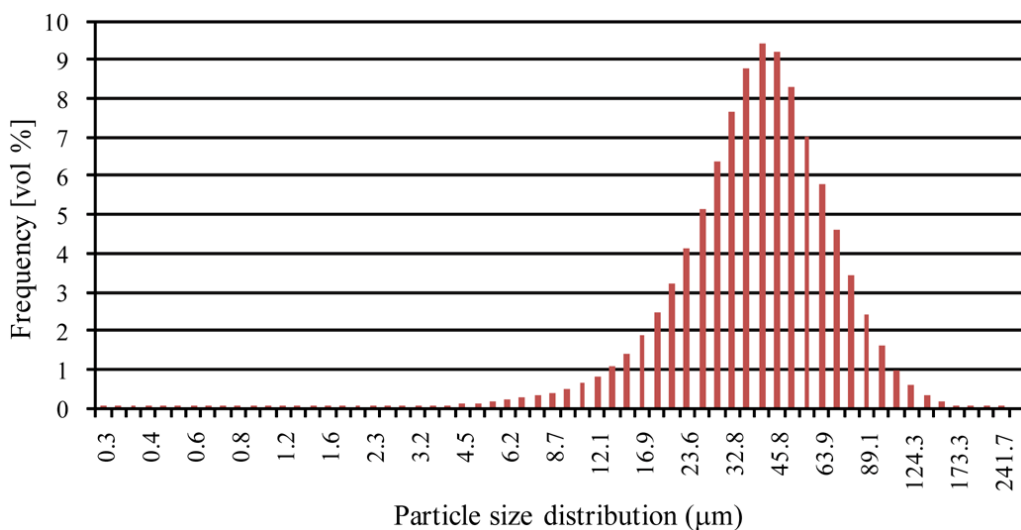
Figure 3. The as-received aluminum alloy powder observed by field emission scanning electron microscope (FESEM).



The numerous smallest particles, with mean diameters less than 10 μm , tend to agglomerate on the surface of the bigger ones (Figure 3b), creating some clusters of about 60 to 80 μm , and this could be detrimental for the final density of the DMLS parts, considering that the layer thickness employed in this research is of 30 μm .

This tendency is confirmed by the granulometric analyses reported in Figure 4. The diameters corresponding to 10% (d_{10}), 50% (d_{50}) and 90% (d_{90}) of the cumulative size distribution are 19.3 μm , 40.7 μm and 74.8 μm , respectively. In the graph of Figure 4, the frequency distribution is based on a volumetric assumption. This means that even if the small particles are far more than the bigger ones in number, their mean volume is three orders of magnitude less than the big ones: for this reason, they could not be displayed.

Figure 4. Particle size distribution of as-received aluminum alloy powder.



In addition to the particles size and distribution, also their chemical composition could affect the densification in DMLS process, as observed by Olakanmi *et al.* [22]. The values of the chemical analyses conducted via ICP test are summarized in Table 2. As can be seen, the main alloying elements are silicon and magnesium, as expected, but there is also an appreciable quantity of iron.

Table 2. Chemical composition of aluminum alloy powder as determined by inductively coupled plasma (ICP) test.

Element	Weight (%)
Si	10.08
Fe	0.16
Cu	0.001
Mn	0.002
Mg	0.35
Zn	0.002
Ti	0.01
Al	balance

3.2. Mechanical Characterization

In Table 3 are summarized the mean values for density, Young's modulus and Vickers Hardness. Moreover, considering for the AlSiMg alloy a theoretical density of 2.68 g/cm^3 [28], the percentage of the residual porosity can be calculated: it ranges from 0.7% to 0.8%, so it is indeed low.

Table 3. Density, Hardness and Young's Modulus of aluminum alloy DMLS specimens.

Orientation	Density (g/cm^3)	Residual Porosity (%)	Hardness (HV)	Young's Modulus E (GPa)
xy -plane	2.66	0.8	105 ± 2	73 ± 1
z axis	2.66	0.7	108 ± 3	72 ± 1

It was observed that the AlSiMg DMLS samples have isotropic properties when built on the xy -plane, as expected from the scanning strategy adopted in this study. For this reason, a single mean value for each property is reported in the table. Considering the samples built along the z axis direction, there are some differences, but they could be considered negligible.

Hardness is well recognized as a first indication for mechanical properties: using micro-Vickers, the measurements could be done relatively close to each other, making it possible to investigate the change of hardness of the DMLS parts with depths. The mean value profiles obtained along the total length of four rectangular bars for each orientation are very close and with flat trends. Thus, in a first approximation, it can be assumed that the samples were also homogeneous in terms of microstructure along the whole section.

Considering tensile tests, the results are summarized in Table 4. Variations were not found among performances of samples with different orientations on the powder deposition plane, while there are some differences with the values obtained along the direction perpendicular to it.

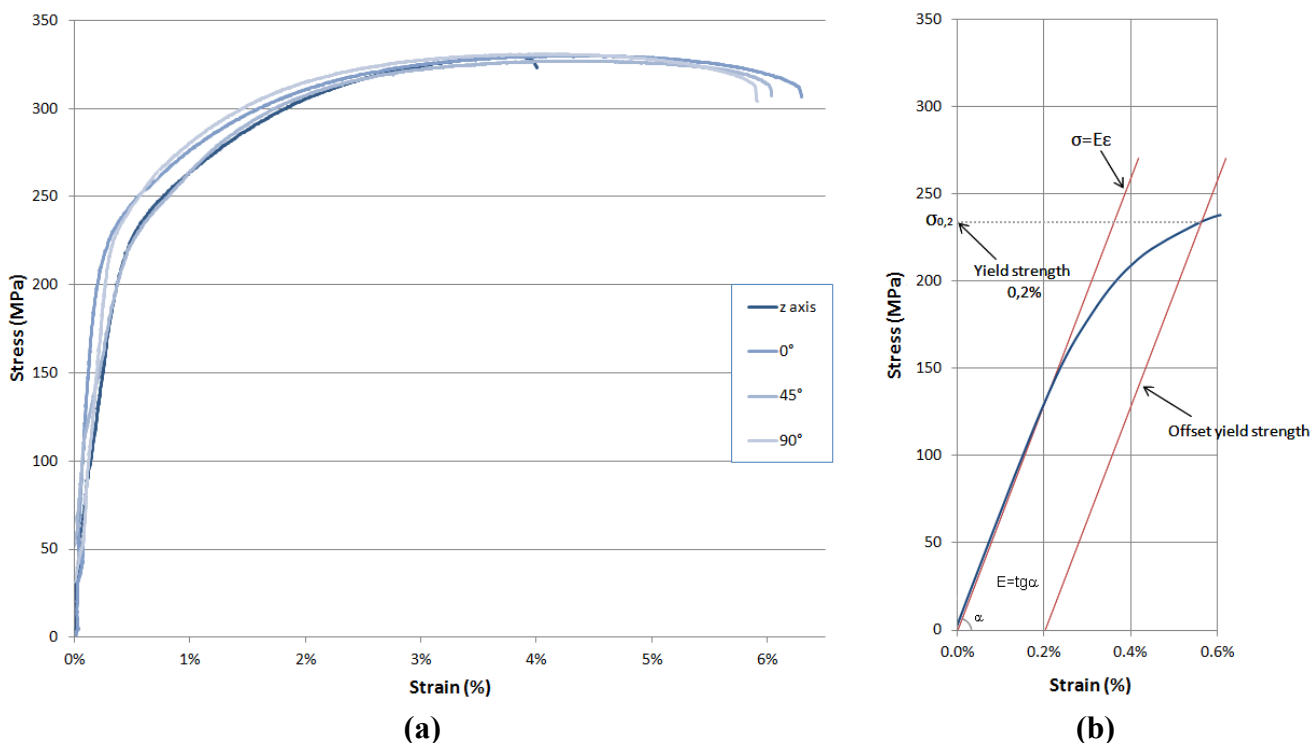
In Figure 5a are shown the representative trends of stress-strain curves for each orientation considered. As can be seen, the results are well reproducible. In Figure 5b, it is graphically explained how the yield strength values were calculated: this is shown for a typical stress-strain curve of a sample along the build direction. Considering the tangent to the curve in the elastic region, the values for the Young's modulus could also be estimated: it was confirmed that they are in good agreement with the results obtained by the impulse excitation technique.

Table 4. Mean values of tensile properties of aluminum alloy DMLS specimens produced according the standard ASTM E8M along different orientations, compared to a similar alloy as-fabricated.

Material	Orientation	Yield Strength $\sigma_{0.2}$ (MPa)	Ultimate Tensile Strength σ_{UTS} (MPa)	Elongation at break (%)
AlSiMg after DMLS	xy -plane	243 ± 7	330 ± 3	6.2 ± 0.3
	z axis	231 ± 3	329 ± 2	4.1 ± 0.2
A360.0 F *	—	170	317	5

* Temper and product form: as-fabricated [28].

Figure 5. (a) Typical stress-strain curves for aluminum alloy DMLS specimens built along four different orientations; (b) yield strength and Young's modulus evaluation for the representative curve of a specimen along z axis.



3.3. Microstructure and Fracture Surface Analyses

The AlSiMg DMLS samples microstructure was initially analyzed by light microscopy. Figure 6 shows micrographs of two cross sections: a section parallel to the build direction, indicated by the black arrow (Figure 6a), and a section perpendicular to it (Figure 6b). The images refer to the core of the parts.

The etching with Weck's reagent is useful to highlight the molten pools and their contours. During the process, upon irradiation, the powder material is heated, melts and forms a liquid pool. Afterwards, the molten pool solidifies and cools down quickly, and the consolidated material starts to form the product. After a complete layer is scanned, the building platform is lowered by an amount equal to the layer thickness, and a new layer of powder is deposited, following a pattern rotated 67° around z axis, as illustrated in Figure 1.

The laser beam intensity is modulated in such a way as to ensure that the new powder layer is melted and penetrates the previous layer, so remelting it to accomplish a good connection of the layers (wetting of the layer underneath) at the same time. Therefore, considering a section along the build direction, these melt pools are all oriented in the same way (Figure 6a), being a section made by the superimposition of subsequent layers. However, due to the scanning strategy adopted in this study and in account of the above mentioned partial re-melting, the shape of these melt pools is not simply half-cylindrical. Consequently, in this case, it is not possible to define their mean depth. On the other hand, considering the section parallel to the powder deposition plane, it could be assumed to observe the cross-section of melt pools of different layers (Figure 6b): due to the different depth, their contours overlap originating shapes with irregular geometries.

Looking at the micrographs of Figure 6, even if some porosity is visible in the samples investigated, the pores dimension is very little. Going at higher magnifications, it is possible to appreciate their mean size: in Figure 7a, two pores are visible, with a dimension of about 20 μm , while Figure 7b is focused on a single melt pool and its region of contour. As can be observed, the rapid and localized melting and cooling of DMLS originate very fine microstructures.

Figure 6. Optical microscope images of an aluminum alloy DMLS sample after etching with Weck's reagent: (a) a section along the build direction (z axis); (b) a section parallel to the powder deposition plane (xy -plane).

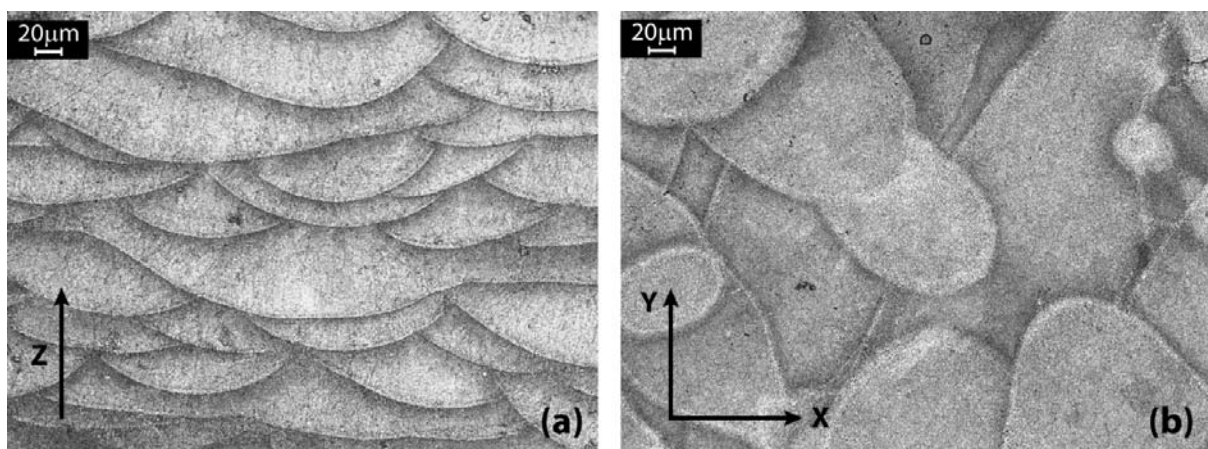
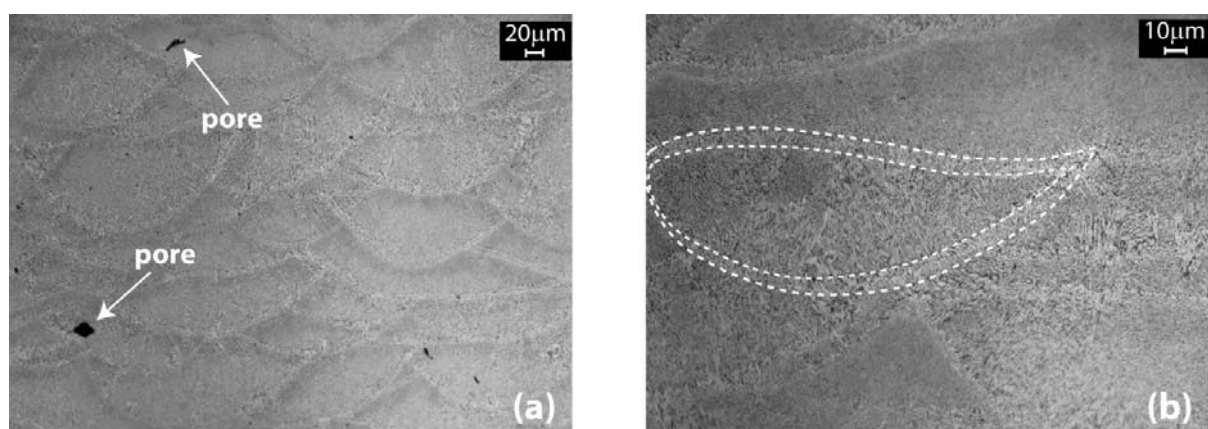


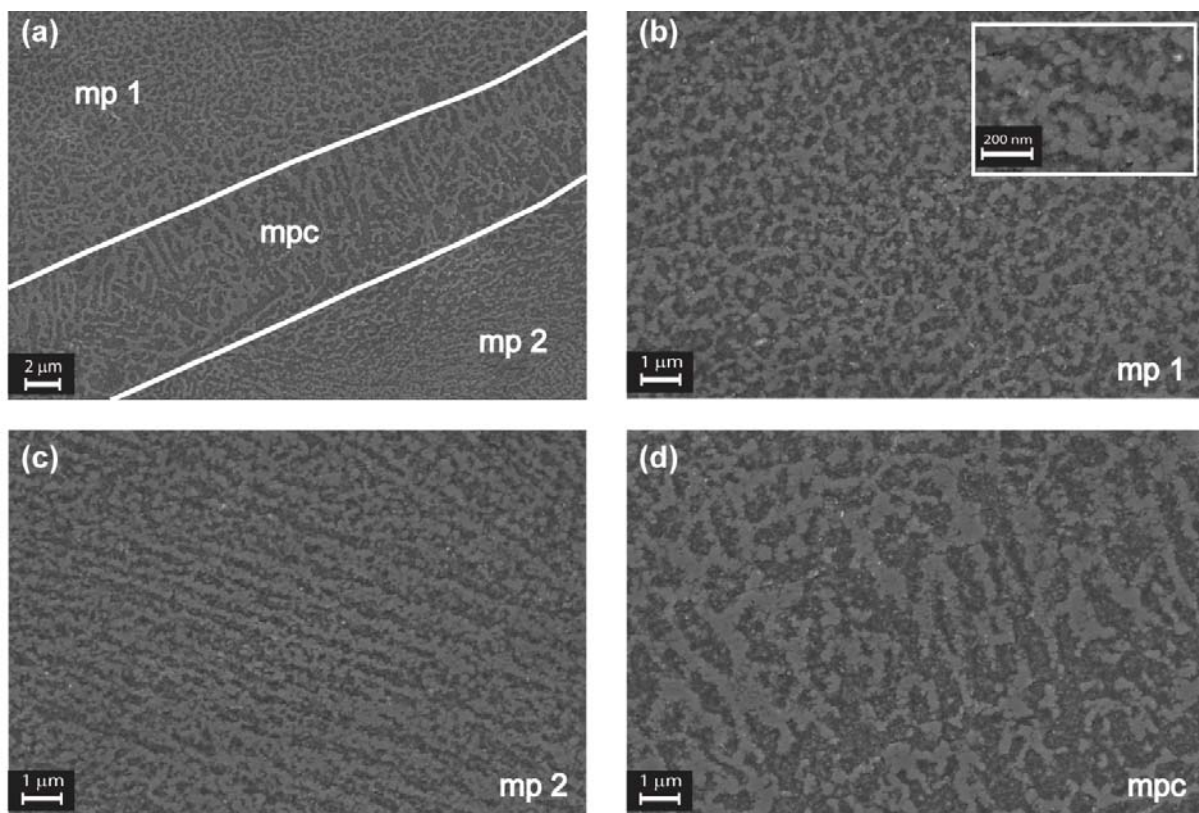
Figure 7. Optical microscope images after Weck's etching showing: (a) the presence of pores and at a higher magnification; (b) the shape of a melt pool with its contour.



To appreciate this small grain size, the section along the build direction was observed by FESEM, focusing on a region between two melt pools, as shown in Figure 8a. The area inside the white parallel lines corresponds to the melt pool contour (mpc), with a mean height of about 8 μm . At higher magnifications, from Figure 8b–d, it can be seen that the three regions (mp_1 , mp_2 and mpc) are characterized by a fine cellular-dendritic structure made by agglomerates of grains with mean diameters of 80 nm or less. It was found that these agglomerates are different in length, thickness and aspect ratio in the three regions.

According to Olakanmi *et al.* [21] it can be assumed that there is little or no free-energy barrier to the phase transformation from liquid to solid. It is due to the complete wetting of the substrate by the molten metal and the nearly ideal interface provided by the partially melted heat affected zone (HAZ) grains at the fusion boundary. In this way, the grains grow epitaxially, and the grain direction is parallel with the local conductive heat transfer, as shown in Figure 8b–d.

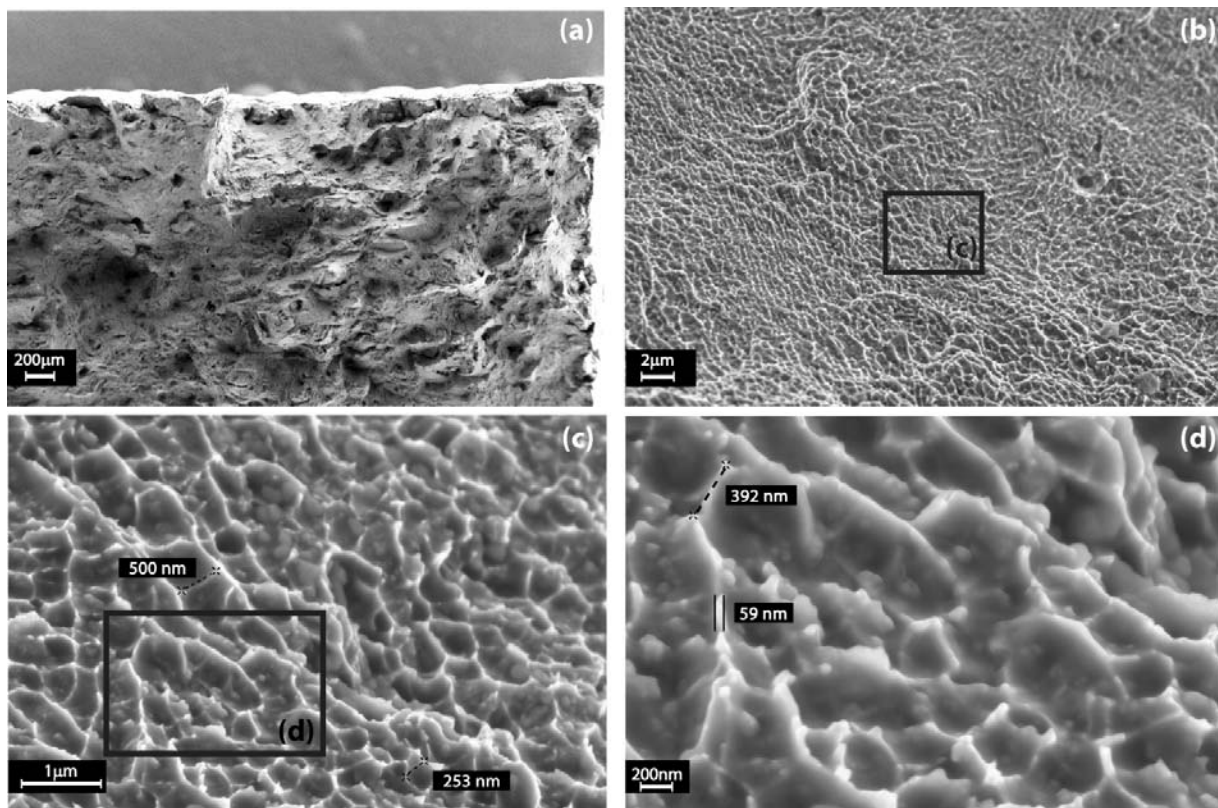
Figure 8. FESEM images of an aluminum alloy DMLS sample after etching with Weck's reagent, sectioned along the z axis: (a) mp_1 and mp_2 are areas of two adjacent melt pools, while the region delimited by the white lines correspond to the melt pool contour (mpc); (b–d) the three regions at higher magnifications. In the inset, it possible to observe the nanometric grain size.



Also, fracture surfaces after tensile tests were investigated by FESEM, as illustrated by Figure 9. It may be assumed that all the samples failed, because of ductile fracture as the result of growth and coalescence of micro-voids. In fact, as observed at higher magnifications reported in Figure 9c,d, the fracture surface is completely covered by very fine dimples, demonstrating also a great ability to

dissipate the energy of fracture. It is possible to appreciate the micro-voids dimensions, from 250 to 500 nm per side, and the dimple thickness, of about 60 nm, a peculiarity of this process.

Figure 9. FESEM images of an aluminum alloy DMLS fracture surface at increasing magnifications: (a–d) it is covered by sub-micrometric voids and dimples with a nanometric thickness.



4. Discussion

From the combination of FESEM and granulometric analyses, it could be stated that the AlSiMg powders employed in this study are made of a large amount of very small spheres and only a few bigger ones. As observed by Simchi [9], finer particles provide a larger surface area to absorb more laser energy, leading to a higher sintering rate. However, before starting the additive process, it is fundamental to sieve the powder to ensure a maximum particle size in agreement with the layer thickness when filling the DMLS machine. Considering the powder chemical composition and comparing it to the literature [28], it could be assumed that this aluminum alloy is similar to the A360.0 alloy, in particular A360.2, which has a nominal density of 2.68 g/cm^3 and a melting temperature around 570°C , due to its near-eutectic composition. This alloy is a typical casting alloy used for example for parts with thin walls and complex geometry. Even if the as-received powders are gas atomized under a nitrogen atmosphere, a thermal treatment for drying them at 80°C for five hours was conducted prior to perform the DMLS process in order to avoid any traces of humidity.

Regarding the mechanical properties investigated (Tables 3 and 4), it could be assumed that they are isotropic for samples built on the building platform plane and slightly different for samples built along a direction perpendicular to it. In particular, if compared with the commercial A360.0 alloy in

as-fabricated conditions [28], AlSiMg DMLS specimens show very high values of yield strength, with an enhancement of about 43% for samples built in the xy -plane and 36% for samples along the z axis. The ultimate tensile strength is a little higher, while for the elongation at break, there is an enhancement on the xy -plane and a decrease along the build direction, as already observed in literature by Tolosa *et al.* [29]. It is well known that this is the weakest direction for samples produced by DMLS. However, the elongation at break is only slightly lower than conventionally processed material.

During the DMLS process, on account of the short interaction times and high conductive heat transfer rate, a very fine microstructure originates. The exposure period of the laser irradiation is in the range of milliseconds. In fact, the process can be considered as “high power density-short interaction time” [9]. The very high cooling rates, ranging between 10^3 and 10^{11} K/s [30], promote greater undercooling, thus producing finer grains and a gradual change in the solidification regime from dendritic to cellular-dendritic. At the same time it is difficult to ascertain the nature of the small amount of precipitates that could be formed due to the non-equilibrium conditions and the solidification conditions associated with the DMLS process. In this study, using the AlSiMg alloy described, Si and Mg₂Si precipitates were expected, but probably they were removed preferentially by the chemical etching employed.

However, looking also at the fracture surfaces analysis, it can be concluded that this very fine microstructure is responsible for the superior overall mechanical properties without the need of a further heat treatment, as usually happens with casting alloys.

5. Conclusions

After characterization and analysis of the starting powders’ size, morphology and chemical composition through to the evaluation of mechanical properties of DMLS as-built specimens, along with microstructural observations, it can be concluded that:

- The AlSiMg powders employed in this study are spherical in shape with an average size of 21–27 μm , but very fine particles with a diameter lower than 10 μm tend to agglomerate, forming bigger clusters of irregular shape. These clusters can adversely affect the flowability of the powders: so, it is fundamental to sieve them before starting the DMLS process.
- Density evaluation of samples indicates a residual porosity of about 0.8%. Microscopic observations show that porosities are very small, on the order of 20 to 30 μm .
- In comparison to the properties of a commercial as-cast A360.0 alloy, AlSiMg DMLS specimens show very high values of yield strength, with an enhancement of about 43% for samples built in the xy -plane and 36% for samples along the z axis. The ultimate tensile strength is slightly higher in both cases, while for the elongation at break, there is an enhancement on the xy -plane and a small decrease along the build direction.
- Microstructure observations show a very fine cellular-dendritic structure by agglomerates of grains with mean diameters of about 80 nm, responsible for the superior overall mechanical properties without the need for a further heat treatment.
- Fracture’s surfaces analysis reveals also a very peculiar behavior: the fracture was caused by coalescence of submicrometric voids, with dimples of nanometric thickness.

This analysis could be the base to properly design lightweight structural components in AlSiMg through DMLS by means of a FEA, for envisaged applications in different fields, such as aerospace, automotive and robotics.

Acknowledgments

The authors gratefully acknowledge Lombardi for her experimental assistance in determining powders distribution.

References

1. Atzeni, E.; Salmi, A. Economics of additive manufacturing for end-useable metal parts. *Int. J. Adv. Manuf. Tech.* **2012**, *62*, 1147–1155.
2. Tuck, C.; Hague, R. The pivotal role of rapid manufacturing in the production of cost-effective customised products. *Int. J. Mass Cust.* **2006**, *1*, 360–373.
3. Kathuria, Y.P. Microstructuring by selective laser sintering of metallic powder. *Surf. Coat. Technol.* **1999**, *116–119*, 643–647.
4. Hopkinson, N.; Hague, R.J.M.; Dickens, P.M. *Rapid Manufacturing: An Industrial Revolution for the Digital Age*; Wiley: New York, NY, USA, 2006.
5. Gibson, I.; Rosen, D.W.; Stucker, B. Design for Additive Manufacturing. In *Additive Manufacturing Technologies*, 1st ed.; Springer: New York, NY, USA, 2010; pp. 283–316.
6. Simchi, A.; Pohl, H. Effects of laser sintering processing parameters on the microstructure and densification of iron powder. *Mater. Sci. Eng. A* **2003**, *359*, 119–128.
7. Simchi, A.; Petsoldt, F.; Pohl, H. On the development of direct metal laser sintering for rapid tooling. *J. Mater. Process. Tech.* **2003**, *141*, 319–328.
8. Kumar, S. Selective laser sintering: A qualitative and objective approach. *JOM* **2003**, *55*, 43–47.
9. Simchi, A. Direct laser sintering of metal powders: Mechanism, kinetics and microstructural features. *Mater. Sci. Eng. A* **2006**, *428*, 148–158.
10. Rochus, P.; Plesseria, J.Y.; van Elsen, M.; Kruth, J.P.; Carrus, R.; Dormal, T. New applications of rapid prototyping and rapid manufacturing (RP/RM) technologies for space instrumentation. *Acta Astronaut.* **2007**, *61*, 352–359.
11. Santos, E.C.; Shiomi, M.; Osakada, K.; Laoui, T. Rapid manufacturing of metal components by laser forming. *Int. J. Mach. Tools Manuf.* **2006**, *46*, 1459–1468.
12. Kumar, S. Selective laser sintering: Recent advances. In *4th Pacific International Conference on Applications of Lasers and Optics*, Wuhan, China, 23–25 March 2010.
13. Yang, J.; Ouyang, H.; Wang, Y. Direct metal laser fabrication: Machine development and experimental work. *Int. J. Adv. Manuf. Tech.* **2010**, *46*, 1133–1143.
14. Niu, H.J.; Chang, I.T.H. Selective Laser Sintering of Gas Atomised M2 High Speed Steel. *J. Mater. Sci.* **2000**, *35*, 31–38.
15. Kruth, J.P.; Mercelis, P.; Van Vaerenbergh, J.; Froyen, L.; Rombouts, M. Binding mechanisms in selective laser sintering and selective laser melting. *Rapid Prototyp. J.* **2005**, *11*, 26–36.
16. Kruth, J.P.; Levy, G.; Klocke, F.; Childs, T.H.C. Consolidation phenomena in laser and powder-bed based layered manufacturing. *CIRP Ann. Manuf. Technol.* **2007**, *56*, 730–759.

17. Wright, C.S.; Dalgarno, K.W.; Dewidarin, M.M. Processing conditions and mechanical properties of high speed steel parts fabricated using direct selective laser sintering. *Proc. Inst. Mech. Eng. B J. Eng. Manuf.* **2009**, *217*, 1651–1663.
18. Wohlers, T. *Additive Manufacturing and 3D Printing State of the Industry: Wohlers Report*; Wohlers Associates Inc.: Fort Collins, CO, USA, 2011.
19. Brandl, E.; Heckenberger, U.; Holzinger, V.; Buchbinder, D. Additive manufactured AlSi10Mg samples using Selective Laser Melting (SLM): Microstructure, high cycle fatigue, and fracture behavior. *Mater. Design* **2012**, *34*, 159–169.
20. Buchbinder, D.; Schleifenbaum, H.; Heidrich, S.; Meiners, W.; Bültmann, J. High power selective laser melting (HP SLM) of Aluminium parts. *Phys. Procedia* **2011**, *12*, 271–278.
21. Olakanmi, E.O.; Dalgarno, K.W.; Cochrane, R.F. Densification mechanism and microstructural evolution in selective laser sintering of Al-12Si powders. *J. Mater. Proc. Tech.* **2011**, *211*, 113–121.
22. Olakanmi, E.O.; Dalgarno, K.W.; Cochrane, R.F. Laser sintering of blended Al-Si powders. *Rapid Prototyp. J.* **2012**, *18*, 109–119.
23. Bartkowiak, K.; Ullrich, S.; Frick, T.; Schmidt, M. New developments of Laser Processing Aluminium Alloys via additive manufacturing technique. *Phys. Procedia* **2011**, *12*, 393–401.
24. Simchi, A.; Godlinski, D. Effect of SiC particles on the laser sintering of Al-7Si-0.3Mg alloy. *Scr. Mater.* **2008**, *59*, 199–202.
25. Ghosh, S.K.; Saha, P.; Kishore, S. Influence of size and volume fraction of SiC particulates on properties of *ex situ* reinforced Al-4.5Cu-3Mg metal matrix composite prepared by direct metal laser sintering process. *Mater. Sci. Eng. A* **2010**, *527*, 4694–4701.
26. Kumar, S.; Kruth, J.P. Composites by Rapid Prototyping Technology. *Mater. Design* **2010**, *31*, 850–856.
27. Calignano, F.; Manfredi, D.; Ambrosio, E.P.; Iuliano, L.; Fino, P. Influence of process parameters on surface roughness of aluminum parts produced by DMLS. *Int. J. Adv. Manuf. Tech.* **2012**, doi:10.1007/s00170-012-4688-9.
28. ASM International. *ASM Handbook, Volume 2, Properties and Selection: Non ferrous Alloys and Special-Purpose Materials*; ASM International the Materials Information Company: Materials Park, OH, USA, 1990.
29. Tolosa, I.; Garciandía, F.; Zubiri, F.; Zapirain, F.; Esnaola, A. Study of mechanical properties of AISI 316 stainless steel processed by “selective laser melting”, following different manufacturing strategies. *Int. J. Adv. Manuf. Tech.* **2010**, *51*, 639–647.
30. Steen, W.M. *Laser Material Processing*, 3rd ed.; Springer: Berlin, Germany, 2003; pp. 279–284.

© 2013 by the authors; licensee MDPI, Basel, Switzerland. This article is an open access article distributed under the terms and conditions of the Creative Commons Attribution license (<http://creativecommons.org/licenses/by/3.0/>).

Research on rapid manufacturing of CoCrMo alloy femoral component based on selective laser melting

Changhui Song · Yongqiang Yang · Yunda Wang ·
Di Wang · Jiakuo Yu

Received: 16 January 2014 / Accepted: 7 July 2014 / Published online: 23 July 2014
© Springer-Verlag London 2014

Abstract In order to meet the high suitability requirements of a femoral component in total knee arthroplasty (TKA), direct and rapid manufacturing of customized CoCrMo alloy femoral components by selective laser melting (SLM) was studied in this paper. When directly manufacturing CoCrMo alloy femoral component by SLM, the processability of CoCrMo alloy is an important factor in successful manufacturing and was firstly analysed in this paper, including the optimizing process for high density and high mechanical properties. Then the femoral component designed to meet the requirement of customized, the display and corresponding supports were discussed to achieve less production time and cost. At last, accuracy of femoral components directly manufactured by SLM was obtained by a contrastive detection method between a 3D scan model of manufactured customized femoral component and designed digital 3D model. The results show that a customized total knee replacement femoral component can be processed with high efficiency and high quality by the direct SLM manufacturing method. This study provides an important method for customized implant rapidly manufactured by SLM.

Keywords Additive manufacturing · CoCrMo alloy · Selective laser melting · Customized femoral component · Rapid response

C. Song · Y. Yang · Y. Wang (✉)
School of Mechanical and Automotive Engineering, South China University of Technology, Guangzhou, Guangdong 510640, China
e-mail: mewdlaser@scut.edu.cn

C. Song
e-mail: song_changhui@163.com

Y. Yang
e-mail: meyqyang@scut.edu.cn

J. Yu (✉)
Institute of Sports Medicine, Peking University Third Hospital, Beijing 100083, China
e-mail: yujiakuo@126.com

1 Introduction

Currently used total knee replacement component is mainly the standard prosthetic systems. Many researchers studied the difference of knee anthropometry in terms of genders and races, all these studies revealed statistically significant differences [1–3]. Traditional standardization and serialization of prosthetics cannot currently meet the needs of patients, and high suitability, low cost, and rapid response manufacturing are the development directions of such medical products. Particularly, in recent years, with the development of digital orthopedics, doctors and engineers have conducted 3D knee joint reconstruction as well as anatomical and morphology measurement by using reverse engineering, and this work has revealed an urgent requirement for high suitability component in clinical medicine and surgery. However, while most traditional manufacturing technologies focus on standardized mass production, a computer numerical control (CNC) machine can process small-batch single products, but the response speed still cannot meet the needs, and the requirements for machine tool operation are high.

The problem of slow production of customized femoral component with the traditional manufacturing methods needs to be solved. Additive manufacturing (AM) technology has been used for more than a decade and has been widely implemented in the medical field [4–6]. The rapid prototyping provides reference models used for diagnosis, treatment, and surgical guide splints for optimal positioning in surgery, for example, Kontio et al. used individual CAD/CAM rapid prototyping in reconstruction surgery to repair maxillary orbits [7]. In recent years, with the development of electron beam melting (EBM) and selective laser melting (SLM) technologies, the manufacture of metal surgical guide splints and customized prosthetics has become increasingly easier [8, 9].

CoCrMo alloys have been defined as effective metallic biomaterials in the ASTM Standards (2008 Annual Book of ASTM Standards, Section Thirteen, Medical Devices and Services). Gaytan et al. summarized that CoCrMo alloys have been used as materials for orthopedic, cardiovascular, and dental wires because of their excellent mechanical properties, high corrosion resistance, high wear resistance, and so on [10]. Their wear resistance propensities are particularly excellent compared with those of other metallic biomaterials such as titanium (Ti) alloys and stainless steels, which is a major advantage for sliding parts in artificial joints. Researchers are now paying attention to the additive manufacturing processes of CoCrMo alloys. Pupo et al. studied scanning space analysis in selective laser melting of CoCrMo powder [11], Monroy et al. studied the pore formation on CoCrMo alloys by an SLM manufacturing process [12], and many application studies have focused on dental applications, such as a study by Averyanova et al. on manufacturing of Co-Cr dental crowns and bridges by SLM technology [13]. However, there has been little study on implants for total knee arthroplasty.

This article delves into the SLM manufacturing process of customized CoCrMo alloy femoral component, which includes density optimization of the CoCrMo alloy SLM process, testing of mechanical properties, display and supports, accuracy of SLM manufacturing femoral components, and so on. The obtained results provide a case reference for directly and precisely manufacturing customized implants for total knee arthroplasty.

2 Experiment apparatus and method

2.1 SLM system and material

The study was conducted with the independently developed SLM RM system Dimetal-100. Its main process parameters are shown in Table 1. The processing procedure follows the basic principles of rapid prototyping, as shown in Fig. 1.

A gas-atomized CoCrMo alloy powder was used in this experiment. Table 2 shows the powder's chemical composition. The powder is spherical and its size distribution is $d(v, 0.5) < 28.5 \mu\text{m}$, its mean diameter is $22 \mu\text{m}$, and its apparent density is 4.2 g/cm^3 .

Table 1 Main process parameters of Dimetal-100

Item	Parameter	Item	Parameter
Wavelength of fiber laser	1,075 nm	Focus length	163 mm
Max laser power	200 W	Max fabrication size	100×100×150 mm
Beam coefficient M2	≤1.1	Range of scanning speed	50–2,000 mm/s
Focus beam size	50–70 μm	Layer thickness	20–50 μm

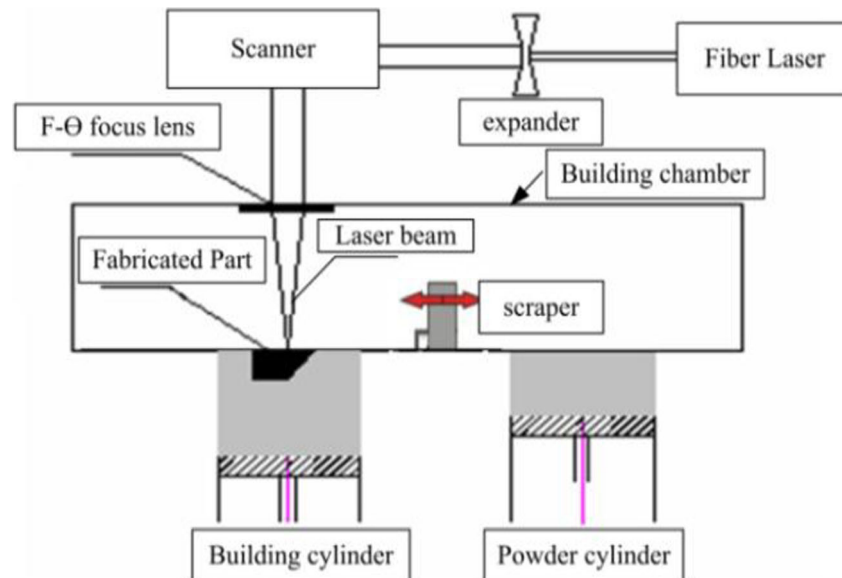
2.2 Experiment procedures

In order to optimize the manufacturing process of the CoCrMo alloy, an “inter-layer stagger” scanning strategy, in which scanning lines of the scanning layer lie between the two consecutive scanning lines of the previous scanning layer, was added to the orthogonal X-Y scanning so as to enhance density [14], as shown in Fig. 2. As did by Yadroitsev et al. in their studies, the main effect of scanning laser line power ψ was used to experimentally evaluate the relative density [15]. ψ , as the ratio laser power P and scanning speed v , could be expressed with the formula $\psi = P/v$. The specimens with the dimension of $10 \times 10 \times 10 \text{ mm}$ were manufactured under the same conditions and environment, except different powers and scanning speeds (see Table 3). The repeatability is considered to be three times, therefore, the total number of samples was $3 \times 16 = 48$, whose densities ρ are measured by drainage. Firstly, the samples' masses m are measured in the air, and then mass after sealing by wax m_0 is measured. Finally, the masses after sealing wax in water m_1 are measured. The density formula is $\rho = m \cdot l_0 \times 100 / [(m_0 - m_1) \times l_1]$. The temperature is 20°C in measurement, the distilled water density l_0 is 0.988 g/cm^3 under the standard atmospheric pressure, and the CoCrMo alloy density l_1 is 8.29 g/cm^3 in this paper.

Using the optimized processing parameters with highest density, the standard tensile specimens, designed according to Chinese national standard GB/T2002, were directly manufactured by SLM while being placed orthogonal to the direction of the laser beam as shown in Fig. 3. A Model GP-TS2000M/100 kN high temperature electronic universal tester with a displacement speed of 1 mm/min was used to obtain fracture load of these samples. The microstructures and microhardness are examined by SEM and microhardness.

Referring to a CT image (DICOM format) of a Chinese female, a femoral STL format 3D model is obtained by means of thresholding with predefined thresholds set as 226–1,792 Hu and regional growth and 3D calculation by using Mimics 16.0 software. The surgeon conducted a cutting operation on a 3D femoral model by using Geomagic Studio software and measured the characteristics of osteotomy by

Fig. 1 SLM manufacturing principles



using the included measurement function of the Geomagic Studio software. According to anatomical data, characteristic modification was conducted on commercialized products of CAD models so as to reach high suitability for femoral osteotomy morphology of patients; the modified 3D model of a highly suitable prosthesis is shown in Fig. 4.

The 3D model was placed and underwent an addition optimization through Magic 14.0 software, then was directly fabricated by Dimetal-100. The accuracy of the customized femoral component was tested by comparing the designed 3D model with a 3D scanning model gained from a Vtop200BS device.

3 Results and discussions

3.1 Analysis of CoCrMo alloy processability

3.1.1 Optimization of process parameters

Only when a dense part is fabricated can the strength be guaranteed. The cubes with different parameters fabricated by Dimetal-100 are shown in Fig. 5. The density testing results are shown in Fig. 6. Polynomial fitting is conducted between laser power/scanning speeds (P/V)

Table 2 CoCrMo alloy powder chemical compositions (mass fraction %)

Cr	Mo	Si	Mn	Fe	N	C	Ni	p	Co
29.4	6	0.8	0.75	0.26	0.19	0.15	0.09	0.008	Bal.

and corresponding density values, as shown in Fig. 7. We can find that the density value follows a trend of increasing and then decreasing. When the energy input is below 0.36 J/s, the density increases with an increase of energy input. This is a process in which powders tend to completely melt and total metallurgical bond with an increase of energy input. When the energy input is more than 0.36 J/s, however, the density begins to reduce, which the melt pool may vaporized partly since the energy input is too large, resulting in gas cavity formation in the powder melting-solidification process, besides energy shockwave bringing surrounding powder makes insufficient powder in laser irradiating powder zone, which causes process defects. In most cases, the density decreases with an increase in scanning speed under the same laser power, however, low density still appears under the situation of excessive laser power and too low scanning speed. A number of experiments

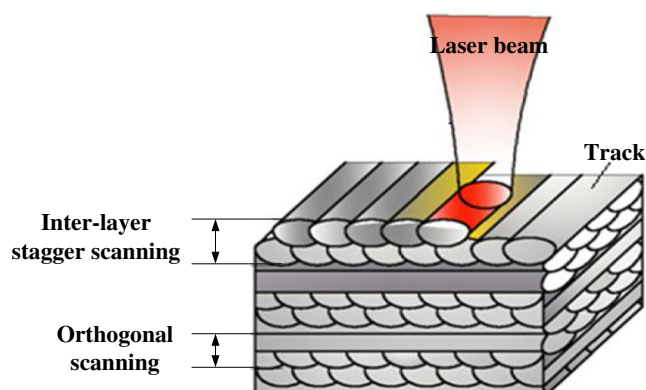


Fig. 2 SLM scanning strategy combining orthogonal scanning and inter-layer stagger scanning together

Table 3 Density optimized experiments of the cube fabricated by SLM

Parameters	Value #1	Value #2	Value #3	Value #4
Laser power (W)	150	160	170	180
Scanning speed (mm/s)	400	500	600	700

verified that when the energy input is 0.36 J/s, the density reaches 99.02 %, given a laser power of 170 W and a scanning speed of 472 mm/s. Figure 8 shows the front and side microstructure of the cube directly fabricated by SLM obtained at this optimization of process parameters.

According to this study and other previous studies, the conditions for fabricating dense parts with CoCrMo alloy are summarized as follows: (1) the laser energy input per unit time and unit area completely melts the metal powder and prevents material vaporization; (2) the weldability of the powder material is good and the oxygen content is low; (3) the powder spreading surface is smooth and the thickness shall be less than 50 μm ; and (4) the oxygen content of the manufacturing chamber is low.

3.1.2 The mechanical properties of CoCrMo alloy manufactured by SLM

As for practical applications, one of the crucial issues is that the component should have enough strength to stand the load. Thus, the mechanical properties are

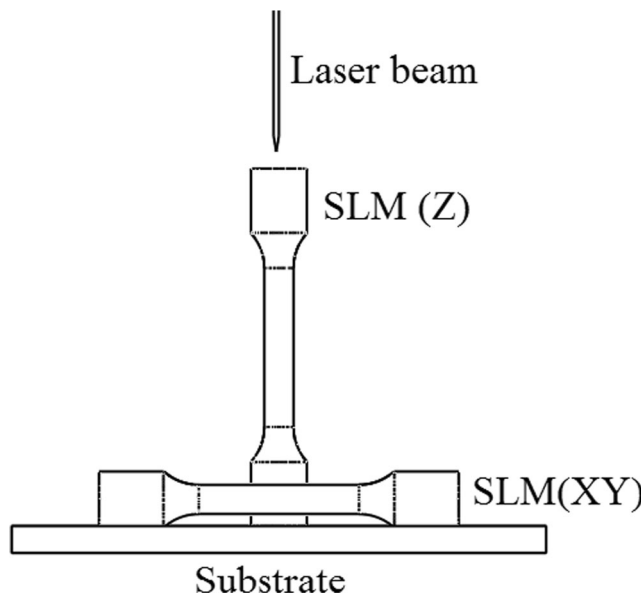


Fig. 3 Tensile specimens placed orthogonal to the direction of the laser beam

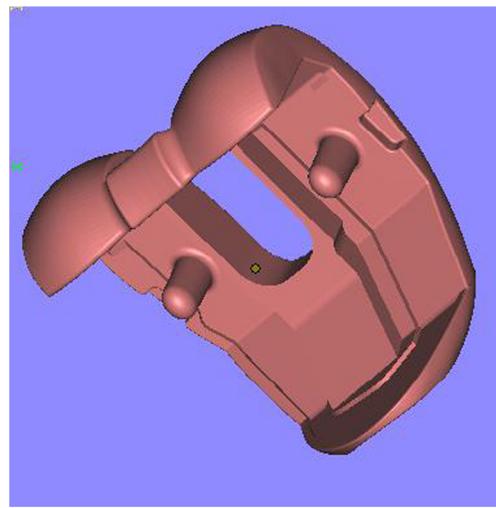


Fig. 4 3D customized femoral components model designed for patient

important. Tensile specimens were manufactured under the optimized process parameters, and the test results were shown in Table 4. The tensile strength and the Rockwell hardness in the XY direction and the Z direction are higher than those of the ASTM F75 standard, but the elongation is lower. This is because SLM process uses a tiny focused spot with high energy density, and the laser beam moves fast. The powder completes the melting-solidification processes in a very short time, so the fine grain strengthening comes into being which improves the tensile strength and hardness. However, according to Hall-Petch, the fine grain strengthening also causes plasticity to slowly increase during the tensile process, which causes the elongation to be lower than that of general castings. The distinctive feature in

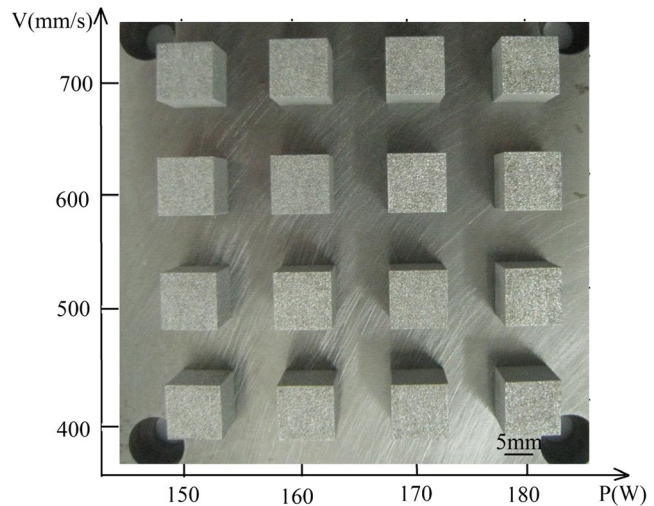


Fig. 5 The cubes fabricated by Dimetal-100 at different process parameters (laser power from 150 to 180 W; scanning speed from 400 to 700 mm/s; scanning space, 80 μm ; and slice thickness, 35 μm)

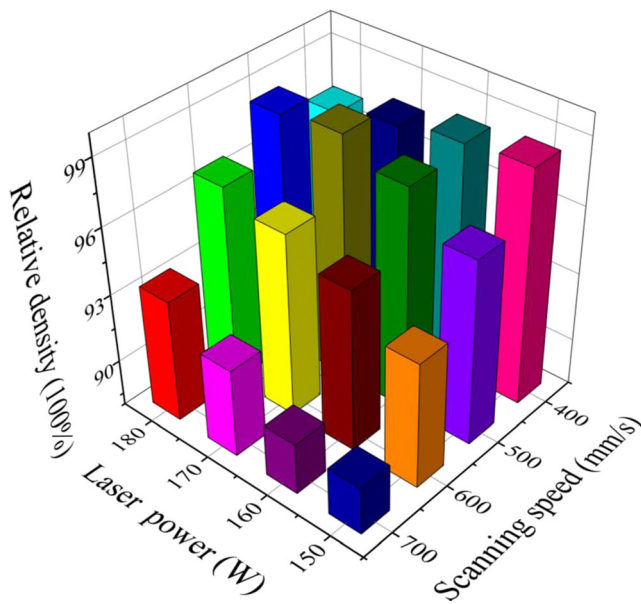


Fig. 6 The densities at different process parameters (laser power from 150 to 180 W; scanning speed from 400 to 700 mm/s; scanning space, 80 μm ; and slice thickness, 35 μm)

XY direction and the Z direction implies that the mechanical properties are anisotropic. The features of Z direction are lower, the main reason could be taken that the interface of the layers is fragile since the specimens were built layer upon layer, and a certain temperature gradient exists when multiple tracks are overlapped or multiple layers build up during the manufacturing process, which causes residual stress to emerge internally. Because of the differences of temperature gradient and residual stress, the mechanical properties are anisotropic. The testing results show that the components by SLM have improved mechanical properties, yet the manufacturing direction should be weighed.

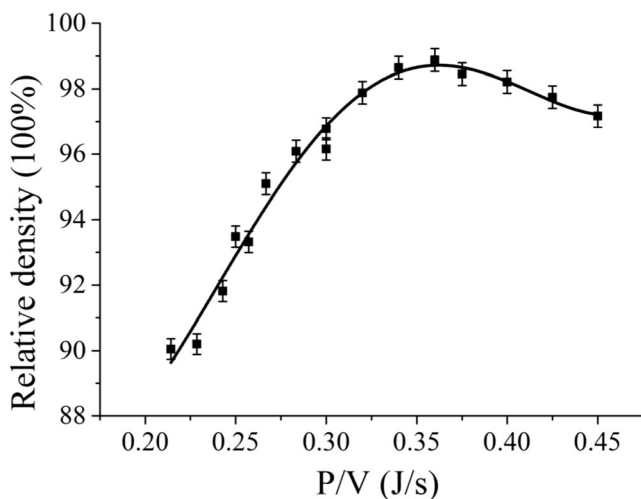
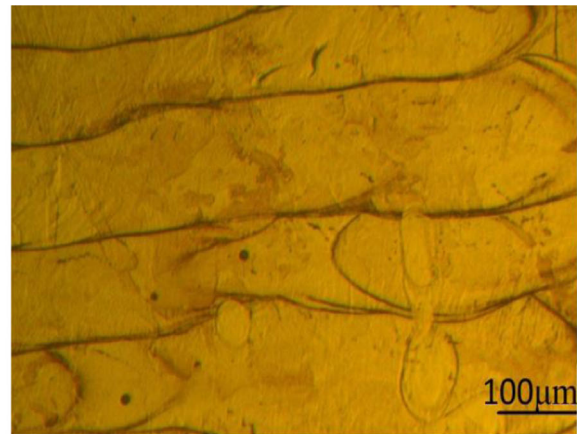
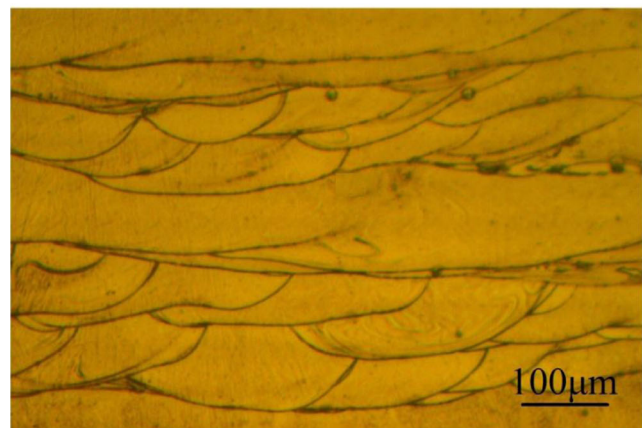


Fig. 7 Relative density with different P/V that from 0.2 to 0.45 J/s



(a) The microstructure of the front surface



(b) The microstructure of the side surface

Fig. 8 The microstructure of CoCrMo sample directly manufactured by SLM ($\times 100$). **a** The front surface fabricated by SLM. **b** The side surface fabricated by SLM

3.2 Data preprocessing for display and support

Display and supports are two important issues in the data process for rapid manufacturing of femoral components. When the femoral components displayed at least height in fabrication direction, the manufacturing time is shortest due to the number of hierarchical layers decrease, the powders-coating time reduce. However, overhang is one of the major structures affecting the manufacturing quality. In the SLM process, the high temperature gradients between melted material and surroundings may lead to warpage as it cools, Kruth et al. also showed when the thermal stress exceeds the strength of the material, and plastic deformation occurs [16]. Meanwhile, the melted liquid-phase material droops due to gravity and capillarity force, the droops deformation on the overhang surface still presence. All could be considered as lack of supports to secure their

Table 4 Mechanical properties of the CoCrMo alloy manufactured directly by SLM

Samples	Number	Tensile strength (Mpa)	Yield strength $\sigma_{0.2}$ (Mpa)	Elongation (%)	Average Rockwell Hardness (HRC)	
					Front	Side
SLM (XY)	1	1,033	740	5.6	38	32
	2	1,061	749	4.8	41	35
	3	1,056	725	5.2	40	33
SLM (Z)	1	982	696	3.6	36	40
	2	970	689	3.9	34	39
	3	958	671	4.1	33	37
ASTM F75	655	450	8		25–35	

firm bonding with the previous layers. Supports are always needed for metal material to avoid defects of collapse, warpage, and so on. But when many support structures are added to the overhang surface, the surface quality may be poor after the supports are removed. Through the overhang test at the optimized process parameters, as shown in the Fig. 9, the maximum overhang angle was determined that when the inclination angle $\theta \geq 40^\circ$ and the overhanging structures were fabricated well, but when the angle $\theta \leq 35^\circ$, the warpage effect occurred. Moreover, the smaller the inclination angle, the more powder would stick to the downward surface of the overhanging structure [17]. Therefore, when the overhanging structures have an inclination angle $\theta \leq 40^\circ$, supports are needed.

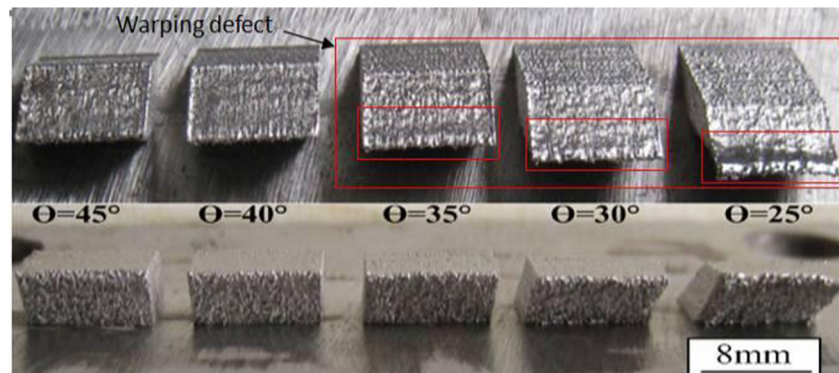
As discussed above, Materialism Company's Magic 14.0 was adopted to generate supports with the

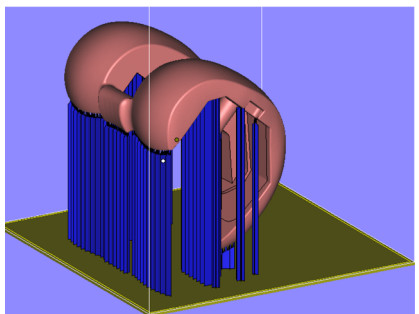
optimized support parameters, wherein the femoral component is marked in red, the supports in blue, and the horizontal substrate in orange. The best display configuration depends on many factors, such as the area of the overhanging structure, building time and cost, and post-processing time. Four displacements are shown in Fig. 10a, b, c, and d, with the type of support, the number of layers, the estimated manufacturing time, and the post-processing time in Table 5.

From the aspects of minimizing the support area, Fig. 10a is the smallest, followed by b, and d, so a can be seen as the optimized display. From the aspects of minimizing post-processing area, since the lateral curved surfaces of femoral component has to be further polished, the unsupported internal bone fixation surface of femoral component needs no additional processing, so in this case b has the larger area for post-processing,

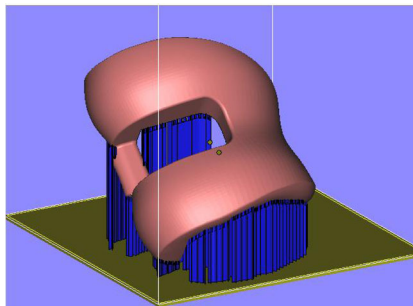
Table 5 Difference between different displacements of femoral component

Item	Layer thickness (μm)	Type of support	Number of layers	Estimated fabrication time (h)	Estimated post-processing time (h)
A	30	Line + block	2,420	7.6	0.7
B	30	Line	2,335	6.9	0.9
C	30	Line + block	2,230	6.7	0.5
D	30	Block	1,689	5.6	0.5

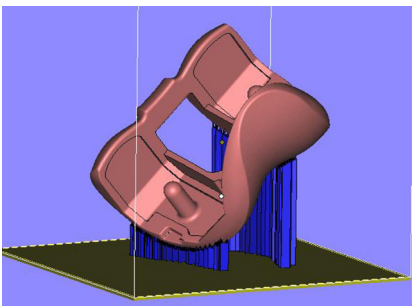
Fig. 9 Experiment of the overhanging structures with different inclined angles



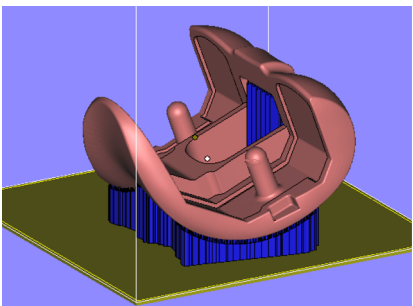
(a) Rotate inside bone fixation surface with X angle of 135°



(b) Rotate inside bone fixation surface with Y angle of 45°



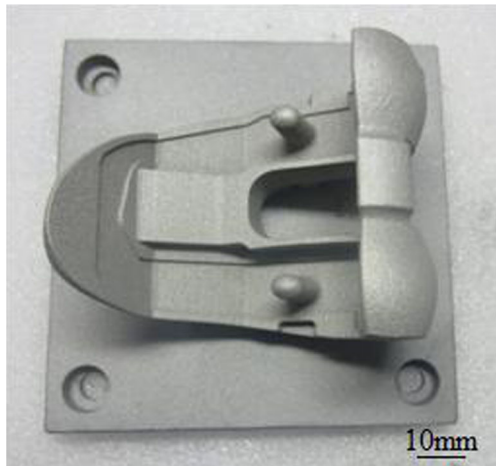
(c) Rotate lateral curved surface with Y angle of 45°



(d) Rotate lateral curved surface with X angle of 15°

Fig. 10 Display and supports for femoral component in Magic14.0. **a** Rotate inside bone fixation surface with X angle of 135°. **b** Rotate inside bone fixation surface with Y angle of 45°. **c** Rotate lateral curved surface with Y angle of 45°. **d** Rotate lateral curved surface with X angle of 15°

c and d have the same area and are the smaller, but for c the added supports for lateral curved surfaces are smallest, so display c as the optimal solution. With manufacturing efficiency and cost aspects taken into consideration, the part displayed at lower height in fabrication direction, the fewer number of hierarchical

**Fig. 11** CoCrMo alloy femoral component directly manufactured by SLM on 10×10 mm substrate

layers lead to shorter manufacturing time, that's we expected. The heights of display a, b, and c in fabrication direction are relatively high, so they need more time for fabrication than d, the display d is the best. From the comprehensive viewpoint, although the display d has a relative large support area at the lateral femoral surface, the post-processing area and fabricating time and cost could be reduced, so in this paper, the display d was adopted.

3.3 Manufacturing and testing in accuracy

Display configuration was determined and shown in Fig. 10d, then the data were imported into Dimetal-100, the part was

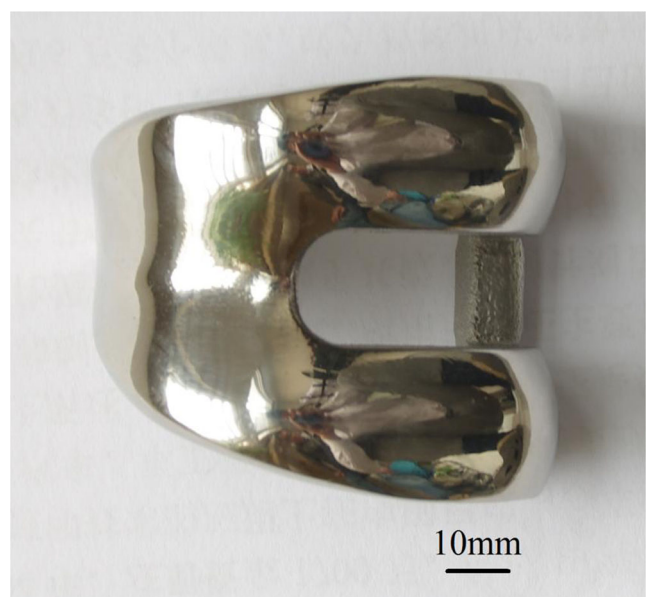
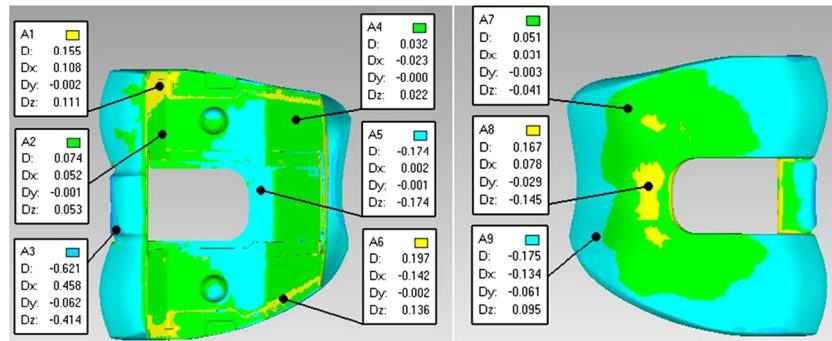
**Fig. 12** The lateral surface of femoral component was polished by hand

Fig. 13 Manufacturing accuracy of SLM detected by reverse engineering



manufactured on the $10 \times 10 \text{ cm}^2$ substrate, and the result is shown in Fig. 11. After removing the supports and simply polishing the outer curved surface by hand, the manufacturing processes were completed and the femoral component was shown in Fig. 12.

The manufactured femoral component was scanned through 3D scanner and packaged as a CAD model. The designed model was then set as a reference model, and the scanned model was set as a contrast model with Geomagic Qualify 2013 software. After automatic overall alignment, their differences were determined and are shown in Fig. 13. While analyzing the accuracy, the maximum positive deviation is 0.621 mm, the maximum negative deviation is 0.458 mm, the average positive deviation is 0.019 mm, the average negative deviation is 0.017 mm, and the standard deviation is 0.030 mm. Therefore, the femoral component manufactured by SLM can meet the requirements of implants in size precision.

The lateral curved surface appeared to have a negative deviation in case of not adding the support and to have a positive deviation in case of adding the support part, which indicates that the lateral curved surface without support was easily warped due to thermal stress in the manufacturing process and that supports can effectively prevent the warpage. The internal bone fixation surface of the model without supports appeared warped with a positive deviation as well. We can say that during the manufacturing, residual stress can lead to warpage and supports can reduce the effect of residual stress on the manufacturing accuracy, however, too many supports can have some influence on follow-up treatments. So, special serious care must be taken to adjust the display and to minimize the supports as much as possible while ensuring accuracy.

4 Conclusions

Several processes for SLM manufacturing of the biomaterial CoCrMo alloy femoral component were discussed, including

the laser power, scanning speed, scanning strategy, display, and supports. The mechanical properties of the CoCrMo alloy manufactured directly by SLM were compared with the ASTM F75 casting standards, which can meet the requirements of medical standards. In order to rapidly obtain the desired biomaterial femoral component manufactured by SLM, this article discussed several key processes as below.

1. Optimizing the SLM manufacturing process of CoCrMo alloy parts, whose density reaches 99.02 %.
2. Obtaining superior mechanical properties under the optimized process parameters.
3. Studying and optimizing the display of the femoral components in the SLM data preprocessing stage.
4. Manufacturing the high accuracy femoral component with standard deviation of 0.03 mm.

This experiment focused on the process feasibility for manufacturing a CoCrMo alloy femoral component by SLM. In practical applications, the biocompatibility, corrosion resistance, wear resistance, and fatigue life should be the next study direction of the authors.

Acknowledgments This study was funded by the National Natural Science Foundation of China (No. 51275179), the Beijing Science and Technology Planning Projects of the Beijing Science and Technology Committee (No. Z131100005213004), and the Instrument Research Project of the National Natural Science Foundation (No. 81327001).

References

1. Bing Y, Kartik MV, Songtao A, Tingting T, Rubash HE, Li G (2011) Differences of knee anthropometry between Chinese and White men and women. *J Arthroplasty* 26:124–130
2. Iorio R, Kobayashi S, Healy WL, Cruz AI Jr, Ayers ME (2007) Primary posterior cruciate-retaining total knee arthroplasty: a comparison of American and Japanese cohorts. *J Surg Orthop Adv* 16: 164–170
3. Mahfouz M, Abdel Fatah EE, Bowers LS, Scuderi G (2012) Three-dimensional morphology of the knee reveals ethnic differences. *Clin Orthop Relat Res* 470:172–185

4. Yang Y, Lu J, Luo ZY, Wang D (2012) Accuracy and density optimization in directly fabricating customized orthodontic production by selective laser melting. *Rapid Prototyp J* 18(6):482–489
5. Xiao D, Yang Y, Su X, Wang D, Sun J (2013) An integrated approach of topology optimized design and selective laser melting process for titanium implants materials. *Biomed Mater Eng* 23(5):433–445
6. Zhang LC, Klemm D, Eckert J, Hao YL, Sercombe TB (2011) Manufacture by selective laser melting and mechanical behavior of a biomedical Ti–24Nb–4Zr–8Sn alloy. *Scr Mater* 65(1):21–24
7. Kontio R, Karri M, Stoor P, Lindqvist C, Westermark A (2013) OP167: rapid prototyped individual orbital wall–Maxillary implant process description of individual reconstruction using 3D CAD–rapid prototyping techniques. *Oral Oncol* 49:S67
8. Chiba A, Kurosu S, Koizumi Y, Matsumoto H, Lee Y (2013) Mechanical properties and microstructures of biomedical grade Co–Cr–Mo alloy produced by additive manufacturing technique using EBM method. *J Bone Joint Surg* 95(SUPP 15):146
9. Stamp R, Fox P, O'Neill W, Jones E, Sutcliffe C (2009) The development of a scanning strategy for the manufacture of porous biomaterials by selective laser melting. *J Mater Sci Mater Med* 20(9):1839–1848
10. Gaytan SM, Murr LE, Ramirez DA, Machado BI, Martinez E, Hernandez DH, Martinez JL, Medina F, Wicker RB (2011) A TEM study of cobalt-base alloy prototypes fabricated by EBM. *Mater Sci Appl* 2(5):355–363
11. Pupo Y, Delgado J, Serenó L, Ciurana J (2013) Scanning space analysis in selective laser melting for CoCrMo powder. *Procedia Eng* 63:370–378
12. Monroy K, Delgado J, Ciurana J (2011) Study of the pore formation on CoCrMo alloys by selective laser melting manufacturing process. *Procedia Eng* 63:361–369
13. Averyanova M, Bertrand P, Verquin B (2011) Manufacture of Co–Cr dental crowns and bridges by selective laser melting technology. *Virtual Phys Prototyp* 6(3):179–185
14. Wang D, Yang Y, Huang Y, Wu W, Sun T, He X (2010) Impact of inter-layer scanning strategy on quality of direct fabrication metal parts in SLM process. *Laser Technol* 34(4):447–451
15. Yadroitsev I, Bertrand P, Smurov I (2007) Parametric analysis of the selective laser melting process. *Appl Surf Sci* 253(19):8064–8069
16. Kruth JP, Froyen L, Van Vaerenbergh J, Mercelis P, Rombouts M, Lauwers B (2004) Selective laser melting of iron-based powder. *J Mater Process Technol* 149(1):616–622
17. Wang D, Yang Y, Yi Z, Su X (2013) Research on the fabricating quality optimization of the overhanging surface in SLM process. *Int J Adv Manuf Technol* 65(9–12):1471–1484

Electron Beam Melted (EBM) Co-Cr-Mo Alloy for Orthopaedic Implant Applications

R.S. Kircher, A.M. Christensen, K.W. Wurth
Medical Modeling, Inc., Golden, CO 80401

Abstract

The Electron Beam Melting (EBM) manufacturing process is emerging as an additional method for producing orthopaedic devices in several materials, including Co-Cr-Mo Alloy. This work presents the chemical, microstructural and mechanical properties of several test specimens produced by the EBM process before and after a post-EBM Heat treatment. Comparisons are made to the properties of Co-Cr-Mo materials used within the orthopaedic implant industry processed by conventional methods such as investment casting and machining from wrought. The results of the work are promising, and demonstrate that EBM produced Co-Cr-Mo material has comparable, and in several cases superior microstructural and mechanical properties to those found in the traditionally-processed materials used today.

Introduction

The last several years have seen many advances towards realizing the goal of additive manufacturing for medical and aerospace applications. The additive manufacturing industry has focused its efforts on producing ‘higher end’ metals including medical grade stainless steels, titanium, titanium alloys and cobalt-chrome alloys. The availability of these materials within the scope of additive manufacturing technology opens the door for many applications in the field. One of the industry-leading additive metal manufacturing processes is the Electron Beam Melting (EBM) Process. The EBM process is an additive fabrication process, which utilizes a scanning electron beam to melt pre-alloyed metal powder in a layered fashion and build a three-dimensional construct, based on input generated from a computer model.

The EBM process is quite different than conventional production techniques, thus it is anticipated that the properties and microstructure of EBM produced materials will differ from what is currently seen today. The EBM process introduces several processing variables which do not exist in current manufacturing methods. It is important to identify these variables, and come to understand their effect on the metallurgical characteristics of the material.

The goal of this paper is to present the metallurgical properties of a particular alloy produced by the EBM process; Co-Cr-Mo. Results of chemical, microstructural, and mechanical evaluations will be presented. The results of these evaluations will be used to compare EBM produced Co-Cr-Mo material to several similar materials used today in the medical industry. In addition, key processing variables that may influence the properties of the material are identified, and their effects on the material are investigated.

The Electron Beam Melting Process

Like many rapid manufacturing techniques, the EBM process creates a physical component from digital CAD models by building the component in a series of layers. The EBM process starts by distributing a 70 μm layer of fine metal powder onto a steel platform. An electron beam is produced by passing current through a Tungsten filament. The electron beam scans areas of the metal powder layer, in an x-y coordinate system (as defined by the computer model) fully melting the powder in the areas scanned. Once the beam has scanned the appropriate areas, the steel platform is lowered by 70 μm and a new layer of powder is distributed on top of the previously melted layer. This process continues, layer by layer, until a complete part is produced. During processing the entire build chamber maintains a temperature

of approximately 800°C. Once the part has been completed, the build chamber is flooded with He gas to expedite cooling. A schematic of the EBM process is shown in **Figure 1**.

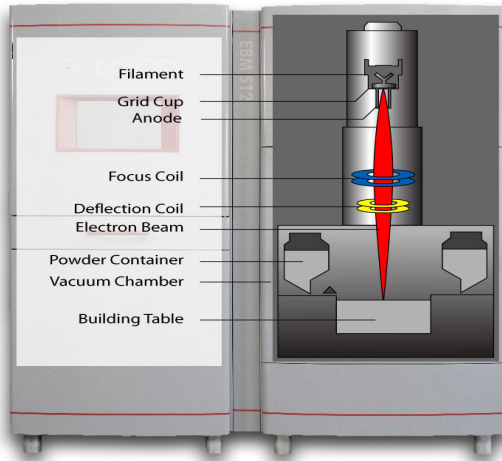


Figure 1: Schematic of an EBM production system.

The use of an electron beam to supply the energy necessary to melt the metal powder mandates that the process be done in a vacuum chamber, which minimizes chemical reactions between the melting metal powder and the surrounding atmosphere. Currently the EBM process is capable of producing parts up to 200x200x200 mm, with a dimensional accuracy of 0.4 mm.

Post EBM Heat Treatment

In addition to evaluating as-produced Co-Cr-Mo samples directly out of the EBM process, samples were also evaluated following a two-stage heat treatment. The heat treatment consisted of a hot isostatic pressing (HIP) cycle and a homogenization treatment. The goals of the heat treatments were to dissolve carbides present in the as-produced material and improve isotropy of the microstructure. **Table A** outlines the parameters used for each heat treatment cycle.

Table A: Heat treatment parameters

Heat Treatment Cycle	Time	Temperature	Pressure	Atmosphere	Quench
HIP	4 hrs	1185	25 ksi	Argon	N/A
Homogenization	4 hrs	1190	N/A	Argon	75°C/Minute

Procedure for Metallurgical Evaluation

The goal of this research was to provide basic metallurgical data from evaluation of EBM produced Co-Cr-Mo alloys, and to compare the results of these evaluations to data in literature and conventionally used standards and specifications. To accomplish this goal, several test specimens were produced to evaluate the chemical composition, microstructure, and mechanical properties of EBM produced material.

Sample Production & Orientation:

Mechanical testing was conducted on samples whose gauge-section was both parallel (Z orientation) and perpendicular (XY orientation) to the beam direction. Z orientation samples were produced as cylinders, whereas XY samples were produced as large slabs which were sectioned into several specimens.

Chemical Composition:

Chemical composition analysis was conducted on virgin Co-Cr-Mo alloy powder prior to EBM production. Solid specimens produced from the same powder were analyzed following EBM production to understand changes in chemical composition during solidification. The analyses were conducted in accordance with ASTM E 354 [1].

Microstructure:

Cross-sections of specimens created by the EBM process were prepared for metallographic examination. The gross microstructure of material was evaluated in two orientations, parallel to the build direction (Z orientation), and horizontal to the build direction (XY orientation). Samples were taken from the mid-section of each specimen, approximately 25mm from the bottom of the build platform. In addition to the EBM produced Co-Cr-Mo alloy, a custom Co-Cr-Mo implant component investment cast in accordance with ASTM F 75[2] was also sectioned and prepared for metallographic examination to allow for a comparison of microstructures. All samples were evaluated by light microscopy and were electrolytically etched in a 5% HCl solution.

Mechanical Properties:

The mechanical properties of EBM produced Co-Cr-Mo material were evaluated by static tensile testing, rotating bending fatigue testing, Rockwell hardness testing, and fracture analysis. The mechanical testing specimens were machined to the appropriate dimensions for each test from the near-net shapes.

The static tensile properties of the EBM produced material were evaluated in accordance with ASTM E 8, using the round powder metallurgy specimen geometry (*Figure 20 of ASTM E8-08*) [3]. Rockwell hardness was measured on cross sections of the grip area on tensile samples following testing. Rotating bending fatigue (RBF) samples were surface polished in the gauge area prior to testing to prevent premature failures. The tests were conducted at a frequency of 100 Hz at room temperature. A run-out value of 10 million cycles was chosen.

Results and Discussion

Table B contains the chemical composition of the virgin powder prior to production as well as the chemical composition of solid test specimens following EBM production. The results indicate that no significant changes in material composition occur during the melting and re-solidification of the pre-alloyed powder during the EBM process. Of particular note, are the consistent levels of interstitial elements such as O, N, C and H. The high vacuum level in the build chamber of the EBM equipment limits the amount of these gasses available for diffusion into the material during production, allowing for tight control on interstitial elements. Alloys containing elements with greatly differing melting points have shown a propensity to ‘burn off’ a fraction of the low melting point element during the EBM process. This phenomenon has been observed with a loss of Al during the EBM production of Ti6Al4V alloys [4]. This does not

appear to be the case for the Co-Cr-Mo alloy system, as all alloying elements remain relatively constant throughout the process.

Table B: Chemical compositions of Co-Cr-Mo powder and EBM solidified material

State	Al wt%	B wt%	C wt%	Cr wt%	Fe wt%	Mn wt%	Mo wt%	N wt%	Ni wt%	P wt%	Si wt%	Ti wt%	W wt%	Co wt%
Powder	<0.010	<0.001	0.24	28.29	0.60	0.59	5.74	0.16	0.14	0.009	0.37	0.026	<0.01	Bal.
EBM Solidified	<0.010	<0.001	0.22	27.69	0.23	0.40	5.96	0.14	0.09	0.009	0.38	0.011	<0.01	Bal.

The microstructure of the Co-Cr-Mo alloys resulting from EBM solidification is unique to the process. Micrographs of as-produced EBM Co-Cr-Mo alloy for both XY and Z orientations are shown in **Figure 2**. These micrographs are representative of the microstructure typical seen in EBM produced Co-Cr-Mo alloys. The microstructure consists of columnar grains orientated along the z-axis. A large number of carbides are also present in both micrographs. It is suggested that the combination of high carbon content along with the elevated 800°C chamber temperature during EBM production encourage the precipitation of carbides out of the matrix material.

Figure 3 contains micrographs of EBM Co-Cr-Mo alloy for both XY and Z orientations following hot isostatic pressing and a homogenizing heat treatment. The heat treatments result in several significant changes in the material microstructure. Heat treatment appears to re-dissolve a portion of the carbides back into solution, increase the overall grain size of the material, and most importantly, results in a much more isotropic microstructure.

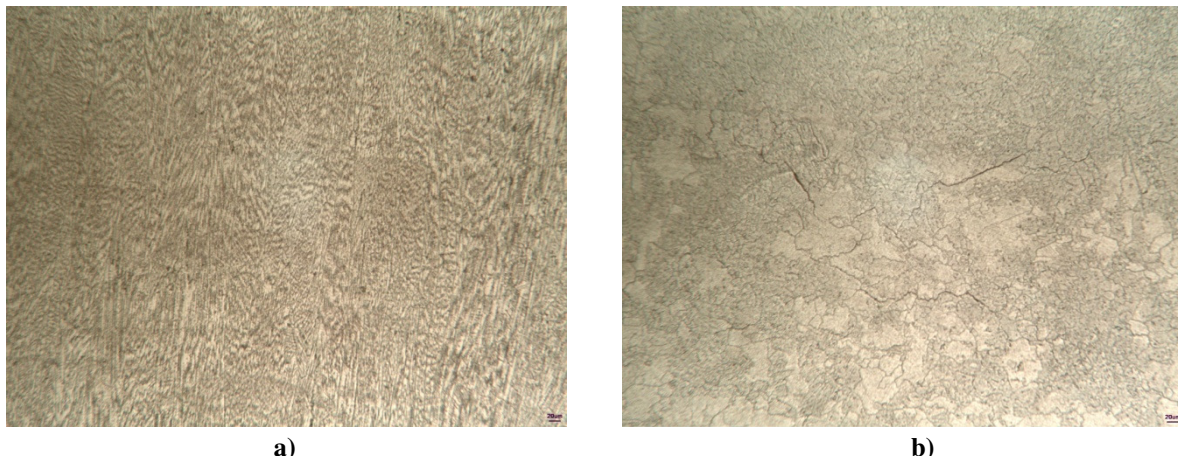


Figure 2: Micrographs of EBM produced Co-Cr-Mo alloy in the as-produced condition orientated in a) the Z direction and b) the XY direction.

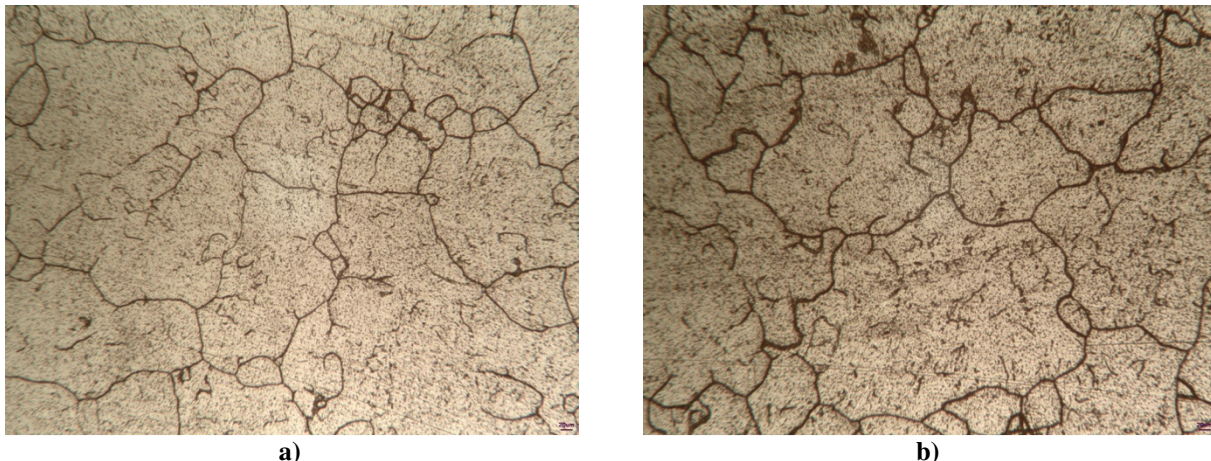


Figure 3: Micrographs of EBM produced Co-Cr-Mo alloy in the HIP and homogenized condition orientated in a) the Z direction and b) the XY direction.

Table C contains the static tensile property results of EBM produced tensile bars in both the as-produced condition and the HIP and heat treated conditions. Test bars from each condition were tested in both the Z orientation as well as the XY orientation. The results indicate that as-produced EBM Co-Cr-Mo material is extremely brittle, especially when stressed along the Z orientation. The low ductility measured in the as-produced material is likely due to large quantity of carbides present in the microstructure. The mechanical property dependence on orientation can be explained by the columnar grains orientated parallel to the beam direction. Heat treatment following EBM production has quite a drastic effect on the mechanical behavior of Co-Cr-Mo material. The 2% offset yield strength is significantly lower and the material exhibits much higher elongation following heat treatment when compared to the as-produced material. The heat-treated samples all exhibited similar mechanical behavior independent of orientation. The average hardness of the heat-treated samples was measured at 33 HRC.

Table C: Static Mechanical Properties of EBM produced Co-Cr-Mo material

State	Orientation (XY or Z)	Number of Samples	Avg. YS ksi (MPa)	Avg. UTS ksi (MPa)	Reduction of Area (%)	Avg. Elong. (%)
As-Produced	XY	5	104 (717)	161 (1110)	7.2	5.0
As-Produced	Z	5	114 (786)	126 (869)	N/A	0.8
HIP & HT	XY	5	85 (586)	166 (1145)	24.3	30
HIP & HT	Z	5	85 (586)	167 (1151)	24.0	30

Fracture analysis was conducted on failed samples following tensile testing utilizing a SEM. **Figure 3a** shows the fracture surface of an as-produced XY orientated tensile sample. The fracture follows the grain boundaries of the columnar grains, and is indicative of a brittle fracture mechanism. **Figure 4b** shows the fracture surface of a XY orientated tensile that has been heat treated. The fracture can be characterized as intergranular, which typically indicates a brittle fracture with little deformation during failure. This sample, however, exhibited approximately 30% elongation which is rather unique. The microstructures in **figure 3** do show a high concentration of carbides at the grain boundaries, which are likely responsible for the intergranular fracture mechanism.

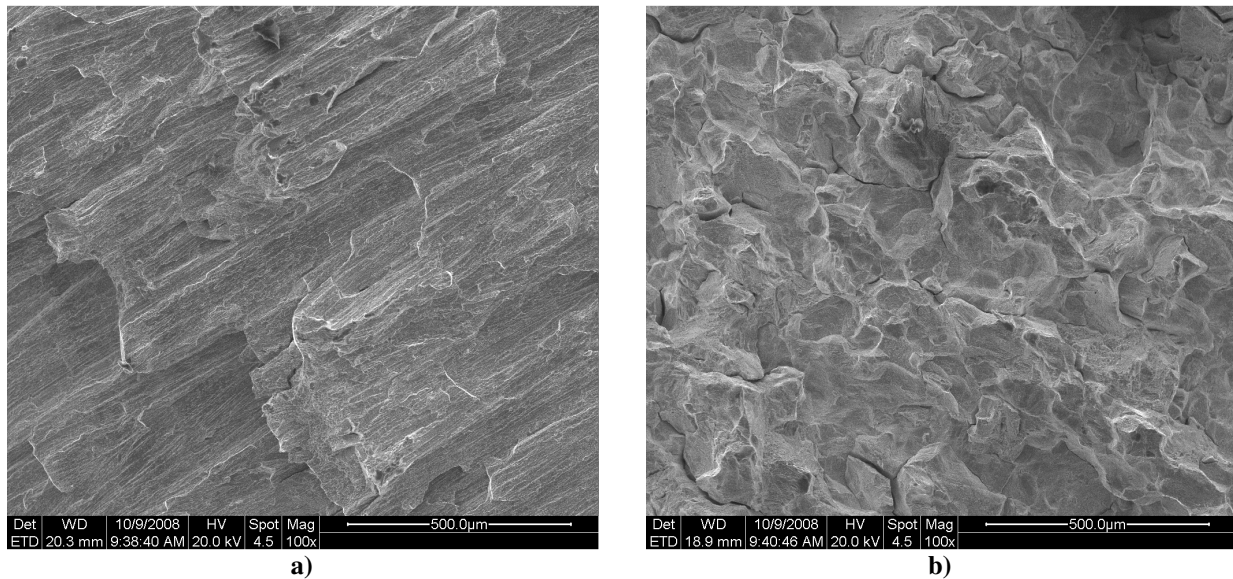


Figure 4: Fracture surfaces of failed static tensile XY orientated samples of EBM produced Co-Cr-Mo alloy in the a) as-produced and b) HIP and homogenized conditions.

The fatigue performance of EBM produced Co-Cr-Mo material is summarized as an S-N curve in **Figure 5**. Two groups of specimens were tested; samples orientated in both XY direction and the Z direction. Both sample groups underwent HIP and homogenization treatments prior to testing. The number of samples in each group is not sufficient to accurately predict the 10 million cycle stress level, however it appears the value will be between 400 and 500 MPa. The data also indicates that samples tested in the Z direction have a slightly lower fatigue limit. This may be a consequence of the layering in the Z direction which could provide crack initiation sites.

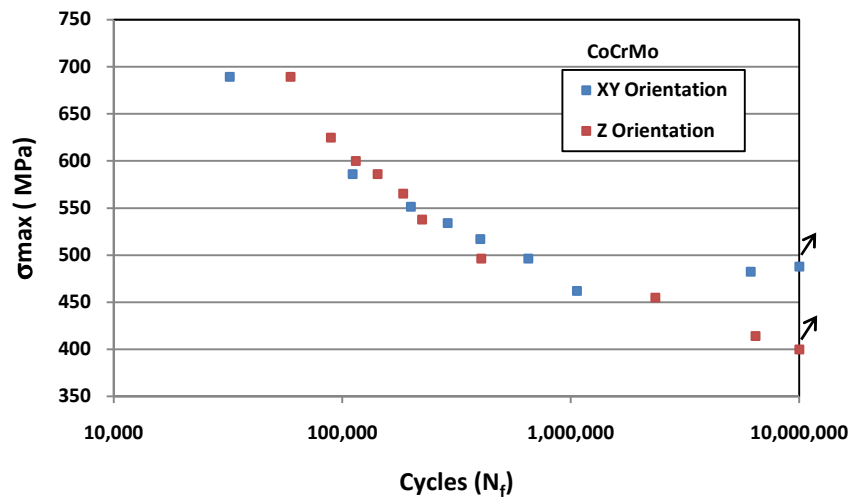


Figure 5: S-N curve for EBM produced C-Cr-Mo material tested in rotating bending fatigue.

If EBM produced Co-Cr-Mo material is going to be used in the medical field it is important to understand how all of the characteristics presented in this study compare to the characteristics of the Co-Cr-Mo materials currently used in the medical industry. **Table D**

summarizes the most commonly used Co-Cr-Mo materials in the medical industry today [2]. The main difference between these alloys is the method of production; forging, casting or wrought alloys. Each alloy has slightly different chemical composition requirements set at the necessary levels to enable proper manufacture and result in the desired mechanical performance. The powder used in this study was produced with the intention of meeting the ASTM F-75 chemical composition requirements. **Table E** compares the chemical composition of the solid EBM Co-Cr-Mo alloy with that of each of the standard materials listed in **Table D**. The ASTM F799 and F1537 standards designate three (3) separate alloys; 1) Low carbon, 2) High Carbon and 3) Dispersion Strengthened. The EBM produced material meets the chemical requirements of ASTM F 75 as well as high carbon (Alloy 2) material.

Table D: Conventional standards for Co-Cr-Mo alloys in the Medical Industry

Specification Designation	Title
ASTM F 75	Standard Specification for Cobalt-28 Chromium-6 Molybdenum Alloy Castings and Casting Alloys for Surgical Implants
ASTM F 799	Standard Specification for Cobalt-28 Chromium-6 Molybdenum Alloy forgings for Surgical Implants
ASTM F 1537	Standard Specification for Wrought Cobalt-28 Chromium-6 Molybdenum Alloys for Surgical Implants

Table E: Chemical composition comparison of EBM produced material and conventional Co-Cr-Mo Alloys

Material	Alloy	Al wt%	B wt%	C wt%	Cr wt%	Fe wt%	Mn wt%	Mo wt%	N wt%	Ni wt%	P wt%	Si wt%	Ti wt%	W wt%	La wt%	Co wt%
EBM Solidified	<0.010	<0.001	0.22	27.69	0.23	0.40	5.96	0.14	0.09	0.009	0.38	0.011	<0.01	N/A	Bal.
ASTM F 75	<0.10	<0.010	<0.35	27.0-30.0	<0.75	<1.0	5.0-7.0	<0.25	<0.50	<0.020	<1.0	<0.10	<0.20	Bal.
ASTM F 799 & F 1537	1	<0.14	26.0-30.0	<0.75	<1.0	5.0-7.0	<0.25	<1.0	<1.0	Bal.
ASTM F 799 & F 1537	2	0.15-0.35	26.0-30.0	<0.75	<1.0	5.0-7.0	<0.25	<1.0	<1.0	Bal.
ASTM F 799 & F 1537	3	0.30-1.00	<0.14	26.0-30.0	<0.75	<1.0	5.0-7.0	<0.25	<1.0	<1.0	0.03-0.20	Bal.

Figure 6 compares the mechanical properties of EBM produced Co-Cr-Mo material following HIP and heat treatment with the mechanical requirements of the alloys listed in **Table D**. There are several important conclusions that can be drawn from the comparison. The elongation and reduction of area properties of the EBM produced materials exceed the requirements for all conventionally produced materials. The EBM produced material also meets or exceeds all mechanical strength requirements for both ASTM F75 and ASTM F1537 Annealed material.

Although none of the ASTM standards for implantable Co-Cr-Mo alloys require a specific microstructure, it is useful to compare the the microstructure of EBM produced materials to that of a conventionally produced implantable device. **Figure 7** is a optical light micrograph of an investment cast commercially available implantable Co-Cr-Mo device which was obtained and sectioned for microstructural evaluation. It is obvious that the microstructure of this implant is quite different than the microstructures presented in **figure 3**. The microstructure in **figure 7** is what one would expect from an investment cast material that experiences a slow solification rate [5]. EBM produced material solidifies very quickly after melting, and experiences an

entirely different thermal history through out its production and subsequent heat treatments, resulting in an entirely different microstructure.

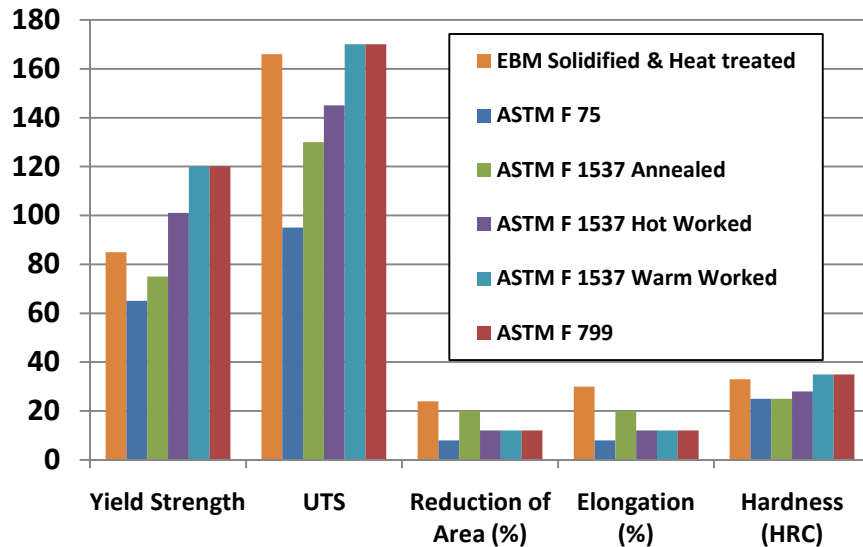


Figure 6: Comparison of mechanical properties of conventional medical grade Co-Cr-Mo alloys and EBM produced Co-Cr-Mo alloy.

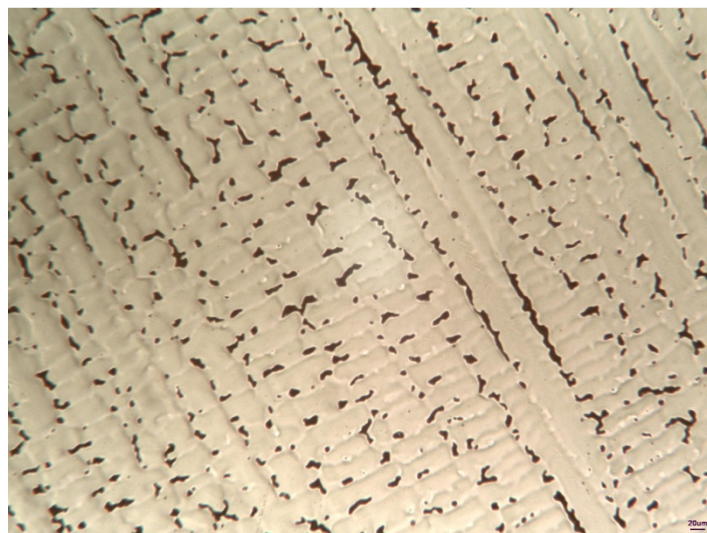


Figure 7: Microstructure of a commercially available investment cast Co-Cr-Mo implant.

Summary and Conclusions

The purpose of this research was to investigate whether EBM produced Co-Cr-Mo alloys exhibit adequate chemical and mechanical properties to be considered acceptable alloys for surgical implant applications. The results demonstrate that as-produced Co-Cr-Mo alloy is quite brittle and exhibits anisotropic mechanical behavior. For these reasons, as-produced Co-Cr-Mo material needs to undergo a two-stage heat treatment in order to satisfy the requirements of standard Co-Cr-Mo medical grade standards. The heat treatment has the effect of dissolving carbides which precipitate out of the matrix during EBM solidification, and removing the anisotropic behavior from the material. Although the microstructure of EBM produced Co-Cr-

Mo alloy is unique when compared to material manufactured by conventional means, its mechanical performance exceeds or meets the requirements for both ASTM F75 material and annealed ASTM F1537 grade material.

References

1. ASTM Standard: E 354 Standard Test Methods for Chemical Analysis of High-Temperature, Electrical, Magnetic, and Other Similar Iron, Nickel, and Cobalt Alloys, 2006.
2. Book of ASTM Standards, Vol. 31.01 Medical and Surgical Materials and Devices, 2006.
3. ASTM Standard: E 8-08 Test Methods for Tensile Tension Testing of Metallic Materials, ASTM, 2008.
4. Christensen, A., Lippincott, A., Kircher, R., *Qualification of Electron Beam Melted (EBM) Ti6Al4V-ELI for Orthopaedic Applications*, MPMD, Palm Desert, CA, 2007.
5. Mishra, A., et al., "Metallurgy, Microstructure, Chemistry and Mechanical Properties of a New Grade of Cobal-Chromium Ally Before and After Porous-Costing", Cobalt-Based Alloys for Biomedical Applications, ASTM STP 1

**STRENGTH
AND PLASTICITY**

Effect of the Regimes of Selective Laser Melting on the Structure and Physicomechanical Properties of Cobalt-Base Superalloys

T. V. Tarasova^a, A. P. Nazarov^a, and M. V. Prokof'ev^b

^a*Moscow State University of Technology (Stankin), Vadkovskii per. 1, Moscow, 127994 Russia*

^b*Moscow Institute of Aviation (National Research University), Volokolamskoe sh. 4, Moscow, 125993 Russia*

e-mail: nazarovstankin@mail.ru

Received August 4, 2014; in final form, September 1, 2014

Abstract—In this article, we give a preferential regime of selective laser melting for the production of parts from a cobalt superalloy using a PTK-PS domestic machine, which can find application upon the production of components from various superalloys in the aviation and atomic industry and in the automobile industry. We have investigated the phase composition and determined the physicomechanical properties of the samples prepared under the preferential regime of selective laser melting. It has been established that the structure of the alloy obtained by selective laser melting consists of two supersaturated solid solutions based on the low-temperature hexagonal and high-temperature cubic cobalt modifications, which leads to an increase in the strength characteristics of the samples in comparison with the cast samples.

Keywords: selective laser melting, cobalt-based alloys

DOI: 10.1134/S0031918X15060101

INTRODUCTION

In contrast to the traditional powder-metallurgy technologies, the method of selective laser melting (SLM) possesses a number of fundamental advantages, including wastelessness; universality; the opportunity of the fabrication of complex-profile components with a high precision (to ± 0.05 mm), which are not inferior to and sometimes even exceed (in their physicomechanical properties) the components obtained by traditional forming.

The SLM method makes it possible to use a wide range of powder materials. High-temperature (high-strength) cobalt-based alloys (superalloys) are some of the most promising objects. The complex-profile parts prepared using SLM from cobalt-based superalloy powder material can find wide application in the aircraft industry, engine production, and automobile industry [1–3].

The purpose of this work is to determine the influence of the regimes of the SLM on the structure and physicomechanical properties of cobalt superalloys.

EXPERIMENTAL

Experimental studies were conducted via standard and original procedures using certified devices and controlling and measuring equipment. The experimental samples (prototypes) and parts were produced on a PTK-PS domestic setup for SLM. The technical characteristics of the setup are as follows: an ytterbium fiber laser with a wavelength of 1070 nm; the maxi-

mum output power of the laser, 200 W; the operation mode of laser, continuous; the scanning velocity, 0–7 m/s; the diameter of the output spot of the laser, 150 μm ; the possibility of using a protective atmosphere (argon, nitrogen, etc.); heating of the working space to the temperature of 100°C.

The scanning by the laser beam was performed according to the “two-zone” strategy with a change in the direction of scanning by 90° when going from track to track.

As the initial material for the production of prototypes and details, the powder of the CoCrMo superalloy obtained by gas atomization was selected. The chemical composition of the powder (in wt %) was as follows: Co, 60–65; Cr, 26–30; Mo, 5–7; Si and Mn, less than 1%; Fe, less than 0.75; C, less than 0.16; and Ni, less than 0.10%. The granulometric composition of the powder was determined using an OCCHIO 500nano (Belgium) with a Callisto built-in software for processing statistical data. It has been established that the average size of the CoCrMo powder particles is $d_{av} = 30.5 \mu\text{m}$. The powder particles have a globular shape and possess a high index of sphericity (67.1% on average) and a low value of size scatter (2.4% on average), which ensures obtaining uniform and homogeneous layer [4, 5].

X-ray diffraction phase analysis was carried out using an ALR X'TRA (Thermo-Fisher Scientific, Switzerland) powder diffractometer by the $\theta-\theta$ scanning technique with the Bragg–Brentano focusing of the X-rays, in Cu $K\alpha$ radiation.

Table 1. Precision of obtained linear dimensions, surface roughness, and density of the prototype samples

Precision of obtaining linear dimensions, μm	Surface roughness Ra, μm	Density, g/cm^3
± 60 (for dimensions less than 15 mm)	8 ± 2	8.3 ± 0.1

The microstructure of the prototypes was analyzed using an Olympus BX51 (Japan) optical microscope and a VEGA 3 LM (Tescan, Czech Republic) scanning electron microscope.

The roughness of the surfaces of the prototypes was measured using a HOMMEL-TESTER T800 (Germany) profilograph—profilometer.

The hardness of the samples was measured via the standard procedure using an automatic ERCOTEST DIGI 25RS hardness meter.

The mechanical properties (tensile strength, yield stress, relative elongation) were measured according to the Russian State Standard GOST 1497-84 using an MTS Insight 100 (MTS Systems Corporation, United States) testing machine. The impact toughness was measured according to the GOST 9554-78 using a Walter and Bai PH 50 (Switzerland) testing machine.

The wear resistance was determined using a kal-MAX NT (Germany) high-precision tester. As the counterbody, a sphere with a diameter of 30 mm made of steel 100Cr6 (according to DIN classification) was used. The sliding distance was 1400–1500 m, the normal load on the sample was 0.54 N, and an abrasive suspension was periodically supplied onto the surface of the sphere.

RESULTS AND DISCUSSION

Based on the technical characteristics of the PTK-PS installation, precision with which the parts should be produced ($\pm 50 \mu\text{m}$), as well as the purpose of achieving the maximum efficiency, the following preferential regime of the process of the selective laser melting of the CoCrMo superalloy was employed: the protective atmosphere was nitrogen, the power of the laser radiation was 200 W, the diameter of the laser spot was

150 μm , the thickness of the powder layer was 50 μm , the rate of scanning was 400 mm/s, and the distance between the laser tracks was 100 μm .

Using these parameters, prototype samples were prepared and some studies were carried out on them.

The precision of linear dimensions, the roughness of the surface, and the density of the prototypes obtained are given in Table 1. Note that the density of the KKhS-D alloy (Russian analog of the CoCrMo powder) after casting is $8.4 \text{ g}/\text{cm}^3$, which is nearly identical to the density of the prototype samples (Table 1).

The prototype samples possess a dense structure; i.e., hardly any pores and cavities are observed in them.

The X-ray diffraction analysis of the alloy after SLM and of the alloy made of the initial powder material has shown that the alloy obtained by the SLM technology is two-phase (Fig. 1), whereas the alloy made of the initial powder is single-phase and presents in itself a solid solution of chromium and molybdenum in the cubic modification of cobalt with the lattice parameter $a = 0.3580(1) \text{ nm}$ (here and below, the digit given in the parentheses indicates the error in the determination of the parameter after the refinement based on the use of all lines of the X-ray diffraction pattern by the method of iterations).

The identification of lines in the diffractograms and the refinement of the parameters of the unit cells made it possible to ensure good agreement between the experimental data and computed values of the interplanar spacings d_{exp} and d_{cal} (Table 3) if we take into account the opportunity of the simultaneous existence of two cobalt modifications in the alloy. The values of d_{cal} (Table 3) were calculated based on the refined parameters of the unit cell. No lines corresponding to the formation of an intermetallic phase with a tetragonal structure and the nominal stoichiometric composition Co_2Cr_3 have been observed in the diffractogram.

As is known [7], the hexagonal modification of pure cobalt (space group $P6_3/mmc$), which is stable at room temperature passes into the cubic modification (space group $Fm3m$) at 427°C. The data concerning the polymorphism of cobalt, chromium, and molybdenum are given in Table 2.

Table 2. Allotropy of cobalt, chromium, and molybdenum [7–9, 10]

Metal	Pauling atomic radius, nm	Space group	Lattice parameters, nm		Temperature stability of allotropic modification, °C
			a	c	
α -Co	0.125	$P6_3/mmc$	0.2505	0.4089	427
β -Co	0.125	$Fm3m$	0.3544		1494
Mo	0.140	$Im3m$	0.3140		2623
Cr	0.127	$Im3m$	0.28845		1890

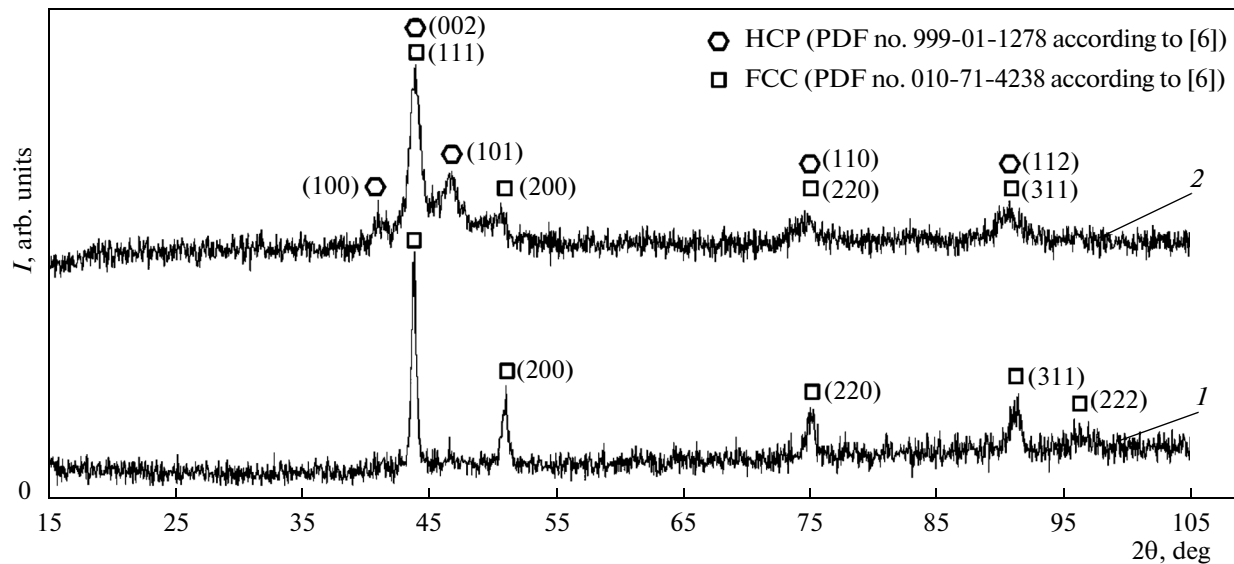


Fig. 1. X-ray diffraction patterns of (1) the initial powder and (2) SLM alloy.

The experimental diffractograms can be completely identified if we assume that the alloying of cobalt simultaneously with chromium and molybdenum under the conditions of rapid cooling can favor the stabilization of the high-temperature phase at temperatures below the temperature of the polymorphic transformation of pure cobalt. The shift of lines in these diffractograms relative to the lines of pure cobalt is explained by the formation of solid solutions based on the hexagonal and cubic modifications. It can be seen from the calculations that the parameters of the unit cells of the hexagonal ($a = 0.255(2)$ nm; $c = 0.413(3)$ nm) and cubic ($a = 0.3595(6)$ nm) modifications of cobalt are enhanced compared to those of pure cobalt. Since the atomic radius of chromium (0.125 nm) [8] is close to that of cobalt (0.127 nm) [7], it is logical to assume the joint presence of all three elements in the alloy. Moreover, the increase in the lattice

parameters is explained by the presence of molybdenum (the Pauling radius of which is 0.14 nm) in these solid solutions [9–11]. The data from indexing the diffractogram are given in Table 3.

Thus, despite the significant difficulties created by the physical broadening of the lines in the diffractograms of the samples after SLM, we can confidently say that it is fairly accurate to interpret this phenomenon as being due to the presence of a mixture of the cubic and hexagonal structures of cobalt.

The significant line broadening that is observed in the diffractograms of the alloys after SLM, can be due to the superimposition of several factors. First, the broadening of the interference lines can arise as a result of diffraction on the alloy crystallites (coherent domains) with a size of less than 100 nm. The formation of these crystallites is possible during rapid cooling after heating by laser. Second, it may be due to the

Table 3. Results of identifying the X-ray diffraction pattern after SLM

2θ, deg	d_{exp} , nm	Relative intensity, %	Cubic unit cell			Hexagonal unit cell			d_{cal} , nm	
			Miller indices			d_{cal} , nm	Miller indices			
			h	k	l		h	k		
40.89	0.2205	49	—	—	—	—	1	0	0	0.2208
43.84	0.2064	100	1	1	1	0.2076	—	—	—	—
46.58	0.1948	67	—	—	—	—	1	0	1	0.1947
50.32	0.1812	51	2	0	0	0.1797	—	—	—	—
74.55	0.1272	51	2	2	0	0.1271	1	1	0	0.1275
90.80	0.1082	53	3	1	1	0.1084	1	1	2	0.1085

Table 4. Mechanical characteristics of prototype samples obtained by selective laser melting using a PTK-PS setup and of samples of the cast alloy KKhS-D

Metal	Yield stress $\sigma_{0.2}$, MPa	Ultimate strength σ_u , MPa	Relative elongation δ , %	Impact toughness KCU , J/m ²	Hardness HRC
SLM, CoCrMo powder	1050 ± 150	1300 ± 150	No less than 6	21 ± 1	42 ± 4
Casting, KKhS-D	600 ± 50	850 ± 50	No less than 7.5	—	34 ± 2

Table 5. Rate of wear of samples produced by SLM in a PTK-PS setup and by casting the KKhS-D alloy

Materials and the preparation method	Wear rate, $10^{-15} \text{ m}^3/(\text{m N})$
SLM, CoCrMo powder	3.1 ± 0.2
Casting, KKhS-D	5.4 ± 0.3

formation of supersaturated solid solutions and, as a result, the presence of significant microstresses in the alloy.

The assumption on the predominant influence of the small coherent domains is confirmed by the microstructure of the alloy revealed by etching. In the micrograph obtained by the method of the scanning electron microscopy (Fig. 2), boundaries of submicroscopic grains can well be seen, the sizes of which are fairly small. Since the size of the features observed upon etching is always greater than the real size, the existence of these subgrains agrees with the data of X-ray diffraction analysis. No coarse grains typical of the

cast alloys and alloys heat treated at high temperatures are observed in the samples of the alloys after SLM.

The results of comparative mechanical tests are given in Table 4. The analysis of the data obtained shows that the mechanical characteristics of the prototype samples are much higher than those of the cast-alloy analog (except for the relative elongation). This phenomenon is characteristic of the alloys obtained as a result of either laser treatment with the melting of the surface or as a result of the application of special coatings [12–17].

The results of comparative tests of wear resistance under the conditions for the abrasive wear of the samples of the cast alloy and of the samples prepared by the SLM method (below, SLM samples) are given in Table 5. It can be seen from Table 5 that the rate of wear for SLM samples is 1.7–1.5 times less than in the case of the cast alloy.

An analysis of our data and the literature data [18–22] makes it possible to conclude that the SLM method has a large potential for the applications in the machine-building field.

CONCLUSIONS

(1) A preferential regime of selective laser melting for the powder material of the CoCrMo alloy has been chosen, which made it possible to prepare prototype samples with a high density and shape precision not inferior to the density and precision of cast samples.

(2) The structure of the alloy obtained by the selective laser melting represents a mixture of two supersaturated solid solutions based on the low-temperature hexagonal and high-temperature cubic modifications of cobalt, which leads to an increase in the strength characteristics of the samples in comparison with the cast samples.

(3) The physicomechanical characteristics of the prototype samples prepared using the preferential regime of the selective laser melting have been determined to be as follows: the density is $\rho = 8.3 \pm 0.1 \text{ g/cm}^3$, hardness is $42 \pm 4 \text{ HRC}$, the precision of linear dimensions is $\pm 0.06 \text{ mm}$, surface roughness R_a is $8 \pm 2 \mu\text{m}$, yield stress is $\sigma_{0.2} = 1000 \pm 150 \text{ MPa}$, the ultimate tensile strength is $\sigma_u = 1250 \pm 150 \text{ MPa}$, the relative elongation δ is no less than 6%, and the impact toughness KCU is $21 \pm 1 \text{ J/cm}^2$. This makes it possible to

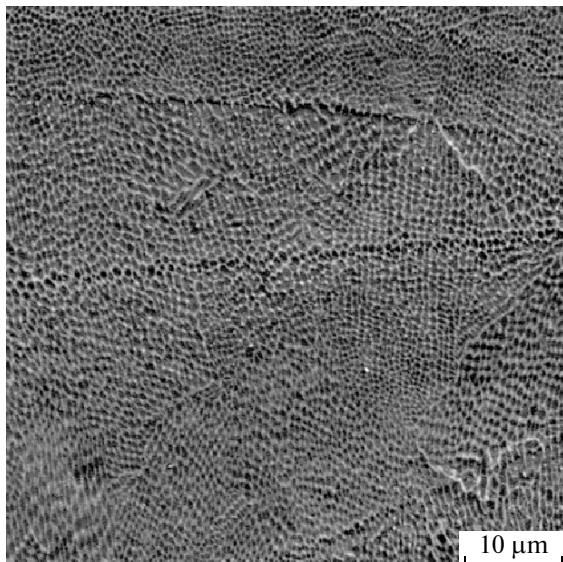


Fig. 2. Microstructure of the CoCrMo alloy after SLM.

produce complex-profile components suitable for exploitation at high mechanical loads.

(4) Comparative tests of wear resistance have shown that the wear rate of SLM samples is 1.7–1.5 times less than that of the samples made of the cast alloy.

ACKNOWLEDGMENTS

This work was supported by the Ministry of Education and Science of the Russian Federation within the framework of the State Task in the sphere of scientific activity.

REFERENCES

1. I. V. Shishkovskii, *Laser Synthesis of Functional-Gradient Mesostructures and Bulk Products* (FIZMATLIT, Moscow, 2009) [in Russian].
2. S. N. Grigor'ev, "Solving problems of mechanical engineering technological reequipment," *Vestn. MGTU "STANKIN"*, No. 3, 5–9 (2008).
3. S. N. Grigor'ev and M. A. Volosova, *Application of Coatings and Modification of Tool Surfaces* (ITs MGTU "STANKIN", Moscow, 2007) [in Russian].
4. T. V. Tarasova and A. P. Nazarov, "The study of the processes of the modification of the surface layer and fabrication of three-dimensional machine parts by selective laser melting," *Vestn. MGTU "STANKIN"*, No. 2, 17–21 (2013).
5. A. P. Nazarov, "Specific Features of the design of machines for selective laser sintering," *Vestn. MGTU "STANKIN"*, No. 1, 76–79 (2013).
6. *The International Centre for Diffraction Data (ICDD) / A Comprehensive Database of Powder Diffraction Patterns (PDF-2)*.
7. *Chemical Encyclopedia*, In 5 vol., Ed. by I. L. Knunyants, (Sovetskaya Entsiklopediya, Moscow, 1990) [in Russian], Vol. 2.
8. *Chemical Encyclopedia*, in 5 vols., Ed. by I. L. Knunyants (Sovetskaya Entsiklopediya, Moscow, 1992) [in Russian], Vol. 3.
9. *Chemical Encyclopedia*, in 5 vol., Ed. by I. L. Knunyants (Sovetskaya Entsiklopediya, Moscow, 1999) [in Russian], Vol. 5.
10. V. K. Pecharsky and P. Y. Zavalij, *Fundamentals of Powder Diffraction and Structural Characterization of Materials* (Kluwer Academic, Dordrecht, 2003).
11. *International Tables for Crystallography. Vol. A: Space-Group Symmetry*, Ed. by Th. Hahn et al. (International Union of Crystallography, Springer, New York, 2006).
12. S. N. Grigor'ev, T. V. Tarasova, G. O. Gvozdeva, and S. Nowotny, "Micro-laser facing of Al–Si system alloys," *Metal Sci. Heat Treat.* **55**, 242–246 (2013).
13. V. Y. Fominskii, R. I. Romanov, S. N. Grigor'ev, and V. N. Nevolin, "Effect of the pulsed laser deposition conditions on the tribological properties of thin-film nanostructured coatings based on molybdenum diselenide and carbon," *Tech. Phys. The Russ. J. Appl. Phys.* 2012, **57**, 516–523.
14. T. V. Tarasova, "Prospects of the use of laser radiation for raising the wear resistance of corrosion-resistant steels," *Metal Sci. Heat Treat.* **52**, 284–288 (2010).
15. S. N. Grigor'ev, R. I. Romanov, and V. Yu. Fominskii, "Dependence of mechanical and tribological properties of diamond-like carbon coatings on laser deposition conditions and alloying by metals," *J. Friction Wear* **33**, 253–259 (2012).
16. S. N. Grigor'ev, V. Yu. Fominskii, and A. V. Gusarov, "Features of micro- and nanostructures of Au–Ni alloys obtained on nickel due to different modes of pulse laser alloying," *Metal Sci. Heat Treat.* **54**, 34–40 (2012).
17. S. N. Grigor'ev, V. Yu. Fominskii, J. P. Celis, R. I. Romanov, and V. B. Oshurko, "Structure and mechanical properties of W–Se–C/diamond-like carbon and W–Se/diamond-like carbon bi-layer coatings prepared by pulsed laser deposition," *Thin Solid Films* **520**, 6476–6483 (2012).
18. V. Yu. Fominskii, S. N. Grigor'ev, R. I. Romanov, A. G. Gnedovets, and P. N. Chernykh, "Laser plasma ion implantation and deposition of platinum for SiC-based hydrogen detector fabrication," *Nucl. Instrum. Meth. Phys. Res., Sect. B: Beam Interactions with Materials and Atoms* **313**, 68–75 (2013).
19. T. V. Tarasova, "Distribution of elements in the molten pool produced by laser alloying," *Met. Sci. Heat Treat.* **44**, 124–127 (2002).
20. T. V. Tarasova and G. O. Gvozdeva, "Study of laser alloying processes of aluminum alloy surface," *Nauka Obrazovanie: Elektron. Nauchn.-Tekhn. Izd.*, No. 3, 48 (2012).
21. T. V. Tarasova and G. O. Gvozdeva, "Structure formation in hypereutectic Al–Si-alloys produced by laser surface treatment," *Uprochn. Tekhnol. Pokryt.*, No. 12, 35–40 (2012).
22. T. V. Tarasova and A. P. Nazarov, "Technological limitations of selective laser melting method," *Appl. Mech. Mater.* **752–753**, 878–883 (2015), DOI:10.4028/www.scientific.net/AMM.752-753.878

Translated by S. Gorin



Effect of energy input on formability, microstructure and mechanical properties of selective laser melted AZ91D magnesium alloy



Kaiwen Wei, Ming Gao*, Zemin Wang, Xiaoyan Zeng

Wuhan National Laboratory for Optoelectronics, Huazhong University of Science and Technology, Wuhan 430074, China

ARTICLE INFO

Article history:

Received 24 December 2013

Received in revised form

13 May 2014

Accepted 30 May 2014

Available online 9 June 2014

Keywords:

Selective laser melting

AZ91D

Formability

Microstructure

Mechanical property

ABSTRACT

Selective laser melting (SLM) technology has been used to manufacture the AZ91D magnesium alloy. The relative density, microstructure, microhardness and tensile properties of the deposited AZ91D samples at different laser energy inputs were characterized. The results indicate that laser energy input plays a significant role in determining formation qualities of the SLMed samples. High density samples without obvious macro-defects can be obtained between 83 J/mm³ and 167 J/mm³. The SLMed AZ91D presents a unique layerwise feature in which the fully divorced eutectic β -Mg₁₇Al₁₂ distributing along the boundary of the equiaxed α -Mg matrix. The average size of α -Mg in overlapping regions is a little larger than that in the center of the scanning tracks due to the remelting process though the element distributions of Mg and Al are quite uniform. The microhardness of all samples shows directional independence. The microhardness and tensile strengths of the SLMed AZ91D at room temperature are superior to those of the die-cast AZ91D due to the combined effect of grain refinement and solid solution strengthening.

© 2014 Elsevier B.V. All rights reserved.

1. Introduction

As the lightest structural alloys, magnesium alloys have the potential to replace steels and aluminum alloys in many applications due to their high specific strength and excellent damping capacity. For example, magnesium alloys are excellent candidates for automotive and aerospace components to reduce weight and realize fuel conservation and emission reduction [1,2]. Besides, in medical field, surgical implants based on magnesium alloys have become a promising invention due to their good degradability in situ and elasticity moduli closer to human bone than other conventional materials [3,4].

The manufacturing methods of magnesium alloys have been paid more attentions to meet the increasing applications. Deformation processing and casting are two conventional methods to manufacture complex magnesium alloy parts. In industry, deformation processing is preferred to obtain metal parts with high performances. However, for magnesium alloys, only two effective slip systems are available at room temperature due to the nature of close-packed hexagonal structure. Deformation processing of magnesium alloys needs to be conducted at elevated temperatures, which causes more fuel consumption, lower efficiency and oxidation of parts. As a result, the consumption of wrought magnesium alloys is merely about 1.5% of total magnesium alloy

demands [5]. At present, die-casting is the dominate method to manufacture magnesium alloys. Although die-casting is of great efficiency together with high precision, gas entrapment is inevitable due to the high filling rates [1,6]. Moreover, complex structures such as internal channels, curved surfaces and ultrafine lattices, are difficult to manufacture by die-casting though their increasing needs in automobiles and surgical implants. Thus, although much of growth is in the area of die-cast parts, new manufacturing methods are still urgently being developed to promote further applications of magnesium alloys.

Selective laser melting (SLM) is one of the most promising laser-assisted additive manufacturing methods that can fabricate near net shape components according to CAD model without any tools or molds in a relatively short cycle [7,8]. With the aid of additive support structures and unirradiated powders, SLM technology has the capability to build any complex shape of metal parts that would otherwise be difficult or impossible to produce using conventional manufacturing methods. On the other hand, small molten pools and heat affected zones are induced by the fast scanning laser beam under the control of the galvanometer, which generates high cooling rates of 10^3 – 10^4 K/s inside the molten pools [9,10]. Such high cooling rates may lead to the refinement of microstructure and help to improve essential performances of parts needed in automotive industry and medical implantation. In summary, SLM is an effective way to expand the applied range of magnesium alloys further.

So far, only a few researches on processing pure magnesium or its mixtures using SLM have been reported. Ng et al. [11] have

* Corresponding author. Tel.: +86 27 87792404.

E-mail address: mgao@hust.edu.cn (M. Gao).

studied the single-track formation of pure magnesium using a home-developed SLM system. They found that the width and height of a single track are almost consistent though the laser energy changes. However, there was no attempt to manufacture the more meaningful three-dimensional components. Zhang et al. [12] successfully obtained a SLM parameter window to process the mixture of pure magnesium and pure aluminum with a weight ratio of 91:9. However, the deposited samples only have a highest relative density of 82% and no data about the mechanical properties are given. Obviously, above studies demonstrate that SLM technology is a promising method to develop magnesium or its alloys. Compared with pure magnesium and magnesium-

aluminum mixtures, commercial magnesium alloys have more important application value in industry and medical area. But no reports have been presented to explain the deposition mechanism, formability, microstructure and mechanical properties of SLMed magnesium alloys despite their importance to further applications.

As one of the Mg-Al-Zn (AZ) alloys, AZ91D is a widely used cast magnesium alloy with excellent comprehensive performance. For example, AZ91D is often used as the material of transmission parts in automobile industry and porous implants in medical domain. AZ91D parts with complex structures and high performance are increasing fast in number to challenge conventional manufacturing methods. SLM technique can be used to solve the above manufacturing problems efficiently only after the basic knowledge has been made clear. Therefore, AZ91D is processed by SLM in this study. Forming ability of AZ91D as well as relationship of laser energy input with microstructure and mechanical properties have been studied. Finally, high-density AZ91D parts with better mechanical strengths than conventional die-cast ones are obtained.

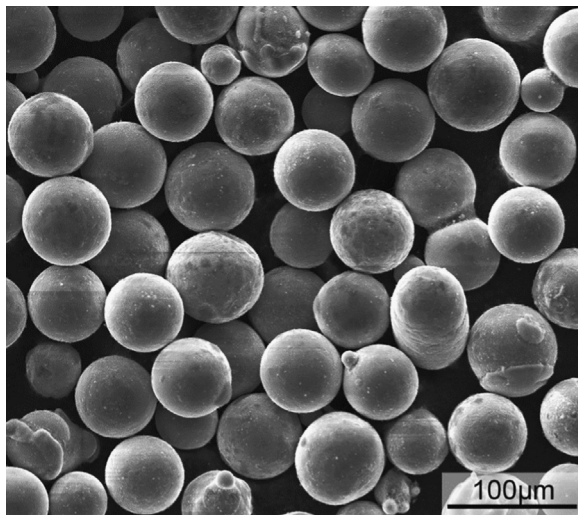


Fig. 1. SEM image showing characteristic morphology of AZ91D powders.

Table 1
Chemical compositions of AZ91D and AZ31B (wt%).

	Al	Zn	Mn	Mg
AZ91D	8.95	0.44	0.19	Bal.
AZ31B	3.34	0.61	0.29	Bal.

2. Experimental procedures

Spherical gas atomized AZ91D powders with a mean particle size of 59 μm and an apparent density of 0.95 g/cm^3 were used as the starting material in SLM experiments, whose morphology is shown in Fig. 1. A commercial die-cast AZ91D ingot with the same composition was also prepared for comparison. Rolled AZ31B plates with a thickness of 35 mm were used as the substrate plates. The chemical compositions of AZ91D and AZ31B used in experiments are listed in Table 1.

All the samples were built by a self-developed SLM system (LSNF-I). Details about the SLM system has been described in our previous publications [13,14], and they will be introduced briefly here. The SLM machine mainly consists of a continuous wave IPG YLR-200 fiber laser ($\lambda = 1.07 \mu\text{m}$), an automatic powder delivery system, a building platform, and a computer system for process control. The manufacturing software controls the movements of the scanner, recoater, powder dispenser and building platform to fabricate parts according to the 3D model. All the SLM experiments were conducted in an argon atmosphere with the concentrations of H_2O and O_2 both controlled below 50 ppm. In addition, a

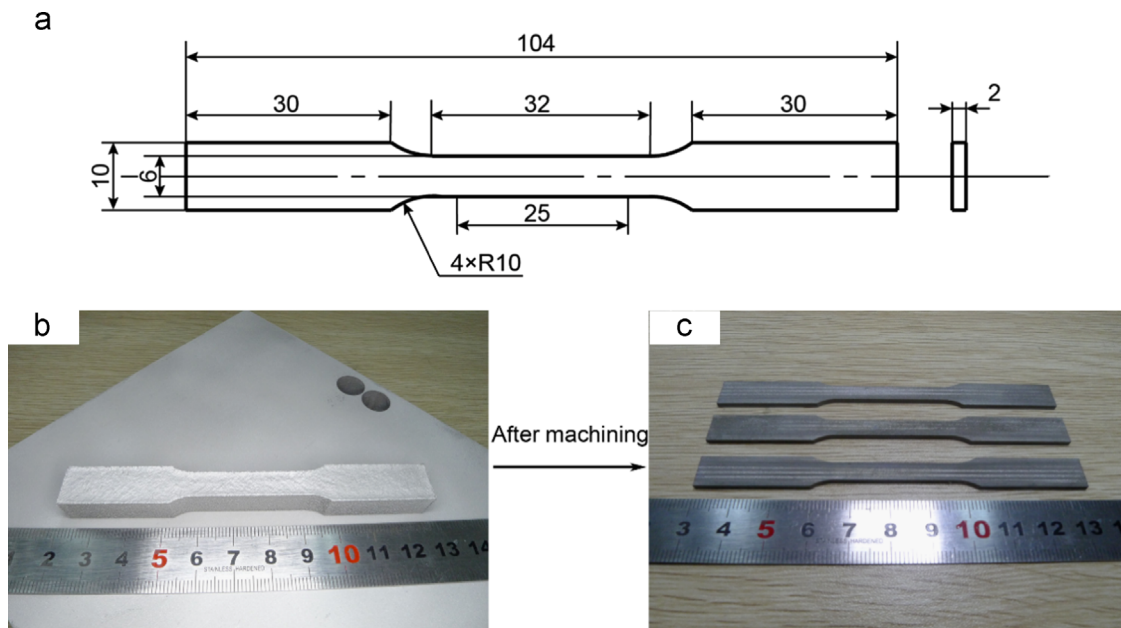


Fig. 2. SLMed AZ91D tensile testpieces in this study. (a) Configuration, (b) SLMed part, (c) tensile testpieces.

standard alternating x/y raster strategy was chosen for laser scanning paths. This strategy features bidirectional hatches of a layer ' n ' performed in x -direction whilst the next layer ' $n+1$ ' turned 90° .

Microstructures of the SLMed samples were observed by standard metallographic techniques using an optical microscopy (Nikon EPIPHOT 300). Phase structure of deposited layers was checked by X-ray diffraction (PANalytical X'Pert PRO) with Cu K α radiation. Surface appearances and microstructures of the samples were characterized by a scanning electron microscopy (FEI Nova NanoSEM 450). The distribution of chemical composition was examined by an energy dispersive spectroscopy (Oxford X-Max 50). Microhardness tests were carried out using an HVS-1000 microhardness tester at a load of 200 g and a holding time of 15 s. As shown in Fig. 2, tensile testpieces were first designed according to the ASTM B557M-10 standard. Then several series of standard AZ91D tensile testpieces manufactured at different laser energy inputs were machined and examined using a Zwick/Roell tester at room temperature. After tensile tests, fracture faces were characterized by the scanning electron microscopy.

Table 2
SLM manufacturing parameters used in this study.

Manufacturing parameters	Value
Laser power P , W	200
Scanning velocity V , m/min	10, 20, 30, 40, 50 and 60
Layer thickness T , mm	0.04
Hatch spacing S , mm	0.07, 0.09, 0.11 and 0.13

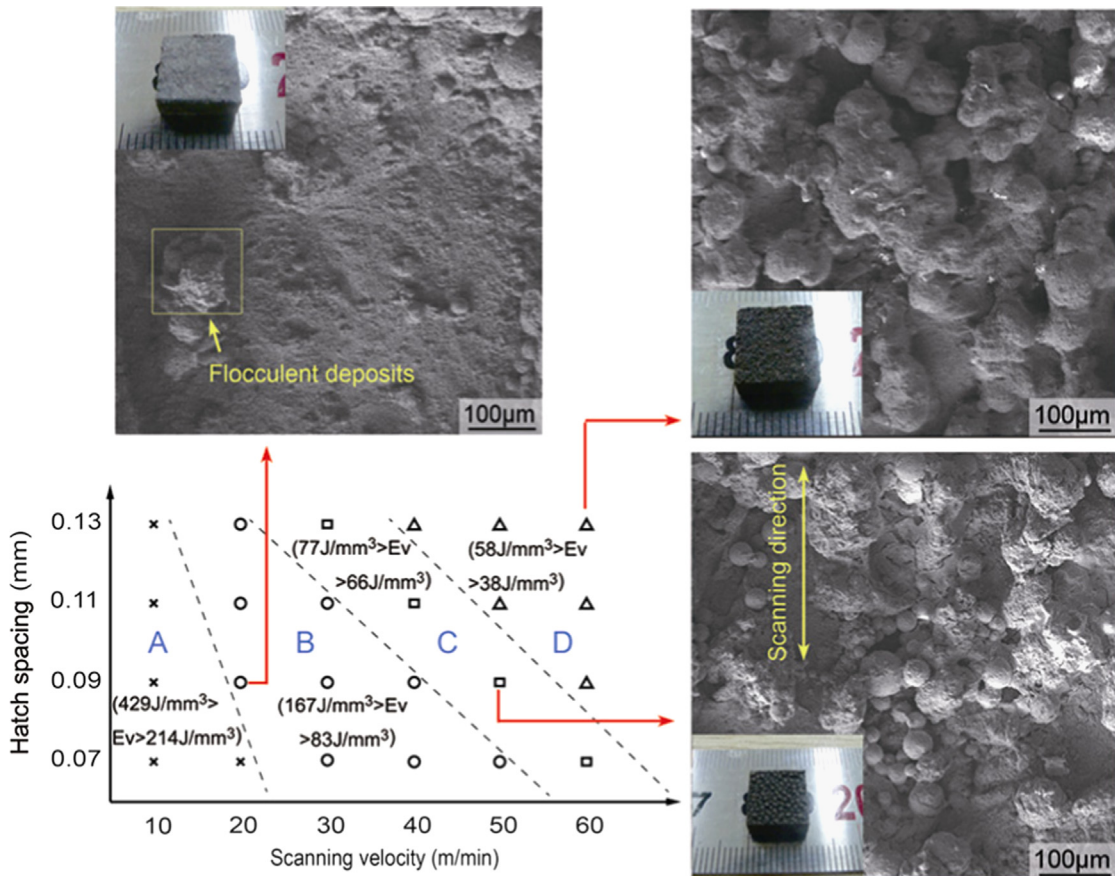


Fig. 3. The processing map of SLM experiments based on laser energy input.

3. Results and discussion

3.1. Formability

During SLM experiments, 24 cubic samples with a size of $10 \times 10 \times 5$ mm 3 were first built to optimize the SLM parameters. Parameters used in this study are presented in Table 2. A processing map based on the formability of AZ91D magnesium alloy powders was then established, as shown in Fig. 3. It could be found that the formability of AZ91D during SLM process directly depends on the input of laser energy. Considering the thickness of powder layer, the input of laser energy during fabrication can be represented better by the volume energy density E_v . Here volume energy density E_v is defined as the laser energy per volume and can be calculated by the following equation:

$$E_v = \frac{P}{STV} \quad (1)$$

where P is the laser power, S is the hatch spacing, T is the layer thickness and V is the scanning velocity.

Based on the calculation of Eq. (1) at different parameter combinations, the processing map in Fig. 3 can be divided into four zones. In zone A, high energy inputs with E_v above 214 J/mm 3 make the temperature in the molten pools increase too much, which causes serious evaporation of the powders due to low boiling point and high vapor pressure of magnesium. The evaporated powders expand rapidly and exert a high recoil pressure on the molten pools. Molten pools together with the surrounding unmelted powders are then blown away to make the SLM process failure. In zone B, AZ91D samples without obvious macro-defects are built in a proper range of E_v between 83 J/mm 3 and 167 J/mm 3 .

However, flocculent depositions together with distorted scanning tracks caused by the evaporation of metal powders can still be found on the surface of sample fabricated at 166.7 J/mm^3 . In zone C, where E_v is in the range of 66 J/mm^3 to 77 J/mm^3 , “balling effect” arises on the surface of SLMed samples. Molten pools with small circumference-to-length ratios generated at relatively low energy inputs are unstable. As described by Yadroitsev et al. [7], scanning tracks decompose into discrete droplets in this condition. Thus, ball-like particles parallel to scanning direction together with large quantities of unmelted powders induce a more deteriorated surface, which can be observed from the fabricated sample at 66.7 J/mm^3 . Finally, in zone D, where E_v is below 58 J/mm^3 , loose samples without mechanical strength are obtained due to incomplete melt of most of the powders.

In order to further understand how the energy input influences formability, relative density of the deposited AZ91D samples was analyzed by measuring the porosity. According to quantitative stereology, the porosity of sample is considered to be equivalent to the area percentage of pores in tested sections [15]. An Image-Pro Plus 6.0 software was utilized to analyze the porosity. First, for each SLMed sample, two sections parallel to deposition direction were taken into account. For each section, after grinding and polishing, optical micrographs of four random selected positions were taken at a magnification of $50\times$. Second, all the micrographs were transformed into the gray mode and a proper threshold value of grayscale was chosen using the segmentation function of the software to mark regions where the grayscale is the same as the pores. Third, the area percentage of pores in each micrograph was determined by calculating the area ratio of the marked regions to the whole micrograph with the help of the statistics function. Finally, the porosity of each SLMed sample was determined by counting the average area percentage of pores based on the eight optical micrographs. Fig. 4 gives the relationship between the relative density and scanning velocity at different hatch spacings. There is a general decreasing trend of the relative density with increasing scanning velocity for all hatch spacings, which demonstrates that the relative density of SLMed samples is decided by the energy input. During SLM process, relatively high E_v induced by slow scanning velocities leads to a sufficient irradiation time. Thus, powders are fully melted and the gas entrapped or generated in the molten pool has enough time to release. On the contrary, short irradiation time induced by relative high scanning velocities results in partial melt of powders and serious entrapment of gas. Thus, poor bond of adjacent scanning

tracks leads to the decrease in relative density. In the present study, the highest relative density of SLMed AZ91D sample is 99.52% at E_v of 166.7 J/mm^3 ($P=200 \text{ W}$, $S=0.09 \text{ mm}$, $T=0.04 \text{ mm}$, $V=20 \text{ m/min}$). Relative density may influence mechanical properties of the SLMed samples and this will be discussed in the subsequent sections.

3.2. Microstructure characterization

XRD patterns of the SLMed samples built at different energy inputs are shown in Fig. 5a. It is evident that samples are all composed of $\alpha\text{-Mg}$, $\beta\text{-Mg}_{17}\text{Al}_{12}$ and a lesser degree of Al_8Mn_5 . No peaks corresponding to MgO and Al_2O_3 are found due to strict control of the concentrations of H_2O and O_2 . Through a close-up view of the XRD patterns, as shown in Fig. 5b and c, $\alpha\text{-Mg}$ peaks slightly shift to low diffraction angles with decreasing E_v . Since atomic radii of Al (0.1199 nm) and Zn (0.1187 nm) are 89.95% and 89.05% of Mg (0.1333 nm) [16], Al and Zn act as substitutive solutes in the $\alpha\text{-Mg}$ matrix according to the theory of solid solution. When E_v decreases from 166.7 J/mm^3 to 66.7 J/mm^3 , temperatures of the molten pools reduce and the evaporation of Mg element becomes weak, which results in decrease of contents of Al and Zn in $\alpha\text{-Mg}$ matrix. Therefore, lattice parameters of $\alpha\text{-Mg}$ become larger and $\alpha\text{-Mg}$ diffraction peaks shift to low angles. Table 3 lists intensity ratios of major peaks of $\beta\text{-Mg}_{17}\text{Al}_{12}$ to $\alpha\text{-Mg}$ phase at different energy inputs. Note that β phase becomes less with decreasing energy input and this phenomenon will be discussed further in subsequent chapter.

Fig. 6 presents the optical micrographs of the AZ91D sample deposited at 166.7 J/mm^3 . In Fig. 6a, molten pools with elliptical bottom induced by the Gaussian distribution of laser energy align layer by layer, which shows a layerwise feature intrinsic to SLM technology. All the ends of melted tracks are close stacked to form a good metallurgical bonding between two neighbor layers though several micropores still exist. In Fig. 6b, it is easy to find that the penetration depth of molten pools can be up to $312 \mu\text{m}$, which is approximately eight times the layer thickness. Therefore, except for the last layer, each layer of the as-deposited sample undergoes remelting process more than once. Multiple remelting processes not only help to improve the quality of metallurgical bond between neighbor tracks and layers, but also play a significant role in determining the microstructure of SLMed samples. From Fig. 6c, close stacked scanning tracks can be seen in the cross section. It is necessary to point out that discontinuous scanning tracks from different layers can also be observed due to the fluctuation of molten pools and the alternating raster filling strategy. Fig. 6d gives the detail of scanning tracks shown in Fig. 6c and it is quite apparent that the microstructure is not uniform. During SLM process, in order to acquire metallurgical bond with high quality, hatch spacing between two neighbor tracks should be smaller than the track width. As shown in Fig. 6d, the overlap regions between two neighbor tracks are defined as the overlapping regions (hereafter called OLR) whilst other regions are defined as the center of scanning tracks (hereafter called CST). The difference in thermal history between OLR and CST induces the nonuniform microstructure of the deposited AZ91D samples.

SEM micrographs of SLMed AZ91D at the energy input of 166.7 J/mm^3 are shown in Fig. 7a and b. The microstructure presents a feature of equiaxed $\alpha\text{-Mg}$ with fully divorced eutectic $\beta\text{-Mg}_{17}\text{Al}_{12}$ distributing reticularly along the boundary. Although Al_8Mn_5 are believed to exist according to XRD patterns, they are not found throughout the micrographs due to the very low content. Grain sizes of $\alpha\text{-Mg}$ matrix are quite fine due to the high cooling rates of SLM. From Fig. 7c and d, the average grain size of $\alpha\text{-Mg}$ in CST and OLR are measured to be $1.0 \mu\text{m}$ and $2.9 \mu\text{m}$,

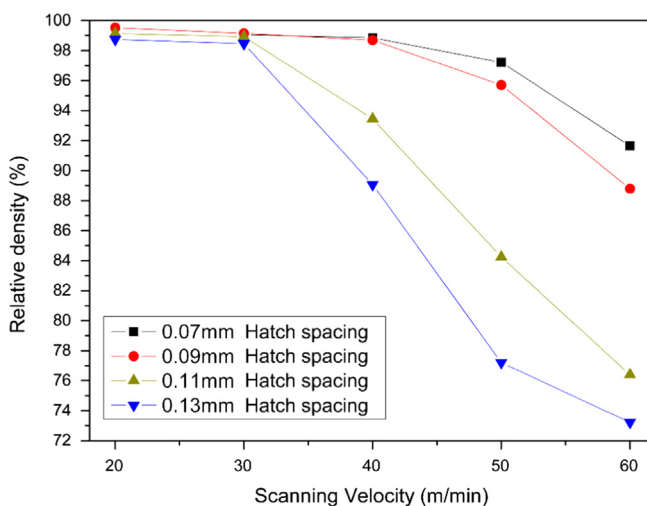


Fig. 4. Relative density of the SLMed samples deposited at different SLM parameters.

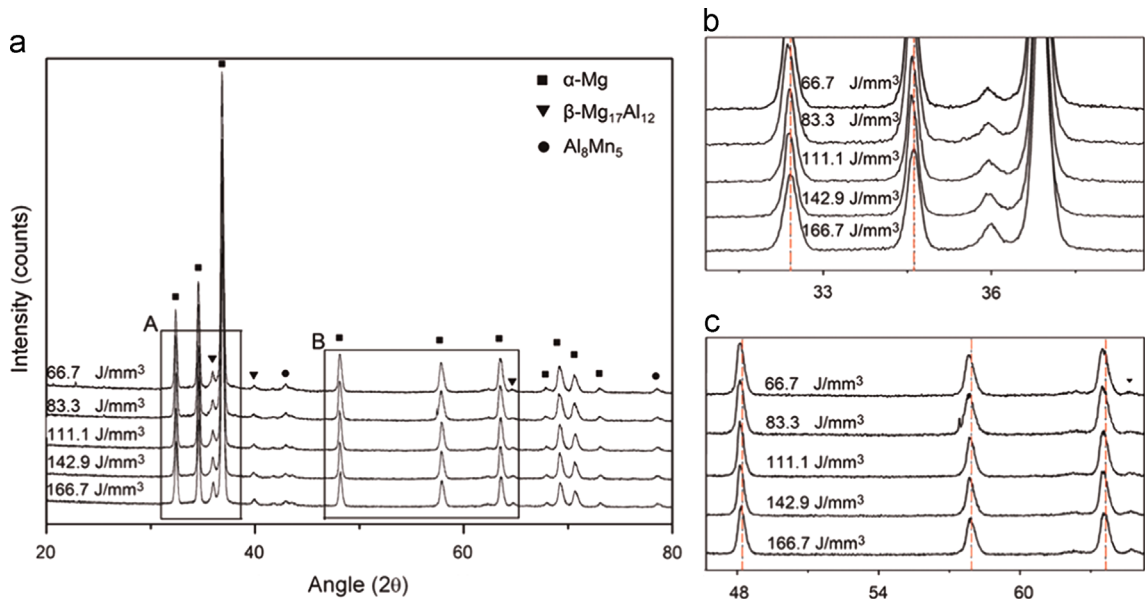


Fig. 5. (a) XRD patterns of the SLMed samples at different E_v , (b) and (c) details about regions marked as A and B shown in (a).

Table 3

Intensity ratios of major X-ray diffraction peaks of β and α phase, I_β/I_α , as measured in the deposited samples at different E_v .

I_β/I_α (%)	As-deposited samples at different E_v				
	166.7 J/mm ³	142.9 J/mm ³	111.1 J/mm ³	83.3 J/mm ³	66.7 J/mm ³
Intensity ratio of (411) peak of β phase to (101) peak of α phase	6.02	5.78	5.04	4.81	3.84
Intensity ratio of (332) peak of β phase to (101) peak of α phase	2.21	1.90	1.98	2.06	1.20

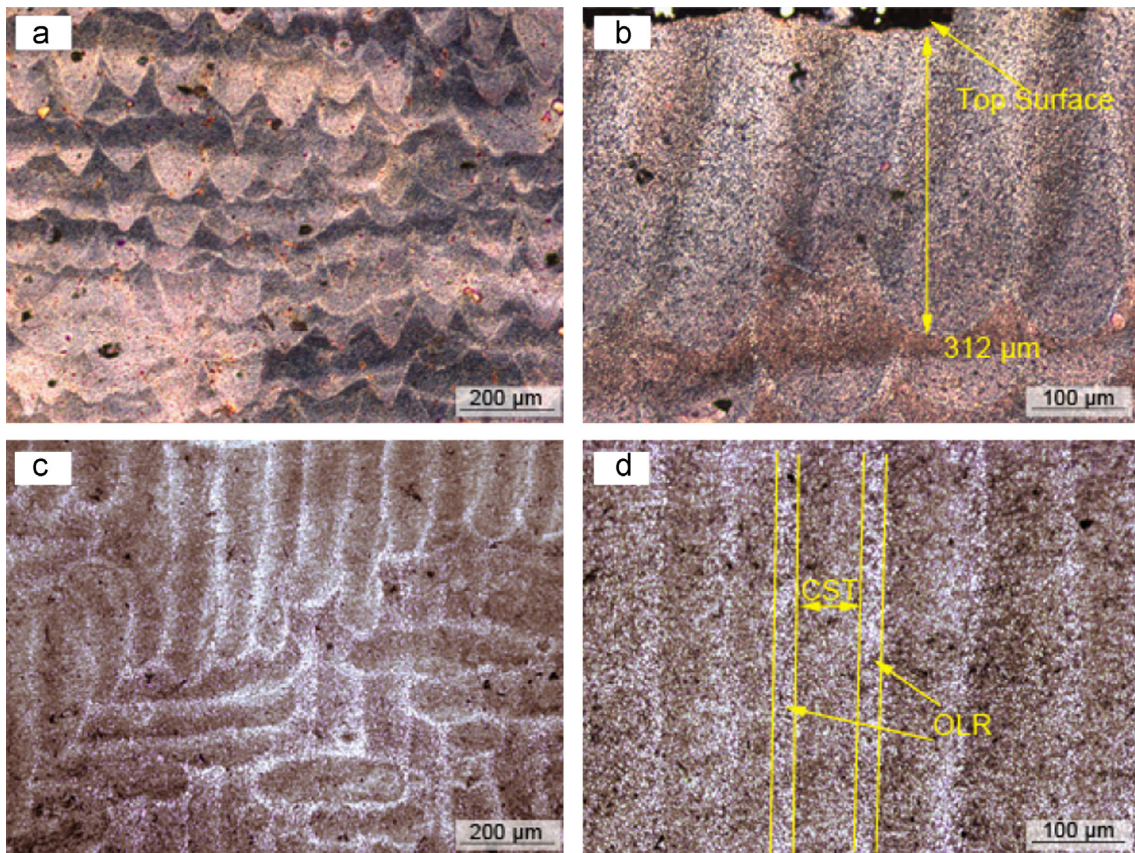


Fig. 6. Optical micrographs of the AZ91D sample deposited at E_v of 166.7 J/mm³. (a) and (b) The vertical section, (c) the cross section, and (d) the detail of scanning tracks shown in (c).

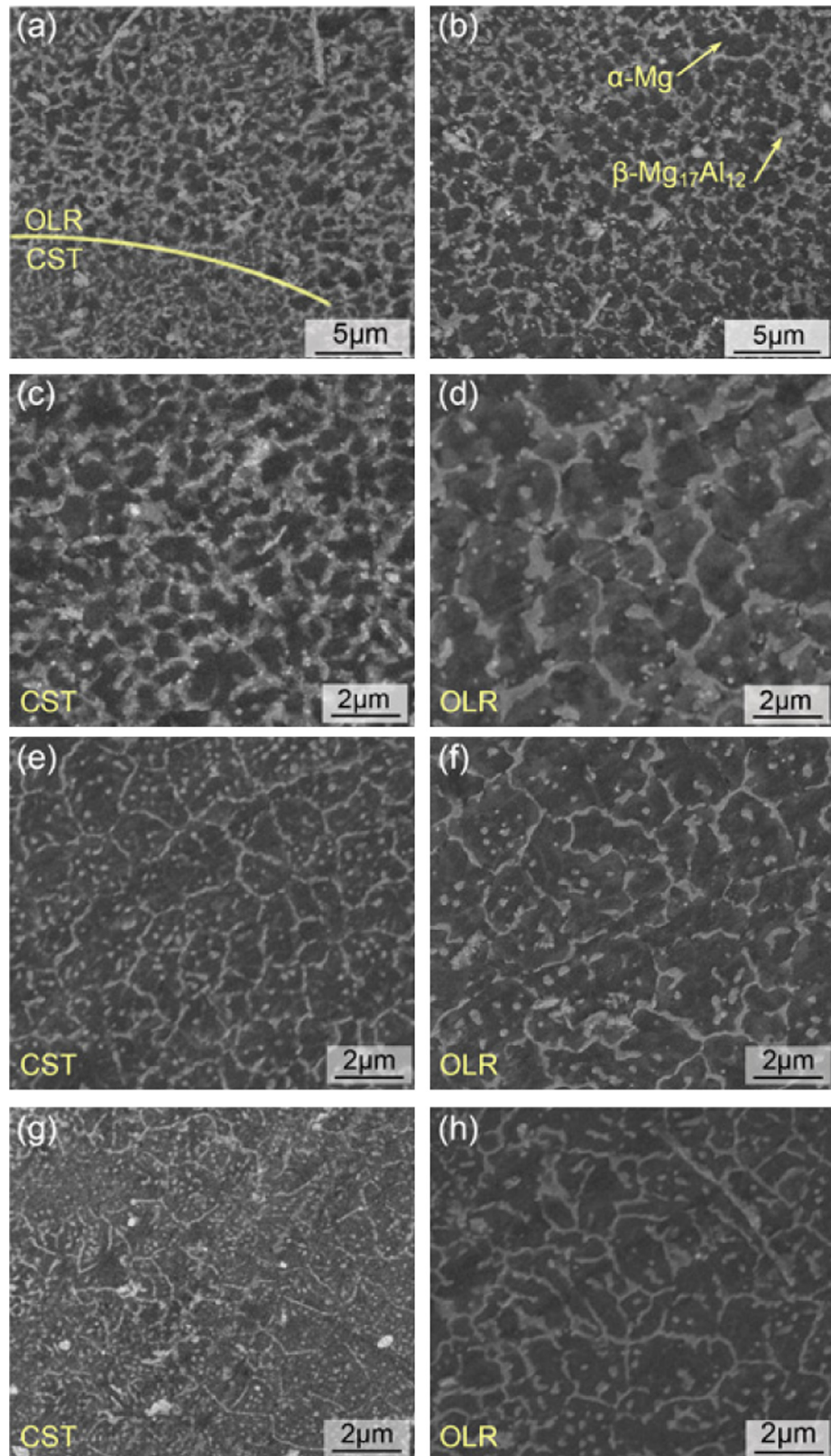


Fig. 7. SEM micrographs of AZ91D samples built at different E_v . (a) The cross section of the sample built at 166.7 J/mm³, (b) the vertical section of the sample built at 166.7 J/mm³, (c) details of CST in (a), (d) details of OLR in (a), (e) and (f) CST and OLR in the cross section of the sample built at 111.1 J/mm³, (g) and (h) CST and OLR in the cross section of the sample built at 83.3 J/mm³.

respectively. Compared with CST, OLR experiences more cycles of remelting process to induce relatively lower cooling rates, which causes the microstructures in OLR coarsen. This phenomenon has also been found by Guan et al. [17] during laser surface melting of

AZ91D. However, this kind of nonuniform distribution of microstructure is in the scale of several microns, which may only lead to the mechanical performance like microhardness fluctuates in a smaller range.

SEM micrographs of samples deposited at 111.1 J/mm³ and 83.3 J/mm³ are also presented in Fig. 7e, f, g and h. The coarsening of microstructures in OLR is observed again. Moreover, β phase becomes lesser and thinner both in OLR and CST with decreasing E_v , which is totally consistent with the variation in intensity ratio of major diffraction peaks of β to α phase shown in Table 3. There may be two reasons to explain this phenomenon. One is lower E_v reduces the evaporation capacity of Mg and then $\beta\text{-Mg}_{17}\text{Al}_{12}$ which is enrichment of Al becomes less with decreasing content of Al. Another reason can be explained by the effect of “solute capture”. According to the model for solute redistribution during continuous growth in rapid solidification established by Aziz [18], solute distribution coefficient of the moving solid–liquid phase interface (k_v) can be calculated by the following formula:

$$k_v = \frac{k_e + R/V_d}{1 + R/V_d} \quad (2)$$

where k_e is the equilibrium segregation coefficient, R is the growth rate of the solid/liquid interface and V_d is the diffusive speed of a solute atom at the interface. From the above formula, k_v is not a constant but a dynamics-dependent variable which changes monotonously from k_e to 1 with the increase of R from 0 to ∞ . During SLM process, R is directly proportional to the scanning velocity V . Under the control of the galvanometer, the scanning velocity adopted in this study is as high as tens of meters per minute, which results in the rapid motion of the solid/liquid

interface. Thus, during solidification of the deposited layers, k_v is considerably larger than k_e and the condition of local equilibrium near the interface is significantly deviated. The diffusion time of Al is insufficient so that “solute capture” phenomenon in the $\alpha\text{-Mg}$ matrix appears and therefore, the formation of Al-rich β phase is inhibited to some extent. By lowering down the energy input from 166.7 J/mm³ to 83.3 J/mm³, in other words, by increasing the scanning velocity from 20 m/min to 40 m/min, the growth rate of the interface R increases to a much higher degree. Therefore, k_v further approaches to 1 and a higher proportion of solute atom is captured in the matrix $\alpha\text{-Mg}$ to further retard the nucleation of $\beta\text{-Mg}_{17}\text{Al}_{12}$.

For comparison, the microstructure of commercial die-cast AZ91D is presented in Fig. 8a and b. The die-cast ingot is also composed of $\alpha\text{-Mg}$ solid solution and $\beta\text{-Mg}_{17}\text{Al}_{12}$ eutectic phase distributing along the grain boundaries. From the magnified micrograph of region A (inset in Fig. 8b), it could be found that some bulky divorced eutectic $\beta\text{-Mg}_{17}\text{Al}_{12}$ are surrounded by the lamellar eutectic. The lamellar structure is believed to form through the cellular growth of alternating plates of the $\beta\text{-Mg}_{17}\text{Al}_{12}$ phase and the $\alpha\text{-Mg}$ phase at high angle boundaries [19]. Thus, in the die-cast AZ91D ingot, β precipitates exist in the form of partially divorced eutectic structure. AZ91D is approximately one of the hypoeutectic Mg-Al alloys due to its low content of Zn. According to Dahle's report [20], the morphology of eutectic in the hypoeutectic Mg-Al alloys depends on the cooling rate. The higher

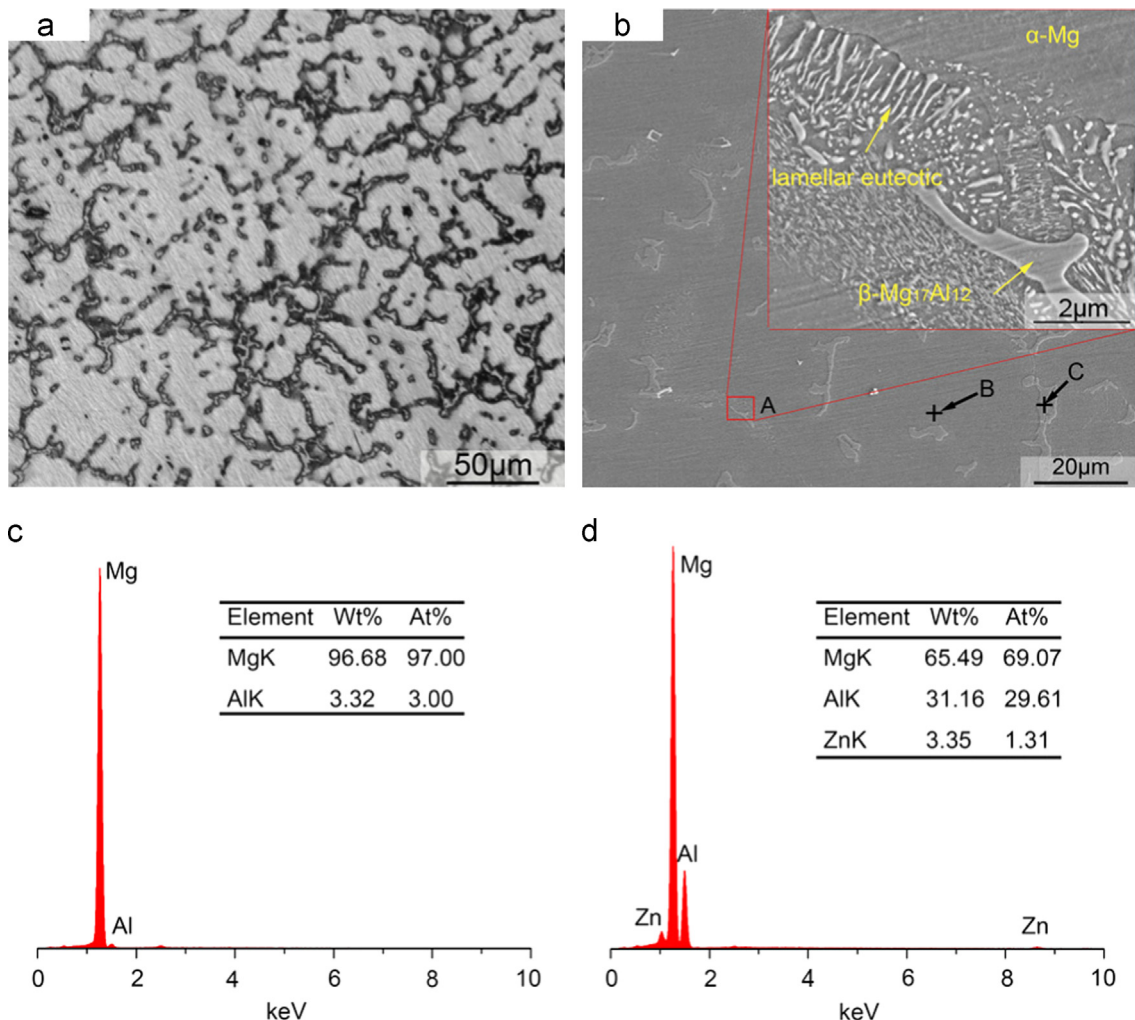


Fig. 8. (a) Optical image and (b) SEM image of the die-cast AZ91D ingot, (c) EDS result of position B in (b), (d) EDS result of position C in (b).

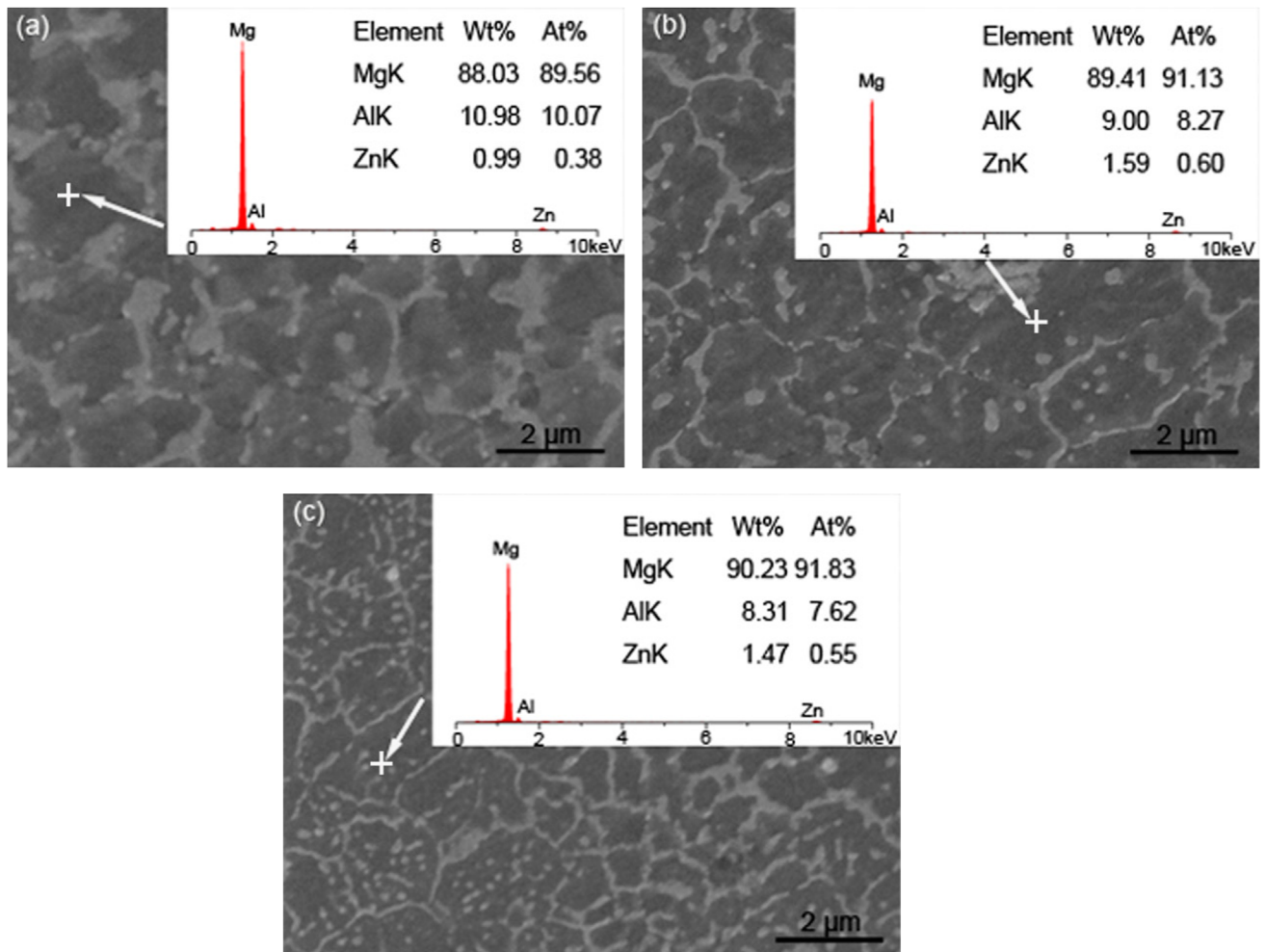


Fig. 9. EDS results of α -Mg matrix of the SLMed AZ91D deposited at E_v of (a) 166.7 J/mm³, (b) 111.1 J/mm³ and (c) 83.3 J/mm³.

cooling rate results in the more divorced structure. Therefore, change in the form of β phase between SLMed and die-cast AZ91D is induced by the high cooling rate inherent to SLM process.

For the die-cast sample, most of the Al and Zn elements concentrate in the β -Mg₁₇Al₁₂ phase, as shown in Fig. 8c and d. The decrease of Al content in α -Mg solid solution not only reduces the effect of solution strengthening but also deteriorates the corrosion behavior [21]. Therefore, element distribution of the SLMed AZ91D is also necessary to be evaluated. Fig. 9 presents EDS results of the α -Mg solid solution of the SLMed samples at different energy inputs. The concentration of Al element in the α -Mg solid solution is much higher than that of the die-cast sample. It could be observed that Al content in the α -Mg matrix decreases from 10.98 wt% to 8.31 wt% with decreasing energy input, which is in accord with the XRD peak shifting shown in Fig. 5. Along with the decrease in energy input, the effect of "solute capture" becomes stronger whilst burning loss rate of Mg atoms reduces. Therefore, under the interaction between "solute capture" and element evaporation, Al concentration in the α -Mg decreases with the decreasing energy input in spite of the fact that more proportion of Al atoms are captured. Fig. 10 compares the dispersion of Mg and Al elements in the AZ91D sample deposited at 166.7 J/mm³ and the die-cast AZ91D ingot sample. It could be found that distributions of Mg and Al are much more uniform in the deposited AZ91D and there is no distinct variation in element contents between OLR and CST. Moreover, the distributions of Mg and Al in deposited samples at other energy inputs are similar

with the result shown in Fig. 10 though they are not given here to save space.

Composition homogenization of the deposited AZ91D should be decided by the solidification procedure during SLM. Firstly, the difference of composition between supersaturated α -Mg and β -Mg₁₇Al₁₂ is diminished by the effect of "solute capture". Secondly, convection in the molten pool helps to homogenize the liquid. According to fluid flow model proposed by He et al. [22], driving force for liquid convection in the molten pool produced by laser irradiation consists of buoyancy and Marangoni force. Which one dominates the convection process can be evaluated from the ratio of surface-tension Reynolds number (Ma) to buoyancy-related Grashof number (Gr):

$$R_{s/b} = \frac{Ma}{Gr} = \frac{L_R |\partial\gamma/\partial T|}{g\rho\delta L_b^3} \quad (3)$$

where L_R is the pool radius taken as half of the width of scanning track, $\partial\gamma/\partial T$ is the temperature coefficient of surface tension, g is the gravitational acceleration, ρ is the density of materials, δ is the thermal expansion coefficient and L_b is the characteristic length for the buoyancy force which is approximately one eighth of the width of scanning track. Take the sample fabricated at 166.7 J/mm³, according to the average width of the scanning track 108 μm measured from Fig. 6 and physical properties of AZ91D recorded in the literature [23], $R_{s/b}$ is about 7.20×10^7 . Thus, fluid flow in the molten pool is mainly driven by Marangoni convection. The maximum liquid velocity in the molten pool is believed to

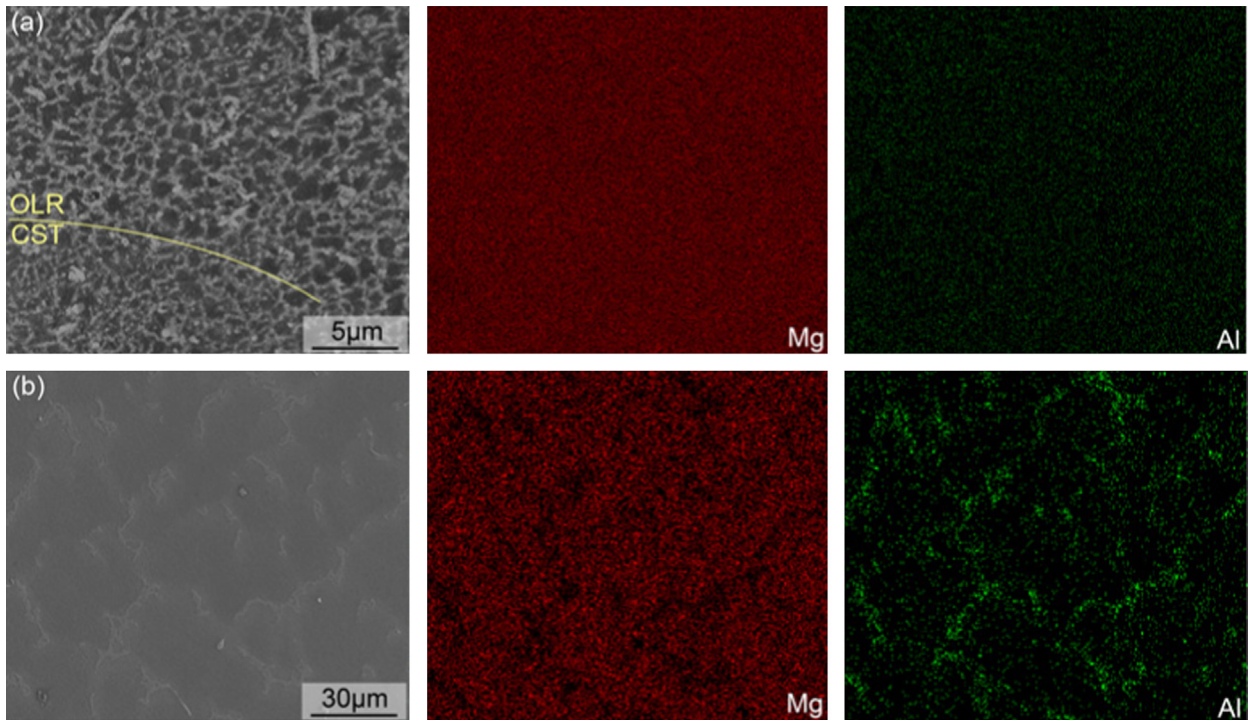


Fig. 10. EDS images of (a) the SLMed AZ91D at E_v of 166.7 J/mm^3 and (b) the die-cast AZ91D.

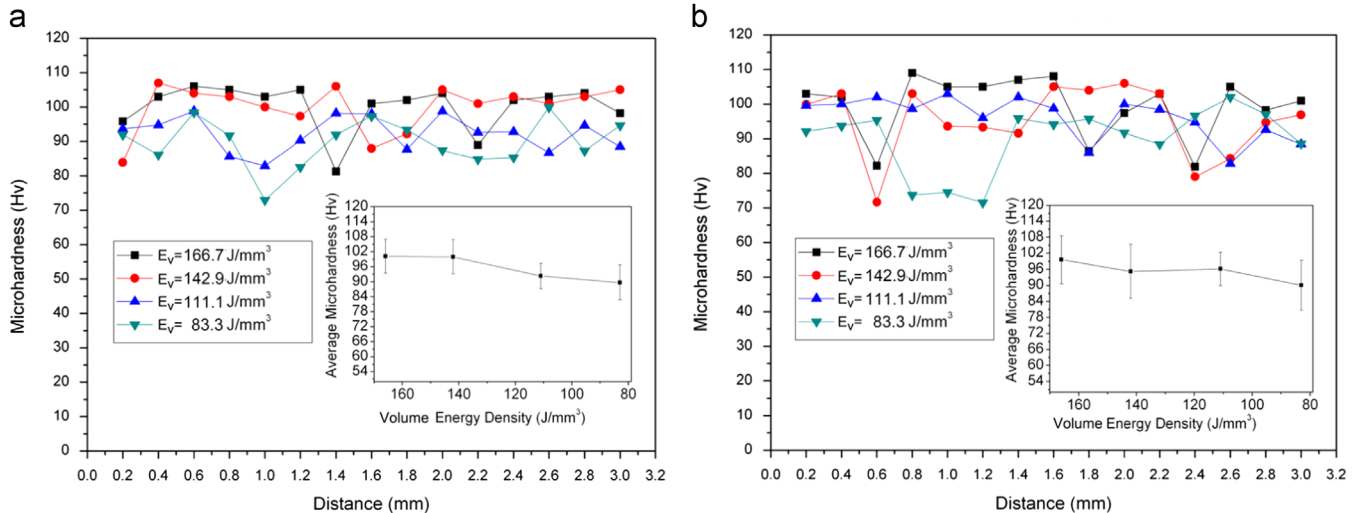


Fig. 11. Microhardness of SLMed AZ91D samples on cross section (a) and vertical section (b).

be positive correlation with the temperature gradient [24]. Due to the Gaussian distribution of incident laser and small size pool inherent to SLM technology, a high temperature gradient between the center and edge of the molten pool is generated, which results in a strong Marangoni convection to improve the homogeneous dispersion of Mg and Al elements.

3.3. Mechanical properties

Fig. 11 presents the microhardness on two sections for AZ91D samples deposited at several representative E_v chosen in zone B of the processing map. Due to the variation in microstructure between OLR and CST, the microhardness fluctuates in a small range on both sections for all tested samples. However, the microhardness of deposited samples shows directional independence. The average microhardness of SLMed samples ranges from 85 to 100 HV, which is much higher than that of the commercial

die-cast ingot (58 HV). Considering the SLMed AZ91D sample built at 166.7 J/mm^3 , the improvement of microhardness should be ascribed to the following reasons.

First, according to the Hall-Petch formula [25], grain refinement can significantly increase the microhardness of magnesium alloys. Due to the variation of grain size between CST and OLR, the average grain size $d_{\alpha-SLM}$ of α -Mg matrix can be evaluated to be $1.2 \mu\text{m}$ using the area-based averaging method [26]:

$$d_{\alpha-SLM} = [f_{CST}/d_{\alpha-CST}^2 + (1-f_{CST})/d_{\alpha-OLR}^2]^{-1/2} \quad (4)$$

where f_{CST} is area fraction of CST (measured as 65% from Fig. 6d), $d_{\alpha-CST}$ ($1.0 \mu\text{m}$) and $d_{\alpha-OLR}$ ($2.9 \mu\text{m}$) are the average size of α -Mg in CST and OLR respectively. Meanwhile, the average grain size of α -Mg in the die-cast sample is measured as $57 \mu\text{m}$. Therefore, grain refinement helps to improve the microhardness of the SLMed AZ91D.

Second, Al concentration in α -Mg of the SLMed sample is much higher than that of the die-cast AZ91D due to the effect of “solute capture”. According to the theory of solid solution strengthening, a higher solid solubility would induce superior mechanical strengths [27]. For Mg-Al alloys, the variation in microhardness is in proportion to the Al content in α -Mg [28]. Therefore, solid solution strengthening also contributes to the high microhardness of the SLMed AZ91D.

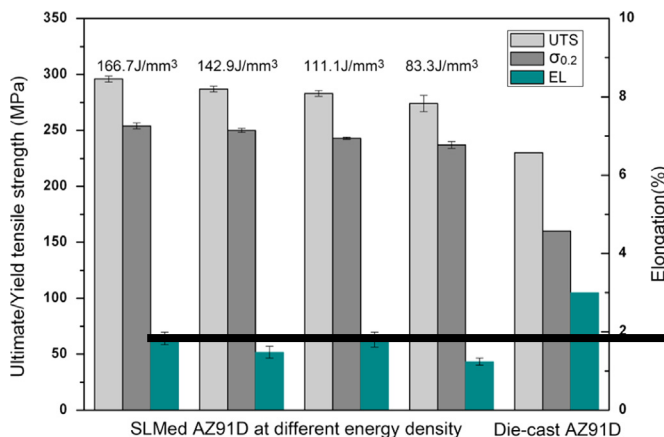


Fig. 12. Tensile performance of samples deposited at different E_v and that of the die-cast AZ91D.

In addition, the hard-brittle β phase can be considered as a strengthening phase when distributing in the soft α -Mg matrix. According to Yang's and Yim's reports [29,30], higher fraction of the strengthening phase would result in the improvement of strength and microhardness. Here, based on the area-based averaging theory [26] and Figs. 7c, d and 8a, the fraction of β phase in the SLMed AZ91D is determined to be 31.7% whilst that of the die-cast AZ91D is 36.2%. Thus, it can be concluded that β phase does not contribute to the improvement of microhardness for the SLMed AZ91D samples.

Under the interaction of “solute capture” and element evaporation, the content of hard-brittle β phase and the solid solubility of solute elements in α -Mg matrix decrease simultaneously with decreasing E_v . Meanwhile, there is no significant difference on the average grain sizes of α -Mg in different SLMed samples. Therefore, the microhardness becomes lower gradually when E_v decreases from $166.7 J/mm^3$ to $83.3 J/mm^3$, as shown in Fig. 11.

Fig. 12 summarizes the tensile properties of samples deposited at those above-mentioned E_v . For comparison, the tensile properties of the die-cast AZ91D (according to ASTM standard B94-07) are also included. Ultimate strength (UTS) and yield strength ($\sigma_{0.2}$) of the SLMed samples are superior to those of the die-cast AZ91D alloy though their elongation (EL) has a slight drop from 3% to 1.24–1.83%. It is apparent that laser energy input can also influence the tensile properties. In Fig. 12, the average UTS and $\sigma_{0.2}$ of the SLMed samples, decrease gradually from 296 MPa and 254 MPa at $166.7 J/mm^3$ to 274 MPa and 237 MPa at $83.3 J/mm^3$. This variation should be first ascribed to the poor relative densities of the SLMed

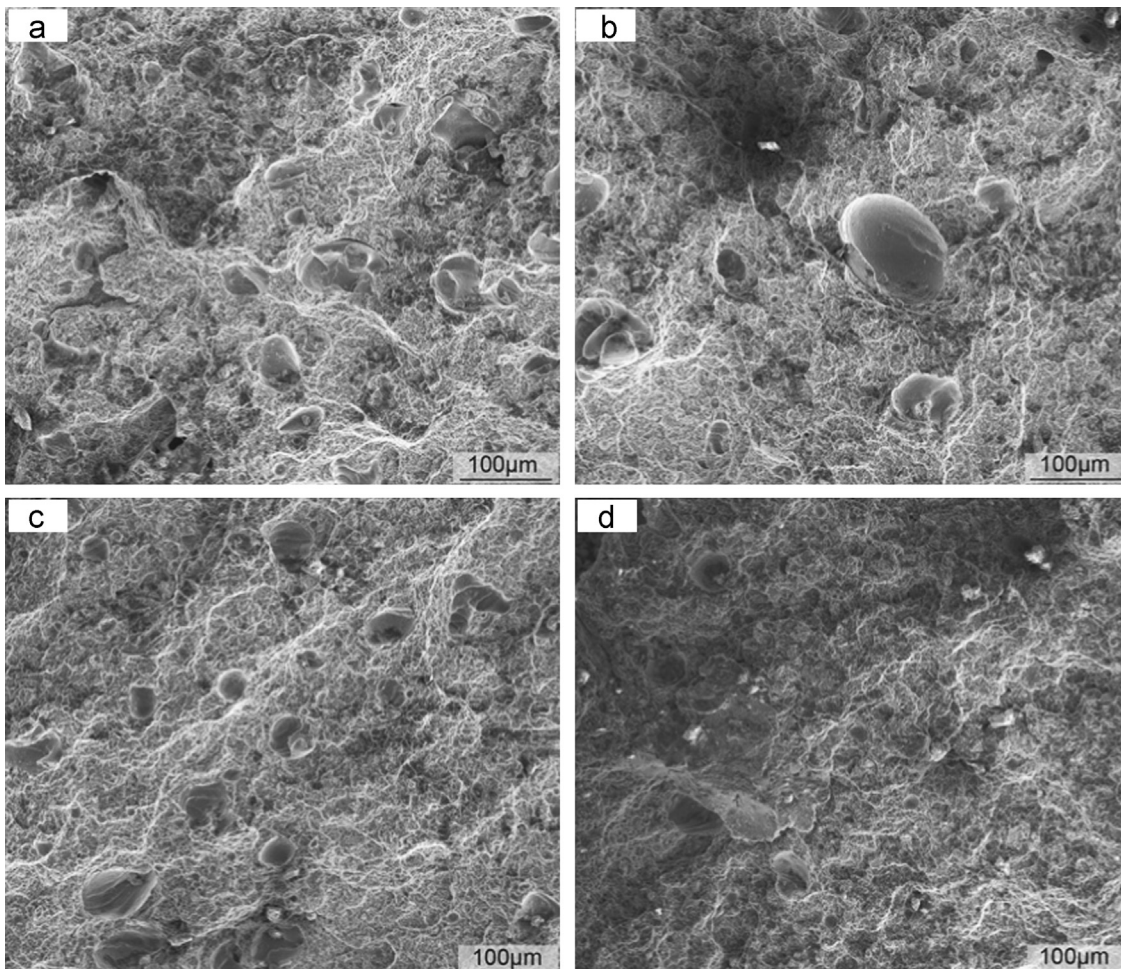


Fig. 13. Fracture morphologies of SLMed tensile samples at different E_v . (a) $166.7 J/mm^3$, (b) $142.9 J/mm^3$, (c) $111.1 J/mm^3$, (d) $83.3 J/mm^3$.

samples obtained at lower energy inputs. Another factor that cannot be ignored to degrade the tensile properties is the lower solid solubility of the α -Mg matrix and smaller quantity of the intermetallic β phase induced by lower energy inputs.

The fracture morphologies of tensile samples were also observed, as shown in Fig. 13. All the tensile samples exhibit the feature of ductile–brittle hybrid fracture for bestrewing dimples and ductile tearing ridges together with quasi-cleavages. This kind of fracture mode should be related to the multiple-phase microstructures and the micropores distributing in the samples. Soft α -Mg matrix results in the ductile feature whereas brittle β phase and the micropores reduce ductility by stress concentration and lead to the formation of cleavage-like brittle characteristics.

4. Conclusions

Selective laser melting of AZ91D has been carried out in this study. Effect of laser energy input on the formability, microstructure and mechanical properties of the SLMed AZ91D samples are analyzed. The major findings are listed as follows:

- (1) Formation qualities of the as-deposited AZ91D samples depend on the laser energy inputs during SLM process. There is a proper processing window to fabricate AZ91D powders, where high density AZ91D without obvious macro-defects can be obtained between 83 J/mm³ and 167 J/mm³. Samples are unable to be deposited at laser energy inputs higher than 214 J/mm³ due to intense evaporation, whereas the fabricated samples are loosened at laser energy inputs below 77 J/mm³ due to “balling effect” and incomplete melt of powders.
- (2) All the deposited AZ91D samples show a layerwise feature with neighbor tracks and layers stacking close together. In microstructure, the SLMed AZ91D consists of equiaxed α -Mg matrix and fully divorced eutectic β -Mg₁₇Al₁₂. The average size of α -Mg in OLR is a little larger than that in CST due to the remelting process though the element contents are quite uniform. Due to the interaction of “solute capture” and element evaporation, the content of hard-brittle β phase and solubility of solute elements in α -Mg matrix decrease simultaneously with decreasing laser energy inputs.
- (3) The microhardness of all samples shows directional independence. There is a fluctuation of microhardness within a narrow range on both sections for all tested samples. The microhardness and tensile strengths of the SLMed AZ91D at room temperature are superior to those of the die-cast AZ91D. Grain refinement and solid solution strengthening are the main strengthening mechanisms for SLMed AZ91D.
- (4) In this study, nearly full dense AZ91D (99.52%) with the microhardness of 100 Hv, UTS of 296 MPa and $\sigma_{0.2}$ of

254 MPa can be obtained using laser volume energy density of 166.7 J/mm³.

Acknowledgment

This work is supported by the National Natural Science Foundation of China through Program no. 51075164 and the Fundamental Research Funds for the Central Universities through Program no. HUST-2014QT006.

References

- [1] B.L. Mordike, T. Ebert, Mater. Sci. Eng. A 302 (2001) 37–45.
- [2] F.H. Froes, D. Eliezer, E. Aghion, J. Miner. Met. Mater. Soc. 50 (1998) 30–34.
- [3] C.K. Seal, K. Vince, M.A. Hodgson, IOP Conf. Ser. Mater. Sci. Eng. 4 (2009) 012011.
- [4] M.P. Staiger, A.M. Pietak, J. Huadmai, G. Dias, Biomaterials 27 (2006) 1728–1734.
- [5] M.K. Kulekci, Int. J. Adv. Manuf. Technol. 39 (2008) 851–865.
- [6] E. Aghion, N. Moscovitch, A. Arnon, Mater. Sci. Eng. A 447 (2007) 341–346.
- [7] I. Yadroitsev, A. Gusarov, I. Yadroitseva, I. Smurov, J. Mater. Process. Technol. 210 (2010) 1624–1631.
- [8] I. Yadroitsev, P. Krakhmalev, I. Yadroitseva, S. Johansson, I. Smurov, J. Mater. Process. Technol. 213 (2013) 606–613.
- [9] T. Vilaro, C. Colin, J.D. Bartout, Metall. Mater. Trans. A 42A (2011) 3190–3199.
- [10] L. Wang, S. Felicelli, Y. Gooroochurn, P.T. Wang, M.F. Horstemeyer, Mater. Sci. Eng. A 474 (2008) 148–156.
- [11] C.C. Ng, M. Savalani, H.C. Man, Rapid Prototyping J. 17 (2011) 479–490.
- [12] B.C. Zhang, H.L. Liao, C. Coddet, Mater. Des. 34 (2012) 753–758.
- [13] Z.M. Wang, K. Guan, M. Gao, X.Y. Li, X.F. Chen, X.Y. Zeng, J. Alloys Compd. 513 (2012) 518–523.
- [14] K. Guan, Z.M. Wang, M. Gao, X.Y. Li, X.Y. Zeng, Mater. Des. 50 (2013) 581–586.
- [15] D. Min, J. Shen, S.Q. Lai, J. Chen, N. Xu, H. Liu, Opt. Lasers Eng. 49 (2011) 89–96.
- [16] C.H. Suresh, N. Koga, J. Phys. Chem. A 105 (2001) 5940–5944.
- [17] Y.C. Guan, W. Zhou, Z.L. Li, H.Y. Zheng, Appl. Surf. Sci. 255 (2009) 8235–8238.
- [18] M.J. Aziz, J. Appl. Phys. 53 (1982) 1158–1168.
- [19] K.N. Braszczyńska-Malik, J. Alloys Compd. 477 (2009) 870–876.
- [20] A.K. Dahle, Y.C. Lee, M.D. Nave, P.L. Schaffer, D.H. StJohn, J. Light Met. 1 (2001) 61–72.
- [21] Z.H. Wen, C.J. Wu, C.S. Dai, F.X. Yang, J. Alloys Compd. 488 (2009) 392–399.
- [22] X. He, J.W. Elmer, T. DebRoy, J. Appl. Phys. 97 (2005) 084909.
- [23] K. Abderrazak, S. Bannour, H. Mhiri, G. Lepalec, M. Autric, Comput. Mater. Sci. 44 (2009) 858–866.
- [24] D. Höche, S. Müller, G. Rapin, M. Shinn, E. Remdt, M. Gubisch, P. Schaaf, Metall. Mater. Trans. B 40 (2009) 497–507.
- [25] N. Xu, J. Shen, W.D. Xie, L.Z. Wang, D. Wang, D. Min, Mater. Charact. 61 (2010) 713–719.
- [26] W.Z. Chen, Y. Yu, X. Wang, E.D. Wang, Z.Y. Liu, Mater. Sci. Eng. A 575 (2013) 136–143.
- [27] H.M. Wen, T.D. Topping, D. Isheim, D.N. Seidman, E.J. Lavernia, Acta Mater. 61 (2013) 2769–2782.
- [28] C.H. Cáceres, D.M. Rovera, J. Light Met. 1 (2001) 151–156.
- [29] Y. Yang, X.D. Peng, H.M. Wen, B.L. Zheng, Y.Z. Zhou, W.D. Xie, E.J. Lavernia, Metall. Mater. Trans. A 44A (2013) 1101–1113.
- [30] C.D. Yim, K.S. Shin, Mater. Sci. Eng. A 395 (2005) 226–232.



The effect of location on the microstructure and mechanical properties of titanium aluminides produced by additive layer manufacturing using in-situ alloying and gas tungsten arc welding

Yan Ma, Dominic Cuiuri, Nicholas Hoye, Huijun Li, Zengxi Pan*

School of Mechanical, Materials, and Mechatronic Engineering, Faculty of Engineering & Information Sciences, University of Wollongong, Northfields Avenue, Wollongong, NSW 2522, Australia



ARTICLE INFO

Article history:

Received 28 December 2014
Received in revised form
17 February 2015
Accepted 19 February 2015
Available online 27 February 2015

Keywords:

In-situ alloying
Additive layer manufacturing
Welding
Titanium aluminides
Microstructure
Mechanical properties

ABSTRACT

An innovative and low cost additive layer manufacturing (ALM) process is used to produce γ -TiAl based alloy wall components. Gas tungsten arc welding (GTAW) provides the heat source for this new approach, combined with in-situ alloying through separate feeding of commercially pure Ti and Al wires into the weld pool. This paper investigates the morphology, microstructure and mechanical properties of the additively manufactured TiAl material, and how these are affected by the location within the manufactured component. The typical additive layer manufactured morphology exhibits epitaxial growth of columnar grains and several layer bands. The fabricated γ -TiAl based alloy consists of comparatively large α_2 grains in the near-substrate region, fully lamellar colonies with various sizes and interdendritic γ structure in the intermediate layer bands, followed by fine dendrites and interdendritic γ phases in the top region. Microhardness measurements and tensile testing results indicated relatively homogeneous mechanical characteristics throughout the deposited material. The exception to this homogeneity occurs in the near-substrate region immediately adjacent to the pure Ti substrate used in these experiments, where the alloying process is not as well controlled as in the higher regions. The tensile properties are also different for the vertical (build) direction and horizontal (travel) direction because of the differing microstructure in each direction. The microstructure variation and strengthening mechanisms resulting from the new manufacturing approach are analysed in detail. The results demonstrate the potential to produce full density titanium aluminide components directly using the new additive layer manufacturing method.

Crown Copyright © 2015 Published by Elsevier B.V. All rights reserved.

1. Introduction

Titanium aluminide alloys based on intermetallic γ phase are widely recognised as promising structural materials due to their attractive combination of low density, unique mechanical properties such as high specific strengths and moduli, and good resistance against oxidation and corrosion [1]. These properties make γ -TiAl alloys attractive for high temperature aerospace and automotive components such as turbine wheels, compressor blades and pistons for reciprocating engines [2].

Despite the desirable characteristics of these alloys, TiAl components are difficult to manufacture by conventional production processes due to relatively low ductility at room temperature. Another drawback is the high processing temperature, owing to the long-range ordering of TiAl up to its melting point. Greater capital investment is required for processing equipment with the necessary

high temperature characteristics [3]. Industrial scale processing routes that have been used to produce γ -TiAl alloy billets and components include investment casting, ingot or powder metallurgy. These techniques are similarly applied to conventional titanium and nickel based alloys. However, for the case of TiAl alloys, these processes often require a series of additional post-processing steps such as hot-isostatic pressing, ageing, annealing, and hot working to improve the mechanical properties to desirable levels and to obtain the desired component geometries. For casting and ingot metallurgy processes, the main difficulties encountered in producing γ -TiAl are the development of cracks, inhomogeneous microstructure and coarse-grained microstructure, resulting in poor mechanical properties. For example, casting defects and strong segregation of impurity elements are found in titanium aluminides produced by various casting methods [4]. Bryant and Semiatin [5] have pointed out that microsegregation is an obvious phenomenon in multicomponent ingot-metallurgy titanium aluminides as well as in binary alloys. Powder metallurgy minimises these problems, but introduces the likelihood of porosity and contamination [6]. Although post-processing operations can solve many of the problems associated with the three main processes, and

* Corresponding author. Tel.: +61 2 42215498.

E-mail address: zengxi@uow.edu.au (Z. Pan).

each process can produce acceptable material, the overall production costs are inevitably increased. High costs have been acknowledged as the chief limitation for titanium aluminides to successfully reach the market in a wide range of part forms.

Efforts have been devoted to explore alternative manufacturing techniques for titanium aluminides, such as direct rolling, laser forming and sintering [7]. Although these techniques are capable of producing material with acceptable properties, processing costs and product shapes are still prohibitive for many commercial applications.

It is well known that joining techniques play an important role in the application of γ -TiAl based alloys. Processes that have been used for joining gamma titanium aluminides include fusion welding (electron beam welding and gas tungsten arc welding), solid state welding and brazing. Considering its high deposition rate and low cost, gas tungsten arc welding is an appealing option for investigating novel fabrication technology based on the study by Wang et al. [8].

Additive layer manufacturing (ALM) has been shown to be a feasible and economical alternative to traditional manufacturing methods for conventional metals. Many consecutive layers are deposited onto a substrate using powder or wire to produce complex, near net shape components. Thus, ALM has the potential to produce geometrically intricate components with major savings in time, material, and hence cost.

Considerable investigation and development have been carried out on ALM processes applied to conventional metals, ranging from aluminium [9,10], nickel [11,12], steel [13] and titanium alloys such as Ti-6Al-4V [14–18]. In comparison, the application of ALM to intermetallics such as titanium aluminide has been limited. Srivastava [19,20] applied direct laser fabrication to fabricate TiAl alloy components using gas atomised TiAl powders. The range of processing parameters was identified and controlled by an intelligent feedback system. The authors also established the relationship of processing parameters and the subsequent heat treatment with the microstructure and mechanical properties. Laser melting deposition (LMD) ALM has been used to produce TiAl intermetallics and the resultant microstructure and mechanical properties were analysed in detail [21]. The effects of heat treatment have also been evaluated [22]. The first successful application of electron beam melting (EBM) on fabricating TiAl components has been reported to consolidate Ti-47Al-2Cr-2Nb powders. Electron beam melting has been first reported to successfully consolidate titanium aluminide powders [23]. Two EBM processing routes of prealloyed TiAl powders have also been explored to successfully produce near net shape parts [24]. Furthermore, Murr et al. [25] demonstrated the potential to build near net shape and complex titanium aluminide products directly using powder-bed EBM technology for aerospace and automotive applications. Biamino et al. [26] recently succeeded in producing γ -TiAl based alloy with low levels of internal defects and consistent tensile properties by using powder-bed EBM.

Nevertheless, the powder based systems frequently used in the above studies are prone to high impurity levels in the output materials. It has been demonstrated that the wire-feed processes

are more economical and less susceptible to contamination from the atmosphere in comparison to processes using powders [27]. Mostly for these reasons, it may be prudent to focus research activities on wire-based processes. However, no information is currently available on the use of material feeding methods other than prealloyed powders to produce titanium aluminide components.

The current investigation concentrates on an innovative additive layer manufacturing approach for titanium aluminides. The gas tungsten arc welding (GTAW) process is combined with separate wire feeding of commercially pure Ti and Al wires to perform in-situ alloying of the two elements. The wire feeding ratios are chosen so that a γ -TiAl alloy is produced. The potential of this new manufacturing method has been proved in our previous studies [28,29]. Processing parameters including arc current, interpass temperature and wire feed rate ratio have been investigated on microstructure and microhardness of γ -TiAl components fabricated by GTAW-ALM. Further, for purpose of producing the components of acceptable quality, repeatability and reproducibility, it is also important to understand the microstructural evolution and the variation of mechanical properties within one build. A few of previous studies have reported the effect of distance from the build plate on the microstructure and microhardness variation within the additive manufactured Ti-6Al-4V part produced by EBM [30], laser-based process [31] and wire and arc based technique [32]. However, no previous literature can be found to specifically study the effect of location on additive manufactured titanium aluminide alloys. Therefore, microstructural features and mechanical properties of the fabricated components as a function of location are the objective of this study, to understand the effectiveness of GTAW-ALM process in producing titanium aluminide components with the desired properties.

2. Experimental procedures

A GTAW current of 120 A and 3.5 mm arc length were applied at a travel speed of 100 mm/min, these parameters being found to be acceptable through several preliminary trials. Commercially pure Ti plates of 6 mm thickness were used as substrates for depositing the alloys. The GTAW torch was focused on the substrate to create a melt pool into which the feed materials were delivered by a twin wire feeder arrangement. The first feed stock was 1.0 mm diameter commercially pure Ti wire at 750 mm/min feeding speed, while the second feed stock was 0.9 mm diameter pure Al wire delivered at 870 mm/min. The deposition process was protected from atmospheric oxidation by using an appropriately designed argon gas shielding device, to produce a final product with minimal oxygen and nitrogen contamination. Fig. 1a and b shows the experimental setup and schematic diagram of the manufacturing process.

The deposited wall components (Fig. 1c and d) typically have a length of 100 mm and a width of 10 mm. Two build heights of 19 mm and 45 mm were used, depending on the specimens

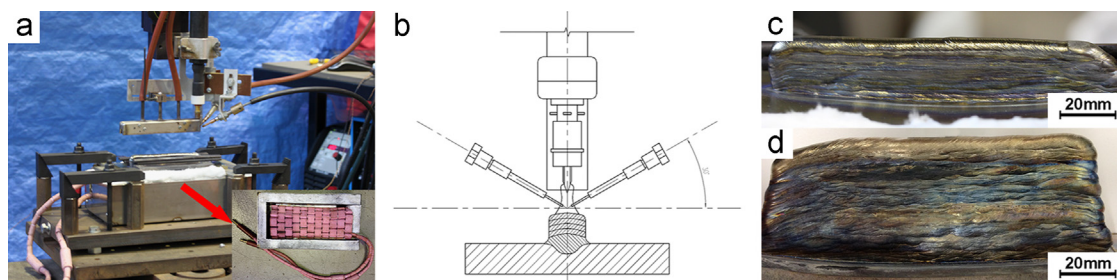


Fig. 1. Experimental setup of the GTAW-ALM process and the typical wall components: (a) experimental setup of the manufacturing process, (b) schematic representation of the process, (c) and (d) examples of titanium aluminide components.

required for testing. The deposited walls were wire-cut from the substrates, and the required specimens were subsequently wire-cut from the deposits. The metallographic specimens were prepared using standard procedures for titanium aluminides. A mixed solution of 6 vol% nitric acid, 3 vol% hydrofluoric acid and water was selected as the etching agent. The microstructure and element distribution in the different regions of the specimens were analysed by scanning electron microscopy (SEM, JEOL JSM-6490LA) equipped with an energy dispersive X-ray spectroscopy (EDS) analysis system. The accuracy of EDS measurements is ± 0.5 at%. A GBC MMA X-ray diffractometer (XRD) with CuK α radiation ($\lambda=1.5418\text{ \AA}$) was used to identify the phase constitutions. Vickers microhardness profiles were measured at a load of 200 g (HV0.2) by a Duramin 70 Hardness Tester. In order to investigate the possible influence of location on hardness within the component, the indentations were started from the interface between substrate and deposited wall, progress along the vertical centre line parallel to the build direction (Z) in cross-section (X-Z plane), and continue to the top in the last layer of the deposited wall in 0.5 mm intervals. Hardness in the lateral direction (X) perpendicular to the centre line was also measured in the near-substrate regions, layer bands and top regions separately. In addition, microhardness measurements were performed parallel to the travel direction (Y) in the longitudinal section (Y-Z plane) of the deposited walls. The location of the indentations and orientation of the reference axes are shown in Fig. 2.

The room-temperature tensile properties of the deposited material were measured in both the vertical build direction (Z) and longitudinal direction (Y). Fig. 3 indicates the direction, location, section shape and size of all the tensile specimens. In the first set of tests that perform a direct comparison between the properties in the two orientations, one component of 45 mm height was fabricated as shown in Fig. 3a to produce three specimens for each orientation. In the second set of tests to assess the consistency of mechanical properties throughout the height of the fabricated wall, three components of 19 mm height were fabricated. From each wall, 10 specimens were cut as shown in Fig. 3b–d at controlled heights to produce a total of 30 specimens. All tensile tests were performed on a MTS370 load unit at a strain rate of 0.05 s^{-1} .

3. Results

3.1. Morphology and microstructure

The typical macrostructure of a cross-section (X-Z plane) and a series of optical micrographs from different regions along the vertical centreline (Z direction) are shown in Fig. 4. Apart from two small areas at the surface and bottom of the component, the macrostructure exhibits strong columnar grains oriented upwards, parallel to the build direction, which is the direction of heat flow. A series of layer bands can be readily observed in this region. This

phenomenon is well documented in a number of studies on different ALM processes that have been referenced in Section 1.

The optical micrographs clearly show that there are significant changes of microstructure in different regions. Large equiaxed α_2 grains are found in the near-substrate region, shown in Fig. 4d. Some fine, irregularly γ laths displaying more contrast variation precipitate at the grain boundaries. The diameters of the α_2 grains are in the range of 50–150 μm .

Above the near-substrate region, optical contrast caused by different microstructure shows the formation of layer bands (Fig. 4c). The sequential layer bands appear to be perpendicular to the build direction (Z) owing to high temperature and heat conduction along the travel direction (Y). Brandl et al. [33] have stated that the layer bands do not coincide with the layers deposited. The number of layer bands is generally less than the number of layers deposited. In the case of components shown here, 20 layers have been deposited while approximately 13 layers can be identified. A band region with about 190 μm thickness can be found between any two layers. Detailed

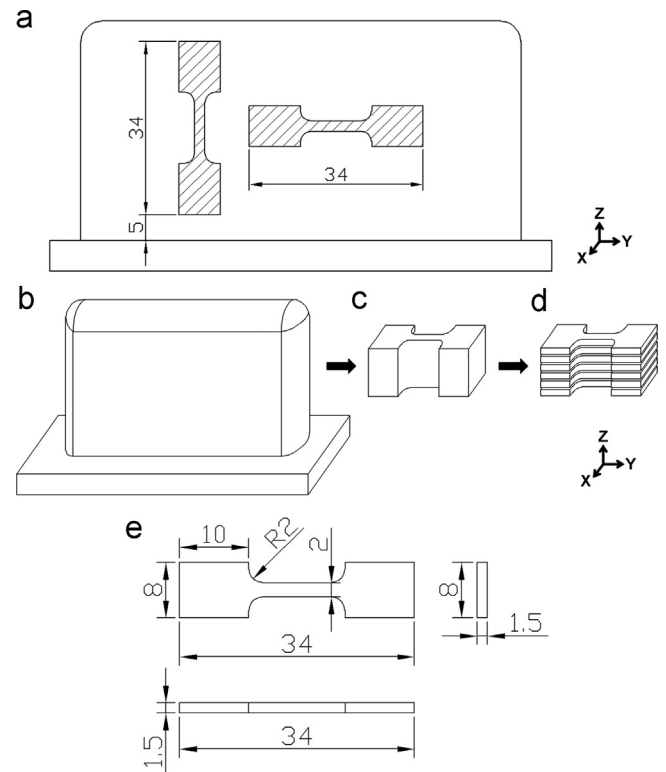


Fig. 3. Sample orientations and dimensions for room temperature tensile tests: (a) sample orientation and designation of directions, (b) GTAW-ALM deposited wall component, (c) bulk tensile sample cut from the centre of deposit, (d) tensile specimens after slicing bulk sample, and (e) dimensions of tensile specimens in mm.

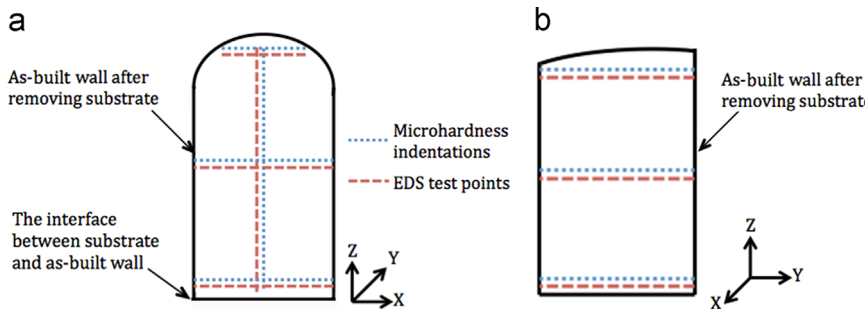


Fig. 2. Schematic showing the locations of microhardness and EDS measurements in different sections of γ -TiAl based wall components produced by GTAW-ALM: (a) cross-section (X-Z plane) and (b) longitudinal section (Y-Z plane).

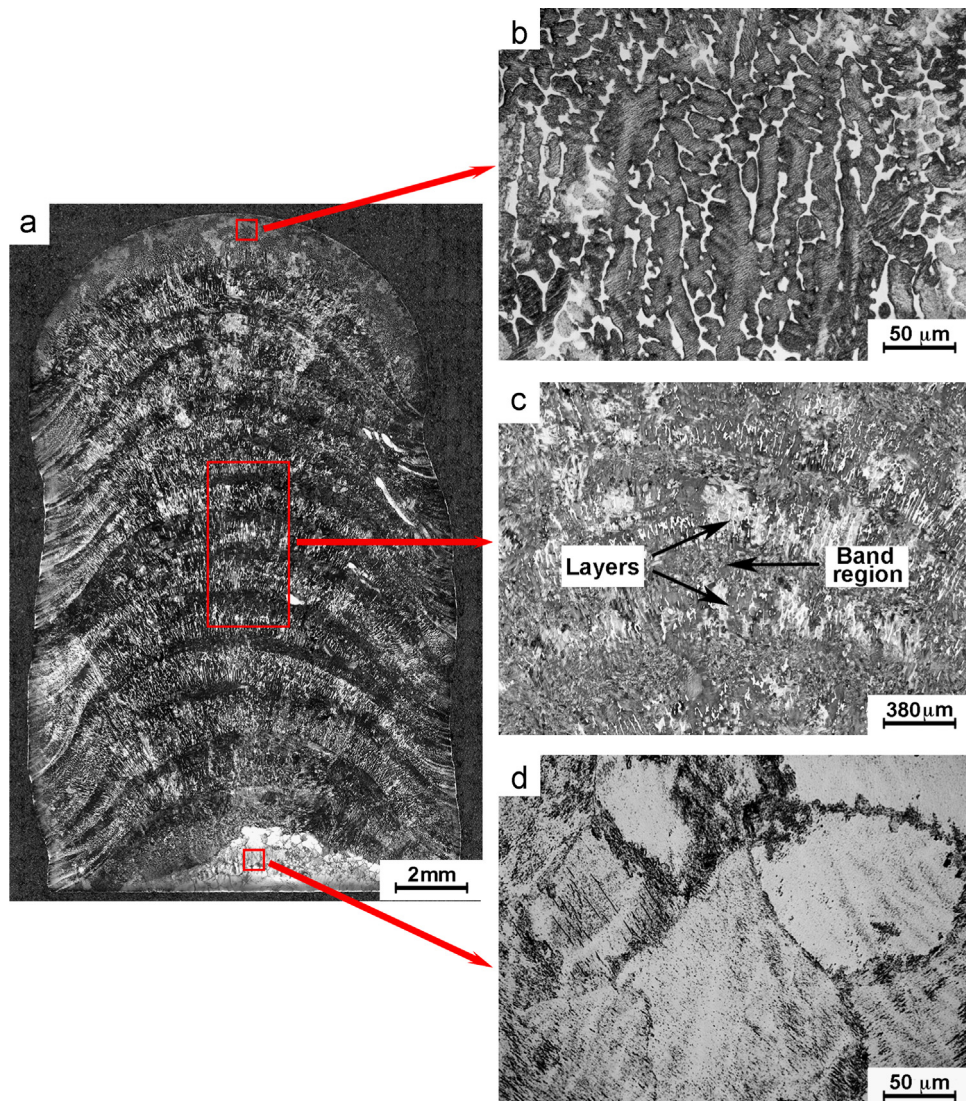


Fig. 4. Morphology and microstructure in cross-section (X-Z plane) of γ -TiAl components produced by GTAW-ALM: (a) cross-section (X-Z plane) morphology, (b) representative microstructure in the top region (c) morphology of the layer bands, and (d) representative microstructure in the near-substrate region.

observation of the microstructure (Fig. 5) shows that the interdendritic phases surrounded by lamellar microstructure are observed in each layer (Fig. 5a), while fully lamellar colonies with different colony sizes consisting of α_2 and γ lamellae content are found in the band region (Fig. 5b and c). Duarte et al. [34] describe similar microstructures in γ -based TiAl cast alloys.

The microstructure seen in the top region (Fig. 4b) is relatively fine and consists of long dark dendrites and white interdendritic phases. Similar microstructures have been observed in titanium aluminide welds produced by both laser [35] and GTAW [36]. The lamellar character of the dendritic structure and the interdendritic regions is revealed at higher magnification (Fig. 6).

3.2. EDS analysis

The results of microchemical analysis at test locations specified by Fig. 2 are summarised in Fig. 7. All EDS measurements were performed either alongside or below the hardness measurement points at approximately 0.1 mm distance. It can be seen that the Al distribution is comparatively homogeneous in the layer bands, where there are small fluctuations in the measurements between 43 at% and 46 at% Al. However, among the layer bands, the Al content is slightly higher in the layers than that in the band regions.

Predictably, the Al concentration is lower in the near-substrate region adjacent to the pure Ti substrate. The particularly higher concentration of Ti in the central area of the near-substrate region also appears as the bright microstructure in Fig. 4d. In the top region, the highest Al concentrations are detected, and large deviations of Al concentration are observed. This can be attributed to Al segregation on solidification and no further heat treatment or temperature cycling, as no subsequent layers are deposited. A line profile (Fig. 8) taken across three dendrite arms in the top region of one specimen shows the Al enrichment in the interdendritic phases.

Correspondingly, the microchemical composition of various microstructures contained within the different regions was identified by EDS analysis, as recorded in Table 1. Lamellae in the top region have an average Al content of around 43.8 at%, while a similar Al concentration can be found in lamellar structures within the layer bands. The interdendritic phase with higher Al content of around 48.7 at% is found in the top region. In addition, the interdendritic phases have comparable Al distribution throughout the entire component.

3.3. Phase identification

In order to identify the phase structure, an XRD analysis was conducted in cross-sections of components produced by

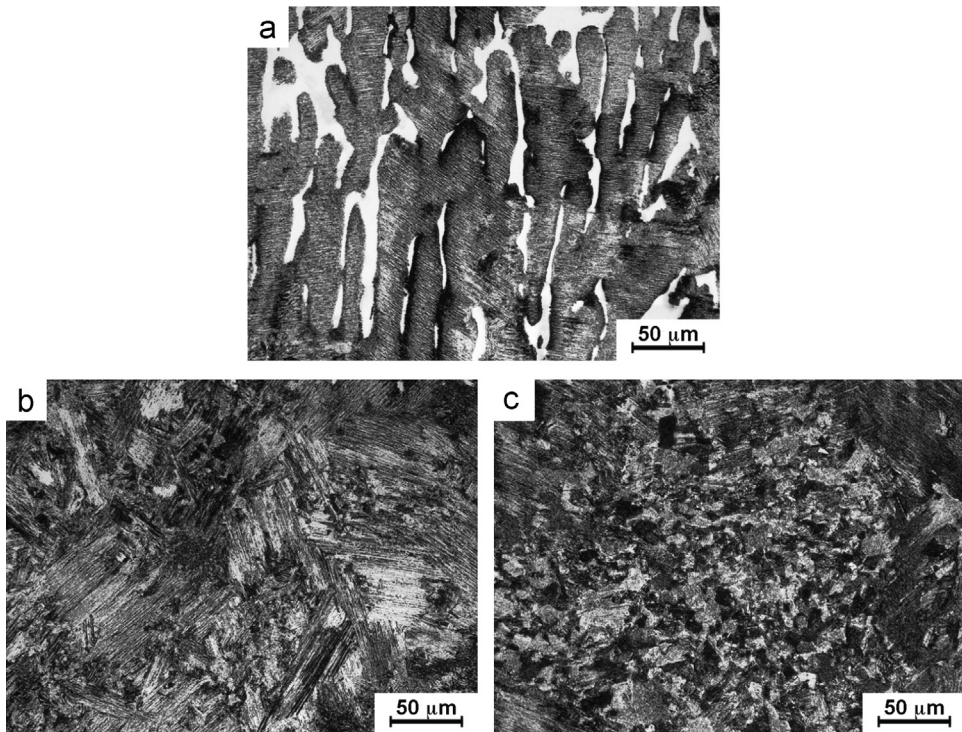


Fig. 5. Representative microstructure of layer bands in cross-section (X-Z plane) of γ -TiAl components produced by GTAW-ALM; (a) microstructure observation in the layer, (b) and (c) microstructure observations in the band region.

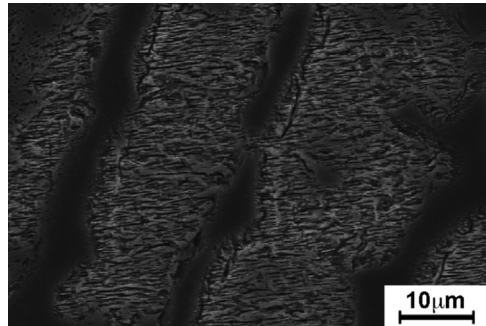


Fig. 6. High magnification SEM image showing microstructure in the top region of cross-section (X-Z plane) of γ -TiAl components produced by GTAW-ALM.

GTAW-ALM. A comparison of the XRD data from different regions of a cross-section is shown in Fig. 9. All the diffraction patterns are found to contain a prominence of γ phase at approximately 39° , which includes both the γ lamellae and the observed interdendritic γ grains. The γ phase peaks of the top region are markedly stronger than those of the other regions. The layer bands are characterised by peaks of γ and α_2 , although only a very small amount of α_2 phase can be found. In comparison to the other areas, the volume fraction of γ phase decreases in the near-substrate region accompanied by a dramatic increase of α_2 phase. This phenomenon is further confirmed by different amounts of α_2 phase in different regions (Fig. 9b). The near-substrate region has an extremely high α_2 phase volume fraction of $52 \pm 3\%$.

3.4. Hardness measurements

Microhardness (HV0.2) values versus location are plotted in Fig. 10. The microhardness appears to be relatively homogeneous within the layer bands, ranging from 287 to 323 HV0.2. The mean microhardness value is 296 HV0.2 when measured in the layer bands together with the top region, despite the slight fluctuation in

the top region due to segregation. The central area of the “bowl shape” in the near-substrate region (Fig. 10b) is much harder than the outer areas near the wall surface. These results are in accordance with the microstructural observations and the microchemical distribution measurements. It is interesting that the highest microhardness value of 437 HV0.2 is found in the first few layers of near-substrate region, rather than in the centre of laser-melting deposited plates as described by Qu and Wang [21]. The difference could be attributed to different morphology and microstructure. This will be discussed further in the following section.

3.5. Tensile properties

The room temperature tensile properties of the deposited material in the vertical build direction (Z) and longitudinal direction (Y) are summarised in Table 2. Three test specimens were used for each orientation. The specimens tested in the Y-direction are found to have higher ultimate tensile strength (UTS) and yield strength (YS) than those tested in Z-direction. However, there is no observable difference in Elongation (% EL).

Fig. 11 shows the effect of vertical location (in the build direction, Z) on the mechanical properties, as measured in the longitudinal (Y) direction. The near-substrate region of the deposited wall exhibits the highest UTS and YS and the lowest ductility. However, no significant variation in tensile strength is found due to the location of a sample within the layer bands. The average values of UTS and YS in the layer bands span 512–552 MPa and 443–466 MPa, respectively. Additionally, the elongation is also almost identical within this area. The consistency of these test results is in agreement with the regularity of microhardness measurements according to the location in the Z-direction (Fig. 10).

Representative fracture surfaces of the tensile samples are shown in Fig. 12. The fracture morphologies after tensile tests are quite similar for the microstructures within different regions. All samples show predominantly transgranular cleavage fracture over the entire fracture surface. The fracture surface of the samples from the near-substrate

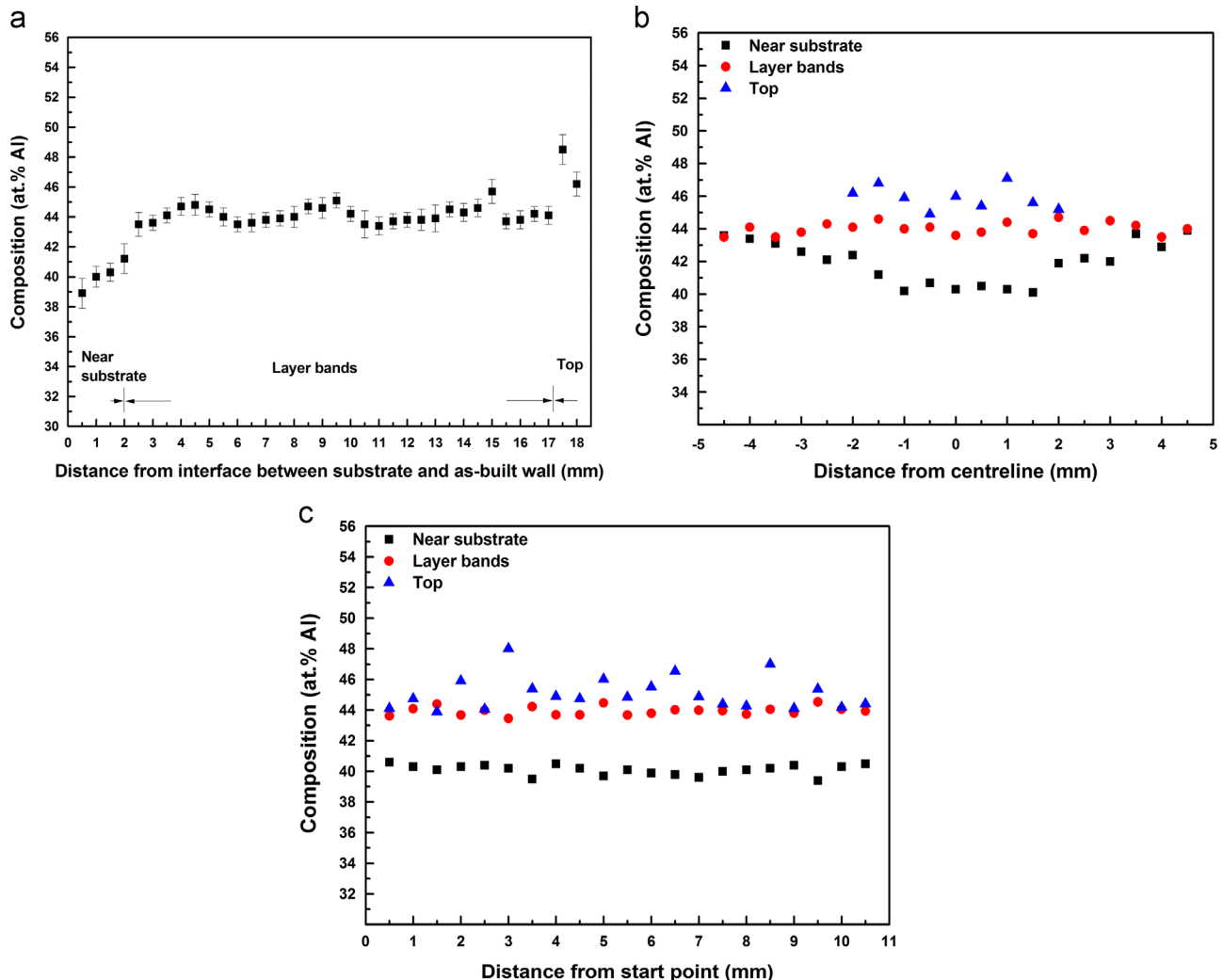


Fig. 7. Quantitative concentration of Al obtained by EDS from cross-section (X-Z plane) and longitudinal section (Y-Z plane) of γ -TiAl components produced by GTAW-ALM: (a) along the build-up direction (Z) in cross-section, (b) across the build-up direction (X) in cross-section, and (c) along the travel direction (Y) in longitudinal section. Each data along different direction was averaged as a result of three measurements on 3 samples. Error bar means one standard deviation. The variation of 0.5–1 at% in Al composition for each point was obtained from the calculated standard deviation.

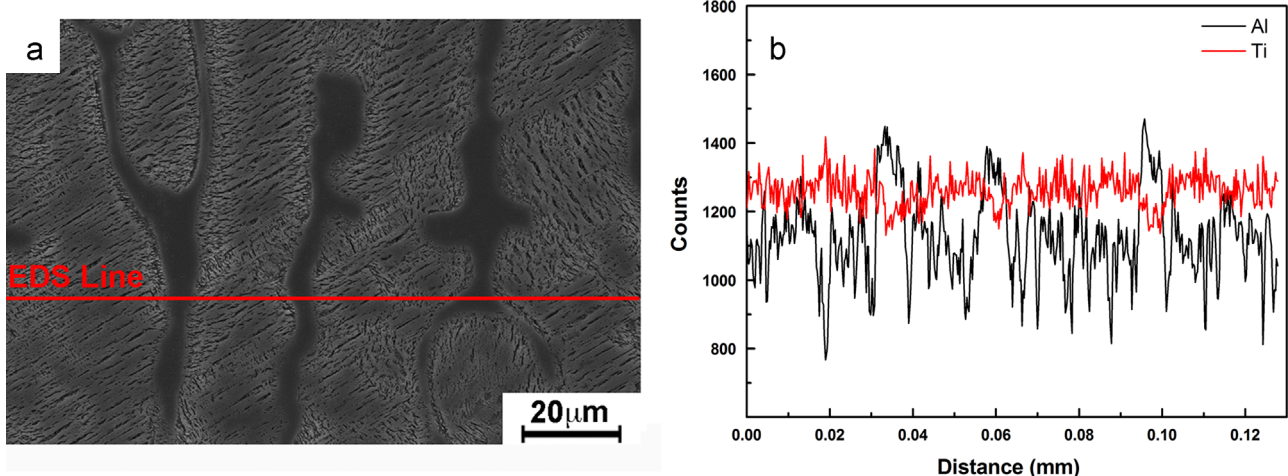


Fig. 8. The distribution of in-situ alloyed elements in the top region: (a) the position of EDS line scan test and (b) the corresponding line profile showing Al enrichment within interdendritic phases.

Table 1

Microchemical composition of γ -TiAl components produced by GTAW-ALM, determined by EDS. The mean composition of different microstructure and their standard deviation were calculated by the results of five measurements for each structure in the same region.

Microstructure	Microchemical composition (at%)	
	Ti	Al
Lamellae in the top region	56.2 ± 0.3	43.8 ± 0.3
Interdendrites in the top region	51.3 ± 0.2	48.7 ± 0.2
Lamellae in the layer bands	55.9 ± 0.3	44.1 ± 0.3
Interdendrites in the layer bands	52.1 ± 0.1	47.9 ± 0.1
Equiaxed α_2 grains in the near-substrate region	59.8 ± 0.2	40.2 ± 0.2

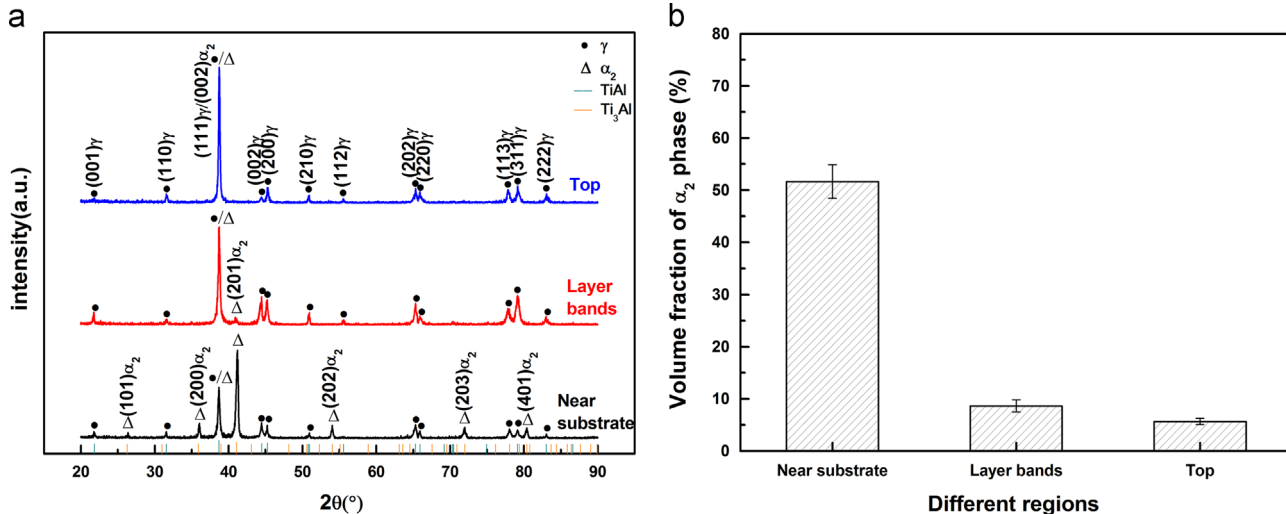


Fig. 9. Phase constitutions of different regions in cross-section of γ -TiAl components produced by GTAW-ALM: (a) XRD diffraction patterns. Three experiments were performed on each region; (b) average volume fraction of α_2 phase. The results were obtained by Rietveld analysis on the three experiments in (a), and error bar shows one standard deviation.

region shows some secondary cracks, which cannot be found in the samples from layer bands. In all cases, the fracture modes are brittle fracture, and no dimples are observed.

4. Discussion

4.1. Morphology and microstructure

The ALM fabrication technique used in this work has many similarities to a multipass arc welding process. During the initial welding pass, many processes take place simultaneously: (i) melting of the constituent ALM elements and also the surface of the substrate; (ii) formation of the main phases, that is, titanium aluminide; (iii) alloying of the main phases, such as TiAl; and (iv) solidification of the different phases. Therefore, immediately below the fusion zone, small β grains present in the pure Ti plate revert to a fully β structure and undergo rapid grain growth. The solidification front epitaxially grows back from these coarsened β grains, which act as nucleation sites at the edge of the fusion boundary, into the weld pool where each growing grain forms as a continuation of the grains that lie along the fusion boundary [37]. When solidification occurs following a moving melt pool, the preferential grain growth direction is perpendicular to the curved surface of the solid/liquid interface in order to follow the maximum temperature gradient. The steepest gradient provides the maximum driving force for solidification, as is commonly observed in ALM-produced Ti-6Al-4V products [38].

As the build-up progresses away from the substrate, the upper region of the previously deposited layer is partially remelted every time the next layer is deposited on top of the existing layer. As a result,

the grains in this region serve as nuclei in the subsequent layer and grow from the previously coarsened grains. When the build-up continues, the unidirectional heat flow characteristic of the additive layer manufacturing process contributes to the columnar grains that develop up through the entire sample. The formation of layer bands can also be attributed to the partial remelting of previously deposited layers and multiple thermal cycles that have occurred with each subsequent deposition pass. A detailed explanation of the layer bands can be found elsewhere. Kelly and Kampe [39] found that the layer bands and gradient morphologies are a result of the complex thermal history experienced by the build material and not a result of segregation or oxidation. The layer bands reflect the beta transus temperature T_β rather than the solidus temperature T_s or liquidus temperature T_L , as proposed by Brandl et al. [33]. Liu et al. [40] have suggested that layer bands are heat-affected zones, which result from the sub-melting-point reheating treatment when a new layer is deposited.

Further, solidification takes place solely through β phase for alloys containing less than 45 at% Al based upon the phase diagram (Fig. 13). Microsegregation for such alloys is significantly lower than predicted by the Gulliver-Scheil equation [1]. This indicates back-diffusion in β phase and solidification relatively close to equilibrium. As illustrated in Fig. 7a, the near-substrate region has around 40 at% Al because of dilution from the pure Ti substrate that is mixed into the weld pool during deposition of the first layer. This effect is reduced as the next few layers are added, since the weld pool penetrates layers that have progressively lower Ti content. Thus, materials within the near-substrate region are able to experience $\beta \rightarrow \beta + \alpha \rightarrow \alpha + \gamma \rightarrow \alpha_2 + \gamma$ phase transition during solid state cooling because of the expectedly lower Al concentration. However, the microstructure seen in the near-substrate region with around

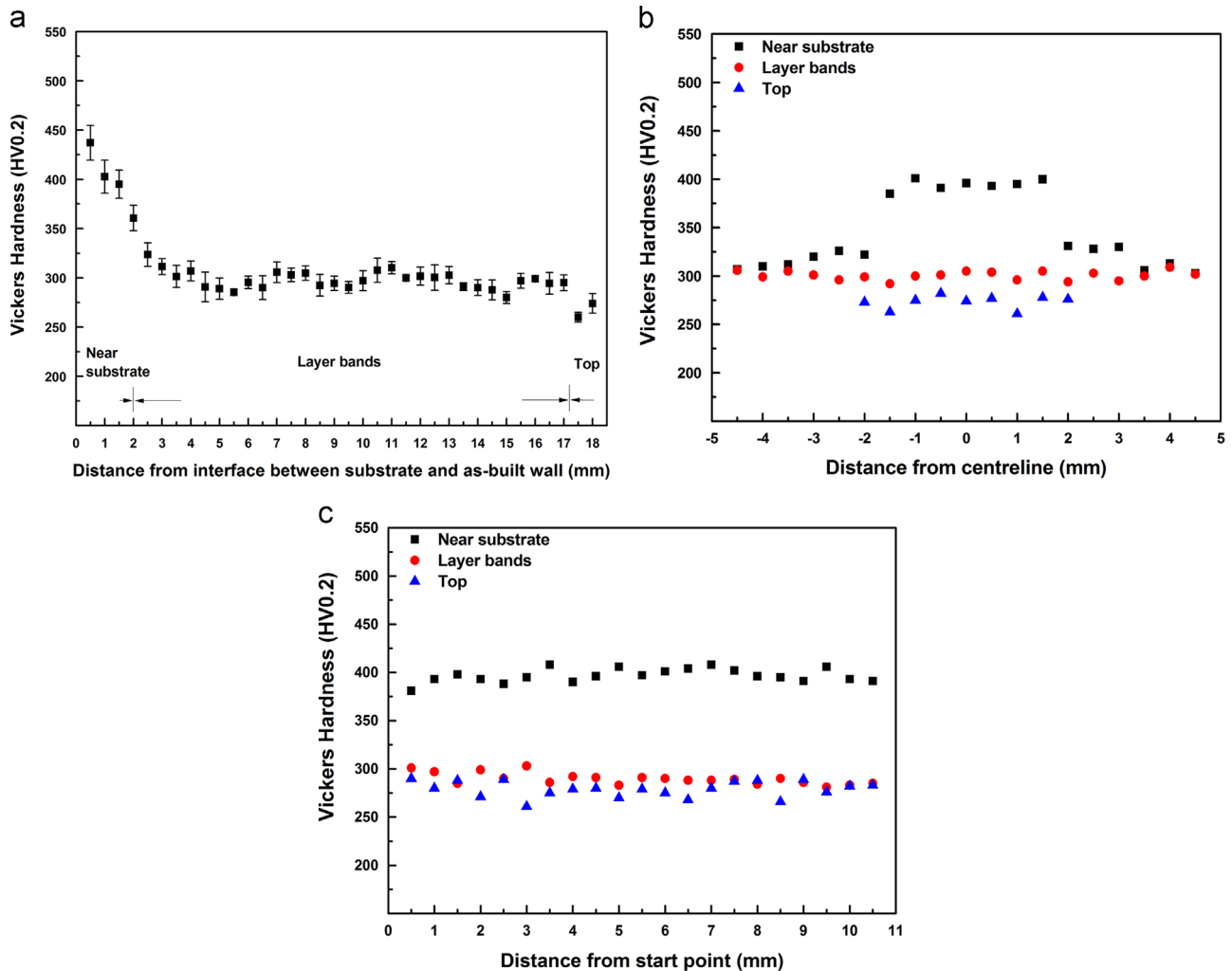


Fig. 10. Microhardness profile as a function of location in cross-section (X - Z plane) and longitudinal section (Y - Z plane) of γ -TiAl components produced by GTAW-ALM: (a) along the build-up direction (Z) in cross-section, (b) across the build-up direction (X) in cross-section, and (c) along the travel direction (Y) in longitudinal section. The presented results for each direction are mean values calculated from 3 measurements of 3 samples. Error bar shows one standard deviation that is in the acceptable range of 3–13 HV0.2 for each data point, while the maximum deviation is found in the top region.

Table 2

Comparison of the mechanical properties of γ -TiAl components produced by GTAW-ALM, tested along the build-up direction (Z) and the travel direction (Y). The results including the average value and their standard deviation were calculated from 3 specimens for each direction.

Direction	Ultimate tensile strength (MPa)	Yield strength (MPa)	Elongation (%)
Longitudinal/travel direction (Y)	549 ± 23	474 ± 17	0.5
Vertical/build direction (Z)	488 ± 50	424 ± 30	0.5

40 at% Al is indicative of a transformation from α to α_2 followed by precipitation of γ at some lower temperature, as evidenced by the thermal APBs in the α_2 that were continuous on either side of the γ plates [41]. It is well known that the volume fraction of different phases is controlled by Al content and also strongly influenced by heat treatment and cooling rate [42], which is implicit in GTAW-ALM building process. As such, the high temperature transformation ($\alpha \rightarrow \alpha + \gamma$) is suppressed by the relatively high cooling rate during initial weld passes, and only the ordering transformation $\alpha \rightarrow \alpha_2$ occurs [36] which plays an important role in the formation of α_2 phase in the near-substrate region.

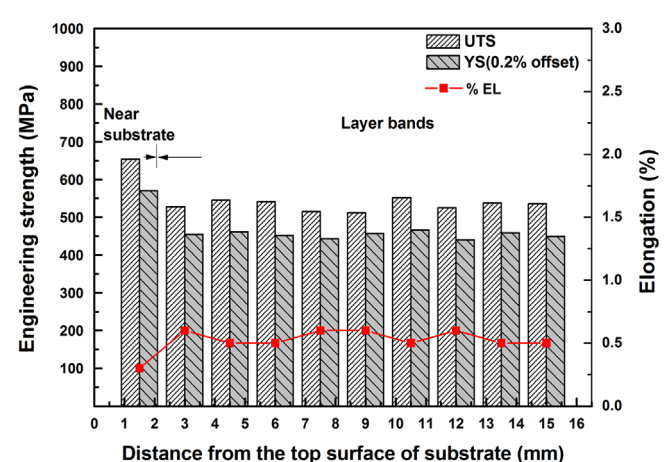


Fig. 11. Location effect on mechanical properties of γ -TiAl components produced by GTAW-ALM. Testing performed in longitudinal/travel direction. Each data point represents the average of 3 tests, corresponding to the 3 wall samples that were produced. The variation in strength within each group of 3 does not exceed 20 MPa, while the variation in ductility is approximately $\pm 0.1\%$.

In contrast to the near-substrate region, $L \rightarrow \beta$ is not the only solidification route for top region and layer bands, which have higher Al content at around 44 at% Al. Because the co-existence of

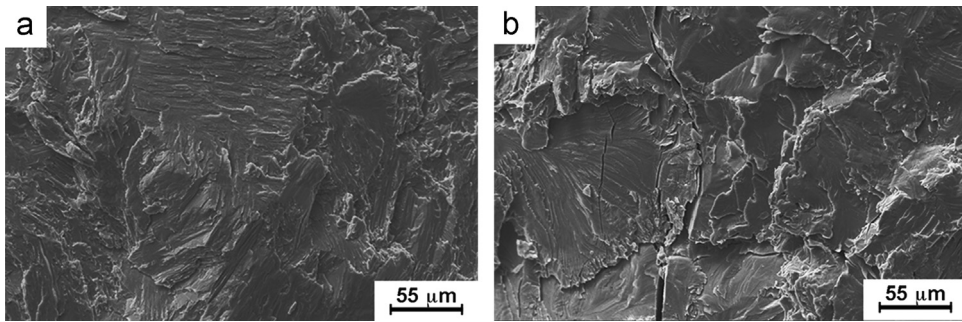


Fig. 12. SEM fractographs in different regions of γ -TiAl components produced by GTAW-ALM: (a) layer bands and (b) near-substrate region.

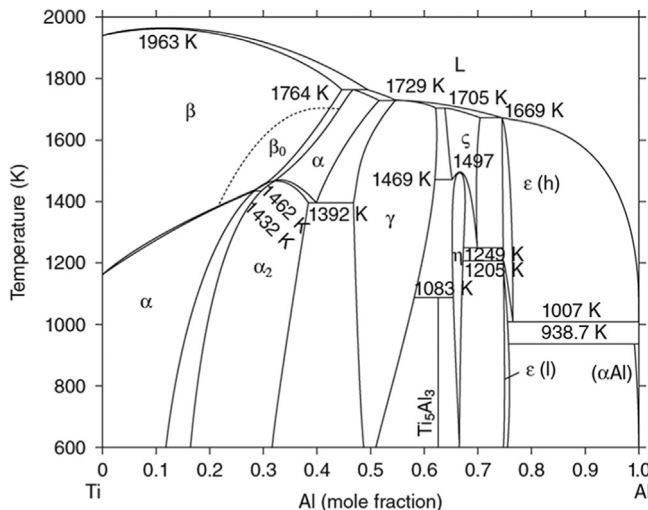


Fig. 13. Binary phase diagram of Ti-Al system according to Witusiewicz et al. [43].

heavy and light metals in the Ti-Al system can still easily cause dendrite segregation, the remaining liquid progressively enriches in Al and then solidifies through the peritectic reaction $L + \beta \rightarrow \alpha$ [44]. The crystallographically oriented α grains form at L/β interfaces with orientation according to Burgers' relationship $\{110\}_{\beta} \parallel \{0001\}_{\alpha}$ and $\langle 111 \rangle_{\beta} \parallel \langle 11\bar{2}0 \rangle_{\alpha}$ [45]. However, limited diffusion and melt undercooling that impede the formation of the pro-peritectic solid phase normally cause the incompleteness of peritectic reaction. The formation of γ grains in the interdendritic areas is mainly ascribed to the occurrence of $\alpha \rightarrow \gamma$ transition or nucleation directly from the β phases [46]. After solidification has been completed, different phase transformations are possible depending on the Al composition and cooling velocity on moving out of the single phase α field. As such, upon further cooling the alloys either pass through the phase transformation $\alpha \rightarrow \alpha + \gamma \rightarrow \alpha_2 + \gamma$ or the path $\alpha \rightarrow \alpha_2 \rightarrow \alpha_2 + \gamma$. All γ lamellae precipitate from α or α_2 grains to form a lamellar structure according to Blackburn's orientation relationship $(0001)_{\alpha_2} \parallel \{111\}_{\gamma}$ and $\langle 11\bar{2}0 \rangle_{\alpha_2} \parallel \langle 1\bar{1}0 \rangle_{\gamma}$ [47,48]. The solid state annealing of existing layers during the deposition of subsequent layers can result in further precipitation of γ laths in non-remelted areas, named as band region in this work. Therefore, a fully lamellar microstructure is obtained in the band regions, while the layers are indicative of remelted material that consists of some interdendritic γ grains and coarse lamellar structure. Similar microstructure but more and finer interdendritic γ grains are consequently obtained in the top region that is not influenced by subsequent weld passes. It is interesting that the α_2 phase could not be readily found in the top region, especially the (201) main plane located at $2\theta \approx 41^\circ$. However, it would be unreasonable to draw a conclusion that there is no α_2 phase in the top region. This is most probably caused by

limitations of X-ray diffraction. Usually XRD cannot detect a phase if it presents at less than 2–5%. The weak intensity of α_2 peaks could be attributed to the ultrafine α_2 lamellae.

4.2. Mechanical properties

It is well known that mechanical properties in metallic materials are strongly dependent on grain or colony size, dislocations and boundaries, solid solution elements and precipitates. In the case of titanium aluminides, there are several competing effects regarding the strength.

Firstly, hardening mechanisms in metallic materials are generally explained in terms of the Hall-Petch relationship [49]. There are three Hall-Petch constants, which account for the effects of grain boundaries, domain boundaries and lamellae interfaces. The mean grain/lamellar colony size has been demonstrated to significantly control a range of mechanical properties in γ -based alloys [50]. However, in most investigations of TiAl alloys with $\alpha_2 + \gamma$ lamellar structure, the strength is ordinarily described as a function of the mean interface spacing. The interaction between interfaces and dislocation motion can be used to interpret their dependency relationship [51]. Investigations by Dehm et al. [52] have shown that the movement of dislocations in the γ phase governs mechanical properties when mean interface spacing is more than 100 nm. The high interface density can distinctly improve the mechanical properties since the slip of dislocations can be hindered by interfaces comprising γ/α_2 and γ/γ .

Secondly, the Al level in binary alloys determines the initial phase to precipitate and the subsequent phase transformations that occur on solidification. The mechanical properties of γ -TiAl based alloys can be controlled not only by the γ phase but also by the α_2 phase. Consequently, the volume contents of the γ and α_2 lamellae and also their mean widths should be taken into account. In the case of polysynthetically twinned (PST) crystals [53], a significant difference in hardness has been found between γ and α_2 phase. The hardness of γ phase is almost half of α_2 phase. The increased strength of the low Al content is likely to result from the increased α_2 phase content.

Nevertheless, Cha et al. [54] have reported that in γ -based TiAl alloys with ultrafine $\alpha_2 + \gamma$ lamellar structures, the strength is decided by both the volume fraction and lamellar thickness of the two phases. On one hand, when the volume fraction of α_2 phase is dominating, the α_2 phase, especially the width of α_2 laths, is the primary factor affecting the strength of lamellar colonies. On the other hand, the strength of titanium aluminides having a lamellar structure can be enhanced under the significant influence of nanometer-sized γ laths and their volume fraction. Generally, if the width of the laths is too small to allow dislocations to move or even to be generated, the strength is expected to be extremely high and most likely constant [55]. Therefore, the small size of γ laths acts as the obstacle for dislocation movement, to make the ultrafine γ lamellae harder than the much wider α_2 lamellae. It should be noted

that theoretical hardness of the individual γ and α_2 phase could be obtained in the nano-scale region, and the strength of lamellar structure in titanium aluminides accordingly depends on the volume contents of both the nanometer-sized γ and α_2 laths.

In addition, the different orientation of γ lamellae should be taken into account when discussing the obtained strength. Strength variations were observed by Sato et al. [56] between γ lamellae of different orientation with relatively large thickness. Very thin γ lamellae do not show reproducible strength variations.

With respect to the fabricated γ -based TiAl alloys in the current study, anisotropic tensile properties are expected for both directions owing to anisotropic microstructure. Crack nucleation sites tend to locate at the interface of layered microstructure. This leads to poorer tensile properties in the Z-direction. However, less interface and more homogenous microstructure along the Y-direction are conducive to superior mechanical properties in this direction. Considering the location effect in the Z-direction, Al content is the key factor that influences the strength. One hypothesis involves the change of stacking fault energy with composition. Calculations of interatomic potential and charge distribution have indicated that stacking fault decreases with decreasing Al concentration [57]. Besides, the volume fraction of γ phase decreases accompanied by an increase in α_2 phase when the Al content decreases. The critical resolved shear stresses for dislocations to glide in the α_2 -Ti₃Al phase are considerably larger than those for activation of slip in γ -TiAl phase [58]. Furthermore, the higher cooling rates in components produced by GTAW-ALM lead to more microstructures (α_2 phases), which have higher strength and hardness than in the case of lower cooling rates. Based upon this discussion, it is believed that higher volume fraction of α_2 structures (Fig. 9b) results in considerably higher microhardness values, UTS and YS in the near-substrate region. Although larger grains normally have lower strength because of the reduced number of boundaries and/or dislocations in the large-scale microstructure, the fine γ laths precipitated from the large α_2 grains could be obstacles to dislocation slip and hence the strength in the near-substrate region could be improved.

Additionally, the temperature in the layer bands and top region of the fabricated wall is higher and more homogeneously distributed than that in the near-substrate region, and hence, a softer and less heterogeneous material is obtained in these areas. However, the impact of multiple deposition cycles (i.e. multiple annealing cycles) on the strength of each layer and the band region between them cannot be seen clearly. A generally monotonic microhardness gradient throughout the vertical (Z) axis of the deposit might generally be expected, as each layer has a different thermal history [59]. This is not evident in the microhardness measurements (Fig. 10a) of the layer bands and top region of the fabricated wall components in the current work. The variation of microhardness in these regions probably results from different microstructure characterisation. From the above discussion, critical factors could be the lamellae thickness and interfaces, especially the lamellar spacing. Generally, high cooling rates can result in a decrease of lamellar spacing, which significantly affects translamellar microcracking and the size of shear ligaments. A small lamellae spacing hinders translamellar microcracking, and linkage of the main crack with interlamellar microcracks thus becomes difficult, leading to larger ligament sizes and higher shear ligament toughening [60]. Nevertheless, it is interesting to note that in the case of GTAW-ALM, despite different lamellae spacing in the top region and the layer bands, the hardness is not significantly affected. Lamellar spacing does not appear to be responsible for the different mechanical performance in the current materials. Most probably, the distribution and volume fraction of α_2 and γ phases determine the strength for different areas of the fabricated wall.

5. Conclusions

Full density γ -TiAl based alloy has been successfully produced by using additive layer manufacturing with separate wire feeding of titanium and aluminium components to perform in-situ alloying of these elements. The gas tungsten arc welding (GTAW) process acts as the heat source. In this study, the fabricated material is deposited on a pure titanium substrate, and the deposit can be divided into three distinct regions along the vertical build direction for the purposes of material characterisation as a function of location. In the near-substrate region which extends approximately 2 mm above the substrate surface, equiaxed α_2 grains with sizes ranging from 50 μm to 150 μm are significantly populated by γ lamellae, which precipitate from the grain boundaries. In the top region that comprises the final 2 mm of the additive deposit, the microstructure contains long dendrites interspersed with interdendritic γ phases having a lamellar structure. Between these two relatively narrow bounding regions, the typical morphology exhibits columnar grains that grow epitaxially across a series of layer bands in the build direction. The deposited material is mostly comprised of these layer bands. Fully lamellar colonies consisting of α_2 and γ lamellae are present in the band region, whereas each layer exhibits much coarser interdendritic γ phases surrounded by lamellar microstructure compared with top region.

Within the band region, the tensile properties differ by approximately 11% in the build and travel directions as a result of the anisotropic microstructure in these orientations, although there is no appreciable difference in average microhardness measurements along the two directions. When looking more widely throughout the entire height of the deposited wall component, there are also variations in microhardness, ultimate tensile strength (UTS) and yield strength (YS) that can be ascribed to Al composition and the multiple annealing characteristics of the GTAW-ALM process. In the near-substrate region, considerable increases in microhardness, UTS and YS are a result of the relatively lower Al concentration and higher volume fractions of α_2 phase caused by significantly higher cooling rates in comparison to those experienced by the middle and upper layers. The very fine γ lamellae may be another contributing factor. In the layer bands and top region, a higher Al concentration, a more homogenous Al distribution and comparatively low cooling rates result in lower values of microhardness, UTS and YS. The distribution and volume fraction of α_2 and γ phases are the most likely influences for the measured differences in microhardness and strength between layers and band regions.

Acknowledgement

This work was supported by the China Scholarship Council (CSC), the University of Wollongong and the Welding Technology Institute of Australia (WTIA). The author is also grateful to the UOW Electron Microscopy Centre for the use of their facilities.

References

- [1] F. Appel, J.D.H. Paul, M. Oehring, *Gamma Titanium Aluminide Alloys: Science and Technology*, first ed., Wiley-VCH, Weinheim, Germany, 2011.
- [2] X. Wu, *Intermetallics* 14 (2006) 1114–1122.
- [3] K. Kothari, R. Radhakrishnan, N.M. Wereley, *Prog. Aerosp. Sci.* 5 (2012) 1–16.
- [4] J.-S. Huang, B. Liu, Y.-H. Zhang, W. Zhang, X.-Y. He, Y. Liu, Y.-H. He, B.-Y. Huang, *J. Mater. Sci. Eng.* 3 (2009) 16–21.
- [5] J.D. Bryant, S.L. Semiatin, *Scr. Metall. Mater.* 25 (1991) 449–453.
- [6] M. Thomas, J.L. Raviart, F. Popoff, *Intermetallics* 13 (2005) 944–951.
- [7] H. Clemens, S. Mayer, *Adv. Eng. Mater.* 15 (2013) 191–215.
- [8] F. Wang, S. Williams, M. Rush, *Int. J. Adv. Manuf. Technol.* 57 (2011) 597–603.
- [9] E. Louvis, P. Fox, C.J. Sutcliffe, *J. Mater. Process. Technol.* 211 (2011) 275–284.
- [10] E. Brandl, U. Heckenberger, V. Holzinger, D. Buchbinder, *Mater. Des.* 34 (2012) 159–169.
- [11] F. Wang, *Int. J. Adv. Manuf. Technol.* 58 (2012) 545–551.

- [12] Q. Jia, D. Gu, *J. Alloy. Compd.* 585 (2014) 713–721.
- [13] P. Kazanas, P. Deherkar, P. Almeida, H. Lockett, S. Williams, *Proc. Inst. Mech. Eng. B: J. Eng. Manuf.* 226 (2012) 1042–1051.
- [14] S.M. Kelly, S.L. Kampe, *Metall. Mater. Trans. A* 35 (2004) 1869–1879.
- [15] S.H. Mok, G. Bi, J. Folkes, I. Pashby, *Surf. Coat. Technol.* 202 (2008) 3933–3939.
- [16] S.H. Mok, G. Bi, J. Folkes, I. Pashby, J. Segal, *Surf. Coat. Technol.* 202 (2008) 4613–4619.
- [17] S. Rawal, J. Brantley, N. Karabudak, Recent advances in space technologies (RAST) in: Proceedings of the 2013 6th International Conference on IEEE, 2013, pp. 5–11.
- [18] B. Dutta, F.H. Froes, *Adv. Mater. Process.* 172 (2014) 18–23.
- [19] D. Srivastava, I. Chang, M. Loretto, *Mater. Des.* 21 (2000) 425–433.
- [20] D. Srivastava, I. Chang, M. Loretto, *Intermetallics* 9 (2001) 1003–1013.
- [21] H.P. Qu, H.M. Wang, *Mater. Sci. Eng. A* 466 (2007) 187–194.
- [22] H. Qu, P. Li, S. Zhang, A. Li, H. Wang, *Mater. Des.* 31 (2010) 2201–2210.
- [23] D. Cormier, O. Harrysson, in: Proceedings of the 16th Solid Freeform Fabrication Symposium, Austin, 2005.
- [24] D. Cormier, O. Harrysson, T. Mahale, H. West, *Res. Lett. Mater. Sci.* 2007 (2007) 1–4.
- [25] L.E. Murr, S.M. Gaytan, A. Ceylan, E. Martinez, J.L. Martinez, D.H. Hernandez, B.I. Machado, D.A. Ramirez, F. Medina, S. Collins, R.B. Wicker, *Acta Mater.* 58 (2010) 1887–1894.
- [26] S. Biamino, A. Penna, U. Ackelid, S. Sabbadini, O. Tassa, P. Fino, M. Pavese, P. Gennaro, C. Badini, *Intermetallics* 19 (2011) 776–781.
- [27] E. Brandl, C. Leyens, F. Palm, IOP Conference Series: Materials Science and Engineering, IOP Publishing, 2011, p. 012004.
- [28] Y. Ma, D. Cuiuri, N. Hoye, H. Li, Z. Pan, *Metall. Mater. Trans. B* 45 (2014) 2299–2303.
- [29] Y. Ma, D. Cuiuri, N. Hoye, H. Li, Z. Pan, *J. Mater. Res.* 29 (2014) 2066–2071.
- [30] N. Hrabe, T. Quinn, *Mater. Sci. Eng. A* 573 (2013) 264–270.
- [31] L. Qian, J. Mei, J. Liang, X. Wu, *Mater. Sci. Technol.* 21 (2005) 597–605.
- [32] B. Baufeld, O. Van der Biest, R. Gault, *Mater. Des.* 31 (2010) S106–S111.
- [33] E. Brandl, A. Schobert, C. Leyens, *Mater. Sci. Eng. A* 532 (2012) 295–307.
- [34] A. Duarte, F. Viana, H.M. Santos, *Mater. Res.* 2 (1999) 191–195.
- [35] G.Q. Wu, Z. Huang, *Mater. Sci. Eng. A* 345 (2003) 286–292.
- [36] M.F. Arenas, V.L. Acoff, *Weld. J.* 5 (2003) 110–115.
- [37] F. Wang, S. Williams, P. Colegrove, A.A. Antonyam, *Metall. Mater. Trans. A* 44 (2013) 968–977.
- [38] B. Baufeld, E. Brandl, O. Van der Biest, *J. Mater. Process. Technol.* 211 (2011) 1146–1158.
- [39] S.M. Kelly, S.L. Kampe, *Metall. Mater. Trans. A* 35 (2004) 1861–1867.
- [40] C.M. Liu, X.J. Tian, H.B. Tang, H.M. Wang, *J. Alloy. Compd.* 572 (2013) 17–24.
- [41] S.A. Jones, M.J. Kaufman, *Acta Metall. Mater.* 41 (1993) 387–398.
- [42] B.W. Choi, Y.G. Deng, C. McCullough, B. Paden, R. Mehrabian, *Acta Metall. Mater.* 38 (1990) 2225–2243.
- [43] V.T. Witusiewicz, A.A. Bondar, U. Hecht, S. Rex, T.Y. Velikanova, *J. Alloy. Compd.* 465 (2008) 64–77.
- [44] H. Sun, Z. Huang, D. Zhu, X. Jiang, *J. Alloy. Compd.* 552 (2013) 213–218.
- [45] R. Imayev, V. Imayev, M. Oehring, F. Appel, *Intermetallics* 15 (2007) 451–460.
- [46] Y. Wang, Y. Liu, G.Y. Yang, H.Z. Li, B. Tang, *Trans. Nonferr. Met. Soc. China* 21 (2011) 215–222.
- [47] F. Appel, R. Wagner, *Mater. Sci. Eng. R* 22 (1998) 187–268.
- [48] A.K. Singh, K. Muraleedharan, D. Banerjee, *Scr. Mater.* 48 (2003) 767–772.
- [49] C. Mercer, W.O. Soboyejo, *Scr. Mater.* 35 (1996) 17–22.
- [50] F. Appel, M. Oehring, R. Wagner, *Intermetallics* 8 (2000) 1283–1312.
- [51] D.M. Dimiduk, P.M. Hazzledine, T.A. Parthasarathy, M.G. Mendiratta, S. Seshagiri, *Metall. Mater. Trans. A* 29 (1998) 37–47.
- [52] G. Dehm, C. Motz, C. Scheu, H. Clemens, P.H. Mayrhofer, C. Mitterer, *Adv. Eng. Mater.* 8 (2006) 1033–1045.
- [53] M. Göken, M. Kempf, W.D. Nix, *Acta Mater.* 49 (2001) 903–911.
- [54] L. Cha, C. Scheu, H. Clemens, H.F. Chladil, G. Dehm, R. Gerling, A. Bartels, *Intermetallics* 16 (2008) 868–875.
- [55] E. Arzt, G. Dehm, P. Gumbsch, O. Kraft, D. Weiss, *Prog. Mater. Sci.* 46 (2001) 283–307.
- [56] Y.S. Sato, S.H.C. Park, H. Kokawa, *Metall. Mater. Trans. A* 32 (2001) 3033–3042.
- [57] S.-C. Huang, E.L. Hall, *Metall. Mater. Trans. A* 22 (1991) 427–439.
- [58] J.M.K. Wiezorek, X.-D. Zhang, W.A.T. Clark, H.L. Fraser, *Philos. Mag. A* 78 (1998) 217–238.
- [59] E. Brandl, B. Baufeld, C. Leyens, R. Gault, *Phys. Proc.* 5 (2010) 595–606.
- [60] K. Chan, Y. Kim, *Acta Metall. Mater.* 43 (1995) 439–451.



ELSEVIER

Available online at www.sciencedirect.com**ScienceDirect**

Acta Materialia 84 (2015) 172–189

www.elsevier.com/locate/actamat

Evaluation of defect density, microstructure, residual stress, elastic modulus, hardness and strength of laser-deposited AISI 4340 steel

Guifang Sun,^{a,b,*} Rui Zhou,^c Jinzhong Lu^d and Jyotirmoy Mazumder^{b,*}^a*School of Mechanical Engineering, Southeast University, Nanjing, Jiangsu 211189, People's Republic of China*^b*Center for Laser-Aided Intelligent Manufacturing, University of Michigan, 2041 G G Brown Bldg, 2350 Hayward Street, Ann Arbor, MI 48109-2125, USA*^c*School of Mechanical and Metallurgical Engineering, Jiangsu University of Science and Technology, Zhangjiagang 215600, People's Republic of China*^d*School of Mechanical Engineering, Jiangsu University, Zhenjiang, Jiangsu 212013, People's Republic of China*

Received 9 July 2014; revised 1 September 2014; accepted 3 September 2014

Available online 26 November 2014

Abstract—Laser-aided direct metal deposition (DMD) was used to form a AISI 4340 steel coating on an AISI 4140 steel substrate. Stress in the coating was relieved before mechanical testing. The defect density and microstructural property of the DMD coating were analyzed. The thermal analysis, continuous cooling transformation (CCT), residual stress, micro-hardness, nano-hardness and elastic modulus of the DMD coating before and after stress relief were studied. Tensile testing, lap shear testing and bend testing were done on the stress-relieved DMD coatings. Finally, evaluation of the effect of porosity on fracture behavior was characterized. A porosity and residual stress-based fracture mechanism was proposed. A better deposition strategy is needed to improve the microstructure (decrease porosity), and the mechanical properties of DMD could be tailored through appropriate heat treatments.

© 2014 Acta Materialia Inc. Published by Elsevier Ltd. All rights reserved.

Keywords: Laser deposition; Microstructure; Thermal analysis; Nanoindentation; Fracture

1. Introduction

AISI 4340 steel is widely used in industrial applications because of its toughness, high strength and ability to retain good fatigue strength at elevated temperatures [1], e.g. in fatigue-critical components, such as the rotor hubs and connecting links of helicopters [2,3], in nuclear power plant structures, high-pressure vessels and reactors and shafts [4], and it is regarded as one of the most popular spring materials for typical force transducer applications [5]. These components often fail. Laser-aided direct metal deposition (DMD®) can be used to repair these metal components with a complex geometry.

DMD is a solid free-form fabrication developed at the University of Michigan. It is one of the rapid prototyping technologies, which has the ability to fabricate and to repair a wide range of metal components with a complex geometry, starting from metal powders. It combines computer-aided design, computer-aided manufacturing,

laser cladding and sensors [6,7]. In the fields of rapid tooling and small batch production, DMD can afford considerable commercial benefit by reducing the design-to-market time of a product, and in the die production industry in particular it has the potential to drastically reduce operating costs, and repair or fabricate high-value parts with low production volume [8–10]. Various laboratories have developed similar processes with different names, such as direct light fabrication (DLF) at Los Alamos National Laboratory, Los Alamos, NM [11,12], and laser-engineered net shaping (LENS) at Sandia National Laboratory, Albuquerque, NM [12–14]. The main difference between DMD, DLF and LENS is the closed-loop controlled, though all three use pneumatically delivered powder. Another group selected melting of powders in a powder bed, e.g. selective laser powder remelting or selective laser melting at Fraunhofer ILT, Aachen [15], and selective laser sintering (SLS®) at the University of Texas, Austin (commercialized by the Desktop Manufacturing Corporation) [16]. The basic principles of these pneumatically delivered powder technologies are similar, in that they use a high-power focused laser beam to create a melt pool on the substrate, to which metallic powder is delivered to create a metal cladding. A robot or a computer numerical control system is used to control the motion of the laser beam as per the tool path generated

* Corresponding authors at: School of Mechanical Engineering, Southeast University, Nanjing, Jiangsu 211189, People's Republic of China (G. Sun). Tel.: +86 13770827969; fax: +86 734 763 5772 (J. Mazumder); e-mail: gfsun82@gmail.com

from the computer-aided design model of an object to create a three-dimensional component layer-by-layer [17]. Accurate control of parameters such as laser power, spot diameter, scanning speed and powder mass flow rate is fundamental to obtaining the required geometric dimensions and material property.

Extensive work has been done so far by various research groups to develop novel coatings with high performance by various laser technologies [18–24]. However, a large proportion of the research attention in this field is focused towards the characterization of microstructures, determination of micro-hardness and the evaluation of wear or corrosion behavior of the fabricated coatings.

First, porosity and discontinuities are two important problems in DMD or SLS. Their nucleation, growth and coalescence greatly affect the stiffness, fracture and fatigue resistance of the components [25–28]. All the defects, such as de-bonding, micro-voids, inclusions, pores and weak grain boundary films can cause rupture. The effects on the structural performance of porosity and bonding defects in the DMD coating need to be clarified. Second, induced residual stress of the laser-treated coating is dependent on the elastic modulus, which is one of the important properties that determine the mechanical strength of the coating [29]. Therefore, it is necessary to investigate the relationship between residual stress and elastic modulus and their effects on the mechanical properties of the DMD coating. Third, what is the effect of the stress-relieving treatment on the residual stress, nano-hardness and elastic modulus of each layer of the DMD coating? These aspects are, of course, of utmost importance for the use of DMD manufactured parts when used in actual working conditions, but to the best of the authors' knowledge, none of the studies available so far in open literature has addressed this topic.

Therefore, the current study aims to shed light on the effects of stress-relieving treatment on the microstructure, the full width at half maximum (FWHM) of the presented peaks, the residual stress, nano-hardness and elastic modulus of each layer in the DMD, and on the relationships between strength, fracture, residual stress, porosity and microstructure of the DMD-processed material. A thorough testing procedure combining microstructure, phases and mechanical tests was carried out. The microstructure, FWHM of the presented peaks of the as-deposited and stress-relieved DMD AISI 4340 steel were observed by scanning electron microscopy (SEM) and X-ray diffractometry (XRD). The phase transformation and martensite transformation starting temperature were analyzed by differential scanning calorimetry (DSC) and continuous

cooling transformation (CCT) curves. The residual stress, nano-hardness and elastic modulus were investigated by analyzing the residual stress change and indentation load–displacement curves resulting from the nano-indentation test. Furthermore, evaluation of the effect of process-induced porosity on the strength and fracture behavior of stress-relieved DMD AISI 4340 steel was carried out by tensile, lap shear and three-point bend testing. These fracture surfaces were characterized. A fracture mechanics-based mechanism was proposed to illustrate the failure mechanism.

2. Experimental procedures

2.1. Powder material

The substrate material was AISI 4140 steel with chemical composition Fe–0.38C–1.04Mn–0.026P–0.014S–0.23Si–0.123Ni–0.967Cr–0.18Mo (wt.%). Gas atomized pre-alloyed AISI 4340 steel powders (Fe–0.4C–0.75Mn–0.017P–0.009S–0.18Si–1.9Ni–1.0Cr–0.46Mo (mass%)) with size range 45–109 μm were used as the feedstock material. The powders were manufactured by Carpenter Powder Products (PA, USA). Fig. 1 shows the as-received powder particle morphology. The particles are mainly spherical, with an average particle size of 75 μm and 85% of the particles within the 60–109 μm range. Powder was also mounted in epoxy, ground and polished to examine the powder particle cross sections, using SEM, for particle morphology, size and porosity measurements. A cross section of the as-received powder particles is shown in Fig. 1(b). Approximately 100 particles per micrograph were selected for measurement, and always the largest diameter and the diameter in the direction perpendicular to the long axis were measured. The average powder particle porosity was found to be ~0.45%.

2.2. DMD process

Fig. 2 shows a schematic of the DMD process. The DMD system consisted primarily of a laser generation system, a powder delivery system, a feedback control system and the CNC motion stage [30]. The DMD process could be performed either in air or under a controlled atmosphere. DMD samples for this investigation were prepared at Focus, HOPE, using a 1 kW fiber coupled diode laser (Laserline GmbH, Germany) POM DMD 105D system. The authors have investigated the laser processing

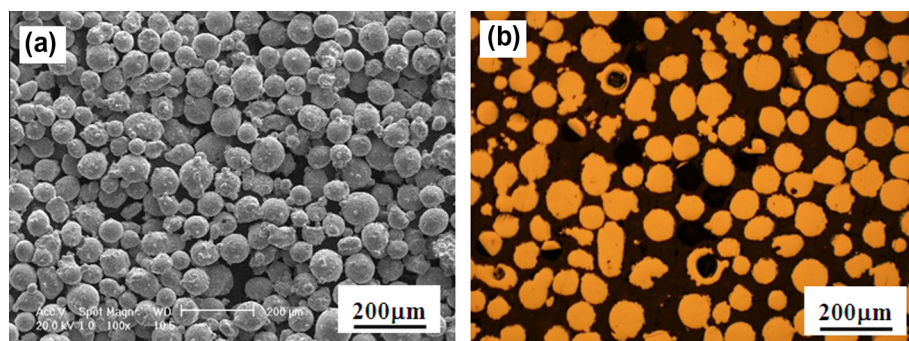


Fig. 1. SEM micrograph of AISI 4340 powders: (a) morphology; (b) cross section.

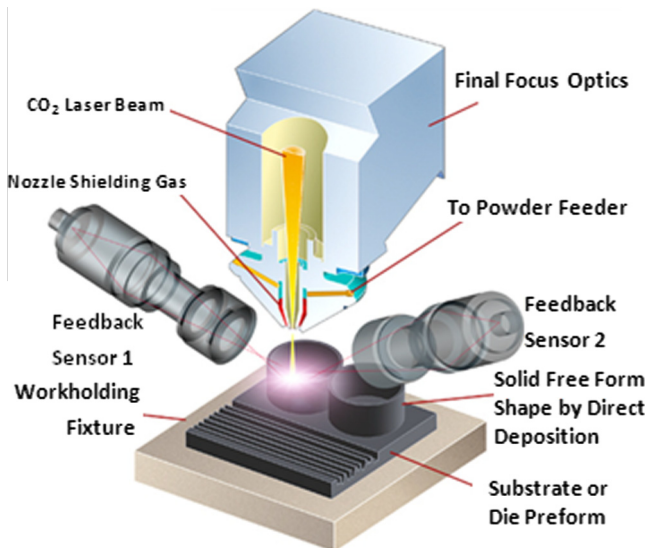


Fig. 2. Schematic diagram showing the DMD process.

parameters and microstructural evolution of laser-deposited 4340 steel coatings [31,32]. Details of the fabrication of 4340 steel DMD coatings were given in an earlier publication [32]. The scanning strategy was that identical layers were scanned using unidirectional scan vectors, and the tracks in the subsequent layer were located directly between two tracks in the previous layer (Fig. 3). The overlap ratio between two tracks in the same layer was 50%. The distance between the nozzle and the substrate surface was 20 mm. The flow rates of the delivering and shielding gas (argon) were 8 l min^{-1} . The laser beam in TEM₀₁ (donut shaped) mode was 4 mm in diameter. The laser power was 3.2 kW, scan speed 1.1 m min^{-1} , and the powder feed rate 45 g min^{-1} . To save time, three layers were deposited for microstructural characterization.

2.3. Heat-treatment process

To analyze the role played by stress relief, a series of specimens were heat-treated after DMD in order to

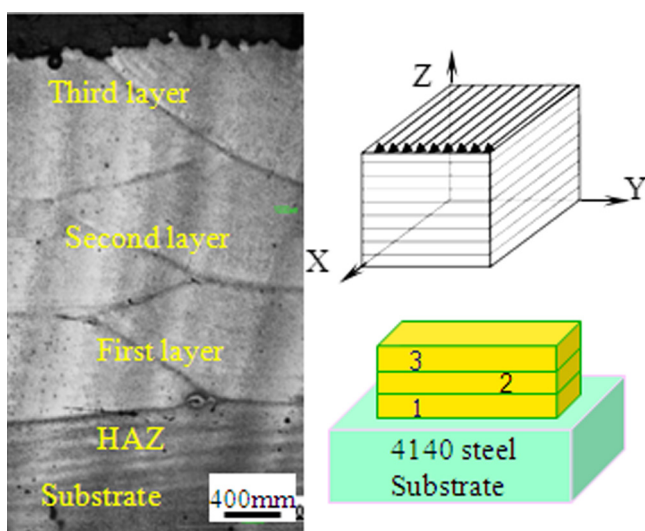


Fig. 3. Morphology of the DMD and schematic of the scanning pattern.

investigate the effects of the partial removal of residual stresses on the mechanical properties of the DMD. Stress in the DMD coatings was relieved in a furnace before tensile, lap shear and bend testing. The processing parameters were as follows: ramping rate, $60\text{ }^{\circ}\text{C min}^{-1}$; holding temperature, $600\text{ }^{\circ}\text{C}$; and holding time, 40 min. All the samples were furnace cooled to the room temperature. Argon was used as the shielding gas.

2.4. DSC experiment

DSC was carried out between room temperature ($25\text{ }^{\circ}\text{C}$) and $700\text{ }^{\circ}\text{C}$ with a heating rate of $10\text{ }^{\circ}\text{C min}^{-1}$, using a heat-flux DSC system (STA 449 C, NETZSCH, Freistaat Bayern, Germany) to observe and differentiate the phase formation and microstructure evolution during solid-state transformation (stress-relieving treatment) of the DMD coating in the as-deposited and stress-relieved states. DSC samples were prepared from the DMD coating. In this device, the samples and reference were contained in small alumina crucibles placed over bases. Thermocouples were attached to the bases, and the whole setup was placed within the same furnaces, i.e. identical thermal conditions. An enthalpy change associated with a phase transformation in the sample induced a small temperature difference compared with the reference. This difference can be recorded and converted to enthalpy, using a suitable calibration. In this case, the reference was an empty alumina crucible.

2.5. CCT

CCT experiments of as-deposited and stress-relieved DMD AISI 4340 steel were carried out using L78RITA Quenching Transformation Measuring Apparatus (LINSEIS, Germany). The geometry of the samples was cylindrical, with height 10 mm and diameter 3 mm. First, the samples were heated on the tip of the thermocouple at a rate of $5\text{ }^{\circ}\text{C s}^{-1}$. Then, they were held at $830\text{ }^{\circ}\text{C}$ for 10 min to homogenize their composition and temperature. After that, the samples were cooled to room temperature at different cooling rates. AISI 4340 alloy steel is heat-treated at $830\text{ }^{\circ}\text{C}$ ($1525\text{ }^{\circ}\text{F}$), followed by quenching in oil [33]. Therefore, the cooling rates used in this investigation were $20, 25, 30, 35$ and $40\text{ }^{\circ}\text{C s}^{-1}$, close to the cooling rates in oil quenching. The start of martensite transformation can be determined by recording the crystallization temperature and the onset time of crystallization at different cooling rates, which can be reflected by the turning points of the expansion curves.

After CCT testing, metallography of the samples was carried out. The etchant solution was 5% nital.

2.6. Microstructure and XRD characterization

After laser treatment and stress relief, the specimens were sectioned, mounted, ground, polished and etched with nital for SEM (Philips XL30 FEG) investigation. Phases presented in the stress-relieved DMD coatings were identified using XRD (Rigaku rotating anode) with $\text{Cu K}\alpha$ generated at 40 kV and 100 mA and a scanning speed of 0.5 deg min^{-1} . The hardness of the stress-relieved specimens was measured using a Vickers micro-hardness tester (Clark, CM-400 AT) with a 500 g load for a dwell time of 15 s.

2.7. Mechanical property test

Nano-indentation and elastic modulus tests on the polished sections of alloyed layers were performed using a CSM + NHT2 + MST nano-indentation tester at room temperature. A loading-unloading test mode was used, and a test force of 10 mN, a loading speed of 20 mN min⁻¹ and a duration of 10 s were adopted. During measurements, the load and indentation depth were recorded. An average value of nano-hardness in each deposited layer was taken from five measurements. The raw data from five measurements were then used to construct loading-unloading plots.

Measurements of residual stress in the as-deposited and stress-relieved DMD AISI 4340 steel were measured using XRD (X-350A) ($\sin^2 \psi$ method). The X-ray beam diameter was ~ 2 mm. The X-ray source was Cr K_{α} X-ray, and the diffraction plane was (111). In the stress calculation, the Poisson's ratio was set to 0.35. The speed of the ladder scanning was 0.1 deg s⁻¹, and the time constant was 1 s. The tube voltage and current were 20 kV and 5 mA, respectively. The scanning angle of 2 θ was in the range 76–84°. Residual stresses determined using XRD were arithmetic average stresses in a volume of material defined by the irradiated area. The penetration depth of the Cr K_{α} X-ray beam on steel is ~ 5.5 μ m according to the instruction

manual of this equipment. The heeling angle was set to 0°. Measurements were repeated five times on the cross section for each layer (in total three layers), and average values were obtained.

Schematic drawings of the tensile test specimen as per ASTM E8 standard, the lap shear test specimen as per ASTM D-3846, and the bend test specimen as per ASTM E290 standard are shown in Fig. 4(a)–(c), respectively. Specimens for tensile and lap shear testing were tested on an Instron® 5982 Universal Testing Instrument at the University of Michigan, with a load cell of 10 kN and loading speed of 3 mm min⁻¹. In the three-point bend test, the DMD coating side was put on the bottom, and the load speed was 0.1 mm min⁻¹. The bend test was tested at Stork Climax Research Services (Wixom, MI). All tests were conducted at room temperature.

3. Results and discussion

3.1. Microtopography analysis

3.1.1. Density defect analysis

Cross-section morphology of the as-deposited DMD AISI 4340 steel coating before etching is shown in Fig. 5.

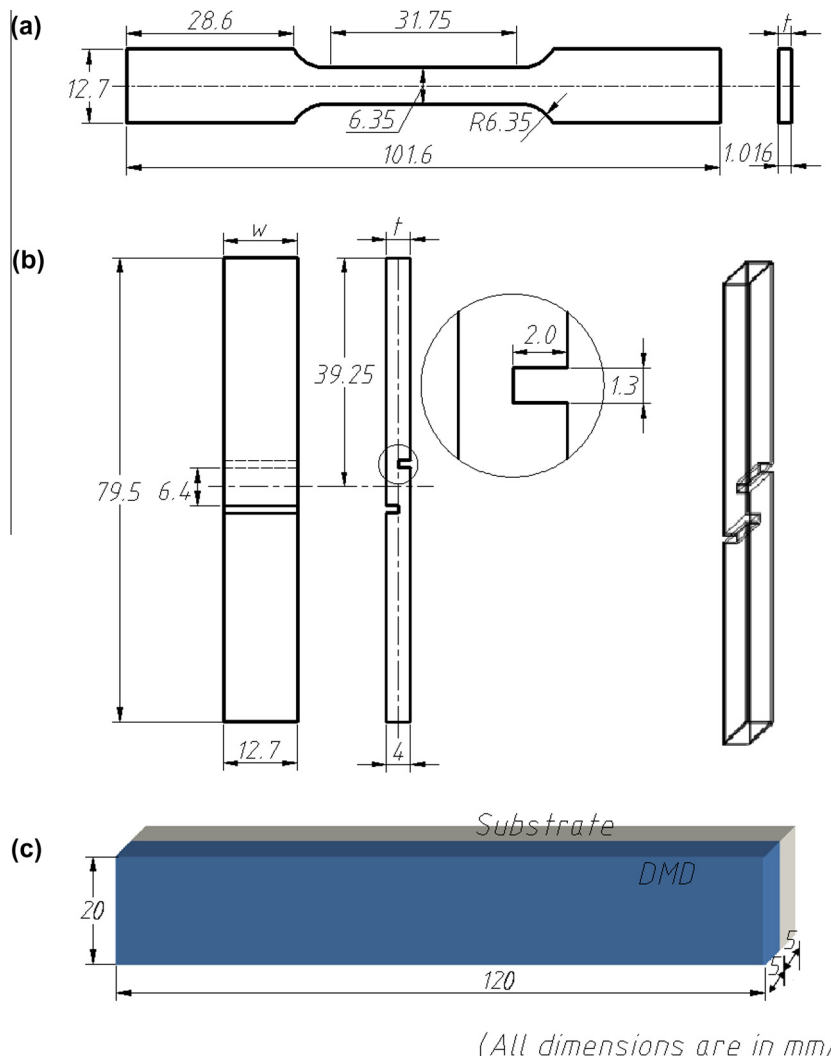


Fig. 4. Schematic of (a) tensile test, (b) lap shear test and (c) bend test specimens prepared from stress-relieved DMD 4340 steel.

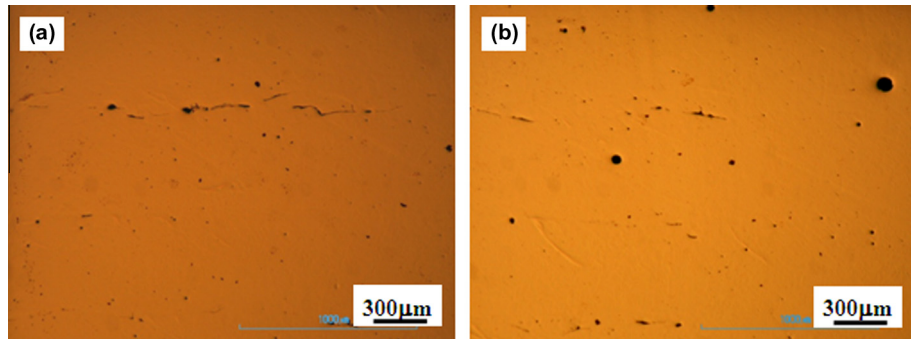


Fig. 5. Cross section of the as-deposited DMD coating.

Porosity in the DMD coating and bonding defects between successive layers can be detected. The porosity ratio (including the de-bonding) of the DMD coating was ~3.3%, calculated from SEM images at 10 different sites and analyzed using one function of Adobe Photoshop image software. Undoubtedly, porosity in the powder contributes partially to the porosity in the DMD coating. Furthermore, smaller powder has a larger surface area, which will tend to introduce more oxygen into the molten material. A negative effect of oxygen on the flow behavior of molten tool steels (M2) and further on the densification process has been reported [34]. If the scanning speed is high, surface tension will cause the molten pool to break up into a row of spheres, leaving areas of porosity between tracks [35]. In addition to the porosity in the powders, pores in the DMD coating are also due to a lack of powder in the regions between the tracks. Adopting a different scan strategy can improve this situation. Morgan et al. [36] adopted a complex scan strategy, i.e. knit-scan strategy, to fabricated 316L stainless steel components that exhibited porosities <1%. Xie et al. [37] reported that the density of H13 tool steel samples was significantly increased by the use of a modified knit-scan strategy.

The cross-section morphology of the stress-relieved DMD AISI 4340 steel coating before etching is shown in Fig. 6(a)–(c). Severe oxidation around porosity in the DMD coating and bonding defects between successive layers can be observed. Oxidation was also observed in the micro-cracks, even with argon as the shielding gas. Investigation of the role of cold work and applied stress on the surface oxidation of 304 stainless steel showed that prior cold work facilitated the oxidation of microstructural features such as grain boundaries and deformation bands by providing a density of dislocations that can act as fast diffusion paths for oxygen and iron. Applied stress was found to magnify the effects of cold work and accelerate oxidation rates [38]. In this case, the micro-cracks and bonding defects that exposed the adjacent DMD materials to air facilitated oxidation by serving as even faster diffusion paths for oxygen and iron than grain boundaries or deformation bands did. A cross section of the stress-relieved DMD AISI 4340 steel after the CCT experiment is shown in Fig. 6(d) and (e). It is apparent that the higher temperature (830 °C in the CCT experiment) stimulates crack propagation around porosities significantly compared with the stress-relieved DMD AISI 4340 steel (600 °C). Oxidation cracks propagate mainly in the intergranular boundaries. A synergistic oxidation effect brought about by a high-temperature and oxidizing environment can significantly

degrade fatigue performance associated with increasingly intergranular fracture features and secondary grain boundary cracking [39]. The oxygen has sufficient time to diffuse along the grain boundary ahead of the crack tip, causing a decrease in the bonding strength of the grain boundary and predominantly intergranular oxidation. To emphasize the effect of stress-relieving heat treatment, cross-section morphology of the as-deposited (Fig. 6(f)) and stress-relieved DMD coating (Fig. 6(g)) after CCT with a cooling rate of 20 °C s⁻¹ is also observed. A thick oxide film was formed in the bonding defects in both. However, more severe oxidation can be reflected by the oxides in the stress-relieved DMD coating (Fig. 6(g)) than by those in the as-deposited coating (inset in Fig. 6(f)). This indicates that the negative effect of porosities on fracture increases with temperature, which will accelerate fracture of DMD coatings. Porosities, in particular, should be avoided in high-temperature thermal cycling.

3.1.2. Microstructure analysis

The morphology of the as-deposited DMD coating is shown in Fig. 7(a), in which martensite and retained austenite, as indicated by red arrows, can be differentiated. The morphology of the stress-relieved DMD coating is shown in Fig. 7(b)–(d). Tempering leads to the formation of tempered martensite with the presence of fine carbide precipitates dispersed among them (Fig. 7(b)). Fig. 7c marks the presence of both blocky and fine carbides dispersed between lath tempered martensite matrix. The precipitation of the fine granular cementite was along the grain boundaries of the tempered martensite, as indicated by red arrows. Fig. 7(d) shows the boundaries of three tempered martensite grains (A, B and C), with a small amount of retained austenite as the grain boundaries. Red and yellow arrows showed the grain boundaries between grains A and B, C and B, and grains A and C, respectively. Furthermore, parallel sub-microstructure in lath martensite, indicated by yellow parallel lines in grain A and red parallel lines in grain B, are highlighted by the precipitation of carbides during the heat treatment. Lath martensite is characterized by a dislocated substructure composed of screw dislocations, which are intrinsic to the transformation lattice invariant shear, plus a forest inherited from the surrounding austenite [40]. In a typical microstructure, martensite laths with the same habit plane are grouped into blocks according to their crystallographic orientation variant. These blocks compose packets, which subdivide the austenite grains [41]. According to the present authors' previous report [32], the orientation relationship between

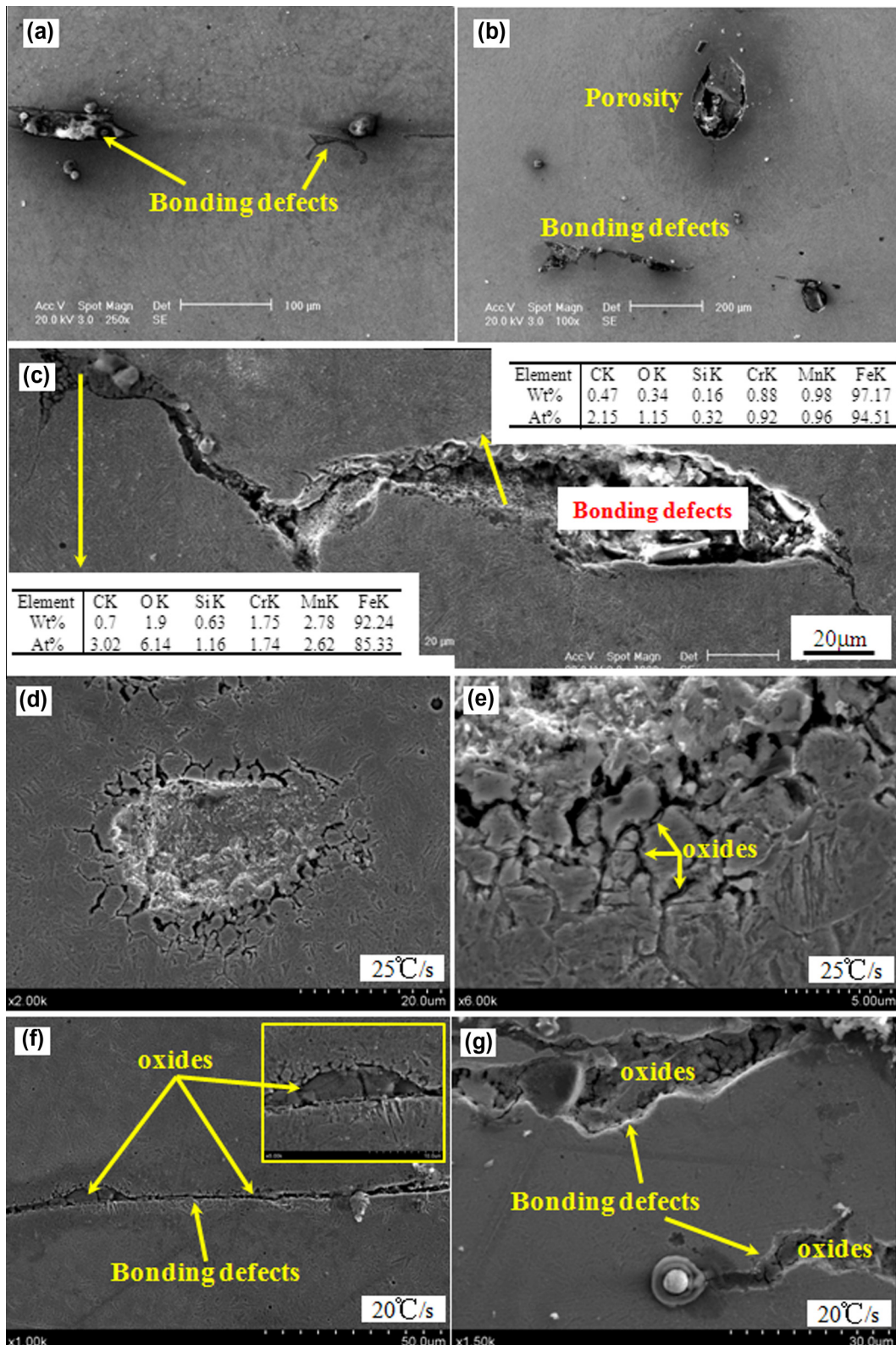


Fig. 6. SEM morphology of a cross section of DMD AISI 4340 steel: (a)–(c) stress-relieved; (d, e) after CCT with a cooling rate of $25\text{ }^{\circ}\text{C s}^{-1}$; (f) as-deposited; (g) stress-relieved after CCT with the cooling rate of $20\text{ }^{\circ}\text{C s}^{-1}$.

martensite and austenite in the as-deposited coating is $[111]\alpha/[110]\gamma$, $(101)\alpha/(111)\gamma$ and $(011)\alpha/(111)\gamma$, which follows the Kurdjumov–Sachs relationship. The orientation relationship between cementite and martensite

is $[212]\text{Fe}_3\text{C}/[311]\alpha$, $(120)\text{Fe}_3\text{C}/(101)\alpha$ and $(101)\text{Fe}_3\text{C}/(211)\alpha$. Martensite forms during the fast solidification process after laser irradiation. Blocks of laths with an energetically preferred variant that propagate from the austenite

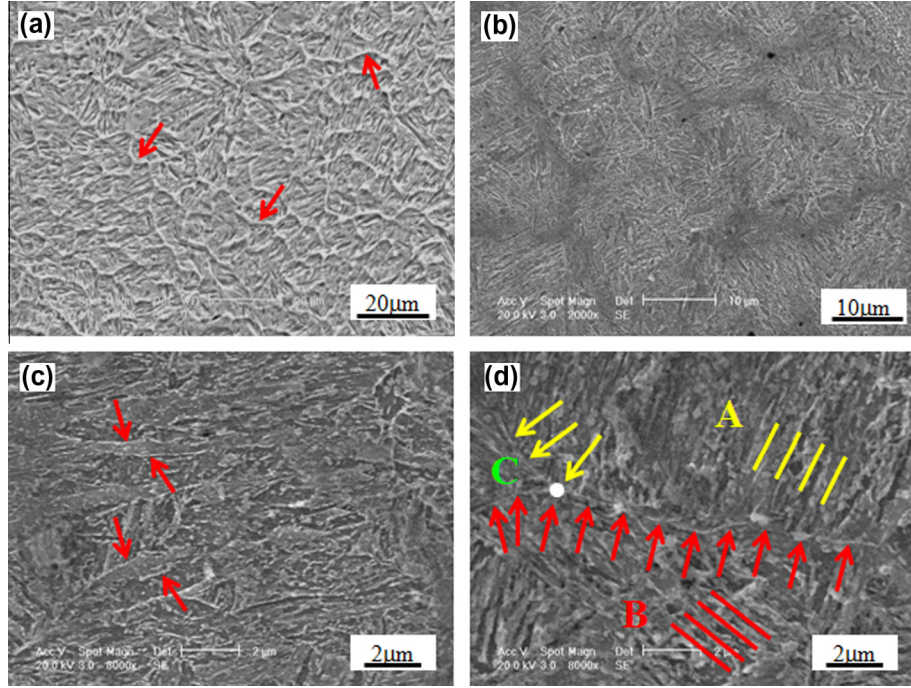


Fig. 7. Microstructure of (a) DMD AISI 4340 steel and (b)–(d) stress-relieved DMD AISI 4340 steel.

grain boundaries initially partition the austenite grains. These partitions are subsequently filled by additional blocks of laths with favorable orientations. This explains why a parallel sub-microstructure (packets of lath martensite) can be observed in Fig. 7(d). According to Zhang's report on the microstructure evolution of the lath martensite microstructure in 12Cr–9Ni–0.066C (wt.%) steel [42], these additional blocks of laths favorably orient to accommodate transformation strains. Cementite precipitates in the oriented lath martensite during the heat treatment, which highlights the boundaries of lath martensite, resulting in the clear parallel lines.

3.2. Phase analysis

The phases detected by X-ray are martensite and retained austenite in the as-deposited DMD coating, and martensite and ferrite in the stress-relieved DMD coating, as shown in Fig. 8. Retained austenite decomposes during the heat treatment process, accounting for the absence of it in the stress-relieved DMD coating. In addition, martensite decomposes into ferrite and cementite, accounting for the observation of ferrite in the stress-relieved DMD coating. This is in agreement with the DSC results. Furthermore, the peak intensity decreases after stress relief.

The DSC curves of the as-deposited and stress-relieved DMD AISI 4340 steel are shown in Fig. 9(a) and (b), respectively. It should be noted that no large peaks are detected when the temperature is lower than the A₁ temperature (727 °C). Two small endothermic peaks are detected in the DSC curve of as-deposited and stress-relieved DMD AISI 4340 steel. Their temperatures are 406.9, 564 and 411.1, 589 °C, respectively. It is believed that the first small peak corresponds to the epsilon (ϵ) carbide dissolution, since non-stoichiometric ϵ -carbide dissolves above 200 °C [43]. It is important to mention that, according to the previous TEM study of the as-deposited DMD AISI

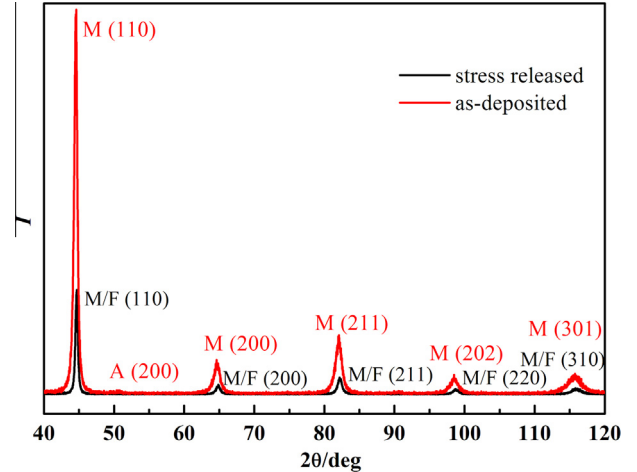


Fig. 8. XRD pattern of as-deposited and stress-relieved 4340 steel DMD.

4340 steel [32], ϵ was absent in specimen 2 (the same as in the present investigation), while it was present in specimen 1, owing to the higher cooling rate in specimen 2 than in specimen 1, which inhibited the carbon diffusion at low temperatures. However, ϵ precipitates from martensite when the tempering temperature is in the range 100–200 °C, with the precipitated tiny flaky ϵ -carbides distributing in the martensite matrix, and martensite tetragonality reducing. In the next stage, residual austenite decomposes to ferrite and carbide with the increase in temperature. After the dissolution of martensite and austenite, ϵ -carbide starts to dissolve and is replaced by cementite as the temperature increases. The temperatures of the first small peaks in the two coatings are close. The second small peak corresponds to the recrystallization of ferrite, accompanied by the formation of tempered sorbite with the granular

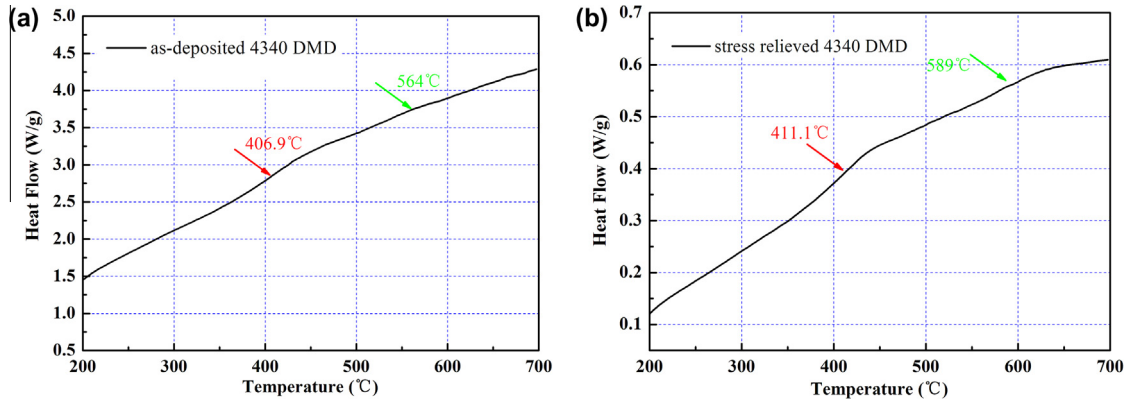


Fig. 9. DSC curves for (a) as-deposited and (b) stress-relieved DMD AISI 4340 steel.

cementite distributing in the polygonal ferrite. Some results indicated that the formation of martensite in the strain-induced martensitic transformation of an austenitic steel followed the sequence $\gamma \rightarrow \varepsilon \rightarrow \alpha$. Nucleation of α phase occurred mainly at the intersections of two ε bands or at the intersection of the ε band and twin or grain boundaries [44]. Recrystallization of deformed ferrite was testified by dilation curves of the cold-rolled steel when heated at a low rate (1 K s^{-1}). It starts at ~ 500 °C and reaches up to 0.1% at 650 °C [45]. The second peak temperatures for the two coatings in this investigation are 564 and 589 °C, respectively. The deformation energy of the cold-rolled steel brings forward ferrite recrystallization at a relatively lower temperature than both the DMD coatings. Investigation of tempering of Fe–13Cr–4Ni–Mo (wt.%) low carbon martensite stainless steels indicates that reversed austenite formation occurs by the diffusion mechanism in the tempering temperature range 570–680 °C when the holding time is 30 min [46]. Addition of Cr, Ni and Mo decreases the martensite transformation starting temperature to ~ 570 °C, much lower than the equilibrium temperature. This may not happen in the low-alloy DMD AISI 4340 steel.

It is obvious that the difference between the two DMD coatings can be attributed to their different heat histories. The stress-relieving treatment decreases the solubility of martensite and therefore decreases the degree of lattice distortion. More energy is needed to drive the recrystallization of ferrite in the stress-relieved DMD coating than that in the as-deposited coating, which accounts for the relatively high peak temperature in the stress-relieved DMD coating. Furthermore, owing to the nature of the temperature control in the heat treatment, it was not always possible to achieve the exact target temperature during rapid heating, or to force a certain cooling schedule. Consequently, overshoots of the target temperature or non-linear cooling trends may occur during the experiment. Since the DSC peaks associated with the ε dissolution and ferrite recrystallization are relatively small, it is always desirable to correlate them with other experimental or thermodynamic studies, such as high-temperature confocal laser scanning microscopy (HT-CLSM). This has been used in several studies investigating both solid–solid phase transformations [47,48] and solid–liquid phase transformations [49–51]. A combination of DSC and HT-CLSM might be a further direction for investigation of phase transformations.

3.3. Residual stress analysis

The FWHM values obtained from the X-ray measurements allowed researchers to obtain important information about the surface state of material. This quantity is related to the grain distortion, to the dislocation density and to the so-called type II micro residual stresses [52]. Research focusing on FWHM and its relationship with improving residual compressive stress by shot peening is widely available. The effect of temperature on cyclic deformation behavior and residual stress relaxation of deep-rolled under-aged aluminum alloy AA6110 [53] shows that the reductions in the FWHM values are quite similar to the relaxation of the residual stresses as temperature increases. The evolution of residual stress-redistribution associated with localized surface microcracking in shot-peened medium-carbon steel during fatigue testing [54] shows that shot peening increases residual stress and FWHM. However, the heat effect of the laser, such as in laser cladding or laser alloying, on FWHM has not been addressed in detail. FWHM values of the five peaks presented are listed in Table 1. The martensite/ferrite peaks in the stress-relieved DMD are narrower, and peak positions shift to a relatively larger Bragg's angle compared with the martensite peaks in the as-deposited DMD coating. Laser treatment can increase defects in structure and high strain values, resulting in the broadening of the diffraction peaks [55,56]. The narrow diffraction peaks testify to a decrease in defects in structure and high strain values after stress relief. Peaks become sharp again after post-heat treatment followed by laser surface treatment. This observation confirms that stress relief reduced the solid solubility of dissolved alloying elements kept in the martensitic supersaturated solid solution after laser DMD, owing to the precipitation of carbides. Colaco et al. [57] reported a reduction in the supersaturation of martensite induced by post-heat treatment followed by laser surface melting, which is similar to the present results.

Research on improving residual compressive stress by shot peening and its relationship with FWHM is widely available. However, few studies have reported the heat effect of laser and heat treatment on the residual stress of each layer of the deposited DMD coating. Fig. 10 shows residual stress in the three layers in the as-deposited and stress-relieved DMD AISI 4340 steel. Tempering can apparently relieve stress in the DMD coating. Residual

Table 1. FWHM values of peaks in the as-deposited and stress-relieved DMD AISI 4340 steel (20 deg^{-1}).

Sample	Peak 1	Peak 2	Peak 3	Peak 4	Peak 5
As-deposited	0.535	0.947	1.026	1.129	1.872
Stress relieved	0.368	0.647	0.663	0.832	1.283

stress in all the three stress-relieved layers is lower than that in the as-deposited counterparts. The stress in the first layer of the stress-relieved DMD coating is even compressive stress. Surface residual compressive stress is able to improve the fatigue resistance of materials, postpone the initiation and propagation of fatigue cracks, and prolong the service life of materials [58]. The residual stress in the previous layer is lower than that in the subsequent layer, owing to the stress relief in the previous layer induced by the heat effect of the deposition of the subsequent one. Both of these work for DMD coatings.

An illustration of the distribution of residual stress in the substrate and each DMD layer is shown in Fig. 11. The length of the substrate and the first layer is L_0 when the solidification of the molten pool just finishes (Fig. 11(a₁)). The temperature distribution is supposed to be uniform in the substrate and DMD layer. The length of the DMD layer shrinks to L_1 , which is smaller than the original length L_0 during the subsequent cooling process. Shrinkage of the DMD layer would be restrained by the substrate, owing to the metallurgical bonding between them, resulting in tensile stress in the DMD layer. Corresponding compressive stress in the substrate is formed according to the action and reaction principle, owing to the dimensional change (Fig. 11(b₁)). Shrinkage of the DMD layer will form an additional couple in the sample, owing to the asymmetric structure composed of the DMD layer and the substrate. As a result, the sample will bend, and bending stress is formed in the cross section, as shown in Fig. 11(c₁). The bending strength in the DMD layer and substrate is compressive and tensile stress, respectively.

Fig. 11(d₁) shows the incorporated residual stress of thermal stress (b₁) and bending stress (c₁). Furthermore, there is one heat-affected zone in the substrate close to the cladded zone, which undergoes microstructure change during laser processing. Martensite can be formed under

the appropriate processing parameters with the volume expansion, inducing residual compressive stress in the heat-affected zone. At the same time, on both sides of the heat-affected zone, i.e. in the cladded zone and substrate, residual tensile stress can be formed locally, as shown in Fig. 11(e₁). The real stress distribution in the cross section of the sample is the combination of geometry and microstructure change, as shown in Fig. 11(f₁).

For the deposition of the second layer, the same process is repeated. The substrate and the first layer serve as a whole part, while the second layer repeats what the first layer has undergone, and so on. The residual stress distribution shown in Fig. 11(f₂) obtained from qualitative analysis is in good agreement with the measured value as shown in Fig. 10.

Laser surface treatments induce thermal gradients and hence residual stresses. Pilloz and Pelletier [59] determined the stresses in the case of coatings of various metallic materials on two different substrates: a low carbon steel and an austenitic stainless steel. Furthermore, they performed qualitative analysis of experimental results using phenomenological modeling based on decomposition of the specimen into three different parts: the substrate, the heat-affected zone and the coating. This block scheme partition method is similar to the present analysis. The substrate used in this investigation is AISI 4140 medium carbon steel. Even though the specimen is decomposed into two parts—the substrate and the deposited layer—the phase transformation effect in the heat-affected zone has been considered in the present analysis. Analysis of these two typical examples (whether phase transformations can occur during the heat cycle) reveals that their phenomenological approach describes fairly well the process that induces the residual stress field. They have drawn three main conclusions. First, heating induces a creep phenomenon in the heat-affected zone. Therefore, it is realistic to assume a constant length in this zone. The sign and level of stress depend on the creep's magnitude. Second, the differences in thermal expansion coefficients are the main factors that create residual stresses. Thermal contraction effects in the different blocks determine the sign of the residual stresses. Plasticification effects during cooling have only a secondary influence, probably on the magnitude of these stresses, but not on their sign. Third, thermal gradients induced by laser heating influence the dimensions of different blocks.

3.4. Hardness analysis

Average micro-hardness in the as-deposited and stress-relieved DMD is 789.8 and 444.3 HV_{0.5}, respectively. Stress relief decreases the micro-hardness of the DMD coating by 43.7%. Fig. 12(a) and (b) depicts the nano-indentation load-depth curves measured on the polished sections of as-deposited and stress-relieved DMD AISI 4340 steel. One can see that the indentation depth of each layer of the stress-relieved DMD AISI 4340 steel is larger than that of the as-deposited DMD AISI 4340 steel, which can be understood by the larger deformability and lower hardness

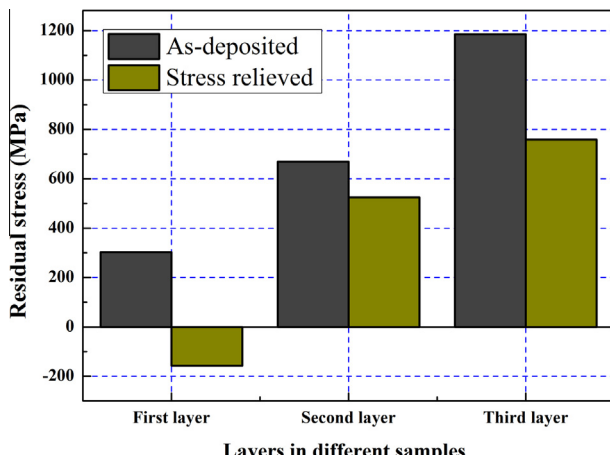


Fig. 10. Residual stress in different layers in the as-deposited and stress-relieved DMD AISI 4340 steel.

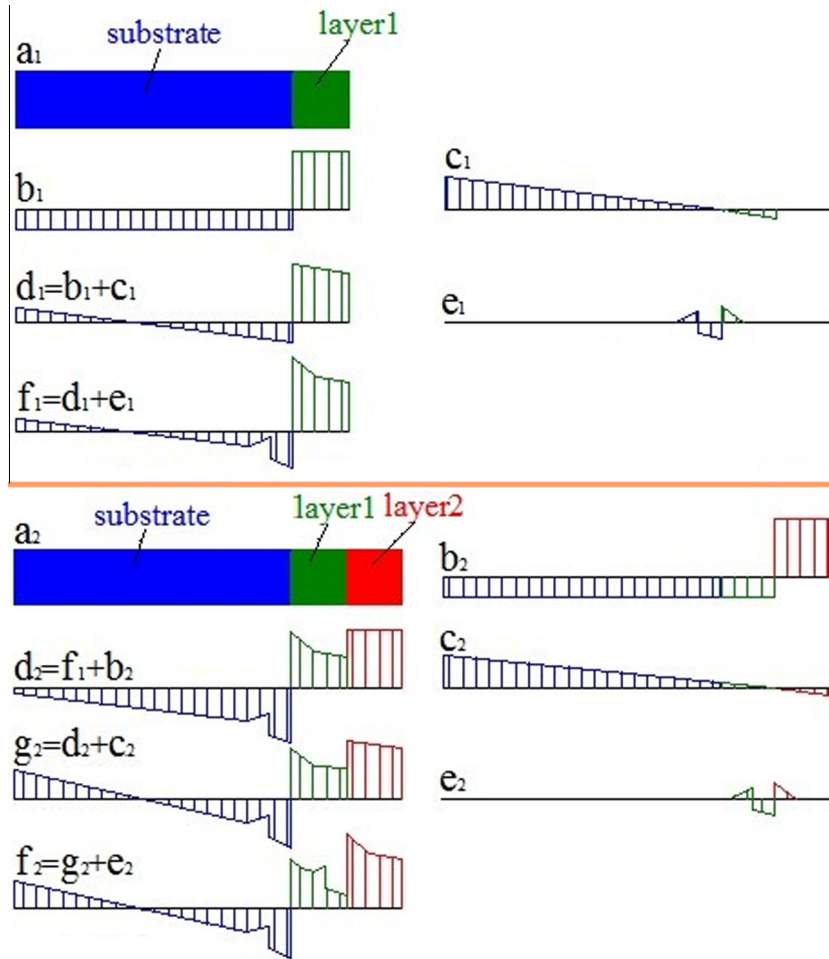


Fig. 11. Illustration of the distribution of residual stress in the substrate and each DMD layer: (a) illustration of sample geometry; (b) thermal stress; (c) bending stress; (d) stress integration of thermal stress and bending stress; (e) transformation stress; (f) residual stress; (a_1-f_1) substrate, first and second layer; (a_2-f_2) substrate, first and second layer.

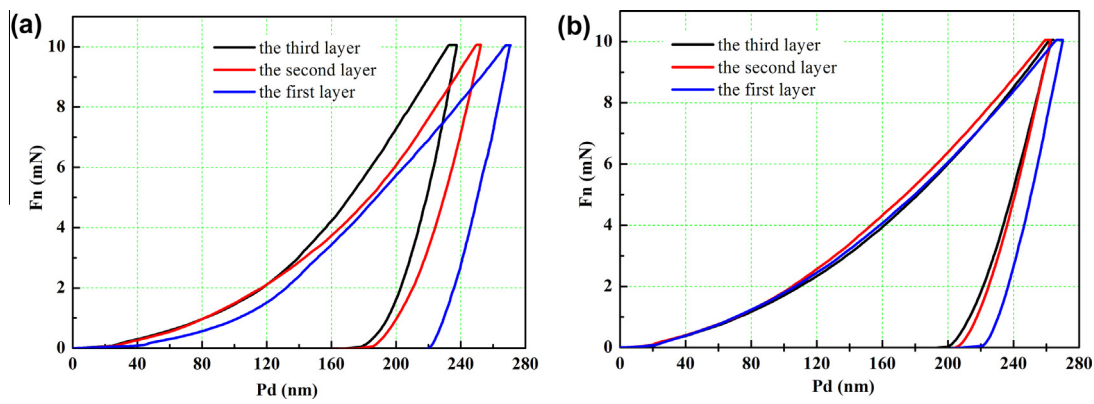


Fig. 12. Loading–unloading curves of (a) DMD AISI 4340 steel and (b) stress-relieved DMD AISI 4340 steel.

of the former. The corresponding indentation hardness (H_{IT}) and indentation elastic modulus (E_{IT}) of each layer are listed in Table 2. The H_{IT} values increase with the deposited layers for both DMD coatings, indicating the heat effect of the subsequent deposition on the previous layer. Furthermore, the increased ratios decrease with deposited layers, with the ratio value of 12%, 7.6% and 7.4%, 2.1% for the as-deposited and stress-relieved layers,

Table 2. Nano-hardness (H_{IT}) and elastic modulus (E_{IT}) values in the as-deposited and stress-relieved DMD AISI 4340 steel (GPa).

Sample	First layer	Second layer	Third layer	
As-deposited	H_{IT}	6.845	7.666	8.247
	E_{IT}	218.292	210.223	284.262
Stress-relieved	H_{IT}	6.391	6.929	7.076
	E_{IT}	223.887	206.607	188.394

indicating the decreased heat effect of the deposition of the third layer on the second layer compared with that of the second layer on the first layer. In addition, the H_{IT} value of each stress-relieved layer and the increased ratio are smaller than that of the corresponding as-deposited layer, indicating the heat effect of tempering. The corresponding average dynamic nano-hardness H_{IT} of stress-relieved DMD AISI 4340 steel is 6.799 GPa, while that of the as-deposited sample is 7.586 GPa. Definitions of micro-hardness and nano-hardness display similar results when the plastic deformation plays a main role. Otherwise, the results are quite different when the elastic deformation plays a main role [60]. The similar trends in variation of micro- and nano-hardness revealed in this investigation indicate that the deformation during hardness measurement is plastic deformation, which is in good agreement with the characteristic of the DMD layers.

The elastic modulus E_{IT} values of the stress-relieved layers show an opposite trend to the H_{IT} values. Nevertheless, the elastic modulus value of the third layer in the as-deposited DMD coating shows a large increase. The elastic moduli E_{IT} of the as-deposited and stress-relieved samples are 237.5923 and 206.296 GPa, respectively. Stress relieving remarkably reduces the elastic modulus of the as-deposited DMD coating. The micro-hardness and elasticity modulus of annealed AISI 4340 alloy steel (annealed at 844 °C, furnace cooled) are 228 HV and 190–210 GPa, respectively [33], which are smaller than both the DMD coatings in this study. In addition to the phase transformation strengthening effect and solution strengthening effect, both the grain refinement effect as a result of laser rapid solidification and the high residual stress in the laser-treated coatings favors the enhancement of hardness compared with conventional heat treatment.

3.5. Strength test

3.5.1. Tensile test

The tensile test performance of seven stress-relieved 4340 steel DMD specimens is shown in Fig. 13 (labeled T1–T7). Fig. 13(a) shows pictures of the tensile test specimens. Fracture occurred at different locations in the neck. Some are in the middle part of the neck, and some are close to one end

of the neck. Furthermore, the cross-section morphology of the fracture varies. Specimen 1 exhibits a footstep shape, while specimen 6 exhibits a zigzag shape. Fig. 13b shows the stress–engineering strain curves of three tensile test specimens. The ultimate tensile strength (UTS) and strain of seven specimens are listed in Table 3. The average UTS is 1399 MPa, and average strain is 1.665%. The tensile strength and strain at the break of annealed AISI 4340 alloy steel (844 °C, furnace cooled) are 745 MPa and 22%, respectively [33]. Compared with the annealed 4340 alloy steel, the UTS of the stress-relieved DMD AISI 4340 steel increases by 88%, and the engineering strain decreases by 92.4%. No characteristic of necking around the fracture area is observed in all the tensile specimens, which verifies the low engineering strain of the DMD coating.

Fracture surface of the stress-relieved DMD coating after tensile testing is shown in Fig. 14, which appears to be a combined fracture of ductile and cleavage. The dimple rupture in Fig. 14(a) indicates a ductile fracture, while the tear ridge in Fig. 14(b) indicates a cleavage fracture. Cleavage fracture exists in some local areas, as shown in Fig. 14(c). Because the branches of the river pattern join in the direction of crack propagation, these markings can be used to establish the local fracture direction. Furthermore, some inclusions can be found in Fig. 14(c), as indicated by yellow arrows. They can serve as void-nucleating sites. When overload is the principal cause of fracture, most common structural alloys fail by a process known as microvoid coalescence. The micro-voids nucleate at regions of localized strain discontinuity, such as that associated with second-phase particles, inclusions, grain boundaries and dislocation pile-ups. Discontinuities act as fracture initiation sites, and cause fracture initiation to occur earlier, or at lower loads. The fractures of tearing topography surfaces

Table 3. Ultimate strength and strain values of seven stress-relieved DMD AISI 4340 steel.

Sample	Tensile	Lap shear	Bend
Strength (MPa)	1398.65	511.63	225
Strain (%)	1.665	0.537	–

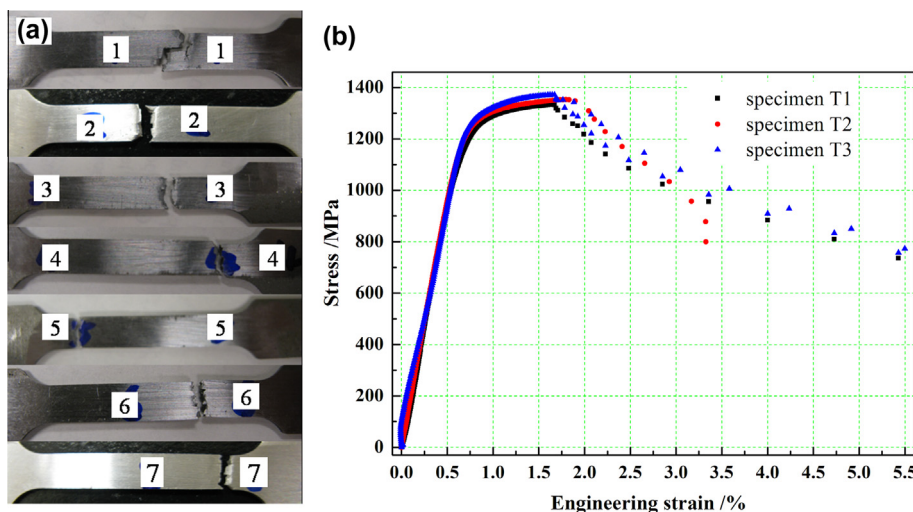


Fig. 13. (a) Tensile test performance and (b) stress–engineering strain curves of stress-relieved DMD AISI 4340 steel.

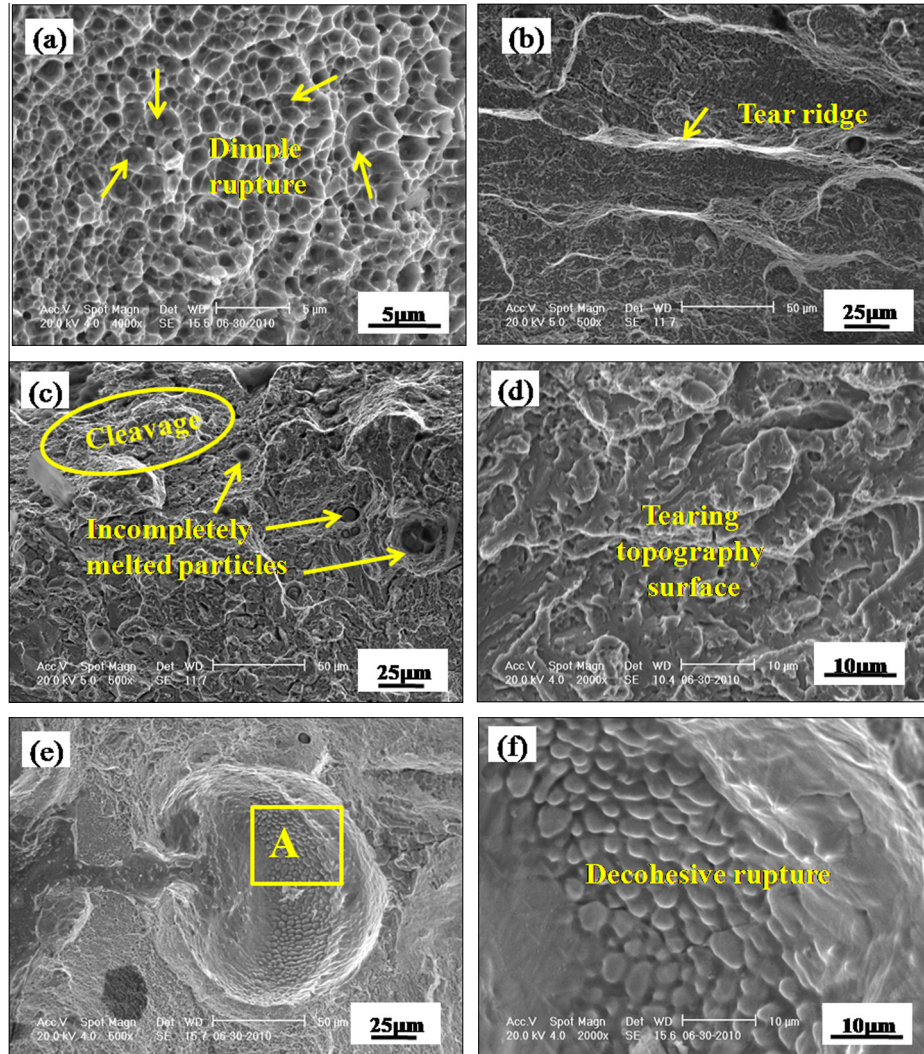


Fig. 14. Fracture morphology of the stress-relieved DMD AISI 4340 steel after tensile testing.

are generally characterized by relatively smooth, often flat, areas or facets that usually contain thin tear ridges (Fig. 14(d)). The fracture of weak grain-boundary films (grain-boundary penetration by low-melting-point metals), the rupture of melted and re-solidified grain-boundary, or the separation of melted material in the boundaries before it solidifies (hot cracking) can produce a de-cohesive rupture (Fig. 14(e)). Fig. 14(f) shows the magnified microstructure of the yellow rectangle in Fig. 14(e). Fig. 14(g) also shows the de-bonding between successive layers or tracks. The magnified microstructure in the yellow rectangle in Fig. 14(g) is shown in Fig. 14(h). Similarly, rupture occurred between dendrites, i.e. in the inter-dendrites, which are weak points during solidification. The second arm distance of dendrites is $\sim 2\text{--}4 \mu\text{m}$. All the defects, such as de-bonding, micro-voids, inclusions and pores and weak grain boundary films can cause de-cohesive rupture.

3.5.2. Lap shear test

Pictures of the stress-relieved DMD AISI 4340 steel after lap shear testing are given in Fig. 15. The fracture surface of the specimen is shown in the inset, where the interface between adjacent DMD layers can be differentiated. All fracture occurs at the DMD coating side, implying that

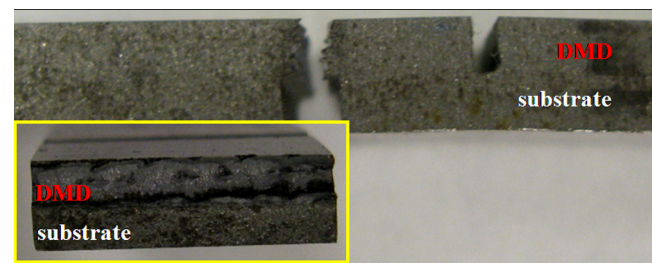


Fig. 15. Morphology of the stress-relieved DMD AISI 4340 steel after lap shear testing.

the densification of the DMD coating affects the strength to a large extent. Average values of five specimens of the shear strength and shear strain are 512 MPa and 0.537%, respectively (listed in Table 3).

Fracture morphology of the stress-relieved DMD AISI 4340 steel after lap shear testing is given in Fig. 16. Fig. 16(a) shows a combined fracture of ductile and cleavage. The dimple rupture indicates a ductile fracture. The fracture surface shows elongated grains, as indicated by arrows in Fig. 16(b). Fig. 16(c) and (d) shows the

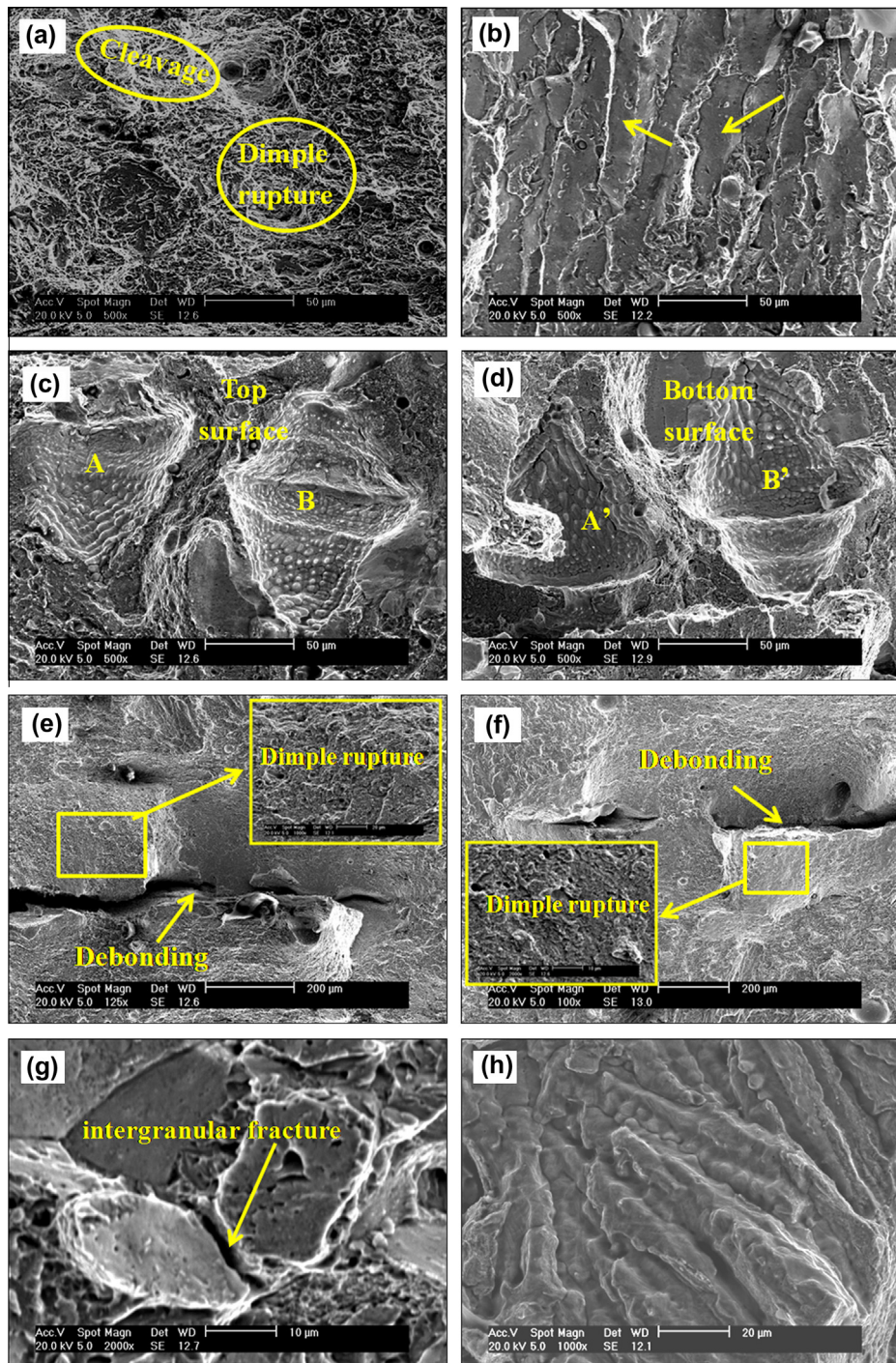


Fig. 16. Fracture morphology of the stress-relieved DMD AISI 4340 steel after lap shear testing.

corresponding spots of the top and bottom of the fracture surface. In shear, elongated microstructure points in opposite directions on matching fracture surfaces. Fig. 16(e) and (f) shows the corresponding spots of the interface between adjacent layers of the top and bottom of the fracture surface. Large discontinuities (de-bonding) may reduce the strength of a part to such an extent that it will fracture under a single application of load. They increase both local stresses and reactions to detrimental environments. However, the fracture close to the de-bonding shows dimple

rupture. This further indicates the bad effect of bonding defects in accelerating fracture. Fig. 16(g) shows the intergranular fracture. The dendrite nodules in the void (Fig. 16(h)) indicate that the cavity was caused by unfavorable directional solidification during laser deposition. The fracture was caused by overload.

3.5.3. Three-point bend test

Pictures of the cross section and top view inset of stress-relieved DMD AISI 4340 steel after bend testing are given

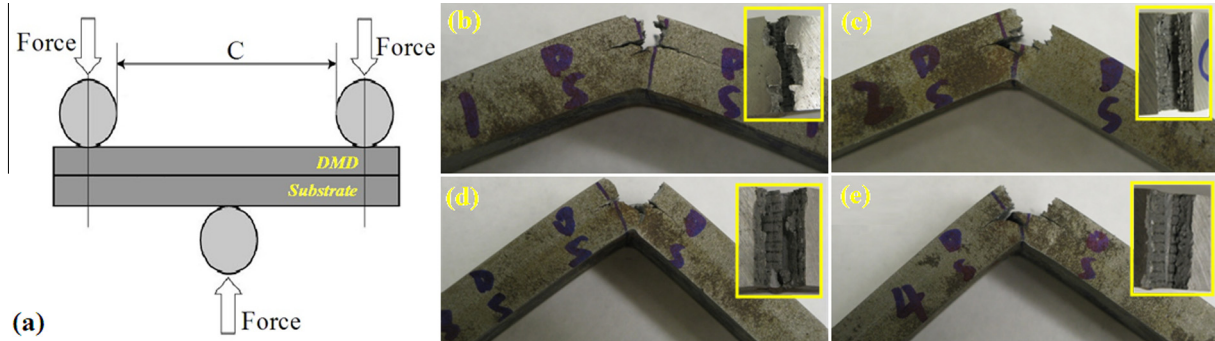


Fig. 17. (a) Schematic and (b) fracture morphology of the stress-relieved DMD AISI 4340 steel after three-point bend testing.

in Fig. 17. A schematic of the bend test is shown in Fig. 17(a). The bending angle varies for four samples (labeled B1–B4), indicating their varied bend strength. Adjacent track boundaries can clearly be differentiated in the insets in Fig. 17(c)–(e). Their load–displacement curves are shown in Fig. 18. The average value of four measurements of the bend strength is 225 MPa (Table 3).

The fracture morphology of the stress-relieved DMD AISI 4340 steel after bend testing is given in Fig. 19. Fig. 19(a) shows the top view of specimen B4. The magnified microstructures of the plan view and cross section are shown in Fig. 19(b) and (c), respectively. The elongated structure in the first layer close to the bending fracture plane is formed as a result of the stretching effect of the bending force, as shown in Fig. 19(b). The elongation direction is parallel to the displacement of the DMD sample. Layers can be differentiated by the layer interface in the cross section shown in Fig. 19(c). The cross section of the sample shown in Fig. 19(d) is etched, and the microstructure is given in Fig. 19(e) to identify where the fracture took place. It is obvious that the fracture occurs at the interface between the first and the second layers. The bonding strength between the first layer and the substrate is strong enough to resist the bending force. The bonding defects or de-bonding between deposited layers is the detrimental factor of fracture. It is especially important in determining the bending strength.

4. Discussion

A schematic illustration of the fracture morphology of the stress-relieved DMD AISI 4340 steel after strength testing is given in Fig. 20. The fracture surface exhibit a mixture of brittle and ductile fracture. Porosity, de-bonding, dimple, cleavage, tearing ridge and decohesion are observed. Elongated microstructure is also observed on the cross section of the fracture surface, parallel to the tensile force. However, it is more obvious on the bend test fracture surface, owing to the shear force subdivided from the loading force. Decohesion is present on the fracture surface as a result of the poor bonding strength at grain boundaries. The reasonable explanation for the presence of a tearing ridge rather than decohesive fracture at some local sites might be that the grain boundary strength is larger than the shear force, which causes tearing ridge fracture preferentially and avoids decohesive fracture. It is noteworthy to mention that the fracture starts at the interface between the substrate and the first deposited layer in the bend test (Fig. 19(e)), which indicates that the side effect of bonding defects is especially obvious in the bend test. Imperfections from the DMD process and their effects on the mechanical properties are discussed in the following.

4.1. Porosity influence on mechanical properties

Porosity is one of the drawbacks in the volume of parts processed by DMD or other additive manufacturing technologies. These pores stem from process-induced defects originating from initial powder contamination, evaporation or local voids after powder-layer deposition [61,62]. Eventually, these pores act as strong stress-raisers, and finally lead to failure. Voids can pre-exist as microporosity and can also nucleate from imperfections such as second-phase particles. After nucleation, voids grow with increasing hydrostatic stress and local plastic straining. As voids nucleate and grow, the void (or porosity) volume fraction increases. The voids begin to interact, and the porosity fraction at which interactions between voids begins is the critical porosity volume fraction. As plastic strain continues to increase, local necking and coalescence occur in the material between voids until a connected chain of voids forms and failure occurs [63]. Areas close to pores, inclusions of foreign materials or incompletely melted particles show cleavage, tear topography or surface (Figs. 14(b)–(d) and 16(a)), indicating very brittle failure or not perfectly bonded material. The effects of porosity on the structural

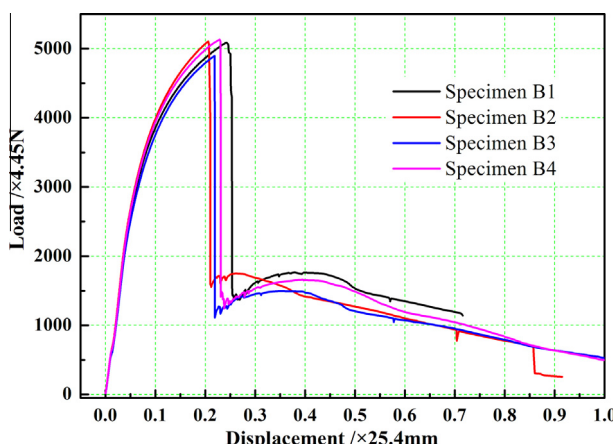


Fig. 18. Load–displacement curves of the stress-relieved DMD AISI 4340 steel during bend testing.

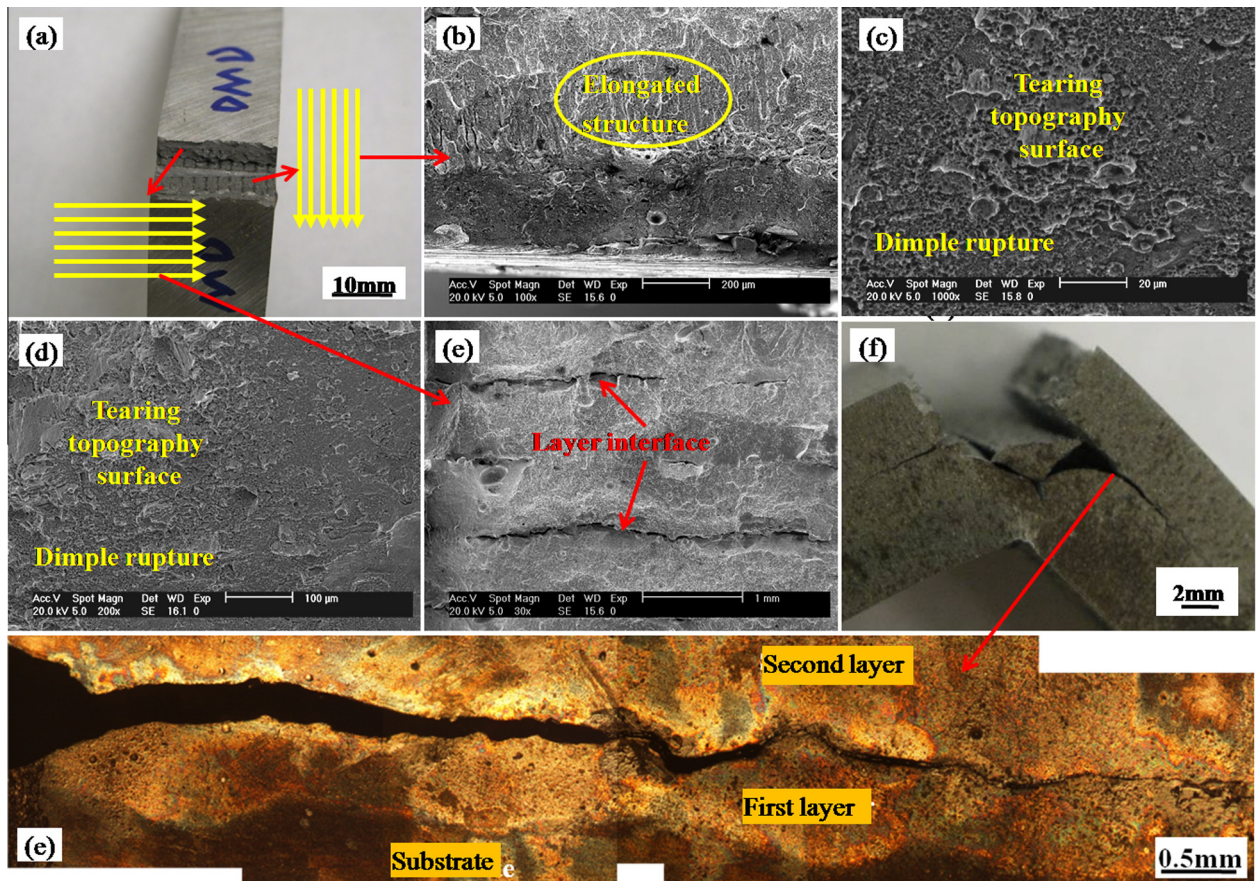


Fig. 19. Fracture morphology of the stress-relieved DMD AISI 4340 steel after bend testing.

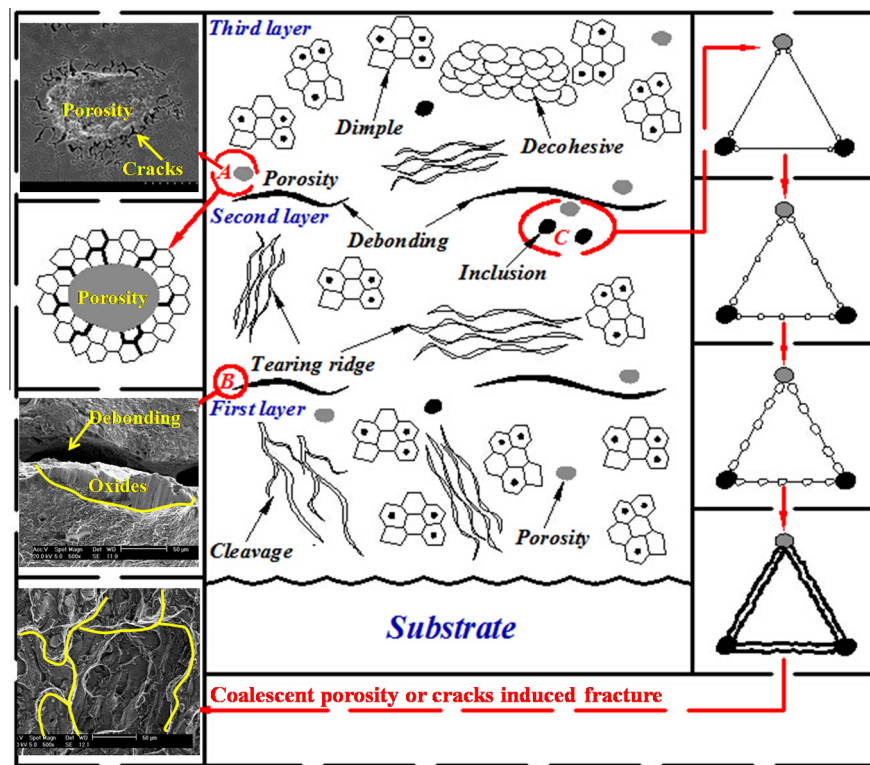


Fig. 20. Schematic illustration showing the fracture morphology of the stress-relieved DMD AISI 4340 steel.

performance of carbon and low-alloy steel castings are clearly defined on the microscopy scale [63]. Porosity lower than a few per cent does not result in a measurable loss of stiffness, or large stress concentrations, or stress distribution, but it greatly affects fatigue resistance [64,27]. Also, the presence of low-level porosity will reduce the ductility of metals, since microvoids pre-exist before any stress is applied and the nucleation stage is bypassed [65]. The behavior of materials with porosity <10% demonstrates a more linear dependence on the amount of porosity, assuming that voids do not interact [66], and considering isolated pores [67] or a uniform distribution of pores [68]. The amount of porosity in the DMD AISI 4340 steel is 3.3%, which is <10%. However, the de-bonding, which can be taken as coalescent porosity to some extent, is even detrimental to determining the material behavior. Compared with the annealed AISI 4340 alloy steel [33], the UTS of the DMD AISI 4340 steel is much higher (increases by 88%) than that of the annealed AISI 4340 alloy steel even with 3.3% porosity, owing to the strengthening effect of solid solution and grain refinement strengthening. However, the ductility decreases by 92.4%, which is more noticeable than the increase in strength. The most noticeable effect of porosity in cast steel is a reduction in ductility [63], which is in agreement with this investigation. Simulated development of average porosity in the gage section of the test plate in Ref. [63] shows that the average porosity in the plate gage section is ~0.75% and increases slowly until the ultimate tensile stress is reached, after which it increases rapidly because of the failure event. These results give additional insight into the complexity of the interaction between the porosity and the elastic–plastic model, and the resulting non-uniform stress and strain fields. The simulated maximum stress increases from ~280 to ~520 MPa. The original average residual stress before tensile testing in the as-deposited and stress-relieved DMD coating is 720 and 376 MPa, respectively. One can conclude that the residual stress in the DMD coating will also increase after tensile testing. Stress-relieving treatment actually improves the ductility of the as-deposited DMD coating. It is difficult to make general statements about the effect of porosity on fracture behavior, since it has been demonstrated here that its effects are dependent on the porosity distribution relative to the load [63].

4.2. Influence of residual stress on microstructure and mechanical properties

Another important aspect strongly affecting the mechanical properties of the components is internal stress resulting from steep temperature gradients and high cooling rates during processing [69]. It needs to be taken into account when evaluating the performance of parts manufactured from any metallic powder using DMD. Stresses in the DMD parts include thermal stress, bending stress and transformation stress. Transformation stress is caused mainly by martensite transformation. Martensite is formed in carbon steels by the rapid cooling (quenching) of austenite at such a high rate that carbon atoms do not have time to diffuse out of the crystal structure in large enough quantities to form cementite (Fe_3C). As a result, the face-centered cubic austenite transforms to a highly strained body-centered cubic form of ferrite that is supersaturated with carbon. It is commonly believed that martensite

transformation includes martensite nucleation and growth. The minimum free energy barrier to nucleation of martensite in a matrix of austenite surrounded by a strong stress field can be expressed as [70]

$$\Delta G^* = \frac{32\pi A^2 \gamma^3}{3(\Delta G_V + \Delta p)^4} \quad (1)$$

where ΔG^* is the minimum free energy, A is the elastic constant, γ is the interfacial free energy, ΔG_V is the volume free energy relieving, and Δp is stress. Generally, for coarse-grained material, the effect of Δp can be ignored in some circumstances, because it is very small; however, the influence is not negligible for the small grain size. Δp increases with decreasing grain size, and in the submicrocrystalline regime, it will significantly affect martensite nucleation and growth. This is because the martensite transformation is a shear-like process in which only if the shear stress is larger than the yield strength of the parent phase could martensite be formed in austenite. As for DMD coatings, grain sizes are small, and the effect of Δp could be taken into consideration. Because the value of ΔG_V is negative, it can be concluded that ΔG^* will increase with increasing Δp . As stress increases, the slip or shear resistance of the parent phase will increase, which is necessary to be mounted in martensitic transformation. Therefore, it becomes more difficult for the martensitic transformation to take place, and the martensite growth is inevitably impeded. A CCT experiment was done to determine the martensite transformation starting temperatures of the as-deposited and stress-relieved DMD AISI 4340 steel. To the best of the present authors' knowledge, this has never been done on laser-treated or fabricated coatings. The detected temperatures of the as-deposited and stress-relieved DMD AISI 4340 steel are 308 and 317 °C, respectively. The higher residual stress in the as-deposited DMD AISI 4340 steel compared with that in the stress-relieved DMD AISI 4340 steel explains well the lower martensite transformation starting temperature of 308 °C in the former compared with 317 °C in the latter. The difference worth noting is that the large stress and strain in the Fe-32%Ni alloy in the literature [70] is caused by severe deformation by multi-axial forging, while that in this investigation is caused by thermal stress and microstructural stress during the laser rapid heating and cooling process. In addition, induced residual stress of the laser-treated coating is dependent on the elastic modulus. The reduced elastic modulus of the stress-relieved DMD coating (Table 2) testifies to the stress relief in the as-deposited DMD coating.

4.3. Interaction between porosity and residual stresses

Pores and bonding defects in the DMD coating can also raise internal stresses and change their distribution. Applied stress was found to magnify the effects of cold work and accelerate oxidation rates [38]. Oxidation cracks propagate mainly in the intergranular boundaries (SEM image and the schematic of area A in Fig. 20). Bonding defects that exposed the adjacent DMD materials to air facilitate oxidation by serving as even faster diffusion paths for oxygen and iron than grain boundaries do. This is confirmed by the thick oxides on the surface of the DMD coating adjacent to the bonding defects, as indicated by the corresponding SEM image of area B in Fig. 20. The bonding defect itself is a synergistic oxidation effect

brought about by the high temperature, and the oxidizing environment can significantly degrade fatigue performance, associated with increasingly intergranular fracture features and secondary grain boundary cracking [39]. Stress concentrations will be introduced at the interface of the matrix and the secondary phases or inclusions. If the second phases cannot harmonize with the plastic deformation, voids will nucleate at the stress concentrated sites. The pre-existing and newly generated micro-pores will grow and interact until coalescence occurs, forming a micro-crack. The main cracks are generated through the propagation and coalescence of micro-cracks. The evolution of this process is shown in the schematic of area C in Fig. 20. The corresponding SEM showing the coalescent porosity or cracks induced fracture is also inserted in Fig. 20. Bonding defects, which can be taken as coalescent porosity and cracks to some extent, are even detrimental in determining the material behavior.

Investigation of fatigue resistance and crack growth performance of TiAl6V4 manufactured by selective laser melting indicates that residual stresses and porosity do not have a strong impact on the monotonic tensile properties, which are dominated by the microstructure. Micron-sized pores mainly affect fatigue strength, while residual stresses have a strong impact on fatigue crack growth. In addition, crack initiation is influenced primarily by the pores, while the main influencing factor on crack growth behavior is residual stress [69]. To what extent these two factors (porosity and residual stress) influence each mechanical property (such as elastic modulus, tensile strength, lap shear strength, bend strength or fatigue strength) or which one is the dominant influencing factor in this investigation remains unclear. Additional unpublished studies by the authors on other alloys showed that the porosity ratio can be decreased or even eliminated if the deposition strategy is successive layer scanned normal to each other. Accordingly, microstructure and mechanical properties can be improved.

5. Conclusions

AISI 4340 steel coating was formed by DMD. The thermal effect of stress-relieving treatment was characterized using DSC, CCT, FWHM, residual stress, micro-hardness, nano-hardness and elastic modulus of the DMD coating before and after stress relief. Defect density, residual stress and their effects on mechanical properties were investigated, and fracture mechanism was proposed. The following conclusions are drawn.

- (1) The porosity ratio in the DMD coating is ~3.3%, including voids and bonding defects, which are the sites for nucleation and propagation of high-temperature oxidation cracks.
- (2) DSC curves show the dissolution of ϵ -carbide and recrystallization of ferrite. Stress relief increases the ferrite recrystallization temperature in the stress-relieved DMD coating to ~25 °C higher than that in the as-deposited DMD coating (564 °C). The higher martensite transformation starting temperature (317 °C) in the stress-relieved DMD coating compared with that (308 °C) in the as-deposited DMD coating is attributed to the relieved residual stress.

- (3) FWHM values in the stress-relieved DMD coating are smaller compared with those in the as-deposited DMD coating. Residual stress and nano-hardness in all three stress-relieved layers are lower than those in the as-deposited counterparts. In addition, their values in the previous layer are smaller than in the subsequent layer in both DMD coatings, as a result of the heat effect of the subsequent deposition on the previous layer.
- (4) Stress relief reduces the elastic modulus of the as-deposited DMD coating from 237.5923 GPa to 206.296 GPa. Compared with annealed AISI 4340 alloy steel (annealed at 844 °C, furnace cooled, 228 HV and 190–210 GPa) [33], the micro-hardness and elasticity modulus of both DMD coatings are higher.
- (5) Compared with the annealed 4340 alloy steel [33], UTS (1399 MPa) of the stress-relieved DMD AISI 4340 steel increases by 88% and the engineering strain (1.665%) decreases by 92.4%. The shear strength, shear strain and bend strength of the stress-relieved DMD coating are 512 MPa, 0.537% and 225 MPa, respectively. Bend fracture occurs at the interface between the first and the second layer. The most noticeable effect of porosity is a reduction in ductility. De-bonding is even detrimental to determining the material behavior.
- (6) The deposition strategy needs to be improved to improve the microstructure (decrease porosity), and mechanical properties of DMD coating can be tailored through appropriate heat treatments.

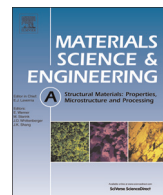
Acknowledgements

Financial support from the National Science Foundation of China (Nos. 51201070 and 51275220), Doctoral Fund of Ministry of Education of China (No. 20113227120006) and the Natural Science Foundation of Jiangsu Province of China (No. BK2012713) is acknowledged by Guifang Sun. The authors would also like to thank their colleagues from the Engineering Department of Focus, HOPE, for the DMD deposition and financial support from Office of NAVAL Research for experimental work on DMD.

References

- [1] R.L. McDaniels, S.A. White, K. Liaw, L. Chen, M.H. McCay, P.K. Liaw, Mater. Sci. Eng. A 485 (2008) 500.
- [2] J.A. Pape, R.W. Neu, Int. J. Fatigue 29 (2007) 2219.
- [3] M.P. Nascimento, R.C. Souza, W.L. Pigatin, H.J.C. Voorwald, Int. J. Fatigue 23 (2001) 607.
- [4] S.K. Maiti, G.K. Kishore, A.H.I. Mourad, Nucl. Eng. Des. 238 (2008) 3175.
- [5] S. Fank, M. Demirkol, Sens. Actuators A 126 (2006) 25–32.
- [6] L. Costa, R. Vilar, T. Reti, A.M. Deus, Acta Mater. 53 (2005) 3987.
- [7] J. Mazumder, A. Schifferer, J. Choi, Mater. Res. Innovations 3 (1999) 118.
- [8] J. Mazumder, J. Choi, K. Nagarathnam, J. Koch, D. Hetzner, JOM 49 (1997) 55.
- [9] W.R. Morrow, H. Qi, I. Kim, J. Mazumder, S.J. Skerlos, J. Clean. Prod. 15 (2007) 932.
- [10] J. Choi, Y. Chang, Int. J. Mach. Tools Manuf. 45 (2005) 597.
- [11] O.J. Milewski, G.K. Lewis, D.J. Thoma, G.L. Keel, R.B. Nemec, R.A. Reiner, J. Mater. Process. Technol. 75 (1998) 165.
- [12] G.K. Lewis, E. Schlienger, Mater. Design 21 (2007) 417.

- [13] D.M. Keicher, W.D. Miller, *Met. Powder Rep.* 53 (1998) 26.
- [14] <<http://www.sandia.gov/mst/pdf/LENS.pdf>>.
- [15] W. Meiners, K. Wissenbach, R. Propawé, in: Proc ICALEO, vol. 31, 1998.
- [16] D.E. Bunnell, D.L. Bourell, H.L. Marcus, Advances in Powder Metallurgy and Particulate Materials, Part 15, Metal Powers Industries Federation (MPIF), vol. 93, Princeton, NJ, 1996 (Section 15).
- [17] G.P. Dinda, A.K. Dasgupta, J. Mazumder, *Scripta Mater.* 67 (2012) 503.
- [18] Y.S. Tian, C.Z. Chen, L.B. Chen, J.H. Liu, T.Q. Lei, *J. Mater. Sci.* 40 (2005) 4387.
- [19] H.C. Man, S. Zhang, F.T. Cheng, X. Guo, *Surf. Coat. Technol.* 200 (2006) 4961.
- [20] S. Liu, W. Zhang, *J. Alloys Compd.* 391 (2005) 146.
- [21] G.F. Sun, C.S. Liu, L.J. Song, J. Mazumder, *Metall. Mater. Trans. A* 41 (2010) 1592.
- [22] L. Thijs, K. Kempen, J.-P. Kruth, J. Van Humbeeck, *Acta Mater.* 61 (2013) 1809.
- [23] V. Ocelík, I. Furar, J. De Hosson, M. Th, *Acta Mater.* 58 (2010) 6763.
- [24] S. Bhattacharya, G.P. Dinda, A.K. Dasgupta, H. Natu, B. Dutta, J. Mazumder, *J. Alloys Compd.* 509 (2011) 6364–6373.
- [25] R.A. Hardin, C. Beckermann, *Metall. Mater. Trans. A* 38 (2007) 2992.
- [26] R.A. Hardin, C. Beckermann, *Metall. Mater. Trans. A* 40 (2009) 581.
- [27] K.M. Sigl, R. Hardin, R.I. Stephens, C. Beckermann, *Int. J. Cast Met. Res.* 17 (2004) 130.
- [28] E. Zhang, B. Wang, *Int. J. Mech. Sci.* 47 (2005) 744.
- [29] M. Masanta, S.M. Shariff, A. Roy Choudhury, *Mater. Sci. Eng. A* 528 (2011) 5327.
- [30] J.L. Koch, J.U.S. Mazumder, Patent Number 6, 122, 564, September 19, 2000.
- [31] G.F. Sun, S. Bhattacharya, G.P. Dinda, A. Dasgupta, J. Mazumder, *Scripta Mater.* 64 (2011) 454.
- [32] G.F. Sun, S. Bhattacharya, G.P. Dinda, A. Dasgupta, J. Mazumder, *Mater. Sci. Eng. A* 528 (2011) 5141.
- [33] <<http://www.azom.com/article.aspx?ArticleID=6772>>.
- [34] H.J. Niu, I.T.H. Chang, *Scripta Mater.* 41 (1999) 25.
- [35] W. Meiners, K. Wissenbach, R. Propawé, *Proc. LANE 2* (1997) 615.
- [36] R.H. Morgan, A.J. Papworth, C. Sutcliffe, P. Fox, W. O'Neill, *J. Mater. Sci.* 37 (2002) 3093.
- [37] J.W. Xie, P. Fox, W. O'Neill, C.J. Sutcliffe, *J. Mater. Process. Technol.* 170 (2005) 516.
- [38] S. Lozano-Perez, K. Kruska, I. Iyengar, T. Terachi, T. Yamada, *Corros. Sci.* 56 (2012) 78.
- [39] R. Jiang, S. Everitt, M. Lewandowski, N. Gao, P.A.S. Reed, *Int. J. Fatigue* 62 (2014) 217–227.
- [40] T. Maki, in: T. Furuhara, K. Tsuzaki, (Eds.), Proceedings of the 1st International Symposium on Steel Science, ISIJ, Tokyo, 2007, p. 1.
- [41] J.R.C. Guimaraes, P.R. Rios, *Metall. Mater. Trans. A* 44 (2013) 2.
- [42] S. Zhang, S. Morito, Y. Komizo, *ISIJ Int.* 52 (2012) 510.
- [43] <<http://en.wikipedia.org/wiki/Cementite>>.
- [44] M.T. Jahn, C.M. Fan, C.M. Wan, *J. Mater. Sci.* 20 (1985) 2757.
- [45] H. Azizi-Alizamini, M. Militzer, W.J. Poole, *Metall. Mater. Trans. A* 42 (2011) 1544.
- [46] Y.Y. Song, X.Y. Li, L.J. Rong, Y.Y. Li, *Mater. Sci. Eng. A* 528 (2011) 4075.
- [47] D. Phelan, M. Reid, N. Stanford, R. Dippenaar, *JOM* 58 (2006) 67.
- [48] D. Zhang, H. Terasaki, Y. Komizo, *Acta Mater.* 58 (2010) 1369.
- [49] J.H. Kim, S.G. Kim, A. Inoue, *Acta Mater.* 49 (2001) 615.
- [50] H. Terasaki, Y. Komizo, M. Yonemura, T. Osuki, *Metall. Mater. Trans. A* 37A (2006) 1261.
- [51] M.M. Attallah, H. Terasaki, R.J. Moat, S.E. Bray, Y. Komizo, M. Preuss, *Mater. Charact.* 62 (2011) 760.
- [52] I.C. Noyan, J.B. Cohen, Residual Stress Measurement by Diffraction and Interpretation, Springer-Verlag, New York, 1987.
- [53] P. Juijerm, I. Altenberger, *Mater. Sci. Eng. A* 452–453 (2007) 475.
- [54] J.C. Kim, S.K. Chenon, H. Noguchi, *Int. J. Fatigue* 55 (2013) 147.
- [55] V.E. Danilchenko, Y.M. Sidorin, *Mater. Sci. Forum* 228–231 (1996) 563.
- [56] M. van den Burg, J.Th.M. De Hosson, *Acta Metall. Mater.* 41 (1993) 2557.
- [57] R. Colaco, E. Gordo, E.M. Ruiz-Navas, M. Otasevic, R. Vilar, *Wear* 260 (2006) 949.
- [58] L. Wagner, *Mater. Sci. Eng. A* 263 (1999) 210.
- [59] M. Pilloc, J.M. Pelletier, *J. Mater. Sci.* 27 (1992) 1240.
- [60] G.F. Sun, R. Zhou, Y.K. Zhang, G.D. Yuan, K. Wang, Ren Xudong, D.P. Wen, *Opt. Laser Technol.* 62 (2014) 20.
- [61] L.E. Murr, S.M. Gaytan, A. Ceylan, E. Martinez, J.L. Martinez, D.H. Hernandez, B.I. Machado, D.A. Ramirez, F. Medina, S. Collins, R.B. Wicker, *Acta Mater.* 58 (2010) 1887.
- [62] B. Gorny, T. Niendorf, J. Lackmann, M. Thone, T. Troster, H.J. Maier, *Mater. Sci. Eng. A* 528 (2011) 7962.
- [63] R.A. Hardin, C. Beckermann, *Metall. Mater. Trans. A* 44 (2013) 5316.
- [64] P. Heuler, C. Berger, J. Motz, *Fatigue Fract. Eng. Mater. Struct.* 16 (1992) 115.
- [65] C.T. Herakovich, S.C. Baxter, *J. Mater. Sci.* 34 (1999) 1595.
- [66] J.M. Dewey, *J. Appl. Phys.* 18 (1947) 578.
- [67] A.L. Gurson, *J. Eng. Mater. Tech.* 99 (1977) 2.
- [68] V. Tvergaard, *J. Int. Fract. Mech.* 17 (1981) 389.
- [69] S. Leuders, M. Thone, A. Riemer, T. Niendorf, T. Troster, H.A. Richard, H.J. Maier, *Int. J. Fatigue* 48 (2013) 300.
- [70] B.J. Han, Z. Xu, *Mater. Sci. Eng. A* 31 (2006) 109.



Effects of process time interval and heat treatment on the mechanical and microstructural properties of direct laser deposited 316L stainless steel

Aref Yadollahi ^{a,b}, Nima Shamsaei ^{a,b,*}, Scott M. Thompson ^{a,b}, Denver W. Seely ^b

^a Department of Mechanical Engineering, Box 9552, Mississippi State University, Mississippi State, MS 39762, USA

^b Center for Advanced Vehicular Systems (CAVS), Box 5405, Mississippi State University, Mississippi State, MS 39762, USA

ARTICLE INFO

Article history:

Received 30 April 2015

Received in revised form

27 June 2015

Accepted 18 July 2015

Available online 21 July 2015

Keywords:

Additive Manufacturing (AM)

Laser Engineered Net Shaping (LENS)

Direct Laser Deposition (DLD)

Mechanical Properties

Microstructure

Stainless Steel

ABSTRACT

The mechanical and microstructural properties of 316L stainless steel (SS) fabricated via Direct Laser Deposition (DLD), a laser-based additive manufacturing method, are presented and compared with those of conventionally-built counterparts. Using a Laser Engineered Net Shaping (LENS[®]) DLD system, the time interval between successive layer deposits, or inter-layer/idle time, for fabricating cylindrical specimens vertically-upward was varied by building either one or nine samples per build plate – thus increasing total assembly volume per build. Subsequently, the effect of thermal history, as well as heat treatment, on microstructural (i.e. grain size and morphology) and mechanical (i.e. tensile, compression, and microhardness) properties of DLD parts were investigated. Results indicate that the DLD 316L SS samples produced herein have a higher yield and ultimate tensile strength relative to their cast and wrought forms. Furthermore, the thermal history, microstructural evolution, and mechanical properties of DLD 316L SS are shown to be dependent on the time interval between deposits. Longer local time intervals result in higher cooling rates, leading to finer microstructures, higher/uniform strength and lower elongation to failure. In addition, porosity and less integral metallurgical bonds are found to be more prevalent in locations further upward from the build plate due to reduced laser penetration depths (e.g. previous-layer remelting decreases). Conversely, parts manufactured with shorter time intervals were found to possess a coarser microstructure, lower strength and higher elongation to failure – attributable to lower cooling rates caused by an increased bulk temperature in the part. These results may aid in future design and control of more efficient, constant-power DLD processes – especially with regard to building multiple and/or larger parts; an approach desirable for minimizing small-to-medium lot production times.

© 2015 Elsevier B.V. All rights reserved.

1. Introduction

During the past few decades, additive manufacturing (AM) has evolved significantly; from prototype-scale production to fabrication of functional parts for service [1–3]. In contrast to traditional, ‘subtractive’ fabrication methods, AM techniques allow parts to be built vertically-upward, layer-by-layer, with combined material deposition and energy delivery. For metals, there are two common laser-based additive manufacturing (LBAM) techniques employed, including: Powder-Bed Fusion-Laser (PBF-L), such as Selective Laser Melting (SLM) [4], and Direct Laser Deposition (DLD) [5], a Directed Energy Deposition method that employs blown powder and in-situ laser heating; such as Laser Engineered Net Shaping

(LENS). In a typical DLD process, a high power laser and blown powders are used to create a melt pool that subsequently solidifies for generating tracks/layers. Using this method, parts are consequently built track-by-track and layer-by-layer within an inert atmosphere upon a build plate (or substrate) that moves relative to the laser source via a predefined tool path, or scanning pattern, realized via Computer Numerical Control (CNC). Direct Laser Deposition has demonstrated to effectively fabricate a wide range of materials such as: titanium alloys, tool steels, austenitic steels, martensitic steels, nickel-base superalloys and cobalt-base alloys [6–15].

There are many process parameters that can be assigned to, or controlled during, DLD such as: laser power, laser-to-substrate relative speed (i.e. traverse speed), powder feed rate, layer thickness and hatching space (track-to-track distance). These parameters influence the laser-induced melt pool shape/dynamics and degree of localized heating (and cooling) during DLD – thus

* Corresponding author. Tel.: +1 662 325 2364.

E-mail address: shamsaei@me.msstate.edu (N. Shamsaei).



impacting the thermal history experienced by parts during fabrication. This thermal history will then directly impact the formation of pores/voids and the encumbered microstructural features (e.g. grain size, morphology), and thus mechanical properties, of the as-built part [3,5].

Success of DLD, and inevitably the thermal history of parts, also depends on 'design' parameters, such as: part orientation during the build, number/size of parts (or total part volume), complexity of parts (e.g. constant vs. non-constant cross-section) and scanning strategy/pattern. Some design parameters, such as part complexity/size, are limited by the DLD machine and build envelope, while others can be set before, or controlled during, DLD – such as the part orientation and scanning strategy/pattern.

Various combinations of process and design parameters will impact the time elapsed between successive deposits and/or layers, i.e. DLD 'time intervals'. Two time intervals can be readily defined, including: (1) time elapsed between successive layer completions, or the inter-layer time interval, and (2) time elapsed between successive deposits over (or adjacent to) a common coordinate/point in space – the intra-layer time interval. Based on these time intervals, a build schedule (a vector or matrix corresponding to layer number or coordinate space) can be defined so that each layer completion and/or deposit occurs at specified times. The total time for any build schedule to be completed is then the manufacturing time.

The inter-layer time will generally change with part orientation and assembly size/complexity, while the intra-layer time will generally depend more on the laser/track patterns employed. A part with constant cross-sectional area (with respect to build height) can consist of a uniform inter-layer build schedule, while the intra-layer build schedule can vary for a specific point along the cross-section for successive layers. Although manufacturing time is limited by traverse speed and assembly size/complexity, the DLD user can control intra- and inter-layer schedules. For instance, the intra-layer time interval can be controlled by employing various scan patterns, which can remain consistent or alternate during the build, while the inter-layer time interval can be altered by intentionally stopping, or 'idling', the DLD process after completion of a layer. Inter-layer idling can be accomplished by turning off the DLD laser or holding the deposition head still, with no deposition/heating occurring on the part. As a result, the inter-layer time is a function of traverse speed and idle time. Note that the entire build schedule can be controlled by changing traverse speed with layer number; however, other process parameters may also have to be changed in order to ensure successful deposition (i.e. powder feed rate, laser power). The optimal combination of scan patterns, or intra-layer build schedule, will depend on the complexity/geometry of the part.

The build schedule will also change with respect to part orientation. For example, a simple rectangular bar will undergo a different thermal history when built with its length parallel (horizontally-built) or perpendicular (vertically-built) to the substrate (with all process parameters held constant) [7,16]. Yadollahi et al. [17] recently demonstrated the effect of orientation of stainless steel 17-4 PH rods during SLM and demonstrated that the additively-manufactured specimens will have orientation-dependent microstructures and mechanical properties for a given set of process parameters. Horizontally-built AM parts, for use in uniaxial loading applications, were shown to have different tensile properties than vertically-built parts as the inter-layer porosity distribution will greatly affect the end-service performance of manufactured specimens [7,17].

For time-invariant DLD process parameters, it has been demonstrated that bulk heating can occur in smaller-sized specimens – causing layer-dependent cooling rates [18]. This bulk heating can be combated with increased idle times. Zheng et al.

numerically demonstrated that as the inter-layer time interval decreases, by decreasing idle time, the severity of bulk heating effects will increase significantly and that the initial temperature of the previously-deposited layer will have a strong influence on the cooling/solidification rates of the subsequent layer [15,19].

Costa et al. numerically investigated the effect of inter-layer idle time on the microstructure and hardness of a DLD AISI 420 steel, thin-walled part [20]. It was found that hardness decreases along the part as inter-layer idle time increases. Further, the inter-layer idle time was shown to directly affect the melt pool size, and consequently, the transient temperature distribution of the part during the DLD process [18,20–22]. These findings suggest that the microstructural evolution of a part during DLD can be altered significantly by varying idle times, i.e. inter-layer time intervals [8,20]. However, due to relatively high cooling rates of a single layer/track, long idle times can adversely affect layer-to-layer adhesion and thus lead to lack of fusion [23,24].

For uncontrolled DLD (i.e. time invariant process parameters), the variation of thermal history along a part leads to anisotropic features that impact mechanical properties – in particular tensile and fatigue behavior [5,7,25]. Fine microstructures can evolve in size due to successive layer passes (i.e. thermal cycles) and bulk temperature rise in the part [26]. For these uncontrolled/performance-limited DLD processes, one can strategically employ, or deal with, design parameters (i.e. scanning strategy and building orientation) to combat anisotropy and to gain more control on thermal history. Although process/design parameters can be altered to make the thermal history more uniform, post-DLD heat treatments may also be utilized to fully or partially rectify inhomogeneity in microstructure due to non-uniform thermal history [27].

The current study focuses on the microstructural features and mechanical properties (i.e. tensile, compression, and microhardness) of DLD 316L stainless steel (SS) and their dependence on thermal history, as controlled via two different inter-layer time intervals, and post-DLD heat treatment. These effects are investigated by fabricating one-specimen/build plate or nine-specimens/build plate while holding other DLD process parameters constant. This scenario is of relevance for using DLD in small-lot production operations, as it demonstrates how maximizing the number of parts-per-build plate, as well as part size in the build envelope, affects part quality.

2. Experimental procedure

Gas-atomized 316L SS powder was used for DLD of cylindrical specimens accomplished via an OPTOMECH LENS 750 with 1 kW Nd:YAG laser. The alloys nominal chemical composition (in weight %), as determined via a SPECTROMAXx stationary metal analyzer (Spectro Analytical Instruments GmbH), is shown in Table 1. The cylindrical specimens were 8 mm in diameter and 75 mm in height, and were fabricated vertically-upward atop 316L SS build plates using build patterns depicted in Fig. 1. Process parameters were selected via a trial-and-error/"build-and-inspect" method to ensure a low level of porosity in the LENS parts. In this method, several cylindrical rods were printed using various process parameters and their density was measured using Archimedes' principle. Final process parameters utilized in this study are provided

Table 1

Chemical composition (weight %) of the DLD 316L SS.

Elements (wt.%)	C	Cr	Ni	Mn	Si	Mo	S	P	Fe
316L SS	0.042	19.95	10.87	1.41	0.61	2.45	0.011	0.025	63.7

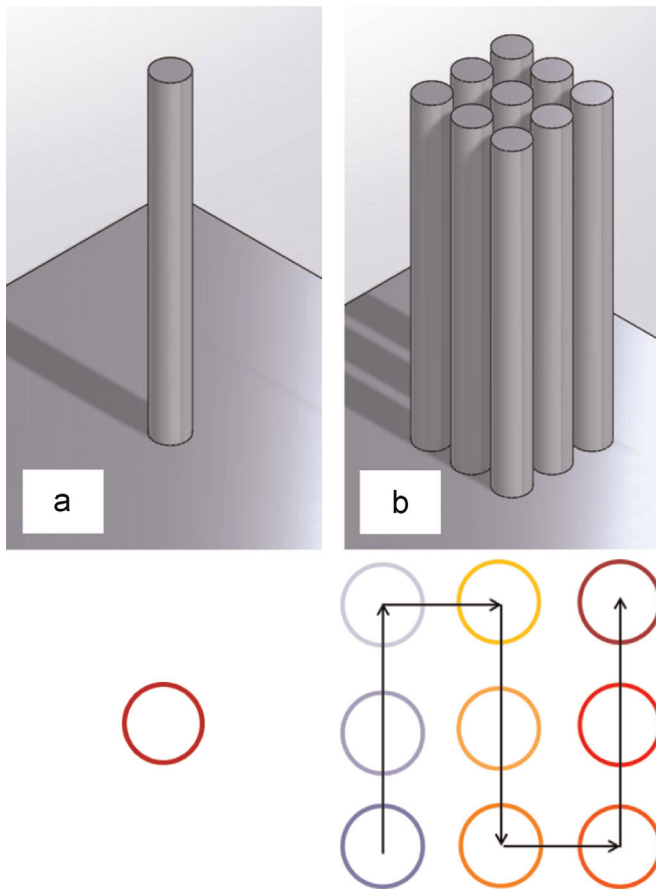


Fig. 1. Schematic of fabricated cylindrical rods (a) first group: one cylindrical rod built at a time, i.e. single-built, and (b) second group: nine samples built at a time, i.e. nine-built (arrows in this figure describe the build schedule for each layer).

Table 2
Utilized LENS process parameters for fabricating 316L SS.

Laser Power (W)	Beam Transverse Speed (mm/sec)	Powder Feed Rate (g/sec)	Hatching Pitch (mm)	Layer Thickness (mm)	Oxygen content (ppm)
360	8.5	0.09	0.5	0.5	0-17

in Table 2.

Using the identified process parameters, vertically-built, cylindrical rods were either: (1) fabricated one-per-plate ('single-built') or (2) fabricated nine-per-plate all together ('nine-built'), as shown in Fig. 1 – to expose effects of inter-layer build schedule which can exist due to multiple part or large part fabrication. For the 'single-builds', each sample was fabricated continuously layer-by-layer with minimal time between layers, which due to specimen size and utilized machine, was approximately 10 s. For the nine-built rods, one layer of all nine samples was deposited before moving to the next layer; therefore, the inter-layer idle time for each sample was approximately ten times longer (i.e. about 100 s) than the single-built samples. This allowed each cylindrical specimen to experience different build schedules and heating/cooling rates during fabrication. Note that one can describe multi-part AM build schedules as being either 'in-series' or 'in-parallel'. For the investigated nine-per-plate experiment, the deposition process is 'in-parallel', with each part increasing in height at a similar rate. However, it is also possible for one specimen to be completely built before moving to the first layer of the next specimen – which

can be described as an 'in-series' deposition process, such as the single-built rods in this study. The thermal history experienced by a part undergoing in-series fabrication should have a similar thermal history as single-built parts made using the same process parameters. Any major differences in thermal history would primarily depend on the inter-part build schedule employed and material being fabricated (e.g. heat capacity, radiative surface properties).

For the current study, specimens were fabricated in close-proximity to each other, as presented in Fig. 1, to simulate a more efficient multi-part manufacturing process. Due to this chosen setup, rod-to-rod heat transfer, consisting of mixed convection and radiation, can cause asymmetric, location-dependent cooling rates. This can result in, for example, the centrally-located rod having a different thermal history than a corner-located rod. The severity of these boundary heat transfer effects will depend primarily on the number/size/type of parts and the inter-layer build schedule used.

For most in-parallel, multi-part AM procedures (i.e. 3-axis DLD), the net heat flux direction of the solidifying melt pool (i.e. solidification heat flux direction) is predominantly towards previously-deposited layers of the part it sits atop, since the radiative view factor between previous-layers from neighboring parts and the deposited part's melt pool is relatively low. For in-parallel DLD part fabrication, thermal interaction amongst parts should only influence microstructural evolution in their heat affected zones (HAZs). The HAZs can interact with neighboring media/environment of lower temperature via radiation and/or convection and the net heat transfer will primarily depend on material/surface properties and relative proximity (e.g. radiative view factor, merging of convective boundary layers between parts), as well as the DLD chamber conditions (e.g. inert gas flow rate) and employed build schedules. For the current study, the microstructures from various-located, nine-built rods were inspected and no significant location-dependent features (e.g. direction of grain growth, grain size) were observed. Based on this preliminary investigation, it was determined that any comparison between single-built and nine-built samples would not be substantially biased by nine-built specimen location.

After fabrication, the specimens were removed from the build plate and machined for monotonic tension and compression tests.

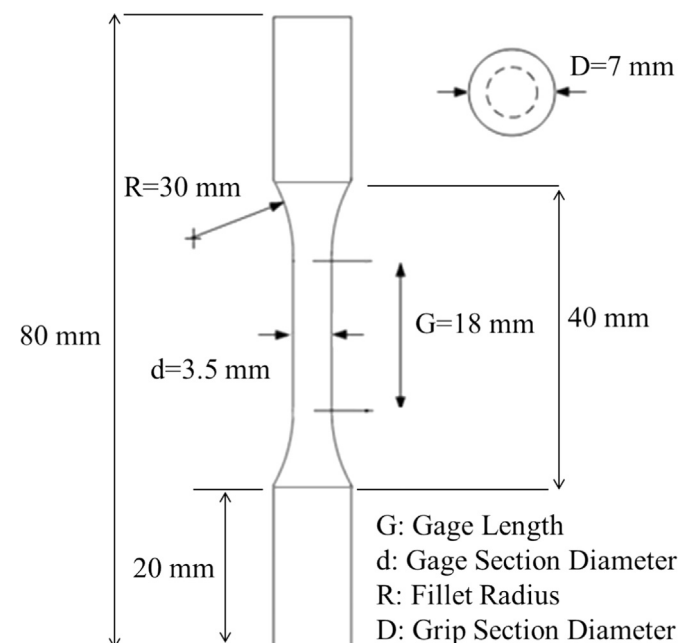


Fig. 2. Dimensions of investigated tensile specimens based on ASTM E8 [28].

Fig. 2 provides the final dimensions of LENS-produced tensile samples according to ASTM E8 [28]. Cylindrical compression specimens were sectioned off at five different regions along the longitudinal axis of each cylindrical rod according to the ASTM E9 [29]. Some specimens from the single-built group underwent a standard homogenizing heat treatment [30] for 2 hours at 1150 °C followed by air cooling, while the remaining specimens were left as-built. In summary, three sets of specimens were created for characterization, namely: single-built, single-built with post-DLD heat treatment and nine-built.

Tension and compression experiments were performed on an Instron 5882 servo-hydraulic testing machine with a ± 100 kN maximum loading capacity. Tensile tests were conducted using four specimens from each set (i.e. single-built, heat treated single-built, and nine-built) at room temperature at a 10^{-3} s⁻¹ nominal strain rate. One specimen from each set was mounted and polished for microstructural observation and microhardness testing. Samples were polished with colloidal silica in an alkaline (pH: 9.8) suspension for SEM/EBSD/EDS investigations. The microstructures, crystallographic texture and orientation and phase fraction of cylindrical sections from these three sets of samples were examined using optical microscopy (OM) (ZEISS Axiovert 200) and scanning electron microscopy (SEM) (FEG SEM Zeiss SUPRA™ 40) equipped with an electron backscatter diffraction (EBSD) detector. Chemical composition analysis of the DLD 316L SS was carried out by SEM-energy dispersive spectroscopy (EDS). Hardness measurements were conducted via a Vickers microhardness tester (Micro-indentation Hardness Testing System, LECO) on the polished surface of mounted samples under a 500-g load for a dwell time of 10 s using a diamond indenter.

3. Experimental results

3.1. Microstructural features

Optical micrographs of a single-built and nine-built sample, at three different regions (i.e. bottom, middle and top) are presented in **Fig. 3**. It may be seen that the porosity is higher near the build plate (bottom region) for both sample sets. As shown in **Fig. 3(b)**, there is significantly more porosity in all sections of the nine-built sample as compared to the single-built sample.

Electron backscatter diffraction (EBSD) was used to quantify the crystallographic texture, microstructure (e.g. grain size and orientation), and volume fraction of the austenite and ferrite phases of specimens from each group (i.e. single-built, heat treated single-built, and nine-built). The EBSD inverse pole map and misorientation angle distribution from the bottom region of each inspected specimen are shown in **Figs. 4–6**. The various colors correspond to orientation of grains with respect to crystal lattice, and each color corresponds to the unique combination of Euler angles. Therefore, grains with the same crystallographic orientation have similar colors.

The average grain size along the bottom region of a single-built sample (**Fig. 4(a)**) was found to be approximately 60 μ m, while the average grain size for the middle and top regions were approximately 140 μ m and 100 μ m, respectively. The majority of grain boundaries were found to exhibit very low misorientation angles (1°–4°) indicating a near-monocrystalline texture. Average misorientation angles were measured to be approximately 14°, 15° and 30° for the single-built specimen, nine-built specimen and heat treated single-built specimens, respectively. The as-built samples, single-built and nine-built, (see **Fig. 4(b)** and 6(b)) were found to possess less variation in the crystalline misorientation relative to the heat treated sample (see **Fig. 5(b)**). In addition, the

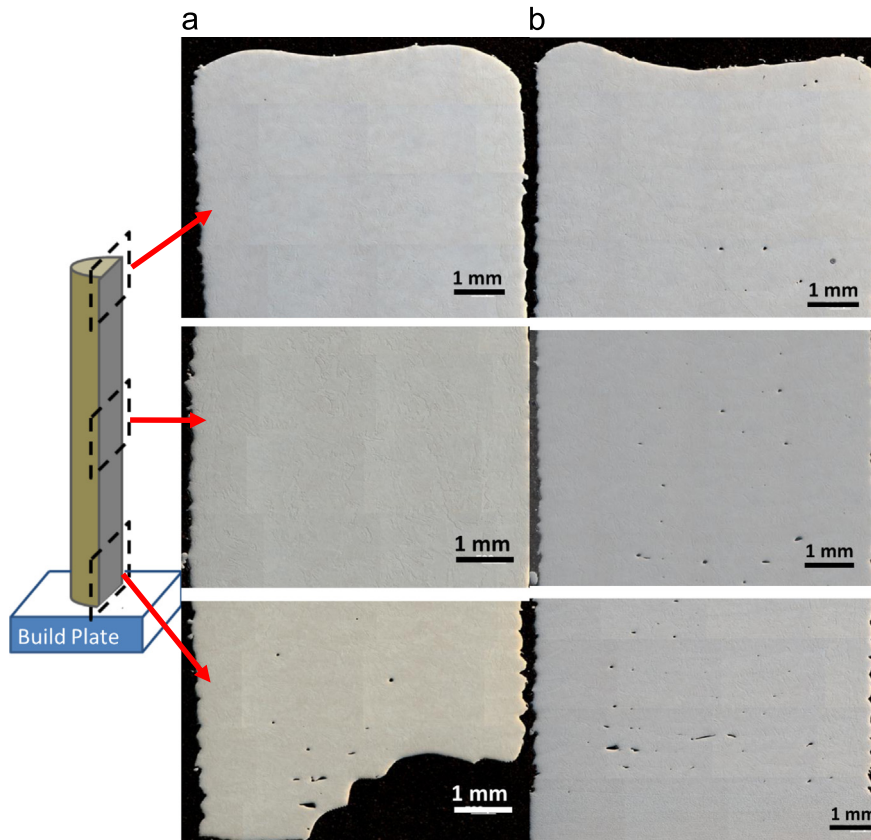


Fig. 3. Porosity observed for (a) single-built (not heat treated) and (b) nine-built samples at three different regions (bottom, middle, and top).

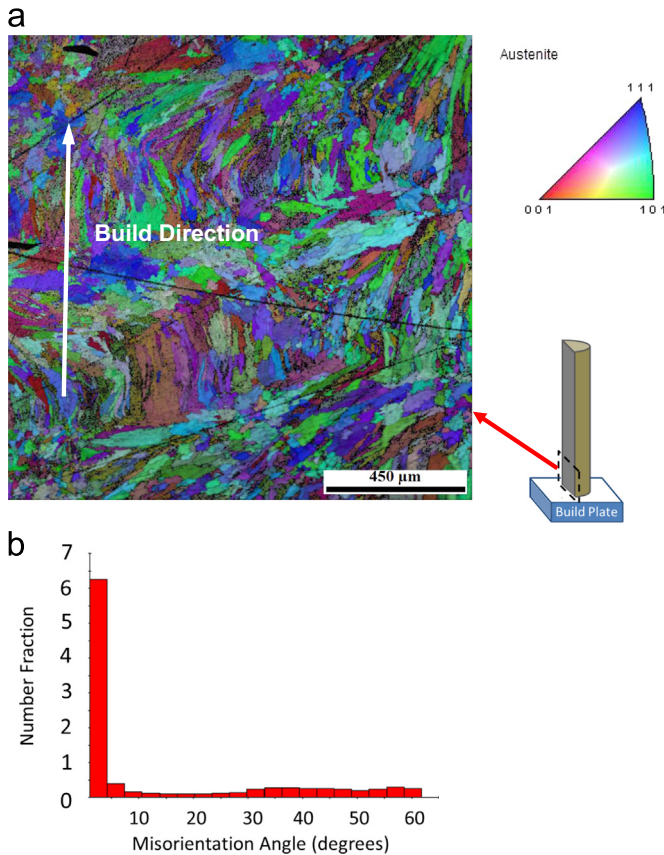


Fig. 4. (a) EBSD inverse pole map and (b) misorientation angle distribution of austenite phase in bottom region of a single-built sample (red: [001]; blue: [111]; green: [101]).

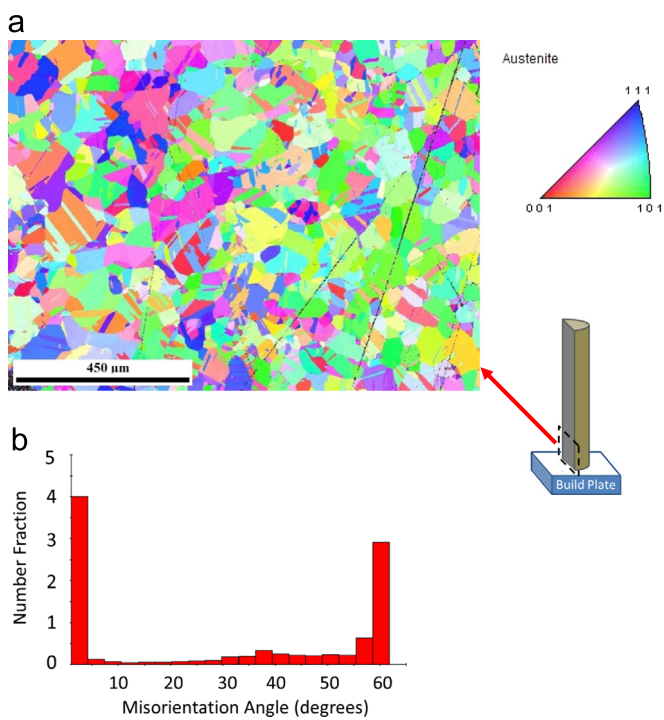


Fig. 5. (a) EBSD inverse pole map and (b) misorientation angle distribution of austenite phase in bottom region of a heat treated single-built sample (red: [001]; blue: [111]; green: [101]).

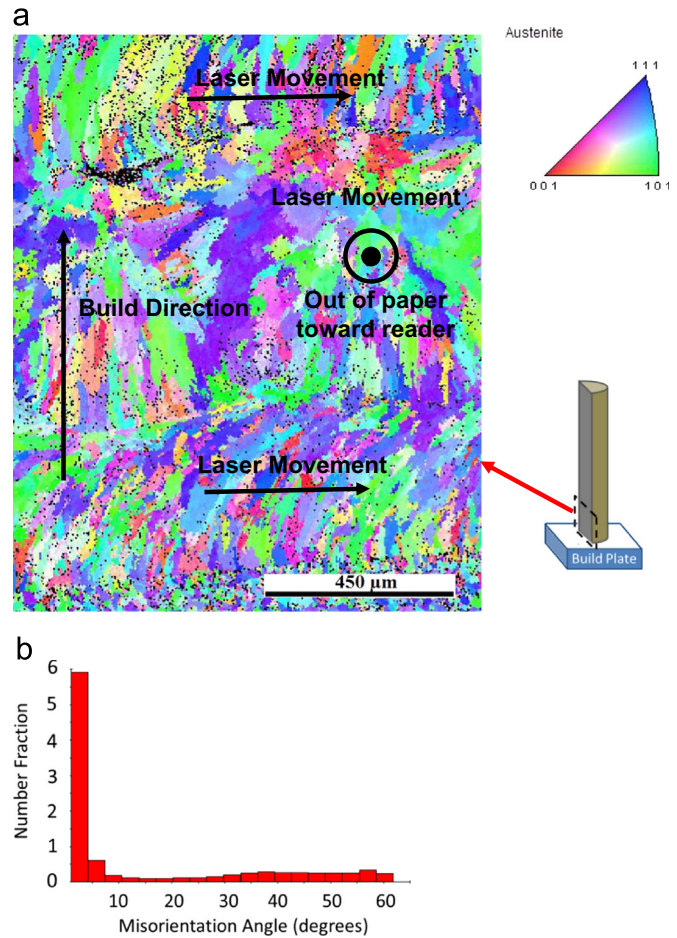


Fig. 6. (a) EBSD inverse pole map and (b) misorientation angle distribution of austenite phase in bottom region of a nine-built sample (red: [001]; blue: [111]; green: [101]).

average grain size for the bottom region of the nine-built sample was found to be approximately 45 μm, which indicates that the grains are slightly finer due to the increased layer time interval employed. Heat treatment was found to increase the grain size and misorientation angle. As can be seen in Fig. 5, the elongated grains parallel to build directions became fully recrystallized after heat treatment. These recrystallized grains possess a more isotropic configuration and average size of approximately 80 μm.

Electron backscatter diffraction maps from the middle region of the single-built sample before and after heat treatment are presented in Figs. 7 and 8. Figures 7–8 reveal the distribution of two iron-based phases, consisting of a dominant austenitic (γ) phase with face centered cubic (FCC) structure and less-prevalent, finely-dispersed ferrite (δ) phase with body centered cubic (BCC) structure. The EDS microanalysis was carried out at different regions of the single-built sample to determine the segregation/depletion of alloying elements. The EDS analysis of the top region is presented in Fig. 9 and the scanning line is also included. It may be seen that the distribution of compositions is rather uniform with very small inter-grain segregation of nickel and chromium elements.

3.2. Mechanical properties

3.2.1. Microhardness

Microhardness measurements were taken along the longitudinal axis of specimens from each group, to determine effects of inter-layer time interval. In Fig. 10, the Vickers hardness values are plotted versus distance from the build plate for all three sets of

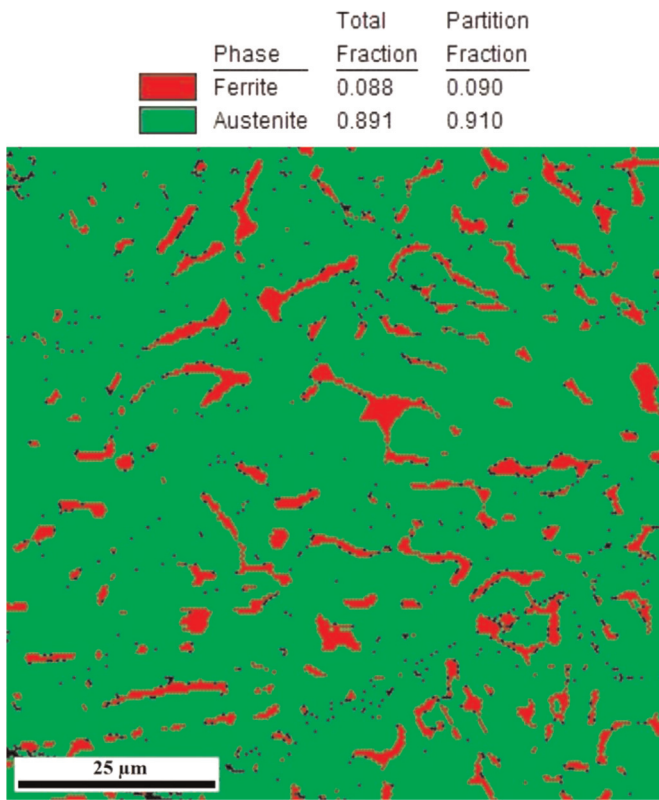


Fig. 7. EBSD phase fraction map of a selected area in the middle region of a single-built sample (red: ferrite; green: austenite).

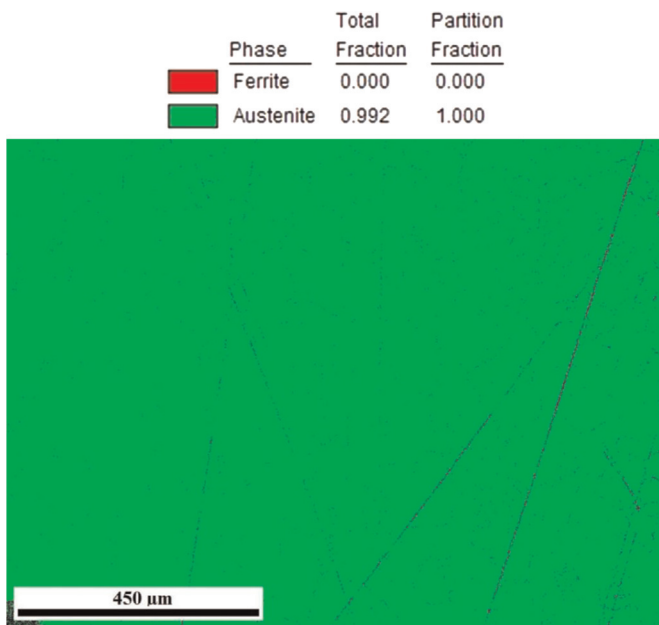


Fig. 8. EBSD phase fraction map of a selected area in the bottom region of a single-built sample after heat treatment.

samples. Note that each data point, which represents the Vickers hardness, is an average value of seven microhardness measurements along the sample length performed at equidistant locations. As can be seen in Fig. 10, the single-built set (as-built condition) shows Vickers hardness values that are lower than those of the nine-built specimens, but higher than those of the heat treated single-built specimens. This variation in Vickers hardness values clearly indicates the effect of thermal history originating from

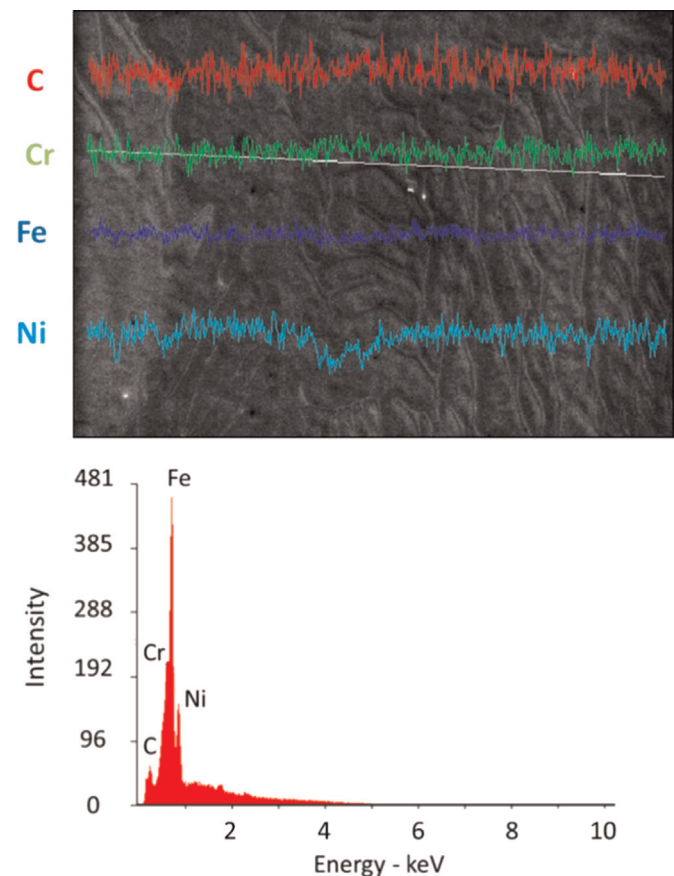


Fig. 9. EDS line spectrum along top region of a single-built sample.

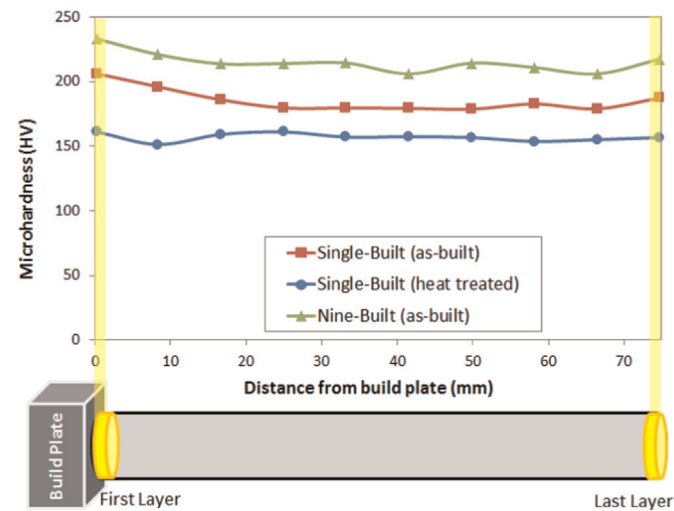


Fig. 10. Variation in Vickers hardness values of LENS 316L SS vs. distance from build plate for various build/post-build conditions.

different inter-layer time intervals, as well as the effect of post-DLD heat treatment on microstructure.

3.2.2. Compressive Behavior

Since the experienced thermal history for each part/layer varies at different distances from the build plate, DLD parts can have anisotropic microstructural distributions. Therefore, short compression specimens, from a single part, favor the more-accurate evaluation of bulk mechanical properties of the LENS 316L SS rods. Samples from each set were cut into five sections at equidistant

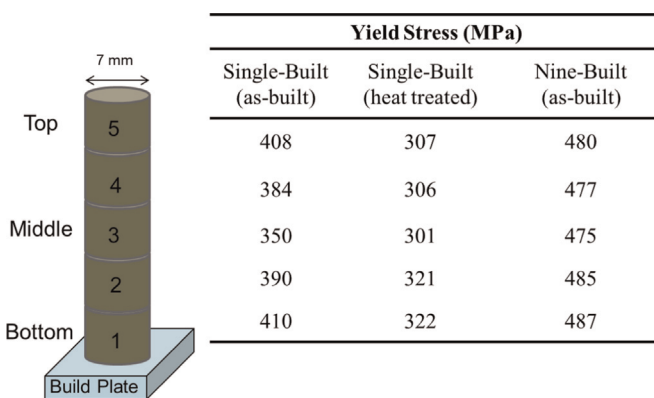


Fig. 11. Compressive yield strength of LENS 316 L SS at different regions and various build/post-build conditions.

locations along their axis, as shown in Fig. 11, which also includes their compressive yield strength (0.2% offset). These yield strengths were determined from the stress-strain plots derived from load-displacement data recorded during compression tests. As can be observed, single-built specimens in the as-built condition exhibit higher compressive yield values compared to heat treated single-built ones, but lower than nine-built specimens.

3.2.3. Tensile Behavior

The stress-strain curves of LENS 316L SS rods from the single-built (both as-built and heat treated) and nine-built sets are shown in Fig. 12; where error bars present the ranges in yield and ultimate strengths, as well as elongation to failure, observed for each set. It is important to note that since all specimens were fabricated vertically, the tensile loading axis for each specimen is parallel to the utilized (upward) build direction – resulting in inter-layer/interfacial porosity being perpendicular to loading. Measured tensile properties and their comparison with cast and wrought materials [31], as well as other DLD studies [15,32], are provided in Table 3. Results demonstrate that the yield and ultimate tensile strength of LENS 316L SS is higher than their conventionally-built counterparts; independent of process time interval or heat treatment. Increasing the layer-to-layer time interval increased the yield and tensile strengths of the specimens, while heat treatment was shown to decrease yield/tensile strength.

Significantly lower elongation to failure can be seen for the nine-built specimens compared to that of the cast and wrought materials, whereas for the single-built specimens (in both as-built and heat treated conditions), the elongation to failures are in the same range. Monotonic tension results indicate that the ultimate and yield tensile strengths of all three sets of the LENS 316L SS

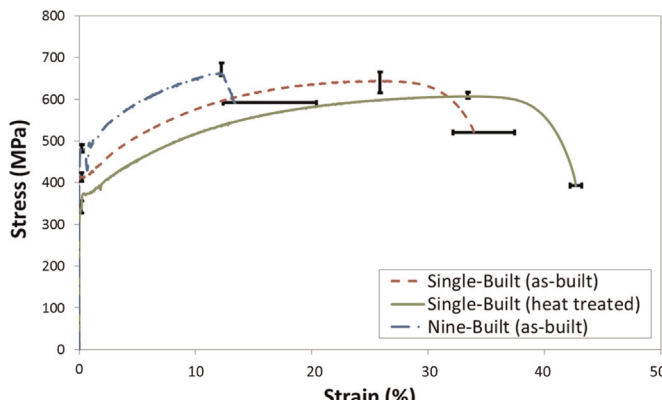


Fig. 12. Engineering tensile stress-strain curve of LENS 316L SS for various build/post-build conditions.

specimens are higher than those of cast and wrought 316L SS. Specimens from the single-built set (as-built condition) show lower yield and tensile strengths than those from nine-built specimens, but are higher than those from the heat treated single-built.

4. Discussion of experimental results

4.1. General comments on microstructure

Due to the unique thermal history, and heat treatment, experienced at each point within the single-built parts, finer microstructures are found near the bottom and top regions where the melt pool cooling rate is relatively high. For the bottom region, heat is quickly conducted away by the build plate, and at the top region, radiation/convection heat loss is more prevalent due to increased surface area and fewer re-heating cycles. Near the substrate, relatively high cooling rates were experienced along the initially-cold build plate employed in this study. This relatively high heat transfer can result in gas-entrapment within the melt pool due to vapor recoil. Lower cooling rates, and more cyclic re-heating, in the middle region causes tempering and aging, and typically, a coarser microstructure, and this is consistent with the observations of Zheng et al. [15].

As shown by the EBSD grain-structure map (of a longitudinal section from the bottom region of a single-built specimen) in Fig. 4(a), columnar growth of dendrites with the same orientation throughout their entire length can occur during DLD. Some deposited layers are also found to be epitaxial with previously-deposited layers, meaning that the colony growth direction can be the same as the crystallographic orientation of previously-deposited grains. This indicates that the crystallographic relationship between layers is a factor that influences the crystallization process in DLD parts. The laser penetration depth during fabrication of the single-built samples can encompass multiple pre-deposited layers, thus, the interface regions of deposited layer boundaries are not clearly visible in Fig. 4(a).

Due to lower initial temperatures of previously-deposited layers on the nine-built parts, resulting in higher solidification rates and a more-unidirectional heat flux, elongated austenite grains can be noticed in the direction of solidification in Fig. 6(a). It may be seen that the orientation of the columnar grains tends to incline from the building direction (vertical) towards the laser beam or melt pool movement direction in each layer. This can be explained by grains developing in a direction parallel with the local conductive heat transfer, and solidifying in the direction perpendicular to the isotherms [33,34]. Experimental results confirm that the local heat transfer conditions, in particular the solidification heat flux direction, dictates grain orientation and texture evolution [34,35]. As the height of a relative-small, single-built (with no time interval) part increases, its bulk temperature becomes higher, and consequently, heat transfer via part-to-build plate conduction may become lower than that due to part convection/radiation. As a result, directional growth of nuclei more perpendicular to the build direction will occur [33].

4.2. Melt pool Behavior

Despite the more uniform thermal history inherent to the nine-built samples, microhardness values were not homogeneous throughout the thickness of an individual deposited layer compared to single-built samples. This indicates that each deposited track consists of regions with distinct microstructure and microhardness, as shown in Fig. 13(a)-which provides a cross-sectional view of a solidified track perpendicular to the laser scan direction.

Table 3

Tensile properties of investigated DLD 316L SS samples and their comparison with cast and wrought materials [31] as well as other DLD studies [15,32].

Conditions	Yield Strength (MPa)	Ultimate Tensile Strength (MPa)	Elongation (%)	References
DLD/Single-Built (as-built)	405–415	620–660	32–40	Present Study
DLD/Single-Built (heat treated)	325–355	600–620	42–43	Present Study
DLD/Nine-Built (as-built)	465–485	660–685	12–20	Present Study
Cast	262	552	55	[31]
Wrought (cold finished)	255–310	525–623	30	[31]
Wrought (hot finished-annealed)	170	480	40	[31]
DLD/Other Studies	330–395	540–625	35–85	[15,32]

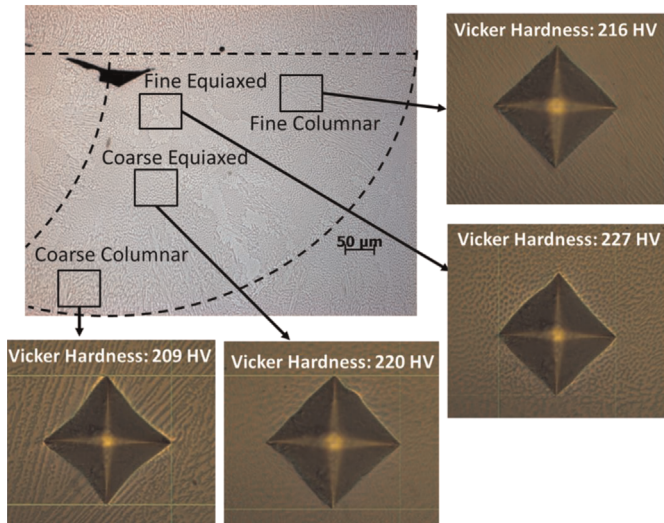
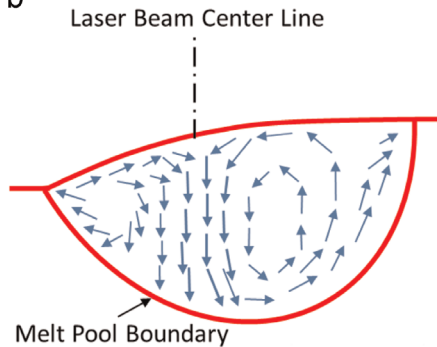
a**b**

Fig. 13. (a) Microstructure and microhardness of a nine-built sample at different regions of an individual layer (solidified melt pool cross-section perpendicular to the laser track), and (b) schematic of the melt pool flow directions (shown by blue arrows) during initial solidification.

Inferences regarding the nature of melt pool solidification can be made from Fig. 13(a) by observing the various microstructural distributions/features.

Due to temperature variation in the melt pool [36,37], the cooling rate varies along its single-phase volume [38]. The melt pool solidifies rapidly and consists of highly-transient, and spatially-dependent cooling rates. Heterogeneous and/or homogeneous nucleation can occur; thus forming intermediate zones of both liquid/solid phases. Solidification rates, i.e. local changes-in-volume due to phase-change, will dictate encumbered microstructure, i.e. columnar vs. equiaxed, while single-phase/sensible cooling rates will dictate grain size/evolution. Microstructure development can occur for grains formed during early phases of solidification, as they will experience high cooling rates once formed. The highest solidification rates occur near final stages of

melt pool phase-change and are typically concentrated near the core of the melt pool.

As shown in Fig. 13(a), relatively low solidification rates result in columnar/dendritic structures near the track perimeter. Since the melt pool boundary is large at the onset of solidification, the heat flux is more unidirectional away from the center of the molten core, influencing grain elongation in this direction. In regions near the melt pool center, fine equiaxed structures (cellular structure) are observed. These fine structures result from very high solidification rates that occur amid final stages of melt pool collapse. Based on Fig. 13(a), it appears that coarser equiaxed structures are generally found between the columnar and fine equiaxed regions. It may also be observed that relatively large equiaxed grains can form near the center of the track – and this may be indicative of homogeneous nucleation during solidification.

The Marangoni number, Ma , a dimensionless measure of thermally-driven surface tension forces with respect to viscous forces, is defined as:

$$Ma = \frac{\partial \gamma}{\partial T} \frac{r_m^2 [T - T_L]}{\mu \alpha} \quad (1)$$

where $\frac{\partial \gamma}{\partial T}$ is the temperature sensitivity of the molten metal surface tension (or surface tension coefficient), T is the local melt pool temperature, T_L is the liquidus temperature, r_m is melt pool radius, μ is the melt pool dynamic viscosity and α is the melt pool thermal diffusivity. Here, for sulfurous stainless steels (e.g. 316L SS), the surface tension coefficient, $\frac{\partial \gamma}{\partial T}$ is positive [39]; meaning, the surface tension of the melt pool increases with temperature. Since the melt pool is superheated, with temperatures above liquidus, the temperature difference, $T - T_L$, is positive.

Relative to melt pools of pure metal (no additive/contaminants) with $Ma < 0$, melt pools with $Ma > 0$ will tend to spread less and be deeper. Furthermore, the $Ma > 0$ melt pool will consist of convective, Bénard–Marangoni flow patterns directed inward from its free surface [40]. These convection currents flow through the hot region below the laser beam center line and recirculate along the melt pool circumference [40], as shown in Fig. 13(b). The convection will consist of jets due to intersecting vortices, thus deepening the melt pool and increasing layer height. The dominant, inward Bénard–Marangoni flow direction will provide a solidification front near-parallel with the laser beam center line.

Positive Marangoni number flow can help in describing the microstructural distribution observed for the cross-section of a solidified track presented Fig. 13(a). For example, an atypically-large columnar structure exists near the laser beam center line; possessing a slightly tortuous and continuously-elongated form. This irregular columnar grain morphology may be a result of downward-jetting Bénard–Marangoni flows existing during early phases of solidification. Based on Fig. 13(a), it appears that, due to convection effects, the molten metal near the jetting zone will solidify to more elongated grains and then coarsen due to high cooling rates in the HAZ.

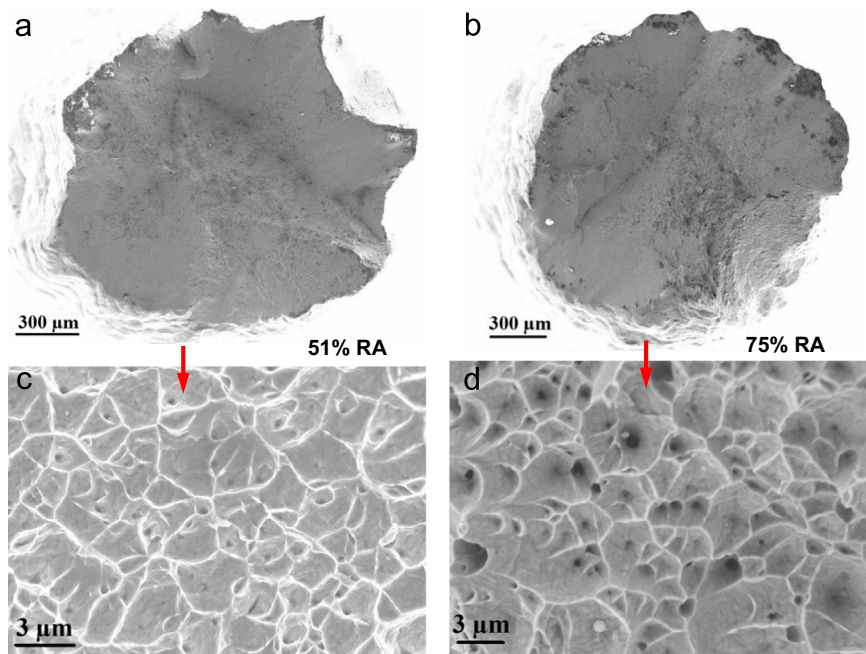


Fig. 14. Tensile fracture surfaces of single-built specimens in (a) as-built and (b) heat treated conditions (RA: reduction in area). Higher magnification of dimples on fracture surfaces of (c) as-built and (d) heat treated specimens.

The corresponding values of the Vickers microhardness at different regions of the solidified melt pool are presented in Fig. 13 (a). It may be seen that the microhardness decreases from the center of solidified melt pool (227 HV) towards its boundary (209 HV) due to an increase in the grain size resulting from lower local solidification rates at the boundary. It may also be seen from Fig. 13 (a) that the lowest microhardness value is obtained at the melt pool/previous-deposited layer interface, and this confirms other findings in the literature [9,15,41].

4.3. Effect of post-DLD heat treatment

In general, heat treating the single-built sample was found to increase the size of its grains. Furthermore, due to homogenizing effects of heat treatment on microstructure, there is little inconsistency in the microstructure among different regions observed. The interface regions of deposited layer boundaries (i.e. inter-layer porosity) and the laser track footprint are completely vanished. The low angle boundaries (1° – 4°) for non-heat treated samples, shown in Fig. 4(b), change to high angle boundaries (60°) after heat treatment as shown in Fig. 5(b). The low misorientation angles are indicative of the pre-heat treated material being near-monocrystalline resulting in less dislocation densities, and thus its ability to restrain more slip systems [42], since dislocation activity typically decreases with a reduced misorientation angle [43]. Twinned austenitic grain structures (FCC) appear after heat treatment, which may have formed during grain growth due to a decrease in the interfacial free energy of grain boundaries, as can be seen in Fig. 5(a). It has been found that for FCC structures, annealing twins possess a misorientation angle of 60° about the $<111>$ [44]. Therefore, increasing the high angle boundaries (60°) after heat treatment most likely is the result of twin boundary misorientations.

Fig. 7 clearly shows that the austenite phase (91%) is the dominant phase within the single-built specimen. However, a relatively small volume fraction of ferrite (approximately 5–10%) is observed at different regions along the specimen, as can be seen in Fig. 7. Although fully-austenitic material can be obtained at equilibrium according to the chemical composition of 316L SS [45],

small amounts of δ -ferrite “islands” were homogeneously formed within the boundaries of austenite grains due to rapid solidification and the presence of chemical elements conducive for ferrite formation (i.e. Cr, Mo, and Si), as can be seen in Fig. 7. The EBSD phase fraction map in Fig. 8 demonstrates the corresponding distribution of the austenite and ferrite phases after heat treatment. It can be observed that fully-austenitic grains are prevalent, thus demonstrating that the employed heat treatment significantly decreases the volume fraction of the δ -ferrite phase. Note that the volume fraction of δ -ferrite can have a significant effect on the mechanical properties of materials [46].

As can be seen in Fig. 10, the hardness of a heat treated single-built sample is significantly lower due to microstructural coarsening imposed by the heat treatment process. Since the δ -ferrite phase is harder than the austenite phase at room temperature [47], decreasing the δ -ferrite phase during heat treatment can be responsible for the lower hardness values observed.

It was found that heat treatment results in a reduction of approximately 17% in yield strength and 5% in ultimate tensile strength for the investigated DLD 316L SS specimens, as well as a 26% increase in elongation to failure – indicating an increase in ductility. Increasing the grain size via heat treatment is the main reason for the reduced tensile strength of the heat treated specimens. Less deviation in yield strength can also be observed for heat treated samples at each section (Fig. 12). This is mainly due to the homogenizing effect of heat treatment on the initially-anisotropic microstructure.

Decreasing the amount of the δ -ferrite phase, which has a higher strength than the austenite phase, via heat treatment, can be responsible for observed lower tensile strengths. A higher strain hardening rate was also observed for heat treated specimens ($n=0.31$) as compared to the as-built specimens ($n=0.27$). The higher dislocation density resulting from a higher misorientation angle in heat treated specimens, may also contribute towards the higher strain hardening rate. A higher misorientation angle increases dislocation densities [43], resulting in more strain hardening.

Scanning electron microscope (SEM) morphologies from the tensile fracture surface of the single-built and heat treated single-

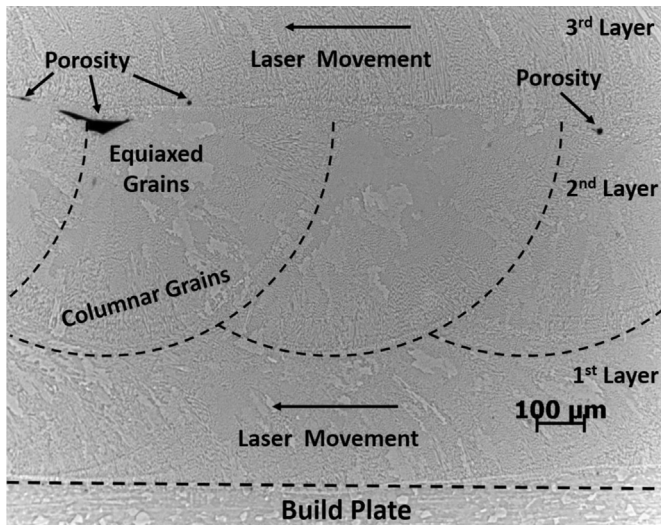


Fig. 15. Micrograph showing a section of three layers with porous features atop the build plate.

built specimens are presented in Fig. 14. A large number of dimples and micro-voids were observed on the tensile fracture surface of the as-built and heat treated single-built specimens – indicative of a ductile fracture, as depicted in Fig. 14. Moreover, un-melted powder particles resulting from lack of fusion can be noticed on the tensile fracture surface of the heat treated single-built sample in Fig. 14(d). This indicates that unmelted powders are, to some extent, immune to the homogenizing heat treatment selected.

4.4. Effect of DLD inter-layer time interval

4.4.1. Microstructure

Variation in grain size was observed for the single-built samples due to (indirectly) imposing a relatively-fast build schedule non-conducive for uniform microstructure as it promotes a thermal history with bulk temperature rise and inconsistent, initial layer temperature throughout the build. When this is the case, the net heat transfer into the part is positive for longer time, and this allows for grain growth, and in fact, ‘during-the-process heat treatment’ that is unique to each region of the part (i.e. bottom, middle, top). Note that the frequency of thermal cycling experienced by the single-built part was also higher due to the reduced inter-layer time interval. Finally, since the intra-layer build schedule consisted of an alternating scan pattern, adjacent inter-layer points experienced a different thermal history. If one were constrained in manufacturing time, the intra-layer build schedule could be modified as to allow for more-optimal, alternating scan patterns for increased temperature uniformity. In addition, the part could be oriented differently, as to allow for less layer deposits and thus longer inter-layer time intervals.

No significant differences are observed in microstructure for the bottom, middle, and top regions of the nine-built samples. As the inter-layer time interval increases, the part will reach thermal equilibrium with its surroundings before deposition of a new layer; thus, each layer will experience more similar heating/cooling rates. Therefore, uniform thermal history is experienced by each deposited layer resulting in a more uniform microstructure for the nine-built rods.

Since the thermal histories experienced by the first few deposited layers for both the single-built and nine-built samples are somewhat similar, these layers share more similar grain sizes. However, in contrast to single-built samples, the examined average grain size at the middle and top regions of a nine-built sample

was consistent with the bottom region (approximately 50–60 μm) as they all experienced relatively high, and similar, cooling rates. Generally, nine-built samples contain finer microstructures due to these higher cooling rates resulting from longer inter-layer time intervals, while reduced time intervals result in lower cooling rates and high-temperature aging – favoring the creation of coarser microstructure, especially in the middle and top regions.

There is no significant difference in austenite and ferrite phase volume fractions between nine-built and single-built samples. In addition, similar to single-built samples, no significant grain-boundary segregation/depletion of alloying elements was observed for nine-built samples. Although the volume fractions of these phases may depend on process parameters [48], it appears that different thermal histories, resulting from different time intervals between layers, do not have a significant effect on phase fraction, or composition.

4.4.2. Porosity

Depending on the combination of process and design parameters, unique thermal histories are realizable, thus impacting formation of pores/voids—which can form due to lack of fusion between layers, entrapped gas/debris or utilization of porous powders. At layers further from the build plate, lack of fusion can occur due to insufficient laser power [49,50], while closer to the substrate, they can form due to very high heat transfer rates.

For nine-built samples, the laser penetration depth, or HAZ size, is altered due to colder, initial layer temperatures and this will impact the degree of previous-layer remelting, as depicted in Fig. 15. Therefore, due to this lower laser penetration depth, previously deposited layers cannot become molten enough to achieve sufficient metallurgical bonding. This allows the ‘footprint’ of the laser track to be more visible for the nine-built samples as compared to the single-built ones. As compared to the single-built samples that consisted of long columnar grains well-bonded to the previously-deposited layer, nine-built samples show less bonding between layers, via comparison Figs. 4(a) and 6(a). The weak bonding between layers may be attributed to lower laser penetration depths [33] reducing the tendency for extensive epitaxial growth in the nine-built samples.

4.4.3. Ductility and tensile strength

More reduction in area (RA) can be noticed for the single-built specimens, in both as-built (RA: 51%) and heat treated conditions (RA: 75%), as compared to the nine-built ones (RA: 17%), which indicates more ductility in single-built specimens. However, as shown in Fig. 16, a lower amount of dimples on the tensile fracture surfaces of nine-built specimens existed – indicating a more brittle-behaving fracture. In addition, voids and un-melted regions can be seen along the tensile fracture surface of the nine-built specimens in Fig. 16. These features can be attributed to the lack of fusion (or lower HAZ depth) during DLD of this particular plane in which fracture occurred, justifying the observed lower elongation to failure for the nine-built specimens. The layers are essentially colder prior to deposition during the nine-built fabrication, and this increases the cooling rate – generating finer microstructures and a less ductile behaving sample.

An energy dispersive spectroscopy (EDS) spot analysis was conducted to determine the elemental composition of an inclusion found on the tensile fracture surface of a nine-built specimen, as shown in Fig. 17. The EDS micro-chemical analysis demonstrated that the inclusion comprised of predominantly oxygen, manganese, chromium, and silicon, with no iron content. The high oxygen concentration indicates that this inclusion is an oxide consisting of manganese (MnO) and silicon (SiO_2). Even during DLD in an inert atmosphere, the existence of oxygen can be unavoidable. From Fig. 17, it appears that the nine-built rods were exposed to

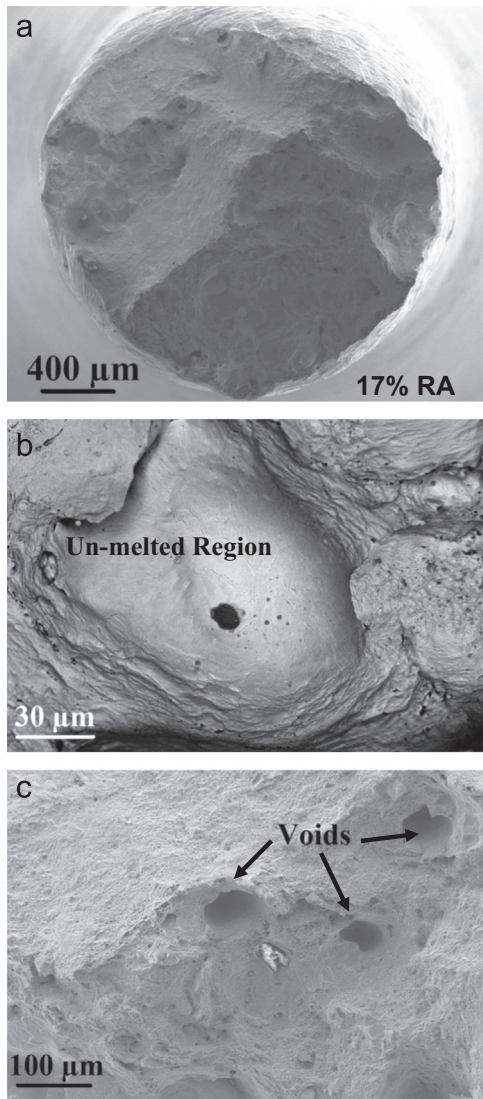


Fig. 16. (a) Tensile fracture surfaces of a nine-built sample (RA: reduction in area), (b) higher magnification of an un-melted region, and (c) higher magnification of typical voids.

oxygen, and this exposure time was longer relative to the single-built samples in which such inclusions were not observed. The existence of oxygen between layers can impact the melt pool wetting characteristics, and thus, the layer-to-layer bonding efficiency.

The elongation to failure of the nine-built specimens is significantly lower than the other sets, as well as both cast and wrought materials. However, the elongation to failure of the single-built specimens in both as-built and heat treated conditions were observed to be within the same range as the conventionally-built materials. The lower ductility of the nine-built samples is attributed to the higher cooling rates experienced during their fabrication. In addition, the presence of more micro-porosity and intra-layer oxides in the nine-built samples (due to lack of fusion) may have contributed to the observed lack of ductility.

4.4.4. Compression

For single-built samples, the bottom and top sections have the highest compressive yield strength due to their finer microstructures, as can be seen in Fig. 11. Lower cooling rates and cyclic reheating of subsequent layers, in the middle of the part, leads to a coarser grain size, causing lower yield strength. Nine-built samples

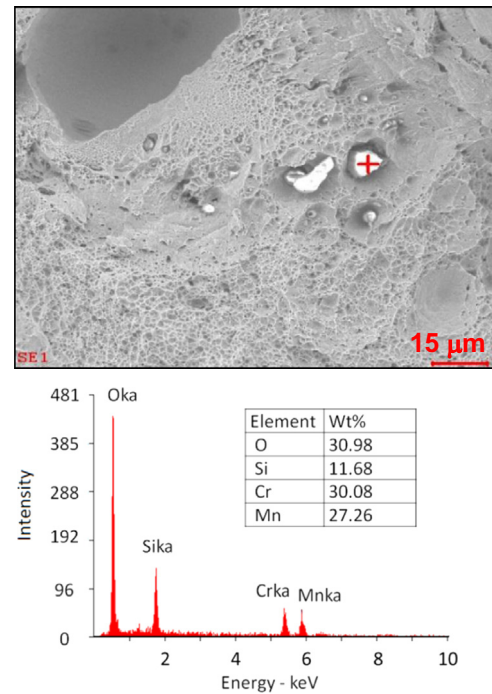


Fig. 17. EDS spot spectrum of an inclusion along a tensile fracture surface of a nine-built sample (marked with "+").

exhibit more-uniform yield strengths at different distances from the build plate, which can be explained by the more-uniform thermal history experienced at each deposited layer. Despite having lubricated contact surfaces, longitudinal cracks were observed for specimens under compression tests due to barreling effects resulting from frictional resistance to lateral deformation. Furthermore, since voids do not grow under compression loading, the effect of porosity and weak metallurgical bonding between layers is less pronounced during monotonic compression tests.

4.4.5. Microhardness

The hardness of the nine-built samples is noticeably higher than the single-built samples due to finer grain sizes encumbered via higher cooling rates. As shown in Fig. 13(a), significant microhardness variations were observed in each layer of the nine-built samples. The average microhardnesses for single-built samples in as-built and heat treated conditions, as well as for nine-built ones, are 185, 157 and 215 HV, respectively. These measurements confirm the direct relationship of the densification level with microstructure for DLD 316L SS. Furthermore, the first layer (at the build plate junction) has the highest Vickers hardness irrespective of time interval, which can be attributed to the heat sinking effects imposed by the initially-cold build plate utilized; facilitating rapid quenching. A slight increase in microhardness for the last deposited layer is also observed and this can be explained by the increased convection and radiation heat transfer at these locations (increased surface area) – resulting in higher cooling rates, and consequently, finer microstructures. Due to cyclic re-heating and lower cooling rates within the middle region, slightly lower microhardnesses are measured for all the samples.

5. Conclusions

As the utilization and appeal of larger build envelopes and multi-part/large-part manufacturing schemes for Direct Laser Deposition (DLD) increases, important design parameters to consider are the elapsed time between successive deposits, i.e. build

schedule or time intervals, and the post-manufacture heat treatment utilized, as these both will impact overall manufacturing time and efficiency. Hence, the effects of inter-layer time interval and heat treatment on DLD part quality were assessed. This was accomplished by evaluating the mechanical properties and microstructural features of 316L stainless steel (SS) samples fabricated while employing two different inter-layer time intervals; i.e. either building the samples one-at-a-time or nine-at-a-time (in-parallel), via Laser Engineered Net Shaping (LENS), a DLD additive manufacturing method.

Results indicate that the inter-layer (and intra-layer) time intervals experienced during DLD have a substantial effect on thermal history, and consequently encumbered microstructure (i.e. grain size and morphology) and mechanical properties (i.e. tension, compression, and microhardness) of DLD 316L SS. Based on these findings, DLD process and design parameters should be optimized while considering part size, number and geometry. The appropriate combination of time intervals, or build schedule, should be integrated into manufacturing design; especially if laser power is not controlled. In addition, the following conclusions can be drawn from the experimental results:

1. Longer inter-layer time intervals increase cooling/solidification rates along each layer which leads to finer microstructure and higher yield and tensile strengths, as well as lower elongation to failure. Conversely, shorter inter-layer time intervals decrease cooling rates and increase bulk temperature in the part resulting in a coarser microstructure, lower strengths and larger elongation to failure.
2. Distinct microstructures and yield strengths were observed for single-built 316L SS samples (i.e. without inter-layer time interval), along their longitudinal axis, due to non-uniform/highly-transient heat transfer throughout the part. Each layer of a single-built sample will experience a unique thermal history, with layers near the build plate experiencing more thermal cycles relative to final deposited layers.
3. Homogenizing effects of heat treatment on microstructure (i.e. grain size, morphology, and orientation) impacted mechanical properties of the LENS-produced 316L SS. Heat treatment increased grain size which resulted in lower yield and ultimate tensile strengths and microhardness. Heat treated samples were shown to be more ductile as compared to as-built specimens.
4. Nine-built samples (i.e. with constant inter-layer time interval) showed more-uniform microstructure and yield strengths; near-independent of height-wise location relative to build plate and this is attributed to each layer having a similar thermal history during fabrication.
5. As solidification rates increase during melt pool collapse, various microstructures with distinct microhardness can populate along a deposited track of DLD parts. A cross-section of a solidified track from a nine-built sample was observed and it was found that coarse columnar grains, with lower microhardness, exist along its boundary, while fine equiaxed grains with higher microhardness are concentrated near its center region. The observed microstructural distributions can be partially attributed to Bénard–Marangoni convection pulling liquid from the free surface of the melt pool towards its bottom – characteristic of thermally unstable liquids with a positive Marangoni number – such as 316L SS.
6. No significant differences between the nine-built samples and single-built samples were observed with regard to austenite and ferrite phase volume fraction or chemical composition distribution.
7. The inspected LENS specimens (single-built and nine-built) were found to have higher ultimate and yield strengths as

compared to their cast and wrought forms and this is attributed to the higher cooling rates inherent to DLD.

8. Occurrence of imperfections (e.g. voids and un-melted powders) and weak metallurgical bonding between layers resulted in the LENS specimens having a lower elongation to failure compared to cast and wrought forms. This effect was more pronounced for specimens with longer inter-layer time intervals (i.e. nine-built samples). Finer microstructures in the LENS specimens may be also responsible for the decreased ductility.

Acknowledgments

This work was supported by Mississippi State University's Office of Research and Economic Development (ORED) and Center for Advanced Vehicular Systems (CAVS).

References

- [1] S. M. Thompson, L. Bian, N. Shamsaei, A. Yadollahi, An overview of direct laser deposition for additive manufacturing; Part I: Transport phenomena, modeling and diagnostics, *Additive Manufacturing* (2015). <http://dx.doi.org/10.1016/j.addma.2015.07.001>.
- [2] W.E. Frazier, Metal additive manufacturing: a review, *J. Mater. Eng. Perform.* 23 (2014) 1917–1928.
- [3] C. Selcuk, Laser metal deposition for powder metallurgy parts, *Powder Metall.* 54 (2011) 94–99.
- [4] G. Tapia, A. Elwany, A Review on Process Monitoring and Control in Metal-Based Additive Manufacturing, *J. Manuf. Sci. Eng.* 23 (2014) 1917–1928.
- [5] L. Bian, S.M. Thompson, N. Shamsaei, Mechanical properties and microstructural features of direct laser deposited Ti-6Al-4V, *JOM* 67 (2015) 629–638.
- [6] J. Mazumder, J. Choi, J. K. Nagarathnam, Koch, D. Hetzner, The direct metal deposition of H13 tool steel for 3D components, *JOM* 49 (1997) 55–60.
- [7] P.A. Kobryn, S.L. Semiatin, Mechanical properties of laser-deposited Ti-6Al-4V, in: *Solid Freeform Fabrication Proceedings*, Austin, 2001: pp. 179–186.
- [8] L. Costa, R. Vilar, T. Réti, Simulating the effects of substrate pre-heating on the final structure of steel parts built by laser powder deposition, in: *Proc. 15th Solid Free. Fabr. Symp.*, Austin, USA (2004) 643–654.
- [9] H. El Kadiri, L. Wang, M.F. Horstemeyer, R.S. Yassar, J.T. Berry, S. Felicelli, et al., Phase transformations in low-alloy steel laser deposits, *Mater. Sci. Eng. A* 494 (2008) 10–20.
- [10] G.P. Dinda, a. K. Dasgupta, J. Mazumder, Laser aided direct metal deposition of Inconel 625 superalloy: Microstructural evolution and thermal stability, *Mater. Sci. Eng. A* 509 (2009) 98–104.
- [11] P. Ganesh, R. Kaul, C.P. Paul, P. Tiwari, S.K. Rai, R.C. Prasad, et al., Fatigue and fracture toughness characteristics of laser rapid manufactured Inconel 625 structures, *Mater. Sci. Eng. A* 527 (2010) 7490–7497.
- [12] Y. Xiong, W.H. Hofmeister, Z. Cheng, J.E. Smugeresky, E.J. Lavernia, J. M. Schoenung, In situ thermal imaging and three-dimensional finite element modeling of tungsten carbide–cobalt during laser deposition, *Acta Mater.* 57 (2009) 5419–5429.
- [13] Y. Xue, a. Pascu, M.F. Horstemeyer, L. Wang, P.T. Wang, Microporosity effects on cyclic plasticity and fatigue of LENS™-processed steel, *Acta Mater.* 58 (2010) 4029–4038.
- [14] D. Wu, X. Liang, Q. Li, L. Jiang, Laser rapid manufacturing of stainless steel 316L/Inconel718 functionally graded materials: microstructure evolution and mechanical properties, *Int. J. Opt.* 2010 (2010) 1–5.
- [15] B. Zheng, Y. Zhou, J.E. Smugeresky, J.M. Schoenung, E.J. Lavernia, Thermal behavior and microstructure evolution during laser deposition with laser-engineered net shaping: part II: experimental investigation and discussion, *Metall. Mater. Trans. A*. 39 (2008) 2237–2245.
- [16] H.K. Rafi, T.L. Starr, B.E. Stucker, A comparison of the tensile, fatigue, and fracture behavior of Ti-6Al-4V and 15-5 PH stainless steel parts made by selective laser melting, *Int. J. Adv. Manuf. Technol.* 69 (2013) 1299–1309.
- [17] A. Yadollahi, N. Shamsaei, S.M. Thompson, A. Elwany, L. Bian, Mechanical and microstructural properties of selective laser melted 17-4 PH stainless steel, in: *ASME International Mechanical Engineering Conference and Exposition*, 2015.
- [18] B. Zheng, Y. Zhou, J.E. Smugeresky, J.M. Schoenung, E.J. Lavernia, Thermal behavior and microstructural evolution during laser deposition with laser-Engineered net shaping: part I. numerical calculations, *Metall. Mater. Trans. A*. 39 (2008) 2228–2236.
- [19] R. Ye, J.E. Smugeresky, B. Zheng, Y. Zhou, E.J. Lavernia, Numerical modeling of the thermal behavior during the LENS® process, *Materials Science and Engineering* 428 (2006) 47–53.
- [20] L. Costa, R. Vilar, T. Réti, A.M. Deus, Rapid tooling by laser powder deposition: Process simulation using finite element analysis, *Acta Materialia* 53 (2005) 3987–3999.
- [21] H. Yin, L. Wang, S.D. Felicelli, Comparison of two-dimensional and three-

- dimensional thermal models of the LENS® process, *J. Heat Transfer.* 130 (2008) 102101.
- [22] V.D. Manvatkar, a a Gokhale, G. Jagan Reddy, a Venkataramana, a De, Estimation of melt pool dimensions, thermal cycle, and hardness distribution in the laser-engineered net shaping process of austenitic stainless steel, *Mater. Mater. Trans. A.* 42 (2011) 4080–4087.
- [23] S. Barua, F. Liou, J. Newkirk, T. Sparks, Vision-based defect detection in laser metal deposition process, *Rapid Prototyp. J.* 20 (2013) 77–85.
- [24] G.K. Lewis, E. Schlienger, Practical considerations and capabilities for laser assisted direct metal deposition, *Mater. Des.* 21 (2000) 417–423.
- [25] N. Shamsaei, A. Yadollahi, S.M. Thompson, L. Bian, An overview of direct laser deposition for additive manufacturing; part II: Mechanical behavior, process parameter optimization and control, *Additive Manufacturing* (2015), <http://dx.doi.org/10.1016/j.addma.2015.07.002>.
- [26] M.L. Griffith, M.E. Schlienger, L.D. Harwell, M.S. Oliver, M.D. Baldwin, M.T. Ensz, et al., Understanding thermal behavior in the LENS process, *Mater. Des.* 20 (1999) 107–113.
- [27] J. Hunt, F. Derguti, I. Todd, Selection of steels suitable for additive layer manufacturing, *Ironmak. Steelmak* 41 (2014) 254–256.
- [28] ASTM Standard, ASTM E8 / E8M-13a, Standard test methods for tension testing of metallic materials, (2013).
- [29] ASTM Standard, ASTM E9-09, Standard test methods of compression testing of metallic materials at room temperature, (2009).
- [30] ASM Handbook, *ASM Handbook Volume 4, Heat Treating*, Mater. Park. OH ASM Int. (1991).
- [31] A.S.M. Metals, Handbook, Properties and selection: stainless steels, tool materials and special-purpose metals, Met. Handbook, in: 9th Edn, in: D. Benjamin, C.W. Kirkpatrick (Eds.), ASM Int. Met. Park, 1980, pp. 113–121.
- [32] L. Costa, R. Vilar, Laser powder deposition, *Rapid Prototyp. J.* 15 (2009) 264–279.
- [33] X. Wu, R. Sharman, J. Mei, W. Voice, Direct laser fabrication and microstructure of a burn-resistant Ti alloy, *Mater. Des.* 23 (2002) 239–247.
- [34] L. Thijs, F. Verhaeghe, T. Craeghs, A study of the microstructural evolution during selective laser melting of Ti-6Al-4V, *Acta Mater.* 58 (2010) 3303–3312.
- [35] T. Niendorf, S. Leuders, A. Riemer, H.A. Richard, T. Tröster, D. Schwarze, Highly anisotropic steel processed by selective laser melting, *Mater. Mater. Trans. B.* 44 (2013) 794–796.
- [36] M.L. Griffith, M.E. Schlienger, L.D. Harwell, M.S. Oliver, M.D. Baldwin, M.T. Ensz, et al., Thermal behavior in the lens process, in: Proc. 9th Solid Free. Fabr. Symp., Austin, USA, 1998: pp. 89–96.
- [37] L. Wang, S.D. Felicelli, J.E. Craig, Experimental and numerical study of the lens rapid fabrication process, *J. Manuf. Sci. Eng.* 131 (2009) 041019.
- [38] V. Neela, a De, Three-dimensional heat transfer analysis of LENSTM process using finite element method, *Int. J. Adv. Manuf. Technol.* 45 (2009) 935–943.
- [39] Z. Li, K. Mukai, M. Zeze, K.C. Mills, Determination of the surface tension of liquid stainless steel, *Journal of Materials Science* 40 (2005) 2191–2195.
- [40] A. Kumar, S. Roy, Effect of three-dimensional melt pool convection on process characteristics during laser cladding, *Comput. Mater. Sci.* 46 (2009) 495–506.
- [41] G.P. Dinda, a K. Dasgupta, S. Bhattacharya, H. Natu, B. Dutta, J. Mazumder, Microstructural characterization of laser-deposited al 4047 alloy, *Mater. Mater. Trans. A.* 44 (2012) 2233–2242.
- [42] J.B. Jordon, J.B. Gibson, M.F. Horstemeyer, H. El Kadiri, J.C. Baird, A.A. Luo, Effect of twinning, slip, and inclusions on the fatigue anisotropy of extrusion-textured AZ61 magnesium alloy, *Mater. Sci. Eng. A.* 528 (2011) 6860–6871.
- [43] J.Shi, Predictive Microstructural Modeling of Grain-boundary Interactions and Their Effects on Overall Crystalline Behavior, 2009.
- [44] Y. Jin, M. Bernacki, G.S. Rohrer, A.D. Rollett, B. Lin, N. Bozzolo, Formation of annealing twins during recrystallization and grain growth in 304L austenitic stainless steel, *Mater. Sci. Forum.* 753 (2013) 113–116.
- [45] G. Bouche, J.L. Bechade, M.H. Mathon, L. Allais, A.F. Gourguès, L. Naze, Texture of welded joints of 316L stainless steel, multi-scale orientation analysis of a weld metal deposit, *Journal of Nuclear Materials* 277 (2000) 91–98.
- [46] A. Imandoust, A. Zarei-Hanzaki, S. Heshmati-Manesh, S. Moemeni, P. Changizian, Effects of ferrite volume fraction on the tensile deformation characteristics of dual phase twinning induced plasticity steel, *Mater. Des.* 53 (2014) 99–105.
- [47] A. Kocjan, D.K. Merl, M. Jenko, The corrosion behaviour of austenitic and duplex stainless steels in artificial saliva with the addition of fluoride, *Corros. Sci.* 53 (2011) 776–783.
- [48] L. Costa, T. Reti, A.M. Deus, R. Vilar, Simulation of layer overlap tempering kinetics in steel parts deposited by laser cladding, in: Int. Conf. Met. Powder Depos. Rapid Manuf. April, San Antonio, Texas, USA, 2002.
- [49] L. Wang, S. Felicelli, Process modeling in laser deposition of multilayer ss410 steel, *J. Manuf. Sci. Eng.* 129 (2007) 1028–1034.
- [50] A. Yadollahi, D. Seely, B. Patton, N. Shamsaei, S.M. Thompson, Mechanical and microstructural properties of lens-produced aisi 316L stainless steel, in: AIAA SciTech, 10.2514/6.2015-1355, 2015.

Mechanical Properties of INCONEL 718 Parts Manufactured by Shaped Metal Deposition (SMD)

Bernd Baufeld

(Submitted December 9, 2010; in revised form July 7, 2011)

INCONEL 718 parts have been manufactured by shaped metal deposition (SMD), an additive layer manufacturing technique applying wire-based tungsten inert gas welding. This technique is aimed toward mass customization of parts, omitting time- and scrap-intensive, subtractive fabrication routes. SMD results in dense, “near net-shaped” parts without pores, cracks, or fissures. The microstructure of the SMD parts exhibit large, columnar grains with a fine dendritic microstructure. The interdendritic boundaries are decorated by small Laves phase precipitates and by MC carbides. Tensile tests were performed with different strain rates (10^{-4} , 10^{-3} , and 2×10^{-3} 1/s), but no dependency on strength or strain at failure was observed. The ultimate tensile strength was 828 ± 8 MPa, the true plastic strain at failure $28 \pm 2\%$, the micro Vickers hardness 266 ± 21 HV200, and the dynamically measured Young’s module was 154 ± 1 GPa.

Keywords additive manufacturing, aerospace, electron microscopy, fabricated metal, mechanical testing, shaped metal deposition, welding

1. Introduction

Additive manufacturing is a novel concept, where near net-shaped parts are created layer wise. In comparison with traditional subtractive methods, scrap material and machining times are largely reduced. Additive manufacturing allows accelerating the introduction of new designs, shortening the product implementation cycle, and being applied for the repair of expensive components. While additive manufacturing is not suitable for mass production, it is ideal for mass customization (Ref 1). Different methods, each with their characteristic pros and cons, are under investigation applying different heat sources, such as laser beam, electron beam, or welding torch, and supplying the material either in form of powder or wire. The method applied for the present article is called shaped metal deposition (SMD), which is utilizing a tungsten inert gas (TIG) welding torch and is fed by wire.

Until now SMD has been used mostly to build Ti-6Al-4V parts (Ref 2–9), which is the most widely applied Ti alloy (Ref 10). Ti alloys are expensive and difficult to machine, which makes additive manufacturing a perfectly fitting technique. SMD was also applied for Ti and intermetallics (Ref 11), different steels (Ref 12, 13), and INCONEL 718 (Ref 14). The latter is today’s superalloy of choice for a wide variety of turbine engine applications, making up 55–70% of the nickel base superalloys in modern jet engines (Ref 15). The emphasis of the present article is on the material properties of SMD parts

of this alloy, which has not been studied by Clark et al. (Ref 14). While here the properties of as-fabricated parts are investigated, a future article will show the influence of heat treatment (Ref 16).

Detailed knowledge of the microstructure and the properties is the prerequisite to achieve reliability and consistency of an additive manufacturing technique, which is necessary for a successful transition from the experimental state to manufacturing (Ref 17). It was predicted, but not proven by Clark et al., that SMD has the inherent potential to outperform polycrystalline castings of the same chemistry in terms of mechanical properties, because of the more consistent solidification conditions made possible by a deposition process (Ref 14). The microstructure and mechanical properties for INCONEL 718 parts fabricated by other additive manufacture techniques, such as electron (Ref 18, 19) or laser beam (Ref 20–22), have already been investigated, and the results will be compared in this study.

2. Experimental

2.1 SMD Unit

The SMD unit consists of a 6-axis KUKA KR16 robot manipulating a Fronius Tungsten Inert Gas (TIG) welding head and a 2-axis DKP400 turntable, all located in an airtight chamber filled with argon of 99.999% purity. The INCONEL 718 wire of 1.2-mm diameter is supplied by a Fronius wire feeder located outside of the chamber. The material was deposited by single track, layer by layer with a step height of 1 mm on an INCONEL 718 plate. The geometry of the targeted part was a square-based tube with 0.17-m side length, 0.12-m height, and 0.01-m wall thickness (Fig. 1). The applied SMD parameters were a wire feed speed of 1.5 m/min, a deposition speed of 0.3 m/min, and an electrical current of 220 A. These parameters lead to fully dense parts without pores, cracks, or fissures.

Bernd Baufeld, Nuclear Advanced Manufacturing Research Centre, University of Sheffield, Brunel Way, Rotherham S60 5WG, UK. Contact e-mail: b.baufeld@sheffield.ac.uk

The coordinate system applied in the present article attributes x to the travel direction of the TIG head relative to the base plate, y to the direction perpendicular to the wall surface, and z to the direction perpendicular to base plate.

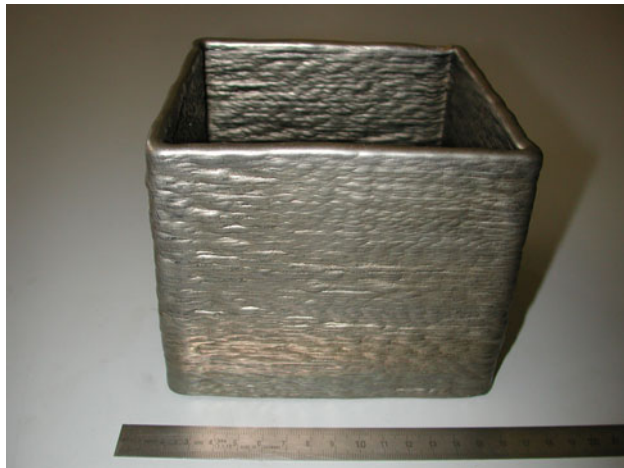


Fig. 1 View on a square-based, tubular INCONEL 718 part



Fig. 2 Top area of part in y - z cross section

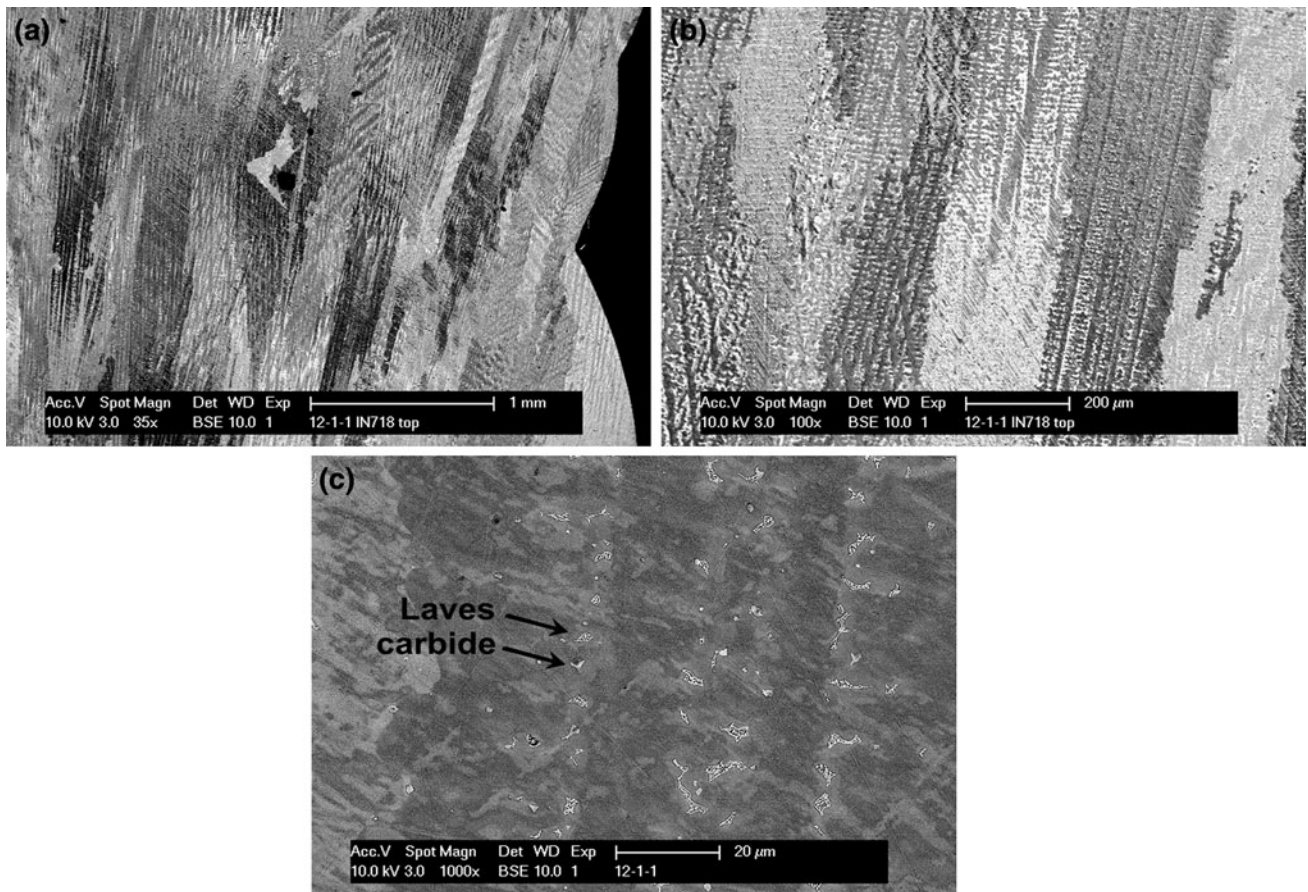


Fig. 3 SEM micrographs (y - z plane) exhibiting the elongated grains and the dendritic microstructure at different magnifications (a–c). (a) Contour of the wall surface at right

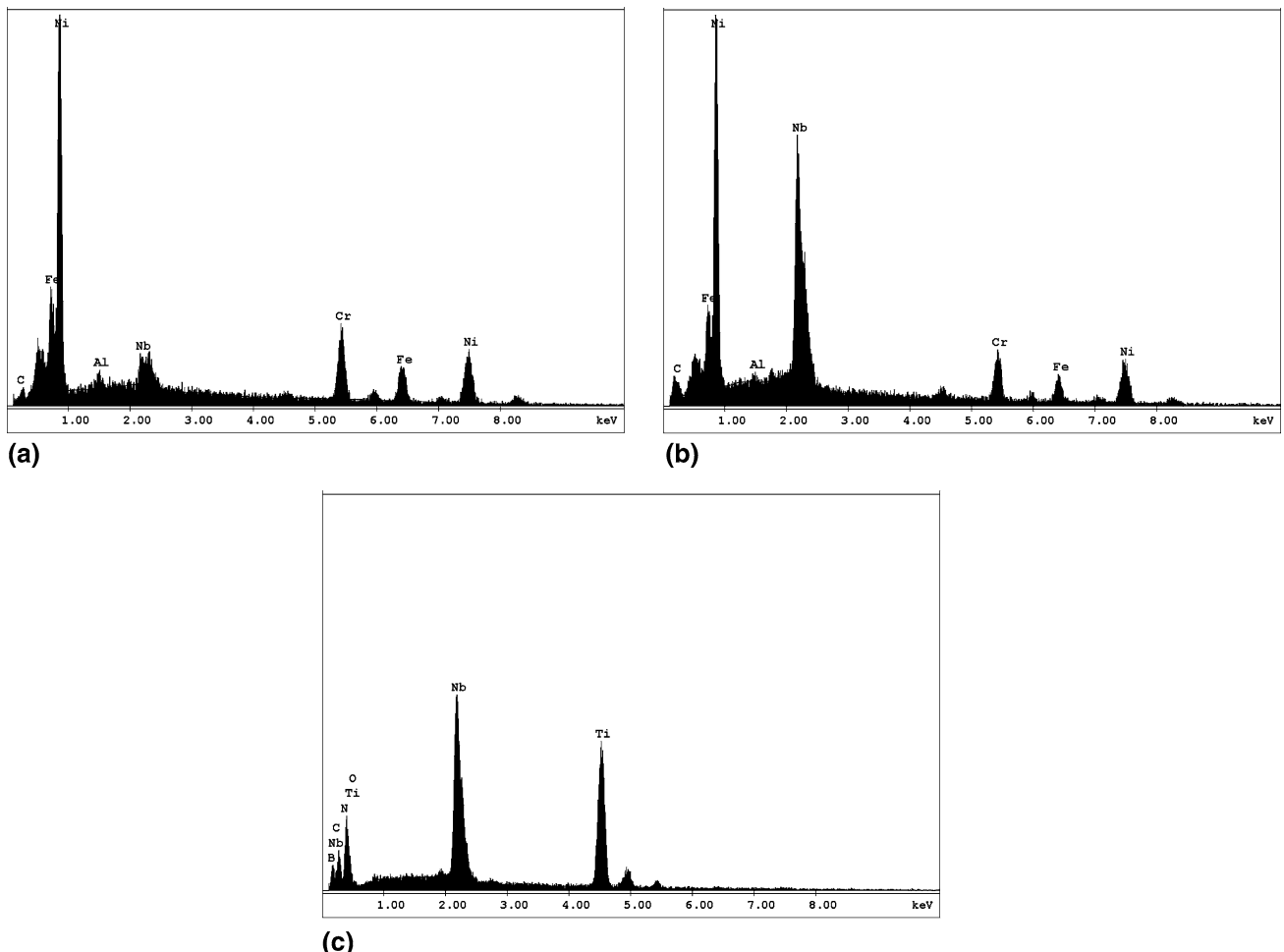


Fig. 4 EDX spectra from matrix (a), Laves phase (b), and MC-type carbide (c)

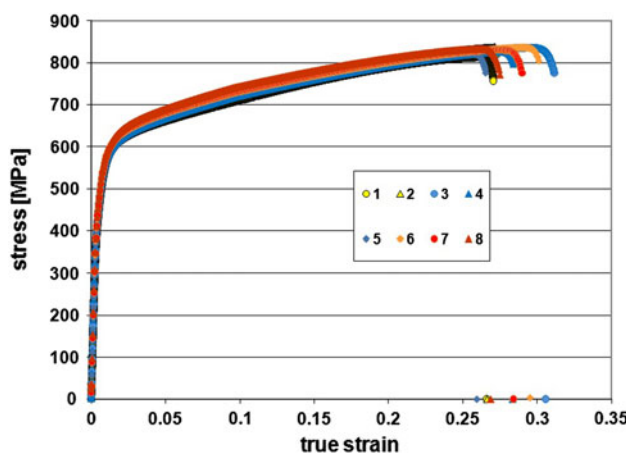


Fig. 5 Stress–true strain curves of INCONEL 718 SMD specimens tested with different strain rates: 10^{-4} 1/s (1, 2), 10^{-3} 1/s (3, 4, 5), and 2×10^{-3} 1/s (6, 7, 8)

2.2 Mechanical Testing and Microstructure Characterisation

The tensile testing was performed with an Instron testing machine model 4505 under strain rate control, applying an extensometer with a gauge length of 25 mm, and different strain rates, namely, 10^{-4} 1/s (specimen 1 and 2), 10^{-3} 1/s

(specimen 3, 4, and 5), and 2×10^{-3} 1/s (specimen 6, 7, and 8). The strain at failure was determined from the plastic true strain at failure. Flat dog bone-shaped tensile specimens with a $4 \times 2 \text{ mm}^2$ cross section were cut by electrical discharge machining, with their tensile axis perpendicular to the deposition plane, and then grinded. The Young's modulus was not only derived from the elastic part of the stress-strain curve, but also by applying the impulse excitation technique (Ref 23) (IMCE, Diepenbeek, Belgium). The specimen was a bar with the dimensions of $25 \times 8 \times 3 \text{ mm}^3$.

Optical and scanning electron microscopy (SEM, FEI XL30FEG) on polished or etched (with NITAL) cross sections was applied to investigate the microstructure. Energy dispersive x-ray spectrometry was applied for elemental analysis.

The Vickers microhardness was measured with a Leitz microhardness tester with a load of 200 g. Several indents on a $y-z$ plane at different heights relative to the base plane were executed.

3. Results

3.1 Shape, Morphology, and Microstructure

The surface of the INCONEL 718 SMD walls is rippled reflecting the layerwise deposition. The top side is round due to

the surface tension in the liquid state (Fig. 1). The optical micrograph of the etched cross section exhibits large, columnar grains extending in the direction of the wall height across many deposition layers (Fig. 2). No pores, cracks, or regions of bad fusion are observed.

The SEM of Fig. 3(a) shows in more detail these grains in addition to the contour of the rippled surface. The ripples derive from the melt of subsequent SMD steps, and it is worthy to note that no interrelation between the grains and the ripples is observable. In contrast to reports from additive manufacturing

of INCONEL 718 applying laser (Ref 21) or electron beam techniques (Ref 18), no evidence of banded structures reflecting the individual passes of the deposition is found.

The grains consist of a fine dendritic microstructure with different precipitates, characterizing the interdendritic boundaries (Fig. 3b, c). After etching the cross section, one type of precipitates shows a substructure, while the other does not. Examples of EDX spectra from the matrix and from the two different types are given in Fig. 4. Compared to the matrix (Fig. 4a), the precipitates with substructure is rich in Nb (Fig. 4b), while the other type contains Nb, Ti, and lighter elements, such as C, N, and B (Fig. 4c). According to the literature, the microstructure of Inconel 718 is governed by the fcc lattice structure of the γ matrix and a number of characteristic precipitates, where not only the chemical compositions of the precipitates but also by their distribution, location, and possible coagulation during thermal and mechanical treatments are decisive in the microstructural development (Ref 24). In weld metals and heat-affected zones, the two main

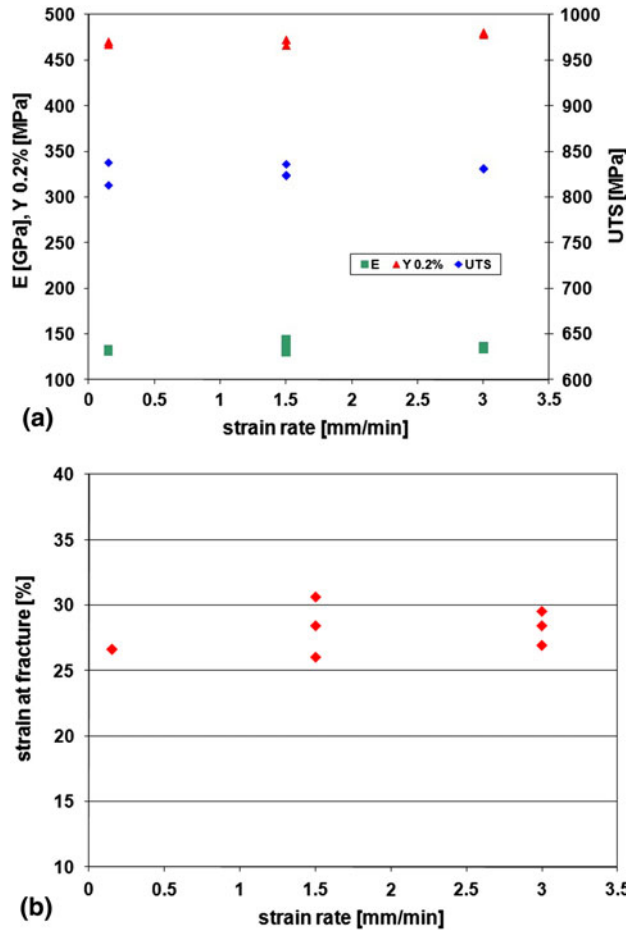


Fig. 6 Compilation of test results depending on the strain rate. (a) Ultimate tensile strength (UTS), yield strength at 0.2% $\sigma_{0.2\%}$, and Young's modulus E . (b) Plastic true strain at failure

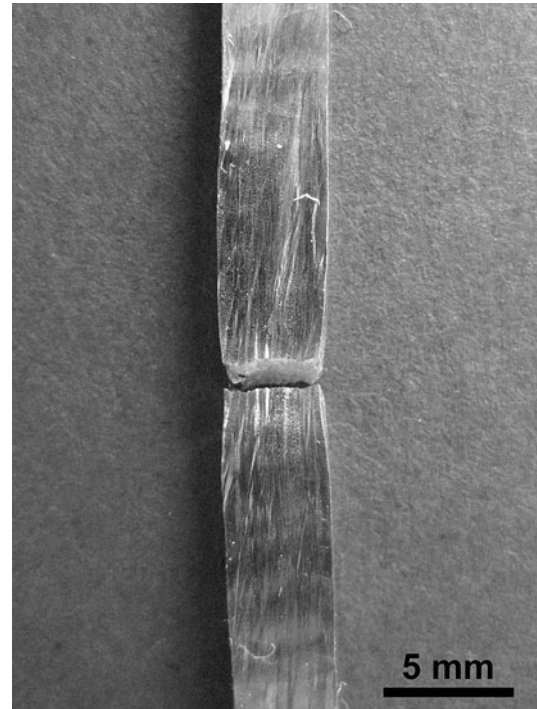


Fig. 7 Tensile specimen after failure

Table 1 Mechanical properties of SMD parts in comparison of additive manufactured by laser or electron beam and of as-cast material

	UTS, MPa	$\sigma_{0.2\%}$, MPa	E , GPa	$\varepsilon_{\text{plastic}}$, %
SMD	828 ± 8	473 ± 6	Stress-true strain: 135 ± 4 IET: 154 ± 1	28 ± 2
Laser (Ref 19)	845	590	n.a.	11
Laser (Ref 20)	1000	650	n.a.	n.a.
Laser (Ref 21)	904	552	n.a.	16
Electron beam (Ref 18)	910	580	159	22
As cast (Ref 18)	786	488	n.a.	22

n.a.: not analyzed

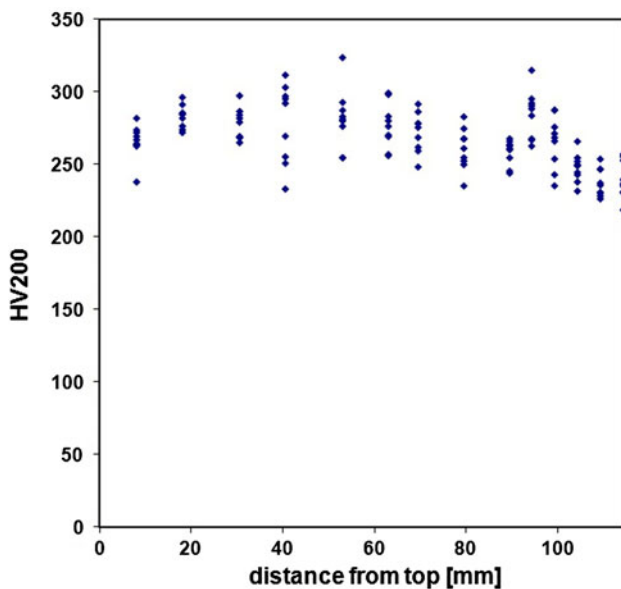


Fig. 8 Micro Vickers hardness in dependence on the distance from the top (y - z plane)

types of precipitates are Nb-rich Laves phase and Nb(Ti)-rich MC-type carbides (Ref 25). Accordingly, the precipitates with substructure have been attributed to the Laves phase, and the other to the MC carbides (Fig. 3).

3.2 Mechanical Testing

Figure 5 presents the stress-true strain curves for different strain rates. All the curves exhibit yielding, extensive plasticity with strain hardening, and comparable values of strength and strain at failure. As the compilation of the results shows (Fig. 6), no strain rate sensitivity is observed. In Table 1, the averages, from all the eight experiments, of the ultimate tensile strength, UTS, the yield strength $\sigma_{0.2\%}$, the Young's modulus E , and the plastic true strain $\varepsilon_{\text{plastic}}$ as an indication for the ductility are compared with results of parts additive manufactured by laser and electron beam, and, in addition, with the properties of as-cast material. The strength and strain values of SMD specimens are comparable or slightly better than as reported for the as-cast material. Compared with specimens from additive manufactured by laser or electron beam, their strengths are inferior, and their plastic strain at failure values are superior. Naturally the strength of the as-deposited material is lesser in comparison to that of wrought material or to that of material subjected to special heat treatment for performance improvement, and dedicated heat-treatment promises improvements (Ref 20-22). However, improved strength may be accompanied with decreased ductility (Ref 20-22). This will be investigated in a future article (Ref 16).

The Young's modulus, derived from the stress-true strain curve, is 135 GPa. However, the determination of the Young's modulus by this method may include some experimental error (IET); a much more reliable method, gives 154 GPa. This value agrees very well with results reported for INCONEL 718 parts additive manufactured by electron beam (Ref 18). Nevertheless, these results are much lower than the Young's modulus of 206 MPa reported by Fukuhara for INCONEL 718 (Ref 26). The authors of Ref 18 have attributed the low values to the strong texture of additive manufactured parts.

Figure 7 shows a specimen after failure exhibiting a distinctive surface relief and necking due to the extensive plasticity before the final fracture. Noteworthy is the development of a banded structure parallel to the deposition plane of the SMD component, possibly reflecting the deposition layers.

Figure 8 shows the micro Vickers hardness depending on the distance from the top. As usually observed for microhardness measurements, the results exhibit a large scatter. Within this scatter, no clear dependency of the results on the location can be reported. If at all, the values are slightly lower near the base plate. The average of all the results gives 266 ± 21 HV200.

4. Conclusions

It has been shown that the additive layer manufacturing method of SMD is suitable for near net-shaped processing of dense INCONEL 718 parts, introducing this technique for mass customization. The tensile strengths of these parts are slightly higher than that of the as-cast material but lower than those of parts fabricated by other additive layer manufacturing techniques. This is possibly related to the lower cooling rates than in the case of techniques based on laser or electron beam. The true strain at failure of SMD specimens proved to be superior to specimens from parts fabricated by other additive layer manufacturing techniques or from the as-cast material. Dedicated heat treatment possibly can increase the strength of SMD parts, but probably at the expense of the ductility. The choice of this technique will therefore depend on the application according as whether a higher strength or ductility is preferred.

Acknowledgments

The research has been performed as part of the RAPOLAC STREP project under contract number 030953 of the Sixth Framework Programme of the European Commission (<http://www.RAPOLAC.eu>), which is gratefully acknowledged. The parts have been built at AMRC, Sheffield, the United Kingdom in association with the team of Dr. Rosemary Gault, and the experimental evaluation has been performed at the Katholieke Universiteit Leuven, Belgium, in association with the team of Prof. Omer van der Biest. The supports provided by them and their staff are highly acknowledged.

References

1. K. Cooper and S. Lambrakos, Thermal Modeling of Direct Digital Melt-Deposition Processes, *J. Mater. Eng. Perform.*, 2011, **20**, p 48–56
2. C. Charles and N. Järvstrat, Development of a Microstructure Model for Metal Deposition of Titanium Alloy Ti-6Al-4V, *11th World Conference on Titanium (Ti-2007)* (Kyoto, Japan), 2007, p 1201–1204
3. C. Charles and N. Järvstrat, Modelling Ti-6Al-4V Microstructure by Evolution Laws Implemented as Finite Element Subroutines: Application to TIG Metal Deposition, *8th International Conference on Trends in Welding Research*, (Pine Mountain, GA), 2008
4. B. Baufeld and O. van der Biest, Mechanical Properties of Ti-6Al-4V Specimens Produced by Shaped Metal Deposition, *Sci. Technol. Adv. Mater.*, 2009, **10**, p 10
5. B. Baufeld, O. van der Biest, and S. Dillien, Texture and Crystal Orientation in Ti-6Al-4V Builds Fabricated by Shaped Metal Deposition, *Met. Mater. Trans. A*, 2009, **41**, p 1917–2010

6. B. Baufeld, O. van der Biest, and R. Gault, Microstructure of Ti-6Al-4V Specimens Produced by Shaped Metal Deposition, *Int. J. Mater. Res.*, 2009, **100**, p 1536–1542
7. B. Baufeld, O. van der Biest, and R. Gault, Additive Manufacturing of Ti-6Al-4V Components by Shaped Metal Deposition: Microstructure and Mechanical Properties, *Mater. Des.*, 2010, **31**, p S106–S111
8. B. Baufeld, O. van der Biest, R. Gault, and K. Ridgway, Manufacturing Ti-6Al-4V Components by Shaped Metal Deposition: Microstructure and Mechanical Properties, *TRAM 2009, IOP Conference Series: Materials Science and Engineering* (Sheffield, UK), 2010
9. A.K. Swarnakar, O. van der Biest, and B. Baufeld, Thermal Expansion and Lattice Parameters of Shaped Metal Deposited Ti-6Al-4V, *J. Alloy Compd.*, 2011, **509**, p 2723–2728
10. C. Leyens and M. Peters, *Titanium and Titanium Alloys*, Wiley-VCH, Weinheim, 2003
11. M. Katou, J. Oh, Y. Miyamoto, K. Matsuura, and M. Kudoh, Freeform Fabrication of Titanium Metal and Intermetallic Alloys by Three-Dimensional Micro Welding, *Mater. Des.*, 2007, **28**, p 2093–2098
12. T. Skiba, B. Baufeld, and O. van der Biest, Microstructure and Mechanical Properties of Stainless Steel Component Manufactured by Shaped Metal Deposition, *ISIJ Int.*, 2009, **49**, p 1588–1591
13. T. Skiba, B. Baufeld, and O. van der Biest, Shaped Metal Deposition of 300M Steel, *Proc. IME B J. Eng. Manufact.*, 2011, **255**, p 831–839
14. D. Clark, M. Bache, and M. Whittaker, Shaped Metal Deposition of a Nickel Alloy for Aero Engine Applications, *J. Mater. Process. Technol.*, 2008, **203**, p 439–448
15. R.A.J. Jeniski and R.L. Kennedy, Nickel-base Superalloy Designed for Aerospace, *Adv. Mater. Process.*, 2006, **164**, p 19–22
16. B. Baufeld and A.K. Swarnakar, Influence of Heat Treatment on the Mechanical Properties of IN718 Parts Built by Shaped Metal Deposition (SMD), in preparation
17. S.G. Lambrakos and K.P. Cooper, An Algorithm for Inverse Modeling of Layer-by-Layer Deposition Processes, *J. Mater. Eng. Perform.*, 2009, **18**, p 221–230
18. R.K. Bird and J. Hibberd, Tensile Properties and Microstructure of INCONEL 718 Fabricated with Electron Beam Freeform Fabrication (EBF3), *NASA* (Hampton, VA), 2009, p 14
19. J.E. Matz and T.W. Eagar, Carbide Formation in Alloy 718 During Electron-Beam Solid Freeform Fabrication, *Metall. Mater. Trans. A*, 2002, **33**, p 2559–2567
20. X. Zhao, J. Chen, X. Lin, and W. Huang, Study on Microstructure and Mechanical Properties of Laser Rapid Forming INCONEL 718, *Mater. Sci. Eng. A*, 2008, **478**, p 119–124
21. P.L. Blackwell, The Mechanical and Microstructural Characteristics of Laser-Deposited IN718, *J. Mater. Process. Technol.*, 2005, **170**, p 240–246
22. H. Qi, M. Azer, and A. Ritter, Studies of Standard Heat Treatment Effects on Microstructure and Mechanical Properties of Laser Net Shape Manufactured INCONEL 718, *Metall. Mater. Trans. A*, 2009, **40**, p 2410–2422
23. G. Roebben, B. Bollen, A. Brebels, J. van Humbeeck, and O. van der Biest, Impulse Excitation Apparatus to Measure Resonant Frequencies, Elastic Moduli, and Internal Friction at Room and High Temperature, *Rev. Sci. Instrum.*, 1997, **68**, p 4511–4515
24. A.J. Brand, K. Karhausen, and R. Kopp, Microstructural Simulation of Nickel Base Alloy INCONEL 718 in Production of Turbine Discs, *Mater. Sci. Technol.*, 1996, **12**, p 963–969
25. G. Knorovsky, M. Cieslak, T. Headley, A. Romig, and W. Hammetter, INCONEL 718: A Solidification Diagram, *Metall. Mater. Trans. A*, 1989, **20**, p 2149–2158
26. M. Fukuhara and A. Sanpei, Elastic Moduli and Internal Frictions of INCONEL 718 and Ti-6Al-4V as a Function of Temperature, *J. Mater. Sci. Lett.*, 1993, **12**, p 1122–1124

The mechanical and microstructural characteristics of laser-deposited IN718

P.L. Blackwell*

QinetiQ Ltd., Cody Technology Park, Room G069, A7 Building, Ively Road, Farnborough GU14 0LX, UK

Received 4 May 2004; accepted 16 May 2005

Abstract

The paper is concerned with the application of laser deposition to the nickel-based superalloy INCONEL™ 718 (IN718). Several blocks of material were manufactured using the LENS™ process and subsequently heat treated and tensile tested. Following this, further sections of the original blocks were hot isostatically pressed (HIPed) and then reassessed for mechanical properties and microstructure. It was found that prior to HIPing the deposit exhibited anisotropic properties that appeared to be associated with non-optimised processing conditions. HIPing led to a reduction in anisotropy within the deposit, but generated considerable grain growth within the (IN718) substrate.

© 2005 Qinetiq. Published by Elsevier B.V. All rights reserved.

Keywords: INCONEL™ 718; Laser deposition; Nickel; LENS™

1. Introduction

The direct laser deposition (DLD) process, sometimes also referred to as the direct laser fabrication technique, is a manufacturing method that allows the die-less production of metal parts direct from powder. It is essentially a derivative of a rapid prototyping process that has been used for some years for polymeric materials. The DLD process involves feeding the metal powder through a nozzle into the focal point of a laser beam, which then melts the powder producing a deposit onto a pre-existing substrate. For generating structural shapes, the powder nozzle and the beam are moved relative to the metal surface in a raster pattern. A component is then built up layer by layer until the required shape is obtained. Modern systems feature five axis heads that allow complex geometries to be built up using computerised control similar to those found on CNC machining centres. Applications for the DLD process include the repair of worn parts, e.g. turbine blades, and the manufacture of components that feature complex internal geometries that would be difficult to machine or cast, e.g. plastic injection moulding dies.

The present investigation centred on the nickel-based superalloy IN718. This alloy is one of the most widely used

superalloys, having found numerous applications in the aero-engine, e.g. as a turbine disk material, for shafts and as compressor blades. It is also used in cryogenic applications. The alloy is age-hardenable via the precipitation of the metastable form of the delta (δ) phase (Ni_3Nb), known as δ' .

The purpose of the investigation was to examine some commercially produced IN718 deposit and to compare its mechanical and microstructural characteristics to wrought product. The deposition technology used was that of the LENS™ process. This features a 4 kW Nd-YAG laser, which is capable of close control in terms of the accuracy of deposition.

2. Experimental procedure

The deposit was laid down on wrought IN718 substrate material; the block dimensions are shown in Fig. 1. The original substrate measured 170 mm × 40 mm × 30 mm and the deposit was built up on top of this to a final size of 170 mm × 80 mm × 30 mm. Fig. 1 illustrates the location of the tensile testpieces that were taken from the blocks following deposition. It will be noted that testpieces 1–3 were taken across the bond-line and included both the substrate and deposit; the intention being to assess any bond-line weakness.

* Tel.: +44 1252 392000; fax: +44 1252 397491.

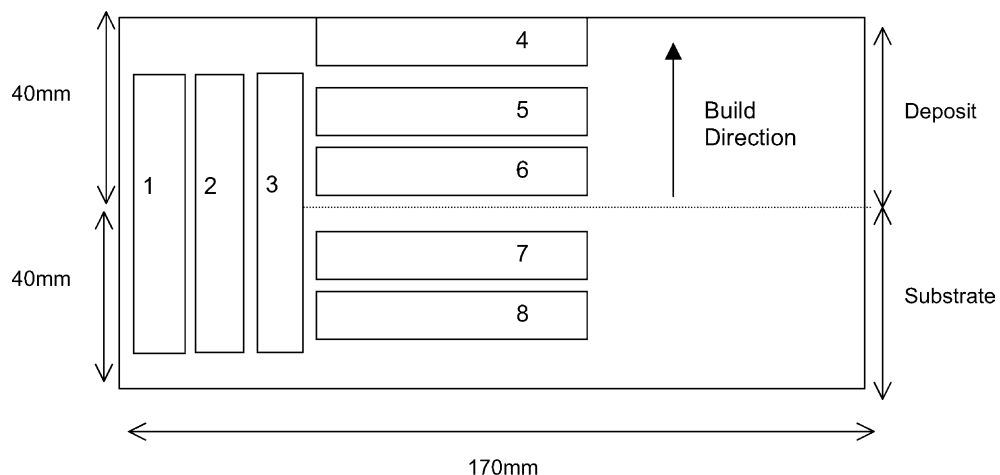


Fig. 1. Cut-up diagram for the laser-fabricated blocks.

The tensile tests were carried out using an applied strain rate of 10^{-3} s^{-1} at room temperature.

Several states of heat treatment were examined; tests were carried out on the deposit in either the as-deposited, deposited + (double) aged, or, in the fully heat-treated condition. The heat treatment used was a 980°C , 1 h, air cool solution treatment followed by a double age (720°C , 8 h, furnace cool + 620°C , 8 h, air cool). This is a standard heat treatment used for this material. In addition, a number of as-deposited blocks were hot isostatically pressed (HIPed) at 1160°C for 3 h with a pressure of 100 MPa and then fully heat-treated.

Following testing, several of the fracture faces were examined using scanning electron microscopy, while the microstructure was examined using an electron backscatter pattern (EBSP) technique.

3. Experimental results

One of the blocks from which the testpieces were extracted is shown in Fig. 2. In practice, the blocks were fabricated with the substrate at the bottom (Fig. 1)—the picture shows the block standing on one end. It will be noted that the deposit surface was reasonably smooth and accurately laid down onto the substrate.

3.1. Mechanical properties

The tensile test results are presented in Table 1. It may be seen that the as-deposited material gave relatively low proof (PS) and ultimate tensile strengths (UTS) with a high ductility. Reference figures for fully heat-treated wrought material are included in the Table 1 [1].

Following ageing, the PS and UTS of the deposit rose considerably to give values above that typical for wrought material. However, the elongation at 13% was low. If the deposit was fully heat-treated then the strengths increased still further. It was notable that the elongation figure for the

substrate was unusually high although the PS and UTS were broadly in line with that for wrought material.

The testpieces that were positioned across the bond-line (cross-bond) tended to exhibit strengths that reflected those of the deposit, albeit at a reduced level, and all gave very poor elongations.

The tensile strengths following HIPing are presented in Table 2. It is notable that the strength values obtained for



Fig. 2. Overall view of test-block. The substrate is on the right hand side, the dimensions were as given in Fig. 1.

Table 1
Tensile test results

Sample description	0.2% PS (MPa)	UTS (MPa)	Reduction in area (%)
As-deposited	650	1000	38
Deposit + age	1204	1393	13
Deposit + full heat-treatment	1257	1436	13
Substrate	1152	1358	47
Cross-bond (as-deposited)	612	650	4.6
Cross-bond (aged)	1110	1162	4.6
Cross-bond (fully heat-treated)	1142	1244	5
Wrought IN718 (typical)	1125	1365	20

the cross-bond testpieces and from the substrate were closely comparable. However, the elongation for the cross-bond testpieces was about half of that for the substrate. Examination of the gauge area of the tensile specimens suggested that the cross-bond testpieces had failed within the substrate and that very little deformation had occurred within the deposit. This would explain both the similarity of the tensile strength noted above and the reduction in elongation for the cross-bond testpieces. Testpieces taken from the deposit exhibited strengths and ductilities similar to that for wrought product.

Comparing these results with those for the non-HIPed samples shows that for the cross-bond testpieces the HIP operation had produced a considerable increase in ductility. This was, however, accompanied with a reduction in strength. For the testpieces taken from the deposit there was an improvement in ductility, albeit of a more modest level than that noted for the cross-bond testpieces. Within the substrate region there had been a marked decrease in ductility together with a reduction in strength.

3.2. Microstructural observations

Fig. 3a shows the fracture face from one of the cross-bond testpieces with the deposit left in the as-received state, i.e. with no heat treatment or HIPing. It may be seen that the surface exhibited a clear patterning. At a higher magnification

Table 2
Tensile results following HIPing and full heat treatment

Testpiece no.	0.2% PS (MPa)	UTS (MPa)	Reduction in area (%)
Cross-bond	1003	1159	17.5
	984	1138	14.5
	997	1158	16.5
	997	1155	17.5
	978	1148	16.0
Deposit	1147	1381	19.5
	1121	1355	20.5
	1173	1389	20.0
	1178	1393	21.5
Substrate	957	1162	30.0
	966	1174	30.5
	956	1161	29.0
	958	1173	32.0

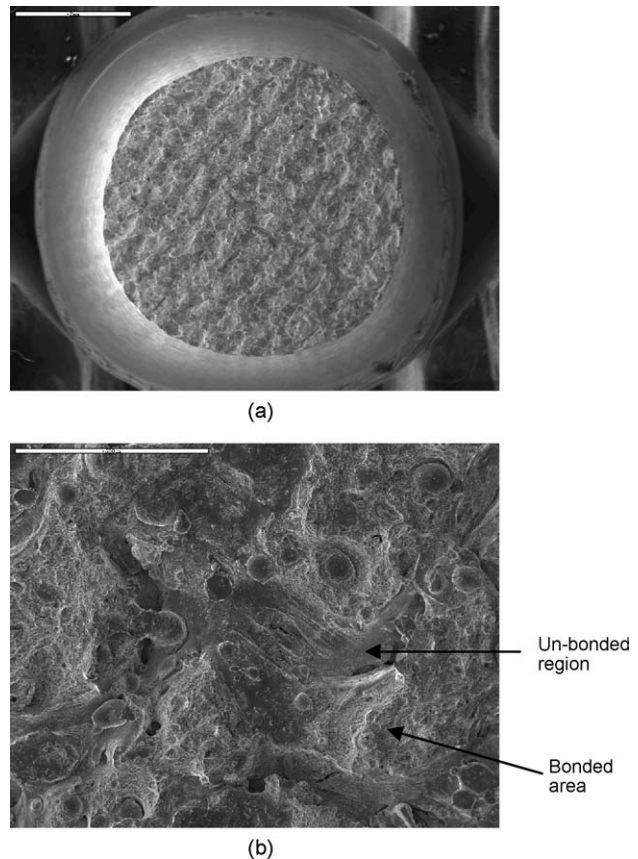


Fig. 3. Fracture face from a cross-bond testpiece prior to heat treatment or HIPing; (a) shows the overall fracture face which exhibited a patterning effect (marker 2 mm) and (b) close-up showing areas that were apparently not bonded (marker: 500 μm).

the surface appeared as shown in Fig. 3b. A number of features may be noted. Firstly, there were areas where micro-void formation had occurred indicating a ductile failure. There were, however, other areas where the surface was relatively smooth and where it appeared that there was a lack of bonding between successive layers of the deposit. In addition, numerous spherical particles could be seen, which were likely to be non-melted powder particles from the original deposition process.

Fig. 4a shows the overall view of the fracture face of a testpiece that was taken from within the deposit; in this case, the IN718 had been fully heat-treated (though not HIPed). It is not entirely apparent from Fig. 4a but the fracture had formed shear lips around the outer circumference of the gauge; though apart from this the fracture face was fairly flat. At a higher magnification there was again evidence of a significant amount of un-melted powder, which may be clearly seen in Fig. 4b and c. Apart from this there was considerable micro-void formation.

Fig. 5 shows the fracture face from one of the cross-bond testpieces following heat treatment. The majority of the fracture surface was relatively flat (Fig. 5a) and a visual inspection revealed a pattern similar to that shown in Fig. 3. Again, there

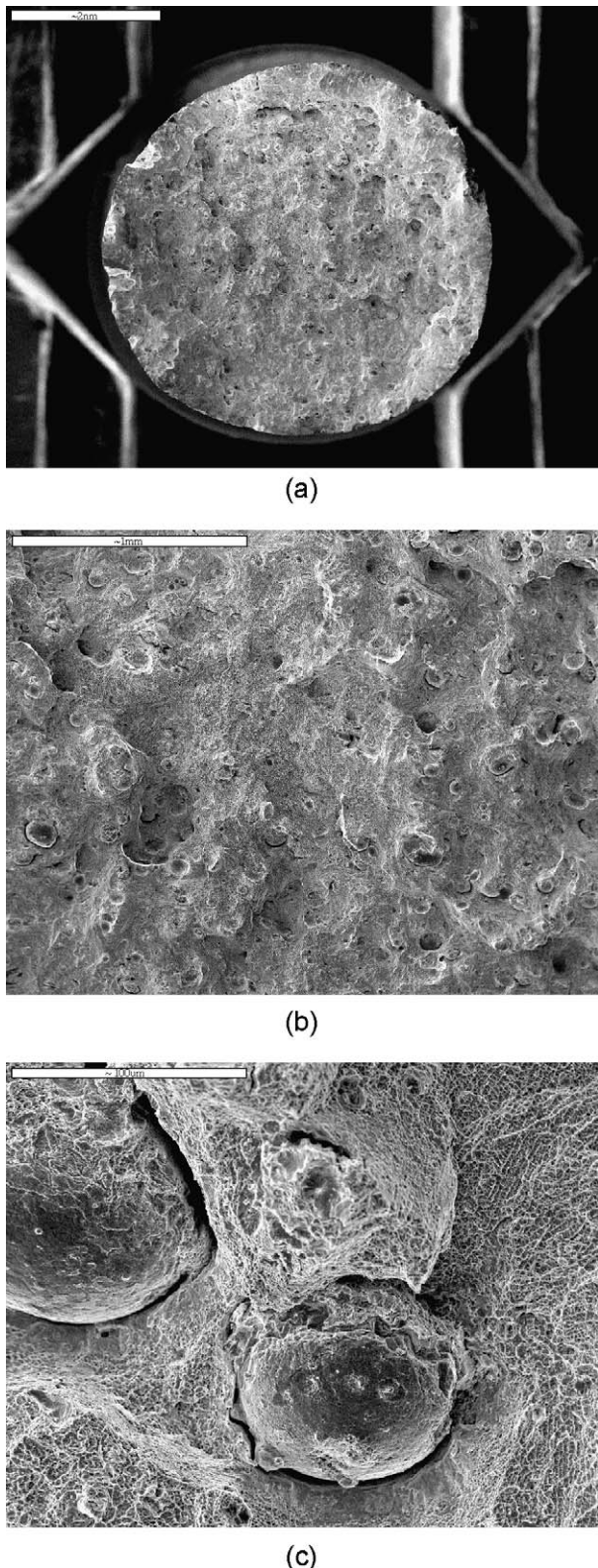


Fig. 4. Heat-treated deposit: (a) overall fracture surface (marker 2 mm) and (b and c) evidence of un-melted powder (marker: 1 mm and 100 μm , respectively).

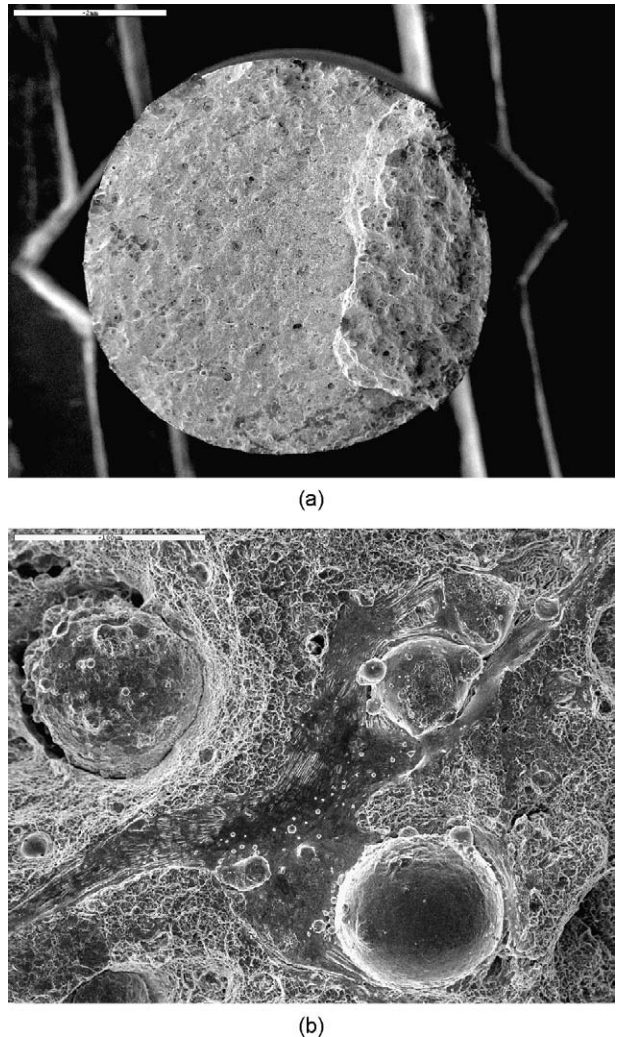
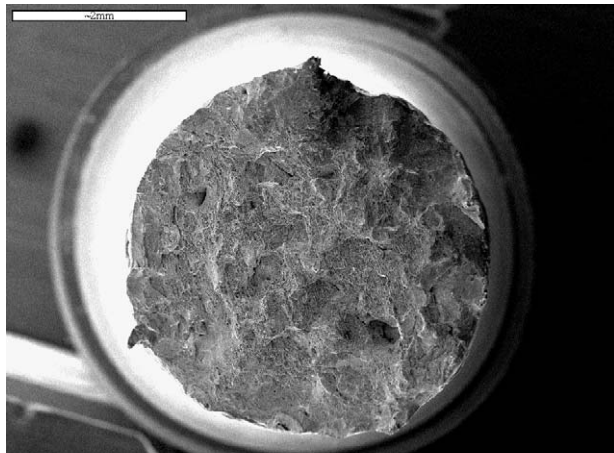


Fig. 5. Fully heat-treated cross-bond testpiece: (a) overall fracture face (marker: 2 mm) and (b) high magnification view (marker: 100 μm).

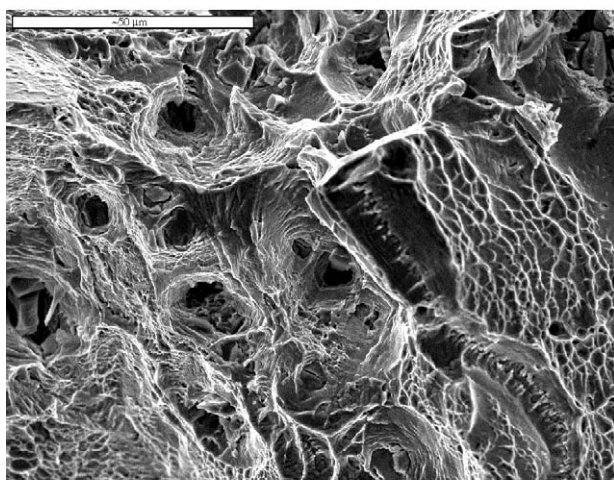
was extensive evidence of non-assimilated particles and areas that had not bonded. Fig. 6 shows the fracture surface from a post-HIP and fully heat-treated testpiece that was taken across the bond-line. The testpiece appeared to have failed within the substrate. Failure appeared to be primarily via micro-void coalescence (Fig. 6b).

Fig. 7 shows metallographic detail from the as-deposited material. At a high magnification a fine dendritic cast structure was apparent, indicative of a high cooling rate. At lower magnification, evidence of the individual passes of the laser could be seen in the form of a series of arcs, each arc corresponding to a specific pass. Similar structures have been noted in Ti-6Al-4V by Gorman et al. [2].

Fig. 8 shows the grain structure within the fully heat-treated deposit (prior to HIP); the image was obtained using EBSP. The different shades of grey represent different orientations. This revealed a banded structure within the deposit with some of the bands containing fine equiaxed grains and others containing coarser columnar grains.



(a)



(b)

Fig. 6. Deposit following HIPing and heat treatment: (a) overall fracture face (marker: 2 mm) and (b) micro-void coalescence (marker: 50 μm).

The interface region is featured in Fig. 9, with the deposit lying on the right hand side of the figure. This is included for reference against Fig. 10, which shows a similar area following HIPing. This difference was dramatic. The high temperatures associated with the HIP operation had allowed considerable grain growth to take place within the substrate. In the deposit, the grains had become equiaxed though little grain growth had taken place.

4. Discussion

Based on the evidence of the tensile tests, it appeared that in the as-deposited state the IN718 was effectively in a solution-treated condition. Subsequent ageing generated a marked increase in strength accompanied by some loss of ductility. The elongation, at 13%, was low when compared to fully heat-treated wrought material, but might be acceptable

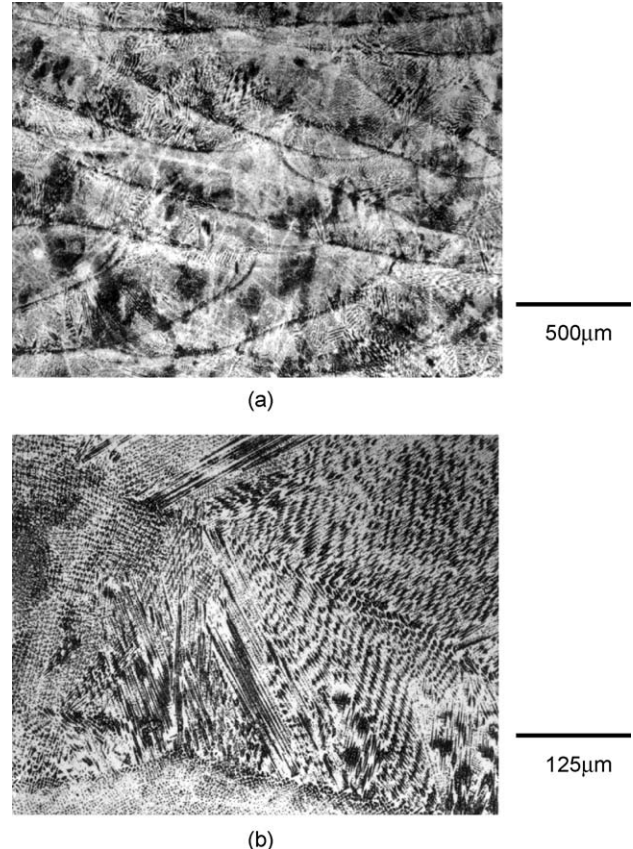


Fig. 7. As-deposited IN718 showing evidence of individual passes and (b) detail of dendritic structure within a single pass.

in some applications. The post-deposition full heat treatment produced a slight improvement in strength compared to the as-aged properties, but this was not particularly significant. With respect to the use of this technology for repair then,

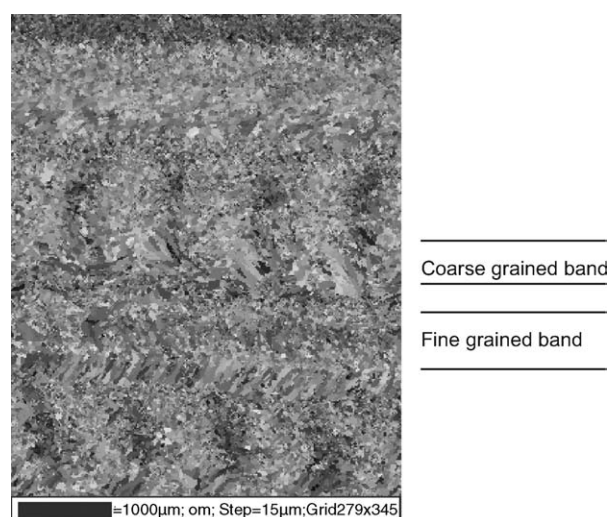


Fig. 8. Electron back-scatter patterned (EBSP) image showing grain structure within as-deposited material. The grain colours correlate to different orientations. There was no evidence for epitaxial growth.

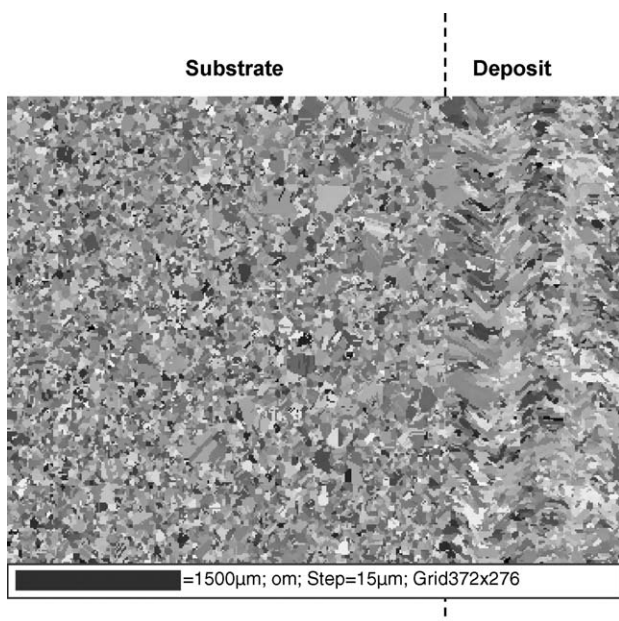


Fig. 9. EBSP image of the interface region following heat treatment.

based on the above, it would be necessary to use a post-deposition ageing treatment to develop acceptable properties.

The fact that such a strong ageing response was obtained indicates that the cooling rates following deposition were significant—at least rapid enough that ageing was suppressed. With regard to the substrate, the results indicated that the deposition process was not unduly affecting the substrate, although, the high ductility noted for the substrate in Table 1 suggests that the material may have been slightly under-aged.

The low strengths noted for the cross-bond testpieces were probably related to the low elongations. There appeared to be two possible reasons for the poor ductility:

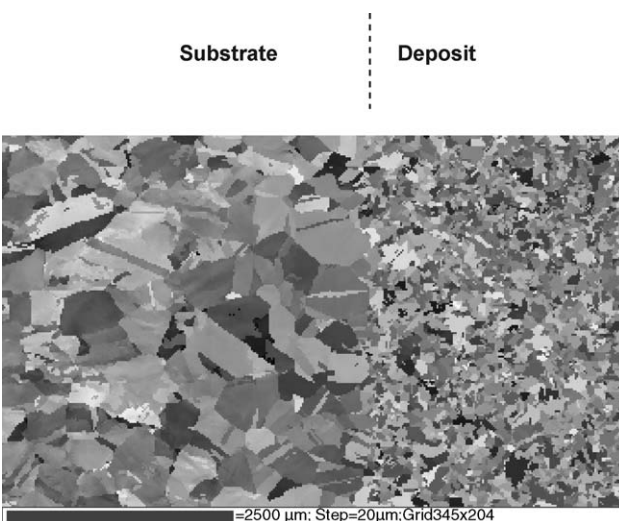


Fig. 10. Interface zone following HIPing and heat treatment. This shows that considerable grain growth occurred within the substrate material.

- (1) the substrate/deposit bond was weak, or,
- (2) the deposit was strongly anisotropic.

This can be resolved with reference to the fractographic results. Considering firstly the pre-HIPed material, it was noted that testpieces, which have been taken parallel to the build direction, often exhibited a criss-cross pattern on the fracture face (Fig. 3a). This was almost certainly a result of the rastering pattern of the laser during the original deposition process. For the production of the blocks used in this investigation a step spacing of ~0.4 mm was used for each pass across the surface; this correlates well with the pattern size. There also appeared to be areas where the bonding between successive layers was interrupted (Figs. 3b and 5b). A rough estimation would suggest that up to 30% of the fracture surface may not have been bonded. The low ductilities measured in this direction for the pre-HIP material was, therefore, not surprising.

Another feature of the fracture faces shown in Figs. 3–5 was the presence of what appeared to be un-melted powder. This may have been present either as a result of the fact that during the initial deposition there was excessive powder being sprayed into the melt pool, or it may be over-spray powder that settled onto the semi-molten surface after the deposition head had moved away. Whatever the cause, there was evidence to suggest that the process was not under optimum control. Following HIPing, the patterning effect was not observed and it may be assumed that the HIPing operation had successfully bonded any previously un-bonded areas. Similar effects were noted by Kobryn et al. [3]. They used Ti–6Al–4V alloy and found that when tested parallel to the build direction the elongations were as low as 0.8%; HIPing increased this to ~12%.

Fig. 8 reveals that the deposit had a complex grain structure. To manufacture blocks as large as those examined here, laser passes were made both along the length of the blocks (170 mm) and also across the width (30 mm). This was alternated—one layer would be deposited length-wise and then one across the width. Now, given that the deposition parameters (laser speed and step size) were held constant then, for any point on the surface, the time between the laser passing over that point and returning for the next, adjacent pass (in the same layer), was much shorter when the material was being deposited across the width. Hence, the cooling rates for the two deposition directions would have reflected this. The bands of finer grains, associated with higher cooling rates, would have been the result of the longitudinal passes. Much of the work that has been carried out to examine the structure of laser-deposited material has focused on titanium alloys and often on relatively thin-walled sections created using a few longitudinal passes. These often feature elongated grain structures generated as a result of the occurrence of epitaxial growth between layers [4]. There was no evidence of epitaxial growth in the present material. This may be due to the significant difference in the relative thermal conductivity of titanium and nickel, leading to

higher cooling rates for IN718 which may have suppressed any tendency for epitaxial growth. The EBSP data indicated that the crystallographic texture within the deposit was random.

The effect of HIPing on the material behaviour was significant. As noted, the high temperature used for the HIPing process allowed considerable grain growth to take place within the substrate (see Figs. 9 and 10). Prior to HIPing the substrate grain size was $\sim 125 \mu\text{m}$; following HIPing this increased to $\sim 500 \mu\text{m}$. The increase in grain size accounts for the reduced strengths and elongations noted in the substrate results from Table 2. The grain growth also produced a significant change in the failure behaviour of the cross-bond testpieces; prior to HIPing these testpieces failed in the deposit (Figs. 3 and 5). Following HIPing, failure occurred in the substrate. The effect of the HIPing in generating an improved bond between successive layers within the deposit, combined with the substrate grain growth, appeared to have led to the substrate becoming weaker than the deposit.

The reason for the difference in grain size stability between the deposit and the substrate was unclear. The HIPing operation was performed at 1160°C . This is well above the delta solvus for IN718 and hence grain growth was expected. What was surprising was that the grain size within the deposit did not increase to the same degree. It is possible that fine second phase particles (oxides, carbides) may have been incorporated into the material from the original powder surfaces, or, that they could be generated during the deposition process. Such particles would tend to inhibit grain growth. A systematic investigation of this issue was not carried out, but it is intended that further work will be performed as part of a follow-on programme.

5. Summary

Investigation of commercially sourced laser-deposited IN718 has shown that, prior to HIPing, the deposit exhibited strongly anisotropic properties. This appeared to be associated with a lack of bonding between successive layers of the deposit and points to the need for further research on deposition parameters. A subsequent HIPing operation significantly reduced the anisotropy and eliminated any evidence of poor interlayer bonding.

Acknowledgements

The author gratefully acknowledges both the MOD and the DTI who jointly funded this project as part of ARP 04 and the DTI Aeronautics Research Programme (formerly CARAD), respectively.

References

- [1] High-Temperature, High-Strength Nickel Base Alloys, No. 393, Nickel Development Institute (NiDI), 1995.
- [2] P. Gorman, J.E. Smugeresky, D.M. Keicher, Enhanced process window evaluation for laser engineered powder metal deposition, Proc. Int. Conf. on Metal Powder Deposition for Rapid Manufacturing, Compiled by D. Keicher, J.W. Sears, J.E. Smugeresky, Metal Powder Industries Federation, 2002, pp. 121–127.
- [3] P.A. Kobryn, S.L. Semiatin, Mechanical properties of laser-deposited Ti-6Al-4V, in: D.L. Bourell, J.J. Beaman, R.H. Crawford, H.L. Marcus, K.L. Wood, J.W. Barlow (Eds.), Proceedings of the Solid Freeform Fabrication Symposium 2001, The University of Texas, Austin, TX, August 6–8, 2001, pp. 179–186.
- [4] P.A. Kobryn, S.L. Semiatin, The laser additive manufacture of Ti-6Al-4V, *JOM* 53 (9) (September 2001) 40–42.

Study on microstructure and mechanical properties of laser rapid forming Inconel 718

Xiaoming Zhao, Jing Chen, Xin Lin, Weidong Huang *

State Key Laboratory of Solidification Processing, Northwestern Polytechnical University, Xi'an 710072, PR China

Received 31 March 2007; received in revised form 21 May 2007; accepted 22 May 2007

Abstract

InconelTM 718 (IN718) has been deposited using laser rapid forming (LRF) from the gas atomized (GA) and plasma rotation electrode preparation (PREP) powders. The mechanical properties of LRF IN718 were evaluated and compared in between as-deposited and heat-treated state. The results show that the existence of the porosities in as-deposited samples, caused by the hollow particles in the GA powders, results in the low ductility and stress rupture properties for LRF GA IN718, since it will promote the occurrence of the micro-porous coalescence failure in the tensile samples. However, the ultimate tensile strength for heat-treated LRF GA IN718 is comparable to that of the wrought IN718, which is 1.5 times of that of the as-deposited samples. It is found that there exists a continuous thin film of Nb-rich MC carbides along the grain boundaries on the fracture surface of the stress rupture samples, which makes cracks initiate and propagate along this path easily, which also results in the poor stress rupture life for LRF GA IN718. The porosities and microcracks in LRF sample were successfully eliminated by using PREP powders, which leads to a substantial improvement in both tensile and stress rupture properties of LRF IN718.

© 2007 Elsevier B.V. All rights reserved.

Keywords: Laser rapid forming; IN718; Microstructure; Mechanical properties

1. Introduction

Laser rapid forming (LRF), also referred to as laser engineered net shaping (LENS), direct light fabrication (DLF), etc., is a promising technology based on a new additive manufacturing principle, which combines laser cladding with rapid prototyping into a solid freeform fabrication process for manufacturing fully dense metallic parts with high performance. During LRF, by moving the laser beam and CNC working table to generate certain trajectories, fine metal powders are laser deposited onto the substrate to fabricate three-dimensional components layer by layer in near-net shape without die, thus leading to the savings of delivery time and manufacturing cost. Meanwhile, fine microstructure can be obtained due to the non-equilibrium rapid solidification process, which leads to superior mechanical properties. Recently, with rapid development of LRF, more and more focuses have been directed to the manufacture of components [1–6], some with complex internal geometries, e.g. injection molding die, and the applications in the

repairing of damaged parts [7–9], e.g. damaged turbine blades, disk and so on. In fact, the high replacement costs of gas turbine engine components (disks, blades, etc.) bring LRF an important potential application in the repair of worn or damaged components. LRF can be used to repair and even produce gas turbine components with lower heat input and local heating. It provides remarkable benefits over the conventional welding processes through accurate control of the solidification microstructure and heat input.

IN718 is a niobium-modified nickel-base superalloy, which has been widely used in aeronautic, astronautic and nuclear industries for its good strength, excellent resistance to oxidation at high temperatures, and favorable weldability. It derives its good mechanical properties with temperature being elevated from a fine dispersion of D0₂₂-ordered γ'' and L1₂-ordered γ' precipitates in a face centered cubic matrix γ . But niobium segregation generally could not be avoided in wrought products made from large size ingots, which will lead to the formation of macro-segregation, freckles, laves phase and white spots, and result in a large scatter in the mechanical properties. So the dimension of IN718 ingots is usually limited to a certain value. In order to eliminate such segregation, powder metallurgy (P/M) route was also introduced into the preparation of

* Corresponding author. Tel.: +86 29 88494001; fax: +86 29 88494001.

E-mail address: huang@nwpu.edu.cn (W. Huang).

Table 1
Chemical composition of IN718 powder alloy(wt%)

Element	IN718 powders	AMS:5663
Fe	18	16–20
Cr	19	17–21
Al	0.5	0.2–0.8
Ti	1	0.65–1.15
Mo	3	2.8–3.3
Nb	5	4.75–5.5
C	0.042	0.08 max
Ni	Balance	Balance

this alloy [10,11]. On comparison with P/M, LRF has the same advantage due to its rapid solidification process which results in fine microstructure and getting free of such defects. With this in mind, the present work focuses on the experimental investigation on the microstructure and mechanical properties of LRF IN718 deposited from gas atomized (GA) and plasma rotation electrode preparation (PREP) powder, and the influencing factors for the improvement in mechanical properties were also analyzed.

2. Experimental

The experiments were carried out on a LRF equipment, which consists of a 5 kW ROFIN-SINAR continuous wave CO₂ laser, a LPM-408 CNC working table, a DPSF-1 powder feeding system with the error of powder feeding rate of $\pm 2\%$ and an off-axial nozzle. Pure argon was used as shielding gas, which constrains the powder particles into a jet stream with the diameter of about 3.5 mm and simultaneously prevents both the molten pool and the heat affected zone from being contaminated. The GA and PREP IN718 powders with the powders sizes of 44–150 μm , were laser deposited, respectively on the stainless steel substrate with the size of 100 mm \times 50 mm \times 6 mm. The substrate surface was ground with SiC paper and cleaned with acetone prior to be laser-deposited. The dimension of the LRF samples is designed as 85 mm \times 15 mm \times 15 mm. The chemical composition of IN718 powders is shown in Table 1. The processing parameters are illustrated in Table 2. The as-deposited samples were heat treated with the following schedule: homogenization treatment (1080 °C, 1.5 h/air cooling) + solution treatment (980 °C, 1 h/air cooling) followed by double aging (720 °C, 8 h/furnace cooling + 620 °C, 8 h/air cooling). Samples were machined to prepare the standard tensile and stress rupture testing bars, the shape and size of which are shown in Fig. 1. Rockwell hardness tests after each treatment were also carried out, and each data presented was the average of nine measurements.

Table 2
Processing parameters of the LRF route

Laser powder (W)	2350
Scanning velocity (mm/s)	8
Spot diameter (mm)	3
Powder feeding rate (g/min)	6
Shielding gas flow (l/min)	7.5

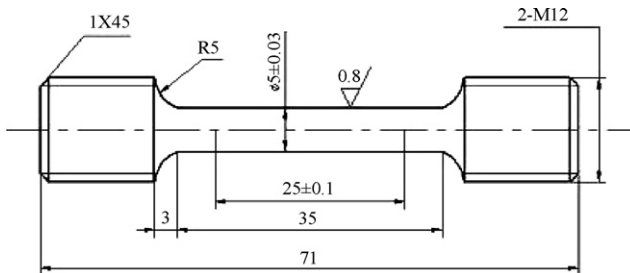


Fig. 1. Sketch of standard tensile and stress rupture testing bars.

LRF IN718 samples for microstructure observation were machined by wire electrolytic-discharge machine. The microstructure of the material was revealed using an etchant of a mixture of H₂O, HCl and H₂O₂ with the volume ratio of 8:4:2. The microstructure were examined by optical microscope. The fracture surface was characterized by scanning electron microscopy (SEM) to correlate the fracture characteristics with microstructure and properties. Energy dispersive X-ray spectrometer (EDS) was also utilized to characterize the chemical compositions of the selected fracture surface.

3. Results and discussion

3.1. The typical mechanical properties of LRF GA IN718

The tensile and stress rupture properties of LRF GA IN718 in as-deposited and heat-treated state, are presented in Tables 3 and 4, respectively. For comparison, the properties of wrought and cast IN718 are also included. Tensile strength (ultimate strength (UTS) and yield strength (0.2% YS)) of the as-deposited GA samples, are inferior to that of typical wrought alloy, but its ductility is much higher (reduction in area (RA), 26%). After heat treatment, the tensile strength of LRF GA IN718 is comparable with that of wrought IN718, which is approximately 1.5 times of that of the as-deposited samples. However, there is a remarkable decrease in ductility for heat treated LRF GA samples ((RA): from 26% to 6%, the elongation (EL): from 11% to 9%). however these properties might be acceptable in some applications, such as the repair of worn parts. The stress rupture tests were carried out for heat-treated

Table 3
Tensile testing results of LRF GA IN718

Material condition (25 °C)	UTS (MPa)	0.2% YS (MPa)	EL (%)	RA (%)
As-deposited	845	590	11	26
LRF + heat treatment	1240	1133	9	16
Wrought IN718	1340	1100	12	15

Table 4
High temperature stress rupture properties of LRF GA IN718

Material condition	Test condition	Rupture life (h)	EL (%)
LRF + heat treatment	650 °C/620 MPa	9	2.8
Cast IN718	650 °C/620 MPa	≥23	≥3

LRF GA IN718 under the condition of 650 °C/620 MPa. Both the rupture life and ductility of LRF GA IN718 were much less than those of cast IN718. It is also shown that the average hardness (HRC41) for heat-treated samples increased remarkably on comparison with as-deposited samples (HRC17). It is noticeable that for aging-hardening IN718, a significant improvement can be obtained through the suitable heat treatment which cause the sufficient precipitation of γ'' and γ' . The high cooling rates (about 10^3 K s $^{-1}$) during the LRF actually suppresses the subsequent aging of the alloy after laser rapid solidification, leading to a poor strength for as-deposited samples. Thus, if LRF is used to repair the worn IN718 components or manufacture the IN718 components, it is necessary to develop reasonable heat treatment schedule to obtain sufficient aging γ'' and γ' precipitates.

3.2. Typical microstructure of LRF IN718

Fig. 2(a)–(c) shows the morphology of GA IN718 powder and the microstructure of LRF GA IN718. It can be seen there are many hollow particles in the GA IN718 powder (**Fig. 2(a)**), which should be caused by the gas entrapping in the GA powder preparation process. During the LRF process, the inert gas entrapped in the hollow particles, could not escape easily from the molten pool due to the high cooling rate, which results in the porosities in the LRF GA IN718 samples (**Fig. 2(b)** and (c)). **Fig. 2(d)** shows the typical as-deposited microstructure of LRF PREP IN718, which is free of porosities. Comparing between **Fig. 2(b)** and (d), it can be seen that microstructure of LRF GA

and PREP IN718 alloy was similar except the porosities existing in the GA IN718 samples.

Typical microstructure of the as-deposited samples is featured in **Fig. 2(b)–(d)**. LRF IN718 sample completely consists of columnar dendrites which grow epitaxially from the substrate, and generally along the $\langle 100 \rangle$ crystallographic orientation, being parallel to the deposition direction. There also exists a thin layer at the top of the sample where the dendrites grow along the laser scanning direction, referred as the direction changing dendrites (**Fig. 2(c)**). The average primary arm spacing is about 5 μm due to the rapid solidification process in LRF, which was an important reason for the superior mechanical properties of LRF IN718 samples free of defects. After heat treatment, recrystallization takes place in the LRF samples (**Fig. 3**). Insufficient recrystallization can be clearly seen along the deposition direction in the samples. In this paper, the homogenization treatment operation was performed at 1080 °C. This is higher than the delta solvus temperature of 1010 °C for IN718. Hence after subsequent quenching, recrystallization is expected, a group of curved, or serrated, grain boundaries were developed (**Fig. 3**). On the other hand, the reserved deforming energy, due to the high residual stress [12] introduced by LRF, also further drove recrystallization. The average grain size after recrystallization is about 200 μm . As compared to the grain size obtained by wrought and the HIP treatment, this grain size is relatively coarser. However, at elevated temperature, it leads to the superior stress rupture properties of LRF PREP IN718 samples (**Table 6**).

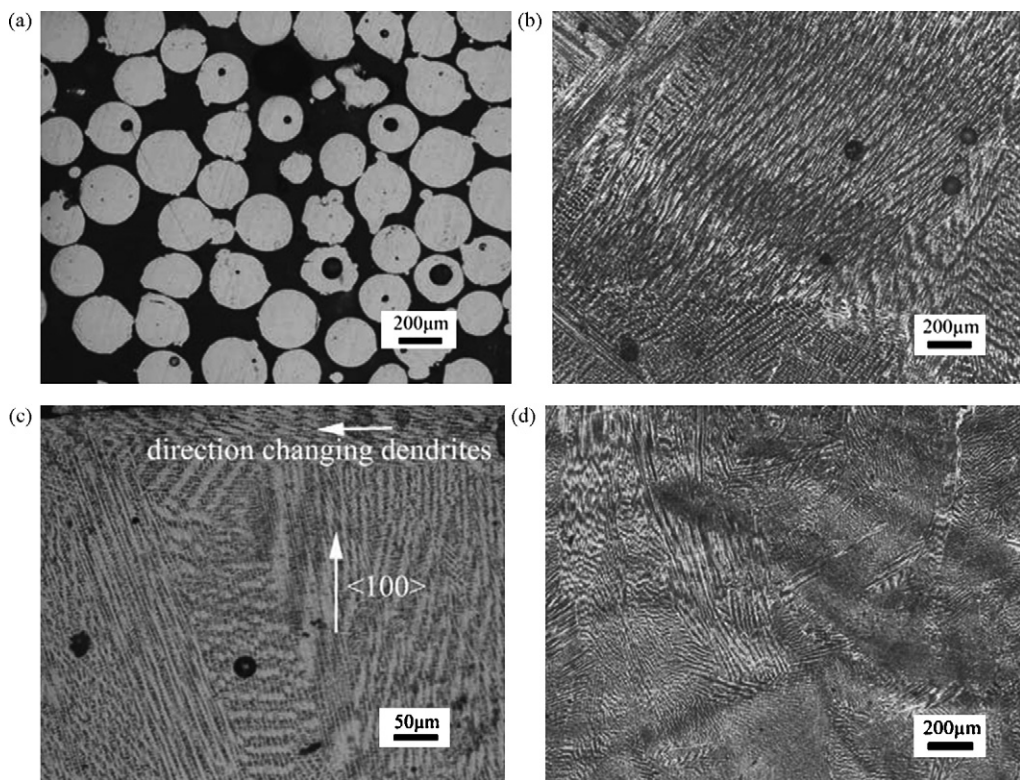


Fig. 2. Optical micrograph of IN718 powder particles and microstructure of LRF In718: (a) GA IN718 powder particles; (b) typical as-deposited microstructure of LRF GA IN718; (c) the direction changing dendrites at the top section of the GA IN718 samples; (d) typical as-deposited microstructure of LRF PREP IN718, free of porosities.

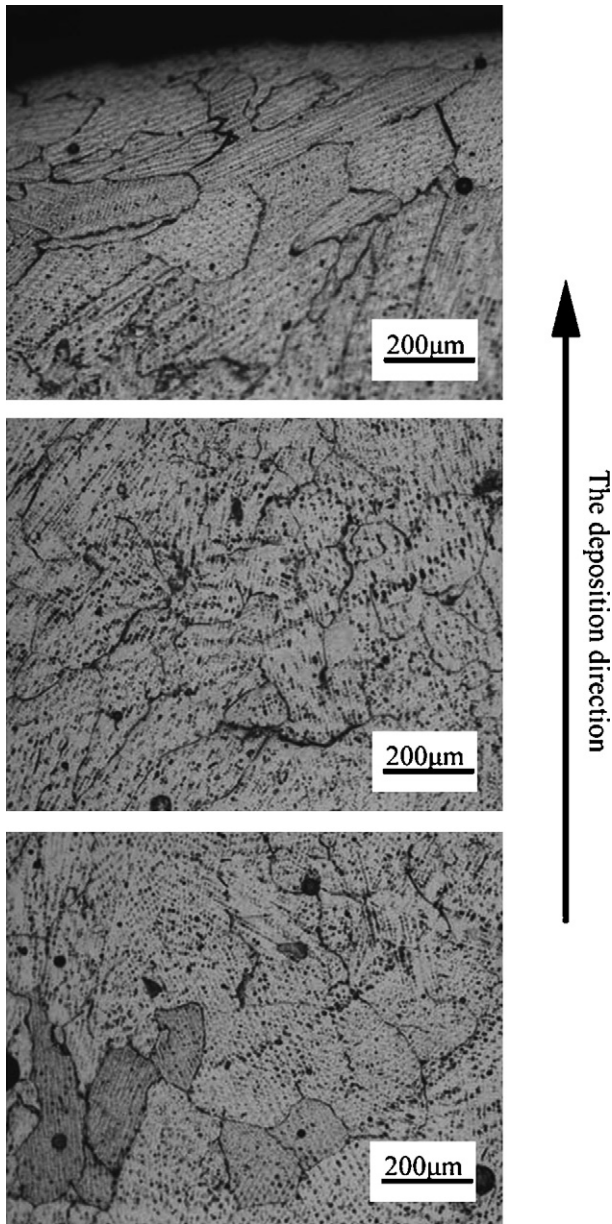


Fig. 3. Recrystallized microstructure of LRF GA IN718 after heat treatment.

3.3. Fracture mechanism

As shown in Fig. 2(b) and (c), there are porosities in the LRF GA IN718 samples. Fig. 4(a) reveals the porosities are coalescing to form a crack under the stress induced by the tensile testing. Actually, the existence of the porosities is easy to cause direct micro-porous coalescence, without the micro-pores initiating during the general fracture course of such alloy. So the tensile strength of as-deposited sample shows a little lower than that of the Wrought IN718. In addition, both the fractography of as-deposited (Fig. 4(b)) and heat-treated (Fig. 4(c)) samples exhibit a considerable amount of dimples, which is the typical characteristic of ductile fracture. It can also be seen that the dimples after the heat treatment are much smaller and more uniform than that in the as-deposition state, which is attributed to a small

dispersion ordered γ'' and γ' coherent precipitates, this enhances yielding strength after heat treatment.

Fig. 4(d) shows the fractography of the stress rupture samples. Microcrack surface can be found. The microcrack plays a role as the crack initiator. EDS spectrum of the crack initiation site in Fig. 4(f), reveals that the selected area is Nb-rich MC type carbides. In fact, during LRF of IN718, if the scanning velocity is relatively low and the forming time interval between two deposition layers is short, MC formation elements will segregate to the grain boundaries, and final MC phases show a continuous distribution. Fig. 4(e) shows a typical HAZ liquation microcrack surface during LRF. Similar influence of minor elements C, B and P on the weldability of Inconel 718-Type superalloy has been discussed elsewhere [13]. At elevated temperature, the crack will initiate and easily propagate along this path, and presents a characteristic of cleavage fracture. So the LRF IN718 samples with such microcrack result in the poor stress rupture life.

3.4. Improvement in mechanical properties of LRF IN718

Based on the above knowledge, it can be deduced the relative low mechanical properties in LRF GA IN718 is mainly attributed to the existence of microcracks and the porosities in the samples due to the hollow particles in GA powders. In order to achieve acceptable mechanical properties, PREP IN718 powder, which is free of hollow particles, was used. It is interesting to note that the average hardness of heat-treated LRF PREP IN718 is same as that of the heat-treated LRF GA IN718, but the average hardness (HRC₂₀) of as-deposited PREP IN718 samples is higher than that of as-deposited GA IN718. The mechanical properties of LRF PREP IN718 are presented in Tables 5 and 6. It is noticeable that both the tensile strength and ductility are superior to wrought IN718. Meanwhile, as compared with the rupture life of 23 h for cast IN718, the stress rupture life (186 h) of heat treated LRF PREP IN718 samples are higher than that of the cast by a factor of approximately 8.0. However, the ductility (1.6%) of the stress rupture samples is still lower than that of the cast IN718 (3%), which might be solved by the reasonable heat treatment. The same problem existing in the HIP route [11] has been relieved by the additional solution treatment at 1270 °C for 1 h followed by re-HIPing, while to some extent, this suggests that the heat

Table 5
Tensile testing results of LRF PREP IN718

Material condition (25 °C)	UTS (MPa)	0.2% YS (MPa)	EL (%)	RA (%)
LRF + heat treatment	1360	1170	18	26
Wrought IN718	1340	1100	12	15

Table 6
High temperature stress rupture properties of LRF PREP IN718

Material condition	Test condition	Rupture life (h)	EL (%)
LRF + heat treatment	650 °C/620 MPa	186	1.6
Cast IN718	650 °C/620 MPa	≥23	≥3

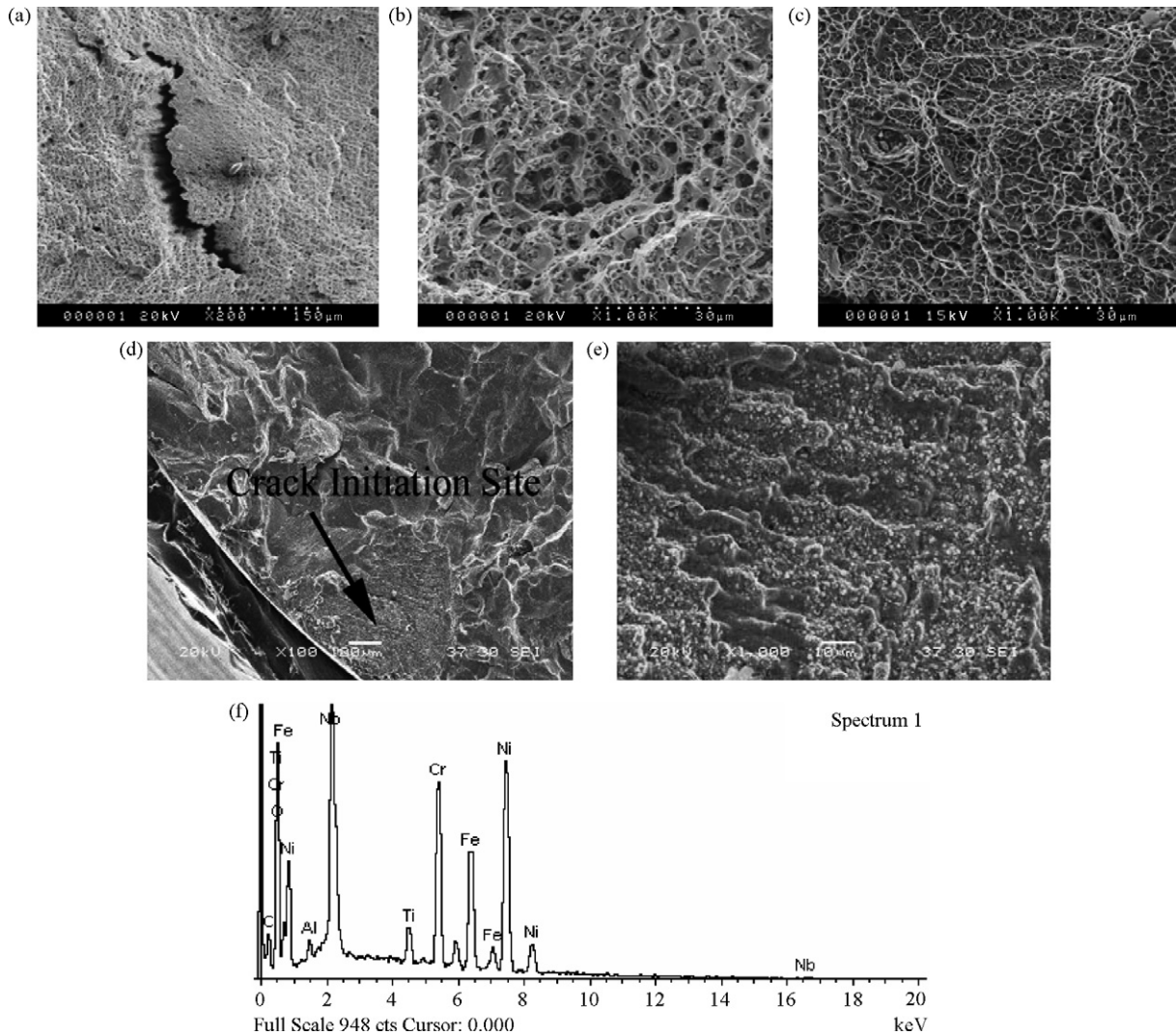


Fig. 4. Fracture surface of the LRF GA IN718: (a) fracture surface showing micro-porous coalescence; (b) fractography of the as-deposited samples; (c) fractography of the LRF + heat treated samples; (d) fractography showing crack initiation site of the stress rupture samples; (e) magnification of the crack initiation site area; (f) EDS spectrum of the crack initiation Site in (d).

treatment used in this paper should be further modified to realize the optimum properties.

4. Conclusions

- (1) Through heat treatment, the tensile strength of LRF GA IN718 samples is comparable with wrought IN718, which is approximately 1.5 times of that of the as-deposited samples. But there is a remarkable decrease in ductility. Both the rupture life and ductility of LRF GA IN718 have been found to be much less than the specified figures for cast IN718. The average hardness (HRC41) for heat-treated samples increased remarkably on comparison with as-deposited samples (HRC17).
- (2) Porosities exist in the LRF In718 samples due to the gas entrapped GA powders. The thin and dense columnar dendrites, whose primary arm spacing is about 5 μm , was an important reason for the superior mechanical properties of LRF IN718 samples free of defects. After heat treatment,

recrystallization takes place in the LRF samples, and the grain size measurement showed an average value of 200 μm , relatively coarser as compared to the grain size by wrought and the HIP route. However, it makes up for the superior stress rupture properties of LRF PREP IN718 at elevated temperature.

- (3) Micro-porous coalescence is the main fracture mechanism of LRF GA IN718 samples during the tensile test. It is recommended that PREP powder should be used in the LRF in order to achieve acceptable mechanical properties. Nb-rich MC type carbides show continuous thin film distribution along the grain boundaries. Crack will initiate and easily propagate along this path, and presents a characteristic of cleavage fracture, which results in the poor stress rupture life.
- (4) The improvement in mechanical properties accomplished by the use of PREP powders, generally meet the specification figures for conventional processed IN718, which makes it possible to explore the near net shape capa-

bility of LRF in the manufacturing and repair of IN718 components.

Acknowledgements

This work was funded by National Natural Science Foundation of China under Grant No. 50331010 and No. 50405038. The work was also supported by Program for New Century Excellent Talents in University.

References

- [1] M. Zhong, L. Yang, W. Liu, Proc. SPIE 5629 (2002) 59–66.
- [2] W. Liu, J.N. DuPont, Acta Mater. 52 (2004) 4833–4847.
- [3] G.K. Lewis, E. Schlienger, Mater. Design 21 (2000) 417–423.
- [4] P.A. Kobryn, E.H. Moore, S.L. Semiatin, Scripta Mater. 43 (2000) 299–305.
- [5] K.I. Schwendner, R. Banerjee, P.C. Collins, C.A. Brice, H.L. Fraser, Scripta Mater. 45 (2001) 1123–1129.
- [6] P.L. Blackwell, J. Mater. Process. Technol. 170 (1–2) (2005) 240–246.
- [7] M. Gaumann, C. Bezencon, P. Canalis, W. Kruz, Acta Mater. 49 (2001) 1051–1062.
- [8] H. Sun, M. Zhong, Proc. SPIE 5629 (2002) 84–92.
- [9] L. Sexton, S. Lavin, G. Byrne, A. Kennedy, J. Mater. Process. Technol. 122 (2002) 63–68.
- [10] G. Appa Rao, Mahendra Kumar, M. Srinivas, D.S. Sarma, Mater. Sci. Eng. A 355 (2003) 114–125.
- [11] G.A. Rao, M. Srinivas, D.S. Sarma, Mater. Sci. Eng. A 418 (2006) 282–291.
- [12] M.L. Griffith, M.E. Schlienger, L.D. Harwell, et al., Mater. Design. 20 (1999) 107–113.
- [13] S. Benhadad, N.L. Richards, M.C. Chaturvedi, Metall. Mater. Trans. A Phys. Metall. Mater. Sci. 33 (2002) 2005–2017.

NASA/TM-2009-215929



Tensile Properties and Microstructure of Inconel 718 Fabricated with Electron Beam Freeform Fabrication (EBF³)

R. Keith Bird
NASA Langley Research Center, Hampton, Virginia

Joshua Hibberd
Old Dominion University, Norfolk, Virginia

NASA STI Program . . . in Profile

Since its founding, NASA has been dedicated to the advancement of aeronautics and space science. The NASA scientific and technical information (STI) program plays a key part in helping NASA maintain this important role.

The NASA STI program operates under the auspices of the Agency Chief Information Officer. It collects, organizes, provides for archiving, and disseminates NASA's STI. The NASA STI program provides access to the NASA Aeronautics and Space Database and its public interface, the NASA Technical Report Server, thus providing one of the largest collections of aeronautical and space science STI in the world. Results are published in both non-NASA channels and by NASA in the NASA STI Report Series, which includes the following report types:

- TECHNICAL PUBLICATION. Reports of completed research or a major significant phase of research that present the results of NASA programs and include extensive data or theoretical analysis. Includes compilations of significant scientific and technical data and information deemed to be of continuing reference value. NASA counterpart of peer-reviewed formal professional papers, but having less stringent limitations on manuscript length and extent of graphic presentations.
- TECHNICAL MEMORANDUM. Scientific and technical findings that are preliminary or of specialized interest, e.g., quick release reports, working papers, and bibliographies that contain minimal annotation. Does not contain extensive analysis.
- CONTRACTOR REPORT. Scientific and technical findings by NASA-sponsored contractors and grantees.

- CONFERENCE PUBLICATION. Collected papers from scientific and technical conferences, symposia, seminars, or other meetings sponsored or co-sponsored by NASA.
- SPECIAL PUBLICATION. Scientific, technical, or historical information from NASA programs, projects, and missions, often concerned with subjects having substantial public interest.
- TECHNICAL TRANSLATION. English-language translations of foreign scientific and technical material pertinent to NASA's mission.

Specialized services also include creating custom thesauri, building customized databases, and organizing and publishing research results.

For more information about the NASA STI program, see the following:

- Access the NASA STI program home page at <http://www.sti.nasa.gov>
- E-mail your question via the Internet to help@sti.nasa.gov
- Fax your question to the NASA STI Help Desk at 443-757-5803
- Phone the NASA STI Help Desk at 443-757-5802
- Write to:
NASA STI Help Desk
NASA Center for AeroSpace Information
7115 Standard Drive
Hanover, MD 21076-1320

NASA/TM-2009-215929



Tensile Properties and Microstructure of Inconel 718 Fabricated with Electron Beam Freeform Fabrication (EBF³)

R. Keith Bird
NASA Langley Research Center, Hampton, Virginia

Joshua Hibberd
Old Dominion University, Norfolk, Virginia

National Aeronautics and
Space Administration

Langley Research Center
Hampton, Virginia 23681-2199

September 2009

Trade names and trademarks are used in this report for identification only. Their usage does not constitute an official endorsement, either expressed or implied, by the National Aeronautics and Space Administration.

Available from:

NASA Center for AeroSpace Information
7115 Standard Drive
Hanover, MD 21076-1320
443-757-5802

Abstract

Electron beam freeform fabrication (EBF³) direct metal deposition processing was used to fabricate two Inconel 718 single-bead-width wall builds and one multiple-bead-width block build. Specimens were machined to evaluate microstructure and room temperature tensile properties. The tensile strength and yield strength of the as-deposited material from the wall and block builds were greater than those for conventional Inconel 718 castings but were less than those for conventional cold-rolled sheet. Ductility levels for the EBF³ material were similar to those for conventionally-processed sheet and castings. An unexpected result was that the modulus of the EBF³-deposited Inconel 718 was significantly lower than that of the conventional material. This low modulus may be associated with a preferred crystallographic orientation resultant from the deposition and rapid solidification process. A heat treatment with a high solution treatment temperature resulted in a recrystallized microstructure and an increased modulus. However, the modulus was not increased to the level that is expected for Inconel 718.

Introduction

Over the past several years NASA Langley Research Center (LaRC) has been developing Electron Beam Freeform Fabrication (EBF³) for the manufacture of near-net-shape and net-shape metallic components (ref. 1, 2). EBF³ offers the potential for efficient streamlined manufacturing of intricate components due to its ability to directly deposit material to only the regions where it is needed. A wide variety of markets is interested in this direct deposition technology which can improve the materials usage efficiency by eliminating the need for machining large quantities of material from wrought blocks and forgings or the fabrication of highly-detailed molds for castings.

Utilization of the EBF³ process for fabrication of Inconel 718 components for high-temperature structural applications is being investigated. Inconel 718 is a widely used superalloy with good weldability (ref. 3), which makes it a good candidate for the EBF³ process. One step in this evaluation process is to determine the mechanical properties of EBF³ deposits and the ability to tailor these properties to specific applications. Two different Inconel 718 EBF³ deposition product forms were fabricated for evaluation of microstructure and room temperature tensile properties. Thin walls were fabricated such that the wall thickness comprised the width of one EBF³ deposit bead. Successive layers were deposited upon each other to fabricate the wall builds. In addition, a bulk deposit was fabricated by making multiple layers of several side-by-side EBF³ deposition passes.

Electron Beam Deposition

Figure 1 shows a photograph of the primary components of the EBF³ system at NASA LaRC used for this investigation. The system uses a high-power electron beam gun in a vacuum environment. The feedstock wire is fed from a spool through the wire feed mechanism. The gun and wire feed are mounted onto a gantry with the capability of translating back and forth along one axis, up and down along the vertical axis, and tilting. The substrate is supported on a table that travels in the transverse direction and has the capability to rotate and tilt. The system is housed within a vacuum chamber with approximate dimensions of 9 ft by 7 ft by 9 ft.

The EBF³ system can be operated manually or via computer code to control the electron beam, wire feed, and translation/rotation parameters to build the desired geometric shapes. During operation, the tip of the wire feed nozzle is brought into close proximity to the substrate. At any given instant the electron beam forms a small molten pool in the substrate. The wire is fed into the beam and the molten pool, thus depositing material at that location. As the electron beam moves away due to the substrate/gun translation the molten pool rapidly solidifies. Detailed discussions of the EBF³ process and this particular system can be found in references 1 and 2.

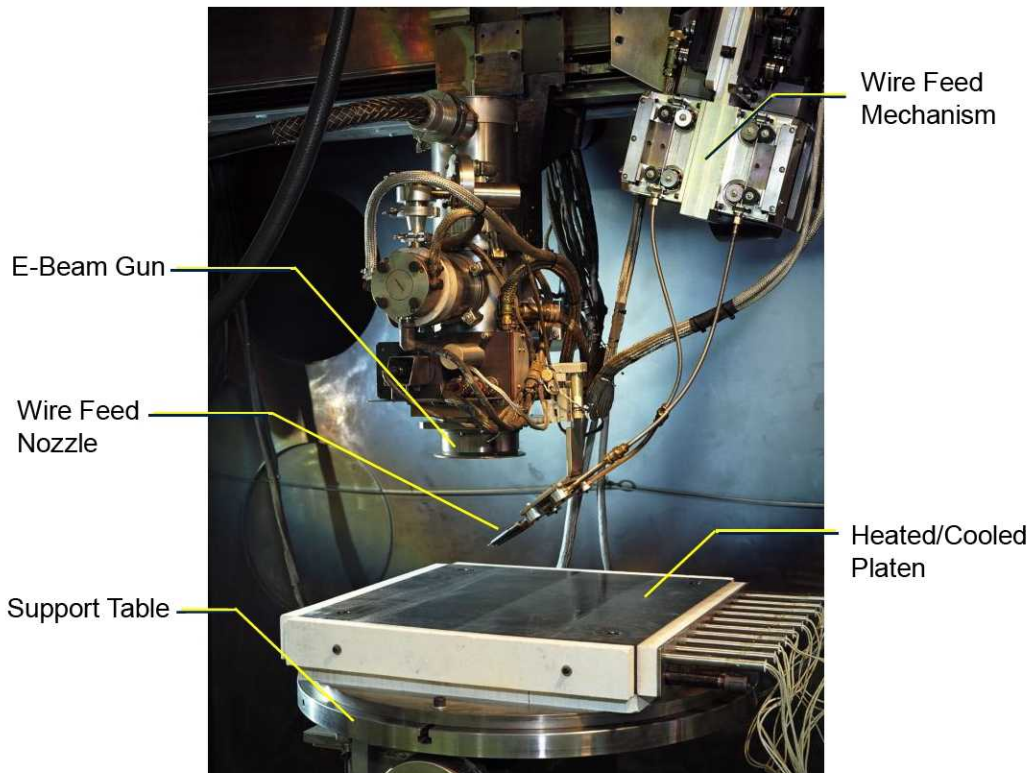


Figure 1. Electron beam freeform fabrication system.

Materials

The base plates and the wires used for the EBF³ wall and bulk block builds were Inconel 718 alloy with nominal composition, in weight percent, of Ni - 19 Cr - 18 Fe - 5.1 (Nb + Ta) - 3 Mo - 0.9 Ti - 0.5 Al (ref. 3). For the wall builds, the base plate was 6 inches by 4 inches by 0.25 inch thick. The wire diameter was 0.045 inch. The block build used a base plate with dimensions of 12 inches square by 0.125 inch thick and a wire diameter of 0.093 inch.

Experimental Procedures

Electron-Beam Freeform Fabrication (EBF³) Process

The base plate was clamped at the four corners to the EBF³ system support table. (The heated/cooled platen shown in Figure 1 was not used for these experiments.) The system was evacuated to the 10⁻⁶ torr range. Parameters for electron beam gun power and deposition rates were selected based on previous work. The electron beam gun was used to preheat the base plate and remove surface oxides in the vicinity of the wall and block builds prior to deposition.

Two walls were fabricated on the same base plate (see Figure 2). The target dimensions of the walls were 5 inches long with height of 2 inches. The wall width was approximately 0.125 inch, which was the width of a single deposit bead using the 0.045-inch diameter wire. The first wall was fabricated with a deposition travel speed of 75 in/min. The second wall was fabricated with a 50-in/min deposition travel speed. During the wall build process, four single-pass beads were deposited successively on top of each other after which the system was allowed to cool for two minutes. This process was repeated until a wall height of nominally two inches was attained. Approximately 50 layers were required to complete each wall.

The target dimensions for the block build were 5 inches long by 1 inch wide with a height of 1 inch (see Figure 3). Preliminary EBF³ deposition studies indicated that the width of a single deposit was approximately 0.180 inch (twice the 0.090-inch wire diameter). To achieve a 1-inch wide block, eight deposits were made side-by-side with a 0.150-inch center-to-center spacing. This spacing produced a 0.030-inch overlap between adjacent deposits to fully fill the volume and avoid porosity. A total of 18 layers were required to build the 1-inch tall block. Each layer was built from the outside towards the center. The left edge was deposited followed by the right edge. Deposits were then made adjacent to the outermost deposits. This process was continued until the two innermost of the 8 deposits were completed for that layer. The block was allowed to cool for approximately 1 minute after each layer was deposited.

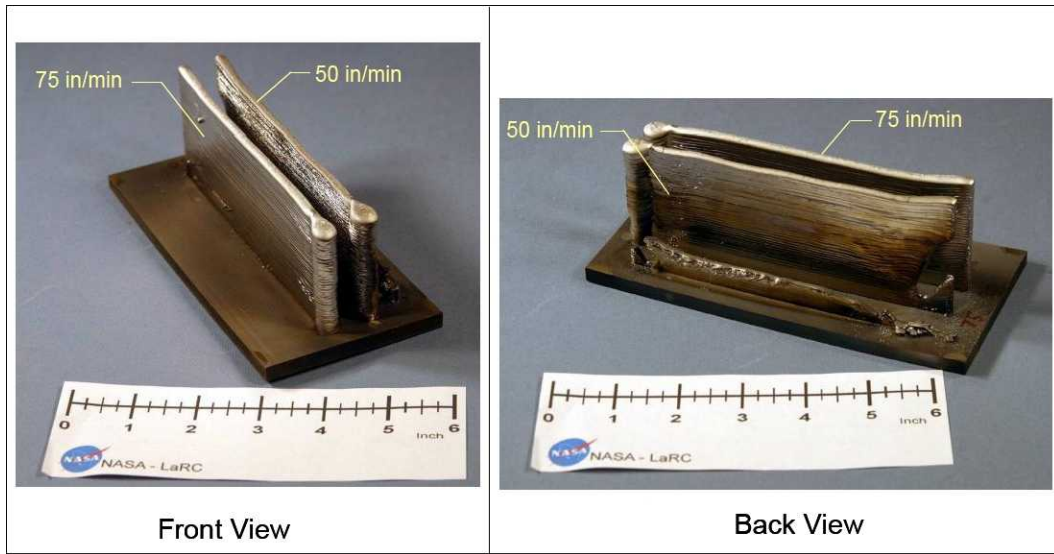


Figure 2. Inconel 718 wall builds.

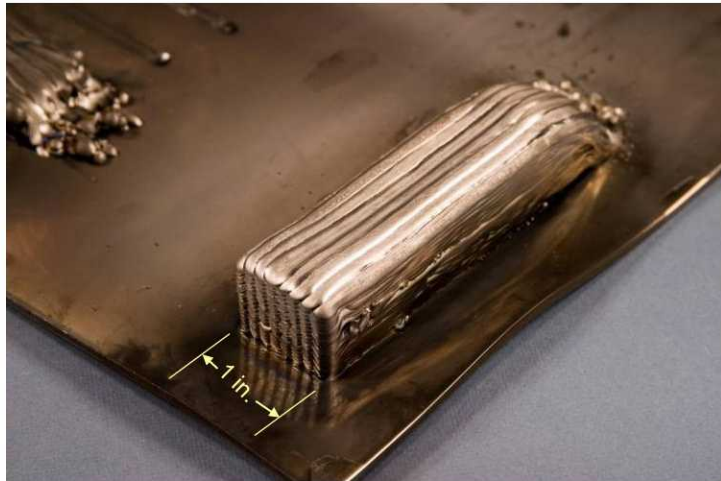


Figure 3. Inconel 718 block build.

Tensile Specimens

Tensile specimens were machined from the two wall builds as shown in Figure 4. The specimens were oriented such that the specimen length was parallel to the wall length (deposition direction) and the specimen width was parallel to the wall height direction. The walls were cut from the base plate and the wall faces were machined to produce flat parallel surfaces. Four tensile specimens were machined from each wall with specimen #1 being located near the base plate and specimen #4 being located near the top of the wall.

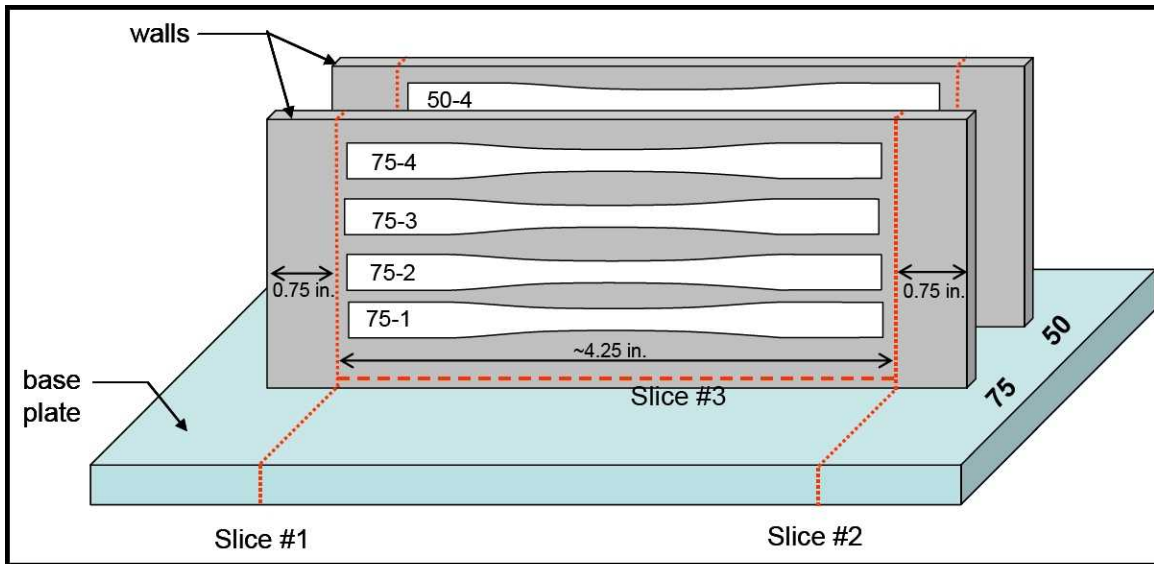


Figure 4. Tensile specimen machining diagram for wall builds.

The EBF³-deposited block was cut into lengthwise through-the-thickness slices (see the slicing information in Figure 5 and Figure 6). One tensile specimen was machined from the top portion and one from the bottom portion of each slice in order to evaluate differences in properties through the height of the block (see Figure 7). The specimen length was parallel to deposition direction (block length) and the specimen width was parallel to the block height. A total of 10 specimens were machined: 5 from the top and 5 from the bottom portions of the block. Tensile specimens from both of the wall builds and the block build were machined in accordance with ASTM specification E8 (ref. 4), as depicted in Figure 8.

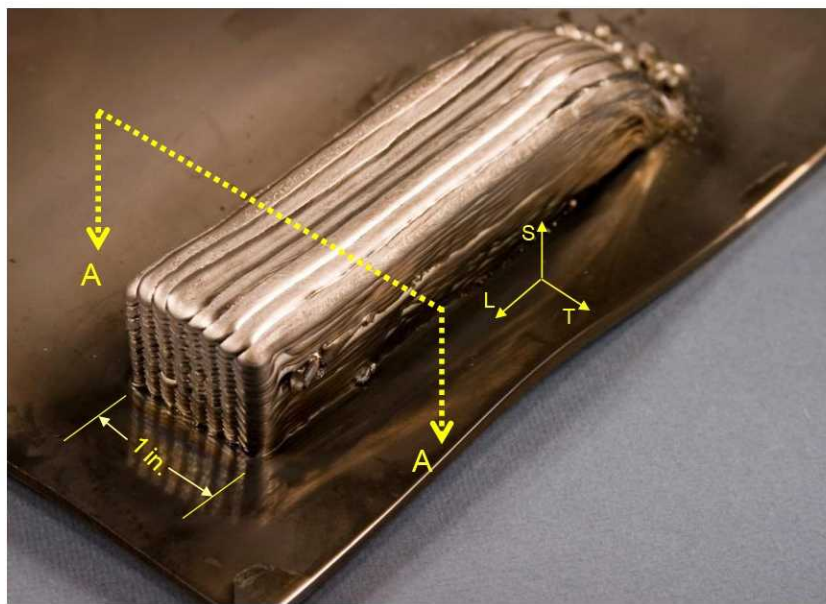


Figure 5. Block build Section A-A for reference in tensile specimen machining.

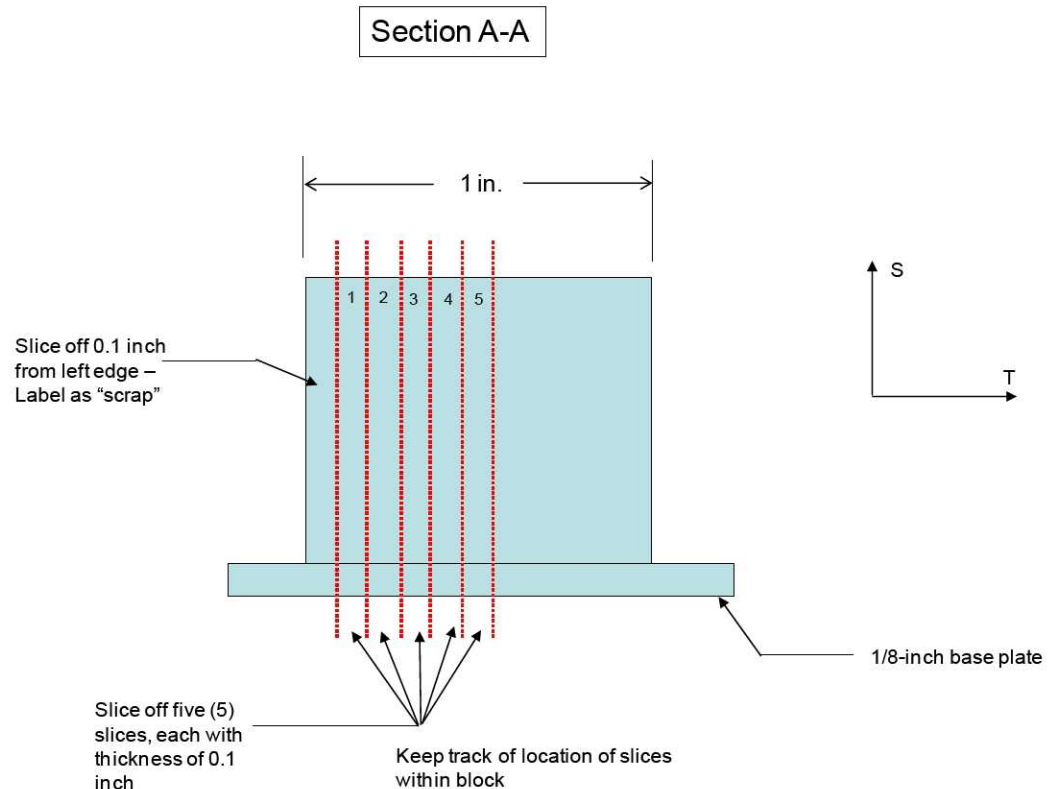


Figure 6. Slicing diagram of block build cross section (Section A-A) for tensile specimens. (Deposition direction is perpendicular to plane of page.)

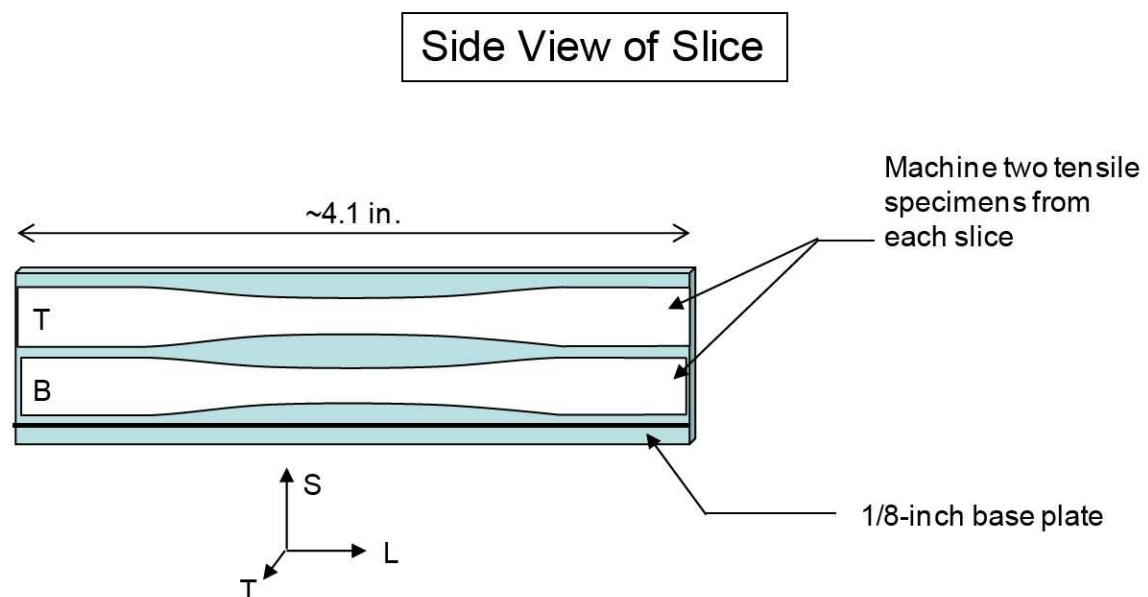


Figure 7. Tensile specimen locations within block build slices. (Deposition direction is left-to-right.)

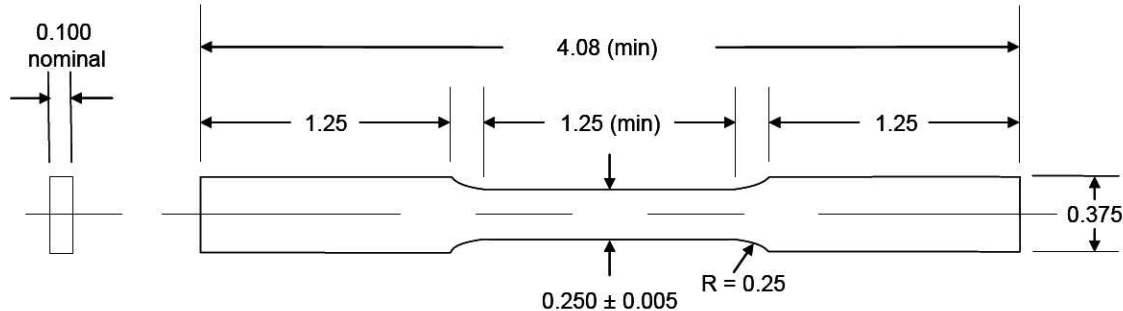


Figure 8. ASTM E8 standard subsized tensile specimen (ref. 4). All dimensions are in inches with tolerance of ± 0.010 , unless noted.

Heat Treatment

Some of the specimens machined from the block build were heat treated to determine the effect of post-EBF³ thermal processing on the properties and microstructure. Table 1 shows the two heat treatment conditions used. None of the specimens machined from the wall builds were heat treated.

Two specimens from the top and two from the bottom portions of the block were kept in the as-deposited condition. One specimen each from the top and bottom portions of the block were processed with heat treatment HT1 and one specimen each from the top and bottom portions of the block were processed with HT2. HT1 is a typical heat treatment for wrought Inconel 718 product forms and is used to solutionize and precipitate the γ' and γ'' strengthening phases (ref. 3). HT2 is a variant of the heat treatment for Inconel 718 castings documented in reference 3. Since this reference heat treatment was designed for large castings, the solution anneal time for the small EBF³ specimens was reduced from 50 hours to 4 hours. This heat treatment has the goal of solutionizing the brittle Laves phase that forms during casting and homogenizing the dendritic microstructure (ref. 3). Following heat treatment, the specimens were lightly polished to remove the surface oxide that formed.

Table 1. Heat treatments for tensile specimens machined from the Inconel 718 EBF3 block build.

HT1	<ul style="list-style-type: none"> • 1750°F for 1 hr; air cool to RT • 1325°F for 8 hrs; furnace cool to 1150°F • 1150°F for 8 hrs; air cool to RT
HT2	<ul style="list-style-type: none"> • 2175°F for 4 hrs; air cool to RT • 1325°F for 8 hrs; furnace cool to 1150°F • 1150°F for 8 hrs; air cool to RT

Precision modulus test procedures

Precision modulus tests were conducted on the specimens in the as-deposited condition in accordance with ASTM specification E111 (ref. 5). Strain was measured using back-to-back extensometers with 1-inch gage length. Each specimen was loaded to a strain level of 0.1% and unloaded. This process was repeated a total of three times. The precision modulus (E_{prec}) was calculated by taking a linear regression of the stress-strain data from the loading portion of the test.

Tensile test procedures

Tensile tests were conducted on the specimens in the as-deposited and heat treated conditions in accordance with ASTM specification E8 (ref. 4). Strain was measured using back-to-back extensometers with 1-inch gage length and a maximum extension range of 0.5 inch (50%). The specimens were loaded at a displacement rate of 0.010 in/min until a strain of 2% was attained; then the displacement rate was increased to 0.050 in/min until specimen failure. Ultimate tensile strength (UTS), 0.2%-offset yield strength (YS), total strain to failure (e_{tot}) and ductility in terms of plastic strain to failure (e_p) were calculated from the stress-strain data. Modulus (E) was calculated using a linear regression of the stress-strain data over the strain range of 0 to 0.2%.

Microstructural Analysis

Microstructures were analyzed using optical microscopy. Composition of the wall and block builds and the wire feed stock was measured using direct current plasma emission spectroscopy.

Results and Discussion

Chemical Composition

Table 2 shows the chemical composition measured for the wall build fabricated with deposition travel speed of 50 in/min and the block build. The compositions measured for the 0.045-inch diameter wire used to fabricate the wall and the 0.093-inch diameter wire used to build the block are also tabulated. For comparison, the nominal composition for Inconel 718 from reference 3 is shown.

The compositions of the feed-stock wires match the nominal composition. The compositions of the final EBF³ products (wall and block) also match the nominal composition of Inconel 718 and the compositions of the respective feed-stock wires. Thus, none of the Inconel 718 alloy elements were volatilized to any significant degree during the e-beam fabrication process.

Table 2. Composition of Inconel 718 wall and block builds and feed wire (nominal composition is from reference 3).

Element	Composition (wt %)				
	Nominal	0.045-in wire	wall build	0.093-in wire	block build
Ni	bal.	53.4	53.4	54.08	52.8
Cr	19	18.9	18.0	18.02	18.5
Fe	18	17.7	17.8	17.93	18.3
Mo	3	3.1	3.2	3.17	3.07
Nb	---	5.1	5.7	4.93	5.12
Ta	---	0.0	0.0	0.002	0.002
Nb + Ta	5.1	5.1	5.7	4.93	5.12
Ti	0.9	0.9	1.1	0.89	1.06
Al	0.5	0.6	0.6	0.45	0.52

Tensile Properties

Table 3 shows the tensile properties measured for the wall builds as well as reference properties for conventionally-processed Inconel 718 (rolled sheet and castings). The tensile properties of the two walls fabricated at different deposition travel rates were almost identical, within the scatter range. The UTS and YS results showed significant variation from specimen to specimen. The average UTS and YS values of the wall builds were about 15-20% greater than those for as-cast Inconel 718 and about 35-50% less than those for rolled Inconel 718 sheet. This result is expected since the EBF³ process is essentially a rapid-solidification casting process and does not include mechanical deformation processing associated with rolled product. The specimens machined from the portion of the wall closest to the base plate had the lowest strength, with the strength tending to increase as the specimen location moved away from the base plate (refer to Figure 4 for specimen locations within the wall build). The average ductility (ϵ_p) values for the wall builds were similar to the as-cast material ductility and were about 10% greater than the ductility reported for rolled sheet. An unexpected result was that the modulus (E) for the wall builds was significantly less (about 20%) than that of conventionally-processed Inconel 718.

Table 3. Tensile properties of Inconel 718 EBF³ wall builds

Deposition travel rate	Spec. No.	UTS (ksi)	YS (ksi)	E (Msi)	ϵ_{tot} (%)	ϵ_p (%)
50 in/min	50-1 (a)	119.3	82.1	25.1	17.5	17.1
	50-2	132.3	86.0	22.8	29.6	29.1
	50-3 (a)	139.5	85.5	21.9	22.4	21.8
	50-4	138.0	83.0	22.9	22.4	21.8
	avg	132.3	84.2	23.2	23.0	22.4
75 in/min	75-1	124.7	75.3	23.5	37.1	36.6
	75-2	131.6	81.9	20.5	26.2	25.6
	75-3	134.2	90.7	22.5	11.5	10.9
	75-4	141.0	90.6	24.7	18.2	17.7
	avg	132.9	84.6	22.8	23.3	22.7
Ref. Data (b)	rolled sheet (0.125-in thick)	203.1	175.0	29.4	---	20.8
Ref. Data (c)	as-cast	114.0	70.8	----	----	22.0

(a) Specimen failed outside gage length.

(b) Report: AFWAL-TR-85-4128 (ref. 6)

(c) Aerospace Struct. Metals HB; code 4103; Table 3.2.1.14 (ref. 3)

The tensile properties measured for the 1-inch wide block build in the as-deposited condition and in two different heat treated conditions are shown in Table 4. Specimens labeled with “B” were machined from the bottom portion of the EBF³ deposit and specimens labeled with “T” were machined from the top portion. The UTS and YS of the as-deposited specimens were greater than those measured for the wall builds. Also, the UTS and YS of the specimens machined from the bottom portion of the block were greater than those for the specimens from the top portion. This trend is the reverse of the trend observed in the wall builds. As was the case with the wall builds, the modulus of the EBF³ as-deposited specimens was significantly lower than that for conventionally-processed Inconel 718. Since the wall builds and the block build had low modulus values and there were no compositional changes associated with EBF³ deposition of Inconel 718, the deposition process may have produced a low-modulus preferred crystallographic orientation along the direction of deposition.

The heat treatments resulted in more uniform properties with respect to the top and bottom locations indicating that they successfully homogenized the properties. The higher-temperature heat treatment (HT2) resulted in a greater modulus compared to the as-deposited condition, but still lower than for conventional Inconel 718.

Table 4. Tensile properties of Inconel 718 EBF³ block build.

Condition	Location within block	Spec. No.	UTS (ksi)	YS (ksi)	E (Msi)	e _{tot} (%)	e _p (%)	E _{prec} (Msi)
As-Deposited	top	T1	146.6	91.6	22.9	31.1	30.5	23.5
		T2	139.9	86.1	23.1	31.5	31.0	23.4
		ave	143.3	88.9	23.0	31.3	30.8	23.4
	bottom	B1	153.3	103.9	24.3	21.0	20.4	24.6
		B2	152.8	104.5	24.6	20.5	19.8	24.2
		ave	153.1	104.2	24.4	20.8	20.1	24.4
HT 1	top	T3	179.5	137.1	23.9	22.8	22.1	---
	bottom	B3	180.8	137.6	24.3	24.2	23.5	---
HT 2	top	T4	164.2	136.6	25.8	21.8	21.2	---
	bottom	B4	163.0	133.8	25.7	22.6	21.9	---

Microstructural Analysis

Figure 9 shows low and high magnification views of the microstructure of the wall build that was fabricated with a deposition travel rate of 50 in/min. The wall fabricated with a rate of 75 in/min had similar microstructural characteristics. The layered nature of the microstructure is apparent. The microstructure consisted of a fine dendritic structure resultant from the rapidly solidified melt pool. These dendrites extended in the direction of the wall height across multiple deposition layers. In addition to the long dendrite colonies, examination at higher magnification shows that new dendrite colonies formed at each boundary between adjacent deposition layers.

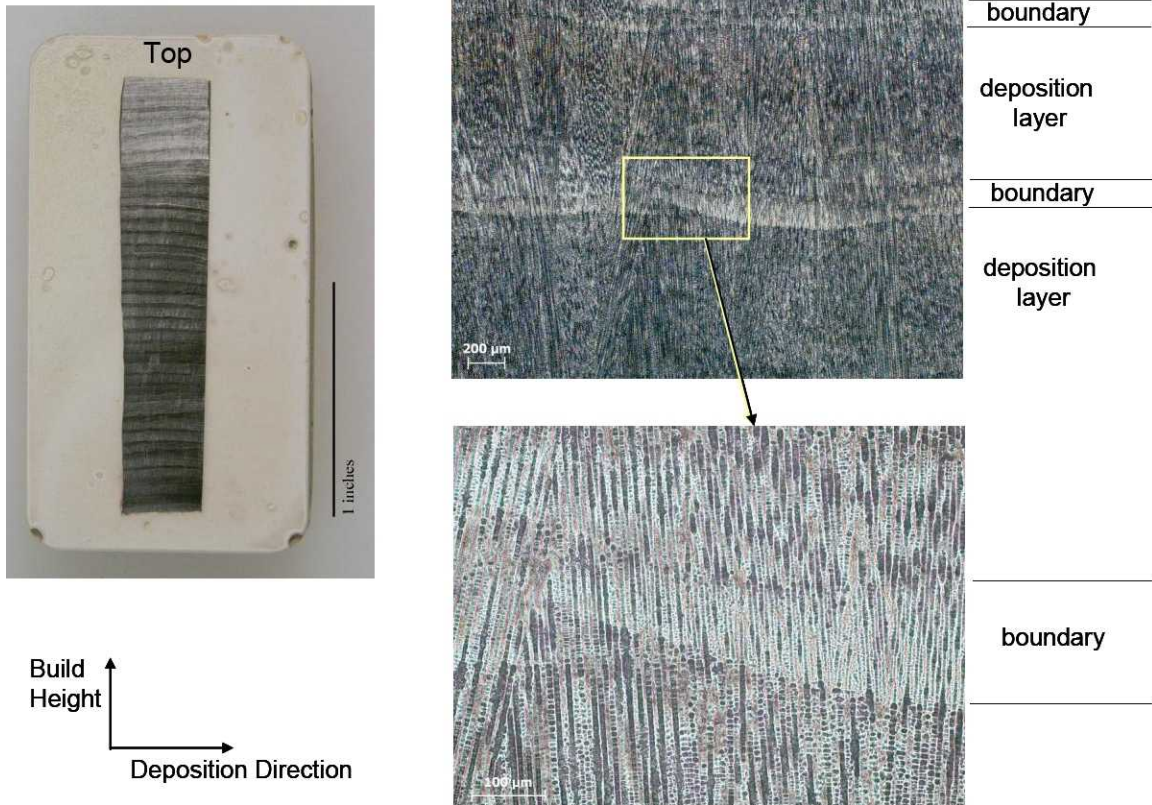


Figure 9. Microstructure of wall build fabricated with deposition rate of 50 in/min.

The microstructures of the Inconel 718 block build material in the as-deposited and heat treated conditions are shown in Figure 10. The microstructure of the as-deposited material is very similar to that of the wall build. Heat treatment HT1 did not have a major effect on the appearance of the microstructure. However, the high solution treatment temperature used with heat treatment HT2 resulted in recrystallization and elimination of the original deposition layer boundaries. The microstructure consisted of a bimodal distribution of large and small grains. Based on the modulus data associated with the HT2 condition, this heat treatment reoriented the microstructure to allow a modest increase in modulus along the deposition direction.

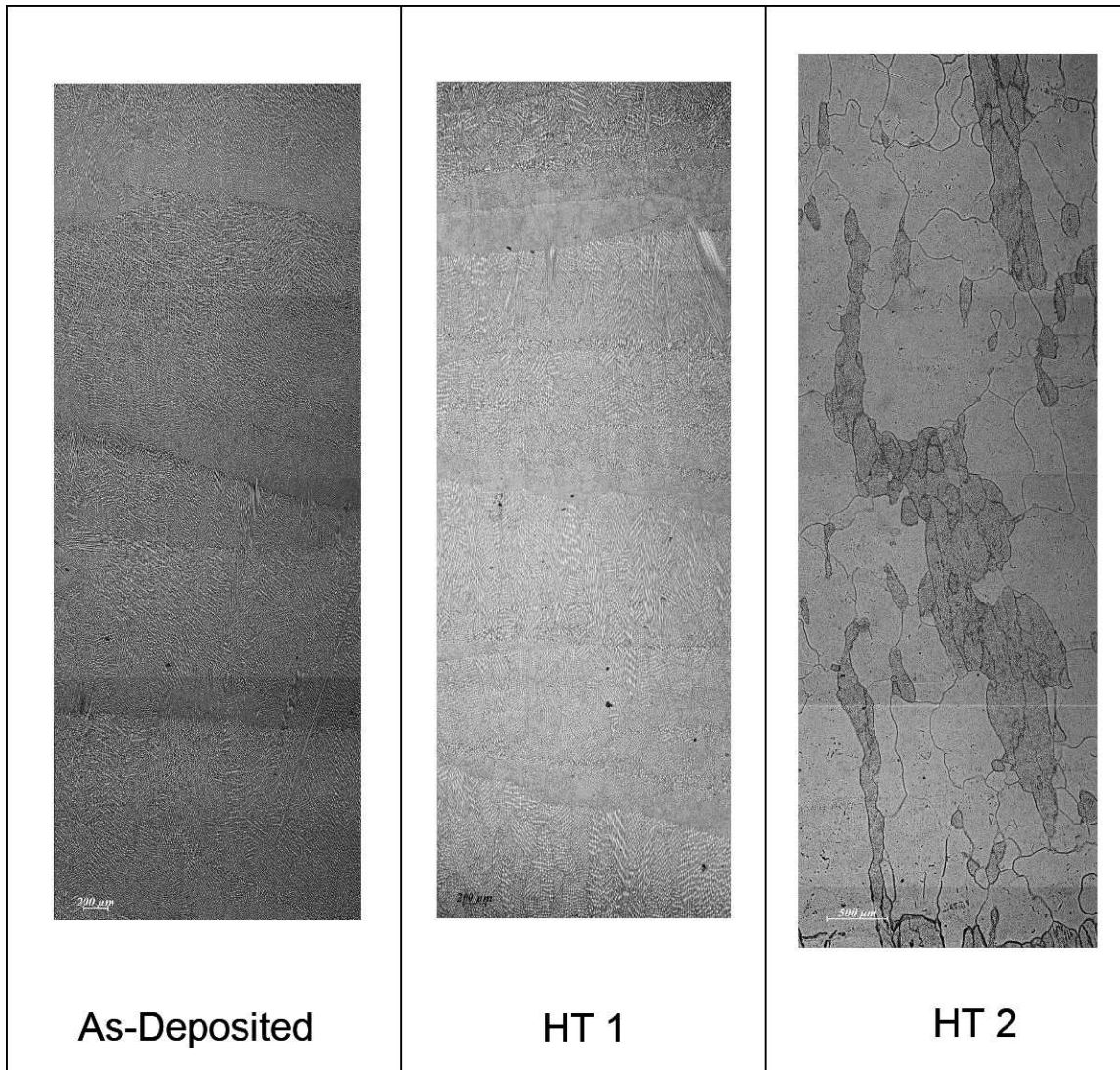


Figure 10. Microstructure of block build in as-deposited and heat treated conditions.
(Deposition direction is left-to-right; wall height is vertical.)

Concluding Remarks

Electron beam freeform fabrication (EBF³) direct metal deposition processing was used to fabricate two Inconel 718 wall builds and one block build. Specimens were machined from the builds to evaluate microstructure and room temperature tensile properties. The properties were measured only in the direction of deposition due to the dimensions of the wall and block builds.

The tensile strength and yield strength of the as-deposited material from the wall and block builds were greater than those for conventional Inconel 718 castings. Since the EBF³-deposited material had no cold work, the strength levels were lower than those for conventional cold-rolled sheet. Ductility levels for the EBF³ material were similar to those for conventionally-processed sheet and castings. An unexpected result was that the modulus of the EBF³ material was

significantly lower than that of the conventional material. This low modulus may be associated with a preferred crystallographic orientation resultant from the deposition and rapid solidification process. A heat treatment with a high solution treatment temperature resulted in a recrystallized microstructure and an improved modulus. However, the modulus was not increased to the level that is expected for Inconel 718. Analysis of the crystallographic structure of the EBF³ Inconel 718 material will be required to better understand this phenomenon.

A more detailed microstructural analysis of EBF³-deposited Inconel 718 will be conducted in the future to better understand the relationship between the deposition process and the properties, especially the low modulus values. In addition, larger-scale Inconel 718 EBF³ builds will be fabricated to allow measurement of properties in directions other than just parallel to the deposition direction.

References

1. Taminger, Karen and Hafley, Robert. "Electron Beam Freeform Fabrication: A Rapid Metal Deposition Process"; Proceedings of the 3rd Annual Automotive Composites Conference, September 9-10, 2003, Troy, MI. Society of Plastics Engineers (2003).
2. Taminger, Karen and Hafley, Robert. "Electron Beam Freeform Fabrication (EBF³) for Cost Effective Near-Net Shape Manufacturing"; NASA Technical Memorandum TM-2006-214284, March 2006.
3. Aerospace Structural Metals Handbook – Volume 6, Code 4103. Brown, Mindlin, and Ho, eds. 39th Edition, CINDAS/USAF CRDA Handbook operation, Purdue University, West Lafayette, Indiana, 2005.
4. "Standard Test Methods for Tension Testing of Metallic Materials." Annual Book of ASTM Standards. Vol. 03.01. Designation E8-04 American Society for Testing and Materials, West Conshohocken, PA 2004.
5. "Standard Test Methods for Young's Modulus, Tangent Modulus and Chord Modulus." Annual Book of ASTM Standards. Vol. 03.01. Designation E111-97 American Society for Testing and Materials, West Conshohocken, PA 2004.
6. Ruff, Paul E. "Effect of Manufacturing Processes on Structural Allowables – Phase I." Air Force Wright Aeronautical Laboratories Technical Report No. AFWAL-TR-85-4128. January 1986.

Acknowledgement

Joshua Hibberd contributed to this work as a Governor's School student while attending Princess Anne High School in Virginia Beach, Virginia, during the summer of 2006.

REPORT DOCUMENTATION PAGE				Form Approved OMB No. 0704-0188	
<p>The public reporting burden for this collection of information is estimated to average 1 hour per response, including the time for reviewing instructions, searching existing data sources, gathering and maintaining the data needed, and completing and reviewing the collection of information. Send comments regarding this burden estimate or any other aspect of this collection of information, including suggestions for reducing this burden, to Department of Defense, Washington Headquarters Services, Directorate for Information Operations and Reports (0704-0188), 1215 Jefferson Davis Highway, Suite 1204, Arlington, VA 22202-4302. Respondents should be aware that notwithstanding any other provision of law, no person shall be subject to any penalty for failing to comply with a collection of information if it does not display a currently valid OMB control number.</p> <p>PLEASE DO NOT RETURN YOUR FORM TO THE ABOVE ADDRESS.</p>					
1. REPORT DATE (DD-MM-YYYY)	2. REPORT TYPE		3. DATES COVERED (From - To)		
01-09 - 2009	Technical Memorandum				
4. TITLE AND SUBTITLE			5a. CONTRACT NUMBER		
Tensile Properties and Microstructure of Inconel 718 Fabricated with Electron Beam Freeform Fabrication (EBF3)			5b. GRANT NUMBER		
			5c. PROGRAM ELEMENT NUMBER		
6. AUTHOR(S)			5d. PROJECT NUMBER		
Bird, R. Keith; Hibberd, Joshua			5e. TASK NUMBER		
			5f. WORK UNIT NUMBER		
7. PERFORMING ORGANIZATION NAME(S) AND ADDRESS(ES)				8. PERFORMING ORGANIZATION REPORT NUMBER	
NASA Langley Research Center Hampton, VA 23681-2199				L-19731	
9. SPONSORING/MONITORING AGENCY NAME(S) AND ADDRESS(ES)				10. SPONSOR/MONITOR'S ACRONYM(S)	
National Aeronautics and Space Administration Washington, DC 20546-0001				NASA	
				11. SPONSOR/MONITOR'S REPORT NUMBER(S)	
				NASA/TM-2009-215929	
12. DISTRIBUTION/AVAILABILITY STATEMENT					
Unclassified - Unlimited					
Subject Category 26					
Availability: NASA CASI (443) 757-5802					
13. SUPPLEMENTARY NOTES					
14. ABSTRACT					
Electron beam freeform fabrication (EBF3) direct metal deposition processing was used to fabricate two Inconel 718 single-bead-width wall builds and one multiple-bead-width block build. Specimens were machined to evaluate microstructure and room temperature tensile properties. The tensile strength and yield strength of the as-deposited material from the wall and block builds were greater than those for conventional Inconel 718 castings but were less than those for conventional cold-rolled sheet. Ductility levels for the EBF3 material were similar to those for conventionally-processed sheet and castings. An unexpected result was that the modulus of the EBF3-deposited Inconel 718 was significantly lower than that of the conventional material. This low modulus may be associated with a preferred crystallographic orientation resultant from the deposition and rapid solidification process. A heat treatment with a high solution treatment temperature resulted in a recrystallized microstructure and an increased modulus. However, the modulus was not increased to the level that is expected for Inconel 718.					
15. SUBJECT TERMS					
Inconel 718; Direct metal deposition; Electron beam freeform fabrication; Mechanical properties					
16. SECURITY CLASSIFICATION OF:			17. LIMITATION OF ABSTRACT	18. NUMBER OF PAGES	19a. NAME OF RESPONSIBLE PERSON
a. REPORT	b. ABSTRACT	c. THIS PAGE	UU	19	STI Help Desk (email: help@sti.nasa.gov)
U	U	U			19b. TELEPHONE NUMBER (Include area code) (443) 757-5802

See discussions, stats, and author profiles for this publication at: <https://www.researchgate.net/publication/273561125>

Correlation Between Microstructure and Mechanical Properties in an Inconel 718 Deposit Produced Via Electron Beam Freeform Fabrication

Article in *Journal of Manufacturing Science and Engineering* · December 2014

DOI: 10.1115/1.4028509

CITATIONS
25

READS
800

5 authors, including:



Wesley A. Tayon

NASA

28 PUBLICATIONS 192 CITATIONS

[SEE PROFILE](#)



Robert A Hafley

NASA

42 PUBLICATIONS 598 CITATIONS

[SEE PROFILE](#)

Some of the authors of this publication are also working on these related projects:



Electron Beam Freeform Fabrication [View project](#)



Integrally Stiffened Cylinders, is a low cost production method for cylindrical structures in Space Applications [View project](#)

Correlation Between Microstructure and Mechanical Properties in an Inconel 718 Deposit Produced via Electron Beam Freeform Fabrication

Wesley A. Tayon¹

NASA Langley Research Center,
Hampton, VA 23681

e-mail: wesley.a.tayon@nasa.gov

Ravi N. Shenoy

Northrop Grumman,
Technical Services
Hampton, VA 23681

MacKenzie R. Redding

Engineering Physics Department,
University of Virginia,
Charlottesville, VA 22904

R. Keith Bird

NASA Langley Research Center,
Hampton, VA 23681

Robert A. Hafley

NASA Langley Research Center,
Hampton, VA 23681

Electron beam freeform fabrication (EBF³), a metallic layer-additive manufacturing process, uses a high-power electron beam in conjunction with a metal feed wire to create a molten pool on a substrate, which on solidification produces a component of the desired configuration made of sequentially deposited layers. During the build-up of each solidified layer, the substrate is translated with respect to the electron beam and the feed wire. EBF³ products are similar to conventional cast products with regard to the as-deposited (AD) microstructure and typical mechanical properties. Inconel 718 (IN 718), a high-temperature superalloy with attractive mechanical and oxidation properties well suited for aerospace applications, is typically used in the wrought form. The present study examines the evolution of microstructure, crystallographic texture, and mechanical properties of a block of IN 718 fabricated via the EBF³ process. Specimens extracted out of this block, both in the AD and in a subsequently heat treated (HT) condition, were subjected to (1) microstructural characterization using scanning electron microscopy (SEM); (2) in-plane elastic modulus, tensile strength, and microhardness evaluations; and (3) crystallographic texture characterization using electron backscatter diffraction (EBSD). Salient conclusions stemming from this study are: (1) mechanical properties of the EBF³-processed IN 718 block are strongly affected by texture as evidenced by their dependence on orientation relative to the EBF³ fabrication direction, with the AD EBF³ properties generally being significantly reduced compared to wrought IN 718; (2) significant improvement in both strength and modulus of the EBF³ product to levels nearly equal to those for wrought IN 718 may be achieved through heat treatment.

[DOI: 10.1115/1.4028509]

1 Introduction

EBF³ is a near-net-shape additive manufacturing technique for large-scale metal components being developed at NASA Langley Research Center (LaRC) for aerospace applications [1,2]. The EBF³ system uses a high-power electron beam gun in a vacuum environment and, together with wire feedstock fed into the beam, produces a molten pool on the substrate. As the electron beam moves away due to the substrate/gun translation, the molten pool rapidly solidifies and forms a three-dimensional component layer-by-layer from a computer-aided design file.

Use of the EBF³ process for fabrication of superalloy IN 718 components for high-temperature structural applications is being actively investigated at NASA LaRC. Inconel 718 is weldable [3], making it a viable candidate material for the EBF³ process. Previous work [4] showed the EBF³-processed IN 718 product to have (a) good strength in the direction of the deposition; (b) higher tensile and yield strengths (YSs) than those obtained in conventional IN 718 castings, but lower than those for conventional cold-rolled sheets; but (c) significantly lower Young's modulus (E) compared to conventionally processed wrought or cast products.

In a pure nickel single-crystal, E varies strongly with crystal direction (Table 1). This crystallographic anisotropy might satisfactorily explain the observed orientation-dependence of E and other mechanical properties in the EBF³ product. To explore this relationship, in-plane mechanical property measurements (tensile and hardness) together with microtexture evaluations were conducted. These evaluations characterized both the AD and the HT conditions of the EBF³ product. The latter was meant to document the extent to which a high temperature heat treatment might improve the isotropy of measured E and other mechanical properties through modification of the texture in the EBF³ product. Understanding the influence of processing on microstructure and mechanical properties for the EBF³ process and other additive manufacturing techniques is critical for qualification, enabling future designs to take advantage of these new techniques. Several recent studies have examined the relationship between additive manufacturing processes, microstructure/texture, and mechanical properties [6–9], as is sought in this paper. These studies represent the first step toward qualifying new materials and parts fabricated via additive manufacturing.

Table 1 Elastic modulus (GPa) dependence on crystal direction for pure Ni [5]

$E_{(111)}$	$E_{(110)}$	$E_{(100)}$
296	220	124

¹Corresponding author.

Contributed by the Manufacturing Engineering Division of ASME for publication in the JOURNAL OF MANUFACTURING SCIENCE AND ENGINEERING. Manuscript received April 8, 2014; final manuscript received September 2, 2014; published online October 24, 2014. Assoc. Editor: Joseph Beaman.

This material is declared a work of the US Government and is not subject to copyright protection in the United States. Approved for public release; distribution is unlimited.

1.1 Materials and EBF³ Test Block. The base plate (12.7 mm thick) and feed wire (1.14 mm diameter) used for building an EBF³ test block were both IN 718 alloy with a nominal composition (in weight percent): Ni–19 Cr–18 Fe–5.1 (Nb + Ta)–3 Mo–0.9 Ti–0.5 Al [3]. The details of the EBF³ process as relevant to the fabrication of this test block are provided in Ref. [4]. The directions within the EBF³ deposit were as follows: *L* (deposition direction); *T* (normal to the deposition direction); and *S* (through-thickness direction). The test block deposit was approximately 117 mm long (*L*) by 104 mm wide (*T*) by 28 mm high (*S*) and was comprised 40 additive layers, each approximately 0.7 mm thick (Fig. 1).

The chemistries of the base plate, the feed wire, and the EBF³ test block were analyzed via direct current plasma emission spectroscopy, and the results are shown in Table 2. The results indicate that (a) the EBF³ test block and base plate have a very similar composition and (b) there is a small decrease (~1.5 wt%) in Cr content and a corresponding increase in Ni content in the AD block relative to the feed wire. This small chemistry difference is within the composition range for the alloy and is therefore not expected to affect mechanical properties of the EBF³ product.

2 Experimental Procedures

The microstructure of the EBF³ test block in the AD condition was analyzed using SEM. The AD microstructure (Fig. 2) shows the dendritic morphology typical of a rapidly solidifying melt pool. The primary dendrites in Fig. 2 tend to be coarse and have two primary growth directions oriented at approximately ±45 deg to the *S* direction.

Four subsize tensile specimens were machined from the EBF³ IN 718 test block, as per ASTM specification E8 [10], in each of the orientations of interest (*L*, *T*, 45 deg) labeled in Fig. 1. The gage section was 6.35 × 2.54 mm. One set of specimens was kept in the AD condition while a second set was HT using the conditions shown in Table 3. The goal of this heat treatment was to dissolve the brittle Laves phase that forms during casting, to minimize solute segregations in the dendritic microstructure [3], and to reduce the mechanical property anisotropy observed in the

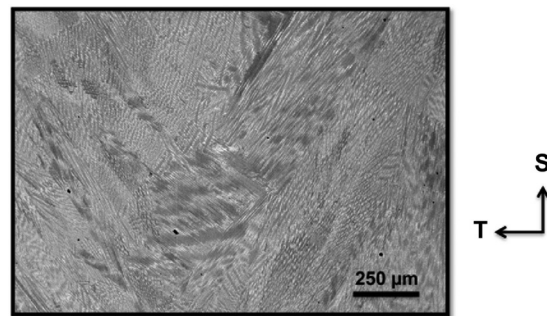


Fig. 2 Back-scattered SEM image of the dendritic microstructure in the *S*–*T* plane of the IN 718 EBF³ block (AD condition)

Table 3 Heat treatment parameters for tensile specimens machined from the EBF³ test block

- 1464 K for 4 h + air cool to room temperature
- 991 K for 8 h + furnace cool to 894 K
- 894 K for 8 h + air cool to room temperature

as-fabricated condition via a modified grain structure and associated texture. The Laves phase is an undesirable intermetallic compound that has a complex and varied chemistry.

Precision modulus and tensile tests, both performed at room temperature, were conducted according to ASTM specification E111 [11] and ASTM specification E8 [10]. Four specimens in each condition and orientation were tested. The precision modulus (*E*_{prec}) was calculated via a linear regression of the stress–strain data from the loading portion of each test. Ultimate tensile strength (UTS) and 0.2% offset YS were calculated from the stress–strain curves. *E*_{prec}, UTS, and YS evaluations of the base plate were not undertaken.

A Knoop microhardness indentation with long diagonal to short diagonal ratio of ~7:1 is widely employed for eliciting texture-dependent hardness of anisotropic metals and alloys [12]. A microhardness evaluation of the *L*–*T* plane in the base plate and the EBF³ product in both the AD and the HT conditions were therefore conducted using a Knoop indenter in conjunction with a 100 g load. The long diagonals of the indentations were positioned perpendicular to each of the directions, *L*, *T*, and 45 deg. Such a procedure provides an indication of anisotropy along these directions. Forty indentations per direction were performed in the *L*–*T* plane.

EBSM was used to determine crystallographic orientation information on samples extracted from the base plate, and the AD and HT conditions of the EBF³ block. The EBSD samples were mechanically polished using SiC paper, followed by diamond slurry and a final polish of 50 nm colloidal silica. The EBSD scans were subsequently analyzed using Orientation Imaging Microscopy (OIMTM) software to obtain information on crystallographic texture, average Taylor factor, and an estimated *E* based on orientation.

The *E* and Taylor factor [13] values for loading conditions parallel to the *L*, *T*, and *S* directions, as predicted from the EBSD data, are reported as average values for the entire scanned EBSD area. These predictions were compared to mechanical test data to assess the agreement between the two and thence to confirm the extent of anisotropy present in the EBF³ product. The OIM software computes an *E* value based on the Bishop-Hill average [14,15] of elastic stiffness and the compliance tensors as described by Voigt [16] and Reuss [17]. The Voigt and Reuss solutions, respectively, provide theoretical upper and lower bounds for the elastic stiffness calculation. In contrast, the Bishop-Hill average is the volume-weighted, arithmetic mean of the Voigt and Reuss solutions and thus represents a more reasonable estimate of the

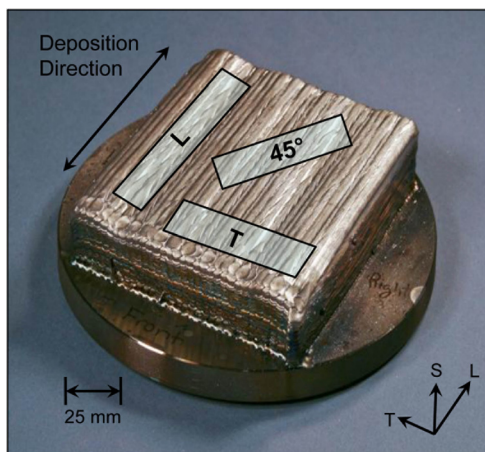


Fig. 1 The IN 718 EBF³ block (AD condition) showing tensile specimen orientations *L*, *T*, and 45 deg in the *L*–*T* plane

Table 2 Chemical composition of IN 718 wire, base plate, and EBF³ deposit in weight percent

	Ni	Cr	Fe	Mo	Nb	Ta	Ti	Al
Wire	52.5	19.6	17.8	2.99	5.27	<0.002	0.94	0.50
Base plate	53.7	18.2	17.9	2.93	5.24	<0.002	0.98	0.51
EBF ³ deposit	54.0	18.1	17.5	3.18	5.30	<0.002	0.98	0.53

Table 4 Elastic constants [18] used for EBSD-computed elastic stiffness values (in units of GPa)

C_{11}	C_{12}	C_{44}
234.6	145.4	126.2

material's elastic stiffness as a function of crystal orientation. For computing E values based on the above, single crystal elastic constants need to be input into the OIM software. In the present study, the elastic constants (shown in Table 4) were obtained from published data for IN 600 [19], which is a similar alloy to IN 718.

3 Results and Discussion

3.1 Precision Modulus. Table 5 shows the experimentally measured and EBSD-computed E values for the base plate and the EBF³ block in the AD and the HT conditions. The published E values for typical as-cast and wrought products are also reported for comparison. Wrought property values in Tables 5 and 6 were obtained from Ref. [20] for IN 718 following solution heat treatment and age in accordance with AMS 5596 [3]. As-cast properties in Tables 5 and 6 were obtained from Ref. [21]. The salient observations from this comparison are

- (a) For the EBF³ block in the AD condition, the measured E was significantly lower (~30%) than in wrought IN 718 plate along the L direction (deposition direction in the EBF³ block). In comparison, either along the T or the 45 deg direction, the measured E of the EBF³ block was very close to the typical E value for wrought plate.
- (b) In the HT condition of the EBF³ block, there was a significant increase in the measured E along the L direction relative to its AD condition. However, the improved E through heat treatment was still measurably lower relative to the wrought plate (~15% lower). In contrast, for both the T and the 45 deg orientations, the measured E values were equivalent to the wrought plate.
- (c) Both (a) and (b) strongly suggest a high concentration of grains with the low- E , $\langle 100 \rangle$ directions oriented along the L orientation and more so in the AD condition than in the HT condition.
- (d) There was good agreement between the measured and the texture-based EBSD-computed E values in both the AD

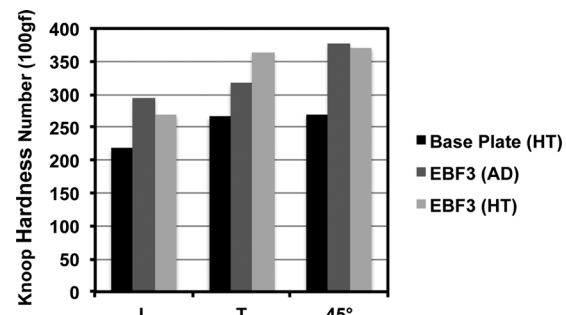


Fig. 3 Microhardness (Knoop hardness number) evaluation of crystal anisotropy in the $L-T$ plane in various conditions of IN 718

and the HT conditions of the EBF³ block, fully attesting to the contribution of texture to mechanical anisotropy in the IN 718 products.

3.2 Tensile Strength, YS, and Knoop Hardness. Table 6 documents the experimentally measured tensile properties (YS and UTS) of the EBF³ block in the AD and HT conditions. Published mechanical properties for typical as-cast and wrought products are shown for comparison. The salient observations from this comparison are

- (a) The average UTS and YS values for the L orientation in the EBF³ block (either in the AD or the HT condition) were greater than those for the as-cast IN 718 but less than those for rolled IN 718 sheet. A similar study examining tensile properties of IN 100 in AD and HT conditions fabricated via laser aided additive manufacturing found excellent mechanical properties which were also superior to castings [6].
- (b) A moderate degree of in-plane mechanical anisotropy was observed, with YS increasing along $L \rightarrow T \rightarrow 45$ deg for the AD condition.
- (c) The heat treatment significantly increased both UTS and YS relative to the AD condition and reduced the in-plane anisotropy in the EBF³ product. In addition, the heat treatment increased strength levels in the EBF³ product to near that of wrought properties reported in Ref. [20].

Table 5 Comparison of measured (E_{prec}) and EBSD-computed E values (GPa) for the IN 718 EBF³ block in the AD and the HT conditions. Additional data from the base plate and literature are provided for reference.

Orientation	Base plate		AD		HT		Typical cast	Typical wrought
	EBSD (computed)	E_{prec} (measured)	EBSD (computed)	E_{prec} (measured)	EBSD (computed)	Ref. [21]		
L	188	138	156	174	170	199	198	
T	188	194	210	192	184	199	206	
45 deg	187	207	210	193	188	—	—	

Table 6 Tensile YS and UTS in the ($L-T$) plane of the IN 718 EBF³ block in the AD and the HT conditions

Orientation	Property	AD (measured) (MPa)	HT (measured) (MPa)	Cast (literature) [21] (MPa)	Wrought (literature) [20] (MPa)
L	YS	655	986	488	1182
	UTS	978	1114	786	1369
T	YS	699	998	—	1208
	UTS	936	1162	—	1374
45 deg	YS	703	995	—	—
	UTS	993	1171	—	—

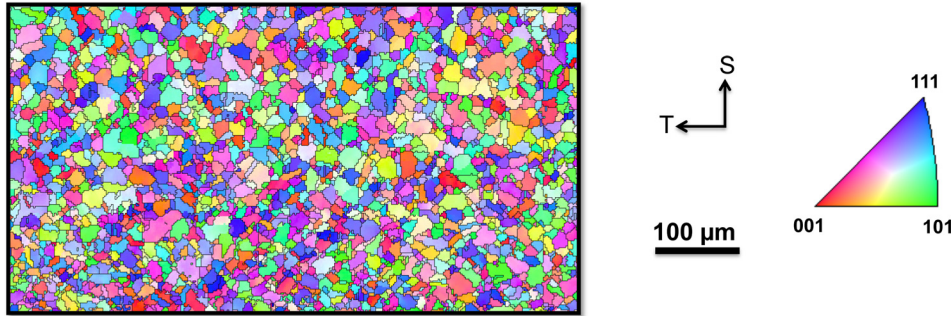


Fig. 4 *L*-axis inverse pole figure microstructural map for IN 718 base plate with colors referenced to stereographic triangle. Thin black lines denote high-angle grain boundaries.

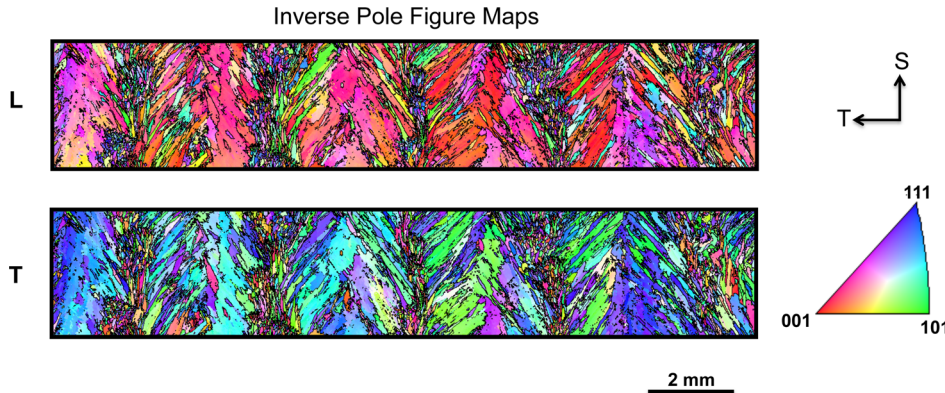


Fig. 5 Inverse pole figure maps for IN 718 EBF³ block (AD condition), referenced to direction *L* (top) and direction *T* (bottom). Thin black lines denote high-angle grain boundaries. The legends apply to both maps.

Figure 3 illustrates the overall hardness anisotropy observed in the EBF³ block in the AD and the HT conditions relative to the base plate after heat treatment. The salient observations evident from Fig. 3 are as follows:

- (a) Microhardness (which involves compressive stresses) revealed anisotropy to be present not only in the EBF³ product (in both the AD and the HT conditions), but also in the base plate (for which neither Eprec nor UTS and YS were evaluated); with the *L* being the least hard, the 45 deg being the hardest, and the *T* lying in between.
- (b) The EBF³ product, in both the AD and the HT conditions, was harder than the base plate in the HT condition.
- (c) In the EBF³ product, the HT tended to reduce the anisotropy in hardness between the *T* and 45 deg orientations observed in the AD condition, while the hardness along *L* showed no appreciable change.
- (d) There was broad agreement among the various data of *E*_{prec}, UTS, YS, and Knoop hardness number regarding anisotropy in the deposited material.

4 Microstructure and Texture Evaluations With EBSD: Correlation With Computed *E* and Taylor Factor

4.1 Base Plate. Figure 4 is an *L*-axis inverse pole figure microstructural map plotted relative to the stereographic triangle, indicating a fairly random texture in the base plate with a grain size of approximately 10 μm . The EBSD-computed *E* and Taylor factor values for this microstructure were 188 GPa and 3.07, respectively. Similarly, the computed *E* and Taylor factor values along *T* and 45 deg directions in the *L*-*T* plane were similar to

those along *L*, thus attesting to the overall isotropic properties in the base plate.

4.2 EBF³ AD Condition. The microstructure within the EBF³ product was highly textured as evident from the inverse pole figure maps presented in Fig. 5. The microstructure displays a range of strong texture components for *L* that are largely concentrated around $\langle 001 \rangle$ (top figure). Similar $\langle 001 \rangle$ textures aligned with the deposition direction have been reported in other cubic metals fabricated via additive manufacturing processes [7]. These directions are known to be low-modulus orientations for Ni. In contrast, texture along *T* has $\langle 111 \rangle$ and $\langle 101 \rangle$ directions (bottom figure), both known to be higher-modulus orientations. Five distinct EBF³ deposited layers with a distinctly dendritic grain pattern in each of them may also be identified in these maps, with much smaller grains present at the interlayer regions. Grain sizes ranged from approximately 1 mm down to several microns in diameter.

The EBSD-generated pole figures shown in Fig. 6 revealed a strong Goss texture (slightly rotated about the *S* direction) and a preferential alignment of the $[001]$ grains along the *S* direction of the EBF³ deposit. In addition, a strong $[001]$ texture parallel to the *L* direction was also evident. Together, these data suggest the presence of a strong $\{001\} \langle 100 \rangle$, Goss texture within the deposited layers.

As a result, significant variations are expected in the measured mechanical properties in the EBF³ product, as illustrated by the EBSD-generated *E* maps presented in Fig. 7. For example, the computed-*E* values for the *L* direction were ~25% lower than those for the *T* and 45 deg orientations (see Table 5). Thus, the variations in the measured *E* values are largely attributable to a

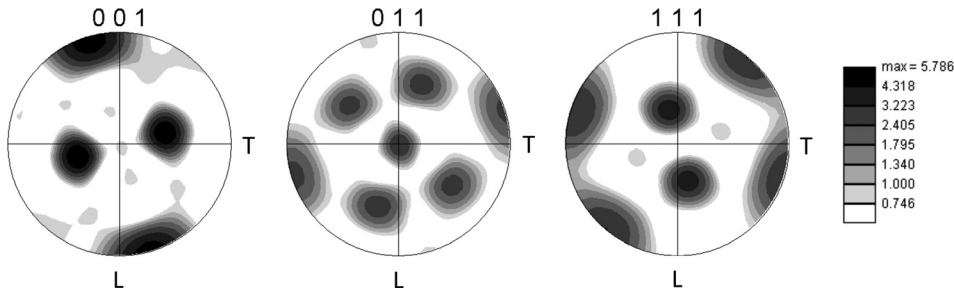


Fig. 6 001, 011, and 111 pole figures for the IN 718 EBF³ block in the AD condition

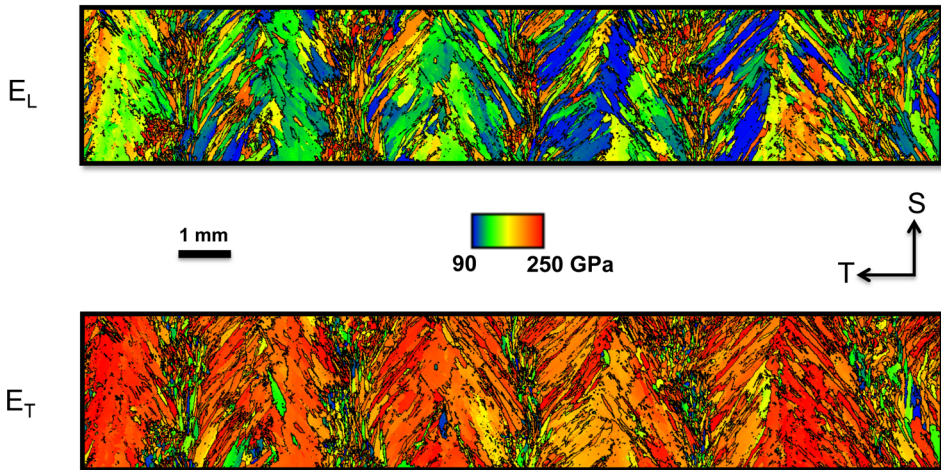


Fig. 7 Elastic modulus maps for the L (top) and T (bottom) directions for IN 718 EBF³ block in the AD condition

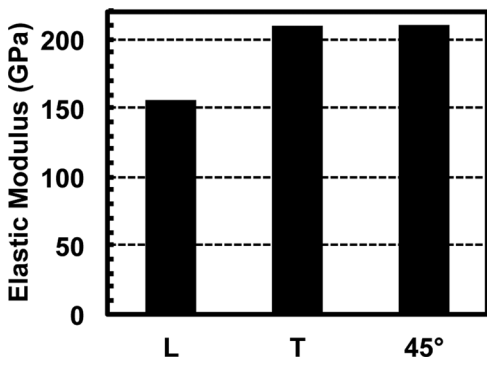


Fig. 8 In-plane ($L-T$) variations in EBSD-computed elastic modulus for the AD IN 718 EBF³ block

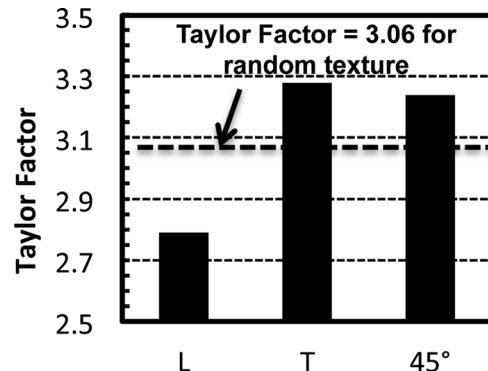


Fig. 9 In-plane ($L-T$) variations in average Taylor factor in the AD IN 718 EBF³ block

strong crystallographic texture that developed within the AD microstructure. Similar results highlighting the impact of texture-induced anisotropy resulting from additive manufacturing have been reported elsewhere [8].

The texture-induced anisotropy in E and Taylor factor for L , T , and 45 deg directions in the $L-T$ plane are presented in Figs. 8 and 9, respectively. The Taylor factors were calculated for uniaxial tensile loading. As shown in these figures, predicted E values were the lowest (~156 GPa) along L and the highest (~210 GPa) for both T and 45 deg orientations. All these values are in good agreement with the measured values. Once again, the significant texture-induced variations in the computed Taylor factor were in good agreement with the measured YS (refer to Table 6).

4.3 EBF³ HT Condition. Figure 10 is an L -axis inverse pole figure microstructural map plotted relative to the stereographic triangle. It clearly shows that the high temperature heat treatment substantially recrystallizes the EBF³ deposited microstructure and appreciably decreases the extent of texture. Additionally, a more uniform grain size (~100–400 μm diameter) and a near equi-axed grain morphology were realized through this heat treatment compared to the AD condition.

The EBSD-generated pole figures shown in Fig. 11 reveal a weak edge-on cube texture component present in the product. Such a texture is not uncommon in face centered cubic metals subjected to static recrystallization [22]. This observed level of weaker texture compared to the AD material should reduce the overall mechanical anisotropy.



Fig. 10 *L*-axis inverse pole figure map in IN 718 EBF³ block in the HT condition

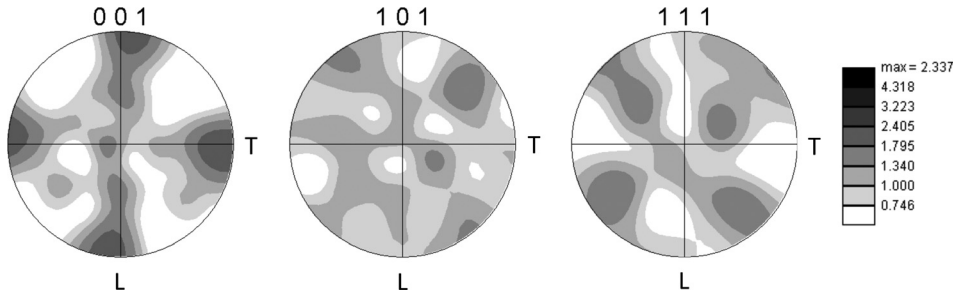


Fig. 11 001, 011, and 111 pole figures for IN 718 EBF³ block (HT condition). The contours are scaled to match with the pole figures for the AD EBF³ condition in Fig. 6.

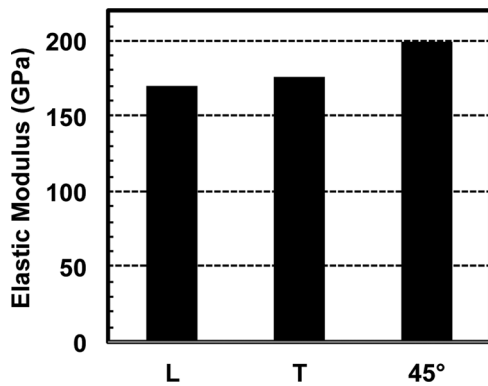


Fig. 12 Variation in EBSD-computed elastic modulus for the IN 718 EBF³ block (HT condition)

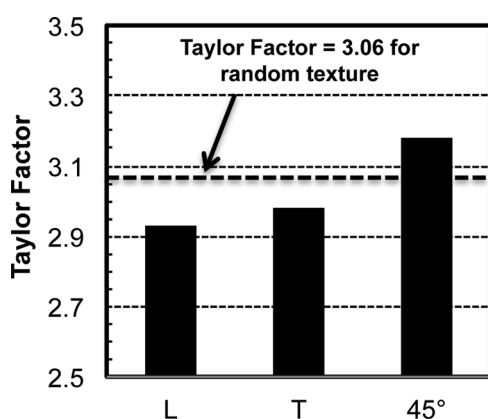


Fig. 13 Variations in average Taylor factor for the IN 718 EBF³ block (HT condition)

The EBSD-computed E variations for L , T , and 45 deg direction in the $L-T$ plane for the EBF³ block in the HT condition are presented in Fig. 12 and those for Taylor factor in Fig. 13. As shown in these figures, the E values were moderately more isotropic for

the HT condition compared to the AD condition. For example, in the L direction the AD block had an estimated E value of 156 GPa while the HT block had an estimated value of 175 GPa. Additionally, in the HT condition, the computed E agreed well with the measured E for other directions in the $L-T$ plane. The YS of the HT EBF³ deposit as compared to the computed Taylor factor variations showed a similar heat treatment response. Subsequent to the heat treatment, Taylor factor varied within a narrow range of 2.95–3.18 as shown in Fig. 13. Based on this plot, the peak YS in the $L-T$ plane may be predicted for an orientation close to 45 deg while the lowest YS would be along L , in agreement with the measured values (see Table 6).

5 Summary

A metallurgical characterization of an IN 718 block fabricated via the EBF³ process showed the following:

- (1) In the AD condition, the EBF³-processed block had a highly inhomogeneous microstructure together with a strongly textured grain structure.
- (2) E , UTS, and YS in the AD condition were strongly affected by texture as evidenced by their dependence on orientation relative to the EBF³ fabrication direction L . In the L direction, many grains were preferentially aligned with the low-modulus $\langle 100 \rangle$ direction in the deposition direction. Hence, the L direction was associated with the lowest values of E , UTS, and YS in the product.
- (3) Significant improvement in grain structure, texture randomization, and isotropy of the strength and modulus properties of the EBF³ product to levels nearly equal to those for wrought IN 718 were achieved through a high-temperature heat treatment.

References

- [1] Taminger, K., and Hafley, R., 2006, Electron Beam Freeform Fabrication (EBF³) for Cost Effective Near-Net Shape Manufacturing, NASA Technical Memorandum Paper No. TM-2006-214284.
- [2] Taminger, K., and Hafley, R., 2003, "Electron Beam Freeform Fabrication: A Rapid Metal Deposition Process," 3rd Annual Automotive Composites Conference, Troy, MI, Sept. 9–10, Society of Plastics Engineers, Troy, MI.
- [3] Brown, W. F., and Setlak, S., eds., 2005, *Aerospace Structural Metals Handbook*, CINDAS/USAF CRDA Handbook Operation, Purdue University, West Lafayette, IN.

- [4] Bird, R. K., and Hibberd, J., 2009, "Tensile Properties and Microstructure of Inconel 718 Fabricated With Electron Beam Freeform Fabrication (EBF³)," NASA Technical Memorandum Paper No. TM-2009-215929.
- [5] Reed, R., 2006, *The Superalloys: Fundamentals and Applications*, Cambridge University Press, Cambridge, UK.
- [6] Bi, G., Sun, C.-N., Chen, H.-C., Ng, F. L., and Ma, C. C. K., 2014, "Microstructure and Tensile Properties of Superalloy IN100 Fabricated by Micro-Laser Aided Additive Manufacturing," *Mater. Des.*, **60**, pp. 401–408.
- [7] Antonysamy, A. A., Meyer, J., and Prangnell, P. B., 2013, "Effect of Build Geometry on the β -Grain Structure and Texture in Additive Manufacture of Ti6Al4V by Selective Electron Beam Melting," *Mater. Charact.*, **84**, pp. 153–168.
- [8] Thijss, L., Montero Sistiaga, M. L., Wauthle, R., Xie, Q., Kruth, J.-P., and Van Humbeeck, J., 2013, "Strong Morphological and Crystallographic Texture and Resulting Yield Strength Anisotropy in Selective Laser Melted Tantalum," *Acta Mater.*, **61**(12), pp. 4657–4668.
- [9] Edwards, P., O'Conner, A., and Ramulu, M., 2013, "Electron Beam Additive Manufacturing of Titanium Components: Properties and Performance," *ASME J. Manuf. Sci. Eng.*, **135**(6), p. 061016.
- [10] Designation E8: Tension Testing of Metallic Materials, 2010, *Annual Book of ASTM Standards*, Vol. 3.01, American Society for Testing and Materials, West Conshohocken, PA.
- [11] Designation E111-97: Standard Test Methods for Tension Testing of Metallic Materials, 2010, *Annual Book of ASTM Standards*, Vol. 3.01, American Society for Testing and Materials, West Conshohocken, PA.
- [12] Vander Voort, G. F., 1984, *Metallography, Principles and Practice*, McGraw-Hill, New York.
- [13] Taylor, G. I., 1938, "Plastic Strain in Metals," *J Inst. Met.*, **62**, pp. 307–324.
- [14] Bunge, H. J., Kiewel, R., Reinert, T., and Fritzsche, L., 2000, "Elastic Properties of Polycrystals—Influence of Texture and Stereology," *J. Mech. Phys. Solids*, **48**(1), pp. 29–66.
- [15] Bishop, J. F. W., and Hill, R., 1951, "A Theory of the Plastic Distortion of a Polycrystalline Aggregate Under Combined Stresses," *Phil. Mag.*, **42**(327), pp. 414–427.
- [16] Voigt, W., 1910, *Lehrbuch der Kristallphysik*, Teubner, Berlin.
- [17] Reuss, A., 1926, "Berechnung der Fließgrenze von Mischkristallen auf Grund der Plastizitätsbedingungen für Einkristalle," *Z. Angew. Math. Mech.*, **9**(1), pp. 49–58.
- [18] Holden, T. M., Holt, R. A., and Clarke, A. P., 1998, "Intergranular Strains in Inconel-600 and the Impact on Interpreting Stress Fields in Bent Steam-Generator Tubing," *Mater. Sci. Eng. A*, **246**(1–2), pp. 180–198.
- [19] Dupond, O., Feuilly, N., Chassignole, B., Fouquet, T., Moysan, J., and Corneloup, G., 2011, "Relation Between Ultrasonic Scattering and Microstructure of Polycrystalline Materials," *J. Phys.*, **269**(1), p. 012014.
- [20] Ruff, P. E., 1986, "Effect of Manufacturing Processes on Structural Allowables—Phase I," Air Force Wright Aeronautical Laboratories, Technical Report No. AFWAL-TR-85-4128.
- [21] U.S. Department of Defense, 1999, *Military Handbook—MIL-HDBK-5H: Metallic Materials and Elements for Aerospace Vehicle Structures*, Washington, DC.
- [22] Doherty, R. D., Hughes, D. A., Humphreys, F. J., Jonas, J. J., Jensen, D. J., Kasner, M. E., King, W. E., McNelley, T. R., McQueen, H. J., and Rollett, A. D., 1997, "Current Issues in Recrystallization: A Review," *Mater. Sci. Eng. A*, **238**(2), pp. 219–274.

See discussions, stats, and author profiles for this publication at: <https://www.researchgate.net/publication/272037573>

Tensile properties of laser additive manufactured Inconel 718 using filler wire

Article in Journal of Materials Research · September 2014

DOI: 10.1557/jmr.2014.199

CITATIONS
24

READS
1,327

4 authors, including:



Xinjin Cao
Zhejiang University of Technology

188 PUBLICATIONS 4,606 CITATIONS

[SEE PROFILE](#)



P. Wanjara
National Research Council Canada

174 PUBLICATIONS 2,919 CITATIONS

[SEE PROFILE](#)



Mamoun Medraj
Concordia University Montreal

186 PUBLICATIONS 3,182 CITATIONS

[SEE PROFILE](#)

Some of the authors of this publication are also working on these related projects:



thermodynamic modeling of Magnesium alloys [View project](#)



Most of our researchers are concentrating on Dynamic Transformation. We are now looking into the behavior of Ti alloys. [View project](#)

Tensile properties of laser additive manufactured Inconel 718 using filler wire

Yi-Nan Zhang, Xinjin Cao,^{a)} and Priti Wanjara

National Research Council Canada – Aerospace, Montreal, Quebec H3T 2B2, Canada

Mamoun Medraj

Department of Mechanical Engineering, Concordia University, Montreal, Quebec H3G 1M8, Canada

(Received 21 January 2014; accepted 20 June 2014)

A 5 kW continuous wave fiber laser welding system was used to deposit INCONEL[®] alloy 718 (IN718) on service-exposed IN718 parent metal (PM) substrates using filler wire addition. The microstructure of the deposits was characterized in the fully heat treated condition. The service-exposed IN718 PM and the direct laser deposited (DLD) specimens were then evaluated through room temperature tensile testing. The yield and tensile strengths were well above the minimum values, as defined in the aerospace specifications AMS 5596K and 5663M. However, the ductility at room temperature of the DLD and DLD-PM samples was slightly lower than that specified in AMS 5596K and 5663M. The tensile fracture surfaces of the service-exposed IN718 PM, DLD, and DLD-PM specimens were analyzed using scanning electron microscopy (SEM), and the tensile failure mechanisms are discussed in detail, particularly for the important roles of the secondary particles (MC carbides) and intermetallics (platelet Ni₃Nb-δ and Laves phases).

I. INTRODUCTION

As an emerging and sustainable fabrication technology, laser additive manufacturing allows rapid introduction of new designs, shortening of the product implementation cycle, and manufacturing and/or repairing to the near-net shape of the aerospace components, such as aeroengine subassemblies fabricated from nickel-based superalloys.^{1–3} During laser additive manufacturing, both powder and wire have been used as feedstock, but the latter has lower cost, higher material efficiency (reduced waste), lower contaminant pick-up (higher quality), lower oxidation (fewer defects), and higher deposition rate (productivity).^{4–7}

To date, the microstructure and mechanical properties of laser additive manufactured IN718 using conventional CO₂ and Nd:YAG lasers have been extensively studied.^{1,2,5,8–12} The typical tensile properties obtained for the IN718 alloy are summarized in Table I, including the results for the conduction-mode condition generally used for direct laser deposition, as well as the mechanical performance obtained for keyhole-mode laser welding of butt joints. Zhao et al.⁸ evaluated the mechanical properties of laser deposited IN718 using gas-atomized and plasma rotating electrode processed (PREP) powders. The tensile properties of the deposit using PREP powders were superior to the wrought IN718 alloy, while the performance of the gas-atomized powder deposit was

inferior, which was attributed to the presence of gas porosity in the feedstock that rendered porosity and microcracks in the microstructure. In contrast, Blackwell⁹ reported that tensile failure in laser deposited IN718 was caused by the lack of fusion/bonding between the successive layers of the deposit.

Besides the influence of the defects on the tensile properties, the unique microstructural characteristics of the laser deposited IN718, such as the significantly refined substructure, also contribute notably to the mechanical performance. For instance, as compared to the tensile properties of as-cast and wrought alloys, CO₂ laser deposited IN718 obtained using a PREP powder feed exhibited equivalent or even superior mechanical performance due to the small secondary dendrite arm spacing and refined grain structure resulting from the rapid solidification rate.¹ For Nd:YAG laser butt welding of IN718, Cao et al.¹¹ obtained similar results; the welds exhibited equivalent or superior tensile properties, namely yield strength (YS), ultimate tensile strength (UTS), and elongation (El.), as compared to the aerospace specification AMS 5663 for wrought IN718.

The prevailing influences of the intermetallic and carbide phases on the tensile properties have been well documented for IN718. The two main strengthening phases, γ' and γ'', are coherent with the matrix and thus can improve the tensile strength. However, other intermetallic phases such as Laves and Ni₃Nb-δ particles, and secondary Nb/Ti-rich carbides, are all incoherent with the matrix and have different influences on the tensile properties. The Nb/Ti-rich MC type carbides are reported to

^{a)}Address all correspondence to this author.

e-mail: Xinjin.Cao@nrc-nrc.gc.ca

DOI: 10.1557/jmr.2014.199

TABLE I. Room temperature tensile properties of laser additive manufactured and welded IN718.

Laser type	Laser power applied	Wire or powder feed	Welding or deposition	Tensile properties					References
				Heat treatment	UTS (MPa)	YS (MPa)	El. (%)	RA (%)	
1.5 kW CO ₂	250–550 W	Powder	DLD	954 °C solution anneal + 718 °C and 621 °C aging 1093 °C homogenization + 954 °C solution anneal + 718 °C and 621 °C aging	1221	1007	16.0	...	Qi et al. ¹
5 kW CW CO ₂	2.35 kW	Powder (44–105 µm)	DLD	1080 °C homogenization + 980 °C solution anneal + 720 °C and 620 °C aging (gas-atomized powder) 1080 °C homogenization + 980 °C solution anneal + 720 °C and 620 °C aging (PREP powder)	1240	1133	9	16	Zhao et al. ⁸
4 kW Nd-YAG	DLD	980 °C solution anneal + 720 °C and 620 °C aging 980 °C solution anneal + 720 °C and 620 °C aging 1080 °C solution anneal + 720 °C and 620 °C aging + 720 °C and 620 °C aging	1436	1257	...	13	Blackwell ⁹
400 W PW Nd-YAG	400 W	...	2-mm butt welding	1460	1237	16	...	Ram et al. ¹⁰	
4 kW CW Nd-YAG	4 kW	Wire (0.89 mm)	3.18-mm butt welding	1405	1215	19	...	Cao et al. ¹¹	
12 kW CW CO ₂	5–10 kW	...	5-mm butt welding	1314	1079	20.4	...	Hong et al. ¹²	
...	1286	1179	2	...		
			Wrought (STA)	1276	1034	12.0	15	AMS 5663	

Note: STA is the solution treated and aged condition; PW denotes pulse wave; CW denotes continuous wave.

reduce the ductility^{3,13} and have a limited strengthening effect either directly (e.g., through dispersion hardening) or, more commonly, indirectly (e.g., by retarding grain boundary sliding and permitting stress relaxation along the grain boundaries).¹⁴ These carbides are typically present in the interdendritic regions or grain boundaries of the γ -matrix and are able to initiate microvoids. The effect of platelet or needle-like incoherent Ni₃Nb- δ phase on the mechanical properties has not been consistently reported in the literature.^{1,15,16} In general, the Ni₃Nb- δ phase is considered to have poor bonding characteristics with the γ -matrix, leading to the loss of the strength and creep life for IN718.^{1,15} However, it was also reported that the precipitation of the Ni₃Nb- δ phase along the γ grain boundaries can block grain boundary sliding, refine the grain size, strengthen the grain boundary and thus enhance the tensile strength.¹⁶ It appears that the characteristics (morphology, quantity, and distribution) of the Ni₃Nb- δ phase in the γ -matrix may explain the different mechanical performances, as reported in the literature; for instance, when the Ni₃Nb- δ phase is present in large quantities there is no strengthening effect, but a small quantity can refine the grain size and improve the tensile properties, fatigue resistance, and creep rupture ductility.¹⁴ The Laves [(Ni, Cr, Fe)₂(Nb, Mo, Ti)] particles that precipitate in the interdendritic regions or grain boundaries during laser welding or deposition are also reported to exhibit poor bonding with the γ -matrix, and, in turn, deteriorate the mechanical properties, especially the tensile ductility, fracture toughness, fatigue and creep rupture properties.^{1,3,10,17} Particularly, the formation of the Laves phase (i) depletes the γ -matrix of the principal alloying elements required for solid solution strengthening; (ii) results in a weakened structure, especially at the interface between the Laves phase and the γ -matrix; (iii) promotes excessive microvoid nucleation; and (iv) presents preferential sites for easy crack initiation and propagation along its low energy fracture paths.^{1,3,10,11} Moreover, the formation of both Laves and Ni₃Nb- δ phases consumes the available Nb so that it is not available for the precipitation of the coherent strengthening phases, γ'' and γ' . To this end, considerable dissolution of the Laves phase can improve the tensile ductility, which has been well confirmed through post-weld heat treatment by Ram et al.¹⁰

Notwithstanding this current understanding of the phase constituents and mechanical performance of the laser deposited IN718, information on additive manufacturing or repair of IN718 using wire feeding and a high power continuous wave (CW) fiber laser is limited. From an industrialization perspective, fiber lasers have remarkable advantages including high energy efficiency, good beam quality, flexible fiber beam delivery, small footprint, good process versatility, automation capacity, and low overall costs.¹⁸ In this work, laser deposition with wire feed was performed on service exposed PM substrates. The objective

was to substantiate the process for additive manufacture or repair of IN718 components. Microstructural characterization and mechanical property evaluation of the DLD and DLD-PM IN718 were conducted in the current work and compared with the service-exposed IN718. To understand the tensile failure mechanisms, the fracture surfaces of the PM, DLD, and DLD-PM samples were systematically analyzed using SEM.

II. EXPERIMENTAL

Coupons of the PM substrates were extracted directly from a retired, service-exposed IN718 aerospace component that had nominal and measured chemical compositions as indicated in Table II. Although the details of the manufacturing process for the IN718 aerospace component were not disclosed, it may be reasonably assumed that the alloy was processed through casting and forging followed by a standard solutionizing and aging heat treatment prior to the “normal” long-time service. Hereafter, the term PM refers to the “service-exposed” condition unless otherwise noted, as, for instance, when it was fully heat treated again after laser deposition.

In this study, laser deposition was conducted on the IN718 PM substrate using a 5 kW CW solid-state Yb-fiber laser system (YLR-5000, IPG Photonics, Oxford, MA) equipped with an ABB robot. A collimation lens of 150 mm, a focal lens of 250 mm, and a fiber diameter of 600 μm were used to produce a nominal focusing spot diameter of approximately 1.0 mm. A positive defocusing distance of +12 mm was used to obtain a laser power density of approximately 792 W/mm². The laser head was inclined 2–3° both along the lateral side and from the vertical position toward the scanning direction to avoid any damage to the equipment from the laser beam reflection. The fiber laser beam, with a wave length of about 1.07 μm , was positioned on the top surface of the deposit. To protect the molten metal during deposition, the laser deposited material was shielded using two streams of Ar gas flow. One stream of Ar at a flow rate of 30 cfh ($2.36 \times 10^{-4} \text{ m}^3/\text{s}$) was directed toward the scanning direction at an angle of 18–20° to the deposit surface, while the other was directed opposite to the scanning direction at a flow rate of 20 cfh ($1.57 \times 10^{-4} \text{ m}^3/\text{s}$). The IN718 filler wire, supplied by Haynes Interna-

tional Inc., was ~0.89 mm in diameter and had a nominal composition as given in Table II. The IN718 filler wire was axially fed from the laser scanning direction at an inclination angle of 30° from the top surface of the deposit where interception with the incident laser beam occurred. A schematic of the experimental setup has been reported in an earlier publication.¹⁹ It is noteworthy that each layer was deposited along a single scanning direction on the IN718 PM substrates to produce two types of coupons for the final mechanical property evaluation: (1) DLD IN718 (i.e., 100% direct laser deposited) and (2) DLD-PM (i.e., 50% DLD IN718 and 50% IN718 PM).

After laser deposition, the DLD and DLD-PM coupons were solution treated and aged (STA). The solution heat treatment was carried out in vacuum at a temperature of 954 °C (1750 ± 25 °F) for one hour and then cooled (with inert Ar gas) at a minimum rate of 16.7 °C/min (30 °F/min) to a temperature of 538 °C (1000 °F) followed by rapid cooling in Ar. The aging consisted of the following steps: heating to 732 °C (1350 ± 25 °F), soaking for 8 h, furnace cooling under Ar to 599 °C (1110 ± 25 °F) and holding for 8 h, and finally Ar quenching.

The metallographic samples were characterized in both the as-deposited and post-deposition heat treated (PDHT) conditions. Each laser deposited coupon was sectioned transverse to the scanning direction using a precision cut-off saw to extract specimens for metallographic examination. After sectioning, the specimens were mounted, ground, and polished to a surface finish of 0.04 μm , followed by electrolytic etching in a saturated solution of 10 g oxalic acid in 100 mL distilled water using a voltage of 6 V for 8 s. Optical microscopy (OM) on a GX-71 system (Olympus Corporation, Tokyo, Japan) was used for examining the macrostructural features in the deposited material zone (DMZ).

The microhardness was measured using a load of 300 g and a dwell period of 15 s on a Vickers microhardness (HV) machine (Struers Duramin A300, Struers DuraScan, Salzburg, Austria), equipped with a fully automated testing cycle (stage, load, focus, measure). At an indent interval of 0.2 mm, at least three hardness lines were measured to determine the average hardness profile across each deposit. Standard tensile samples with a gage length of 16.26 mm (0.640" ± 0.005") and a

TABLE II. Nominal and measured chemical compositions of IN718 PM, filler wire, and laser deposits (wt%).

Elements	Ni	Cr	Fe	Co	Nb	Mo	Ti	Al	C	Mn	Si	B	Cu
IN718 ^a	50–55	17–21	Bal.	1.0	4.75–5.50	2.8–3.3	0.35	0.80	0.08	0.35	0.35	0.06	0.3
Filler wire ^a	52	18	19	1	5	3	0.9	0.5	0.05	0.35	0.35	0.009	0.1
IN718 ^b	51.3	18.2	18.6	0.9	5.1	2.9	1.2	0.20
DLD IN718 ^b	50.2	18.6	19.4	1	4.9	2.9	1.3	0.22

^aIndividual values represent the upper limit for the nominal composition.

^bMeasured values using an Olympus Delta X-ray Fluorescence (XRF) analyzer at a beam voltage of 40 V and current 35 A.

diameter of 4.06 mm ($0.160'' \pm 0.003''$) were machined in accordance with ASTM-E8-04 from the IN718 PM, DLD, and DLD-PM coupons. Room temperature tensile testing was conducted at a strain rate of $8.3 \times 10^{-5} \text{ s}^{-1}$ before the yield point and $8.3 \times 10^{-4} \text{ s}^{-1}$ after yielding using a United SFM-30 system. The microstructural constituents in the DMZ and on the fracture surface of the IN718 PM, DLD, and DLD-PM specimens were observed using SEM (Hitachi S-3400N, Tokyo, Japan) with secondary electron imaging (SEI) and backscattered electron imaging (BSEI). Energy dispersive x-ray spectroscopy (EDXS) was used to identify the chemical composition of the different secondary and intermetallic phases. To further improve the reliability of the phase identification on the fracture surfaces, the secondary and intermetallic phases were carefully focused and their compositions were measured at a distance of approximately 10 mm from the EDXS detector. Then these secondary and intermetallic particles were further confirmed by comparing and contrasting with the same phases obtained from metallography and literature.

III. RESULTS AND DISCUSSION

A. Microstructure

As shown in Fig. 1(a) (OM) and Fig. 1(b) (SEM), a multibead and multilayer deposit with no visible macroporosity and macrocracks could be produced under optimized process conditions using a high power fiber

laser with wire feed addition. Three distinct regions are identifiable in the images shown in Figs. 1(a) and 1(b): (1) the IN718 PM, (2) the heat-affected zone (HAZ) that includes the partially melted zone (PMZ), and (3) the DMZ.

1. Parent metal

The microstructures of the IN718 PM in the service-exposed (i.e., as-received) and heat treated conditions are shown in Figs. 1(c) and 1(d), respectively. The PM in both conditions consisted primarily of the equiaxed austenitic γ grains, MC carbide particles, and platelet $\text{Ni}_3\text{Nb}-\delta$ precipitates as well as the age-hardening/strengthening phases γ'' and γ' . The γ grains comprise the face-centered-cubic (fcc) Ni-based continuous matrix phase with solid solution elements (e.g., Co, Cr, Mo, and W). Randomly distributed Nb-rich MC type primary carbides with sizes up to 10 μm were observed at the γ -matrix grain boundaries. Platelet $\text{Ni}_3\text{Nb}-\delta$ precipitates, approximately 1–5 μm in length, were distributed within the γ grains and at the grain boundaries. Their presence and morphology are mainly attributed to the multiple thermal cycles during service of the IN718 aerospace component (from which the PM substrates were extracted).^{3,20,21} An average γ grain size of 14 μm was determined for the service-exposed condition [Fig. 1(c)]. In the fully heat treated

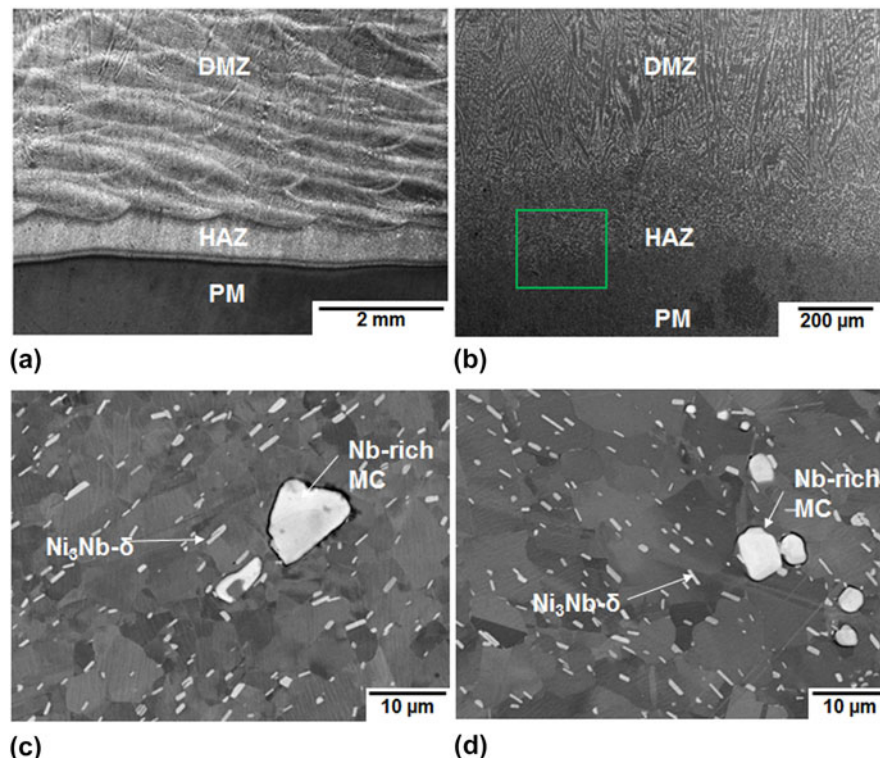


FIG. 1. A multibead and multilayer deposit in the (a) as-deposited condition, OM image and (b) the heat treated condition, SEM image. BSEI of the PM in the (c) service-exposed condition and the (d) reheat treated condition after laser deposition.

condition (after laser deposition), slight coarsening of the γ grains (approximately 17 μm) was observed, as shown in Fig. 1(d).

2. HAZ between PM and DMZ

Figure 2 shows the details of the HAZ [located within the inset in Fig. 1(b)] of the multibead and multilayer deposit in the heat treated condition. Compared to the PM, more complex microstructures were observed in the HAZ between the PM and the DMZ. In particular, within the HAZ close to the DMZ, referred to as the near-HAZ, a large amount of the needle-like $\text{Ni}_3\text{Nb}-\delta$ precipitates were apparent, but no evidence of the Nb- and/or Ti-rich MC type carbides could be ascertained, as shown in Figs. 2(a) and 2(b). The precipitation of these needle-like $\text{Ni}_3\text{Nb}-\delta$ precipitates in the near-HAZ occurs during post-deposition solution heat treatment from the liquid “particle” structure

that forms due to the dissolution of the $\text{Ni}_3\text{Nb}-\delta$ or γ'' in the matrix during the heating stage of laser deposition.^{20,21} Clearly, the temperature in the DMZ is higher than the melting temperature of the IN718 alloy (1350 °C); thus the near-HAZ (i.e., the HAZ close to the DMZ) may experience temperatures surpassing the γ/MC type carbide eutectic temperature (1250 °C). As such, the MC carbides can completely dissolve into the γ -matrix, which reasonably accounts for the absence of the carbides in the near-HAZ [Figs. 2(a) and 2(b)].

Similarly, a large amount of the needle-like $\text{Ni}_3\text{Nb}-\delta$ precipitates were observed in the mid-HAZ [Figs. 2(c) and 2(d)]. However, MC type carbides were also present in this region though some partial dissolution was evident. Hence, as compared to the near-HAZ, the temperatures in the mid-HAZ are lower but most likely close to or below the γ/MC type carbide eutectic temperature.

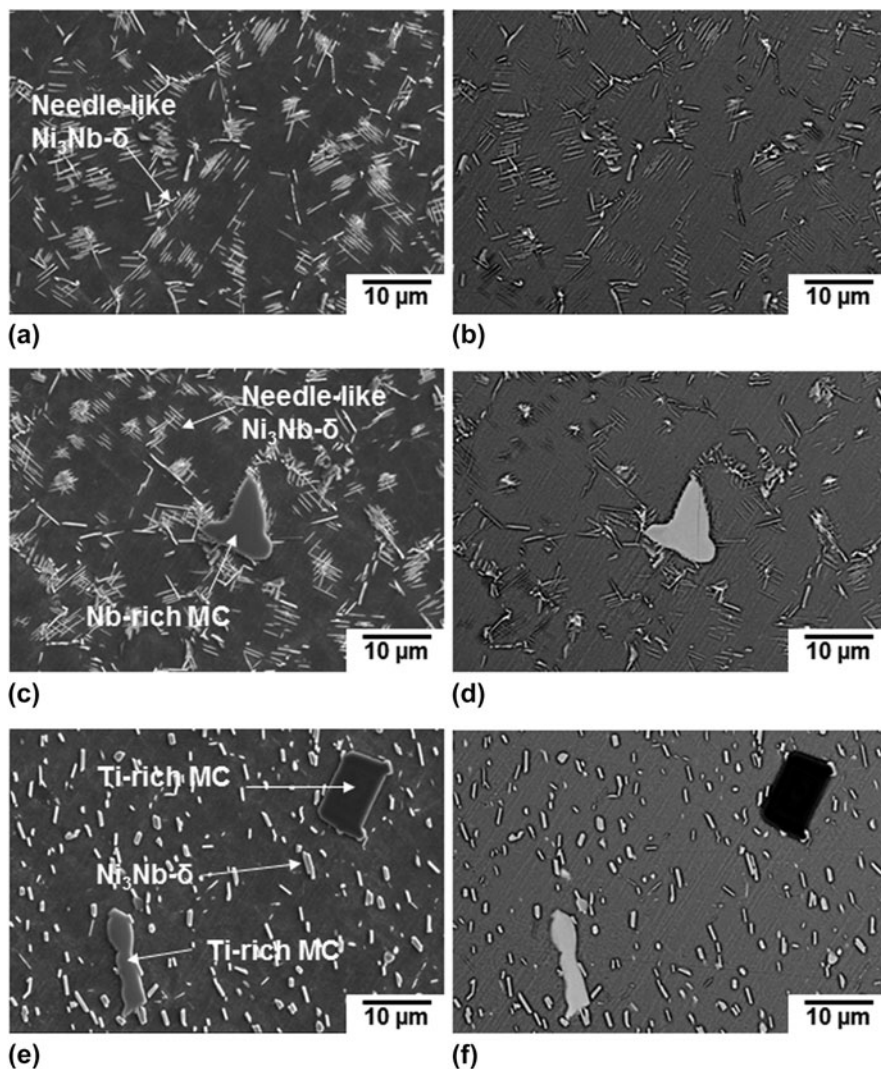


FIG. 2. Microstructures of the multibead and multilayer deposit in the heat treated condition, located within the inset shown in Fig. 1(b): (a–b) near-HAZ, (c–d) mid-HAZ, and (e–f) far-HAZ.

In the far-HAZ (i.e., the HAZ close to the PM), the MC type carbides appeared intact without any evidence of dissolution [Figs. 2(e) and 2(f)]. Also, considering that the solution heat treatment was carried out at 954 °C, which is lower than the solvus temperature (995 °C) of the Ni₃Nb-δ precipitates, neither the carbides nor the Ni₃Nb-δ precipitates in the HAZ and PM were dissolved in the PDHT condition. Although the far-HAZ after the heat treatment appears to have a microstructure similar to that of the PM (i.e., consisting of the γ-matrix, platelet Ni₃Nb-δ, Nb-rich and/or Ti-rich MC primary carbides), the strengthening phase γ' can transform to Ni₃Nb-δ when the temperature is above 861 °C.³

3. Deposited material zone

The DMZ, which had a chemical composition similar to the IN718 PM (Table II), exhibited typical dendritic structures, as shown in Fig. 3(a). Solidification of IN718 starts with the precipitation of primary γ, which causes the enrichment of Nb, Mo, Ti, and C in the interdendritic liquid. The subsequent liquid transforms to γ and NbC through a eutectic reaction that consumes most of the carbon available in the material until another eutectic type reaction, liquid → (γ + Laves phases), occurs and terminates the solidification process.^{3,8,22–24} From EDXS, spot analyses on the Laves particles demarcated in Fig. 3(a) revealed that they consist of Ni, Cr, Fe, Nb, Mo, and Ti, as shown in the typical spectrum given in Fig. 3(b). With due

consideration of the smaller size and fraction of the Ni₃Nb-δ particles within the interdendritic regions, an EDXS line scan across the dendrites in the DMZ [Figs. 3(c) and 3(d)] can further attest to the Laves phase being rich in Nb, Ti, and Mo, but lean in Fe, Cr, and Ni, as compared to the γ-matrix. In the PDHT condition, the solution annealing temperature of 954 °C used resulted in partial dissolution of the Laves particles (the eutectic temperature of (γ + Laves) is 1200 °C) and led to Nb accumulation in the interdendritic regions. Sufficient concentration of Nb around the Laves particles can then initiate the formation of the needle-like δ phase [Fig. 3(a)], an equilibrium orthorhombic incoherent Ni₃Nb precipitate that has a precipitation temperature range of 860–995 °C.²²

B. Defects

HAZ liquation cracks were observed in the PMZ close to the DMZ in the as-deposited condition [Figs. 4(a)–4(d)]. In the PDHT condition, the extent of HAZ microfissuring was markedly reduced, as shown in Fig. 4(d), and can be attributed to healing. HAZ liquation cracking can occur in the wrought IN718 substrate due to (i) the constitutional liquation of Nb/Ti-rich MC carbides and (ii) the segregation of B, S, and P in the HAZ grain boundaries.³ The low equilibrium distribution coefficients of solute and/or impurity elements B (0.04 in Ni), S (nearly 0 in Ni), and P (0.02 in Ni) lead to their segregation into the grain boundaries, cause a local depression of the melting temperature and thus promote the formation of liquation

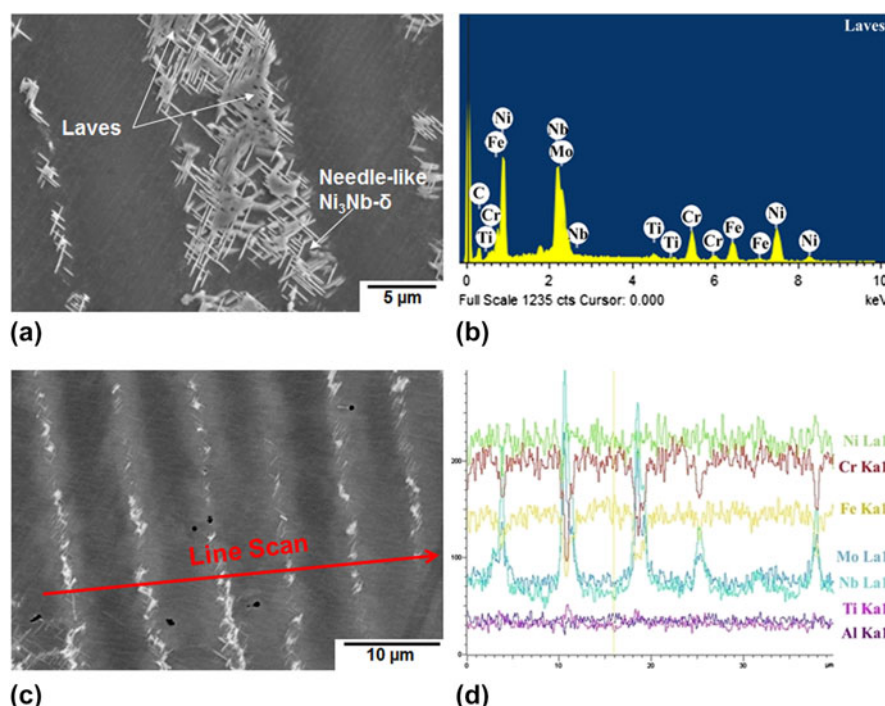


FIG. 3. (a) Microstructure consisting of Laves phase and needle-like Ni₃Nb-δ precipitates in the heat treated condition, (b) typical EDXS point spectrum from a spot analysis on the Laves phase, and (c, d) EDXS line scan across the dendritic structure in the DMZ.

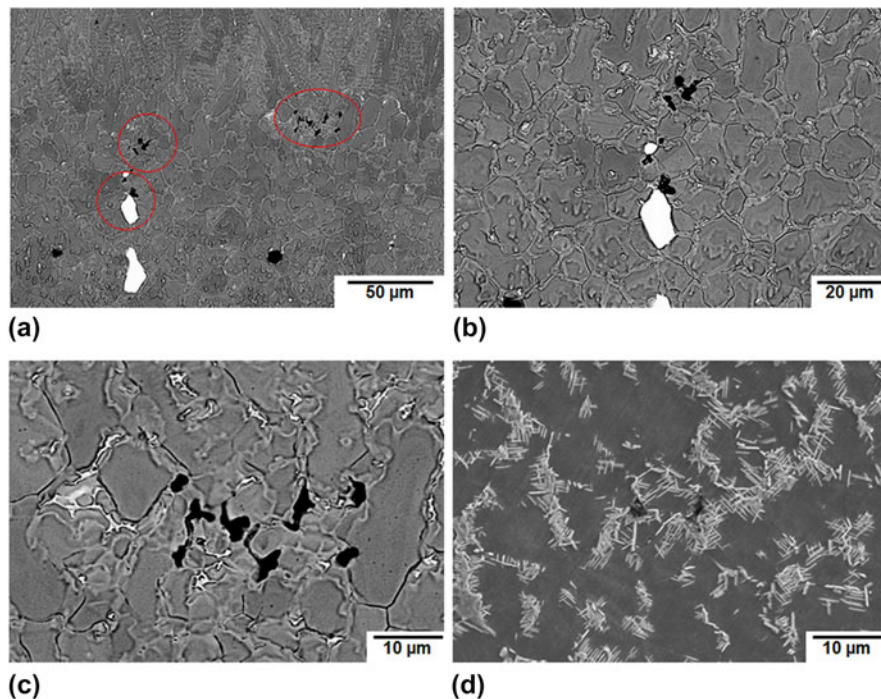


FIG. 4. Liquation cracking in the PMZ of the HAZ in the (a–c) as-deposited and (d) PDHT conditions.

films along the grain boundaries.^{3,20} In spite of the presence of the HAZ liquation cracking in the DLD-PM coupons, tensile fracture occurred exclusively in the DLD region, which suggests that the HAZ liquation cracks are not the dominating factor for the failure of the DLD-PM tensile samples.

In the DMZ, weld metal liquation cracking was frequently observed in the lower beads near the interfacial layer in the as-deposited condition, as shown in Fig. 5. This region of the lower beads acts as the HAZ of the adjacent upper layer beads that are deposited subsequently. Therefore, these microcracks are quite similar to the HAZ microfissures or liquation cracks, as widely encountered in IN718 welds,³ and are usually termed as weld metal liquation cracking in multipass welding.³ The DMZ has a rapidly solidified cast microstructure after laser deposition and thus liquation cracking is promoted by the melting of the Laves phase rather than constitutional liquation of the Nb/Ti-rich carbides, given that the former precipitates at a lower temperature and the latter has a much lower fraction. As shown in Figs. 5(a)–5(c), the weld metal liquation cracks can propagate from the lower beads near the interfacial area along the grain boundaries and even extend into the upper newly deposited layer. In the PDHT condition, the absence of weld metal liquation cracks in the interfacial area, as shown in Fig. 5(d), can be attributed to healing that occurs due to (i) the lower amount of Laves phase available due to its partial dissolution during the heating stage of the solution heat treatment, (ii) the improved strength of the DMZ due to the release of Nb into the γ -matrix caused by the partial

dissolution of the Laves phase at the heating stage and the precipitation of the γ' and γ'' strengthening phases at the aging stage, and (iii) the release of thermal strains and shrinkage stresses (that are a result of rapid solidification after laser deposition) during the solution heat treatment.^{3,20} The healing of the weld metal liquation cracks in the DMZ during the heat treatment after laser deposition is deliberated to diminish the deterioration in the mechanical performance.

C. Mechanical properties

The average Vickers microindentation hardness profiles across the deposits (from DMZ to PM) in the as-deposited and PDHT conditions are shown in Fig. 6. The hardness of the DMZ in the PDHT condition (457 ± 15 HV) is much higher than that in the as-deposited condition (275 ± 30 HV). In the PDHT condition, the DMZ has a hardness that is similar to but slightly lower than the fully heat treated PM (463 ± 16 HV), indicating that the hardness can be essentially recovered to that of the PM. The slightly lower hardness is due to the presence of undissolved Nb-rich Laves particles and the formation of the needle-like $\text{Ni}_3\text{Nb}-\delta$ phase particles in the DMZ that lowers the amount of Nb available for reprecipitation of strengthening phases γ' and γ'' during the heat treatment after laser deposition.

Although the overall tensile properties of the DLD and DLD-PM coupons are lower than the PM, both the UTS and YS are well above the minimum values as defined in the specifications AMS 5596K and AMS 5663M.

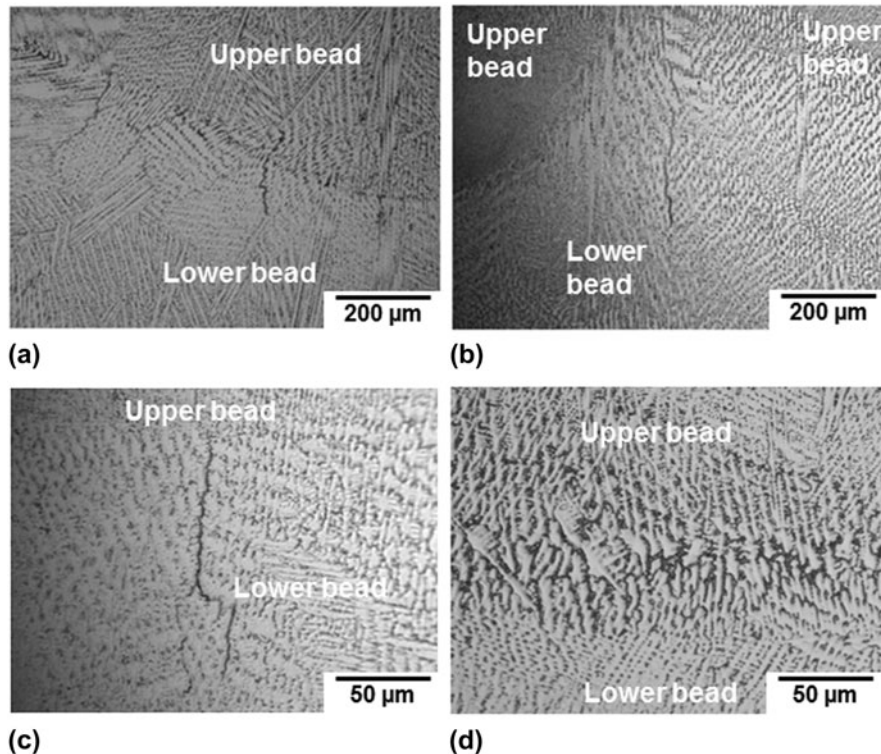


FIG. 5. Weld metal liquation cracks in the (a–c) as-deposited condition and healing with the (d) PDHT condition.

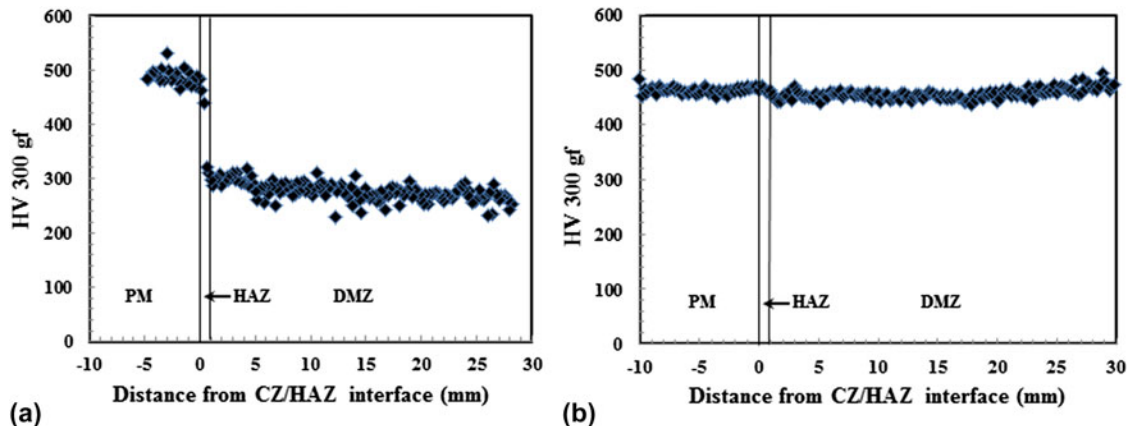


FIG. 6. Average hardness profiles in the (a) as-deposited and (b) PDHT conditions, which indicate that the hardness in the DMZ is nearly recovered to the value of the PM in the fully heat treated condition.

However, the ductility values of the DLD and DLD-PM coupons are slightly lower than the specifications. Both DLD and DLD-PM coupons have similar UTS, YS, and elongation, but the DLD-PM coupon has twice the ductility (RA) of the DLD IN718. All the DLD-PM coupons fractured in the DLD portion of the tensile specimen, indicating that the DMZ is weaker than the service-exposed PM.

D. Fractography

To better understand the tensile failure mechanisms, the fracture surfaces of the IN718 PM, DLD, and DLD-PM

coupons were examined using SEM and EDXS. It is noteworthy that all the DLD-PM coupons failed in the DLD section of the tensile specimens and thus similar fracture surface results were obtained for both the DLD and DLD-PM coupons. As shown in Figs. 7(a) and 7(b), the tensile fracture surfaces of the PM that are indicative of transgranular ductile failure exhibited fine, deep, and uniform equiaxed dimples, within which platelet $\text{Ni}_3\text{Nb}-\delta$ particles were frequently present. Some MC carbides can also be observed on the fracture surface, as shown in Fig. 7(a). In contrast, the tensile fracture surfaces of both the DLD and DLD-PM coupons revealed irregular and

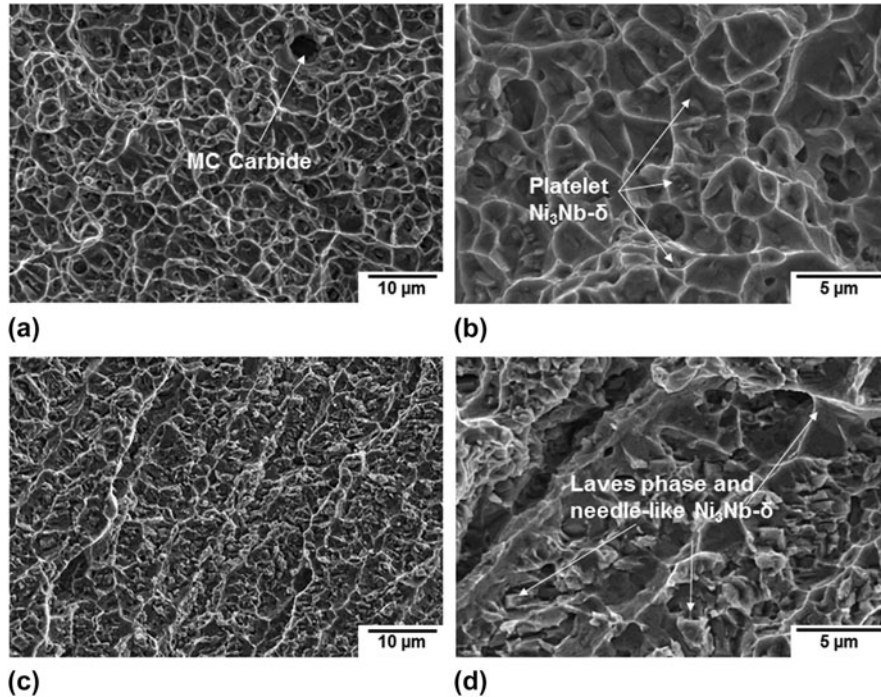


FIG. 7. Typical tensile fracture surfaces of the (a, b) PM and (c, d) laser deposited IN718 (taken from a DLD-PM coupon).

shallow dimple structures and preferential failure along the interdendritic regions or grain boundaries, where evidence of Laves and needle-like Ni₃Nb-δ particles was observed, as shown in Figs. 7(c) and 7(d).

Both Nb-rich and Ti-rich MC carbides were observed on the tensile fracture surfaces of the PM, DLD, and DLD-PM coupons, as shown in Figs. 8 and 9, respectively. Compared with the size of the MC carbides in the PM (approximately 15 μm as shown in Fig. 8), the size of those in the DLD and DLD-PM coupons was finer (approximately 8 μm as shown in Fig. 9), probably due to the rapid cooling conditions during laser deposition that may suppress the γ/NbC eutectic reaction. As illustrated in Figs. 8(a) and 8(b), the Nb-rich MC carbides appeared darker in SEI mode than under BSEI, which indicates the presence of heavier elements, as compared to the γ-matrix. The composition of the MC carbide was confirmed by EDXS to consist mainly of Nb and C. In addition, Ti-rich MC carbides were observed on the fracture surfaces of the PM, DLD, and DLD-PM tensile samples, as shown in Figs. 8(c), 8(d), and 9. In particular, these carbides appeared to be dark in both SEI and BSEI modes, which indicates the presence of lighter elements, as compared to the γ-matrix. Through EDXS, the composition of this MC carbide [Figs. 8(c) and 8(d)] was ascertained to mainly consist of Ti and C. The presence of Nb-rich and Ti-rich MC carbides on the tensile fracture surfaces of the PM, DLD-PM, and DLD coupons can be related to the segregation of the elements C, Nb, and Ti. In particular, both Nb and Ti have low values of equilibrium distribution

coefficient, k , in IN718, i.e., 0.48 for Nb and 0.69 for Ti, as well as negligible solid state diffusion coefficients.³ Therefore, both Nb and Ti will tend to segregate to form Nb-rich or Ti-rich compounds through eutectic reactions, which usually locate at the interdendritic regions or grain boundaries during solidification.

It is noteworthy that Ti-rich MC carbides were found on the mating fracture surfaces of the DLD tensile specimens, as shown in Figs. 9(a)–9(d); this suggests that besides the possibility of carbide-matrix decohesion/debonding, fracture can also occur within these particles and render cleavage characteristics. Moreover, it is evident that the cracks that form in the MC carbides of the PM [Figs. 8(e) and 8(f)] and DLD [Figs. 9(e) and 9(f)] IN718 may subsequently propagate along the grain boundaries or interdendritic regions, respectively, which seems to be consistent with the conventional view of the brittle Nb-rich and Ti-rich MC carbides as crack initiators that can lead to the premature failure of the materials.

As mentioned above, platelet Ni₃Nb-δ particles were frequently apparent at the bottom of the dimples on the tensile fracture surface of the PM; thus, microvoids initiate at the platelet Ni₃Nb-δ particle and decohesion may appear at the particle/matrix interfaces [Figs. 10(a) and 10(b)]. In contrast, at the bottom of the dimples on the tensile fracture surfaces of the DLD IN718, the Laves particles were mainly observed with the needle-like Ni₃Nb-δ phase located around the partially dissolved Laves phase. In particular, the considerable dissolution of the Laves phase during solution heat treatment leaves a sufficient

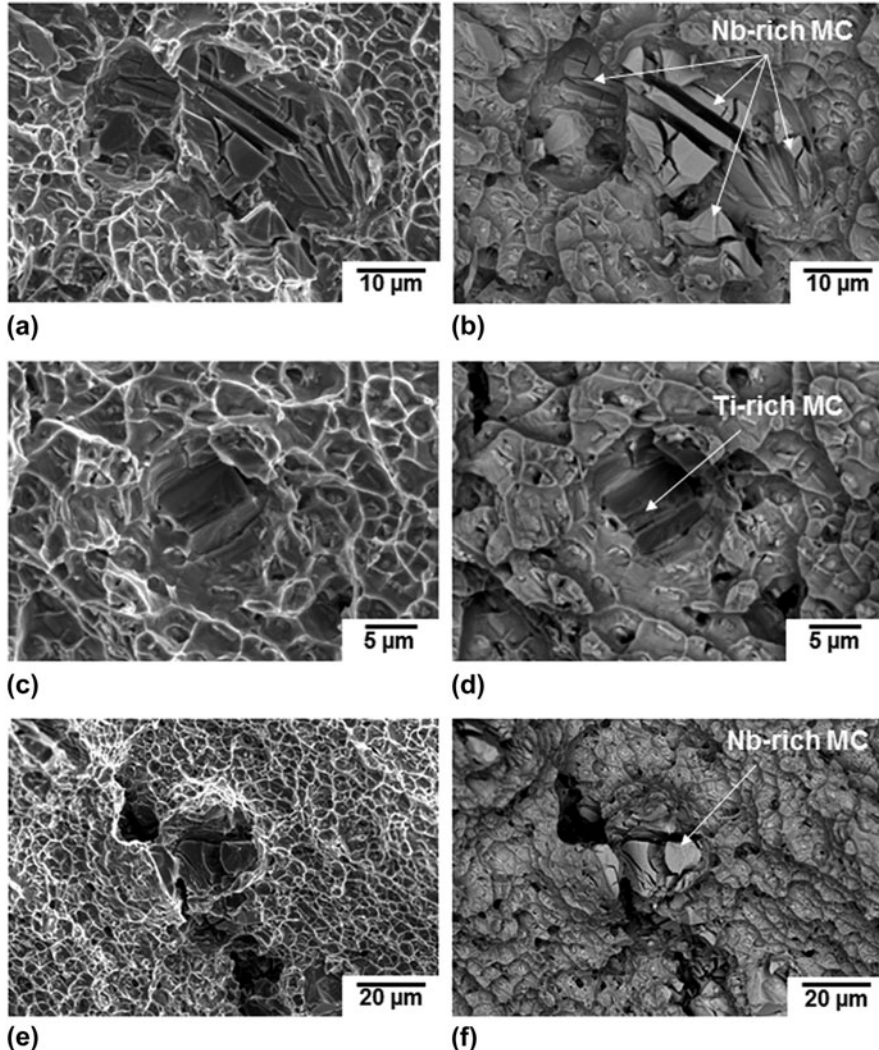


FIG. 8. Tensile fracture surface characteristics of PM showing (a, b) a cracked Nb-rich MC carbide, (c, d) a fractured Ti-rich MC carbide exhibiting cleavage features, and (e, f) evidence of cracks having formed at the brittle MC carbide particles with propagation along grain boundaries (a, c, e are with SEI whereas b, d, f are with BSEI).

amount of Nb around the partially dissolved Laves particles, which then become favorable nucleation sites for the formation of the needle-like $\text{Ni}_3\text{Nb}-\delta$ phase.¹

For the DLD and DLD-PM coupons, Figs. 11 and 12 show further evidence of fracture initiating initially through cracking in the Laves particles, or debonding/decohesion and void growth at the Laves particle/matrix interfaces. Specifically, the Laves particles that are propitious nucleation sites for considerable microvoid initiation (Fig. 11) facilitate the fracture process and lead to the growth of macroscopic cracks along the particle/matrix interfaces, as shown in Fig. 12. It is noteworthy that element mapping of the DLD fracture surface [Figs. 12(d) and 12(e)] using a SEM with EDXS demonstrates that (1) the Laves particles are rich in Nb, Mo, and Ti but lean in Fe, Cr, and Ni as compared with the matrix and (2) the cracks initiate and propagate along the Laves particles. On the basis of these

fracture surface observations, it can be reasoned that the reduced tensile strength and ductility of the PDHT DLD and DLD-PM coupons, as compared to the IN718 PM (Table III), can be attributed primarily to the presence of Laves phase in the DMZ microstructure, which agrees well with the findings reported previously for IN718 weldments and deposits.^{1,3,10,11}

According to aerospace specifications AMS 5596K and 5663M, the laser deposited IN718 (DLD and DLD-PM) in the PDHT condition has adequate tensile strength (YS and UTS) but does not strictly meet the minimum requirements of the ductility (Table III). In addition, all the tensile properties (both strength and ductility) of the laser deposited IN718 in the PDHT condition are markedly lower than the IN718 PM. The occurrence of tensile failure exclusively in the DLD portion of the DLD-PM specimens indicates that

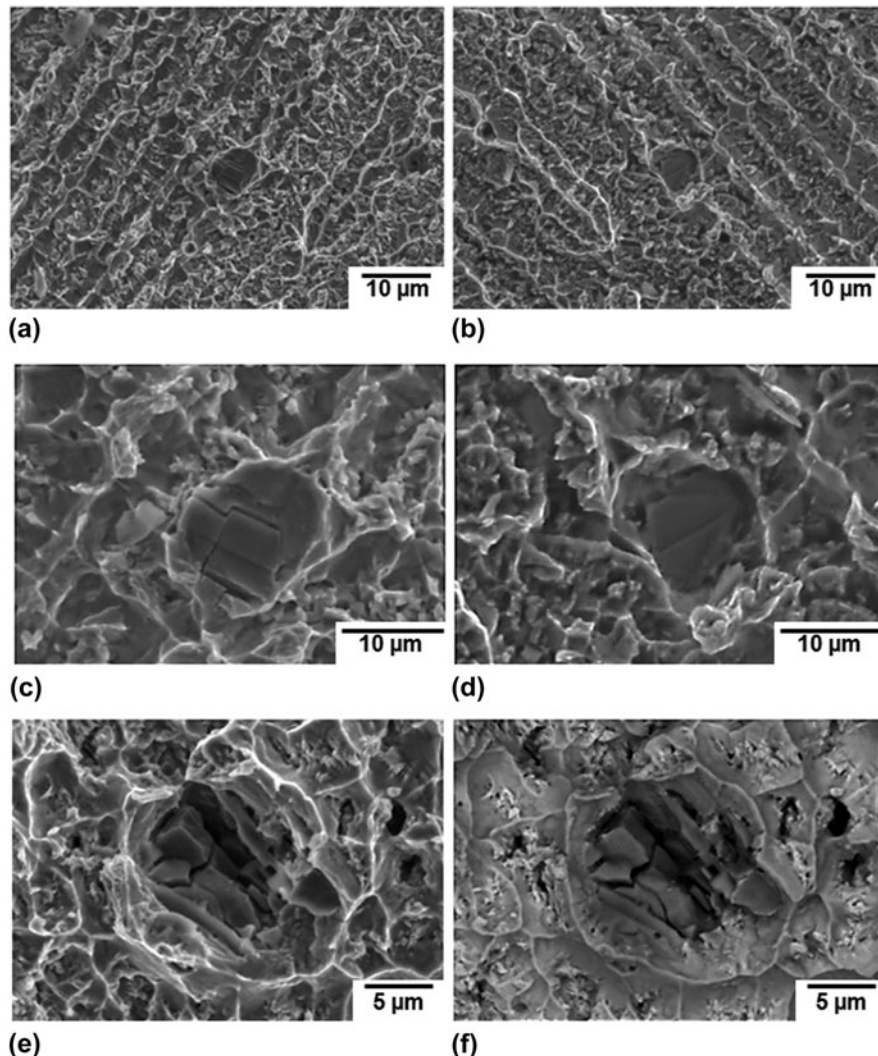


FIG. 9. Tensile fracture surface characteristics of DLD IN718 showing (a-d) a Ti-rich MC carbide on the mating surfaces and (e, f) a cracked Ti-rich MC carbide (all are with SEI except for the image (f) that was taken with BSEI).

(i) the bonding between the successive layers of the laser deposited materials is also weaker than that between the PM and DLD IN718 and (ii) the HAZ liquation cracking appearing in the PM substrate may not be the dominating factor for tensile failure. Similarly, the weld metal liquation cracks are not expected to be responsible for the tensile failure in the DLD specimens since these cracks somehow healed during the heat treatment applied after laser deposition. However, if both the HAZ and weld metal liquation cracks fail to fully heal during this heat treatment applied after laser deposition, they may contribute to a reduction in the tensile ductility. As compared to the DLD specimen, the DLD-PM specimen, consisting of 50% DLD IN718 and 50% IN718, exhibited better deformation ability and improved ductility, inevitably due to the PM characteristics.

The fracture surface characteristics of the laser deposited IN718 revealed dendritic patterns with preferential

cracking along the interdendritic regions or grain boundaries as compared to the transgranular ductile failure (presence of small, uniform, and deep dimples) of the IN718 PM. Also the fracture surface of both the laser deposited IN718 and IN718 PM revealed the presence of many secondary particles, such as MC carbides and intermetallics (platelet or needle-like $\text{Ni}_3\text{Nb}-\delta$, Laves phases), which are generally known to be inherently brittle (with extensive internal cracks) and play a critical role during the tensile failure of IN718,^{1,3,8,10,11} in particular vis-à-vis the poor ductility. Essentially, during tensile loading, the carbides and intermetallic phases are preferential sites for easy crack initiation and microvoid formation, as well as low energy fracture paths for crack propagation.^{1,3,10,15} Since fracture is usually reported to appear at the particle/matrix interfaces, poor bonding between the carbide/intermetallic phases and the matrix along with the brittleness of the carbides and intermetallics

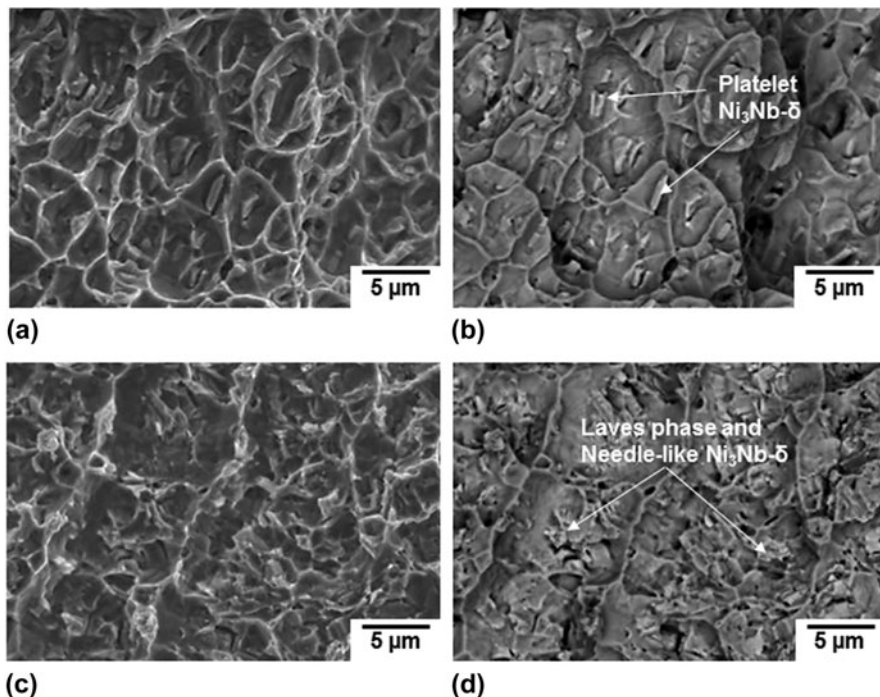


FIG. 10. Tensile fracture surfaces showing (a, b) platelet Ni₃Nb-δ in the PM and (c, d) needle-like Ni₃Nb-δ in DLD coupon.

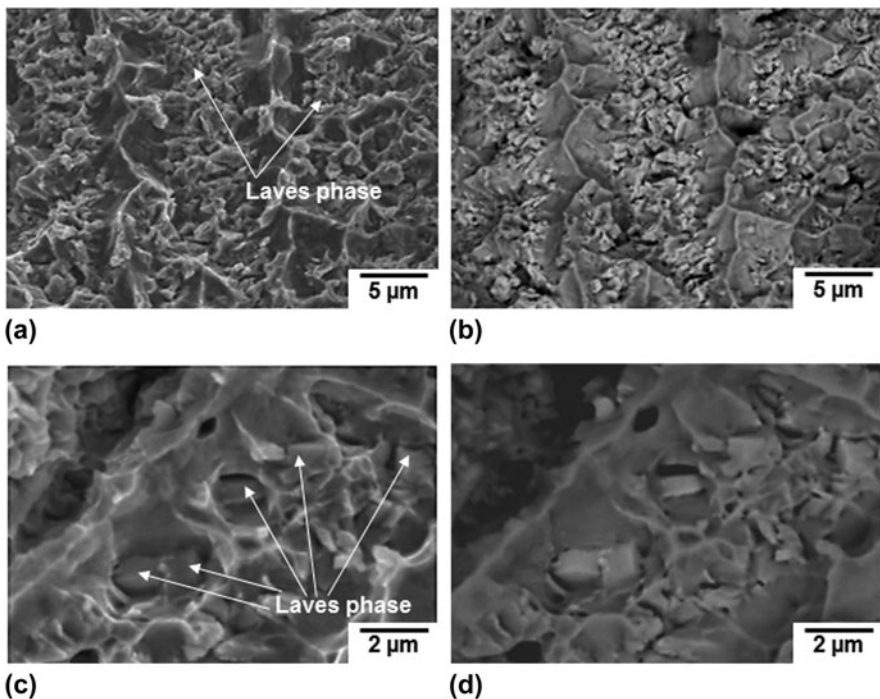


FIG. 11. The presence of Laves phase on the tensile fracture surfaces of (a, b) DLD and (c, d) DLD-PM coupons.

has generally been considered to be responsible for the tensile failure of the IN718 alloy.^{1,3,10,15}

However, the carbides and intermetallic phases have been observed to fracture within themselves and exhibit cleavage characteristics, as demonstrated in Figs. 9(a)–9(d)

for the case of an MC carbide particle that was apparent on both fractographs of the mating fracture surfaces of a DLD tensile specimen. Similar evidence for the Laves and Ni₃Nb-δ phases has been found in laser additive manufactured IN718 deposited using powder feed,²⁵ where these

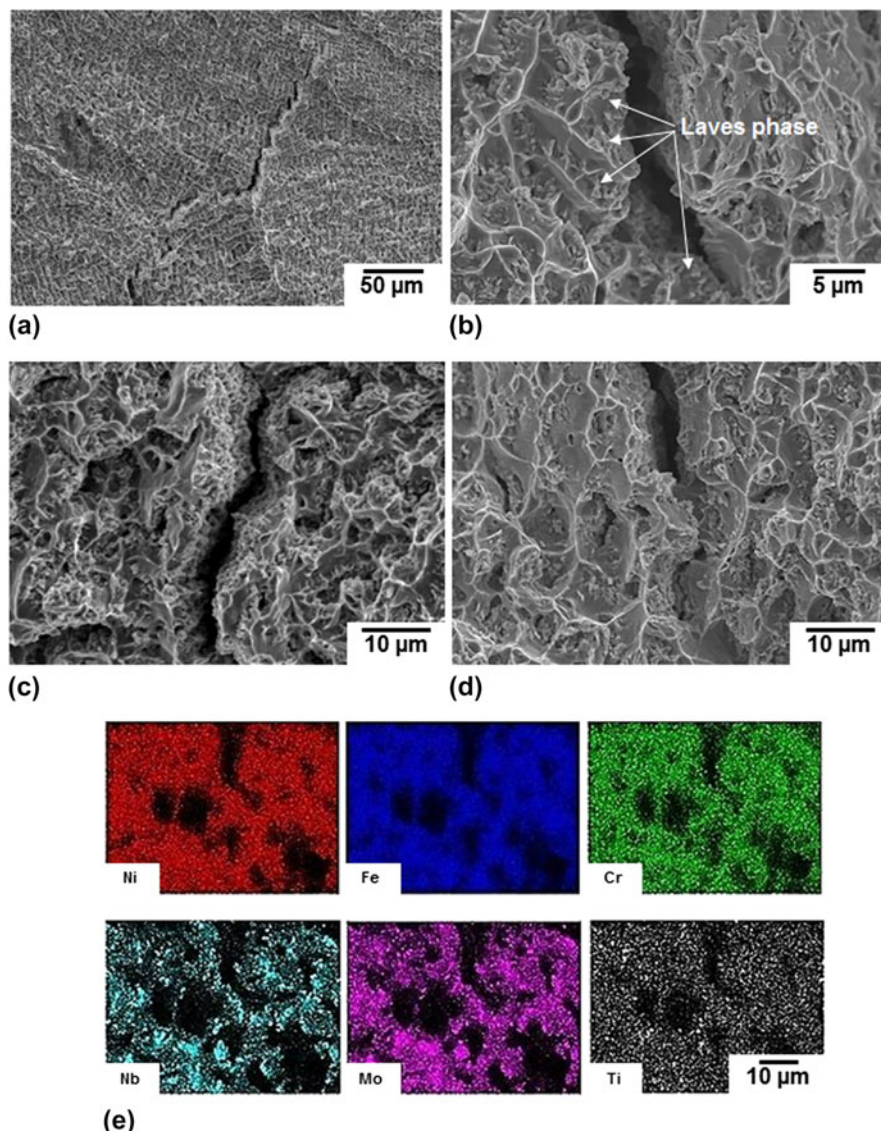


FIG. 12. Tensile fracture surface characteristics of DLD and DLD-PM coupons: (a–c) Laves particles along the cracks, (d, e) EDXS mapping indicating that Laves particles are associated with cracks and are rich in Nb, Mo, Ti but lean in Fe, Cr, and Ni as compared to the γ -matrix.

TABLE III. Room temperature tensile properties of IN718 in the PDHT condition.

Room temperature tensile properties	AMS 5596K sheets and plates (STA)				AMS 5663M bars, forgings, flash welded rings, and stock for forgings or flash welded rings (STA)		
	PM	DLD	DLD-PM	0.010–1.00"	Longitudinal	Long-transverse (forgings)	Transverse (bars)
UTS (MPa)	1448.6	1321.0	1298.3	≥ 1241.1	≥ 1275.5	≥ 1241.1	≥ 1241.1
YS (MPa)	1172.8	1097.6	1152.8	≥ 1034.2	≥ 1034.2	≥ 1034.2	≥ 1034.2
El. in 4D (%)	19.3	9.8	10.3	≥ 12	≥ 12	≥ 10	≥ 6
RA (%)	36.5	11.5	24.8	...	≥ 15	≥ 12	≥ 8

intermetallics were also fractured within themselves and observed on the two mating fracture surfaces. The tensile fracture within the MC carbides and/or the intermetallic particles suggests that the bonding force between the

particle/matrix is even greater than that associated with the close packed planes of the carbides or intermetallics themselves. Therefore, initiation and propagation of the cracks within the MC carbides and intermetallics also seem

to be another alternative failure mechanism, in addition to the well-recognized failure path at the particle/matrix interfaces. This is further supported by the lack of cracks between the matrix and the particles, as demonstrated in Figs. 8 and 9. Also, the premature fracture within the intermetallics or MC carbides [Figs. 9(a)–9(d)] fails to initiate microvoids and then the cracks propagate into the matrix along the interdendritic regions or grain boundaries [Figs. 8(e) and 8(f)]. In view of this, the fracture along the cleavage planes of the secondary MC carbides or intermetallics (Laves, $\text{Ni}_3\text{Nb}-\delta$, and γ' phases) is probably mainly due to their brittleness, as evidenced by the extensive presence of internal cracks. Recently, however, it was observed that the MC carbides or intermetallics in IN718 alloy can nucleate on oxide films.¹⁹ It is still not clear whether the fracture of the MC carbides or intermetallic particles is somehow related to the presence of the oxide films although this mechanism has been well investigated in cast Al–Si and Al–Cu^{26–28} alloys. Further work is still needed to clarify this in the future.

IV. CONCLUSIONS

(1) The yield and tensile strengths of the service-exposed IN718 PM, direct laser deposited (DLD) IN718, and DLD-PM coupons were well above the minimum values defined in the aerospace specifications AMS 5596K and AMS 5663M. However, the elongation at fracture for both the DLD and DLD-PM coupons was slightly lower than the specifications; the degraded ductility is the primary concern for the manufacturing and remanufacturing (repair) of DLD IN718. The service-exposed IN718 PM exhibited the highest tensile performance (both strength and ductility).

(2) The tensile fracture surface of service-exposed PM coupons consisted entirely of dimpled rupture features; the fine and uniform equiaxed dimples indicate transgranular ductile failure that corroborates the good strength and ductility properties. In contrast, the tensile fracture surfaces of the DLD-PM and DLD coupons revealed dendritic features with evidence of preferential cracking along the interdendritic structure or grain boundaries, where secondary MC carbides and intermetallics, such as Laves and needle-like $\text{Ni}_3\text{Nb}-\delta$ particles, were frequently observed.

(3) The HAZ liquation cracking in the DLD-PM coupon may contribute to the reduction in the ductility, but since the failure occurred in the DLD portion of the tensile specimen, the PM appears to have stronger bonding with the IN718 deposit relative to the bonding between the successive layers of deposited materials. The weld metal liquation cracking occurring in the deposited material was healed during post-deposition heat treatment, which effectively mitigated its harmful influence on the tensile properties.

(4) Secondary phase particles such as MC carbides and intermetallics ($\text{Ni}_3\text{Nb}-\delta$ or Laves phases) are usually

thought to be brittle and/or have poor bonding with matrix, leading to the low ductility in laser deposited IN718. However, the initiation and propagation of the cracks within the secondary particles and/or intermetallics also seem to be another alternative failure mechanism, in addition to the well-recognized failure path at the particle/matrix interfaces.

ACKNOWLEDGMENTS

The authors are grateful to X. Pelletier and E. Poirier for the preparation of the laser deposited IN718 coupons and their technical support for metallographic preparation. The following statement pertains only to authors X. Cao, Y.-N. Zhang and P. Wanjara: Published with permission of the Crown in Right of Canada, i.e., the Government of Canada.

REFERENCES

1. H. Qi, M. Azer, and A. Ritter: Studies of standard heat treatment effects on microstructure and mechanical properties of laser net shape manufactured Inconel 718. *Metall. Mater. Trans. A* **40A**, 2010 (2009).
2. G.K.L. Ng, G.J. Bi, and H.Y. Zheng: An investigation on porosity in laser metal deposition. The International Congress on Applications of Lasers & Electro-Optics (ICALEO) 2008 Proceedings, Paper #105, Temecula, California, October 2008; p. 23.
3. J.N. Dupont, J.C. Lippold, and S.D. Kiser: *Welding Metallurgy and Weldability of Nickel-base Alloys* (John Wiley & Sons, Inc., Hoboken, NJ, 2009).
4. J. Andersson and G.P. Sjoberg: Repair welding of wrought superalloys: Alloy 718, Allvac 718plus and Waspaloy. *Sci. Technol. Weld. Joining* **17**, 49 (2012).
5. B. Baufeld: Mechanical properties of Inconel 718 parts manufactured by shaped metal deposition (SMD). *J. Mater. Eng. Perform.* **21**, 1416 (2011).
6. N.I.S. Nussein, J. Segal, D.G. McCartney, and I.R. Pashby: Microstructure formation in Waspaloy multilayer builds following direct metal deposition with laser and wire. *Mater. Sci. Eng., A* **497**, 260 (2008).
7. J.C. Ion: *Laser Processing of Engineering Materials; Principles, Procedure and Industrial Application* (Elsevier Butterworth-Heinemann, Oxford, UK, 2005).
8. X. Zhao, J. Chen, X. Lin, and W. Huang: Study on microstructure and mechanical properties of laser rapid forming Inconel 718. *Mater. Sci. Eng., A* **478**, 119 (2008).
9. P.L. Blackwell: The mechanical and microstructural characteristics of laser-deposited IN718. *J. Mater. Process. Technol.* **170**, 240 (2005).
10. G.D.J. Ram, A.V. Reddy, K.P. Rao, G.M. Reddy, and J.K.S. Sundar: Microstructure and tensile properties of Inconel 718 pulsed Nd-YAG laser welds. *J. Mater. Process. Technol.* **167**, 73 (2005).
11. X. Cao, B. Rivaux, M. Jahazi, J. Cuddy, and A. Birur: Effect of pre- and post-weld heat treatment on metallurgical and tensile properties of Inconel 718 alloy butt joints welded using 4 kW Nd:YAG laser. *J. Mater. Sci.* **44**, 4557 (2009).
12. J.K. Hong, J.H. Park, N.K. Park, I.S. Eom, M.B. Kim, and C.Y. Kang: Microstructures and mechanical properties of IN718 welds by CO₂ laser welding. *J. Mater. Process. Technol.* **201**, 515 (2008).

13. G.X. Yang, Y.F. Xu, L. Jiang, and S.H. Liang: High temperature tensile properties and fracture behavior of cast nickel-base K445 superalloy. *Prog. Nat. Sci.* **21**, 418–425 (2011).
14. M.J. Donachie and S.J. Donachie: *Superalloys: A Technical Guide* (ASM international, The Materials Information Society, Materials Park, OH, 2002).
15. E.A. Loria: *Proceedings of the International Symposium on the Metallurgy and Applications of Superalloy 718*, Pittsburgh, PA, TMS, Warrendale, PA, 2005, p. 135.
16. G.A. Rao, M. Kumar, M. Srinivas, and D.S. Sarma: Effect of standard heat treatment on the microstructure and mechanical properties of hot isostatically pressed superalloy Inconel 718. *Mater. Sci. Eng., A* **335**, 114 (2003).
17. S. Biswas, G.M. Reddy, T. Mohandas, and C.V.S. Murthy: Residual stresses in Inconel 718 electron beam welds. *J. Mater. Sci.* **39**, 6813 (2004).
18. H.C. Chen, A. Pinkerton, and L. Li: Fibre laser welding of dissimilar alloys of Ti-6Al-4V and Inconel 718 for aerospace applications. *Int. J. Adv. Manuf. Technol.* **52**, 977 (2011).
19. Y.N. Zhang, X. Cao, P. Wanjara, and M. Medraj: Oxide films in laser additive manufactured Inconel 718. *Acta Mater.* **61**, 6562 (2013).
20. Y.N. Zhang, X. Cao, and P. Wanjara: Fiber laser deposition of Inconel 718 using filler wire. *Int. J. Adv. Manuf. Technol.* **69**, 2569 (2013).
21. J.W. Hooijmans, J.C. Lippold, and W. Lin: Effect of multiple postweld heat treatment on the weldability of alloy 718. *Superalloys 718, 625, 706 and Various Derivatives*, edited by E.A. Loria. TMS, Warrendale, PA, 1997.
22. G.D.J. Ram, A.V. Reddy, K.P. Rao, and G.M. Reddy: Microstructure and mechanical properties of Inconel 718 electron beam welds. *Mater. Sci. Technol.* **21**, 1132 (2005).
23. J.F. Radavich: The physical metallurgy of cast and wrought alloy 718. *Conference Proceedings on Superalloy 718 – Metallurgy and Applications*, edited by E.A. Loria. TMS, Warrendale, PA, 1989; p. 229.
24. F.J. Xu, Y.H. Lv, Y.X. Liu, F.Y. Shu, P. He, and B.S. Xu: Microstructural evolution and mechanical properties of Inconel 625 alloy during pulsed plasma arc deposition process. *Mater. Sci. Technol.* **29**, 480 (2013).
25. Y.N. Zhang, X. Cao, P. Wanjara, and M. Medraj: Fatigue properties of laser additive manufactured Inconel 718 using powder feed. (2014, in preparation).
26. X. Cao and J. Campbell: The nucleation of Fe-rich phases on oxide films in Al-11.5Si-0.4Mg cast alloys. *Metall. Mater. Trans. A* **34A**, 1409 (2003).
27. X. Cao and J. Campbell: Solidification characteristics of Fe-rich phases in cast Al-11.5Si-0.4Mg alloy. *Metall. Mater. Trans. A* **35**, 1425 (2004).
28. K. Liu, X. Cao, and X-G. Chen: Formation and phase selection of iron-rich intermetallics in Al-4.6Cu-0.3Mg-0.5Fe cast alloys. *Metall. Mater. Trans. A* **44**, 682 (2013).

Studies of Standard Heat Treatment Effects on Microstructure and Mechanical Properties of Laser Net Shape Manufactured INCONEL 718

H. QI, M. AZER, and A. RITTER

Laser net shape manufacturing (LNSM) is a laser cladding/deposition based technology, which can fabricate and repair near-net-shape high-performance components directly from metal powders. Characterizing mechanical properties of the laser net shape manufactured components is prerequisite to the applications of LNSM in aircraft engine industrial productions. Nickel-based superalloys such as INCONEL 718 are the most commonly used metal materials in aircraft engine high-performance components. In this study, the laser deposition process is optimized through a set of designed experiments to reduce the porosity to less than 0.03 pct. It is found that the use of plasma rotating electrode processed (PREP) powder and a high energy input level greater than 80 J/mm are necessary conditions to minimize the porosity. Material microstructure and tensile properties of laser-deposited INCONEL 718 are studied and compared under heat treatment conditions of as deposited, direct aged, solution treatment and aging (STA), and full homogenization followed by STA. Tensile test results showed that the direct age heat treatment produces the highest tensile strength equivalent to the wrought material, which is followed by the STA-treated and the homogenization-treated tensile strengths, while the ductility exhibits the reverse trend. Finally, failure modes of the tensile specimens were analyzed with fractography.

DOI: 10.1007/s11661-009-9949-3

© The Minerals, Metals & Materials Society and ASM International 2009

I. INTRODUCTION

LASER net shape manufacturing (LNSM) is a laser cladding based freeform fabrication technology that uses a high energy laser beam to create three-dimensional geometries by precisely cladding thin layers of metal powder on a base material. As a rapid manufacturing method without the assistance of tooling, this technology enables quick access to new design concepts, shortens the new product introduction cycle, and enables near-net-shape repairs of costly components. One of the important applications of the LNSM technology developed at the General Electric Global Research Center is to provide an economic and flexible method to fabricate and repair high-performance components in aircraft engines, *i.e.*, blisk blades, compressor blades, and turbine components. Geometric accuracy and material properties are the two basic, but challenging, requirements for final implementation of LNSM technology in the aircraft engine industry.

INCONEL^{*} 718 (IN718) has been the most widely

*INCONEL is a trademark of Inco Alloys International, Huntington, WV.

used nickel-based superalloy in the aircraft engine industry over the past 40 years. It has been used in many aircraft engine components, *i.e.*, critical rotating parts, airfoils, supporting structures, and pressure vessels, accounting for over 30 pct of the total finished component weight of a modern aircraft engine.^[1,2] IN718 was designed to retain high strength, creep resistance, and good fatigue life at high temperature up to 650 °C. It can be strengthened by precipitating γ'' (Ni_3Nb) and γ' ($\text{Ni}_3(\text{Al},\text{Ti})$) phases in the γ matrix at normal volume fractions of approximately 16 and 4 pct, respectively, after a full heat treatment.^[3] IN718 is known to have good weldability due to its relatively slow precipitation strengthening kinetics; however, the solidification process of cast or welded IN178 is often associated with segregation of high concentration refractory elements, such as Nb and Mo. As a result, a Nb-rich brittle intermetallic compound called Laves phase, represented as $(\text{Ni},\text{Cr},\text{Fe})_2(\text{Nb},\text{Mo},\text{Ti})$, often forms at the interdendritic regions.^[4] Laves phase is known to be detrimental to the material tensile ductility, fatigue, and creep rupture properties,^[3,5,6] as it depletes the principle elements needed for precipitation strengthening and aids in easy crack initiation and propagation.

H. QI, Laser Processing Engineer, and M. AZER, Manager, Laser and Metrology Systems Laboratory, Material Systems Technologies, and A. RITTER, Principal Scientist, Ceramics and Metallurgy Technologies, are with General Electric Global Research Center, Niskayuna, NY 12309. Contact e-mail: qih@research.ge.com

Manuscript submitted January 17, 2009.

Article published online August 14, 2009

Previous research showed that the morphology and composition of Laves phase depended strongly on the heat input and the cooling rate of a welding process;^[7] *i.e.*, welding processes with lower heat input and higher cooling rates produce less Laves phase, and consequently better material properties.

Previous literature has reported the tensile properties of laser-deposited IN718 (typically after solution and precipitation heat treatment) and has claimed properties equivalent or superior to the wrought properties. This is due to the fine grain size and small dendrite arm spacing as the results of the rapid solidification rate associated with laser deposition. Blackwell^[8] studied the tensile properties of laser-deposited IN718 by the LENS**

**LENS is a trademark of Optomec, Albuquerque, NM.

system and found the deposit exhibited anisotropic properties, which are the result of a weak substrate/deposit bond or lack of bonding between successive layers of the deposit. He also found that a subsequent hot isostatic pressing treatment can significantly reduce the anisotropic ductility of the deposit, but also substantially coarsen the base material grain size. Kelbassa *et al.*^[9] used a short aging method (732 °C for 4 hours) to heat treat the laser-deposited IN718 and achieved properties equivalent to forged tensile properties at room temperature and at 650 °C. Zhao *et al.*^[10] compared the microstructure and mechanical properties of IN718 deposited with the gas-atomized (GA) powder and the plasma rotating electrode processed (PREP) powder. They found that the GA powder produces inferior tensile and stress rupture properties due to the existence of hollow particles in the GA powder, which cause microcracks and porosity in laser-deposited samples.

The aim of this work is to optimize the laser deposition process parameters for high-quality deposits, to evaluate the industrial standard heat treatment methods on laser-deposited IN718, and to characterize the resultant material microstructures and tensile properties of deposited IN718 for the applications of net shape manufacturing and repair of aircraft engine components. The tensile properties of the alloy in the as-deposited, direct-aged, STA-treated, and homogenization-treated conditions are compared and correlated with their corresponding microstructure features.

II. EXPERIMENTAL PROCEDURE

A LNSM system consists of a CO₂ laser, a multiaxis CNC platform, an argon environment glove box, a multihopper powder feeder, and a four-way powder delivery nozzle. Figure 1 shows the schematics of the laser powder deposition process. A 1.5 kW PRC CO₂ laser with a “D” mode (a combination of the TEM00 and TEM01* modes) beam is used in the LNSM system. This mode produces an intensity profile with a relatively flat top and steep sides compared to a

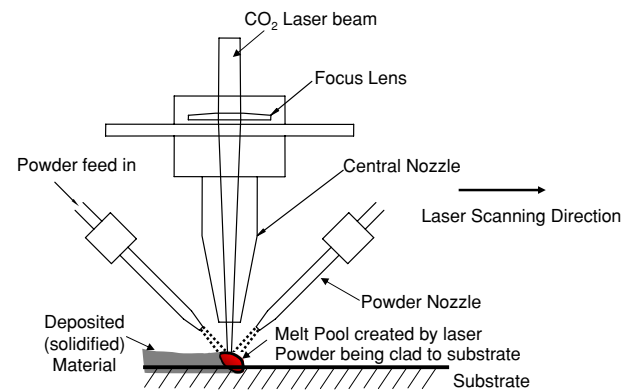


Fig. 1—Schematic of the laser powder deposition process.

Table I. Chemical Compositions of IN718 Powders (Weight Percent)

Element	GA Powder	PREP Powder
Ni	53.05	54.82
Fe	17.58	17.00
Cr	18.23	18.08
Mo	3.06	3.10
Nb + Ta	5.10	5.17
Ti	0.94	0.89
Al	0.44	0.53
Co	0.27	0.17
C	0.04	0.03
Si	0.12	0.08

Gaussian beam. The laser beam is focused by a lens with 127-mm focusing length through a central nozzle. Argon gas is supplied into the central nozzle to protect the focus lens from contamination and provide shielding to the melt pool. Four powder feed nozzles with 0.97-mm inner diameter deliver fine powder streams to the melt pool symmetrically from four directions. The powders used in this study are commercially available IN718 powder (mesh size –100/+325) manufactured by the GA and PREP methods, respectively. The chemical compositions of the GA and PREP IN718 powders used in this study are given in Table I. All the deposition experiments were conducted inside a glove box, where the concentration of oxygen was maintained below 20 ppm.

In order to manufacture the test samples with good quality and obtain the best capable mechanical property results, the following procedures were followed in this study:

- (1) toolpath optimization for multipass deposition;
- (2) porosity assessment;
- (3) process improvement, if needed;
- (4) heat treatment study;
- (5) metallographic study;
- (6) manufacturing of tensile test samples;
- (7) machining samples; and
- (8) tensile testing.

A. Process Optimization

Prior to making the samples for mechanical property tests, experimental studies were performed to investigate factors affecting the porosity levels in the laser-deposited samples, as porosities are known to deteriorate the ductility and fatigue life of the deposited material. Porosity generated in the laser deposition process is identified primarily from three sources: lack of fusion between deposition passes and layers, hollow powder particles produced during the GA or PREP process, and processing gas entrapped during deposition. Lack of fusion normally appears as irregular shapes along the fusion lines between two passes or layers and is associated with partially melted powders. The latter two porosity sources often result in circular-shaped pores. Lack-of-fusion pores can be eliminated by optimizing the laser heat input and geometric toolpath parameters, *i.e.*, bead overlap ratio and bead aspect ratio.^[11] In this study, experiments were designed in order to minimize the porosity caused by hollow powders and entrapped gas bubbles. Three types of IN718 powders with different particle size distributions and manufacturing methods were investigated (as shown in Table II). Figure 2 shows the representative micrographs of these three powders. It can be observed from Figure 2 that the GA powders generally contain a certain fraction of hollow particles. The coarse GA powder contains more hollow particles and larger pores than the fine GA powder. In contrast, hardly any hollow particles can be found in the PREP powder. Laser deposition parameters, laser power, travel speed, and layer height were varied in these experiments to reveal the effect of these parameters on the resulting porosities. Table III gives the ranges of each parameter used in this study. Within the selected range of each parameter, a

high level value (+1) and a low level value (-1) were selected, respectively, for the designed experiments. A set of two-level, three-factor (eight conditions) full factorial designed experiments was conducted with each type of the IN718 powder shown in Table II. This resulted in a total of 24 deposition runs. Solid rectangular blocks of 19 mm × 6 mm × 6 mm were deposited with the raster pattern toolpath. Each of the samples was sectioned at two transverse locations for examination of its internal porosities. The porosities were then measured with imaging analysis software based on the microscopic images of the sectioned surface and calculated as percentage values of the analyzed areas.

B. Porosity Results

Figure 3 shows the microscope pictures of sectioned surfaces from three samples deposited with the same set of process parameters but different IN718 powders. These samples were deposited with the same laser power 425 W (+1), speed 5 mm/s (+1), and layer height 0.127 mm (-1), which is one of the eight designed experiment conditions, but resulted in different porosity levels due to the different powder sources. The coarse GA powder produces a mean porosity of 0.75 ± 0.03 pct, the fine GA powder produces 0.51 ± 0.02 pct, and the PREP powder produces 0.03 ± 0.03 pct. To examine the effects of the process parameters, linear energy was calculated for each experiment condition, which is defined as laser power/speed (J/mm). Figure 4 shows the measured porosity values at the four different linear energy levels from the designed experiments. It is observed that the resultant porosities are inversely proportional to the linear energy. This trend is more obvious with the GA powders, where the porosities are minimized to 0.33 pct for the coarse GA powder and 0.19 pct for the fine GA powder at the highest energy input 111.5 J/mm. The PREP powder has produced

Table II. Three Types of Commercial IN718 Powders

Powder	Manufacturing Method	Mesh Size	Micron
GA coarse	gas atomized	-120/+200	74 to 125
GA fine	gas atomized	-200/+325	44 to 74
PREP	plasma rotating electrode processed	-100/+325	44 to 149

Table III. Ranges of Laser Parameters for Porosity Study

Parameters	Laser Power (W)	Travel Speed (mm/s)	Layer Height (mm)
Range	250 to 550	2.0 to 8.0	0.1 to 0.4



Fig. 2—Micrographs of the three types of IN718 powder used in this study.

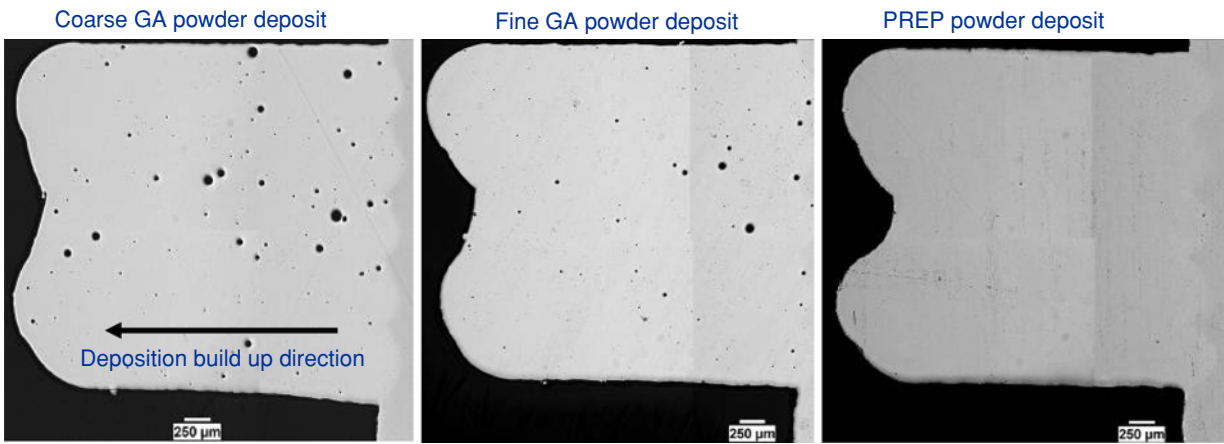


Fig. 3—Sectioned surfaces of the deposition samples fabricated with the same set of process parameters, *i.e.*, laser power 425 W (+1), speed 5 mm/s (+1), and layer height 0.127 mm (-1), but different sources of IN718 powder. Sectioned surfaces exhibit clearly different porosity levels.

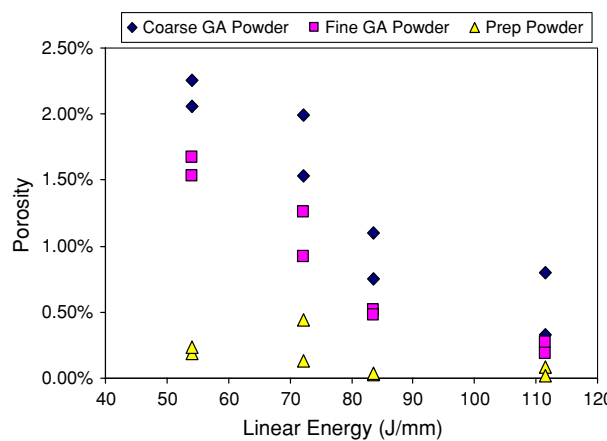


Fig. 4—Effect of the laser linear energy input (laser power/scanning speed) on the resultant porosity of each deposit. Four linear energy values are from the eight runs of the designed experiments.

significantly lower porosities compared to the GA powders. It can be seen that the porosity is reduced to less than 0.08 pct with PREP powder when the linear energy input is kept above 80 J/mm. Based on this study, all the following deposition experiments were performed with PREP IN718 powder and appropriate linear energy values for the best quality of deposition.

C. Heat Treatment and Microstructure Evaluation

Postweld heat treatment is necessary to relieve the residual stresses and enable the precipitation of strengthening phases. Microstructures from a laser deposition process are usually different from those resulting from the conventional cast and wrought processes due to the inherent rapid solidification rate associated with laser deposition. It is necessary to investigate how the industrial standard heat treatment methods (usually for cast and wrought IN718) affect the laser-deposited microstructures and eventually the mechanical properties of the material. In this study, three heat treatment

Table IV. Three Heat Treatment Methods for Laser-Deposited IN718

Homogenized STA* (Steps 1 + 2 + 3)	STA** (Steps 2 + 3)	Direct Aging (Step 3)
Step 1 homogenization	heat to 1093 °C ± 14, hold for 1 to 2 h, air cool or faster	
Step 2 solution	heat to 954 to 982 °C, hold for >1 h, air cool or faster	
Step 3 aging	heat to 718 °C ± 8, hold for 8 h, furnace cool to 621 °C ± 8, hold for 10 h, air cool or faster	

*According to AMS-5383D for cast IN718.

**According to AMS-5662M for forged IN718.

methods conforming to Aerospace Material Specifications (AMS) were evaluated for laser-deposited IN718 samples, *i.e.*, direct age, solution treatment and age (STA), and homogenization followed by STA. Table IV presents the detailed conditions for each heat treatment method used in this study. Solid rectangle samples with dimensions of 20 mm (L) × 8 mm (W) × 8 mm (H) were deposited with IN718 PREP powder and a constant 96 J/mm linear energy for these heat treatment studies. Samples were heat treated, sectioned, polished, and etched with a Kallings etchant. Microstructures at different heat treatment conditions were examined by optical microscopy and scanning electron microscopy (SEM). Energy dispersive X-ray spectroscopy (EDAX) analysis was performed for qualitative elemental characterization of featured phases based on the SEM observations.

Figure 5 demonstrates the microstructures of the transverse cross section of the as-deposited IN718 sample. Staggered individual deposit layers can be observed from the low-magnification microscopy

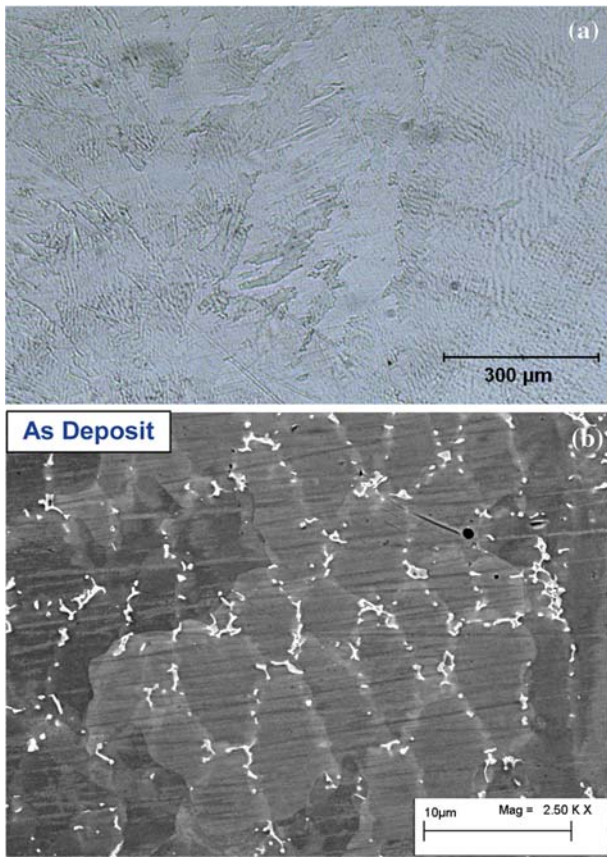


Fig. 5—Microstructure of transverse cross sections of the as-deposited IN718 sample: (a) optical micrograph picture at low magnification and (b) high-magnification SEM picture.

picture (Figure 5(a)). The deposition layers are delineated by bands of thin remelted nucleation zones formed at the layer interface. Extensively grown dendritic grains across a number of deposit layers (several millimeters) can also be seen occasionally. A high-magnification SEM picture in Figure 5(b) shows the detailed microstructure of the as-deposited material, where fine secondary dendrites are formed within a grain with an averaged dendrite arm spacing around $5\text{ }\mu\text{m}$. In contrast to the dark austenite matrix, small white particles in globular and irregular shapes that have precipitated along the interdendritic boundaries can be seen. They are identified as the Laves phase and some minor MC and TiN phases that are segregated during the fast solidification process. Figure 6 shows the EDAX analysis on the major phases appearing in the as-deposited microstructure. Comparing Figures 6(b) and (c), one can observe that the matrix of the dendrite's core area is rich in Fe, Cr, and Ni, while the white segregation particles are rich in Nb, Mo, and Ti, which are the major compositional elements of the Laves phase.

Figure 7 shows the microstructure that went through a direct age heat treatment. Compared to the as-deposited microstructure, the direct-age treatment did not change the size of the dendrites and the morphology of interdendritic Laves phase. Elemental analysis by EDAX on the direct-aged matrix phase and

primary segregation phases shows similar results to the as-deposited phases, as shown in Figure 6. The aging temperatures are designed to precipitate γ'' and γ' strengthening phases in the γ matrix, but these temperatures are not high enough to dissolve the interdendritic Laves phase.

Figure 8 illustrates the microstructure after solution and aging heat treatment. As can be seen, most Laves phases have been transformed to needlelike structures (δ phase) at the interdendritic regions. Since the δ phase requires less Nb than the Laves phase, the transformation indicates that the as-deposited high concentration of Nb at interdendritic regions has been partially dissolved into the matrix after solution treatment. However, the solution temperature at $980\text{ }^{\circ}\text{C}$ did not dissolve the Laves phase completely. It is found by EDAX that there are still occasionally some partially transformed Laves phase particles connecting with the δ -phase plates remaining in the interdendritic regions.

Figure 9 shows the microstructure that went through the complete homogenization (at $1093\text{ }^{\circ}\text{C}$) and STA heat treatment. As can be observed, the high temperature of homogenization results in considerable grain coarsening. Most Laves phase has been dissolved into the matrix and resulted in recrystallized large grains with bands of annealing twins. The primary MC and TiN phases, which appear in white small particles, are relatively stable phases and can still be found in the homogenized microstructure. The microstructure has a more isotropic appearance with recrystallized grains. As a result, one would expect more isotropic properties and increased ductility from this heat treatment. Figure 10 shows the EDAX elemental analysis results for the major phases after homogenization heat treatment, *i.e.*, NbC particles, the remaining δ phase, and the matrix phase.

III. TENSILE PROPERTY TESTS

A. Test Sample Fabrication

Two types of deposition geometries were used for making the tensile specimens: (1) deposition of thin-walled geometry on the direct-aged wrought IN718 (DA718) coupon with the final size of $42\text{ mm} \times 81\text{ mm} \times 3\text{ mm}$, as shown in Figures 11(a); and (2) fully deposited block with the size of $64\text{ mm} \times 15\text{ mm} \times 7\text{ mm}$ on stainless steel substrate ($25\text{ mm} \times 25\text{ mm} \times 6\text{ mm}$), as shown in Figure 11(b). The former sample is designed to represent the repair situations for compressor and blisk blades, where only direct-age heat treatment can be applied after repair. The strength of the interface between the deposited material and the wrought DA718 base material is evaluated in the tensile test. The base DA718 coupon was verified to have a microstructure consisting of fine equiaxed grains with a size of ASTM 11. The DA718 samples, as shown in Figure 11(a), were tested in two heat treatment conditions, *i.e.*, as deposited and direct aged. No solution and homogenization heat treatments were applied to these samples due to the potential degradation risk to the

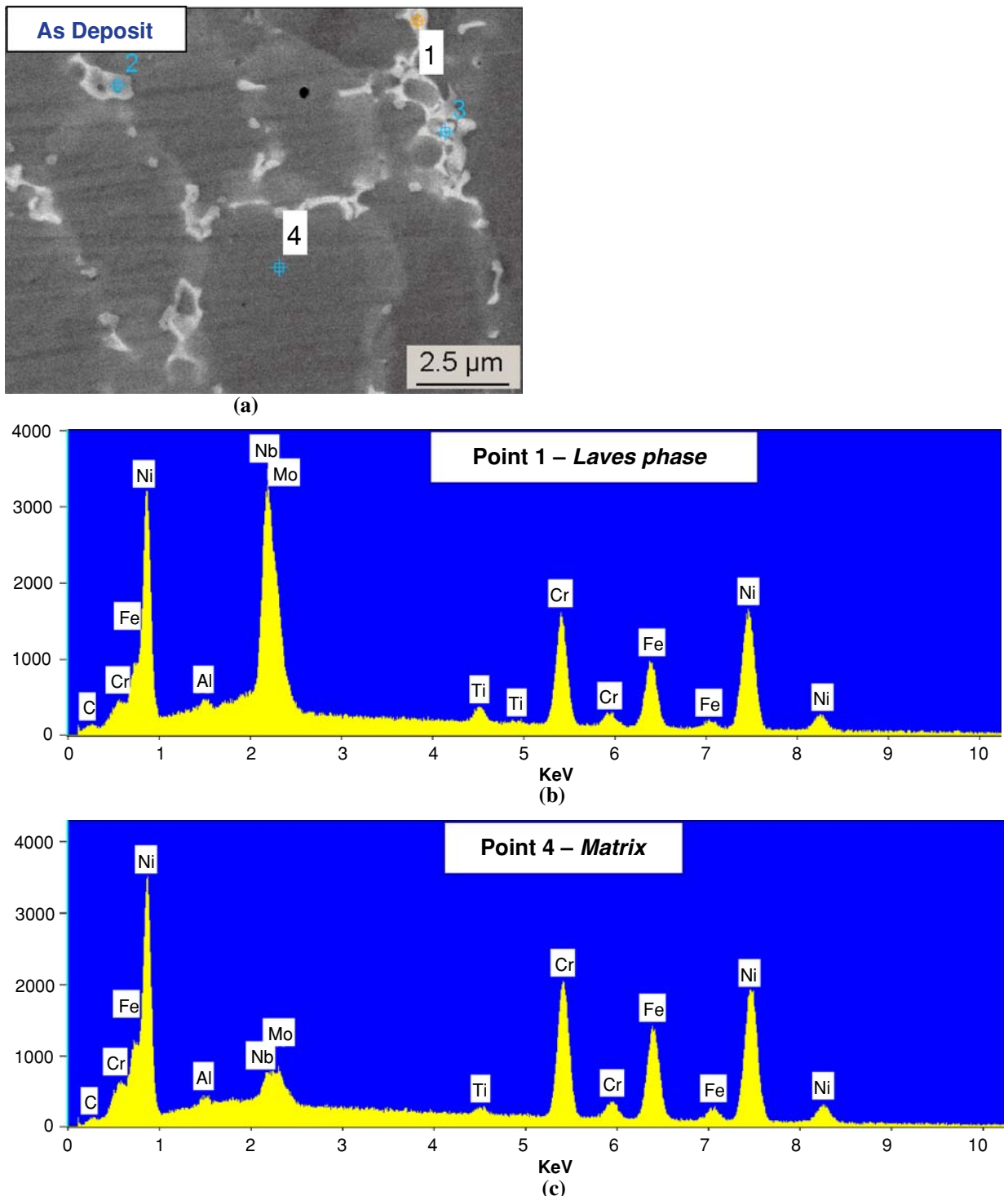


Fig. 6—EDAX elemental analysis on the major phases that appear in the as-deposited microstructure: (a) area of interest in SEM observation, (b) matrix elements, and (c) interdendritic Laves phase elements.

base material as a result of recrystallization and grain size coarsening. The fully deposited samples (Figure 11(b)) were divided into two groups and heat treated by standard STA and the homogenization STA method, respectively. The goal was to evaluate the laser deposition as a potential viable rapid manufacturing technique for new make parts. After

heat treatment, flat tensile bars 60.3 mm (L) × 12.7 mm (W) × 1.5 mm (T) that conformed to GE Aviation specifications were cut from the deposition samples by wire electrical discharge machining. For each heat treatment condition, two to four specimens were prepared and tested. All the tensile tests were conducted at room temperature.

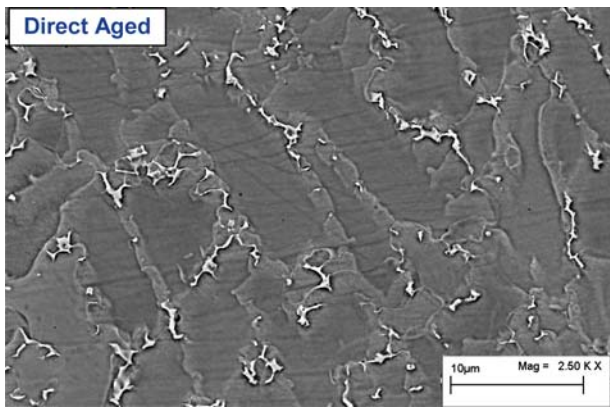


Fig. 7—Direct-aged microstructure shows similar dendrites and interdendritic phases as were seen in the as-deposited microstructure.

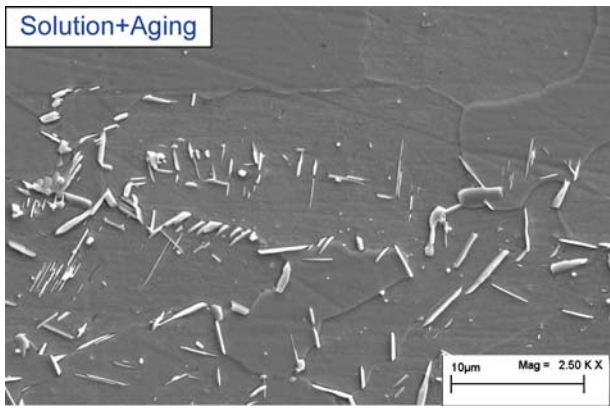


Fig. 8—Microstructure after solution and aging heat treatment shows most of the Laves phase has been transformed to needlelike δ phase at the interdendritic regions.

B. Tensile Test Results

Figure 12 demonstrates the average ultimate stress, 0.2 pct yield stress, and plastic elongation of the tensile test results. These results were compared with different heat treatment conditions and the minimum properties from the AMS specifications for cast and wrought IN718, respectively. All the DA718 specimens (from Figure 11(a)) failed in the gage sections of the laser-deposited portions. The as-deposited material produces low yield stress (552 MPa) and ultimate stress (904 MPa) but relatively high plastic elongation (16.2 pct). After direct-age heat treatment, the ultimate stress increased by 47 pct to 1333 MPa, while the yield stress almost doubled and reached 1084 MPa. However, the plastic elongation of the direct-aged material compared with the as-deposited material dropped significantly from 16.2 to 8.4 pct. Although the direct-aged elongation value is still above the AMS cast property, it is much lower than the AMS wrought property, which is at 12 pct. The STA treatment condition produced slightly lower tensile strength (ultimate stress 1221 MPa) than wrought material, but it produced much better plastic elongation at 16.0 pct compared to

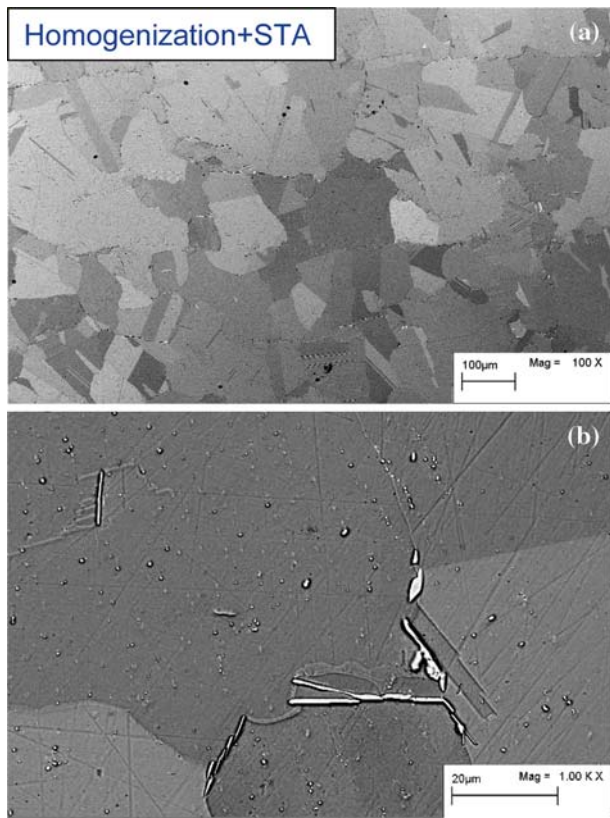


Fig. 9—Microstructure after the homogenization (at 1093 °C) and STA heat treatment shows (a) considerable grain growth with (b) occasional δ phase and MC phase at the grain boundaries.

the direct-aged condition. The material that underwent homogenization treatment produced slightly lower tensile strength (ultimate stress 1194 MPa) but even better elongation (19.9 pct) than the STA-treated material. In all cases, the heat-treated materials exhibited better tensile properties than the AMS cast properties but only marginally approached the wrought properties. Direct-aged tensile stress results were comparable to the wrought alloy, but they showed inferior ductility. The STA and homogenized STA treatments generated good ductility, which exceeded the minimum wrought elongation, but their tensile strength values were slightly below the wrought properties.

To compare the tensile behavior from different heat treatment conditions, one typical tensile test curve was chosen from each group of heat treatment specimens and plotted in Figure 13. Compared to the heat-treated materials, the as-deposited material was relatively soft and produced low yield and ultimate stresses, while demonstrating intermediate ductility. The heat-treated materials exhibited steeper elastic responses (higher modulus of elasticity) but yielded at different stress levels. The direct-aged curve yielded at the highest point followed by the STA curve and then the homogenization STA. After yielding, the three heat treatment conditions exhibited almost parallel stress-strain curves in the plastic elongation periods before necking. The direct age treatment improved the tensile strength of the

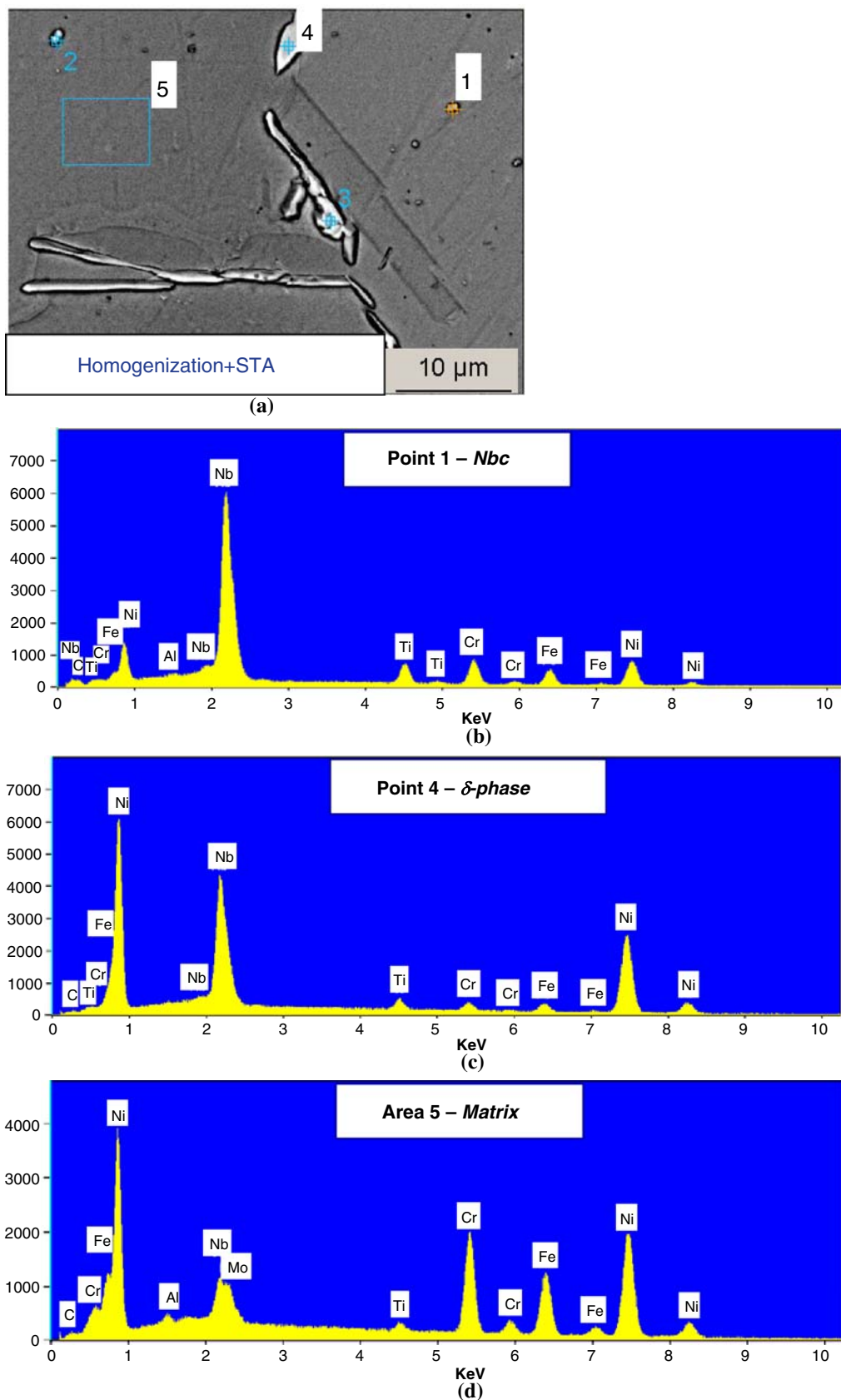


Fig. 10—EDAX elemental analysis shows the major phases after homogenization heat treatment: (a) area of interest in SEM observation, (b) NbC phase, (c) δ phase, and (d) matrix phase.

deposit material substantially with a relatively short plastic elongation period. With the solution and age heat treatment, the plastic deformation curve was slightly lower than the direct-aged curve, but the ductility was significantly improved. When treated with a full cycle of homogenization, solution, and age, the material demonstrated extended plastic elongation

before failure. This came at the cost of slightly lower yield and ultimate stresses.

The fracture surfaces of the tested specimens were examined under SEM. The as-deposited fracture surface exhibited a fine dimpled surface (Figure 14(a)), indicating a transgranular ductile mode of failure associated with good elongation. By contrast, the direct-aged fracture surface (Figure 14(b)) showed shallow dimples with protuberances composed of white particles, which are believed to be the Laves phase and MC carbides. This suggests the failure took place at the interdendritic regions or grain boundaries and was relatively brittle. Figure 15(a) shows the fracture surface of the STA heat-treated sample, which exhibits dendritic patterns with dimpled fracture features. This indicates that the fracture occurred preferentially along the interdendritic

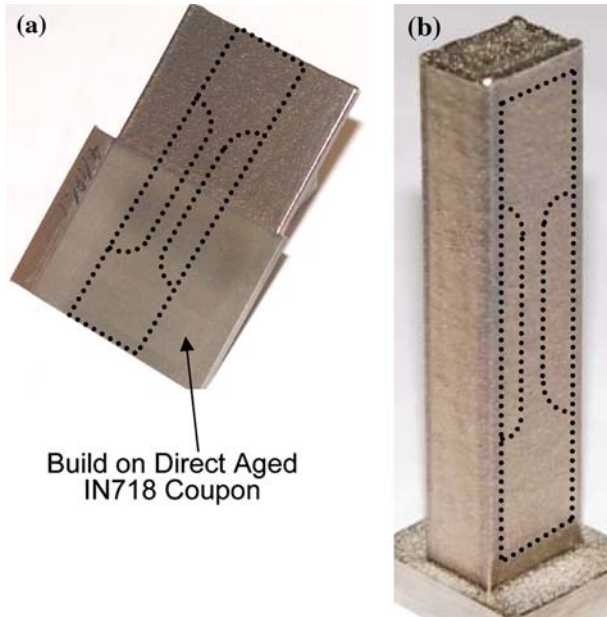


Fig. 11—Tensile samples fabricated by laser powder deposition. (a) Thin-walled sample deposited on the wrought DA718 coupon for as-deposited and direct-age evaluations and (b) fully deposited block sample for STA and homogenization treatment evaluations.

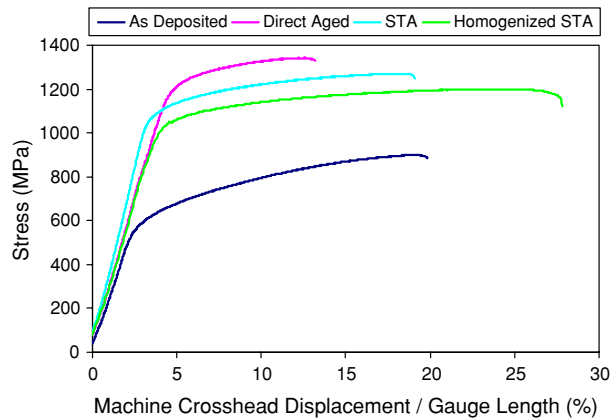


Fig. 13—Tensile test curves comparing the different heat treatment conditions.

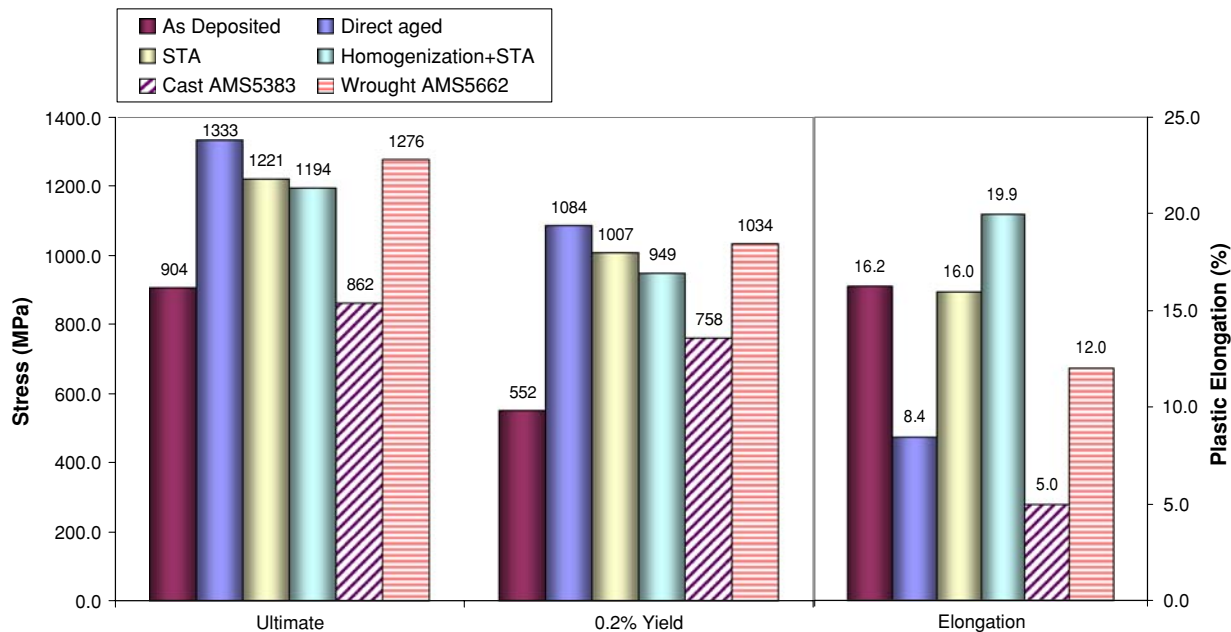


Fig. 12—Tensile test results showing the averaged ultimate stress, 0.2 pct yield stress, and plastic elongation compared with different heat treatment conditions and the AMS specifications for cast and wrought IN718, respectively.

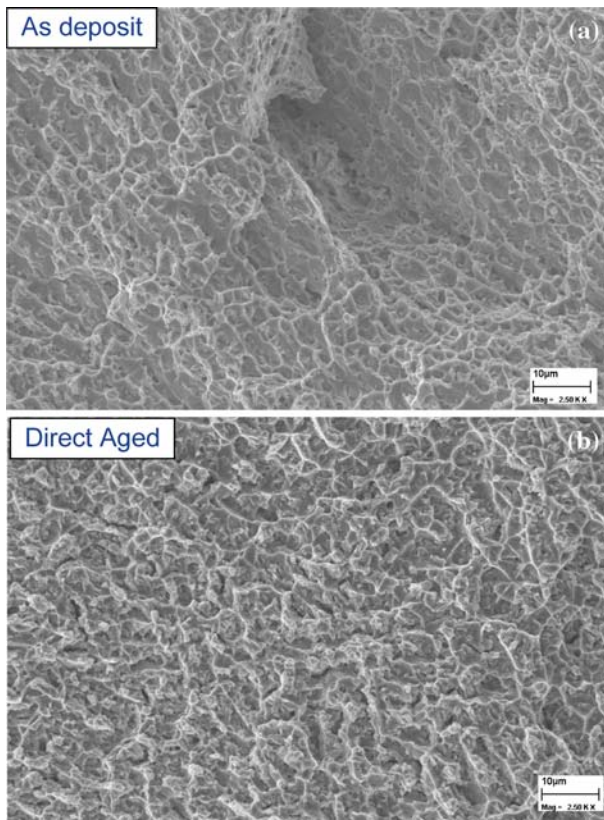


Fig. 14—Fracture surfaces of (a) the as-deposited sample and (b) the direct-aged sample.

regions and was a ductile failure. It was also observed that some white particles, *i.e.*, mostly δ phase and carbide particles, are present inside the dimples of the fracture surface, which suggests that these particles are the microvoid initiation sites associated with particle-matrix decohesion or particle fracture and eventually lead to the final transgranular fracture by void coalescence. In contrast to this, the fracture surface in the homogenized condition consisted of mostly fine shallow dimples and occasionally a few islands of flat surface areas approximately 100 μm in size. Figure 15(b) shows one such flat island in the fracture surface. This suggests that the failure has initiated from the relatively flat grain boundaries and propagated through coarsened grains, which were formed in the homogenization treatment.

IV. DISCUSSION

The microstructure of laser-deposited IN718 alloy exhibited various grain morphologies and size distributions. This was obviously caused by the dynamic heat transfer of the moving heat source and layered material formation mechanism. During laser deposition, material is built up layer by layer. When depositing a new layer of material, a thin top portion of the previous layer is remelted. As the molten pool solidifies, a thin nucleation zone at the layer interface is formed. As a result, layer boundaries consisting of fine grains can be observed,

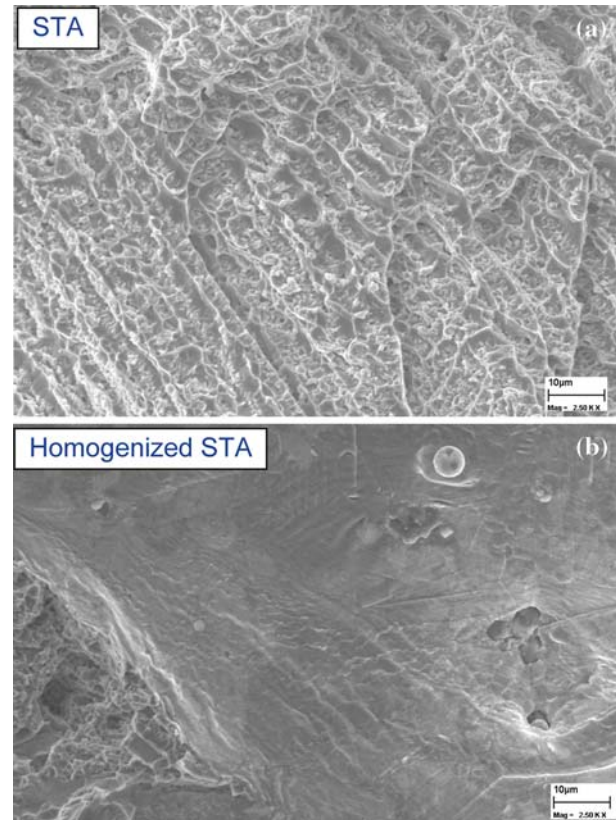


Fig. 15—Fracture surfaces of (a) the STA-treated sample, (b) the homogenization, and the STA-treated sample.

clearly delineating the deposit layers in the cross-sectional microstructure (Figure 5(a)). These layer interface regions are usually associated with sharp changes in grain size and degree of microsegregations; therefore, they can be the weak sites of tensile stress. Figure 16 compares the electron backscatter diffraction (EBSD)-generated grain/twin boundary overlay maps on the standard STA and homogenized STA microstructures, where the differences of grain morphologies and size distributions from the two heat treatments can be clearly seen. The layer interface regions can still be identified in the STA-treated material as bands of agglomerated fine grains (Figure 16(a)). This feature of layer boundaries disappeared in the homogenized microstructure, where the grains have been recrystallized and have a more isotropic appearance (Figure 16(b)). Figure 17 shows the microstructures of STA-treated material. It can be observed that bands of segregation-depleted regions are formed and also delineate the staggered deposition layers. It is also noticed that the edges of the deposit sample consist of relatively larger size grains (left areas in Figure 16(a)). This is a result of 30 pct higher energy input (high laser power and slower speed) used on the periphery contour of the rectangular sample in order to maintain good geometric accuracy. This portion of material was mostly removed during the preparation of tensile specimens; however, if the final specimen contained this microstructure, it may have contributed to deviations of the tensile properties.

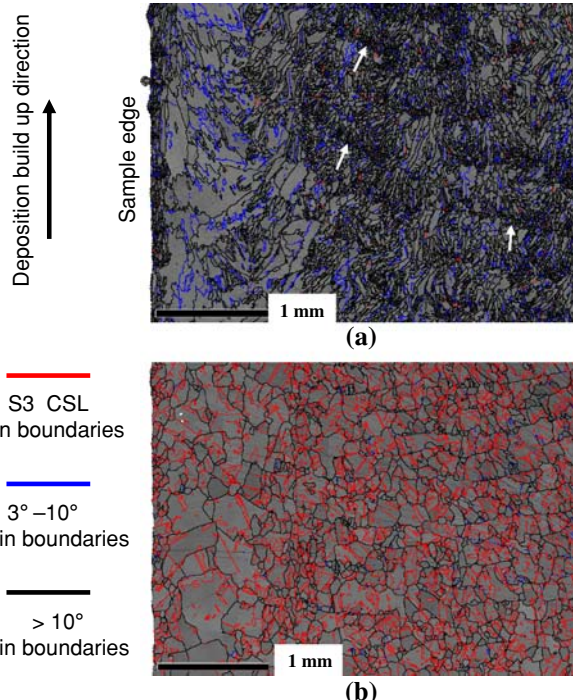


Fig. 16—Grain/twin boundaries overlay maps from EBSD analysis on (a) the standard STA-treated material (arrows pointing to the agglomerated fine grains at layer interfaces) and (b) the homogenization and STA-treated material.

The tensile test results have shown drastic strength changes from the as-deposited status to the direct-aged status. The cause for this is that the direct-aged heat treatment extensively precipitates fine γ'' and γ' strengthening phases in the matrix. These phases were suppressed during laser deposition because of the fast cooling rate. The Laves phase, in the form of fine particles along the interdendritic regions, was observed in both the as-deposited and the direct-aged microstructures with almost the same morphologies and volume fractions. It appears that the brittle Laves phase and carbide particles at the interdendritic regions, coupled with the fine γ'' and γ' precipitates in the matrix that lead to high tensile strength, are also responsible for the low ductility of the direct-aged material. Comparison of the tensile properties of the as-deposited material and the direct-aged material clearly indicates that the ductility of the material is closely related to the relative strength of the interdendritic phases and the matrix phases. The difference between the fractography pictures from the two conditions (Figure 14) indicates that once the matrix was strengthened by the γ'' and γ' precipitates, the brittle laves phase became the relatively weaker sites, initiating the fractures, and caused the reduced ductility of the material.

Standard STA heat treatment dissolved a good portion of the Laves phases and precipitated intergranular δ phase with acicular morphology. The literature has reported^[4] that the Laves phase requires 10 to 12 pct Nb to form, the δ phase requires 6 to 8 pct Nb, the γ'' phase needs 4 pct Nb, and the γ' can form with Nb levels

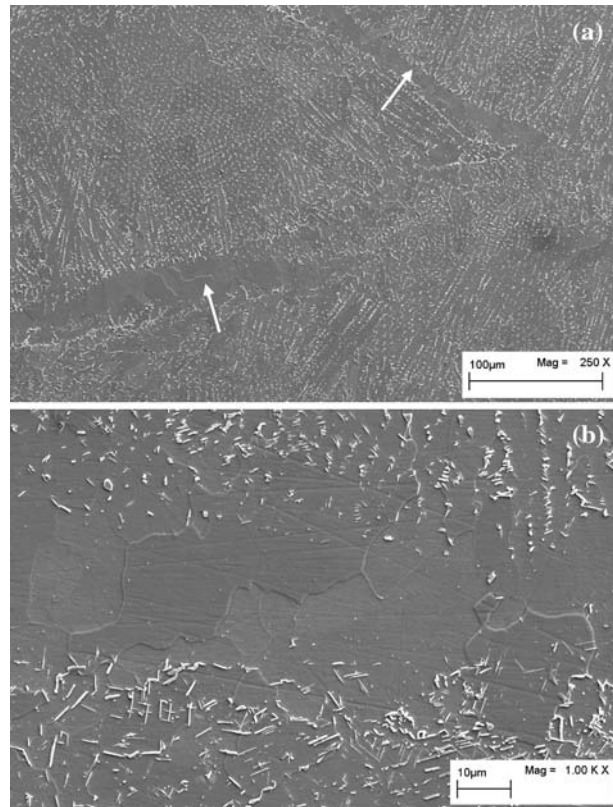


Fig. 17—Microstructure of STA-treated material showing bands of low Nb-rich segregation regions between the deposition layers (arrow pointed regions), which experienced grain growth during solution heat treatment.

below 4 pct Nb. Too much of the Laves phase and δ -phase formation will deplete the available Nb for γ'' and γ' precipitation. The δ phase is an incoherent precipitate and does not contribute to alloy strengthening. Similar to the Laves phase, a large δ phase (Ni_3Nb) at grain boundaries is considered to associate with loss of strength for IN718;^[12] however, the presence of δ phase at the grain boundaries has been reported to be beneficial for enhanced ductility and toughness.^[13] This is because fine acicular δ phase at the grain boundaries provides an irregular morphology to the grain boundaries and thereby restricts grain boundary sliding and improves fracture ductility. Fine grain size is generally controlled during the wrought process using the appropriate δ solvus temperature.^[4] A potential risk of the solution heat treatment is the nonuniformity of Nb concentration in the microstructure, because the δ solvus temperature is dependent on Nb concentration.^[1] The required δ solvus temperature is decreased as the Nb content is decreased, and areas low in Nb will undergo recrystallization and grain growth during the solution heat treatment. The amount of Nb being rejected into the liquid pool from the solidification front is dependent on the temperature gradient and cooling rate along the molten pool boundary during deposition. Variations in these factors will exaggerate or deplete the Nb-rich segregation phases as well as change the grain size at the layer interface regions. During the period of

laser irradiation (laser spot size/scanning speed, on the order of 0.1 second), the high-temperature gradient and the slow cooling rate cause the formation of a thin Nb-depleted solidification layer. As soon as the laser beam moves away, the molten pool is quenched by the surrounding bulk material. The fast solidification speed is initiated and forms the microstructure with fine Nb-rich microsegregation, which is adjacent to the Nb-depleted layers. This microstructure after solution treatment will precipitate fine acicular δ phase at the Nb-rich regions, but it undergoes potential grain growth at the low Nb regions, as shown in the middle part of Figure 17(b). The nonuniformity of microsegregation at the deposition layer interface and the resultant grain size growth at low Nb regions during the STA heat treatment are probably the reason for slightly reduced tensile strength compared to the direct-aged material.

The homogenized STA has dissolved most of the Laves phase at the interdendritic regions; however, it has also caused substantial grain growth, as can be seen in Figures 9(a) and 16(b). The appearance of overwhelming twin boundaries, as shown in Figure 16(b), indicates the extended recrystallization from the homogenization treatment. There is very little δ phase precipitated after the subsequent solution treatment. As a result, recrystallized high-angle grain boundaries become long and prone to remain straight, which provides an easy path for crack propagation and notch brittleness. The SEM fractography observation also confirmed that the failure mode of the intergranular fracture was initiated from the large flat grain boundaries of the homogenized material. The standard 1093 °C/1 h homogenization treatment for cast material is probably overwhelming for the laser-deposited material and causes noticeable grain growth. As observed previously, segregation is not severe in the as-deposited microstructure, due to the fast cooling rate in the laser deposition process. Slightly lower homogenization and solution temperatures and shorter heating time are therefore recommended for the full treatment of the laser-deposited IN718.

V. CONCLUSIONS

This article studied the microstructure and tensile properties of IN718 alloy processed by the laser powder deposition process and the effects of post-heat-treatment methods that comply with the AMS standard specifications. The deposition process was optimized through a set of designed experiments to reduce the porosity caused by hollow powders and entrapped gas bubbles generated during the deposition process. It was found that the use of PREP powder or fine size (~200 mesh size) GA powder combined with a high laser deposition linear energy level (laser power/scanning speed) helps to reduce the porosity. Specifically, the deposit porosity was minimized to less than 0.03 pct when the PREP powder was used with a linear energy level greater than 80 J/mm.

The material microstructure and tensile properties of the laser-deposited IN718 alloy were studied and

compared under the conditions of as deposit, direct age, solution treatment and age (STA), and homogenization followed by STA. It was found that the as-deposited alloy without any heat treatment remains soft and exhibits low tensile strength and good ductility (16.2 pct). The tensile strength was increased dramatically (100 pct improvement yield stress) and shown to be equivalent to wrought material after direct age due to the precipitation of the γ'' and γ' strengthening phases in the matrix; however, the ductility of the direct-aged material is reduced substantially to 8.4 pct due to fine Laves particles that remain at the interdendritic regions. These regions subsequently became relatively weaker sites, initiating fractures during tensile testing. Standard STA heat treatment has transformed most of the Laves phases to fine acicular δ phase at the interdendritic regions. Good ductility (16.0 pct) and slightly lower tensile strength (about 8 pct lower) were obtained from the STA treatment compared to the direct-aged condition. The low Nb bands formed at the deposit layer interfaces and the resultant grain size growth in these regions during the solution heat treatment seem to account for the slightly reduced tensile strength compared to the direct-aged material. The homogenized STA heat treatment completely dissolved the Laves phase but enabled substantial grain growth with isotropic appearance. As a result, this heat treatment produced the best ductility (19.9 pct), the tensile strength decreased 10 pct as compared to the direct-aged material.

ACKNOWLEDGMENTS

The authors thank Jeff Thompson and Chris Canestraro for performing the tensile tests, Renee Rohling and Jim Cournoyer for their support in the SEM fractography analysis, and Michelle Othon and Andrew Deal for their support in the EBSD analysis. Thanks are also due to Todd Rockstroh, Walt Ulanski, and Dave Abbott (GE Aviation) for their support.

REFERENCES

1. R.E. Schaefrik, D.D. Ward, and J.R. Groh: in *Superalloys 718, 625, 706 and Various Derivatives*, E.A. Loria, ed., TMS, Warrendale, PA, 2001, pp. 1–11.
2. D.F. Paulonis and J.J. Schirra: in *Superalloys 718, 625, 706, and Various Derivatives*, E.A. Loria, ed., TMS, Warrendale, PA, 2001, pp. 13–23.
3. G.D. Janaki Ram, A. Venugopal Reddy, K. Prasad Rao, and G.M. Reddy: *Mater. Sci. Technol.*, 2005, vol. 21 (10), pp. 1132–38.
4. J.F. Radavich: in *Superalloys 718—Metallurgy and Applications*, E.A. Loria, ed., TMS, Warrendale, PA, 1989, pp. 229–40.
5. J.J. Schirra, R.H. Cales, and R.W. Hatala: *Superalloys 718, 625, and Various Derivatives*, TMS, Warrendale, PA, 1991, pp. 375–88.
6. G.D. Janaki Ram, A. Venugopal Reddy, K. Prasad Rao, G.M. Reddy, and J.K. Sarin Sundar: *J. Mater. Proc. Technol.*, 2005, vol. 167, pp. 73–82.
7. C.H. Radhakrishna and K. Prasad Rao: *J. Mater. Sci.*, 1997, vol. 32, pp. 1977–84.
8. P.L. Blackwell: *J. Mater. Process. Technol.*, 2005, vol. 170 (1–2), pp. 240–46.
9. I. Kelbassa, E.W. Kreutz, P. Albus, and L. Zhu: *Proc. 24th Int. Congr. on Applications of Lasers & Electro-Optics (ICALEO)*, Laser Institute of America, Orlando, FL, 2005, pp. 660–65.

10. X. Zhao, J. Chen, X. Lin, and W. Huang: *Mater. Sci. Eng. A*, 2008, vol. 478, pp. 119–24.
11. H. Qi, M. Azer, and P. Singh: *Int. J. Adv. Manuf. Technol.*, in press.
12. M.E. Mehl and J.C. Lippold: *Superalloys 718, 625, 706, and Various Derivatives*, TMS, Warrendale, PA, 1997, pp. 731–41.
13. G.A. Rao, M. Kumar, M. Srinivas, and D.S. Sarma: *Mater. Sci. Eng. A*, 2003, vol. 355, pp. 114–25.

Effect of pre- and post-weld heat treatment on metallurgical and tensile properties of Inconel 718 alloy butt joints welded using 4 kW Nd:YAG laser

X. Cao · B. Rivaux · M. Jahazi · J. Cuddy ·
A. Birur

Received: 25 November 2008 / Accepted: 15 June 2009 / Published online: 2 July 2009
© Government Employee: Crown copyright from National Research Council Canada 2009

Abstract The effects of pre- and post-weld heat treatments on the butt joint quality of 3.18-mm thick Inconel 718 alloy were studied using a 4 kW continuous wave Nd:YAG laser system and 0.89-mm filler wire with the composition of the parent metal. Two pre-weld conditions, i.e., solution treated, or solution treated and aged, were investigated. The welds were then characterized in the as-welded condition and after two post-weld heat treatments: (i) aged, or (ii) solution treated and aged. The welding quality was evaluated in terms of joint geometries, defects, microstructure, hardness, and tensile properties. HAZ liquation cracking is frequently observed in the laser welded Inconel 718 alloy. Inconel 718 alloy can be welded in pre-weld solution treated, or solution treated and aged conditions using high power Nd:YAG laser. Post-weld aging treatment is enough to strengthen the welds and thus post-weld solution treatment is not necessary for strength recovery.

Introduction

Inconel 718 is a precipitation-hardenable nickel–iron base superalloy widely used in gas turbines, rocket motors, spacecraft, nuclear reactors, pumps, and tooling due to its excellent combination of corrosion resistance, oxidation resistance, and good tensile and creep properties at temperatures up to 650 °C [1]. The strengthening is mainly produced by lens-like disc shaped γ'' -Ni₃Nb coherent precipitates, with ordered bct DO₂₂ crystal structure, and cubic or spherical shaped γ' -Ni₃(TiAl) coherent precipitates, with ordered fcc Li₂ crystal structure [2]. Niobium is the key alloying element and performs the strengthening role in both the γ'' and γ' phases for Inconel 718 alloy. However, the principal strengthening phase, γ'' , is metastable and can be transformed to detrimental δ -Ni₃Nb when exposed at temperatures above 650 °C [2]. Prior to the introduction of Inconel 718 alloy in 1959, the precipitation-hardened nickel alloys, which were strengthened by either Al and/or Ti compounds underwent a rapid precipitation of the hardening phase during exposure to intermediate temperature range [3]. This rapid reaction caused difficulties in carrying out welding and repair without weld- or post-weld heat treatment associated cracking, which has been frequently encountered in the age-hardenable superalloys such as Waspaloy, Rene 41, Inconel X750, and Udimet 700. The Nb-containing 718 alloy has low Al and/or Ti contents. The introduction of niobium as the primary hardening element in Inconel 718 alloy resulted in a sluggish precipitating reaction of the principal strengthening precipitate γ'' phase, and produced a relatively low-strength, high ductility heat-affected zone during the initial aging treatment. This allowed more time for the alloy to achieve the desired hardness level and enabled stress to be relieved or relaxed before hardening. The improvement in

X. Cao (✉) · B. Rivaux · M. Jahazi
Aerospace Manufacturing Technology Center, Institute
for Aerospace Research, National Research Council Canada,
5145 Decelles Avenue, Montreal, QC H3T 2B2, Canada
e-mail: Xinjin.Cao@nrc-nrc.gc.ca

B. Rivaux
Ecole des Mines de Paris, CEMEF – Materials Processing
Center, Rue Claude Daunesse, BP 207,
06904 Sophia-Antipolis Cedex, France

J. Cuddy · A. Birur
Standard Aero Limited, 33 Allen Dyne Road, Winnipeg,
MB R3H 1A1, Canada

the strain-age cracking resistance and subsequently the prevention of strain-age cracking during post-weld heat treatment (PWHT) drastically improved weldability and repairability of nickel alloys [3, 4]. Strain-age cracking is also termed solid-state cracking, or PWHT stress relaxation cracking. Strain-age cracking usually occurs after welding or during precipitation-hardening heat treatment when the combination of stresses exceeds the material strength. The stresses include the residual welding stresses and those associated with precipitation reactions and fabrication processes.

Inconel 718 alloy has excellent weldability largely because of its resistance to strain-age cracking and reasonably good resistance to solidification cracking. Tungsten inert gas (TIG), electron beam (EB), and plasma welding techniques have been most widely used for precipitation-hardened nickel alloys [5, 6]. One of the major problems associated with the Inconel 718 alloy welding is microfissuring in the HAZ [1]. The HAZ liquation cracks (microfissures) have been frequently observed due to the interaction between grain boundary liquation and tensile stress. The microfissures usually occur under the nail head and are perpendicular to the fusion boundary. Another root concern for Inconel 718 alloy is the segregation of the element Nb and the consequent formation of the Nb-rich Laves phase, a brittle intermetallic compound represented as $(\text{Ni}, \text{Cr}, \text{Fe})_2(\text{Nb}, \text{Mo}, \text{Ti})$, in the interdendritic regions during weld metal solidification. Studies have shown that the formation of the Laves phase (i) depletes principal alloying elements required for hardening from the matrix, (ii) represents a weak-zone microstructure between the Laves phase and the matrix interface, (iii) acts as preferential sites for easy crack initiation and propagation because of its inherent brittle nature, and (iv) deteriorates the mechanical properties, especially tensile ductility, fracture toughness, fatigue, and creep rupture properties [7–9]. Because the formation of Laves phase is due to segregation during weld solidification, any effort to minimize the formation of Laves phase should be directed towards minimizing the segregation. This is well-achieved using a low heat input or high cooling rate welding process such as laser beam technique. High energy density laser beam is characterized with high welding speed, flexibility, and ease of automation. Moreover, its low overall heat input also produces low distortion and minimizes the width of the fusion zone and the HAZ [1]. Therefore, laser welding is very attractive for Inconel 718 alloy. It has been reported that microfissures can even be avoided using a low power pulsing wave Nd:YAG laser [4, 7, 10] and high power CO₂ laser [5].

To date, little work has been carried out using a high power continuous wave solid-state Nd:YAG laser for Inconel 718 alloy welding. It is interesting to investigate

whether the HAZ microfissuring is still an issue for Inconel 718 alloy welded using a high power continuous wave solid-state Nd:YAG laser. It is usually advised that (i) precipitation-hardened nickel alloys should be welded in the solution treated state, and (ii) post-weld solution and aging treatments should be carried out for precipitation hardening [6]. Some interesting topics are therefore to investigate whether a high power Nd:YAG laser can be used to reduce the full post-weld heat treatment to aging only or to weld the materials directly in the solution and aged state. Hence, investigation into the effects of heat treatment conditions prior to and after welding on joint quality is essential. In this study, a 4 kW continuous wave Nd:YAG laser system was used to weld 3.18-mm thick Inconel 718 alloy butt joints and the influence of pre- and post-weld heat treatment conditions on welding quality is investigated in terms of weld defects, microstructure, hardness, and tensile properties.

Experimental procedures

The experimental material used in this article is Inconel 718 alloy with a nominal thickness of 3.18 mm in two pre-weld heat treatment conditions: (i) solution treated (STed) in the as-received material form (980 °C for 1 h and air cooled), and (ii) solution treated and aged (STAed). Solution treating is a high-temperature heat treatment designed to put age-hardening constituents and carbides into solid solution, i.e., solubilizing the Nb-rich Laves phase and producing a homogenized microstructure. The latter is generally obtained only through aging treatment of the as-received material in solution treated condition. The aging consisted of the following steps: solution at 718 °C for 8 h, furnace cool to 621 °C in 2 h, hold at 621 °C for 8 h, and argon quench. The room temperature tensile properties of the 3.18-mm thick Inconel 718 alloy sheets in the roll direction in both the solution treated (STed) and the solution treated and aged (STAed) conditions are indicated in Table 1. The alloy sheet was sheared into 102 × 63 × 3.18 mm coupons with the longitudinal direction (welding direction) normal to the rolling direction. The surface oxides were then removed and cleaned with ethanol prior to laser welding.

Table 1 Mechanical properties of 3.18-mm Inconel 718 base alloy sheets

	Solution treated	Solution treated and aged
Yield strength 0.2% (MPa)	470	1209
Tensile strength (MPa)	887	1398
Elongation (%) at 50-mm gage length	48.8	21.4
Hardness (HV)	210	440

The coupons were clamped using bolts in a restraint fixture designed for a butt joint configuration. The fixture was placed on the electromagnetic table of the laser welding system. The welding machine was a continuous wave solid-state 4 kW Nd:YAG laser system equipped with fiber optic beam transmission and an ABB 4400 industrial robot. In this study, all laser welding experiments were performed using the optimized processing parameters obtained in an earlier work [11] where the effect of joint gap ranging from zero (no gap) to 0.5 mm on the quality of Inconel 718 alloy butt joints was investigated using 0.89 mm (0.035") filler wire with the composition of the parent material. Inconel 718 alloy is usually laser welded autogenously but the use of filler wire can lower the sensitivity to joint gaps, eliminate underfill, and undercut defects, and hence improve welding process. These optimized parameters used in this work are 0.3-mm joint gap, 3.0-m/min welding speed, and 4-kW laser power. To prevent oxidation during welding, argon (at a flow rate of 23.6 L/min) was applied to the top and helium (47.2 L/min) to the tail and the bottom surfaces of the joint. The defocusing distance used is -1.0 mm. The defocusing distance, which refers to the distance of the beam waist (focal spot) from the top surface of the work-piece, is positive above, and negative below, the top surface. Other parameters such as fiber and focusing optics conditions were fixed at fiber diameter of 0.6 mm, collimation lens of 200 mm, focusing lens of 150 mm, and focusing spot diameter of 0.45 mm. Inconel 718 filler wire with a nominal diameter of 0.89 mm (0.035") was used at an angle of 30° with the work-piece surface and wire feed rate of 4.5 m/min. The feed rate of the filler wire was calculated by using the volume flow rate constancy principle. For each pre-weld heat treatment condition, 3 butt joints were prepared: 2 for post-weld heat treatments (i.e., aged, or solution treated and aged) and 1 for as-welded condition (Table 2). The specimens were solution heat treated at 993 °C for 1 h and then argon quenched while the aging process of the weld joints was carried out as described above. The post-weld solution treatment was considered as a possible alternative to overcome the problems associated with niobium segregation and the formation of Laves phase

Table 2 Pre- and post-weld heat treatments for 3.18-mm Inconel 718 sheets

Specimen ID	Pre-weld heat treatment	Post-weld heat treatment
IN80	Solution treated (STed)	As-welded
IN81	Solution treated (STed)	Aged
IN75	Solution treated (STed)	STAed
IN78	Solution treated and Aged (STAed)	As-welded
IN82-2	Solution treated and Aged (STAed)	Aged
IN82-1	Solution treated and Aged (STAed)	STAed

[7]. However, this consideration has practically restricted the solution treatment temperature to approximately 995 °C, which is the solvus temperature of the orthorhombic Ni₃Nb delta phase (the precipitation temperature for delta phase ranges from 860 to 995 °C), to avoid undesirable grain coarsening at higher solution temperatures [8].

Each weld joint was sectioned transverse to the welding direction using a precision cut-off saw to extract two specimens for metallographic examination. The remaining parts of the joints were used for tensile testing. Approximately 15–25 mm was cut from both sides of each joint to avoid edge effects and unstable welding conditions occurring at the start and the end. After cutting, each specimen was hot mounted in conductive Bakelite (Struers LaboPress-3), ground, and polished. Electrolytic etching was usually used, and two different etchants were employed to reveal the microstructure, depending on heat treatment conditions. Specimens were immersed in a solution of 25 g chromium trioxide (CrO₃) with 130 mL acetic acid (50%) and 7 mL distilled water. A voltage of 3.5 V was applied for 30 s with the etching time depending on the sheet thickness and conductive Bakelite. For the two post-weld heat treatments (i.e., aged or STAed), the etchant mentioned above was not suitable to reveal the microstructure of Inconel 718 alloy and thus a new etchant was applied. The specimens were immersed for a few seconds in a solution composed of 95 mL HCl plus 5 mL H₂O₂ for metallographic analysis. An optical microscope (Olympus GX-71) coupled with image analysis software (Analysis Five) was used to study weld geometry and to characterize the microstructure. Microstructure was also observed using a Hitachi S-3600N SEM with EDAX Genesis EDS system. For each sample, weld width (top, middle, and bottom), fusion-zone area, and discontinuities such as porosity, underfill, and weld reinforcement, if any, were measured. Vickers hardness was measured on each specimen at a testing load of 500 g, a dwell time of 15 s, and an indentation spacing of 0.2 mm using a Struers Duramin A300 Vickers microhardness machine. The hardness was usually measured along the middle-thickness of the joint.

For each weld specimen, four subsize tensile specimens were machined according to ASTM E8M-01, to give gauge dimensions of 6.0-mm width, 32-mm parallel length, and 125-mm overall length. The tensile specimens were tested at room temperature using a 50 kN Instron machine (model 1362) with self-locking grips and type 2620-604 Instron extensometer (a gage length of 25 mm used). The cross-head speed was fixed at 2 mm/min. For each tensile test, the data were converted from load and displacement to stress and strain, respectively, in order to obtain the stress-strain curve and to calculate yield strength at 0.2% offset, tensile strength, and plastic elongation percentage.

Results and discussion

Geometries

Figure 1 shows the transverse sections of all joints. The effect of post-weld heat treatment on joint dimensions appears to be insignificant and thus the measured joint dimensions are presented according to the pre-weld heat treatment conditions (Table 3). No significant differences in joint geometries were observed for the two pre-weld heat treatment conditions indicating that similar energy absorptivity of the laser beam is obtained for the STed, or the STAed conditions. In other words, the aging treatment of Inconel 718 alloy has little influence on the energy absorptivity of the laser beam.

Defects

As shown in Table 3 and Fig. 1, some minor underfill defects were observed. Sound joints were obtained, but some porosity was found in the fusion zone in some specimens. Figure 2 shows some microporosity obtained in the STed/as-welded condition. Figure 3 shows some

porosity observed in the STAed/aged condition. Figure 4 shows some microporosity obtained in the STAed/as-welded condition. As shown in Table 3 and Fig. 1, slightly more porosity is observed when the material was welded in the STAed condition. Most of the pores have dimensions less than 0.1 mm and their number is quite low. However, large porosity can occasionally be observed as shown in Fig. 3.

In the fusion zone, neither macrocracks nor microcracks were observed. However, liquation microfissures are frequently observed in the HAZ as shown in Fig. 5. Figure 6 shows the SEM observations obtained in the STed/as-welded condition. It was reported that microfissures can be avoided using a low power pulsing wave Nd:YAG laser [4, 7, 10] and high power CO₂ laser [5]. Therefore, HAZ cracking is still an issue in high power Nd:YAG laser welding for Inconel 718 alloy. The liquation cracks usually occur normal to the fusion line and along the grain boundaries in the HAZ. The backfilling of cracks near the fusion zone was observed, as shown in Fig. 6. They are mainly observed beneath the “nail head” region of the laser welds, similar to those in electron beam welds [12]. As shown in Fig. 7, the composition of the grain boundary

Fig. 1 Transverse sections of all butt joints. Heat treatment conditions are indicated as prior to/after welding (STed Solution Treated, STAed Solution Treated and Aged). **a** STed/As-welded. **b** STAed/As-welded. **c** STed/Aged. **d** STAed/Aged. **e** STed/STAed. **f** STAed/STAed

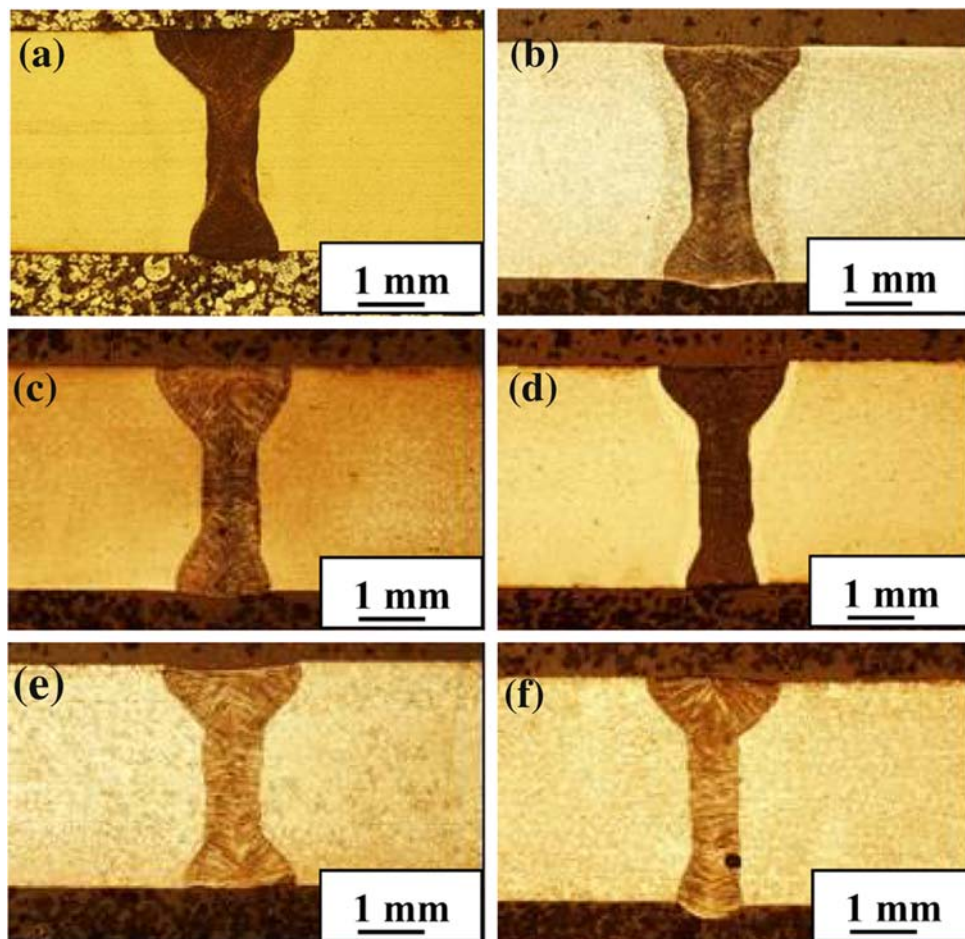
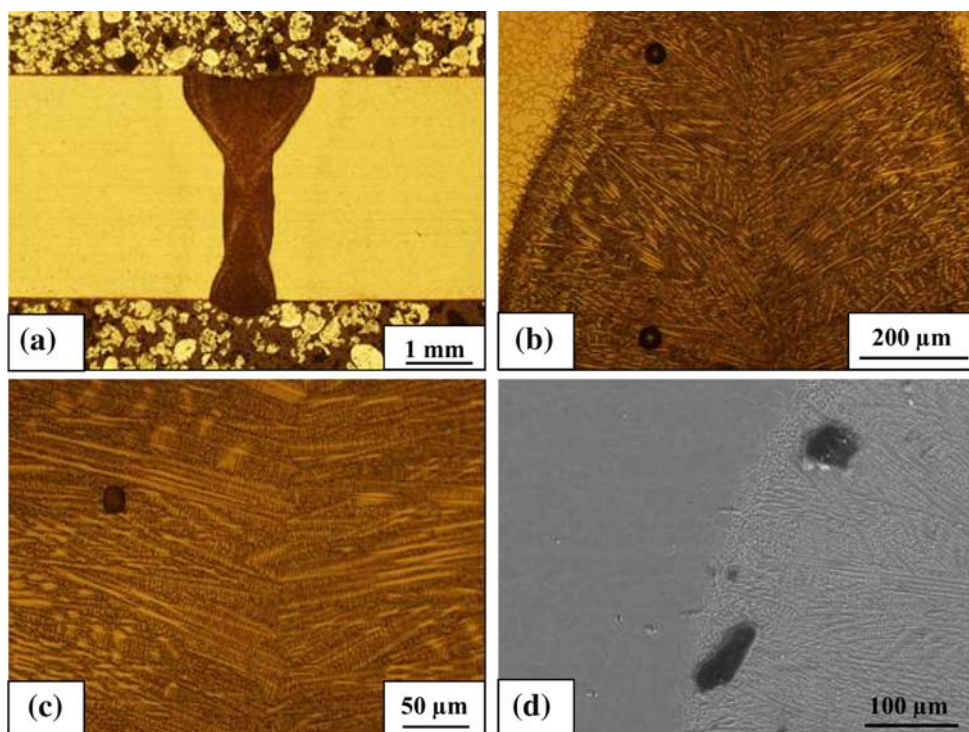
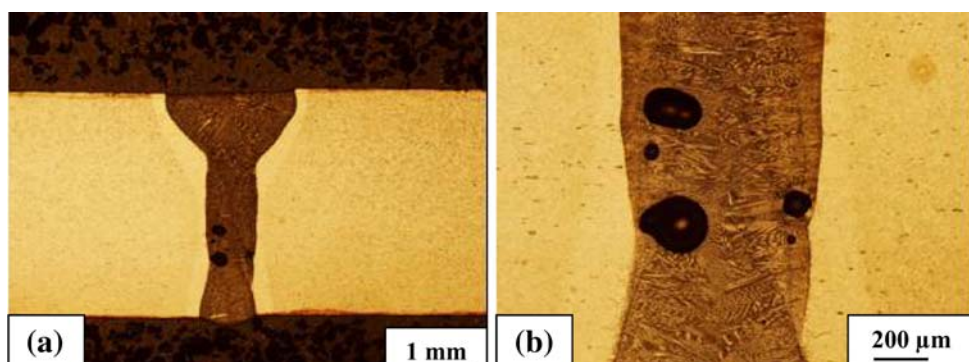


Table 3 Joint geometries and defects

	STEd prior to welding		STAed prior to welding	
	Average	STDEV	Average	STDEV
Top width (mm)	2.06	0.15	1.91	0.11
Middle width (mm)	0.78	0.05	0.79	0.07
Root width (mm)	1.29	0.25	1.20	0.41
Fusion zone area (mm^2)	3.78	0.16	3.53	0.37
Top underfill area (mm^2)	0.05	0.06	0.08	0.10
Crown height (mm)	0.01	0.04	0.02	0.02
Crown area (mm^2)	0.01	0.04	0.01	0.01
Root underfill area (mm^2)	0.00	0.01	0.01	0.03
Root height (mm)	0.14	0.09	0.11	0.07
Root area (mm^2)	0.10	0.06	0.16	0.22
Fusion zone porosity (mm^2)	0.00	0.00	0.02	0.03

STDEV STandard DEVIation

Fig. 2 **a** Overview of the weld joint obtained at STEd/As-welded condition, **b, c** Microporosity in the fusion zone obtained in **(a)** and **d** microporosity obtained in another section of the specimen**Fig. 3** **a** Overview of specimen obtained at STAed/Aged condition and **b** porosity in the fusion zone

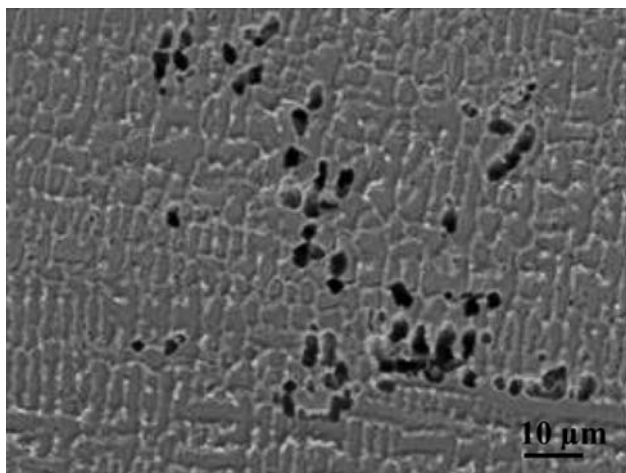


Fig. 4 Microporosity in the fusion zone obtained at STAed/As-welded condition

constituents is compared with that of the adjacent grain interior in the HAZ indicating that the grain boundary constituents have a noticeable higher Nb content. Therefore, the HAZ grain boundary cracking/separation could be associated with Nb-rich constituents in the grain boundary in agreement with the reported data relating the HAZ microfissuring to the constitutional liquation of NbC particles in HAZ grain boundaries [12]. Thompson et al. [13] also suggested that the segregation of the element S at the grain boundary is responsible for HAZ cracking in Inconel 718 alloy. It was also reported that the segregation of the element B, a melting point depressant of Ni, at grain boundaries is a major cause of liquation cracking in Inconel 718 alloy [14]. After the weld joints are solution treated and aged, much less grain boundary liquation cracking is observed (Fig. 5e, f). The mechanism remains to be mysterious. Further work is needed to clarify this in the future.

Previous investigations have shown that, the HAZ microfissuring tends to be enhanced by welding in the aged condition; coarse-grain size; presence of Laves phase; excessive amounts of NbC and delta phases at the grain boundary; higher amounts of boron in the base metal; sharp sectional variations in weld shape as in nail-head shaped welds; and other welding conditions which may promote high solidification stresses [7, 8]. As shown in Fig. 5a–d, no significant difference in the HAZ microfissuring is found in the pre-weld STed, or STAed conditions.

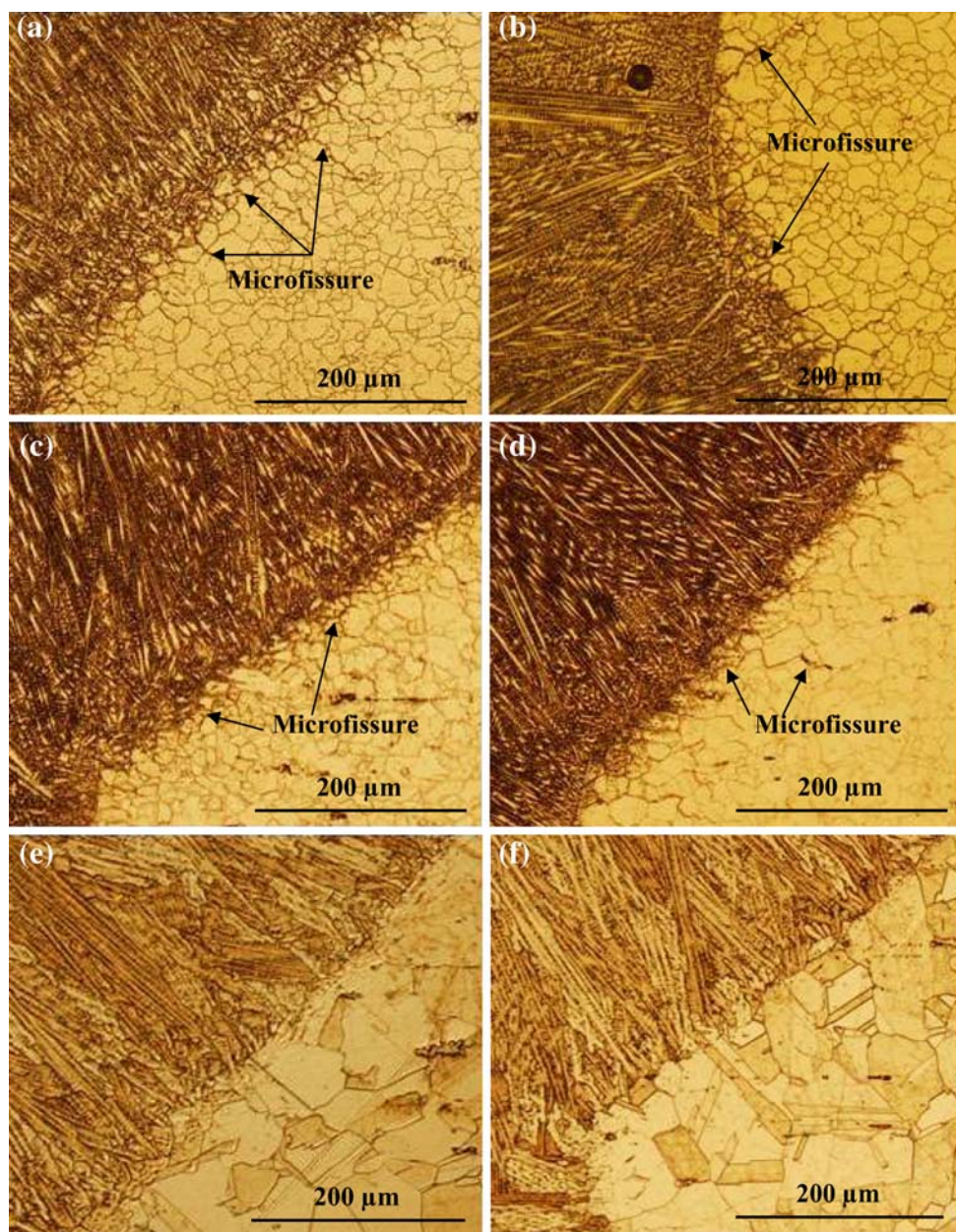
Centerline grain boundary was frequently observed as shown in Fig. 8. It is usually visible from the top surface along the entire joint thickness. Centerline grain boundary should be avoided because it may constitute a potential weldability issue [15, 16]. A centerline grain boundary represents a potentially harmful defect in a weld since it is the last region of the weld to solidify and thus is usually enriched in alloying elements and impurities. Therefore,

centerline grain boundary may contain (i) low melting point constituents, making them potentially subject to incipient melting during heat treatment or service; (ii) eutectic and brittle phases, causing lower mechanical or corrosion resistance than the base material; and (iii) low toughness compared with other grain boundaries in a weldment, making crack propagation along them easier, and potentially harmful owing to their regular nature. In some circumstances, the formation of centerline grain boundaries may be related to the occurrence of solidification cracking due to low ductility and positive transverse stress [15, 16]. Centerline grain boundary is usually formed at high welding speeds, as typically experienced in laser welding. In this case, the weld pool usually has an arrow headed trailing edge or tear-shape and/or is concave [3]. This is due to both the elongation of the temperature field and the increase of growth undercooling with welding speed. The dendrites growing from both sides meet along the centerline of the weld, forming a planar centerline grain boundary [15]. This is a weak plane associated with the high tensile stress caused by the welding and solidification process, which leads to cracking along the weld centerline [3]. In Inconel 718 alloy, the centerline grain boundaries and the interdendritic areas may contain some Nb-rich Laves phases due to the segregation of niobium, which accumulates at the front of liquid–solid interface [4, 7, 8, 17, 18]. The Laves phase morphologies have been reported to be related to dendrites morphologies [7, 8]. In addition, the Laves phase can be interconnected, which is known to be more detrimental to tensile properties than fine Laves particles. To avoid the centerline grain boundary, the weld pool should have an elliptical or rounded shape and be convex. The solidifying grains are more randomly dispersed and do not meet at the center of the weld in a straight line, thus making centerline cracking much less likely [3].

Microstructures

The as-received (solution treated) microstructure of the base material consisted of equiaxed austenitic grains (Fig. 9a). The γ grains are a face-centered-cubic (fcc) nickel base austenitic continuous phase with solid solution elements such as Co, Cr, Mo, and W. Randomly distributed Nb-rich MC type primary carbides and carbonitrides were also observed. In addition, some needle-like δ phase can also be observed, as typically shown in Fig. 9b. The grain size was measured manually using a lineal intercept method according to ASTM E112. For statistically representative results, 1,900–2,000 grains were sampled. Average grain sizes of 15.0 μm (ASTM 8.5–9.0) with standard deviation of 1.7 were obtained for the 3.18-mm base metal sheets in the solution treated condition. Pre- and post-weld aging

Fig. 5 Microfissures in the HAZ. **a** STed/As-welded, **b** STAed/As-welded, **c** STed/Aged, **d** STAed/Aged, **e** STed/STAed, and **f** STAed/STAed



treatment did not result in any perceivable change in the base metal microstructure and thus have insignificant influence on the grain size. For example, the average grain size in the STAed/as-welded condition is approximately 16.7 μm (standard deviation of 1.4), corresponding to ASTM grain size number of 9. Certainly the aging treatment can cause precipitation of the strengthening phases, but they cannot be observed using optical and SEM due to their extremely small size. However, post-weld solution treatment and aging results in considerable grain coarsening in the base metal, as shown in Fig. 9c, d. An average grain size of 44.6 μm with standard deviation of 4.7 (ASTM grain size number of 5.5–6) was obtained in the STAed/STAed condition. Clearly, significant grain

coarsening appears in the post-weld solution treatment, i.e., the base metal was solution treated for a doubled holding time (2 h) compared with the base material in the as-received (STed) condition.

The effect of pre- and post-weld heat-treatment on the fusion zone microstructure is shown in Fig. 10. Typically, elongated dendrites were obtained. Alloy 718, being a heavily alloyed material, solidifies in a dendritic mode. The dendrites extend from the fusion zone boundary to the weld center. In laser welding, rapid cooling rate leads to very fine dendritic structures in the fusion zone. As shown in optical micrographs (Fig. 10), Laves and other hard phases in interdendritic regions become dark after etching compared with the dendritic cores. However, Laves phase

Fig. 6 HAZ liquidation cracking obtained at STed/As-welded condition

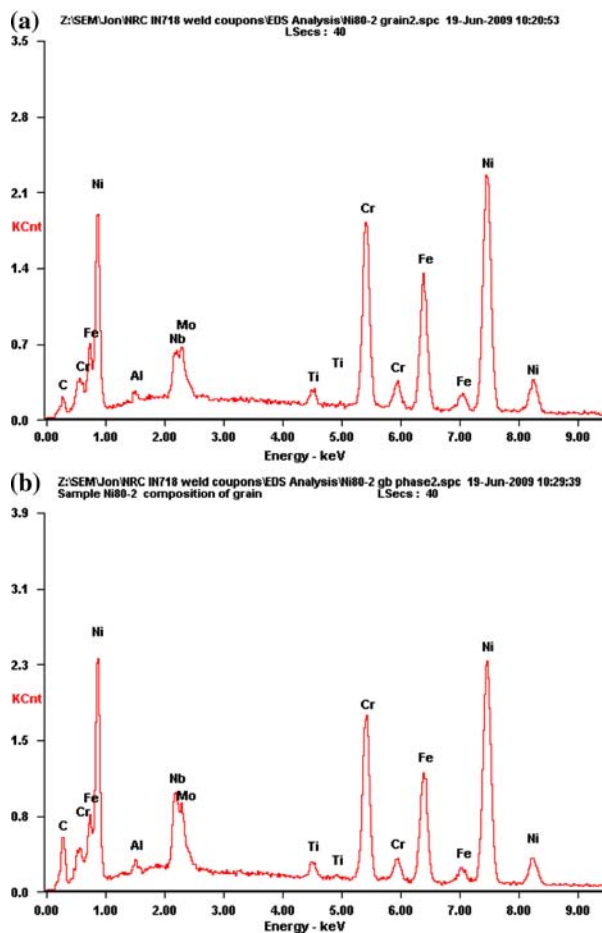
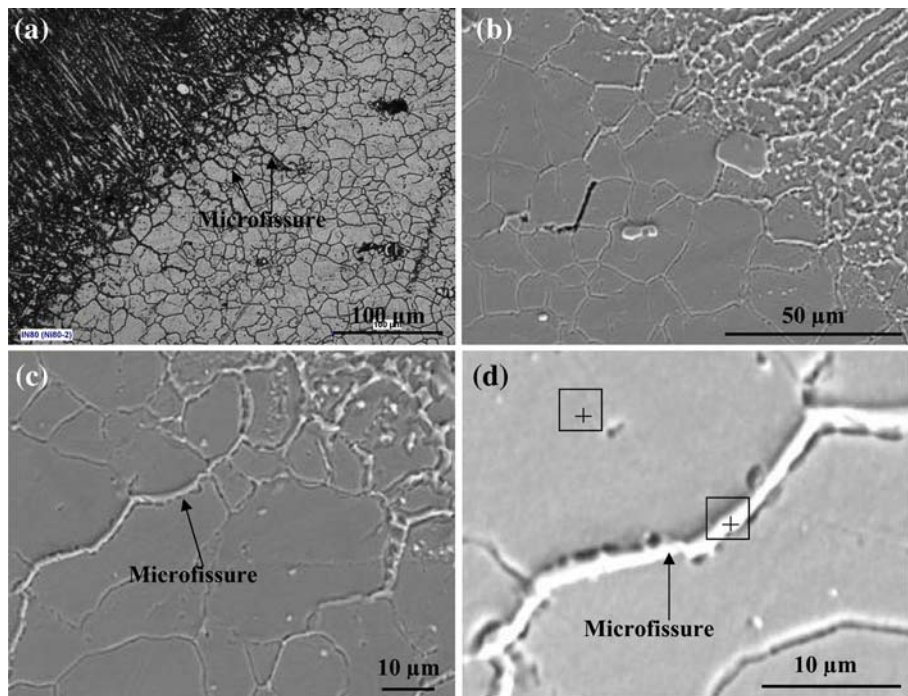


Fig. 7 SEM energy dispersive microanalysis of **a** matrix and **b** grain boundary indicated in Fig. 6d obtained at STed/As-welded condition

appeared to be white in SEM secondary images as shown in Fig. 11 because of higher emission of electrons from Laves phase [19]. In laser welding, the rapid cooling rate can also extend solute solubility which prevents marked segregation and the formation of a large eutectic. During solidification, the elements Nb, Ti, and Mo accumulate at the front of the liquid/solid interface and segregate to interdendritic areas where carbide (NbC , fcc) and Laves (Ni_3Nb , hexagonal $MgZn_2$ type) may form [10]. The gamma + NbC eutectic is suppressed during rapid cooling [10]. As shown in Fig. 11, the interdendritic Nb-rich Laves phase, whose morphologies are related to the dendrites structure, may form an interconnected network [7, 8]. Studies have shown that the formation of the Laves phase (i) depletes principal alloying elements required for hardening from the matrix, (ii) represents a weaker fusion zone microstructure between the Laves phase and the matrix interface by segregation of useful strengthening alloying elements, and (iii) act as preferential sites for easy crack initiation and propagation. The inherent brittle nature of the Laves phase leads to poor tensile ductility, fracture toughness, fatigue, and creep rupture properties in 718 alloy welds and castings [7–9, 20]. Therefore, the Laves phase is detrimental and hence should be carefully controlled. Compared with the as-welded conditions, less Laves particles are observed in the interdendritic regions after post-weld solution and aging treatment. Thus, the post-weld solution treatment at 993 °C resulted in considerable dissolution of the Laves particles. In this case, less interdendritic constituents were observed, as shown in

Fig. 8 Centerline grain boundary obtained at STed/Aged condition

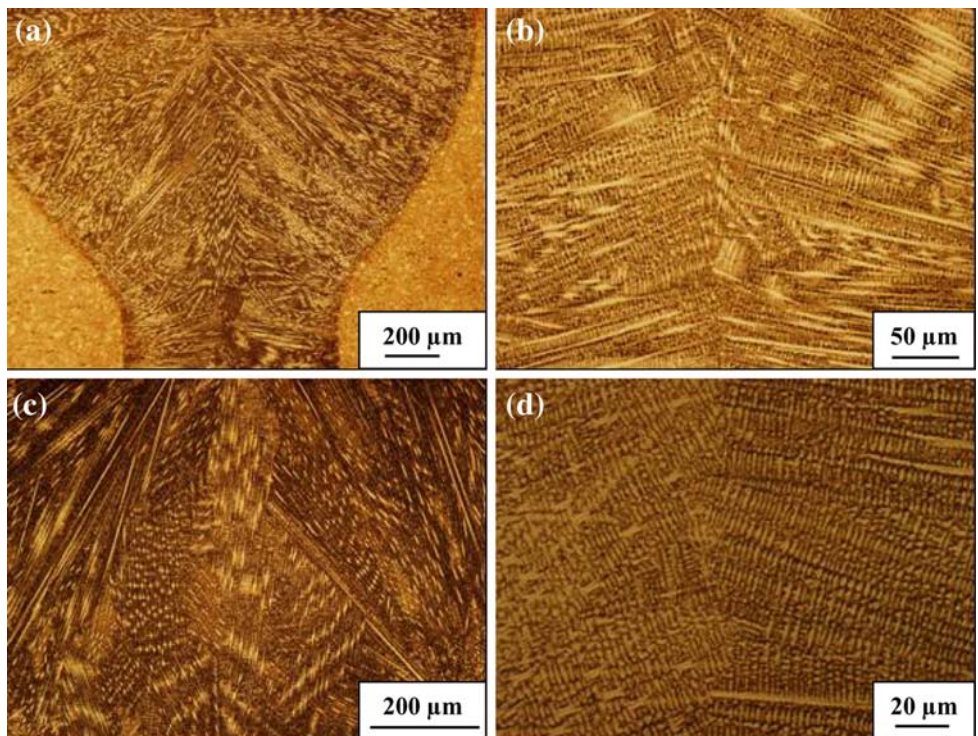


Fig. 9 Microstructures of base metal. **a** STed/As-welded, **b** STAed/As-welded, **c** STed/STAed, and **d** STAed/STAed

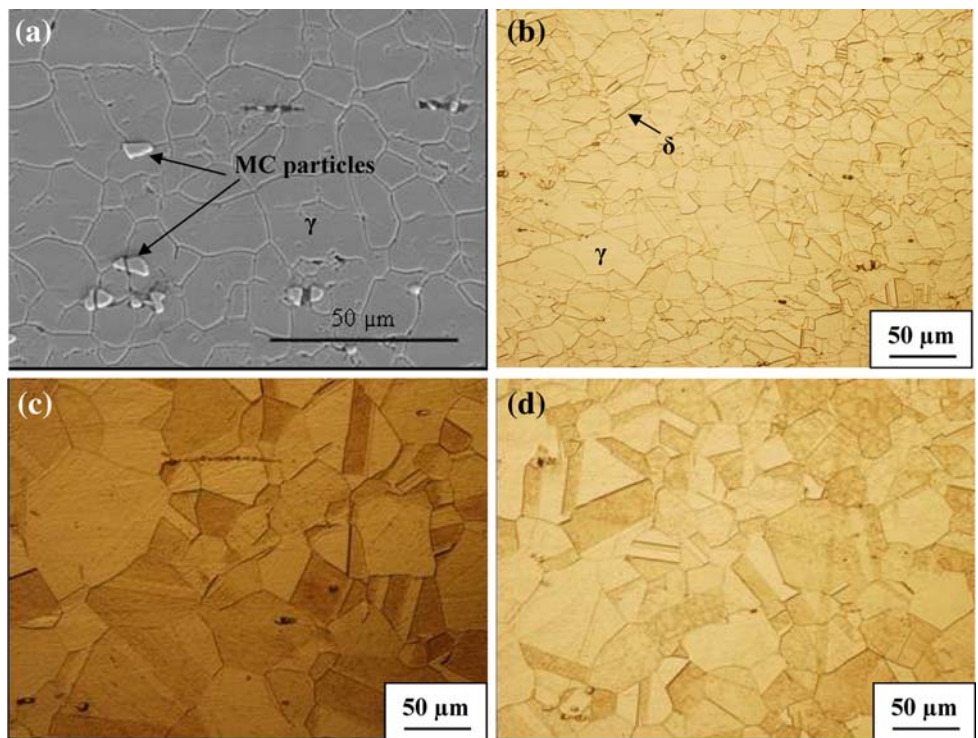
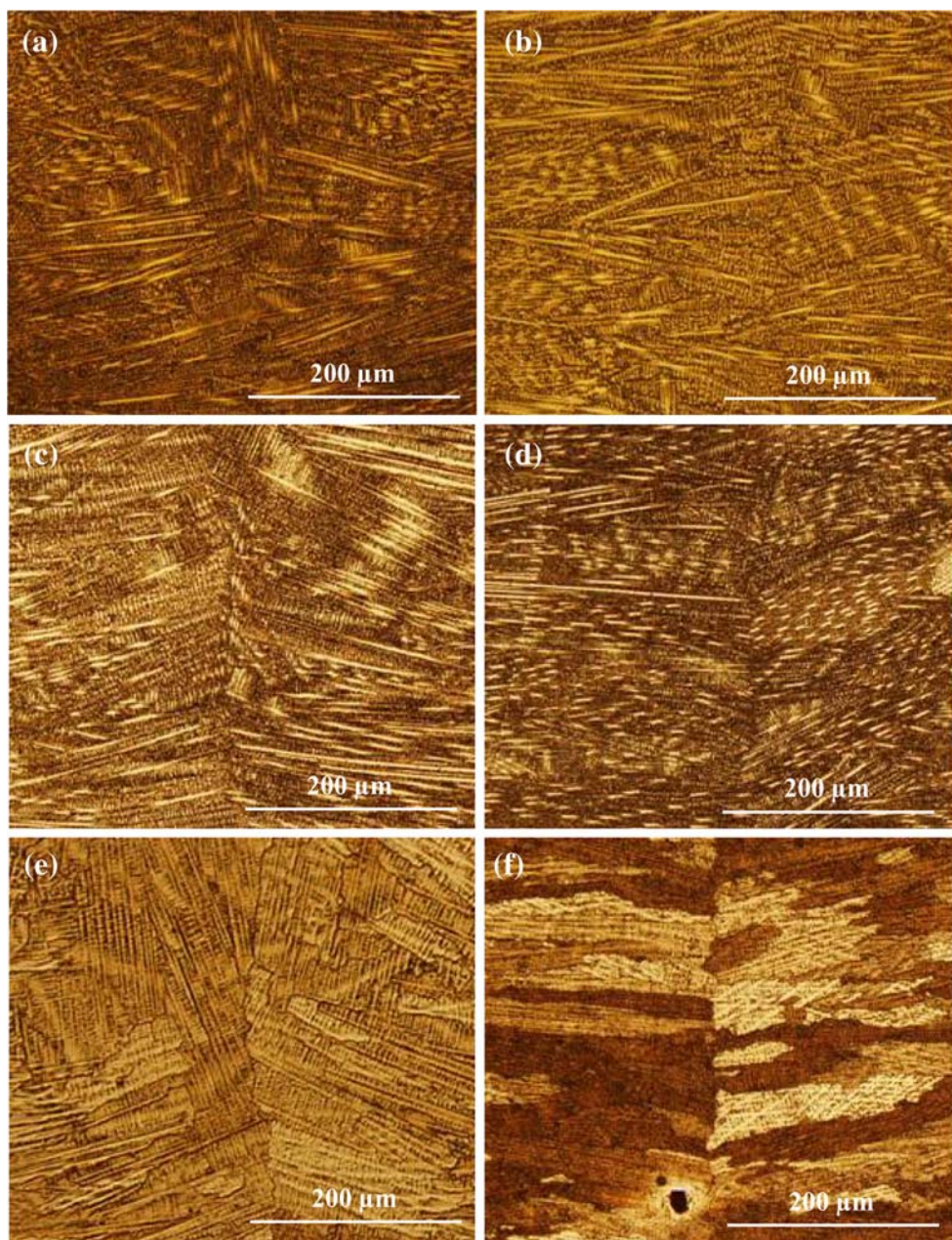


Fig. 12b. The initial solutionizing temperature of Laves phase is about 1,010 °C. Thus temperature of post-welding solution treatment should be higher than 1,000 °C to completely dissolve the Laves phase [10]. However, the improved dissolution characteristics of Laves phase in laser welds as obtained at lower temperature (993 °C) result

from its fine, relatively discrete particle morphology, and low Nb concentration [7].

Solidification in Inconel 718 alloy starts with the primary liquid → γ reaction, causing the enrichment of Nb, Mo, Ti, and C in interdendritic liquid. The subsequent liquid → (γ + NbC) eutectic reaction consumes most of

Fig. 10 Microstructures of the fusion zone. **a** STed/As-welded, **b** STAed/As-welded, **c** STed/Aged, **d** STAed/Aged, **e** STed/STAed, and **f** STAed/STAed



carbon available in the material until another eutectic type reaction $\text{liquid} \rightarrow (\gamma + \text{Laves})$ occurs, terminating the solidification process [7, 8]. The detrimental Laves phase is an unavoidable terminal solidification phase in Inconel 718 alloy. However, solidification conditions can strongly influence the extent of niobium segregation and hence the amount of Laves phase. The Laves particles are usually rich in Nb, Ti, Mo, Si, and lean in Fe, Cr, and Ni compared to the base metal [7]. Both the amount of Laves phase and Nb segregation are a function of solidification conditions. Compared with conventional arc welding processes, the extremely high cooling rate experienced in laser welding results in a much lesser extent of Nb segregation because of

the insufficient time for solute redistribution. Hence, fewer Laves particles and a lower Nb concentration in Laves are obtained [8].

Compared with the base metal microstructure with the same pre- and post-weld heat treatment, similar microstructures are also observed in the HAZ (Figs. 5, 9). The HAZ was observed to be extremely narrow with no significant grain growth.

Mechanical properties

The Vickers microindentation hardness was performed for each welding condition along the middle-thickness.

Fig. 11 SEM secondary electron images indicating the microstructures of the fusion zone. **a** STed/As-welded, **b** STAed/As-welded, **c** STed/Aged, and **d** STAed/Aged

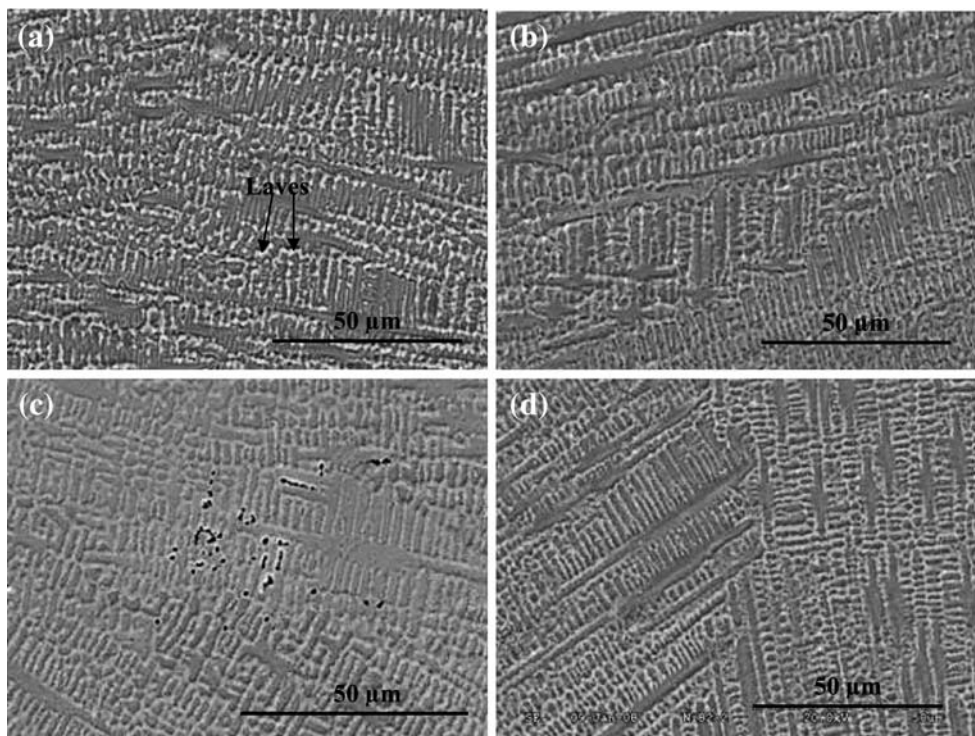
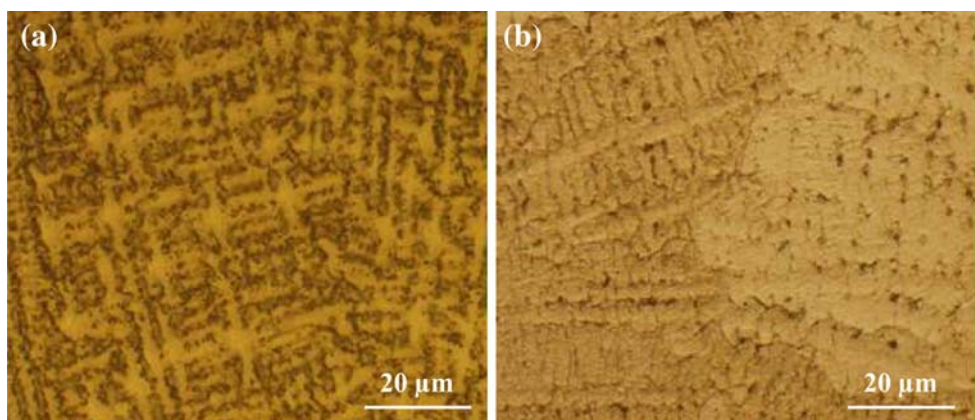


Fig. 12 Optical micrographs indicating the microstructure in the fusion zone. **a** STAed/As-welded and **b** STed/STAed



Typical hardness profiles across the welds are shown in Fig. 13 and the average values are given in Table 4. The base metal has an average value of approximately 221 HV in the solution treated condition. The aging treatment or the full heat treatment (solution treated and aged) either prior to or after welding can double the hardness values of the base metal (see Table 4).

If welded in the as-received condition (solution treated), the highest hardness is achieved in the fusion zone, which is probably due to the refined grain structure (Fig. 13a). For the material welded in the fully heat treated condition (solution treated and aged), however, the fusion zone hardness in the as-welded condition drops by half compared to that of the base material (Fig. 13b). The weld heat cycle occurring during laser welding may dissolve the

principal strengthening phase γ'' , whose dissolution temperature is around 900 °C. However, the fusion zone hardness is still higher than that in the solution treated base metal, probably due to the refined grain structure. The HAZ hardness was found to decrease significantly from the boundary between the base metal and the HAZ to the fusion line. The HAZ width is approximately 0.7 mm on each side of the fusion zone. The narrow HAZ is due to the low heat input and localized heating in laser welding. The softening of the metal in the HAZ is due to annealing [21].

As shown in Fig. 13c, d, the fusion zone has similar hardness to that of the fully heat treated base metal after post-weld aging. These increases in the fusion zone hardness are related to the re-precipitation of γ'' . The full heat treatment (solution treatment and aging) after welding can

Fig. 13 Effect of pre- and post-weld heat treatment on hardness distribution. **a** STed/As-welded, **b** STAed/As-welded, **c** STed/Aged, **d** STAed/Aged, **e** STed/STAed, and **f** STAed/STAed

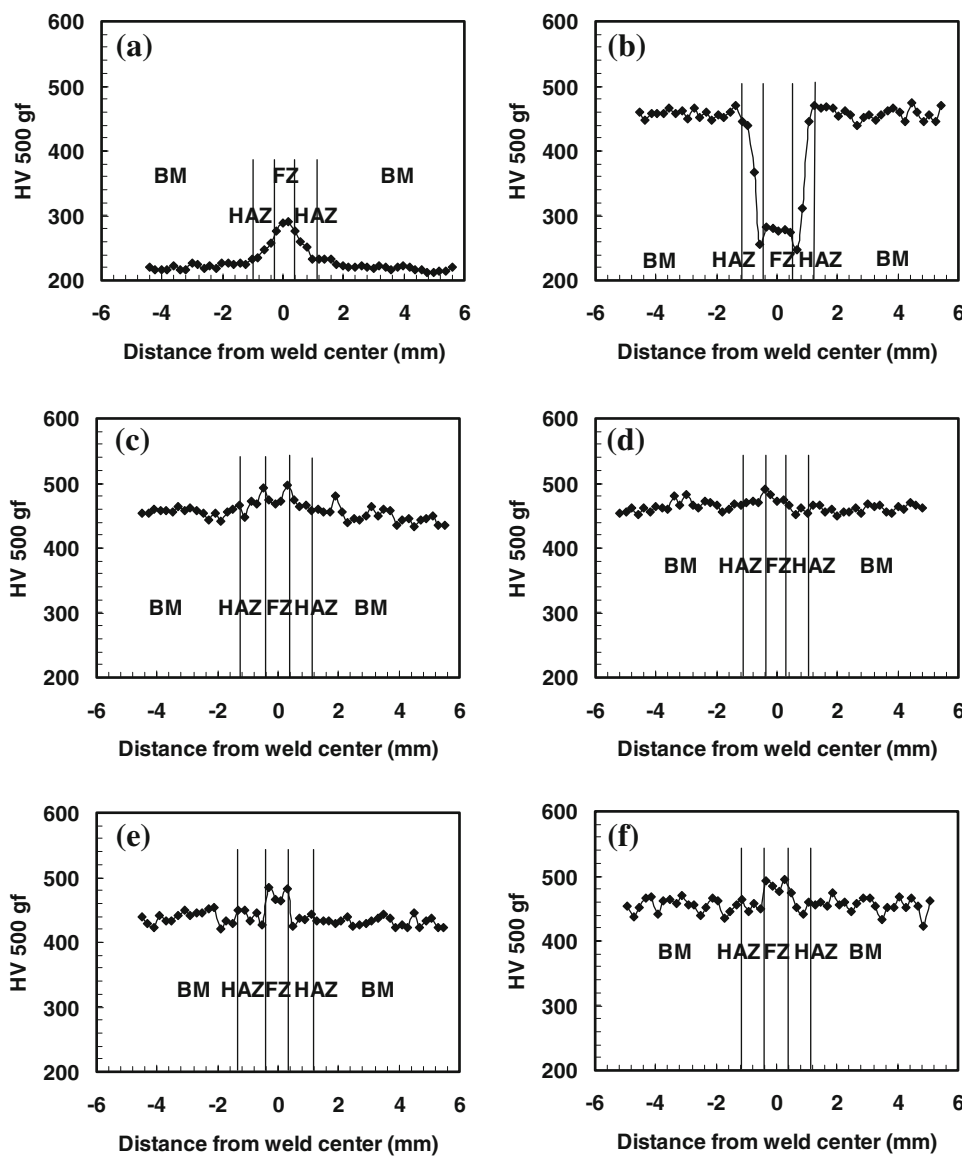


Table 4 Average hardness values

Pre-/post-weld heat treatment	FZ	HAZ	BM
STed/As-welded	287.6 ± 11.9	243.6 ± 27.5	221.1 ± 10.0
STed/Aged	483.1 ± 29.1	463.9 ± 23.8	450.7 ± 17.7
STed/STAed	489.2 ± 19.7	448.2 ± 16.8	445.3 ± 24.9
STAed/As-welded	277.5 ± 11.5	372.9 ± 186.3	459.3 ± 14.5
STAed/Aged	476.5 ± 23.4	463.2 ± 23.9	457.4 ± 15.1
STAed/STAed	489.7 ± 19.0	453.7 ± 20.1	455.3 ± 26.1

Note: Average value \pm Standard deviation

lead to slightly higher hardness in the fusion zone compared with that of the base metal. This slight improvement may be due to the greater dissolution of Laves phases in the fusion zone [7, 8]. Laves phase present in the weld microstructure consumes most of the Nb originally present in the base material, thereby making less Nb available for the precipitation of γ'' , the principal strengthening phase.

During post-weld solution treatment, the dissolution of Laves phases releases niobium. Thus, more Nb is available for γ'' precipitation and hence, niobium segregation may be reduced. This may increase the hardness in the fusion zone after the full post-weld heat-treatment compared with the post-weld aging treatment, in which the Laves phase remained as in the as-welded condition (Fig. 13c–f).

Table 5 Tensile properties

Pre-/post-weld heat treatment	YS (MPa)	TS (MPa)	EI (%)
STed/As-welded	451.9 ± 5.2	897.2 ± 5.8	39.6 ± 1.6
STed/Aged	1177.2 ± 24.5	1401.3 ± 26.6	15.8 ± 14.4
STed/STAed	1075.8 ± 9.6	1318.2 ± 15.6	16.5 ± 1.8
STAed/As-welded	727.2 ± 23.8	1031.1 ± 20.6	2.9 ± 0.2
STAed/Aged	1188.7 ± 12.0	1402.7 ± 3.1	12.9 ± 1.2
STAed/STAed	1079.18 ± 7.2	1314.2 ± 9.9	20.4 ± 2.8

Note: Average value ± 2 Standard deviation

Precipitation of these phases in weld metal cannot take place during welding due to the very rapid thermal cycle, thus necessitating post-weld aging treatment [8].

The tensile specimens used for the base metal (Table 1) and the weld joints (Table 5 and Fig. 14) are different in dimensions and thus ductility results are not compared here. The following observations are mainly concentrated on yield and tensile strengths:

- (i) If welded in the solution treated condition, the weld joints in the as-welded condition have similar yield and tensile strengths to those for the base metal, i.e., 100% joint efficiency can be obtained.
- (ii) If welded in the solution treated and aged condition, the yield and tensile strengths of the weld joints in the as-welded condition are reduced compared with those for the base metal (Approximately 74% joint efficiency is obtained).
- (iii) Higher yield and tensile strengths in the as-welded joints are obtained when welded in the solution treated and aged conditions than in the solution heat treated conditions.
- (iv) If welded in the solution treated condition, the post-weld aging treatment significantly increases the yield and tensile strengths. Approximately 160% joint efficiency was obtained. This is a usual treatment for Inconel 718 alloy, i.e., welded in the solution-annealed condition followed by conventional aging heat treatment, which combines stress relief with precipitation of the strengthening phase [21].
- (v) If welded in the solution treated and aged condition, the post-weld aging treatment can recover the yield and tensile strengths to the levels of the base metal, i.e., 100% joint efficiency can be obtained after post-weld aging treatment only.
- (vi) Compared with the as-welded condition, the post-weld aging or full heat treatment can significantly increase the yield and tensile strengths, particularly if welded in the solution treated condition.
- (vii) If welded in the solution treated condition, the post-weld solution and aging treatment can significantly increase the yield and tensile strengths. Approximately 150% joint efficiency can be obtained.
- (viii) If welded in the solution treated and aged condition, the post-weld solution and aging treatment can recover the yield and tensile strengths almost to the levels of the base metal, i.e., approximately 94% joint efficiency can be obtained.
- (ix) Compared with post-weld aging treatment, the post-weld solution and aging treatment results in slight decreases in yield and tensile strengths. The lower strength in the STAed conditions than in the aged is probably due to the presence of more δ-phase needles which acted as stress raisers in static loading [19]. Post-weld aging treatment is enough to strengthen the weld joints. This is quite different from the results reported by Ram et al. [7]. They concluded that post-weld solution and aging treatment improved all tensile properties, including yield strength, tensile strength, and elongation, compared with post-weld aging treatment in pulsed wave laser welded Inconel 718 alloy. For reasons of weldability and mechanical properties, it is usually advised that (a) these materials should be welded in the solution treated state and (b) post-weld solution and aging treatments with precipitation hardening should be carried out [6]. In the repair welding process of Inconel 718 alloy, the precipitation-hardened superalloys must also undergo PWHT, i.e., solution heat treatment followed by aging after weld repair, to restore the mechanical properties [22]. However, the present work indicates that post-weld aging can lead to better tensile strength than the post-weld full heat treatment. Therefore, the post-weld solution treatment may be eliminated. The solution treatment at high temperature cannot only consume energy but also cause distortion. The aging treatment can also relieve welding residual stress, improve stress corrosion cracking and reduce weld distortion. In addition, no significant grain growth in the HAZ appears during aging.
- (x) As shown in Fig. 14c, higher joint efficiencies can be obtained in pre-weld solution treated than fully heat treated conditions. Post-weld aging or full heat

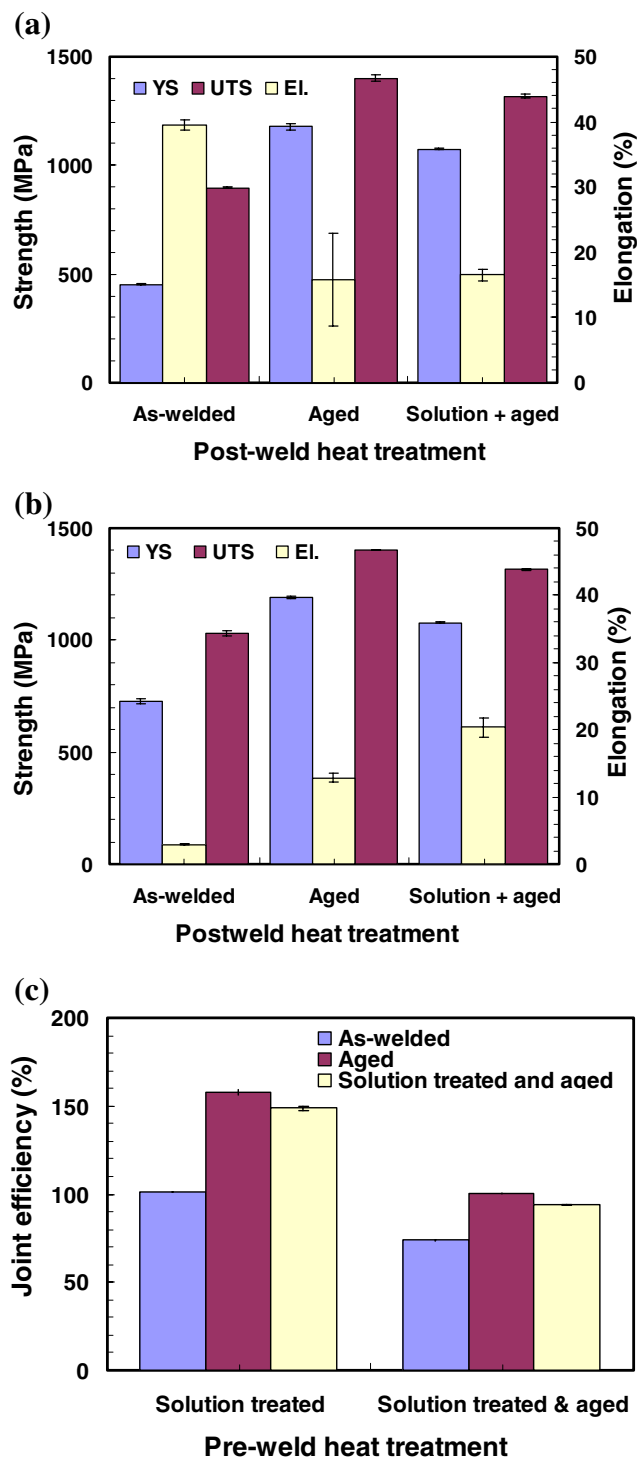


Fig. 14 Tensile properties: **a** solution heat treated prior to welding, **b** solution heat treated and aged prior to welding, and **c** joint efficiency

treatment can increase joint efficiencies. The highest joint efficiencies are obtained in post-weld aging condition.

During tensile failure tests, only one out of four tensile specimens in the solution treated/aged condition was

fractured in the base metal. All other tensile specimens were fractured in the fusion zone indicating that the weld zone is the weakest location for the tensile failure. It has been reported that the interdendritic Laves phase in the weld fusion zone serves as microvoid nucleation sites [1]. The fracture occurred by microvoid coalescence, which was initiated by interdendritic constituents. This causes the fracture in the weld fusion zone and low ductility of the weld joints.

Inconel 718 alloy is usually not recommended to be welded in pre-weld full heat treatment condition [6, 12]. It was also reported that Inconel 718 alloy can be welded in both solution treated and fully heat treated states using 1 kW pulsing wave Nd:YAG and high power CO₂ lasers [4]. The present work indicated that Inconel 718 alloy can be welded using high power Nd:YAG laser in either pre-weld solution treated or fully heat treated conditions. For both pre-weld heat treatment states, no solidification cracking was observed in spite of the presence of HAZ cracking. Even so, pre-weld solution treatment is preferred. After welding, the aging treatment can be used to strengthen the welds.

Conclusions

1. Neither macrocracks nor microcracks are observed in the fusion zone. HAZ liquation cracking, however, is frequently observed in Inconel 718 alloy joints welded using high power Nd:YAG lasers. The liquation microfissures usually appear beneath the “nail head” region of the laser welds, normal to the fusion zone boundary, and along the grain boundaries in the HAZ.
2. Significant increases in the grain sizes of the welds are observed after solution treated and aged.
3. Higher yield and tensile strengths in the as-welded joints are obtained when welded in the solution treated and aged conditions than in the solution treated conditions prior to welding.
4. Compared with the as-welded condition, the post-weld aging treatment can significantly increase the yield and tensile strengths, particularly if welded in the solution treated condition. Compared with the post-weld aging treatment, the post-weld solution treatment and aging results in slight reduction in yield and tensile strength. In other words, only post-weld aging treatment is enough to strengthen the weld joints. The solution treatment at high temperature cannot only consume energy but also cause distortion. Therefore, post-weld solution treatment is not necessary for strength recovery.

Acknowledgements This report is part of the collaborative research Project between IAR-AMTC and SAL (46M3-J017). Thanks are due to E. Poirier and M. Banu, Technical Officers, for the preparation of weld joints, technical support to welding metallurgy, and tensile testing.

References

1. Hirose A, Sakata K, Kobayashi KF (1998) Int J Mater Prod Technol 13(1–2):28
2. Ping DH, Gu YE, Cui CY, Harada H (2007) Mater Sci Eng A 456:99
3. Tillack DJ (2007) Weld J 1:28
4. Gobbi S, Zhang L, Norris J, Richter KH, Loreau JH (1996) J Mater Process Technol 56:333
5. Fontana G, Gobbi S, Rivelia C, Zhang L (1999) Weld Int 13(8):631
6. Cornu D, Gouhier D, Richard I, Bobin V, Boudot C, Gaudin JP, Andrzejewski H, Grevey D, Portrat J (1995) Weld Int 9(10):802
7. Ram GDJ, Reddy AV, Rao KP, Reddy GM, Sundar JKS (2005) J Mater Process Technol 167(1):73
8. Ram GDJ, Reddy AV, Rao KP, Reddy GM, Sundar JKS (2005) Mater Sci Technol 21(10):1132
9. Biswas S, Reddy GM, Mohandas T, Murthy CVS (2004) J Mater Sci 39:6813. doi:[10.1023/B:JMSC.0000045609.86430.19](https://doi.org/10.1023/B:JMSC.0000045609.86430.19)
10. Li Z, Gobbi SL, Fontana G, Richter HK, Norris J (1996) Metall Ital 89:5041–5047
11. Cao X, Rivaux B, Jahazi M, Cuddy J, Birur A (2008) In: Jahazi M, Elboujdaini M, Patnaik P (eds) Aerospace materials and manufacturing: emerging materials, processes, and repair techniques, COM 2008: 47th conference of metallurgists, Winnipeg, Canada, August, 2008, pp 313–323
12. Lingefelter A (1989) In: Loria EA (ed) Superalloy 718—metallurgy and applications. TMS, Warrendale, PA, pp 673–683
13. Thompson RG, Dobbs JR, Mayo DE (1986) Weld Res Suppl 11:299s
14. Chaturvedi MC (2007) Mater Sci Forum 546–549:1163
15. Hunziker O, Dye D, Reed RC (2000) Acta Mater 48:4149
16. Dye D, Hunziker O, Reed RC (2001) Acta Mater 49:683
17. Zhang L, Gobbi SL, Fontana G, Norris J, Richter HK (1997) Metall Ital 89(5):41
18. Ram GDJ, Reddy AV, Rao KP, Reddy GM (2004) Sci Technol Weld Joining 9(5):390
19. Sivaprasad K, Raman SGS (2008) Metall Mater Trans A 39A(9):2115
20. Radhakrishna CH, Rao KP (1997) J Mater Sci 32:1977. doi: [10.1023/A:1018541915113](https://doi.org/10.1023/A:1018541915113)
21. Yaman YM, Kushan MC (1998) J Mater Sci Lett 17:1231
22. Qian M, Lippold JC (2003) Mater Sci Eng A 340:225

WIRE+ARC ADDITIVE MANUFACTURING OF ALUMINIUM

Jianglong Gu^{a,b}, Baoqiang Cong^{a,c}, Jialuo Ding^a, Stewart W. Williams^a, Yuchun Zhai^b

a Welding Engineering and Laser Processing Centre, Cranfield University, MK43 0AL, UK

b School of Materials and Metallurgy, Northeastern University, 110819, China

c School of Mechanical Engineering and Automation, Beihang University, 100191, China

Abstract

Wire+Arc Additive Manufacturing is very suitable for the production of large scale aluminium parts. However implementation is currently limited by issues such as porosity and low mechanical properties. We have studied the utilization of new deposition processes such as pulsed advanced cold metal transfer which allows modification of the thermal profile resulting in refined equiaxed microstructure and elimination of porosity. Standard and new feedstock compositions are being evaluated and developed with ultimate tensile strengths of up to 260 MPa with 17% elongation being obtained in the as-deposited condition. Post build heat treatments compositional changes and high-pressure inter-pass rolling are being investigated in order to increase the strength further.

Key words: Wire+Arc Additive Manufacturing (WAAM), Cold Metal Transfer (CMT), aluminium, porosity, microstructure, mechanical property

Introduction

Wire+Arc Additive Manufacturing(WAAM) is a promising solid freeform fabrication manufacturing technology in reducing the time of products from concept to production, as well as its advantages in rapid processing times, perfect density, materials-saving, flexibility in materials and easy adaptability to automation [1]. However most current research and production in WAAM are focused on titanium and steel [2]. Aluminium alloys, especially high strength ones, have become more and more important in industries such as aerospace and transportation. Therefore research and development of WAAM technology for aluminium is urgently needed. Cranfield University has begun to apply WAAM technology to aluminium and large functional components of ribs and cones in aluminium alloy have been built. It was found that the WAAM process is very suitable for the production of large scale aluminium parts [3]. However the implementation of traditional welding process for WAAM aluminium is currently limited by solidified defects such as porosity and solidification cracks [4], which will exert negative effects on the mechanical properties to some extent. Porosity is the main problem in aluminium alloys, which are far more susceptible to this defect than all other structural metals. This is because merely trace levels of hydrogen usually exceed the threshold concentration needed to nucleate bubbles in the molten pool [5]. Low dilution cladding and welding of aluminium alloy have been

studied using the Cold Metal Transfer (CMT) process [6, 7], which is a modified Gas Metal Arc Welding (GMAW) variant based on a controlled dip transfer mode mechanism. The process delivers excellent performance with excellent welding quality, low thermal heat input (HI) and is nearly spatter-free [8]. A variant of this process is where conventional spray is mixed with the dip transfer mode and this is referred to as CMT pulsed (CMT-P). A further development is the advanced variant of both these processes (CMT-ADV and CMT-PADV). This variant allows for polarity reversal and therefore AC operation. This process has been studied for the WAAM process for aluminium in the present research. This allows modification of the thermal profile resulting in refined equiaxed microstructure and elimination of porosity. Furthermore, neither hot nor cold cracks were observed in the deposited parts.

Experimental

In the present study, aluminium walls were made from ER2319 aluminium alloy wire by the WAAM fabrication system which is shown in Fig.1. 2219-T851 aluminium plates were used as substrates. A Fronius CMT Advanced 4000 R was employed as the power source, which was connected to the ABB robot IRB2400. A home built Cranfield University rolling rig [9] was applied to the inter-pass rolling experiments. Pure argon (99.99%) was used as the shielding gas with a constant flow rate of 25 L/min. The contact tip to work distance (CTWD) was kept constant at 15 mm. Walls dimensions were 500mm long and 200mm high and were built by all four variants of the CMT process using variable wire feed speed (WFS) and deposition travel speed (TS).

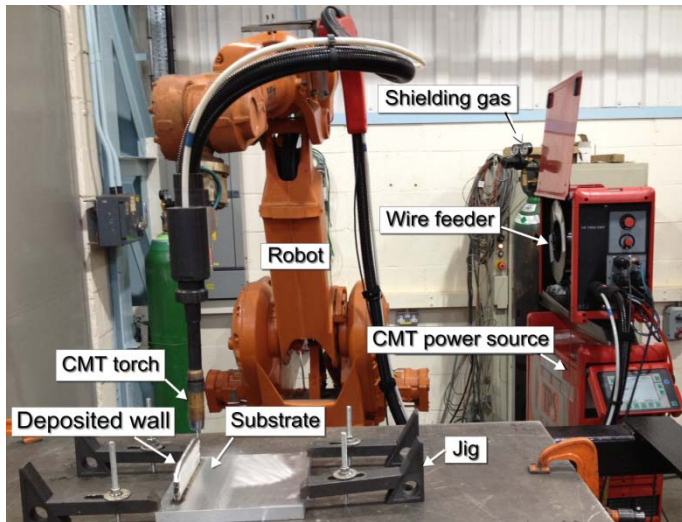


Fig.1 CMT WAAM experimental system

All specimens were naturally aged prior to tests for a minimum of 30 days after deposition. Specimens for porosity and microstructure tests were mechanically taken from the middle part of the wall, then ground and polished to a mirror finish. Specimens were etched with Kroll's reagent

solution to reveal the microstructure. A light optical microscope (OPTIPHOT, Nikon, Japan), scanning electron microscope (SEM) (XL30ESEM, PHILIPS), energy dispersive spectrometry (EDS) were employed for microstructures and porosity analysis. The Vickers micro hardness was tested by auto-C.A.M.S. of Zwick Roell using a load of 200 g for 15 s. Tensile test samples were prepared according to BS EN ISO 6892-1:2009 Standard. Tensile tests were carried out at ambient temperature by an electro-mechanically controlled universal machine at a rate of 0.1 strain min^{-1} .

Results and discussion

Porosity and microstructure

Fig 2 (a) shows that the CMT-PADV process effectively eliminated porosity compared to a wall built by pulsed CMT (CMT-P) process (Fig.2 (b)) where there are many small pores (less than 50 μm in diameter).



Fig.2 Longitudinal porosity of WAAM 2319 deposited by (a) CMT-PADV process, WFS=6m/min, TS=0.6m/min, HI=112.2J/mm, (b) CMT-P process, WFS=6m/min, TS=0.8m/min, HI=189.1J/mm

The narrow finger-shaped molten pool during the CMT-P process or other conventional arc welding processes prevents the escape of gas pores. In addition to that there is a competition correlation between dendrite growth and pore nucleation rate, so the porosity has a close

relationship with the grain size [10, 11]. Fig.3 (b) shows the growing direction of the coarse columnar grain structures of the CMT-P process during solidification, which is normal to the solid/liquid interface and is aligned to the heat-flow direction. Porosity will be increased because cellular dendrite, dendritic solidification interface and some inclusions can be used as heterogeneous nucleation particles for pores. Due to decreased pressure, during solidification small pores float up and can combine into larger ones that were observed at the top part of each deposit layer. Thus, a large number of pores were observed. Grain sizes and morphology are predominantly affected by the HI level. A lower HI can effectively refine the grain structure [12]. The CMT-PADV process was observed to have low dilution and a fine equiaxed grain structure (as shown in Fig.3 (a)). This was due to its lower HI, which is beneficial in eliminating porosity. The alternating polarity of the arc of the advanced CMT process is also beneficial in that it has a significant oxide cleaning effect of the end of the aluminium wire [13]. This reduces the hydrogen content which is contained in the oxidation layer, entering into the molten pool.

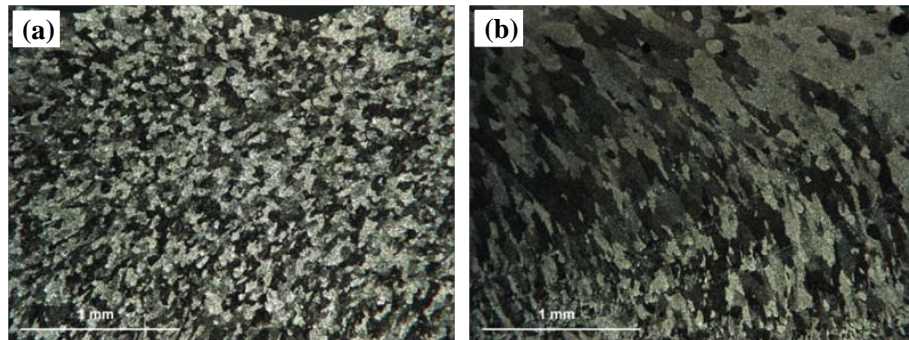


Fig.3 Microstructure of WAAM 2319 deposited by (a) CMT-PADV process, (b) CMT-P process

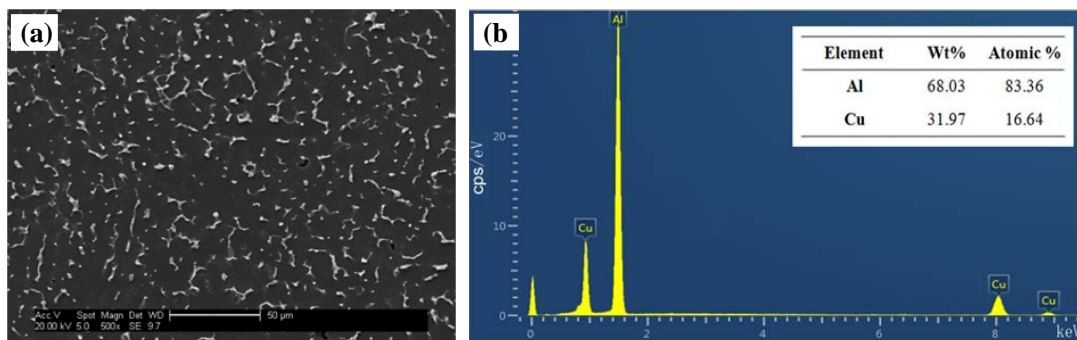


Fig.4 Micro analysis of WAAM 2319 deposited by CMT-PADV process (a) SEM morphology, (b) EDS analysis of the white phases

The precipitated microstructure of the CMT-PADV process is shown in Fig.4 (a). It is composed of a refined dendritic network, where some white phases exist between them. According to EDS analysis in Fig. 4 (b), it indicates that the white particles contain 68.03% Al–31.97% Cu (wt. %). Referring to the Al–Cu binary diagram and a previous study [14], they are identified as α -Al + θ -Al₂Cu eutectics, which were uniformly formed along grain and sub-grain

boundaries. They are caused by dendritic solidification of the non-equilibrium cooling process. During the wire production process most of the Ti, Zr elements will have existed as Al₃Ti, Al₃Zr or Al₃(Ti, Zr) phases. The exception is that some of them will have been dissolved into the aluminium wire matrix. Because of the high melting point of the particles and the low HI of the CMT-PADV process it is likely that there will be more particles retained in the solidified molten pool than other traditional arcing processes. Consequently these particles become to be near perfect heterogeneous nucleation particles due to their similar crystal structures and lattice parameters compared with aluminium matrix, therefore the grain sizes were effectively refined.

Mechanical properties

The experimentally evaluated vertical and horizontal tensile properties of WAAM deposited 2319 aluminium alloy and wrought 2219 alloy are presented in Table 1. The vertical (V) direction refers to samples taken across the build layers whilst the horizontal (H) direction refers to those taken along the layers. Yield strength (YS), ultimate tensile strength (UTS) and elongation of the WAAM alloy are evenly distributed in the whole as-deposited wall. Average YS and UTS are 110 MPa and 260 MPa respectively. Although the strength values are lower than those of the T851-tempered alloy, they are 50% higher than those of the O-tempered alloy. Meanwhile, the excellent 17% plastic elongation is higher than the T-tempered alloy, which will expand their application in the industry to some extent.

Table 1 Tensile properties of WAAM deposited 2319 alloy and wrought 2219 alloy

Property	WAAM alloy						Wrought alloy	
	V1	V2	V3	H1	H2	H3	2219-O	2219-T851
Yield strength /MPa	105	106	107	112	110	121	76	350
Ultimate tensile Strength/MPa	257	261	256	262	263	263	172	455
Elongation /%	15.4	16.8	14.4	18.3	19.0	17.8	18	10

(V-Vertical; H-Horizontal)

Further development of WAAM for aluminium

The strength of T851-tempered 2219 wrought alloy is improved by solution treatment, cold working and artificial aging of O-tempered alloy. In the future developments WAAM built aluminium components will be heat treated to enhance their strength. Although the strength property of the alloy will be definitely improved after heat treatment, the key problem is to control distortion. Therefore inter-pass cold rolling will be applied to the process too, which can significantly reduce the peak residual stress in a straight WAAM wall, thus distortion will be reduced, even eliminated [15]. Furthermore the rolling process also induces additional grain

refinement as well as increased hardness (See Fig.5), therefore mechanical properties of WAAM alloy will be further improved. In addition, compositional changes to the current standard aluminium wires or production of novel aluminium alloy wires are being investigated. For example, strength-enhancing elements such as Magnesium which will react with aluminium-copper alloy to form S phase, will be added into the smelting process of the wire production. Consequently new aluminium wires with advanced compositions will be applied to WAAM to obtain high strength eventually.

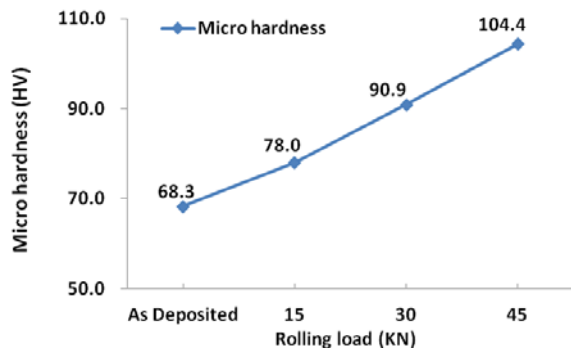


Fig.5 Average micro hardness of WAAM 2319 rolled by increasing rolling load

Conclusion

Conventional processes, which generate high levels of porosity due to their high thermal heat input level, the narrow finger-shaped molten pool and the coarse grain structure, are considered not suitable for the WAAM process for aluminium. Due to its lower heat input, CMT-PADV process is an efficient deposition process in terms of reducing and even eliminating the porosity. In addition fine equiaxed grain structures and uniformly distributed θ -Al₂Cu phases were observed in the WAAM deposits. Consequently, the application of WAAM aluminium alloy deposited by CMT-PADV process will be widened for its perfect strength and excellent plastic elongation. In the near future, new compositional wires, inter-pass rolling and post build heat treatment will be applied to WAAM aluminium alloys to improve their comprehensive properties further.

Acknowledgements

The authors would like to give their gratitude to all the technician members in Welding Engineering and Laser Processing Centre in Cranfield University. The work was supported by the WAAMat programme industry partners.

References

1. Zhang, Y., et al., *Weld deposition-based rapid prototyping: a preliminary study*. Journal of

Materials Processing Technology, 2003. **135**(2-3): p. 347-357.

2. Wang, H. and R. Kovacevic, *A novel welding-based solid freeform fabrication technology for aluminum*, 84th Annual AWS Convention, 2003: Detroit, Michigan, USA. p. 2.
3. Ding, J., et al., *Thermo-mechanical analysis of Wire and Arc Additive Layer Manufacturing process on large multi-layer parts*. Computational Materials Science, 2011. **50**(12): p. 3315-3322.
4. Ouyang, J.H., H. Wang, and R. Kovacevic, *Rapid prototyping of 5356- aluminium alloy based on variable polarity gas tungsten arc welding: process control and microstructure*. Materials and Manufacturing Processes, 2002. **17**(1): p. 103-124.
5. Devletian, J.H. and W.E. Wood, *Factors affecting porosity in aluminum welds - a review*. 1983, New York: Welding Research Council. 18.
6. Pickin, C.G., S.W. Williams, and M. Lunt, *Characterisation of the cold metal transfer (CMT) process and its application for low dilution cladding*. Journal of Materials Processing Technology, 2011. **211**(3): p. 496-502.
7. Pickin, C.G. and K. Young, *Evaluation of cold metal transfer (CMT) process for welding aluminium alloy*. Science and Technology of Welding and Joining, 2006. **11**(5): p. 583-585.
8. Sequeira Almeida, P.M. and S.W. Williams, *Innovative process model of Ti-6Al-4V additive layer manufacturing using Cold Metal Transfer (CMT)*, 21th International Solid Freeform Fabrication Symposium. 2010: Austin, Texas, USA. p. 25-36.
9. Martina, F., S.W. Williams, and P.A. Colegrove, *Improved microstructure and increased mechanical properties of additive manufacture produced Ti-6Al-4V by interpass cold rolling*, 24th International Solid Freeform Fabrication Symposium. 2013: Austin, Texas, USA. p. 490-496.
10. Li, Z., M. Zhu, and T. Dai, *Modeling of microporosity formation in an Al-7%Si alloy*. Acta Metallurgica Sinica, 2013. **49**(9): p. 1032-1040.
11. Lee, P.D. and J.D. Hunt, *Hydrogen porosity in directionally solidified aluminium-copper alloys: a mathematical model*. Acta Materialia, 2001. **49**(8): p. 1383-1398.
12. Pal, K. and S.K. Pal, *Effect of Pulse Parameters on Weld Quality in Pulsed Gas Metal Arc Welding: A Review*. Journal of Materials Engineering and Performance, 2010. **20**(6): p. 918-931.

13. Harwig, D.D., et al., *Arc behavior and melting rate in the VP-GMAW process*. Welding Research, 2006. **3**: p. 52-62.
14. Zhang, C., et al., *Strength improving mechanism of laser arc hybrid welding of wrought AA 2219 aluminium alloy using AlMg5wire*. Science and Technology of Welding and Joining, 2013. **18**(8): p. 703-710.
15. Colegrove, P.A., et al., *Microstructure and residual stress improvement in wire and arc additively manufactured parts through high-pressure rolling*. Journal of Materials Processing Technology, 2013. **213**(10): p. 1782-1791.



Rapid Prototyping Journal

The effects of moisture and temperature on the mechanical properties of additive manufacturing components: fused deposition modeling

Kim Eun-Seob Yong-Jun Shin Sung-Hoon Ahn

Article information:

To cite this document:

Kim Eun-Seob Yong-Jun Shin Sung-Hoon Ahn , (2016), "The effects of moisture and temperature on the mechanical properties of additive manufacturing components: fused deposition modeling", Rapid Prototyping Journal, Vol. 22 Iss 6 pp. - Permanent link to this document:

<http://dx.doi.org/10.1108/RPJ-08-2015-0095>

Downloaded on: 13 September 2016, At: 07:48 (PT)

References: this document contains references to 0 other documents.

To copy this document: permissions@emeraldinsight.com

The fulltext of this document has been downloaded 6 times since 2016*

Access to this document was granted through an Emerald subscription provided by emerald-srm:333301 []

For Authors

If you would like to write for this, or any other Emerald publication, then please use our Emerald for Authors service information about how to choose which publication to write for and submission guidelines are available for all. Please visit www.emeraldinsight.com/authors for more information.

About Emerald www.emeraldinsight.com

Emerald is a global publisher linking research and practice to the benefit of society. The company manages a portfolio of more than 290 journals and over 2,350 books and book series volumes, as well as providing an extensive range of online products and additional customer resources and services.

Emerald is both COUNTER 4 and TRANSFER compliant. The organization is a partner of the Committee on Publication Ethics (COPE) and also works with Portico and the LOCKSS initiative for digital archive preservation.

*Related content and download information correct at time of download.

The Effects of Moisture and Temperature on the Mechanical Properties of Additive Manufacturing Components: Fused Deposition Modeling

1. Introduction

Additive manufacturing (AM) has been widely used in the automotive, aerospace, biomedical, mechanical and jewelry industries (Gibson et al., 2010, Petrovic et al., 2011). AM can be used in the fabrication of complex three-dimensional (3-D) parts, aiding design optimization and the rapid production of customized parts (Huang et al., 2012). During the early development, AM was used only for initial prototypes and visual models owing to the low surface quality and weak strength of fabricated components. Given recent advances, AM is now also used for end-products (Wong and Hernandez, 2012). According to one study, the most common use for AM is in the fabrication of the final products of functional models (Wohlers and Caffrey, 2013). High quality AM components require high load carrying strength.

A typical AM process uses a 3-D printer (Stratasys) for fused deposition modeling (FDM) of acrylonitrile-Butadiene-styrene (ABS) plastic. Parts fabricated by FDM are formed in layers composed of fibers. A heater in the FDM head liquefies the material, which is extruded through a fine nozzle and deposited onto a platform (Upcraft and Fletcher, 2003). The FDM process is shown in **Figure 1**. FDM parts are used under various environmental conditions. For example, FDM components have been used as a mold for fabricating smart soft composites (SSCs) to cure polydimethylsiloxane (PDMS) (Kim et al., 2013, Rodrigue et al., 2014). Therefore, FDM parts are exposed to diverse environmental conditions, and there have been many studies on their mechanical properties and process conditions.

Agarwala et al. developed and implemented processing strategies to reduce internal defects in FDM-processed parts for structural ceramics and metals (Agarwala et al., 1996). Ahn et al. studied the characteristics of ABS parts fabricated by FDM 1650 (Ahn et al., 2002). Parameters such as bead width, air gap, build temperature, raster orientation, and color were investigated to identify their influence on the mechanical properties of FDM components. Air gap and raster orientation were found to be the most influential variables. Anisotropic tensile failure models of FDM parts were produced using composite classical lamination theory, and Tsai-Wu failure criterion (Ahn et al., 2003). The results showed that orientation strategy and raster angle were the most significant parameters in the fabrication of FDM components. Constitutive models of FDM parts have been investigated, demonstrating that finite element analysis can be used to predict their mechanical behavior (Bellini and Güceri, 2003, Mamadapur, 2007).

One quantitative benchmark study, of several RP processes and machines that use polymer materials (Oh and Kim, 2008), compared the mechanical properties of processes including stereolithography (SLA), laminated object manufacturing (LOM) and FDM. Several environmental conditions and build orientations were applied during the SL process, and the effects on the mechanical properties of a final product were studied (Puebla et al., 2012). The effect of moisture on the FDM of ABS material was tested by fabrication under ambient conditions, and in a desiccant chamber (Halidi and Abdullah, 2012).

However, there are insufficient studies on the effect of the environment on properties such as the water absorption, and thermal degradation of FDM parts.

In this study, FDM samples were produced in three different orientations, and the effects of moisture and temperature on their mechanical properties were tested. The results were compared with those collected from injection molded equivalents.

2. Experimental procedure

2.1. Fabrication of specimens

Reference injection molded samples were fabricated from ABS P400 material, which was also used for FDM samples. The fabrication procedure is shown in *Figure 2*. Aluminum molds for ASTM D3039 were fabricated by a three-axis CNC machine. Injection molding pellets were made by cutting 5-mm-long pieces from the FDM spool of ABS P400. A Morgan Press G-100T injection molding machine was used, and the control parameters are given in *Table 1*. Injection molded specimens are denoted by (a) in this paper. The tap for the tensile specimen was fabricated by PLA using an FDM machine (3DISON, Rokit Inc., Seoul, Korea).

A Dimension SST 768 machine (Stratasys®, Edina, MN, US) was used for the fabrication of FDM samples from ABS P400. The Catalysis software package (ver. 2.2) was used to convert 3-D CAD files as required. Catalysis uses an appropriate cross-deposition strategy, irrespective of shape and position. The cross-deposition and definition of the FDM build parameters is shown in *Figure 3*. The machine had no air gap, and cross-deposition meant that the raster angle of the upper and lower layers was at 90°.

As discussed previously, the raster angle is the most important factor in the manufacture of FDM parts (Ahn et al., 2002), but is not a controllable parameter in Catalysis (ver. 2.2). Though raster angle cannot be controlled, the orientation and deposition angle of FDM components can be selected. The plate and orientation controls are shown in *Figure 4*. The x, y and z axes are global coordinates shared between the software and the machine. Axes 1, 2, and 3 in *Figure 4* represent the principal direction of the FDM parts. The raster angle is always parallel to axis 1 or 2. The raster angle of the upper layer should be perpendicular to the lower layer when the lower layer is parallel with axis 1. Test specimens are shown in *Figure 4*. The air gap and layer thickness of the machine were 0 mm and 0.254 mm, respectively.

Three orientation configurations were considered in this experiment. FDM specimens with longitudinal axes that were parallel to the y-axis ((b) [-45°/45°]₅) were considered. As the mechanical properties of specimens whose longitudinal axes were parallel to the y-axis and x-axis were equivalent, specimens parallel to the x-axis were not considered (Mamadapur, 2007). FDM samples were fabricated in the xy plane at an angle of 45° to the machine's x-axis (parallel to the 1-axis) ((c) [0°/90°]₅). Finally, FDM specimens were fabricated with the longitudinal axis parallel to the z-axis ((d) vertical build). All specimens were fabricated based on ASTM 3039 (ASTM, 2000). The FDM sample dimensions were 127 ×

12.7× 2.54 mm.

2.2. Environmental testing

An environmental test was conducted to determine the tensile strength and Young's modulus, as a function of temperature and water absorption. ABS P400 begins to deform at 90°C, and the building temperature of the Dimensions SST 768 was 75 °C (Stratasys, 2006, Stratasys, 2011); tests were carried out at 20°C, 40°C, and 60°C.

Five samples without taps, and three samples with taps, were prepared for the water absorption and tensile tests. Water absorption tests were conducted by immersing specimens in distilled water at room temperature for increasing durations. When samples were removed from the bath, surface water was removed by a dry paper towel. Three specimens were weighed on a precision balance (AUX220, Shimadzu Co., Kyoto, Japan) with 0.001 g resolution, and their relative weight changes were measured. All samples were weighed in 2 hour intervals over 12 hours as the initial absorption rate was expected to be high. All specimens were then weighed at 12 hour intervals over a 100 hour period, followed by 24 hour intervals over 300 hours. Similarly, specimens were placed in a distilled water bath at 60°C to determine the water absorption rate at an increased temperature. For this test, the samples were placed in an environmental chamber (DWTH-155, Daihan, Gangwon-do, Korea). The measuring process and time intervals were kept the same. Tensile strength was tested after 200 hours, and compared with dry samples at room temperature, and at high temperature. A test matrix for these experiments is shown in **Table 2**.

2.3. Mechanical testing

Tensile tests were conducted for each temperature and moisture condition with an Instron 5548 testing unit (Instron®, Norwood, MA, USA). The crosshead speed was set to 2 mm min⁻¹ in accordance with ASTM D3930 (ASTM, 2000). The tensile test unit calculates the tensile strength, elongation, and Young's modulus based on the material behavior. Temperature was controlled by performing the measurements in a forced convection chamber comprising a space heater (KSH-G2-10, KACON Co., Incheon, Korea), forced convection axial flow fan (9225S2HT, Shenzhen Motor Ltd., Quandong, China), temperature controller (FC-142, Taejin Electronics Co., Daejon, Korea), and temperature sensor (NTSE10K; Thinking Electronic Co., Kaohsiung, Taiwan). The forced convection temperature chamber could regulate the temperature within ± 1°C.

3. Results and Discussion

3.1 Water absorption behavior

A composite absorption model was used to calculate the water absorption rate (Shen and Springer, 1976). As FDM is a process based on laminating materials, the final product was considered to be a composite for the analysis of water absorption behavior. Weight gain as a result of water absorption was calculated with the following equation:

$$M(t) = \frac{m_t - m_0}{m_0} \times 100, \quad (1)$$

where $M(t)$ is the moisture content of the specimen at time t as a percentage of its mass, m_0 is the initial mass of the specimen, and m_t is the mass of the specimen after t seconds. The moisture content of the specimen can be expressed by the following equation (Shen and Springer, 1976):

$$M(t) = G(M_m - M_i) - M_i, \quad (2)$$

where M_i is the initial moisture content of the sample, M_m is the maximum moisture content that can be attained under the given environmental conditions, and G is a time-dependent total moisture content parameter that can be expressed by the following equation:

$$G = 1 - \frac{8}{\pi} \sum_{j=0}^{\infty} \frac{\exp\left[-(2j+1)^2 \pi^2 \left(\frac{Dt}{h^2}\right)\right]}{(2j+1)^2}. \quad (3)$$

where j is the summation index, D is the mass diffusivity in the material, and h is the sample thickness (2 mm). The diffusion coefficient, D , is a key parameter in the one-dimensional form of Fick's law (Bullions *et al.*, 2003, Dhakal *et al.*, 2007), according to the following formula:

$$D = \pi \left(\frac{h}{4M_m} \right)^2 \left(\frac{M_2 - M_1}{\sqrt{t_2} - \sqrt{t_1}} \right)^2, \quad (4)$$

where M_1 and M_2 are the moisture content at times t_1 and t_2 respectively. M_1 and M_2 are determined before 100 hours in each condition. **Figure 5** shows the weight change profiles for all specimens. Under each temperature condition, the water absorption behavior exhibited Fickian diffusion. Higher temperatures appeared to increase the water absorption rate. Although little difference was observed between the maximum moisture absorption rates as a function of temperature, the moisture content saturated in approximately half the time at 60°C. The maximum moisture absorption rate and diffusion coefficient of each sample is shown in **Table 3**. For injection molding, cross, crisscross, and vertically built components, the maximum moisture absorption rates at room temperature were 0.339%, 5.972%, 5.131%,

and 7.879%, respectively. The difference between the water absorption rates of the injection molded and FDM components shows that FDM parts have the void (Ahn *et al.*, 2002, Wang *et al.*, 2006).

3.2 Effect of environmental conditions on mechanical properties

Tensile test results showed that the tensile strength of FDM parts had approximately 26–56% of the strength of injection molded parts under dry, room temperature conditions. Stress and strain curves for each sample are given in **Figure 6**. The stress–strain curves differ by sample. Injection molded and cross specimens showed stiff, tough properties. Crisscross specimens showed soft and tough properties while vertically built samples were brittle (**Figure 6**). The temperature-dependent tensile strength profiles of each sample under dry conditions are given in **Figure 7**. The tensile strength of all specimens decreased linearly as temperature was increased. Tensile strength under dry, room temperature conditions was 32.6, 18.0, 15.8, and 8.6 MPa, for injection molded, cross, crisscross and vertical build specimens, respectively. Tensile strength was reduced by 19.9%, 30.6%, 24.5%, and 31.2%, respectively, at high temperatures. The Young's modulus was 1,530, 1073, 995.9, and 848.4 MPa, respectively, under dry, room temperature conditions. The modulus of FDM parts was approximately 55–70% that of the injection molded components.

The decrease in tensile strength, of FDM components as a result of high temperature under dry conditions, was greater than the decrease observed for injection molded components. The failure modes are shown in **Figure 8**. The failure modes of all samples were perpendicular to the loading direction, except for the crisscross specimen. The crisscross specimen was broken at 45° to the loading direction, as failure was caused by both shearing and tension (Ahn *et al.*, 2003). The failure modes did not differ with respect to temperature or moisture. **Figure 9** shows the tensile strength, Young's modulus and strain of each specimen under wet and dry conditions as a function of temperature. The effects of water absorption and temperature on mechanical properties can be quantified by the data given in **Figure 9**. Increasing the temperature of ABS increases strain, but strength and Young's modulus decreases (McKeen, 2007). Absorbing water decreased the strain, and increased temperature increased the strain. Under wet and hot conditions, the tensile strengths of the injection molded, cross, crisscross, and vertical build specimens were 22.0, 12.3, 11.3, and 5.81 MPa, respectively. The Young's modulus of each sample under wet and hot conditions was 1,208, 1,023, 946.5, and 769.1 MPa, respectively.

4. Conclusion

The effects of temperature and water absorption on the mechanical properties of FDM parts in three different orientations was studied and compared to injection molded components. The water absorption behaviors of each sample were also studied following immersion at room and high temperature. The water absorption at all temperatures was found to follow Fickian diffusion. FDM components were found to absorb water at a greater rate than injection molded parts because FDM components have cavities. The water absorption rate was accelerated by an increase in temperature, although the maximum water

absorption volume was not changed. As temperature and water absorption rates increased, the tensile strength and Young's modulus of both the injection molded and FDM components decreased linearly. Moisture had a more significant effect on ABS components. Under wet and hot conditions, the tensile strengths of injection molded, cross, crisscross, and vertical build samples were 67.5%, 68.4%, 71.6%, and 67.6% less, respectively, than under dry, room temperature conditions.

Acknowledgments:

This work was supported by Cooperative R&D between Industry, Academy, and Research Institute funded Korea Small and Medium Business Administration in 2013 (Grants No. C0097484), the Brain Korea 21 Plus Project in 2015, Bio-Mimetic Robot Research Center funded by Defense Acquisition Program Administration, the Industrial Strategic technology development program(10049258) funded by the Ministry of Knowledge Economy(MKE, Korea), and National Research Foundation of Korea (NRF-2010-0029227).

5. Reference

- AGARWALA, M. K., JAMALABAD, V. R., LANGRANA, N. A., SAFARI, A., WHALEN, P. J. and DANFORTH, S. C. (1996). "Structural quality of parts processed by fused deposition". *Rapid Prototyping Journal*, Vol. 2 No. 4, pp. 4 - 19.
- AHN, S.-H., BAEK, C., LEE, S. and AHN, I. S. (2003). "Anisotropic Tensile Failure Model of Rapid Prototyping Parts - Fused Deposition Modeling (FDM)". *International Journal of Modern Physics B*, Vol. 17 No. 8, pp. 1510 - 1516.
- AHN, S. H., MONTERO, M., ODELL, D., ROUNDY, S. and WRIGHT, P. K. (2002). "Anisotropic material properties of fused deposition modeling ABS". *Rapid Prototyping Journal*, Vol. 8 No. 4, pp. 248-257.
- ASTM (2000). Standard Test Method for Tensile Properties of Polymer Matrix Composite Materials. *Annual Book of ASTM Standards, Vol. 15.03*. West Conshohocken, PA: American Society for Testing and Materials.
- BELLINI, A. and G ERI, S. (2003). "Mechanical characterization of parts fabricated using fused deposition modeling". *Rapid Prototyping Journal*, Vol. 9 No. 4, pp. 252-264.
- BULLIONS, T. A., LOOS, A. C. and MCGRATH, J. E. (2003). "Moisture Sorption Effects on and Properties of a Carbon Fiber-reinforced Phenylethynyl-terminated Poly(etherimide)". *Journal of Composite Materials*, Vol. 37 No. 9, pp. 791-809.
- DHAKAL, H., ZHANG, Z. and RICHARDSON, M. (2007). "Effect of water absorption on the mechanical properties of hemp fibre reinforced unsaturated polyester composites". *Composites Science and Technology*, Vol. 67 No. 7-8, pp. 1674-1683.
- GIBSON, I., ROSEN, D. W. and STUCKER, B. (2010). *Additive Manufacturing Technologies*, Springer, New York.
- HALIDI, S. N. A. M. and ABDULLAH, J. "Moisture effects on the ABS used for Fused Deposition Modeling Rapid Prototyping Machine". 2012 IEEE Symposium on Humanities, Science and Engineering Research, 2012 Kuala Lumpur. IEEE, 839 - 843.
- HUANG, S. H., LIU, P., MOKASDAR, A. and HOU, L. (2012). "Additive manufacturing and its societal impact: a literature review". *The International Journal of Advanced Manufacturing Technology*, Vol. 67 No. 5-8, pp. 1191-1203.
- KIM, H.-J., SONG, S.-H. and AHN, S.-H. (2013). "A turtle-like swimming robot using a smart soft composite (SSC) structure". *Smart Materials and Structures*, Vol. 22 No. 1, pp. 014007.
- MAMADAPUR, M. S. A. (2007). *Constitutive Modeling Of Fused Deposition Modeling Acrylonitrile Butadiene Styrene (ABS)*. Master, Texax A&M University.
- MCKEEN, L. W. (2007). *Effect of Temperature and other Factors on Plastics and Elastomers*, Elsevier, Waltham, MA.
- OH, Y. T. and KIM, G. D. (2008). "A benchmark study on rapid prototyping processes and machines: quantitative comparisons of mechanical properties, accuracy, roughness, speed, and material cost". *Proceedings of the Institution of Mechanical Engineers, Part B: Journal of Engineering Manufacture*, Vol. 222 No. 2, pp. 201-215.
- PETROVIC, V., VICENTE HARO GONZALEZ, J., JORD FERRANDO, O., DELGADO GORDILLO, J., RAM N BLASCO PUCHADES, J. and PORTOL S GRI AN, L. (2011). "Additive layered manufacturing: sectors

- of industrial application shown through case studies". *International Journal of Production Research*, Vol. 49 No. 4, pp. 1061-1079.
- PUEBLA, K., ARCAUTE, K., QUINTANA, R. and WICKER, R. B. (2012). "Effects of environmental conditions, aging, and build orientations on the mechanical properties of ASTM type I specimens manufactured via stereolithography". *Rapid Prototyping Journal*, Vol. 18 No. 5, pp. 374 - 388.
- RODRIGUE, H., WANG, W., BHANDARI, B., HAN, M.-W. and AHN, S.-H. (2014). "Cross-shaped twisting structure using SMA-based smart soft composite". *International Journal of Precision Engineering and Manufacturing-Green Technology*, Vol. 1 No. 2, pp. 153-156.
- SHEN, C.-H. and SPRINGER, G. S. (1976). "Moisture Absorption and Desorption of Composite Materials". *Journal of Composite Materials*, Vol. 10 No. 1, pp. 2 - 20.
- STRATASYS (2006). Dimension BST 768/SST 768 User Guide. Eden Prairie, MN: Staratasys®.
- STRATASYS (2011). ABS P400. Eden Prairie: Staratasys®.
- UPCRAFT, S. and FLETCHER, R. (2003). "The rapid prototyping technologies". *Assembly Automation*, Vol. 23 No. 4, pp. 318-330.
- WANG, T.-M., XI, J.-T. and JIN, Y. (2006). "A model research for prototype warp deformation in the FDM process". *The International Journal of Advanced Manufacturing Technology*, Vol. 33 No. 11-12, pp. 1087-1096.
- WOHLERS, T. and CAFFREY, T. (2013). Wohlers Report 2013. *Additive Manufacturing and 3D Printing State of the Industry*.
- WONG, K. V. and HERNANDEZ, A. (2012). "A Review of Additive Manufacturing". *ISRN Mechanical Engineering*, Vol. 2012, pp. 1-10.

Author Biographies:

Eun-Seob Kim is a graduate student at the Innovative Design and Integrated Manufacturing Lab. in Department of Mechanical and Aerospace Engineering at Seoul National University. He received his B.S. degree majoring in mechanical engineering from Gyeongsang National University in 2013. His research interests include additive manufacturing technology, micro contact mechanics and adhesion properties deposited material.

Yong-Jun Shin graduated with master degree from the Innovative Design and Integrated Manufacturing Lab. in Department of Mechanical and Aerospace Engineering at Seoul National University. He received his B.S. degree majoring in mechanical engineering from Korea Advanced Institute of Science and Technology in 2013. He currently works at Hyundai Motor Company as a researcher. His research interests include energy efficient manufacturing and design optimization for a machine tool.

Professor Sung-Hoon Ahn is a director of the Innovative Design and Integrated Manufacturing Lab. in Department of Mechanical and Aerospace Engineering at Seoul National University. He received his B.S. degree in aerospace engineering from the University of Michigan, Ann Arbor, in 1992 and his M.S. and Ph.D. degrees in aeronautics and astronautics from Stanford University in 1994 and 1997, respectively. Before joining Seoul National University, he worked as a research associate at the University of California, Berkeley (1997-2000) and an assistant professor of Department of Mechanical and Aerospace

Engineering at Gyeongsang National University (2001-2003). His research interests include additive manufacturing, smart soft composite materials, green manufacturing, Internet-based design and manufacturing, micro/nano fabrication, nanocomposites, and appropriate technology.

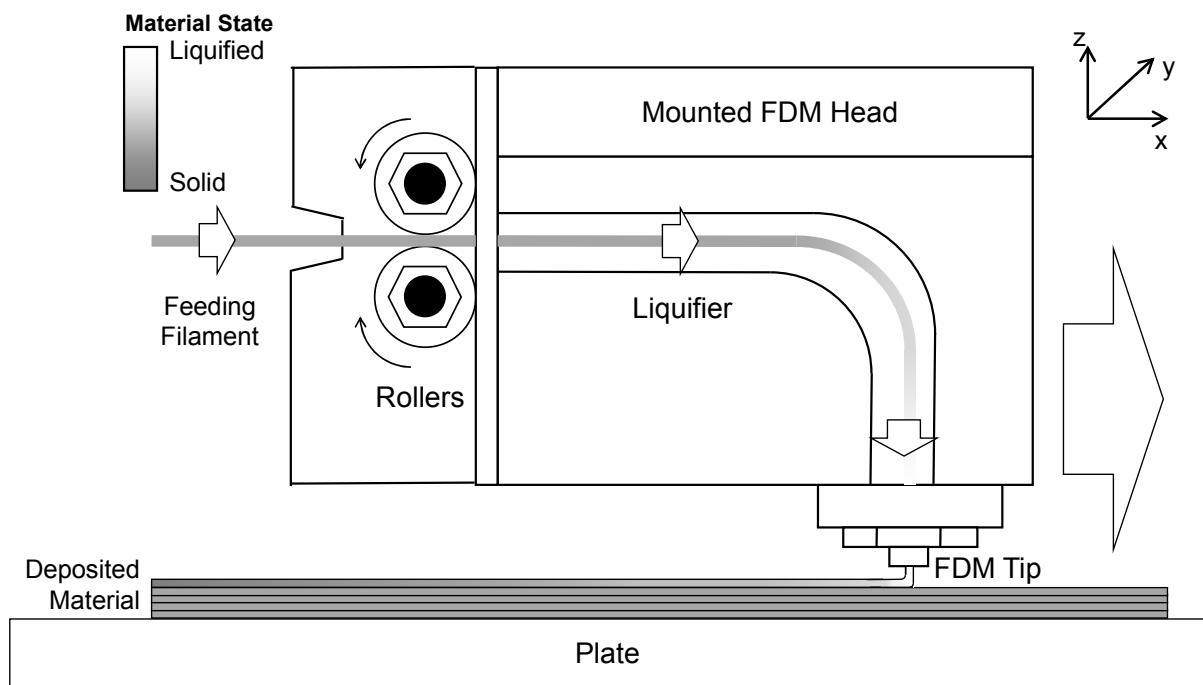


Figure 1 The fused deposition modeling (FDM) process (Ahn et al., 2002).

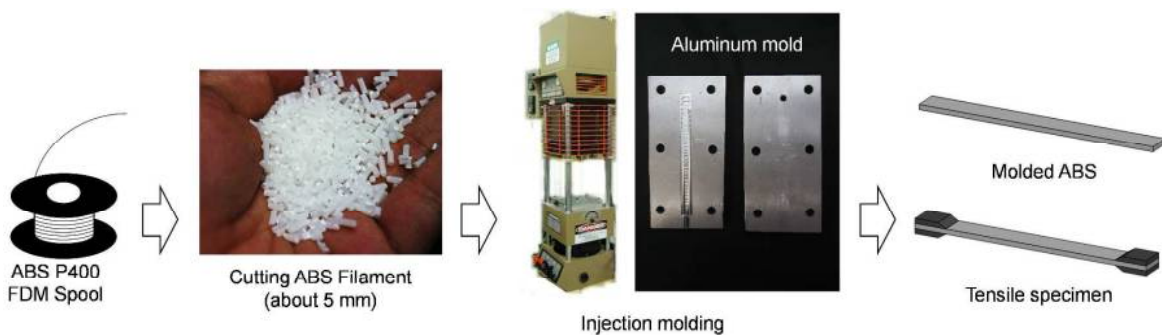


Figure 2 Fabrication procedure of injection molded specimens.

Table 1 Conditions of the injection molding process.

Description	Value
Nozzle temperature	270°C

Barrel temperature	260°C
Mold temperature	120°C
Clamping force	70 kN
Injection pressure	40 MPa

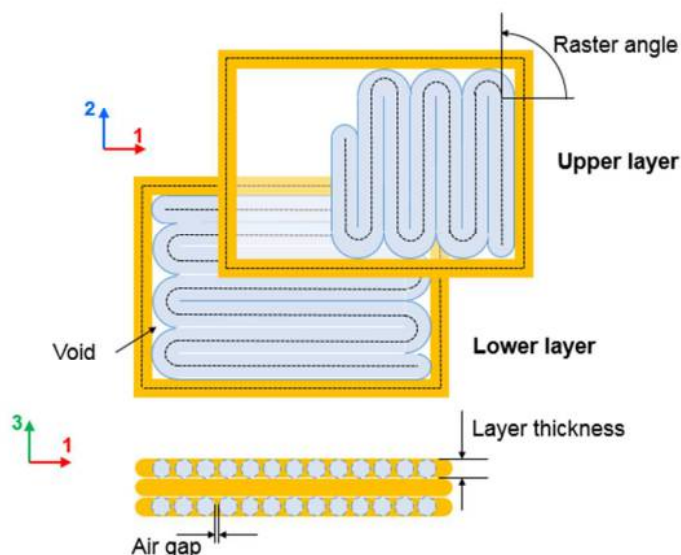


Figure 3 FDM building parameters, and cross deposition.

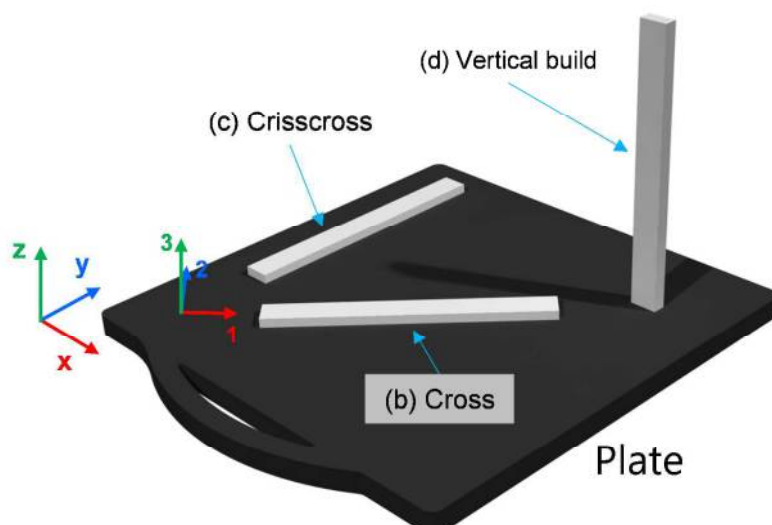


Figure 4 FDM specimens on the plate with coordinates.

Table 2 Test matrix of the environmental test.

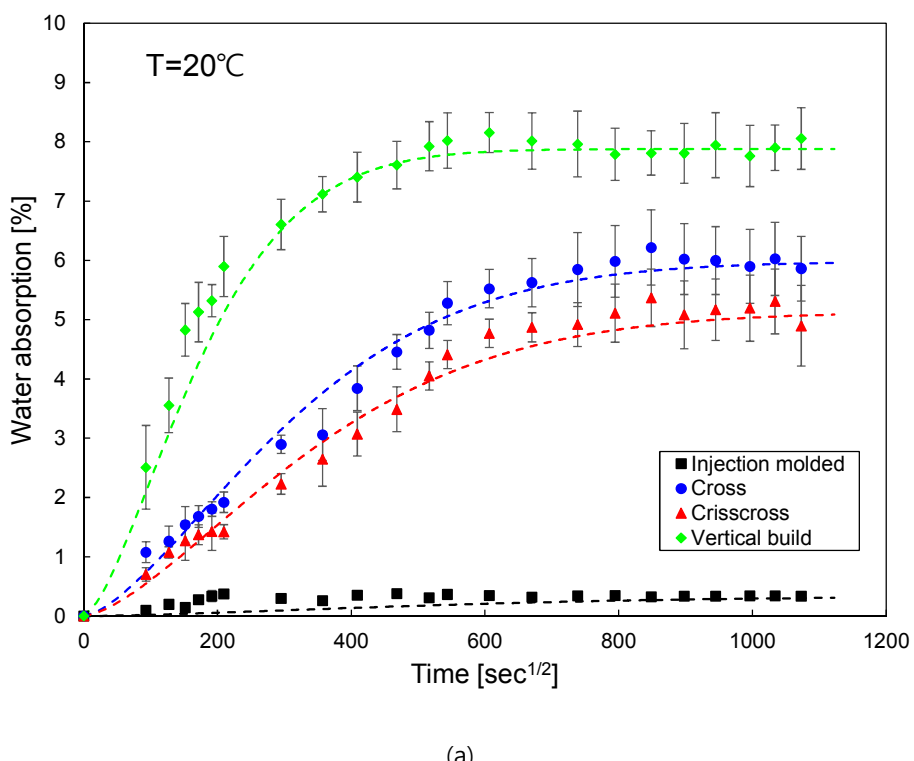
Environmental conditions	Test conditions	Type of specimens
Dry/RT, 40°C, 60°C ^a	RT, 40°C, 60°C	(a) Injection molded
Water/RT (200 hours) ^b	Dry/RT	(b) Cross (c) Crisscross
Water/60°C (200 hours) ^c	Dry/60°C	(d) Vertical build

a Temperature effect test

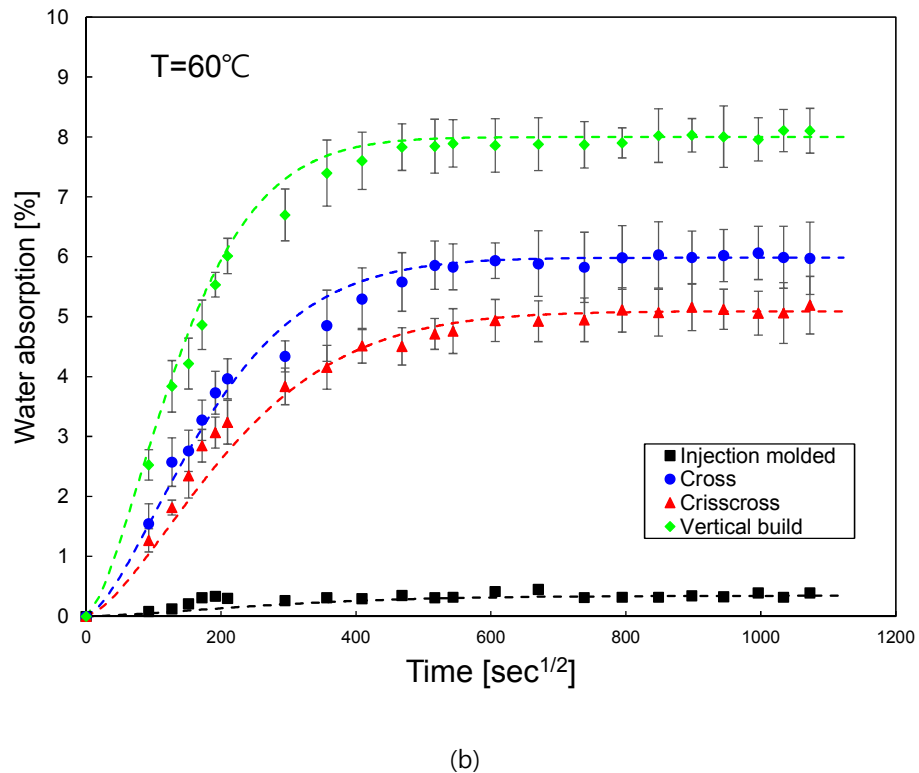
b Humidity effect test

c Temperature and humidity effect test

* Three specimens were used for each test condition.



(a)



(b)

Figure 5 Water absorption rate against square root time according to the environmental conditions: (a) room temperature (RT) and (b) high temperature (dashed lines indicate the theoretical Fickian diffusion).

Table 3 Water absorption results in water at RT and 60 °C

Type of specimen	Maximum water absorption, M_m (%)		Diffusion coefficient, D [mm^2/s] $\times 10^{-5}$	
	RT	60°C	RT	60°C
(a) Injection molded	0.339	0.341	0.176	0.182
(b) Cross	5.972	5.984	0.564	1.545
(c) Crisscross	5.131	5.090	0.428	1.099
(d) Vertical build	7.879	7.998	1.642	2.554

* Data are means of three samples for each specimen group
RT, room temperature

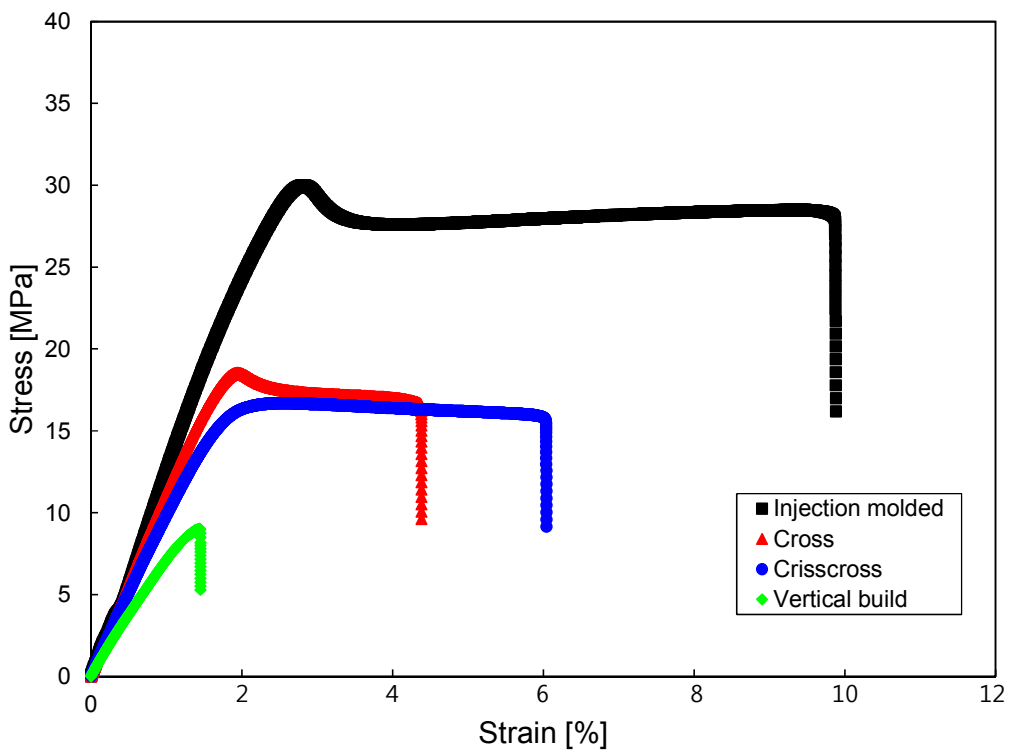


Figure 6 Representative stress-strain curves for specimens under dry, RT conditions.

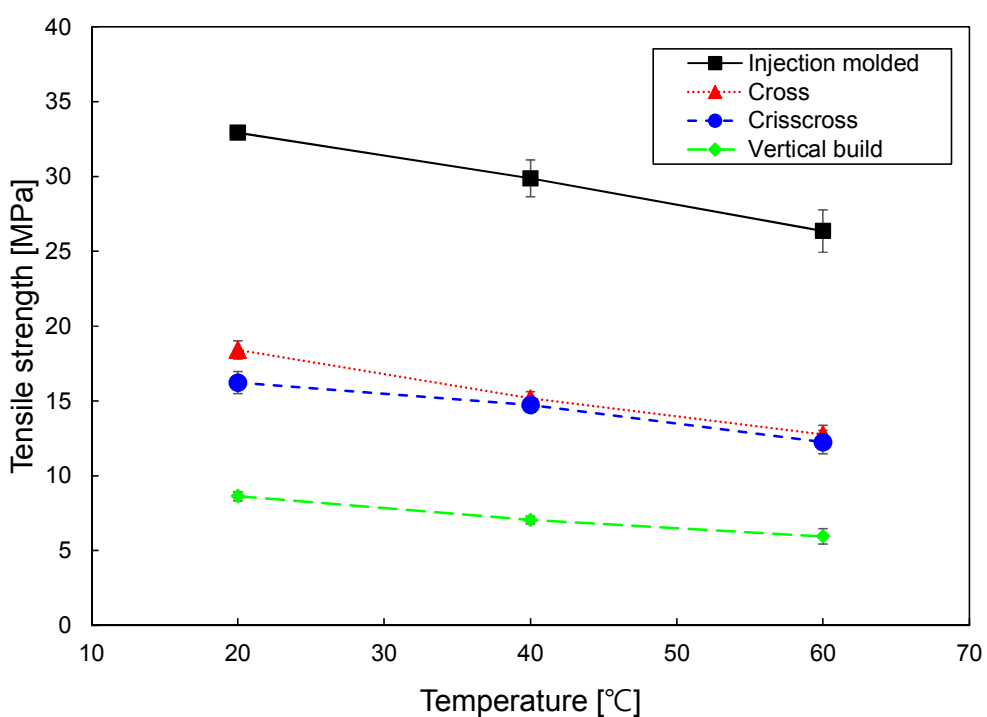


Figure 7 Tensile strength of several specimens under dry conditions at different temperatures.

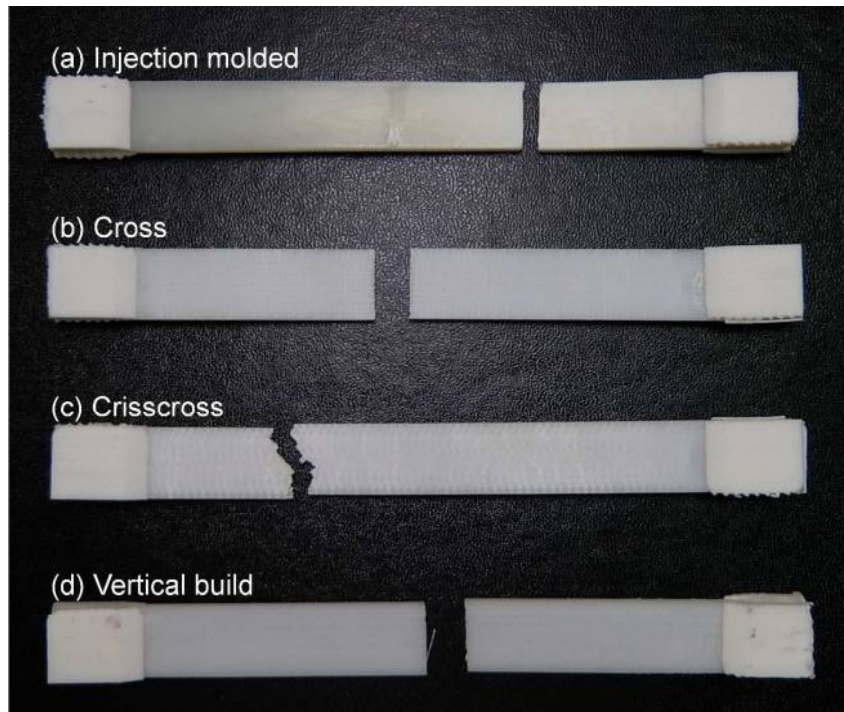
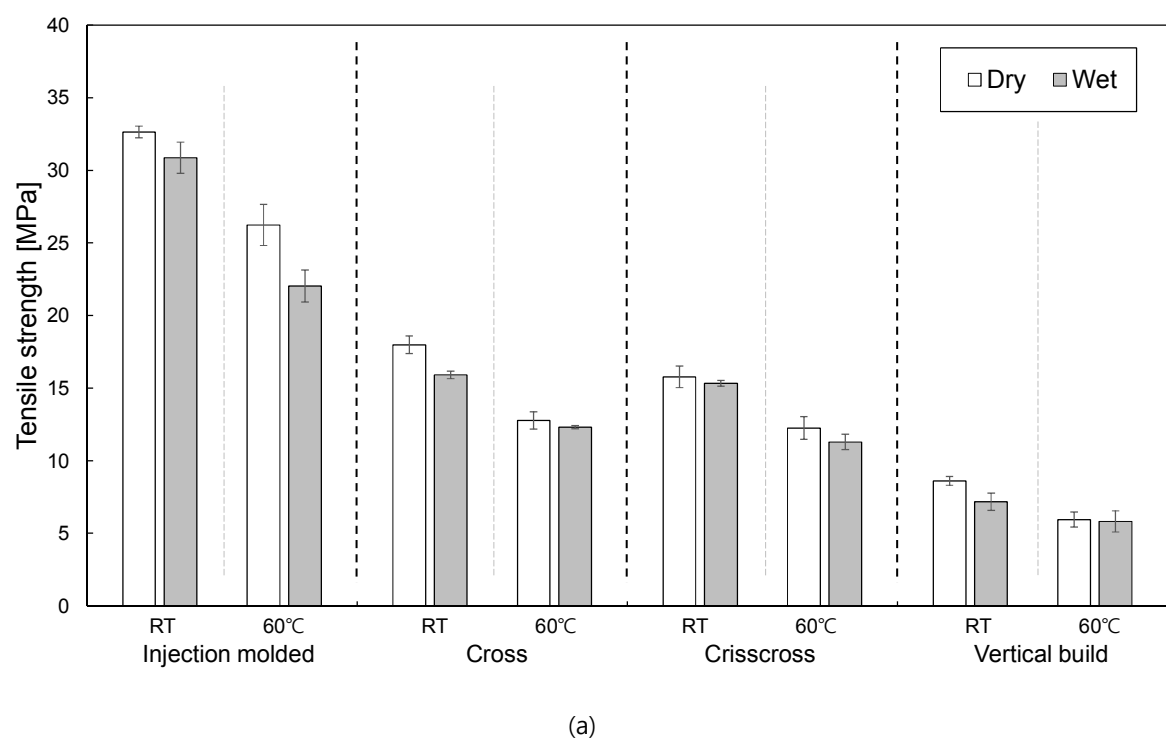


Figure 8 Failure modes of the specimens.



(a)

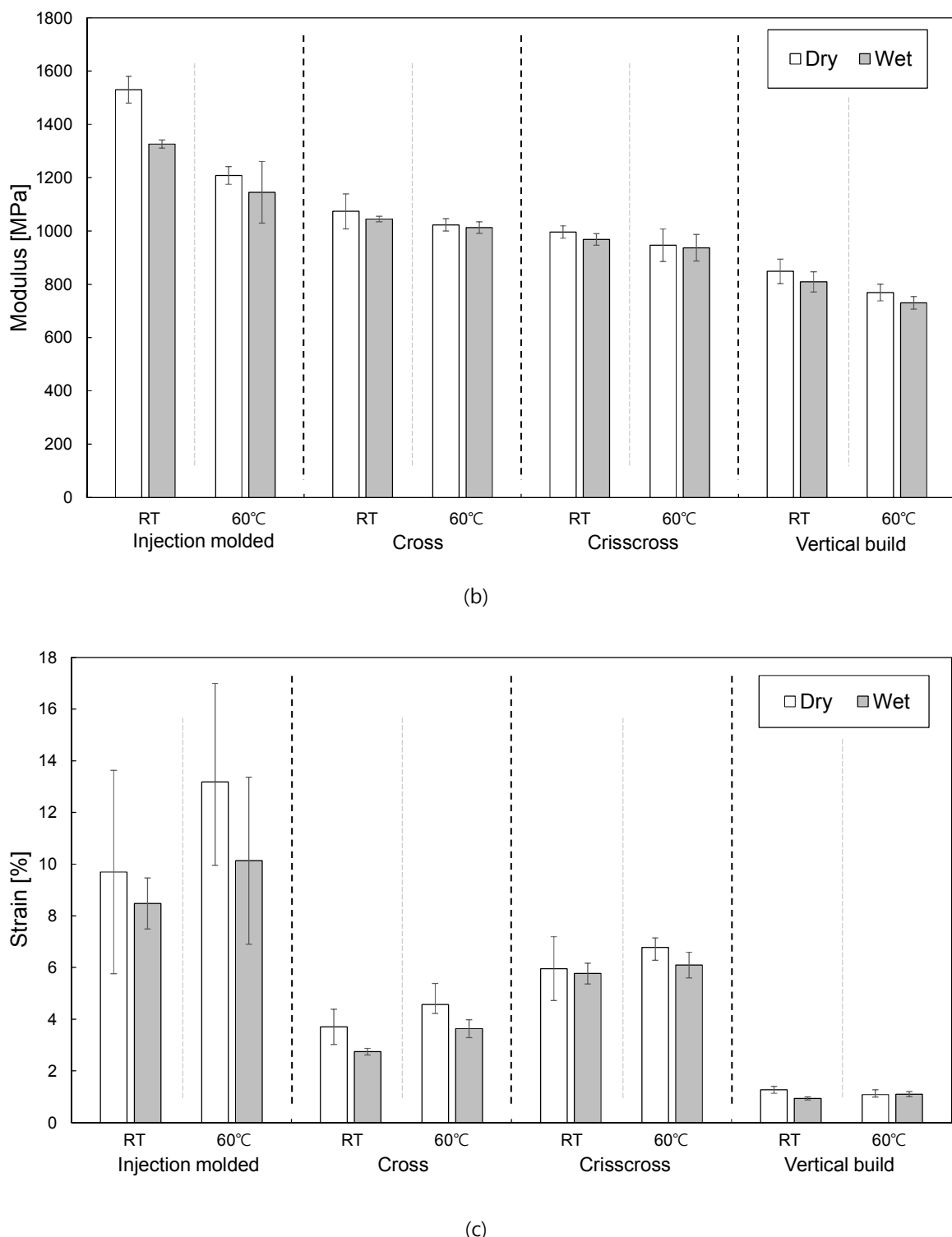


Figure 9 Tensile test results according to temperature and water absorption conditions for each specimen:
 (a) tensile strength, (b) modulus, and (c) strain.